Dissertation

submitted to the

Combined Faculties of the Natural Sciences and Mathematics
of the Ruperto-Carola University of Heidelberg, Germany

for the degree of

Doctor of Natural Sciences

Put forward by

Jan Horak

born in: Paderborn, Germany
Oral examination: 20th of April, 2023

Realtime properties of QCD

Referees: Prof. Dr. Jan M. Pawlowski
Prof. Dr. Manfred Salmhofer

Realtime properties of QCD

We present a novel technique for the calculation of fundamental realtime correlation functions in functional approaches to quantum field theory, the *spectral functional approach*, and demonstrate its potential for the calculation of observables in quantum chromodynamics (QCD). The approach builds on spectral representations for correlation functions, such as the Källén-Lehmann representation of the propagator, and facilitates dimensional regularisation as well as on-shell renormalisation. We apply the spectral functional approach to the two most prominent functional frameworks for the calculation of non-perturbative fundamental correlation functions in QCD, which are Dyson-Schwinger equations and the functional renormalisation group. Building on this conceptual development, we calculate the spectral functions of all fundamental QCD fields, i.e., quark, gluon and ghost. We complement these results with data from spectral reconstruction with Gaussian process regression, inferring gluon and ghost spectral functions from Euclidean lattice QCD data in a Bayesian, non-parametric manner. Finally, as use cases for the spectral functional approach, we present direct computations of several QCD observables, facilitated by realtime correlator data. These include the shear viscosity of the quark-gluon plasma, the non-perturbative, timelike strong coupling constant, a crucial ingredient for scattering amplitudes, and the hadronic vacuum polarisation in the complex momentum plane, the leading QCD contribution to g–2.

Realzeiteigenschaften der QCD

Wir führen eine neue Methode zur Berechnung von fundamentalen Realzeitkorrelationsfunktionen in funktionalen Zugängen zu Quantenfeldtheorie ein, den *spectral functional approach*, und demonstrieren sein Potenzial für die Berechnung von Observablen in der Quantenchromodynamik (QCD). Die Methode basiert auf Spektraldarstellungen für Korrelationsfunktionen, wie beispielsweise die Källén-Lehmann-Darstellung des Propagators, und ermöglicht dimensionale Regularisierung sowie Renormierung auf der Massenschale. Wir wenden den spectral functional approach auf die beiden am weitesten verbreiteten Techniken zur Berechnung von nicht-störungstheoretischen fundamentalen Korrelationsfunktionen in QCD an, die Dyson-Schwinger-Gleichungen und die funktionale Renormierungsgruppe. Basierend auf dieser konzeptionellen Entwicklung berechnen wir die Spektralfunktionen aller fundamentalen QCD-Felder, sprich Quark, Gluon und Geist. Wir komplementieren diese Resultate mit spektralen Rekonstruktionsergebnissen aus Gaussian process regression, indem wir auf Bayes'sche, nicht-parametrische Weise die Spektralfunktionen von Gluon und Geist aus Euklidischen Gitter-QCD-Daten ableiten. Abschließend, als Anwendungsfälle für den spectral functional approach, präsentieren wir direkte Berechnungen von verschiedenen QCD-Observablen, ermöglicht durch Realzeitkorrelatordaten. Diese beinhalten die Scherviskosität des Quark-Gluon-Plasmas, die nichtstörungstheoretische, zeitartige starke Kopplungskonstante, ein zentraler Bestandteil von Streuamplituden, sowie die hadronische Vakuumpolarisation in der komplexen Impulsebene, der führende QCD-Beitrag zu g–2.

Publications

The results presented in this thesis stem from collaborative research. At the time of completion of this dissertation, these results have largely been published, are available as preprint or in preparation for publication. Figures and text taken from these articles are not marked explicitly. Instead, we indicate this at the beginning of the respective sections. The jointly authored publications are:

[1] J. Horak, J. M. Pawlowski, N. Wink, *Spectral functions in the ϕ^4-theory from the spectral Dyson-Schwinger equation*, Phys.Rev.D **102** (2020) 125016, arXiv:2006.09778 [hep-th]

[2] J. Horak, J. M. Pawlowski, N. Wink, *Ghost spectral function from the spectral Dyson-Schwinger equation*, Phys.Rev.D **104** (2021) 074017, arXiv:2103.16175 [hep-th]

[3] J. Horak, J. M. Pawlowski, J. Rodríguez-Quintero, J. Urban, N. Wink, S. Zafeiropoulos, *Reconstructing QCD spectral functions with Gaussian processes*, Phys.Rev.D **105** (2021) 036014, arXiv:2107.13464 [hep-ph]

[4] J. Horak, F. Ihssen, J. Papavassiliou, J. M. Pawlowski, A. Weber, Axel, C. Wetterich, *Gluon condensates and effective gluon mass*, SciPost Phys. **13** (2022) 042, arXiv:2201.09747 [hep-ph]

[5] J. Horak, J. M. Pawlowski, N. Wink, *On the complex structure of Yang-Mills theory*, arXiv:2202.09333 [hep-th], submitted to SciPost Phys.

[6] J. Braun, Y. Chen, W. Fu, A. Geißel, J. Horak, C. Huang, F. Ihssen, J. M. Pawlowski, M. Reichert, F. Rennecke, Y. Tan, S. Töpfel, J. Wessely, N. Wink, *Renormalised spectral flows*, arXiv:2206.10232 [hep-th], submitted to SciPost Phys.

[7] J. Horak, J. M. Pawlowski, N. Wink, *On the quark spectral function in QCD*, arXiv:2210.07597 [hep-ph], submitted to SciPost Phys.

[8] J. Horak, J. M. Pawlowski, J. Turnwald, J. Urban, N. Wink, S. Zafeiropoulos, *Non-perturbative strong coupling at timelike momenta*, arXiv:2301.07785, submitted to Phys.Rev.D

Additionally, we present results from the following manuscripts which are currently being prepared for publication:

[9] J. Horak, F. Ihssen, J. M. Pawlowski, J. Wessely, N. Wink, *Scalar spectral functions from the spectral fRG*

[10] G. Eichmann, A. Gómez, J. Horak, J. M. Pawlowski, J. Wessely, N. Wink, *Scalar bound states from the spectral BSE*

[11] J. Dolgner, J. Horak, J. M. Pawlowski, N. Wink, *Shear viscosity and spectral function of Yang-Mills theory*

Note on the author's contributions

In [1, 2, 5, 7], I performed all practical calculations of the respective works, contributed central ideas and took the leading role in writing the manuscripts. In [8], I developed the central part of the formalism, performed the calculation of the strong coupling spectral function from its spectral representation and took the leading role in drafting the publication. To [4], I contributed a major part of the computation by extracting the gluon mass gap from the effective potential and authored significant parts of the publication.

My contribution to [3] consisted in providing data used as prior information for the spectral reconstruction as well as in preparation of parts of the manuscript. Ref. [6] represents a joint publication of the fQCD collaboration [12], of which I authored in particular the gauge theory part of section IV.

References [9–11] emerged from projects with Master students which I co-supervised during their thesis. I contributed central ideas before and during these projects, provided technical supervision for the students and was sizably involved in writing the respective manuscripts.

In the cases where the practical calculations were not or not solely performed by myself, the collaborators involved in the computation are indicated at the beginning of the sections where the respective results are presented.

Inhaltsverzeichnis

1. Introduction

Systems of strongly correlated quantum matter offer a plethora of fascinating phenomena on a vast range of energy scales. At its lower end lie ultracold atomic gases and condensed matter systems, where strong correlations arise from the Coulomb interaction. These systems also promise industrial application, e.g., for quantum computing and material science. In high energy systems such as the quark-gluon plasma or neutron stars, strong correlations mediated by the strong interaction appear. Finally, even beyond the Planck scale strong correlations can be found in the form of spacetime fluctuations, induced by gravity. The development of quantum field theory (QFT) has brought great success to modern physics in describing these strongly correlated systems. Of particular interest in this thesis will be the strongly coupled infrared regime of Quantum Chromodynamics (QCD), describing the strong interaction between the very constituents of matter, i.e., the quarks.

A very characteristic feature of QCD is that its microscopic degrees of freedom, quarks and gluons, are not directly observable in experiments. Instead, they can only be measured in the form of hadronic bound states. This is due to the phenomenon of confinement. From a theoretical perspective, the mechanism behind it is far from being fully understood. In fact, a particular manifestation of confinement poses one of the seven infamous Millennium Prize Problems [13]: Rigorously establishing a mass gap for the gluon in Yang-Mills theory, the pure gauge part of QCD, has not been achieved until today. Another defining feature of QCD can be found in the matter sector, where the mechanism of spontaneous chiral symmetry breaking generates large parts of the masses of the light quark flavors. While not being directly measurable, these quark masses account for the overwhelming part of the observed masses of protons and neutrons and therefore ultimately of the vast majority of matter around us. Inseparably linked to confinement and chiral symmetry breaking is the phenomenon of asymptotic freedom in QCD. It describes the strong coupling constant's peculiar behaviour of growing big at large, but vanishing at small distances, whose discovery yielded the Nobel Prize for Gross, Politzer and Wilczek in 2004.

A central aspect of the phenomenology of QCD is its phase structure, often summarised in dependence on temperature and net baryon density in the QCD phase diagram. Despite joint theoretical and experimental efforts, there still remain sizable unexplored regions in the phase diagram. For example, the question of the existence and location of a critical endpoint of the first order phase transition between the confined and deconfined region has triggered enormous research activity—without conclusive result so far. From the experimental side, the phase structure of QCD is explored predominantly by the collisions of heavy ions at the facilities of RHIC [14] and LHC [15] as well as, prospectively, CBM [16] and NICA [17]; see [18–22] for an overview. The experimental signatures observed there are the final products of various stages of the far-from-equilibrium evolution that the quark-gluon plasma created in heavy-ion collisions undergoes. Connecting these signatures to the theoretical predictions for the equilibrium phase diagram requires understanding of also non-equilibrium aspects of QCD.

On the theory side, two competing and quite complementary approaches for dealing

with the strongly coupled infrared regime of QCD exist. One of them are lattice simulations, based on a discretisation of a finite, four-dimensional Euclidean spacetime. Lattice QCD has brought significant advances in the description of low-lying hadronic bound states [23–27] and QCD's phase structure at vanishing and small chemical potential [28–31]; for recent reviews on lattice QCD, see [32–34]. The removal of discretisation artefacts via well-defined continuum and infinite volume limits poses a major technical obstacle in lattice simulations. Furthermore, a severe sign problem hampers simulations directly in Minkowski spacetime and at higher baryon chemical potential [35, 36]. Functional approaches to QCD, on the other hand, such as the functional renormalisation group (fRG), Dyson-Schwinger equations (DSEs) or nPI methods, are continuum formulations which do not suffer from sign problems. Accordingly, they can be applied in the entire phase diagram of QCD; see [37–39] for recent results. Within functional approaches, one is often provided with an infinite tower of coupled differential equations for the fundamental correlation functions of the theory, which needs to be truncated to perform calculations. Due to the increase of computer algebraic and numerical capabilities, functional approaches have matured in recent years and are by now quantitatively competitive to lattice simulations of QCD in Euclidean spacetime. Establishing convergence in truncations still poses a central conceptual problem, however.

Despite this rapid progress in particular in the last decade, the reliable, non-perturbative calculation of correlation functions in Minkowski spacetime is still in its infancy; for recent works in different functional approaches, see, e.g., [40–50]. While a formulation of functional equations in Minkowski spacetime (realtime) is generally possible, for most applications Euclidean spacetime (imaginary time) is chosen due to significantly reduced computational costs. Thereby, the extraction of timelike properties of QCD, such as the emergence of the hadronic bound spectrum as well as transport properties of the quark-gluon plasma, remains a notoriously hard task. Besides their strong relevance for connecting experimental observations to the phase diagram, the theoretical description of these inherent non-equilibrium phenomena constitutes a key challenge of our fundamental understanding of QCD.

In this thesis, we tackle the task of describing QCD in the timelike domain by the *spectral functional approach* [1], a particular formulation of functional approaches allowing for efficient calculation directly in Minkowski spacetime. In essence, the spectral functional approach reduces the realtime-induced numerical complexity of functional equations by analytic simplifications, facilitated by using integral representations for correlation functions, so-called *spectral representations*. The most prominent example of such a spectral representation is the Källén-Lehmann representation [51, 52] of the two-point function. In a scalar QFT, the mere existence of a Hilbert space with a positive norm already entails the existence of a Källén-Lehmann representation. The spectral formulation therefore not only facilitates access to observables, but also offers insights into fundamental properties of the underlying quantum field theory. It is this particular combination of simultaneously accessing phenomenological and fundamental aspects of a theory, which constitutes the major appeal of the spectral functional approach. Accordingly, the projects considered in this thesis attempt to contribute to our understanding of QCD in both ways, and their particular relevance will be put into context at the beginning of the respective chapters.

This thesis is structured as follows. The technical tools used in all investigations presented throughout this thesis, i.e., the basic concepts of functional approaches to QFT, are introduced in Chapter 2. In Chapter 3, after briefly reviewing the essentials of non-Abelian

gauge theories and QCD, we discuss mechanisms for the mass generation of the gluon. In Chapter 4, the spectral functional approach is introduced. The conceptual development of this section, and in particular its application to DSEs, is a central element of this thesis, which nearly all results presented in the further course are based on. We present the first of these results already in Chapter 4, consisting in spectral functions of a scalar field theory from both, the spectral DSE and fRG. The motivation for this is twofold: On the one hand, the computations serve as a proof of concept for the spectral functional approach, which we eventually want to use for computing realtime correlation functions in QCD. On the other hand, by comparing the results from these two different functional approaches, we obtain a strong benchmark test for our technique. In Chapter 5, we present results for various realtime correlation functions in Yang-Mills theory and QCD, obtained not just via the spectral functional approach, but also via spectral reconstruction of Euclidean lattice QCD data. After a general discussion of the complex structure of Yang-Mills theory, we present results for the ghost spectral function. The latter serves as an input for the reconstruction of ghost and gluon spectral functions from 2+1 flavor lattice QCD data using Gaussian process regression (GPR), also presented in Chapter 5. With these reconstruction results as an input, we directly compute the quark spectral function in QCD. In Chapter 6, we turn towards the calculation of selected observables, including the non-perturbative, timelike strong coupling constant, bound states, transport coefficients and the hadronic vacuum polarisation. Finally, we present general conclusions, a summary as well as a brief outlook on future prospects in Chapter 7.

2. Functional methods

In this section, we introduce the basic concepts of functional methods. In particular, we give a brief account of the frameworks of Dyson-Schwinger equations (DSE) and the functional renormalisation group (fRG), as these will be used in the further course of this thesis. For exhaustive discussions of these methods, see the reviews [37, 53–56] for DSE and [57–64] for the fRG.

2.1. Generating functionals

Functional methods base on the path integral formulation of QFT; for an introduction into the underlying topics, we refer to the literature [65–69]. In the path integral approach, correlation functions arise as moments of generating functionals. For illustrative purposes, we restrict ourselves to the case of a real scalar field $\varphi(x)$ in this introduction, obeying the classical action

$$S[\varphi] = \int \mathrm{d}^d x \left\{ \frac{1}{2}\varphi(-\partial^2 + m^2)\varphi + \frac{\lambda_\phi}{4!}\varphi^4 \right\}. \tag{2.1}$$

We work in Euclidean spacetime in this section.

Partition function

The correlation functions of the theory can be defined by

$$\langle \varphi(x_1) \dots \varphi(x_n) \rangle_J = \frac{1}{Z[J]} \frac{\delta^n Z[J]}{\delta J(x_1) \dots \delta J(x_n)}, \tag{2.2}$$

where the subscript $_J$ indicates the dependence of the correlation function on the external, spacetime dependent source $J(x)$. We will drop this subscript from now on.

The *partition function* Z introduced in (2.2) is called a generating functional, since all correlation functions can be generated from it by taking functional derivatives. Using the classical action (2.1), the partition function can be represented as

$$Z[J] = \frac{1}{\mathcal{N}} \int \mathrm{d}\varphi \, \exp\left\{ -S[\varphi] + J \cdot \varphi \right\}, \tag{2.3a}$$

and we introduce the shorthand notations

$$J \cdot \varphi = \int_x J(x)\varphi(x), \qquad \int_x = \int \mathrm{d}^d x \,. \tag{2.3b}$$

The normalization constant $\mathcal{N}$ in (2.3) is arbitrary since it drops out of correlation functions, see (2.2). Quantum field theories are fully determined by their corresponding set of correlation functions, promoting correlation functions to a central object of study. The path integral thus encodes the full information about the theory.

Schwinger functional

The correlation functions obtained with (2.2) contain redundant information. This can be seen by splitting correlation functions into connected and disconnected parts. In case of the two-point, this yields

$$\langle\varphi(x_1)\varphi(x_2)\rangle = \langle\varphi(x_1)\varphi(x_2)\rangle_c + \langle\varphi(x_1)\rangle\langle\varphi(x_2)\rangle\,, \tag{2.4}$$

with the subscript $_c$ denotes the connected part of the correlation function. The term 'connected' refers to all external points of the Feynman diagrams of the respective correlators being connected by internal lines. It can be seen that the disconnected part of two-point function is simply given by the product of the two one-point functions. This redundancy can be removed by introducing the *Schwinger functional*,

$$W[J] = \log Z[J]\,, \tag{2.5}$$

which is the generating functional for connected correlation functions,

$$\langle\varphi(x_1)\dots\varphi(x_n)\rangle_c = \frac{\delta^n W[J]}{\delta J(x_1)\dots\delta J(x_n)}\,. \tag{2.6}$$

For the special case of the one-point-function, there is no disconnected component, and we have

$$\langle\varphi(x)\rangle = \langle\varphi(x)\rangle_c = \frac{\delta W[J]}{\delta J(x)}\,. \tag{2.7}$$

Quantum effective action

We can remove further redundant information from correlation functions by noting that Feynman diagrams can be decomposed in one-particle-irreducible (1PI) and one-particle-reducible components. One-particle-irreducibility refers to Feynman diagrams that cannot be divided into two separate diagrams by cutting one internal propagator line. This becomes evident at the example of the propagator, which in functional approaches arises as the second moment of the Schwinger functional (2.5),

$$G(x_1, x_2) = \langle\varphi(x_1)\varphi(x_2)\rangle_c\,. \tag{2.8}$$

In perturbation theory, the propagator is expanded in loop diagrams. This expansion can be organised into a sum over powers of single 1PI kernel, where the different instances of that kernel are connected to each other via single internal lines. Hence, these expressions can be divided into two separate diagrams by cutting the single internal lines connecting the kernels, classifying them as one-particle-reducible diagrams. A closed expression for the propagator can be obtained via Dyson resummation of this sum over powers of 1PI kernels, in analogy of a geometric series. In consequence, the 1PI kernel itself encodes the full information about the propagator. To remove this redundancy, we define the *quantum effective action* or simply *effective action*, which is the generating functional of 1PI correlation functions. The effective action is obtained via Legendre transform of the Schwinger functional,

$$\Gamma[\phi] = \sup_J \Big\{ J\cdot\phi - W[J] \Big\} = J_{\text{sup}}\cdot\phi - W[J_{\text{sup}}]\,. \tag{2.9}$$

Note that the supremum source J_{sup} has an implicit field dependence, $J_{\text{sup}} = J_{\text{sup}}[\phi]$. In the following, we will drop the subscript $_{\text{sup}}$ and implicitly assume the supremum to be achieved in the context of the effective action.

The effective action is a functional of the mean field $\phi = \langle\varphi\rangle$ at a given external source J. This becomes very clear in the situation where the supremum source J is a maximum of Γ,

$$\frac{\delta\Gamma[\phi]}{\delta J(x)} = 0\,. \tag{2.10}$$

Taking a derivative with respect to the supremum source of (2.9) and using (2.10), we obtain

$$\phi = \frac{\delta W[J]}{\delta J(x)} = \langle\varphi(x)\rangle\,, \tag{2.11}$$

stating that the argument of the effective action is indeed the mean field.

The effective actions can be understood as the quantum analogue of the classical action. This can be seen explicitly by taking a derivative with respect to the mean field in (2.9),

$$\frac{\delta\Gamma[\phi]}{\delta\phi(x)} = J\,, \tag{2.12}$$

where we used that the terms originating in the field dependence of J cancel out since we assumed that J is a maximum of Γ, and we can make use of (2.11). The physical theory is obtained at $J = 0$, in which case (2.12) yields the quantum analogue of the classical equation of motion $\delta S/\delta\varphi = 0$.

By taking functional derivatives of (2.9) with respect to ϕ, all higher order 1-PI correlation functions are generated,

$$\Gamma^{(n)}(x_1,\ldots,x_n) = \frac{\delta^n\Gamma[\phi]}{\delta\phi(x_1)\ldots\delta\phi(x_n)}\,. \tag{2.13}$$

Since the effective action is a functional of the mean field, see (2.11), fluctuations are no longer encoded in the field variable. The fluctuations are integrated out and encoded in the operators appearing in the effective action, which can be projected onto using (2.13). In particular, the propagator can be obtained from this relation as the inverse of the 1-PI two-point function. This follows from

$$\int_y \frac{\delta^2 W[J]}{\delta J(x_1)\delta J(y)}\frac{\delta^2\Gamma[\phi]}{\delta\phi(y)\delta\phi(x_2)} = \int_y \frac{\delta\phi(y)}{\delta J(x_1)}\frac{\delta J(x_2)}{\delta\phi(y)} = \delta(x_1 - x_2)\,, \tag{2.14}$$

where in the first step we used (2.7) and (2.12). Hence,

$$G(x_1,x_2) = \left(\Gamma^{(2)}(x_1,x_2)\right)^{-1}. \tag{2.15}$$

Expectation values of composite operators

As a first application of the above general relations for generating functionals, we will derive a very useful expression for expectation values of general composite operators. To

that end, we note that we can pull out functional derivatives with respect to the source term of the partition function by addition of a mean field, i.e.,

$$\frac{1}{Z[J]}\frac{\delta^n Z[J]}{\delta J(x_1)\dots\delta J(x_n)} = \left(\frac{\delta}{\delta J(x_1)} + \phi(x_1)\right)\frac{1}{Z[J]}\frac{\delta^{n-1} Z[J]}{\delta J(x_2)\dots\delta J(x_n)}\,, \tag{2.16}$$

compensating for the fact that the derivative now also hits the normalisation $1/Z[J]$. Recursively applying (2.16), we find

$$\langle\varphi(x_1)\dots\varphi(x_n)\rangle = \prod_{i=1}^{n}\left(\frac{\delta}{\delta J(x_i)} + \phi(x_i)\right). \tag{2.17}$$

Next, we rewrite the source derivative using the propagator,

$$\frac{\delta}{\delta J(x)} = \int_y \frac{\delta\phi(y)}{\delta J(x)}\frac{\delta}{\delta\phi(y)} = \int_y G(x,y)\frac{\delta}{\delta\phi(y)}\,, \tag{2.18}$$

which, substituted in (2.17), yields

$$\langle\varphi(x_1)\dots\varphi(x_n)\rangle = \prod_{i=1}^{n}\left(\int_{y_i} G(x_i,y_i)\frac{\delta}{\delta\phi(y_i)} + \phi(x_i)\right). \tag{2.19}$$

We can straightforwardly generalise (2.19) to any operator $\mathcal{O}$ admitting a series representation in terms of products of fundamental fields. The expectation value of $\mathcal{O}$ can then be obtained as

$$\langle\mathcal{O}[\varphi]\rangle = \mathcal{O}\left[\varphi = G\cdot\frac{\delta}{\delta\phi} + \phi\right], \tag{2.20}$$

which makes apparent the pivotal role of the propagator in functional approaches. The right-hand side of (2.20) is now fully given in terms of 1PI vertices $\Gamma^{(n)}$, which surface by taking field derivatives of the propagator upon noting another useful identity,

$$\frac{\delta}{\delta\phi(x_3)}G(x_1,x_2) = -\int_{y_1,y_2} G(x_1,y_1)\Gamma^{(3)}(y_1,x_3,y_2)G(y_2,x_2)\,. \tag{2.21}$$

Fourier space

In functional approaches to QFT, calculations are usually performed in momentum space, which we will also stick to beyond this introductory chapter. In fact, already in the introduction of the functional renormalisation group in Section 2.3, we will switch to momentum space, since Fourier space allows for a very intuitive understanding of renormalisation group concepts.

The definition of the quantum effective action (2.9) makes apparent that all correlation functions explicitly depend on the background field ϕ. The full, field-dependent propagator $G[\phi]$, as a central correlation function in functional approaches, is obtained via the inverse of the 1PI two-point function (2.15). In Fourier space, this relation reads

$$G[\phi](p,q) = \frac{1}{\Gamma^{(2)}}[\phi](p,q)\,, \tag{2.22}$$

where we made the field-dependence explicit. For simplicity, in functional approaches one usually resorts to spatially homogeneous background fields,

$$\phi(x) = \phi\,, \tag{2.23}$$

with Fourier transform

$$\tilde{\phi}(p) = \phi\,(2\pi)^d \delta(p)\,. \tag{2.24}$$

In this case, propagator and two-point function become diagonal in momentum-space,

$$G[\phi](p,q) = G[\phi](p)(2\pi)^d \delta(p+q)\,, \tag{2.25a}$$

and similarly

$$\Gamma^{(2)}[\phi](p,q) = \Gamma^{(2)}[\phi](p)(2\pi)^d \delta(p+q)\,. \tag{2.25b}$$

In consequence, (2.22) reduces to

$$G[\phi](p) = \frac{1}{\Gamma^{(2)}[\phi](p)}\,. \tag{2.26}$$

If not specified otherwise, we will always work in spatially homogeneous backgrounds in this thesis, where (2.26) holds.

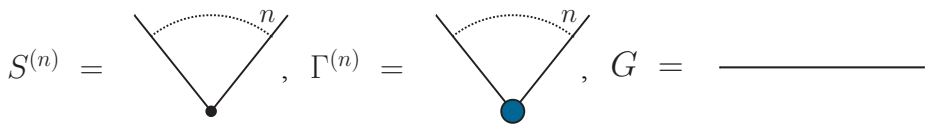

Abbildung 2.1.: Diagrammatic notation employed in this work. We use black dots/blue blobs with n legs for classical/full one-particle irreducible n-vertices $S^{(n)}/\Gamma^{(n)}$, see (2.13). Internal lines always represent full propagators, if not stated otherwise. Note that a full two-vertex corresponds to an inverse full propagator, see (2.26).

2.2. Dyson-Schwinger equations

The language of path integrals allows for an intuitive perspective on the symmetries of the theory at hand. By the assumption of vanishing boundary contributions to the path integral, field transformations whose generators can be represented as total field derivatives leave the path integral invariant. Hence, these transformations correspond to symmetries of the full quantum theory. Letting the corresponding generators explicitly act on the integrand of the path integrals gives rise to a plethora of conservations laws, all captured by a generalised *Dyson-Schwinger equation* (DSE). DSEs can be understood as the equations of motion of the Green's functions of the theory at hand, and were devised by Schwinger [70, 71] basing on earlier work by Dyson [72].

In this section, we will discuss the most prominent representative of the generalised DSE, which is commonly referred to as simply the Dyson-Schwinger equation. It encodes the invariance of the path integral under spacetime-dependent shifts of the field, i.e., $\varphi(x) \to \varphi(x)+\Lambda(x)$. The generator corresponding to this fairly general field transformation is a simple field derivative, resulting in the following simple expression for the DSE,

$$\frac{1}{Z[J]} \int \mathrm{d}\varphi \, \frac{\delta}{\delta\varphi(x)} \exp\Big\{ - S[\varphi] + J \cdot \varphi \Big\} = 0 \,. \tag{2.27}$$

The generalised DSE is achieved by insertion of an arbitrary field operator $\mathcal{O}[\varphi]$ to the right of the field derivative.

Assuming $J = J_{\mathrm{sup}}$ allows to introduce the effective action into (2.27) by the equation of motion of the supremum current (2.12). Explicitly acting with the field derivative on the exponential in (2.27) yields

$$\frac{1}{Z[J]} \int \mathrm{d}\varphi \left[- \frac{\delta S[\varphi]}{\delta\varphi(x)} + \frac{\delta\Gamma[\phi]}{\delta\phi(x)} \right] \exp\Big\{ - S[\varphi] + \frac{\delta\Gamma[\phi]}{\delta\phi} \cdot \varphi \Big\} = 0 \,. \tag{2.28}$$

The derivative of the effective action does not depend on the fluctuation field and can thus be pulled in front of the path integral, which then simply cancels with the normalisation. Remembering the definition of expectation values (2.2), we arrive at

$$\frac{\delta\Gamma[\phi]}{\delta\phi(x)} = \left\langle \frac{\delta S[\varphi]}{\delta\varphi(x)} \right\rangle . \tag{2.29}$$

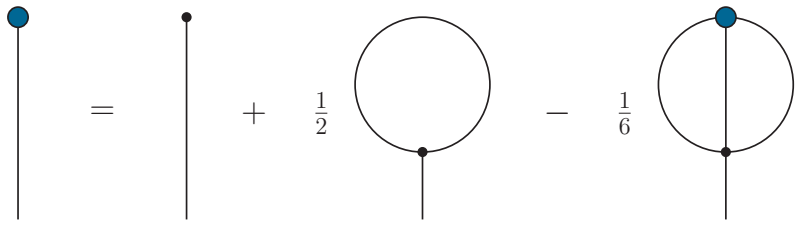

Abbildung 2.2.: Master DSE for a scalar ϕ^4-theory defined by the action (2.1). Notation as defined in Figure 2.1.

Equation (2.29) is the so-called master DSE. It states that the quantum equations of motion (2.12) can be obtained as the expectation value of the classical equations of motion.

Assuming a series representation for the classical action, we can exploit the identity (2.20) to arrive at an algebraic representation of the master DSE,

$$\frac{\delta\Gamma[\phi]}{\delta\phi(x)} = \frac{\delta S}{\delta\varphi(x)}\left[\varphi = G\cdot\frac{\delta}{\delta\phi} + \phi\right]. \tag{2.30}$$

By taking functional derivatives of (2.30), DSEs for correlation functions of all order can be generated. In Figure 2.2, we depict the master DSE for the example of a scalar ϕ^4-theory. The diagrammatic notation is defined in Figure 2.1. In general, the DSE for the correlation function $\Gamma^{(n)}$ is dependent on $\Gamma^{(n+2)}$, as can be anticipated from the master DSE in Figure 2.2. This makes apparent the need for truncation in applications.

2.3. Functional renormalisation group

This section uses parts of [6].

Another important technique in the toolbox of functional methods is the *functional renormalisation group* (fRG) approach. The underlying idea is to successively incorporate quantum fluctuations of different length scales into an effective formulation of the theory, closely resembling the concept of Kadanoff's block spinning on a lattice [73]. The generalisation of this technique to continuum formulations of QFT has been achieved by Wilson [74, 75], and goes by the name of Wilsonian renormalisation. The fRG provides an implementation of Wilsonian renormalisation on the level of generating functionals by integrating out quantum fluctuations momentum shell by momentum shell through the path integral. Here, we will focus on Wetterich's formulation of the fRG in terms of the effective action [76]. Similar formulations exist in terms of other generating functionals; the renormalisation group (RG) flow of the Wilsonian effective action, corresponding to the amputated Schwinger functional, is described by the Polchinski equation [77], for example. Its connection to the Wetterich equation is detailed, e.g., in [78–80].

In the fRG, the successive integration of fluctuations momentum shell by momentum shell is implemented by suppressing modes with momenta below some scale k, and then considering the change of the generating functional upon changing k. Starting from an Ansatz at a (usually perturbatively large) scale $k = \Lambda$, the full theory including the fluctuations of all scales is obtained upon integrating down to $k = 0$. The suppression of modes with momenta $p^2 \lesssim k^2$ can be achieved by an appropriate modification of the path integral measure,

$$\int [\mathrm{d}\varphi]_{p^2 \gtrsim k^2} = \int \mathrm{d}\varphi \, \exp\Big\{ - \Delta S_k[\varphi] \Big\} , \tag{2.31}$$

effectively adding a scale- and momentum-dependent mass term to the classical action,

$$\Delta S_k[\varphi] = \frac{1}{2} \int_p \varphi(p) R_k(p) \varphi(-p) , \qquad \text{with} \qquad \int_p = \int \frac{\mathrm{d}^d p}{(2\pi)^d} . \tag{2.32}$$

This results in an infrared modification of the classical dispersion,

$$p^2 + m^2 \to p^2 + m^2 + R_k(p) . \tag{2.33}$$

The regulator R_k needs to be designed such that while the propagation of modes with $p^2 \lesssim k^2$ is suppressed, those with $p^2 \gtrsim k^2$ remain unchanged. Furthermore, at $k = 0$ we need the regulator to vanish, since we wish to recover our original theory after integrating out all fluctuations. To discuss the implementation of these requirements, it is useful to employ the following parametrisation for the regulator,

$$R_k(p) = Z_\phi \, k^2 \, r(x) , \qquad x = \frac{p^2}{k^2} \quad \text{or} \quad x = \frac{\vec{p}^{\,2}}{k^2} , \tag{2.34}$$

where Z_ϕ is the cutoff dependent wave function renormalisation of the field at hand. The shape function $r(x)$ depends on either full or spatial momenta squared, p^2 or $\vec{p}^{\,2}$, measured in the cutoff scale k^2. It implements both, the vanishing momentum limit associated with an infrared (IR) mass and the ultraviolet (UV) decay,

$$\lim_{x \to 0} r(x) = 1 , \qquad \lim_{x \to \infty} x^{d/2} r(x) \to 0 , \tag{2.35}$$

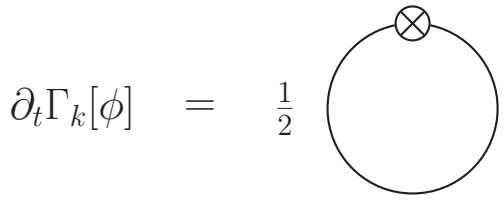

Abbildung 2.3.: Wetterich equation (2.39) for a scalar ϕ^4-theory defined by the action (2.1). The blob with the cross represents the regulator scale derivative $\partial_t R_k$. All other notation is defined in Figure 2.1.

see, e.g., [58] for a respective discussion. The first property in (2.35) implements the desired IR regularisation by suppression of quantum fluctuations of field modes with momenta $p^2 \lesssim k^2$. The second property leads to a suppression of momenta $p^2 \gtrsim k^2$ in momentum loop integrals. This renders the flow equation that we will derive in the following, as well as all its field derivatives, yielding the flows of 1PI correlation functions, UV finite.

Replacing the usual path integral measure in (2.3) by the mode-suppressing one (2.31), we obtain a scale-dependent partition function,

$$Z_k[J] = \exp\Big\{ -\Delta S_k\big[\frac{\delta}{\delta J}\big]\Big\} Z[J]\,, \tag{2.36}$$

with the scale-independent partition function as defined in (2.3). In (2.36) we exploited that we can express the field dependence of ΔS_k as functional derivatives with respect to J, since these bring down factors of φ by hitting the source term in (2.3). The scale-dependent effective action is defined as a modified Legendre transform,

$$\Gamma_k[\phi] = \sup_J \Big\{ J\cdot\phi - W_k[J] - \Delta S_k[\phi]\Big\}\,, \tag{2.37}$$

where the scale-dependent Schwinger functional is obtained via the definition (2.5) from Z_k. Note that also the supremum source acquires a scale dependence now, i.e., $J = J_k[\phi]$. The modification of the ordinary Legendre transform (2.9) is introduced since the RG flow of the Schwinger functional contains trivial contributions only proportional to the flow of the regulator. These are cancelled in the definition (2.37) by subtraction of ΔS_k.

From the definition of the scale-dependent effective action (2.37), its scale evolution is readily obtained by taking a derivative with respect to the cutoff scale k. It is convenient to formulate the scale evolution in terms of dimensionless variables. To that end, we introduce the RG time

$$t = -\log\frac{k}{\Lambda}\,, \tag{2.38}$$

where the initial cutoff scale Λ acts as reference scale. The RG time hence evolves from 0 to ∞ along the RG flow. Acting with a derivative with respect to the RG time on (2.37) then yields the celebrated Wetterich equation,

$$\partial_t\Gamma_k[\phi] = -\frac{1}{2}\,\mathrm{Tr}\,G_k[\phi]\partial_t R_k\,, \tag{2.39}$$

diagrammatically illustrated in Figure 2.3. The scale-dependent propagator in (2.39) is defined as

$$G_k[\phi] = \left(\Gamma_k^{(2)}[\phi] + R_k\right)^{-1}. \tag{2.40}$$

The trace Tr in (2.39) includes summation over all internal degrees of freedom and indices, such as group indices or spacetime/momentum arguments. For a detailed derivation of (2.39), we refer to the literature [58, 61, 81]. By taking derivatives of (2.39) with respect to the mean field, flow equations for all n-point correlation functions can be generated. Similar as in DSEs, see Section 2.2, the functional flow of the correlation function $\Gamma_k^{(n)}$ is generally dependent on $\Gamma_k^{(n+2)}$.

3. Quantum chromodynamics

As the quantum theory of strong interactions, QCD is described by a gauge theory with local $SU(3)$ symmetry. Quarks enter as fermionic fields via the Dirac action, while gluons appear as gauge bosons of the $SU(3)$ gauge group. Except for a brief motivation of gauge theories, in this chapter we restrict ourselves to Yang-Mills theory [82], the pure glue part of QCD, which is sufficient to introduce the concepts needed in this thesis. The non-Abelian nature of the theory results in self-interactions between the gauge bosons. Already in Yang-Mills theory, these self-interactions lead to the phenomenon of color confinement, entailing that colored states, i.e., states which are charged under the $SU(3)$ gauge group, are absent from the physical spectrum. Confinement can be associated with the dynamical generation of a mass gap for the classically massless gluon. Possible mechanisms for this dynamical mass generation are discussed in Section 3.2. To set the stage, we first introduce the basic concepts of non-Abelian gauge theories in Section 3.1.

3.1. Basics of non-Abelian gauge theories

In this section, we introduce the basics of non-Abelian gauge theories; for comprehensive introductions, see, e.g., [68, 69, 81, 83]. To that end, we first approach Abelian gauge theories from a geometric perspective in Section 3.1.1, allowing for an intuitive understanding of the core concepts of gauge theories. We then turn towards Yang-Mills theory in Section 3.1.2, and discuss its quantisation as well as gauge fixing in Section 3.1.3. In Section 3.1.4, we review BRST symmetry, a symmetry of the gauge-fixed action. In Section 3.1.5, we discuss the Hilbert space construction of Yang-Mills theory as well as confinement. We introduce the Slavnov-Taylor identities, a set of conservation laws following from BRST symmetry, and show how these entail transversality of the gluon mass gap, in Section 3.1.6.

3.1.1. Geometric perspective on Abelian gauge theory

The notion of a gauge theory can be introduced intuitively at the example of an Abelian gauge group. Consider a matter quantum field theory with the action

$$S = \int_x \bar{\psi}(\mathrm{i}\partial\!\!\!/ - m)\psi\,, \tag{3.1}$$

with mass parameter m, $\partial\!\!\!/ = \partial_\mu \gamma^\mu$ and the gamma matrices γ^μ. The action in (3.1) is called Dirac action, and is invariant under global transformations $\mathcal{U} \in U(1)$, parametrised by a real constant $\alpha \in \mathbb{R}$,

$$\psi(x) \mapsto \psi^{\mathcal{U}}(x) = \mathcal{U}\psi(x) = e^{-\mathrm{i}e\alpha}\psi(x)\,, \tag{3.2}$$

with charge e. Next, instead of global $U(1)$ transformations, let us consider the case of local ones. These are obtained by promoting the previously constant parameter α to a

spacetime-dependent one, i.e., $\mathcal{U} \to \mathcal{U}(x) = e^{-\mathrm{i}e\alpha(x)}$. Due to the partial derivative term in (3.1), local $U(1)$ transformations are no longer a symmetry of the action (3.1), however. Consider the definition of the derivative term along a unit vector n^μ,

$$n^\mu \partial_\mu \psi(x) = \lim_{\varepsilon \to 0} \frac{1}{\varepsilon} \Big(\psi(x + \varepsilon n) - \psi(x) \Big) \,. \tag{3.3}$$

Acting with a gauge transformation $\mathcal{U}$ on (3.3), we realise that the ordinary derivative compares two fermionic fields ψ transforming differently under the local gauge group, since they 'live' at infinitesimally separated spacetime points. The definition (3.3) is therefore not a meaningful one in the context of gauge theories. As a result, the matter action (3.1) is no longer invariant under local $U(1)$ transformations.

In order to restore the geometric meaning of the derivative term in our matter action, we need to modify it. A more sensible definition is provided by introducing a Wilson line $\mathcal{C}(x, y)$. The Wilson line is implicitly defined via the following transformation property under local $U(1)$ transformations,

$$\mathcal{C}(x, y)\psi(y) \mapsto \mathcal{U}(x)\mathcal{C}(x, y)\psi(y) \,. \tag{3.4}$$

Equation (3.4) allows us to define the action of the so-called covariant derivative D_μ on the spinor field ψ as

$$n^\mu D_\mu \psi(x) = \lim_{\varepsilon \to 0} \Big(\psi(x + \varepsilon n) - \mathcal{C}(x + \varepsilon n, x)\psi(x) \Big) \,, \tag{3.5}$$

which transforms under a local gauge transformation $\mathcal{U}$ as

$$D_\mu \psi(x) \mapsto \mathcal{U}(x) D_\mu \psi(x) \,. \tag{3.6}$$

Promoting the ordinary derivative term in the action (3.1) to a covariant one, we observe that the transformation property (3.6) restores local $U(1)$ symmetry. The Wilson line $\mathcal{C}$ compensates for the fact that the matter field ψ transforms differently at two different points in spacetime. The Dirac action for a gauge theory thus reads

$$S_{\text{Dirac}}[\bar{\psi}, \psi] = \int_x \bar{\psi} \big(\mathrm{i} \not{D} + m \big) \psi \,. \tag{3.7}$$

From (3.6), we can deduce the transformation property of the Wilson line itself under gauge transformations, which is

$$\mathcal{C}(x, y) \mapsto \mathcal{U}(x)\mathcal{C}(x, y)\mathcal{U}^{-1}(y) \,. \tag{3.8}$$

Performing a Taylor expansion of $\mathcal{C}(x + \varepsilon n)$ while demanding $\mathcal{C}(x, x) = \mathbb{1}$, we find that

$$\mathcal{C}(x + n\varepsilon, x) = \mathbb{1} - \mathrm{i}e A_\mu(x) \varepsilon n^\mu + \mathcal{O}(\varepsilon^2) \,. \tag{3.9}$$

The local vector field $A_\mu(x)$ in (3.9) is called connection and effectively carries the information about the local gauge symmetry. Using (3.9), we can recast the transformation property of the covariant derivative in terms of the gauge field $A_\mu(x)$,

$$D_\mu(x) = \partial_\mu + \mathrm{i}e A_\mu(x) \,. \tag{3.10}$$

With (3.6) in addition, we can also deduce the transformation behaviour of the gauge field,

$$A \mapsto A^{\mathcal{U}} = \mathcal{U} A_\mu \mathcal{U}^{-1} + \frac{\mathrm{i}}{g}(\partial_\mu \mathcal{U})\,\mathcal{U}^{-1}\,. \tag{3.11}$$

Using the covariant derivative, we can construct another gauge invariant operator in the action. The curvature or field strength tensor is defined via the commutator of two covariant derivatives,

$$F_{\mu\nu} = \frac{i}{e}\,[D_\mu, D_\nu] = \partial_\mu A_\nu - \partial_\nu A_\mu\,, \tag{3.12}$$

consequently transforming as

$$F_{\mu\nu} \mapsto F^{\mathcal{U}}_{\mu\nu} = \mathcal{U} F_{\mu\nu} \mathcal{U}^{-1}\,, \tag{3.13}$$

under gauge transformations. The absence of a commutator term for the gauge fields in (3.12) entails that $F_{\mu\nu}$ itself is invariant in Abelian gauge theories.

We can use the field strength to construct the following gauge invariant action,

$$S_{\mathrm{QED}}[A, \bar\psi, \psi] = \int_x \left\{ \frac{1}{4} F_{\mu\nu} F_{\mu\nu} + \bar\psi\big(\mathrm{i}\not{D} + m\big)\psi \right\}\,, \tag{3.14}$$

which is the action of quantum electrodynamics (QED).

3.1.2. Yang-Mills theory

We now turn to non-Abelian gauge theories, and in particular Yang-Mills theory. Yang-Mills theory already exhibits some key phenomena of QCD. In particular the deep IR dynamics of QCD is dominated by the gauge sector, which is why many of the mechanisms of Yang-Mills theory readily carry over to QCD. Although Yang-Mills theory is studied intensively since decades, it still poses numerous unanswered questions. The most prominent one certainly is how the classically massless gluon acquires its mass gap.

Yang-Mills theory describes an $SU(N_c)$ gauge theory, where N_c is the number of colors. The gauge field A_μ is element of the corresponding Lie algebra $\mathfrak{su}(N_c)$ with generators t^a,

$$A_\mu(x) = A^a_\mu(x) t^a\,, \quad \text{with} \quad a = 1, \ldots, N_c^2 - 1\,. \tag{3.15}$$

Accordingly, the gauge field transforms in the adjoint representation of the group.

In QCD, one has $N_c = 3$. In that case, the defining representation of the generators t^a are the Gell-Mann matrices. For the electroweak theory with gauge group $SU(2)$, these are the Pauli matrices. As opposed to the Abelian $U(1)$ case, these generators are complex matrices $t^a \in \mathbb{C}^{N_c, N_c}$. Hence, they do not commute. In fact, it is the commutation relation of the generators which fully determines the structure of the Lie algebra $\mathfrak{su}(N_c)$ and hence that of its corresponding Lie group $SU(N_c)$. For general representations, a Lie algebra is defined via its Lie bracket. In the case of a matrix representation, as discussed in the following, the Lie bracket corresponds to the well-known commutator of matrices,

$$[t^a, t^b] = \mathrm{i} f^{abc} t^c\,. \tag{3.16}$$

In (3.16), we have introduced the fully antisymmetric structure constants f^{abc}. As the name says, the structure constants fully determine the algebra and hence the group structure. A typical choice for the normalisation of the generators is

$$\operatorname{tr}\left(t^a t^b\right) = \frac{1}{2}\delta^{ab}\,, \tag{3.17}$$

where the trace is taken in the fundamental representation.

To obtain the curvature tensor of Yang-Mills theory, we only need to replace the electric charge e by the gauge coupling g in the definition (3.12). Since the gauge field is algebra valued, so is the field strength, and we have

$$F_{\mu\nu} = \frac{\mathrm{i}}{g}[D_\mu, D_\nu] = F^a_{\mu\nu} t^a\,, \quad \text{with} \quad F^a_{\mu\nu} = \partial_\mu A^a_\nu - \partial_\nu A^a_\mu + g f^{abc} A^b_\mu A^c_\nu\,. \tag{3.18}$$

Note that in contradistinction to the Abelian case (3.12), (3.18) contains a non-vanishing commutator term for the gauge fields, giving rise to the last term on the very right of (3.18). We can then define the Yang-Mills action via

$$S_{\mathrm{YM}}[A] = \frac{1}{2}\int_x \operatorname{tr} F_{\mu\nu} F_{\mu\nu} = \frac{1}{4}\int_x F^a_{\mu\nu} F^a_{\mu\nu}\,, \tag{3.19}$$

which is gauge invariant due the cyclicity of the trace, again taken in the fundamental representation.

3.1.3. Path integral quantisation & gauge fixing

Next, we discuss the path integral quantisation of QCD at the example of YM theory. The path integral defined by the classical YM action (3.19) contains physically redundant degrees of freedom, which are gauge field configurations

$$A \in \mathcal{A} = \text{space of all gauge fields}\,, \tag{3.20}$$

which are related by a gauge transformation, i.e.,

$$\mathcal{A}^{\mathcal{U}} = \left\{A^{\mathcal{U}}\, \forall\, \mathcal{U} \in U\right\}. \tag{3.21}$$

$\mathcal{A}^{\mathcal{U}}$ is called a gauge orbit. Due to gauge invariance, moving along the gauge orbit by gauge transformations leaves the action invariant, thus corresponding to physically equivalent configurations. The necessity to remove these redundancies is encoded in the non-invertibility of the kinetic operator of the gauge field. Due to its transversality, it has a vanishing eigenvalue,

$$p^\mu S^{(2)}_{AA,\mu\nu} = p^\mu \left(p^2 \delta_{\mu\nu} - p_\mu p_\nu\right) = 0\,. \tag{3.22}$$

In order to single out physically inequivalent configurations, we only want to consider one representative per gauge orbit. These can be represented by the quotient space,

$$\mathcal{A}/U = \left\{A \sim A^{\mathcal{U}} \,:\, A \in \mathcal{A}, \mathcal{U} \in U\right\}. \tag{3.23}$$

We can hence remove all redundancies by restricting our path integral measure to the quotient space. To achieve this, one needs to construct a suitable measure $\mathrm{d}\mu[A]$ such that

the path integral factorises into an integration over gauge transformations and over the quotient space $\mathcal{A}/U$,

$$Z[J_A] = \int_U \mathrm{d}\mathcal{U} \int_{\mathcal{A}/U} \mathrm{d}\mu[A] \, \exp\Big\{ - S[A] + J_A \cdot A \Big\} \,. \tag{3.24}$$

The measure on the gauge group $\mathrm{d}\mathcal{U}$ is called Haar measure and is gauge invariant. With (3.24), configurations on the same gauge orbit can be integrated out, and the resulting factor can be absorbed in the normalisation of the partition function, hence dropping out of correlation functions. Then, we are left with an integration over physically inequivalent field configurations in the quotient space $\mathcal{A}/U$. We will explicitly construct the desired measure in (3.24) in the following.

In order to restrict to one representative per gauge orbit, one imposes a gauge fixing condition. We would like to have that for any $A \in \mathcal{A}$, there exists a unique $\mathcal{U}^\star \in U$ such that, for some function $\mathcal{F}$,

$$\mathcal{F}[A^{\mathcal{U}^\star}] = 0 \,, \tag{3.25}$$

which would allow us to single out one representative $A^{\mathcal{U}^\star}$ per orbit. In fact, it is known that (3.25) cannot always be satisfied, going by the name of Gribov ambiguity [84]. It might happen that the gauge fixing condition does not apply to any element on a particular gauge orbit, or to more than one, which are called Gribov copies. For the moment, we will simply assume that (3.25) holds, and come back to this assumption below.

The gauge fixing condition (3.25) needs to be implemented on the level of the path integral. This can be achieved by Faddeev-Popov quantisation. There, one inserts a functional unity into the path integral,

$$\mathbb{1} = \Delta_{\mathcal{F}}[A] \int_U \mathrm{d}\mathcal{U} \, \delta\big(\mathcal{F}\big[A^{\mathcal{U}}\big]\big) \,, \tag{3.26}$$

with the inverse Jacobian

$$\Delta_{\mathcal{F}}[A] = \det \mathcal{M}_{\mathcal{F}} \,, \quad \text{with} \quad \mathcal{M}_{\mathcal{F}} = \frac{\delta \mathcal{F}[\mathcal{A}^{\mathcal{U}}]}{\delta \mathcal{U}}\bigg|_{\mathcal{U}=\mathcal{U}^\star} \,. \tag{3.27}$$

$\Delta_{\mathcal{F}}$ is called the Faddeev-Popov determinant, and $\mathcal{M}$ is the Faddeev-Popov matrix. In (3.27), we assumed $\mathcal{M}_{\mathcal{F}}$ to be a positive definite operator. We remark that this is assumption is generally not true, ultimately sourcing the Gribov problem. A common technique to soften this problem is to restrict the path integral to a single Gribov region, bounded by the Gribov horizon which marks the first root of the Faddeev-Popov determinant (3.27) around the origin. We discuss this approach briefly in Section 3.1.5.

With (3.27), the path integral measure can be expressed as

$$\int_{\mathcal{A}} \mathrm{d}A = \int_U \mathrm{d}\mathcal{U} \int_{\mathcal{A}} \mathrm{d}A \, \delta\big(\mathcal{F}\big[A^{\mathcal{U}}\big]\big) \Delta_{\mathcal{F}}\big[A\big] \,, \tag{3.28}$$

For the measure (3.28) to factorise as desired in (3.24), we still need to eliminate the $\mathcal{U}$-dependence of the delta distribution carrying the gauge fixing condition. This can be done via a simple gauge transformation $A \mapsto A^{\mathcal{U}^\dagger}$, noting that the path integral measure $\mathrm{d}A$ is gauge invariant due to unitarity of the gauge transformation $\mathcal{U} \in U$. The Faddeev-Popov

determinant (3.26) is gauge invariant as well, owing to the gauge invariance of the Haar measure $\mathrm{d}\mathcal{U}$. We obtain the desired split (3.24) of the path integral measure,

$$\int_{\mathcal{A}} \mathrm{d}A = \int_U \mathrm{d}\mathcal{U} \int_{\mathcal{A}} \mathrm{d}A\, \delta\big(\mathcal{F}[A]\big)\Delta_{\mathcal{F}}\big[A\big]\,, \tag{3.29}$$

from which the explicit form of the measure on the quotient space can be read off,

$$\int_{\mathcal{A}/U} \mathrm{d}\mu[A] = \int_{\mathcal{A}} \mathrm{d}A\, \delta\big(\mathcal{F}[A]\big)\Delta_{\mathcal{F}}[A]\,. \tag{3.30}$$

The integration over the gauge group simply yields a constant factor, which is the volume of the gauge group,

$$\int_U \mathrm{d}\mathcal{U} = \mathcal{V}_U\,. \tag{3.31}$$

Since the normalisation of the partition function drops out of correlation functions, see (2.2), we can simply drop the factor $\mathcal{V}_U$.

The Faddeev-Popov determinant $\Delta_{\mathcal{F}}[A]$ can be calculated explicitly from (3.26). The gauge invariance of the Haar measure allows for expanding the group elements $\mathcal{U}$ about the unit element. This yields the explicit form of the Faddeev-Popov matrix $\mathcal{M}$ defined in (3.27),

$$\mathcal{M}_{\mathcal{F}} = -\frac{\delta\mathcal{F}[A]}{\delta A_\mu} D_\mu\,. \tag{3.32}$$

We can express the determinant of $\mathcal{M}_{\mathcal{F}}$ as a functional Gaussian integral with help of two Grassmann fields $\bar{c}, c$,

$$\Delta_{\mathcal{F}} = \int \mathrm{d}c\, \mathrm{d}\bar{c}\, \exp\Big\{\bar{c}^a \cdot \mathcal{M}^{ab}_{\mathcal{F}} \cdot c^b\Big\}\,. \tag{3.33}$$

It remains to find a representation of the delta distribution in (3.30) carrying the gauge fixing condition, which allows for practical calculations. To that end, we rewrite it via its Fourier representation by introducing an auxiliary field,

$$\delta\big(\mathcal{F}[A]\big) = \int \mathrm{d}B\, \exp\Big\{B^a \cdot \mathcal{F}^a[A]\Big\}\,, \tag{3.34}$$

where B and $\mathcal{F}$ are algebra-valued. The Nakanishi-Lautrup field B will also be useful for the discussion of BRST symmetry, a symmetry of the gauge-fixed action, later.

Since all predictions of our theory need to be independent of how exactly we fix the gauge, the gauge fixing condition (3.25) is arbitrary. Instead of a single gauge fixing condition, we can therefore also consider a Gaussian average over gauge fixing conditions,

$$\delta\big(\mathcal{F}[A]\big) \to \int \mathrm{d}f\, \delta\big(\mathcal{F}[A] - f\big) \exp\Big\{-\frac{1}{2\xi} f^a \cdot f^a\Big\}\,, \tag{3.35}$$

$$= \int \mathrm{d}B\, \exp\Big\{-\frac{\xi}{2} B^a \cdot B^a - B^a \cdot \mathcal{F}^a[A]\Big\}\,, \tag{3.36}$$

where in the last step, we used (3.34) and absorbed a numerical prefactor into the normalisation. Furthermore, we introduced an arbitrary gauge fixing parameter ξ. With (3.35), the gauge-fixed Yang-Mills action reads,

$$S_{\mathrm{YM}}[A,B,\bar{c},c] = \int_x \left\{ \frac{1}{4} F^a_{\mu\nu} F^a_{\mu\nu} + \frac{\xi}{2} B^a B^a + B^a \mathcal{F}^a[A] + \bar{c}^a \mathcal{M}^{ab}_{\mathcal{F}} c^b \right\}. \tag{3.37}$$

Note that the Nakanishi-Lautrup field B has no kinetic term and can hence be integrated out using its equation of motion,

$$B^a_{\mathrm{EoM}} = -\frac{1}{\xi} \mathcal{F}^a[A]\,. \tag{3.38}$$

Specifying to the common case of linear covariant gauges,

$$\mathcal{F}[A] = \partial_\mu A_\mu\,, \tag{3.39}$$

and integrating out the Nakanishi-Lautrup field using (3.38), we eventually obtain the gauge-fixed path integral of Yang-Mills theory,

$$Z[J] = \int \mathrm{d}A\, \mathrm{d}\bar{c}\, \mathrm{d}c\, \exp\left\{ S_{\mathrm{YM}}[A,\bar{c},c] + J_A \cdot A + J_c \cdot c - \bar{c} \cdot J_{\bar{c}} \right\}, \tag{3.40}$$

with $J = (J_A, J_{\bar{c}}, J_c)$ and

$$S_{\mathrm{YM}}[A,\bar{c},c] = \int_x \left\{ \frac{1}{4} F^a_{\mu\nu} F^a_{\mu\nu} + \frac{1}{2\xi} \left(\partial_\mu A^a_\mu\right)^2 - \bar{c}^a \partial_\mu D^{ab}_\mu c^b \right\}. \tag{3.41}$$

3.1.4. BRST symmetry

By construction, the gauge-fixed action (3.41) is no longer gauge invariant. Leaving aside the ghost terms, the gauge fixing term explicitly breaks gauge invariance. The information about the gauge symmetry is not lost however, it is still present in terms of BRST symmetry. A BRST transformation can heuristically be understood as transformation compensating for the gauge variance of the gauge fixing term. This has two immediate consequences: First, the non-gauge-fixed Yang-Mills action (3.19) is BRST invariant,

$$\delta_{\mathrm{BRST}}\, S_{\mathrm{YM}}[A] = 0\,, \tag{3.42}$$

for an infinitesimal BRST transformation δ_{BRST}. Second, the transformation is Grassmanian in nature. Introducing a superfield $\Phi = \{A, B, \bar{c}, c\}$, δ_{BRST} can be written as

$$\delta_{\mathrm{BRST}} \Phi = \epsilon\, s\, \Phi\,, \tag{3.43}$$

where the infinitesimal parameter ϵ is Grassmanian. The BRST variation s has the general form

$$s = \int_x (s\,\Phi_i) \frac{\delta}{\delta \Phi_i}\,, \tag{3.44}$$

and explicitly acts on the Yang-Mills field content as

$$s\, A^a_\mu = D^{ab}_\mu c^b\,, \quad s\, \bar{c}^a = B^a\,, \quad s\, c^a = -\frac{g}{2} f^{abc} c^b c^c\,, \quad s\, B = 0\,. \tag{3.45}$$

From the transformation behaviour (3.45), it can be checked that the BRST variation can be written as a total derivative,

$$s = \int_x \frac{\delta}{\delta \Phi_i} (s\,\Phi_i)\,. \tag{3.46}$$

We can see from (3.45) that, while the $D_\mu c$ term is gauge invariant, it is precisely the antighost which cancels the BRST transformation of the gauge fixing term. In fact, we can exploit (3.45) to recast the gauge-fixed Yang-Mills action as

$$S[\Phi] = S_{\mathrm{YM}}[A] + \int_x s\,\psi[\Phi]\,, \tag{3.47}$$

where S_{YM} stands for the non-gauge-fixed Yang-Mills action (3.19). In (3.47), we also introduced the gauge fixing fermion,

$$\psi[\Phi] = \bar{c}^a \partial_\mu A^a_\mu - \frac{\xi}{2} \bar{c}^a B^a\,. \tag{3.48}$$

Another crucial property of the BRST generator is its nilpotency,

$$s^2 = 0\,, \tag{3.49}$$

which can be verified explicitly with (3.45). Together with (3.47), the nilpotence (3.49) of s directly leads us to

$$s\,S[\Phi] = 0\,, \tag{3.50}$$

i.e., the BRST invariance of the gauge-fixed Yang-Mills action.

3.1.5. Hilbert space and confinement

The path integral quantisation of non-Abelian gauge theories discussed in this chapter in principle allows for the computation of gauge invariant correlation functions. The construction of a corresponding Hilbert space $\mathcal{H}_{\mathrm{phys}}$ requires canonical quantisation of the field operators, however. For the gauge-fixed action (3.37), canonical quantisation relations can indeed be established. A Hilbert space construction based on these operators is required to yield positive-norm states which respect the symmetries of the gauge-fixed theory. Under the assumption of global BRST symmetry, this can be achieved within BRST quantisation. By Noether's theorem, global BRST symmetry entails the existence of a corresponding BRST charge operator Q_{BRST},

$$Q_{\mathrm{BRST}} = \int \mathrm{d}^4 x J^0_{\mathrm{BRST}}\,, \qquad \text{with} \qquad \partial_\mu J^\mu_{\mathrm{BRST}} = 0\,, \tag{3.51}$$

where J_{BRST} is the corresponding conserved Noether current. Since physical states need to respect the symmetries of the gauge-fixed action, they are required to be invariant under BRST transformations. In consequence, they do not carry BRST charge, which is why Q_{BRST} can be used to distinguish between physical and unphysical states,

$$Q_{\mathrm{BRST}} |\psi_{\mathrm{phys}}\rangle = 0\,, \tag{3.52}$$

for $|\psi_{\text{phys}}\rangle \in \mathcal{H}_{\text{phys}}$. As a result of the nilpotency of the BRST generator s, cf. (3.49), Q_{BRST} is nilpotent as well. In consequence, (3.52) also applies trivially to Q_{BRST}-exact states, which are generated via the charge operator,

$$|\psi_{\text{exact}}\rangle = Q_{\text{BRST}}|\psi\rangle \qquad \Rightarrow \qquad Q_{\text{BRST}}|\psi_{\text{exact}}\rangle = 0\,. \tag{3.53}$$

Q_{BRST}-exact states have vanishing norm, which follows directly from the nilpotency of the charge operator. For this reason, we want to exclude these states from the physical spectrum. To that end, one defines the Hilbert space as equivalence class of states which have vanishing BRST charge, but may differ by Q_{BRST}-exact states. More precisely, the Hilbert space is given by the cohomology of the BRST charge operator,

$$\mathcal{H}_{\text{phys}} = \text{Cohom}(Q_{\text{BRST}}) = \frac{\ker(Q_{\text{BRST}})}{\text{im}(Q_{\text{BRST}})}\,, \tag{3.54}$$

where ker is the kernel and im the image of the charge operator, such that for all Q_{BRST}-exact states, $|\psi_{\text{exact}}\rangle \in \text{im}(Q_{\text{BRST}})$. For a more detailed introduction to BRST quantisation, see, e.g., [85].

Confinement

Of course, a successful Hilbert space construction needs to respect the phenomenon of confinement, i.e., it must not contain colored asymptotic states such as single quarks or gluons. In the following, we give a brief account of confinement scenarios on the basis of correlation functions; topological approaches to confinement can be found, e.g., in [86, 87].

The confinement criterion by Kugo and Ojima [88] formulates how, under the assumption of a global color charge, the absence of colored single gluon states can be achieved in Yang-Mills theory. The mechanism entails a particular large distance decay behaviour of the one-particle Green's functions of the theory. In momentum space, this criterion translates into the gluon propagator being less and the ghost propagator being more singular than the propagator of a massless particle in the origin. These requirements are met by the so-called *scaling solution* of Yang-Mills theory, which has been found in various Landau gauge DSE [2, 89–94] and fRG [95, 96] computations. Within the scaling solution, gluon and ghost propagator show a scaling behaviour in the deep IR,

$$G_A^{\text{sca}}(p) \sim (p^2)^{2\kappa-1}\,, \qquad G_c^{\text{sca}}(p) \sim (p^2)^{-1-\kappa}\,, \tag{3.55}$$

with a scaling exponent $1/2 < \kappa < 1$. Numerical estimates yield $\kappa \approx 0.58$ [95], while analytic results predict a value of $\kappa = (93 + \sqrt{1201})/98 \approx 0.5953$ [91, 92].

In lattice simulations, an IR behaviour of ghost and gluon progagators different from the scaling is usually realised [97–101]. It is characterised by a mass-like gapped gluon propagator and a simple massless pole in the ghost propagator for $p \to 0$,

$$G_A^{\text{dec}}(p) \sim 1\,, \qquad G_c^{\text{dec}}(p) \sim \frac{1}{p^2}\,, \tag{3.56}$$

commonly referred to as *decoupling solution*. The fact that lattice simulations so far have not been able to realise the scaling solution has been connected to the difference in gauge fixing between lattice and functional approaches [102]. While not being in line with the Kugo-Ojima confinement scenario, the decoupling solution found in lattice simulations

is consistent with the refined Gribov-Zwanziger scenario for confinement [103, 104]. The Gribov-Zwanziger action imposes an additional gauge fixing condition on the Yang-Mills action (3.37) in order to restrict the configuration space for the gauge field to the first Gribov region. In its initial formulation [105, 106], it predicted a vanishing gluon and an infrared enhanced ghost propagator, which is incompatible with the lattice data. The refined version, however, compensating for non-locality of the additional gauge fixing term, leads to a decoupling-type solution (3.56). Note that the Gribov-Zwanziger action inherently breaks global BRST symmetry [107].

The decoupling solution (3.56) can be also realised in functional approaches, see, e.g., [93, 95, 96]. The DSE solution [2] for the ghost spectral function reported in this thesis in Section 5.2 encompasses both, the scaling and decoupling solution. In functional Landau gauge calculations, the scaling solution usually appears as the IR closure of possible solutions with respect to the initial condition for the gluon mass gap in the system. Therefore, obtaining the scaling solution requires solving a quadratic fine-tuning problem, which gets particularly clear in the context of fRG studies due the RG scaling of the gapping parameter.

Both, the Kugo-Ojima and Gribov-Zwanziger approach to confinement predict a finite value for the gluon propagator at vanishing momentum as a result of confinement, i.e., a mass gap. Through the Slavnov-Taylor identities (STI), which we discuss in Section 3.1.6, BRST symmetry entails that this mass gap only exists in the transverse component of the gluon field. While also the transverse component of the gluon field does not appear in the physical, asymptotic spectrum, as discussed above, its massive excitation eventually gives rise to the physical mass gap of Yang-Mills theory and QCD. The longitudinal component, in contrast, is an unphysical one, which also becomes manifest in the fact that it constitutes a zero-norm state and hence is right away eliminated within the perturbative BRST quantisation procedure described above. However, this begs the question of how the split between longitudinal and transverse component in the gluon propagator comes about on the level of functional equations. The scaling solution (3.55) constitutes a natural mechanism for this split [94]. We turn towards a general discussion of mechanisms for the mass generation of the gluon with focus on condensation in Section 3.2. In the following, we close this introduction to non-Abelian gauge theories with a brief discussion of STIs and the relevant example for this thesis, the STI for the gluon propagator.

3.1.6. Slavnov-Taylor identities

In Section 2.2, we observed that field transformations which can be written as total derivatives lead to non-trivial identities, called Dyson-Schwinger equations. This property is rooted in the shift invariance of the path integral. We will utilise this fact in this section to derive the Slavnov-Taylor identities, which are the non-Abelian counterpart of the Abelian Ward-Takahashi identities.

Utilising that also the BRST variation s can be written as a total derivative (3.46), we can express the normalised generating functional including the Nakanishi-Lautrup field as

$$\frac{1}{Z[J]} \int \mathrm{d}A\, \mathrm{d}B\, \mathrm{d}c\, \mathrm{d}\bar{c}\, s\, \exp\Big\{ - S[A, B, \bar{c}, c] + J_A \cdot A + J_c \cdot c - \bar{c} \cdot J_{\bar{c}} \Big\} = 0\,. \tag{3.57}$$

Explicitly carrying out the BRST variation yields the Slavnov-Taylor identity,

$$\int_x \Big\langle J_A\, s\, A - J_c\, s\, c - J_{\bar{c}}\, s\, \bar{c} \Big\rangle = 0\,. \tag{3.58}$$

The STI (3.58) obtains a much more compact form when casting it in terms of the quantum effective action. To that end, we introduce source terms for the BRST variations,

$$\int_x Q_i \, s \, \Phi_i = \int_x \Big(Q_A \, s \, A + Q_c \, s \, c + Q_{\bar{c}} \, s \, \bar{c} \Big) \,, \tag{3.59}$$

which only represent spectators in the Legendre transform leading to the effective action. Equation (3.59) then allows us to rewrite the STI as

$$\langle s \, \Phi_i \rangle = \frac{1}{Z[J,Q]} \frac{\delta Z[J,Q]}{\delta Q_i} = - \frac{\delta \Gamma[\Phi, Q]}{\delta Q_i} \,. \tag{3.60}$$

Exploiting the equations of motions of the source terms for the fields,

$$J_A = \frac{\delta \Gamma}{\delta A} \,, \quad J_{\bar{c}} = - \frac{\delta \Gamma}{\delta \bar{c}} \,, \quad J_c = - \frac{\delta \Gamma}{\delta c} \,, \tag{3.61}$$

from (3.58) we are directly lead to the quantum master equation,

$$\frac{\delta \Gamma}{\delta Q_i} \frac{\delta \Gamma}{\delta \Phi_i} = 0 \,. \tag{3.62}$$

STI for the gluon two-point function

As a relevant example for this thesis, we now discuss the STI for the gluon two-point-function. It states that the quantum corrections of the gluon propagator are purely transverse, i.e., the gluon mass gap only applies to its transverse degrees of freedom. We discuss mechanisms for the generation of this mass gap in Section 3.2.

Before starting with the derivation of the gluon propagator STI, we introduce a general parametrisation of the gluon two-point function,

$$\Gamma^{(2)}_{AA,\mu\nu}(p) = p^2 \Big(Z_A^{\perp}(p) \Pi^{\perp}_{\mu\nu}(p) + Z_A^{\parallel}(p) \Pi^{\parallel}_{\mu\nu}(p) \Big) \,, \tag{3.63}$$

using the longitudinal and transverse projection operators $\Pi^{\parallel}$ resp. $\Pi^{\perp}$,

$$\Pi^{\parallel}_{\mu\nu}(p) = \frac{p_\mu p_\nu}{p^2} \quad , \quad \Pi^{\perp}_{\mu\nu}(p) = \delta_{\mu\nu} - \Pi^{\parallel}_{\mu\nu}(p) \,. \tag{3.64}$$

In the following, we will take the freedom to swap between super- and subscripts $\perp$ / $\parallel$ for the projection operators (3.64) depending on the position of the Lorentz indices.

We begin deriving the gluon propagator STI by taking a ghost and gluon derivative of the master equation (3.62) at vanishing BRST sources and on the field equations of motion $\Phi_0 = (0, B_{\text{EoM}})$, with B_{EoM} given by (3.38),

$$\begin{aligned} &\frac{\delta^2}{\delta A_\mu(x) \delta c(y)} \left[\frac{\delta \Gamma}{\delta Q_i} \cdot \frac{\delta \Gamma}{\delta \Phi_i} \right]_{\Phi = \Phi_0, Q=0} \\ &= \left[\frac{\delta}{\delta c(y)} \frac{\delta \Gamma}{\delta Q_{A,\nu}} \right] \left[\frac{\delta}{\delta A_\mu(x)} \frac{\delta \Gamma}{\delta A_\nu} \right] + \left[\frac{\delta}{\delta A_\mu(x)} \frac{\delta \Gamma}{\delta Q_{\bar{c}}} \right] \left[\frac{\delta}{\delta c(y)} \frac{\delta \Gamma}{\delta \bar{c}} \right] \Bigg|_{\Phi = \Phi_0, Q=0} = 0 \,. \end{aligned} \tag{3.65}$$

First, we note that we can express the variation of the effective action w.r.t. the anti-ghost BRST source by the equation of motion of the Nakanishi-Lautrup field, i.e.,

$$\frac{\delta \Gamma}{\delta Q_{\bar{c}}(x)} = B_{\text{EoM}} = \frac{1}{\xi} \partial_\mu A_\mu \,, \tag{3.66}$$

where in the last step we again used (3.38). Next, we express the anti-ghost derivative of the effective action by means of the anti-ghost DSE, which reads

$$\frac{1}{Z[J]}\int \mathrm{d}\Phi\,\frac{\delta}{\delta\bar{c}(x)}\left[\exp\left\{-S[A,B,\bar{c},c]+J_A\cdot A-\bar{c}\cdot J_{\bar{c}}+J_c\cdot c\right\}\right]=0\,. \tag{3.67a}$$

Explicitly performing the field variation leads to

$$\left\langle \partial_\mu D_\mu c\right\rangle = J_{\bar{c}}\,. \tag{3.67b}$$

The expectation value on the left-hand side of (3.67b) is a BRST variation, see (3.42). We can hence rewrite it in terms of the effective action using (3.60). Also substituting the equation of motion for the anti-ghost source (3.61), we eventually arrive at

$$\frac{\delta\Gamma}{\delta\bar{c}} = -\partial_\mu\frac{\delta\Gamma}{\delta Q_{A,\mu}}\,. \tag{3.67c}$$

The final form of the anti-ghost DSE (3.67c) entails that we can pull out a common factor with a ghost derivative and a gluon BRST source variation of Γ in the STI (3.65) upon integrating by parts. This yields

$$\left[\frac{\delta}{\delta c(y)}\frac{\delta\Gamma}{\delta Q_{A,\nu}}\right]\left[\Gamma^{(2)}_{AA,\nu\mu}-\partial_\mu\frac{\delta}{\delta A_\mu(x)}\frac{1}{\xi}\partial_\nu A_\nu\right]\Big|_{\Phi=0,Q=0}=0\,. \tag{3.68}$$

The first term on the left-hand side, given by the ghost derivative of the BRST variation of the gauge field, is a Lorentz vector. Since we evaluate (3.68) at vanishing fields and BRST sources, the only non-vanishing Lorentz vector is the partial spacetime derivative. This leads us to the final form of the gluon propagator STI in momentum space,

$$p_\mu\Gamma^{(2)}_{AA,\mu\nu}(p)=\frac{1}{\xi}p_\mu p^2\,. \tag{3.69}$$

Within the parametrisation (3.63), this entails that

$$Z_A^{\parallel}(p)=\frac{1}{\xi}\,, \tag{3.70}$$

stating that the longitudinal dressing function of the gluon propagator is given by its classical value. The gluon mass gap, characteristic of confinement (Section 3.1.5), hence only exists in the physical transverse sector. Any mechanism for gluon mass generation therefore not only needs to explain emergence of the mass itself, but also of the split between the transverse and longitudinal sector of the gluon propagator. In the following section, we will discuss a particular candidate for such a mechanism.

3.2. Mass generation for the gluon via condensation

This section presents results of [4]. The practical calculations were performed in collaboration with fellow PhD student Friederike Ihssen.

Yang-Mills theory exhibits a mass gap, in spite of the fact that the fundamental degrees of freedom are massless at the level of the classical action. While perturbation theory is based on massless gluons, non-perturbative quantum fluctuations lead to exponentially decaying correlation functions for gauge invariant observables, which are characteristic of massive excitations. The lightest excitations are glueballs [108, 109], and the lightest glueball mass sets the mass gap or confinement scale. This dynamical emergence of a mass gap in the gauge sector of QCD has been established by numerous lattice studies, see, e.g., [110–114], and continuum studies, see, e.g., [115–123].

In a gauge-fixed version of QCD, the effects of the mass gap manifest themselves through the appearance of distinctive patterns in the infrared momentum region of correlation functions, see the discussion in Section 3.1.5. Most of the related investigations have been performed in Landau gauge QCD. Especially the infrared behaviour of the gluon propagator in Landau gauge has been explored within large-volume lattice simulations [98, 124–132] and non-perturbative functional methods, such as Dyson-Schwinger equations (DSEs) [107, 133–136] and the functional renormalisation group (fRG) [59, 62, 63, 137]. In combination, these investigations have led to a coherent picture: with exception to the deep infrared regime far below the confinement scale Λ_{QCD}, the results obtained for the gluon propagator in the non-perturbative domain are in excellent agreement. In particular, they are found to be well compatible with a description in terms of an effective gluon mass. Put differently, they show the dynamical emergence of a mass gap in the gluon propagator, and in higher order correlation functions.

The precise relation between the gluon mass in gauge-fixed QCD and the physical mass gap in Yang-Mills theory still eludes us. Nonetheless, in covariant gauges a mass gap in the gluon propagator is required for quark confinement to occur, as has been established through the study of the Polyakov loop expectation value in [138, 139].

This situation asks for the identification and investigation of potential mechanisms which are able to create an effective gluon mass term. Commonly, gauge boson masses are generated by the formation of condensates, even in the absence of fundamental scalar fields. The textbook implementation of such a scenario is realised within the theory of superconductivity. There, the massive photon associated with the Meissner effect is linked to the condensation of the Cooper pairs, see, e.g., [140, 141], and references therein. In pure Yang-Mills theory, a potential connection between the effective gluon mass and gluon condensates of dimension four has mostly been discussed within the operator product expansion (OPE) [142–144]. It has been argued in [145] that a non-perturbative condensate of composite color octets in QCD leads to a simple description of gluon masses by the Higgs mechanism. In this scenario, the massive gluons can be identified with the lowest mass vector mesons, with a rather successful phenomenology [146, 147].

Here, we present a first fRG study of a potential dynamical emergence of the effective mass in the gauge-fixed gluon propagator in QCD color condensates. The condensate is computed from the Euclidean effective potential of a constant field strength $F_{\mu\nu}$ as in [148], with precision ghost and gluon propagators obtained within the fRG [95]. We find minima and saddle points for finite non-zero $F_{\mu\nu}$. The minimum value of $F_{\mu\nu}$ is related to

an effective gluon mass, and the final color-blind result is obtained from an average over color directions. Our computation of the effective gluon mass agrees very well with lattice results and results obtained from alternative dynamical scenarios within the error bars, despite the qualitative nature of the computation. The present study serves as a promising starting point for a systematic exploration of the connection between gluon condensates and gluon mass gap.

This section is structured as follows. In Section 3.2.1, we give a brief introduction to the mechanism of gluon condensation. In Section 3.2.2, we introduce the background field approach, which we use to deal with the non-vanishing background field which gives rise to the condensate studied here. We discuss the computation of the background field effective potential from which the condensate is obtained in Section 3.2.3 and resulting gluon mass gap in Section 3.2.4. In Section 3.2.5, we compare to gluon mass gap results obtained from the Schwinger mechanism. We present our conclusions in Section 3.2.6

3.2.1. Gluon condensates

Gluon condensation can be described by non-vanishing expectation values of composite operators, such as the field strength squared, $F_{\mu\nu}F_{\mu\nu}$, being a scalar under Lorentz transformations. In terms of the free energy or effective action of QCD, this entails that quantum effects would trigger a non-trivial potential in these condensates, with the possibility of capturing also the dynamics of the respective interaction channel. In this context, the classical action of Yang-Mills theory (3.19) is the first (trivial) term of such a non-trivial potential.

3.2.1.1. Color condensates

Color condensates [145, 149–151] could render the gluons massive through a dynamical realisation of the Higgs mechanism. Note that, strictly speaking, a local gauge symmetry cannot be broken spontaneously. Nonetheless, as well-known from the description of the electroweak sector of the Standard Model, the language of spontaneous symmetry breaking in a fixed gauge can be particularly useful, and will be employed in what follows.

Below we discuss a color condensate operator, derived from the field strength $F_{\mu\nu}$ (3.18) in the case of the physical gauge group $SU(3)$. Generally, a possible condensate operator of dimension four is given by the traceless hermitian $N_c \times N_c$ matrices

$$\chi^{AB} = \left(F^{AC}_{\mu\nu} F^{CB}_{\mu\nu} - \frac{1}{N_c} F^{CD}_{\mu\nu} F^{DC}_{\mu\nu} \delta^{AB} \right) , \tag{3.71}$$

where $A, B, C, D = 1, ..., N_c$ are color indices in the fundamental representation, $F^{AB}_{\mu\nu} = F^a_{\mu\nu}(t^a)^{AB}$. The subtraction of the diagonal term makes the operator traceless, $\chi^{AA} = 0$, and for $N_c = 3$ this is an octet operator. In terms of the field strength components $F^a_{\mu\nu}$, the condensate in (3.71) reads,

$$\chi^{AB} = \frac{1}{2} F^a_{\mu\nu} F^b_{\mu\nu} \Big(\{t^a \, , \, t^b\}^{AB} - \frac{1}{N_c} \delta^{ab} \delta^{AB} \Big) , \tag{3.72}$$

We note in passing that the above operator is only present for $N_c \geq 3$. It vanishes in $SU(2)$, as the symmetric group invariant vanishes, $d^{abc} = \mathrm{Tr}\; t^a \{t^b \, , \, t^c\} = 0$. This already suggests that in a realistic condensation scenario leading to a gluon mass gap, (3.71) should be augmented with further color condensate operators.

Introducing the composite color condensate field χ^{AB}, the quantum effective action Γ introduced in Section 2.1 will contain an induced kinetic term,

$$\Gamma_\chi = Z_\chi \int_x (D_\mu \chi)^{AB} (D_\mu \chi)^{BA} , \tag{3.73}$$

with a wave function renormalisation Z_χ. For a non-zero expectation value $\langle \chi^{AB} \rangle$, this induces a mass term for some gluons,

$$m_A^2 \propto Z_\chi g_s^2 \langle \chi \rangle^2 . \tag{3.74}$$

Mass terms for all gluons in $SU(3)$ require condensates of more than one octet in different directions since at least a $U(1) \times U(1)$-subgroup remains unbroken, as for example in [145, 149–151]. This argument also applies to higher gauge groups, $N_c \geq 3$, and we have already pointed out in this context that the color condensate operator (3.72) vanishes for $N_c = 2$. Besides different mass terms, octet condensates can also induce different effective gauge couplings for different gluons, due to terms in the effective action, see, e.g., [152, 153],

$$\int_x F_{\mu\nu}^{AB} \chi^{BC} F_{\mu\nu}^{CA} . \tag{3.75}$$

3.2.1.2. Color condensates and the field strength tensor

The flow equation approach with dynamical composite fields such as the color condensate field discussed in the last section is well understood. It has been introduced and discussed in [38, 58, 154–161], for applications to QCD see [38, 162–166] and the review [63]. However, full computations including the composite field χ^{AB} require a substantial effort, and will be considered elsewhere.

Here, we restrict ourselves to a qualitative study, whose principal aim is to gather insights on the possible role of non-singlet condensates in the confining dynamics. This is done by building on results for the condensation of the field strength tensor within functional renormalisation group investigations in [148, 167, 168]. Such a colored expectation value of $F_{\mu\nu}$ is linked to non-vanishing expectation values of the color condensate operator χ in (3.71) as well as potential non-vanishing expectation values of further color condensate operators. Hence, $\langle F_{\mu\nu} \rangle$ can be used to describe the dynamical emergence of the effective gluon mass via color condensates, for details see Section 3.2.1.3.

We emphasise that a description in terms of $F_{\mu\nu}$ and its expectation value makes it difficult to include the full dynamics of the color condensate sector as well as the condensation pattern, as this requires the computation of the dynamics of higher order terms in $F_{\mu\nu}$ and covariant derivatives. We also note that such an expansion about $\langle F_{\mu\nu} \rangle$ works naturally for observables or more generally, expectation values of gauge invariant operators. There, singling out a color direction is simply a means of computation. In turn, for gauge-variant expressions the expansion about a non-trivial configuration mixes with the gauge fixing, and it is difficult to undo the color selection quantitatively. Still, it can be done with an additional color averaging $\langle \cdot \rangle_{\text{av}}$, which can be implemented systematically. As this concerns the understanding and underlying structure of this section, we further explain this with two simple examples. While important, it is not in our main line of reasoning and hence is deferred to Appendix A.1.

Note, that such an averaging is to date always implied in lattice simulations of gauge-fixed correlation functions as well as in most computations in functional QCD using an

expansion about the only color-symmetric background, $\langle F_{\mu\nu}\rangle = 0$. The intricacies mentioned above only occur for a quantitative implementation in an expansion about a colored background. It is the current lack of a quantitatively reliable averaging procedure, that causes the current investigation to be of qualitative nature, and constitutes our largest source of systematic error.

Here, we compute the respective gauge invariant effective potential $\mathcal{W}_{\text{eff}}(F_{\mu\nu})$ for constant field strength $F_{\mu\nu}$ from the effective action $\Gamma[A]$,

$$\mathcal{W}_{\text{eff}}(F_{\mu\nu}) = \frac{1}{\mathcal{V}}\Gamma[A(F_{\mu\nu})]\,, \tag{3.76}$$

with the spacetime volume $\mathcal{V}$.

Specifically, we choose gauge fields with the following constant self-dual field strengths: the components $F_{\mu\nu} = 0$ for $\mu\nu \neq 01, 10, 23, 32$ vanish, and we have

$$F_{01} = F_{23} = \frac{F^a}{2g_s}t^a\,, \quad F^a_{01} = \frac{F^a}{2g_s}\,, \quad F^a = Fn^a\,, \tag{3.77a}$$

with a constant vector n^a with $n^a n^a = 1$. The field strength (3.77a) can be generated from the gauge fields

$$A^a_\mu = -\frac{1}{2}F^a_{\mu\nu}x_\nu\,. \tag{3.77b}$$

Evidently, the configuration is self-dual,

$$F_{\mu\nu} = \tilde{F}_{\mu\nu}\,, \quad \text{with} \quad \tilde{F}_{\mu\nu} = \frac{1}{2}\epsilon_{\mu\nu\rho\sigma}F_{\rho\sigma}\,, \tag{3.77c}$$

and is covariantly constant, $[D_\rho\,,\, F_{\mu\nu}] = 0$.

The classical action and the classical potential $\mathcal{W}_{\text{cl}}$ as well as the color condensate (3.71) is obtained from the field strength squared, which reads for the configuration (3.77),

$$F_{\mu\nu}F_{\mu\nu} = \frac{F^2}{g_s^2}(n^a t^a)^2\,, \qquad F^a_{\mu\nu}F^a_{\mu\nu} = \frac{1}{g_s^2}F^2\,. \tag{3.78}$$

For example, for the configuration (3.77) with (3.78), the classical potential reduces to

$$\mathcal{W}_{\text{cl}}(F^a) = \frac{1}{2}\ \text{Tr}\ F^a F^b\, t^a t^b = \frac{1}{4g_s^2}F^2\,, \tag{3.79}$$

where Tr is the group trace in the fundamental representation as in (3.19). From now on we only consider configurations of the type (3.77), and hence $\mathcal{W}_{\text{eff}}$ will be written as a function of Fn^a, that is $\mathcal{W}_{\text{eff}}(F^a)$ instead of $\mathcal{W}_{\text{eff}}(F_{\mu\nu})$. The factor $1/g_s^2$ in (3.78) reflects the RG scaling of the field strength, and has been introduced for convenience. Moreover, as both the gauge fields and the field strength in (3.77b) point in direction n^a of the algebra, they can be rotated into the Cartan subalgebra without loss of generality.

Below, we briefly discuss $SU(2)$ and $SU(3)$ gauge groups, the former case as the simplest example, the latter case for its physical relevance:

In the $SU(2)$ gauge group, the Cartan subalgebra is generated by $t^3 = \sigma^3/2$ and the self-dual field strength (3.77) is given by

$$F_{01} = F_{23} = \frac{F}{2g_s}\,t^3\,. \tag{3.80}$$

We have already discussed above that in $SU(2)$ the symmetric group invariant d^{abc} vanishes, and hence $\chi^{AB}_{SU(2)} = 0$, implying $(F_{\mu\nu}F_{\mu\nu})^{AB} = F^a_{\mu\nu}F^a_{\mu\nu}\delta^{AB}/4$ for all configurations. For (3.80) we find

$$(F_{\mu\nu}F_{\mu\nu})^{AB} = \frac{F^2}{4g_s^2}\delta^{AB}\,. \tag{3.81}$$

The explicit computation here is done for the physical gauge group $SU(3)$ with the Cartan generators t^3, t^8. These are related to the Gell-Mann matrices by $t^a = \lambda^a/2$, the respective vector n has the components $n^a = 0$ for $a \neq 3, 8$. A self-dual field strength (3.77) is given by

$$F_{01} = F_{23} = \frac{F}{2g_s}\left(n^3 t^3 + n^8 t^8\right). \tag{3.82}$$

The octet condensate operator (3.71) for the configuration (3.82) reads

$$\begin{aligned}\chi^{AB} &= \frac{F^2}{2g_s^2}\left[n^a n^b \left\{t^a\,,\, t^b\right\}^{AB} - \frac{1}{3}\delta^{AB}\right] \\ &= \frac{F^2}{2g_s^2}\delta^{AB}\left[\delta^{A1}\nu_+ + \delta^{A2}\nu_- + \delta^{A3}\nu_3\right]\,,\end{aligned} \tag{3.83}$$

where

$$\nu_\pm = \frac{1}{2}\left(\frac{n^8}{\sqrt{3}} \pm n^3\right)^2 - \frac{1}{3}\,, \qquad \nu_3 = \frac{2}{3}(n^8)^2 - \frac{1}{3}\,, \tag{3.84}$$

where the trace(less) condition, $\chi^{AA} = 0$, translates into $\nu_+ + \nu_- + \nu_3 = 0$ with $(n^3)^2 + (n^8)^2 = 1$.

Non-vanishing octet condensate expectation values are in one to one correspondence to non-trivial expectation values of its corresponding gauge invariant eigenvalues. Hence, a non-trivial expectation value of the field strength triggers one for the octet condensate χ^{AB} and other color condensate operators. Therefore, in Section 3.2.3, we compute the effective potential for covariantly constant field strength or rather $\mathcal{W}_{\text{eff}}[Fn^a]$ for the field strength amplitude Fn^a defined in (3.77a), and the constant algebra element $n^a t^a$ is rotated into the Cartan subalgebra leading to (3.82). The respective effective potential is shown in Figure 3.1 for the physical $SU(3)$ case with the two Cartan components $F_{01}n^3$ and $F_{01}n^8$.

Our explicit computation of the effective gluon mass is based on an expansion about the minimum $\langle F\rangle(n^a)$ in the three-direction with $n^a = \delta^{a3}$. In $SU(2)$ this is the Cartan direction, and in $SU(3)$ one of the absolute minima points in the three-direction, see Figure 3.1. Then, the expansion about the minimum reads

$$F^a_{01} = F^a_{23} = \frac{\langle F\rangle}{2g_s}\delta^{a3} + \mathcal{O}(a)\,, \tag{3.85}$$

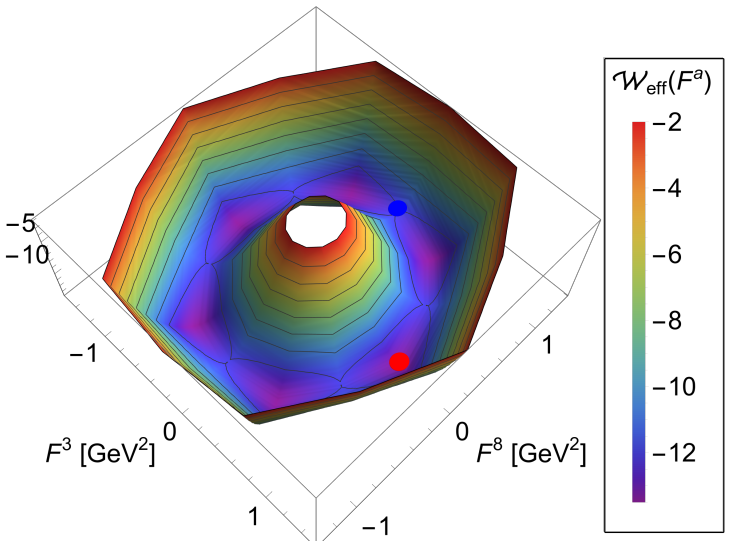

Abbildung 3.1.: Effective potential $\mathcal{W}_{\text{eff}}(F^a)$ in the plane spanned by the Cartan subalgebras. The position of the non-trivial global minimum is highlighted in red.

for both gauge groups, where a_μ is the gauge field, that carries the fluctuations about the field strength expectation value. With (3.77b) we can deduce a gauge field, that generates (3.85). We find,

$$A^a_\mu = \frac{\langle F \rangle}{4g_s}\Big(x_0\delta_{\mu 1} - x_1\delta_{\mu 0} + x_2\delta_{\mu 3} - x_3\delta_{\mu 2}\Big) + a^a_\mu\,, \tag{3.86}$$

which points in the same Cartan direction as the field strength. The fluctuation field a_μ carries the dynamics of the gauge field, leading to the $\mathcal{O}(a)$-terms in (3.85). Within this setting we shall derive our estimates for the effective gluon mass as well as discuss constraints and bounds for this mass.

3.2.1.3. Color condensates and the gluon mass gap

It is left to discuss the emergence of an effective gluon mass term in the presence of gluon condensates via the expectation value $\langle F^a_{\mu\nu}\rangle \propto \delta^{a3}$ in Equation (3.85), or any other algebra direction. This expectation value is computed from the effective potential $\mathcal{W}(F^a)$ introduced in Section 3.2.1.2.

Expanding the effective potential in powers of the fluctuation field gauge field a_μ leads to contributions to the n-point functions of the gauge field, including the two-point function. However, neither a contribution to the mass operator $a^a_\mu a^a_\mu$ is generated, nor do we obtain mass terms in specific algebra directions. In particular, no mass contribution in the Cartan $a = 3$ direction is induced, as is readily shown for $SU(2)$.

While the effective potential does not contribute to the effective mass term, the latter receives contributions from other terms in the full, gauge invariant quantum effective action $\Gamma[A]$. Such an action can be defined within the background field approach, which will be detailed in Section 3.2.2. For the time being we simply assume its existence and consider

the higher order term

$$\Gamma_F[A] = \frac{Z_F}{4}\int_x (D_\mu F_{\nu\rho})^a (D_\mu F_{\nu\rho})^a \,, \tag{3.87}$$

where Z_F is the wave function renormalisation of the condensate term. Equation (3.87) is the lowest order term that generates an effective gluon mass term within an expansion about the condensate $\langle F\rangle$. An obvious generalisation of (3.87) is provided by

$$\frac{1}{4}\int_x (D_\mu F_{\rho\sigma})^a Z_F{}^{ab}_{\rho\sigma\alpha\beta}(F_{\mu\nu})(D_\mu F_{\alpha\beta})^b \,, \tag{3.88}$$

with $Z_F{}^{ab}_{\rho\sigma\alpha\beta}(0) = Z_F\delta_{\rho\alpha}\delta_{\sigma\beta}\delta^{ab}$. In the following we will use the approximation

$$Z_F{}^{ab}_{\rho\sigma\alpha\beta}(\langle F_{\mu\nu}\rangle) \approx Z_F{}^{ab}_{\rho\sigma\alpha\beta}(0) \,, \tag{3.89}$$

hence only considering the term (3.87).

Equation (3.87) leads to an effective gluon mass, but does not contribute to (covariantly constant) solutions of the equations of motions as its first field derivative vanishes for covariantly constant field strengths. The relevant contribution to the effective gluon mass term is obtained by expanding (3.87) in powers of the gauge field, while treating the field strength within the expansion (3.85). To that end we conveniently recast (3.87) into the form

$$\Gamma_F[A] = -\frac{Z_F}{2}\int_x F^{CB}_{\nu\rho}(D^2)^{BA}F^{AC}_{\nu\rho} \,, \tag{3.90}$$

where the factor $1/2$ in (3.87) is now carried by the trace in the fundamental representation. The $\mathcal{O}(A^2)$ term is given by

$$\Gamma_F[A] = \frac{Z_F}{2}\,g_s^2\int_x (F_{\nu\rho}F_{\nu\rho})^{AB}\,(A_\mu A_\mu)^{BA} + \cdots \,, \tag{3.91}$$

and we expand $(F_{\nu\rho}F_{\nu\rho})^{AB}$ about the field strength expectation value (3.85). This implies a non-vanishing condensate expectation value for (3.71) as well as non-vanishing values for other color condensate operators. The expansion about (3.85) leads us to

$$(F_{\nu\rho}F_{\nu\rho})^{AB} = \frac{1}{g_s^2}\langle F\rangle^2[(n^a t^a)^2]^{AB} + \mathcal{O}(a) \,. \tag{3.92}$$

We drop the higher order terms in (3.92) and insert it in (3.91), to wit,

$$\Gamma_F[A] \simeq \frac{Z_F}{2}\langle F\rangle^2\int_x \mathrm{Tr}\,(t^3)^2 A_\mu^2 + \cdots \,, \tag{3.93}$$

with the group trace in the fundamental representation. Now we evaluate (3.93) for the configurations (3.77), which leads to our final expression for the effective gluon mass triggered by an expectation value of the field strength proportional to t^3. For general gauge groups, (3.93) is not color-blind, which originates in the colored expansion point. It can be used to deduce the color-blind mass by a color average discussed in Appendix A.1.

Before we come to our final color-blind estimates, we exemplify (3.93) within $SU(2)$ and $SU(3)$. We first discuss the simple example of an $SU(2)$ gauge group. There, the

configuration (3.85) leads to an $F_{\mu\nu}^2$ that is proportional to the identity tensor $\mathbb{1}$ in the algebra, as $4(t^3)^2 = \mathbb{1}$. Indeed, as discussed below (3.80), general field strength tensors lead to diagonal $F_{\mu\nu}^2$. In summary, in $SU(2)$, a field strength condensate in the t^3-direction leads to

$$\Gamma_F[A] \simeq \frac{1}{2} m_3^2 \int_x A_\mu^a A_\mu^a + \cdots , \quad m_3^2 = \frac{Z_F}{8} \langle F \rangle^2 , \tag{3.94}$$

with a uniform mass m_3 for all gluons. The subscript indicates that, while uniform, the mass is generated by $\langle F_{\mu\nu}^a \rangle \propto \delta^{a3}$. Importantly, (3.94) entails that a color condensate leads to gluons with an effective mass. However, the current procedure with an expansion about a non-vanishing field strength does not allow to directly infer the full effective gluon mass obtained in a color-blind computation from m_3^2 in (3.94). At this stage we only can offer estimates, whose derivation is deferred to the end of the present section.

Before we come to these estimates, we proceed with the $SU(3)$ example. There, we also use the Cartan-valued configuration (3.85) (with $n^8 = 0$) as one of the absolute minima in the full effective potential $\mathcal{W}_{\text{eff}}$ points in this direction, see Figure 3.1. In contradistinction to $SU(2)$, the square $4(t^3)^2$ is not the identity matrix in the algebra, but a projection onto the first two colors,

$$[(t^3)^2]^{AB} = \frac{1}{4} \delta^{AB} \left(\delta^{A1} + \delta^{A2} \right) . \tag{3.95}$$

As expected, the expansion about a minimum of the field strength, related to one about the octet condensate (3.71), breaks color, and indeed, the gluon with the third color is massless if only considering contributions from Γ_F. Hence, while the present expansion shows, that the gluons acquire an effective mass term $\propto \delta^{ab}$, the relation of its *necessarily color-blind* value m_A^2 to the color-sensitive masses derived here is not straightforward.

Therefore, here we simply deduce self-consistency constraints for the effective mass m_A^2 starting with the gluon mass m_3^2, inferred from a field strength in the t^3 direction. To begin with, color symmetry can be restored by averaging over global color rotations as always implied in lattice simulations as well as in most computations in functional QCD. After this averaging, all masses are identical and non-vanishing. A color average of (3.93) leads us to

$$\Gamma_{A^2}[A] = \frac{Z_F}{2} f_{\text{av}}(N_c) \langle F \rangle^2 \int_x A_\mu^a A_\mu^a , \tag{3.96}$$

with $f_{\text{av}}(N_c)$ encodes the color average of the factor $(t^3)^2$ in (3.93),

$$f_{\text{av}}(N_c) = \langle (t^3)^2 \rangle_{\text{av}} . \tag{3.97}$$

The color average in (3.97) necessarily leads to a color insensitive sum over all generators squared in the fundamental representation, which is simply the second Casimir $C_2(N_c) = (N_c^2 - 1)/(2N_c)$ times the identity matrix. Moreover, there is an undetermined prefactor $c_{\text{av}}(N_c)$, which leads us to

$$\left\langle (t^3)^2 \right\rangle_{\text{av}} = c_{\text{av}}(N_c) \sum_{a=1}^{N_c^2-1} (t^a)^2 = c_{\text{av}}(N_c) C_2(N_c) \mathbb{1} . \tag{3.98}$$

Here we will only provide constraints for $c_{\rm av}(N_c)$ and hence for $f_{\rm av}(N_c)$ in (3.97). For example, a 'natural' bound for the averaging factor is unity, $c_{\rm av}(N_c) \leq 1$.

In summary, we arrive at

$$m_A^2 = \frac{Z_F}{2} f_{\rm av}(N_c) \langle F \rangle^2 \,, \tag{3.99}$$

In Section 3.2.2.3 we will show, that self-consistency of the averaging in the large N_c limit entails that in this limit $f_{\rm av}(N_c) \propto N_c$. Indeed, this limit holds true for N_c-independent $c_{\rm av}$. In particular this includes the case, where we saturate the 'natural' bound $c_{\rm av} = 1$, leading to

$$f_{\rm av} = (N_c^2 - 1)/(2N_c) \,. \tag{3.100}$$

For this saturation $f_{\rm av}$ we obtain

$$m_A^2 = \frac{Z_F}{4} \frac{N_c^2 - 1}{N_c} \langle F \rangle^2 \,, \tag{3.101}$$

Equation (3.101) will eventually yield our estimate of the effective gluon mass. In Section 3.2.2, we present the formalism employed for working with the constant field strength configurations in (3.78). The computation of the minimum position $F^a = \langle F \rangle n^a$ is detailed in Section 3.2.3, and an estimate of the wave function of the condensate together with the result for the mass gap is presented in Section 3.2.4.

3.2.2. Background field approach

The condensate $\langle F \rangle$ for the field strength configuration of (3.82) is given by the minimum of an effective potential $\mathcal{W}_{\rm eff}(F\, n^a)$, derived from a gauge invariant effective action $\Gamma[A]$, see (3.76). Such an action is defined in the background field approach [169], building on a linear decomposition of the full gauge field A_μ into a fluctuating and background field. This linear split is given by $A_\mu = \bar{A}_\mu + a_\mu$, where a_μ denotes the fluctuation field and $\bar{A}_\mu$ the background field. On the quantum level, this relation has to be augmented with the respective wave function renormalisations $Z_{\bar{A}} = Z_{g_s}^{-2}$ for the background field $\bar{A}_\mu$ and Z_a for the fluctuation field a_μ, as the two fields carry different RG scalings: As indicated above, the background field scales inversely to the strong coupling, while the fluctuation field carries the RG scaling of the gauge field in the underlying gauge without background field. The gauge fixing condition involves the background field,

$$\bar{D}_\mu a_\mu = 0 \,, \tag{3.102}$$

with the background covariant derivative $\bar{D} = D(\bar{A})$, see (3.10). Note, that (3.102) is invariant under background gauge transformations,

$$a \to a + i\,[\omega, a] \,, \qquad \bar{A} \to \bar{A} + \frac{1}{g_s} \bar{D}\omega \,, \tag{3.103}$$

implying a standard gauge transformation for the full gauge field: $A_\mu \to A_\mu + (1/g_s) D\omega$. Consequently, the full gauge-fixed classical action is invariant under (3.103), and so is the full effective action $\Gamma[\bar{A}, a]$. Moreover, the single-field background field effective action $\Gamma[A] := \Gamma[A, 0]$ is gauge invariant and can be expanded in gauge invariant operators. For this reason, it also allows for a more direct access to observables. In what follows we use the potential condensate background (3.77).

3.2.2.1. Background field effective action

The gauge invariance of the background field effective action allows us to embed the momentum-dependent kinetic terms and vertices in an expansion about a vanishing gauge field in full gauge invariant terms that reduce to the original ones for $A_\mu \to 0$. An important example is given by the (transverse) kinetic term of the gauge field, see, e.g., [138, 139, 148],

$$\Gamma[A] \propto \frac{1}{2}\int_p A^a_\mu(p)\, Z_A(p^2)\, p^2\, \Pi^\perp_{\mu\nu}(p)\, A^a_\nu(-p)\,, \tag{3.104}$$

with the abbreviation $\int_p = \int d^4p/(2\pi)^4$, and the transverse and longitudinal projection operators

$$\Pi^\perp_{\mu\nu}(p) = \delta_{\mu\nu} - \frac{p_\mu p_\nu}{p^2}\,, \qquad \Pi^\parallel_{\mu\nu}(p) = \frac{p_\mu p_\nu}{p^2}\,. \tag{3.105}$$

The kinetic operator $Z_A(p^2)p^2$ is identified as the $A_\mu \to 0$ limit of the second field derivative of a gauge invariant term in the effective action $\Gamma[A]$. This leads us straightforwardly to the parametrisation

$$\Gamma[A] = \frac{1}{2}\int \mathrm{Tr}\, F_{\mu\nu} f_{A,\mu\nu\rho\sigma}(D) F_{\rho\sigma} + \cdots\,, \tag{3.106a}$$

with the split

$$f_{A,\mu\nu\rho\sigma}(D) = \frac{1}{2} Z_A(\Delta_s)(\delta_{\mu\rho}\delta_{\nu\sigma} - \delta_{\mu\sigma}\delta_{\nu\rho}) + F_{\gamma\delta} f_{A,\gamma\delta\mu\nu\rho\sigma}(D)\,. \tag{3.106b}$$

In (3.106b), we have introduced the spin-s Laplacians

$$\Delta_0 = -D^2\,, \qquad \Delta_{1,\mu\nu} = \mathcal{D}_{T,\mu\nu} = -D^2\delta_{\mu\nu} + 2ig_s\, F_{\mu\nu}\,, \tag{3.106c}$$

see also (B.1). Equation (3.106b) represents the most general parametrisation for a covariant function coupled to two field strengths. Since $f_{A,\gamma\delta\mu\nu\rho\sigma}$ is a function of the covariant derivative D, higher order terms in the field strength tensor are contained in the second term of (3.106b). For $A_\mu = 0$, all these decompositions reduce to their the momentum-dependent versions. In particular, the kinetic term (3.104) is obtained from (3.106b) by taking two gauge field derivatives at $A = 0$.

A further relevant example is the sum of the classical action and the term Γ_F in (3.87) that generates the effective gluon mass. This combination is obtained with

$$Z_A(-D^2) = Z_A - Z_F D^2\,, \quad f_{A,\gamma\delta\mu\nu\rho\sigma} = 0\,. \tag{3.107}$$

Here, Z_A is the constant background wave function renormalisation multiplying the classical action, which also entails $Z_A = Z_{g_s}^{-2}$.

The example given in (3.107) is central for two reasons: First, it demonstrates how the condensate studied here emerges from the general, gauge invariant form of the effective action (3.106a), which is defined in the next section within the background field formalism. Second, it establishes a link between the wave function renormalisation of the condensate and the kinetic operator of the gluon field $Z_A(\Delta_s)$. More explicitly, due to the generality of the split (3.106b), (3.107) entails that the wave function renormalisation of the condensate (3.87) is simply given by the D^2-coefficient of the dressing function of the gluon

propagator. In the limit of vanishing background, this simply corresponds to the p^4-term in the inverse gluon propagator.

Note that the use of different Δ_s in the split (3.106b) leads to different forms for $f_{\mu_1\cdots\mu_6}$, thus modifying the parametrisation of the kinetic term. Still, the different field modes carry different spin, and the use of the respective Laplacians makes the split in (3.106b) to be the most natural. Typically, higher order terms within this split are suppressed in the effective action. For example, the second derivative of the classical Yang-Mills action with respect to the gauge field is given by $\Delta_1 = \mathcal{D}_T$, multiplied by a covariant transverse projection operator. For covariantly constant fields with $[D, F] = 0$, we get

$$\frac{\delta^2}{\delta A_\rho \delta A_\sigma} \frac{1}{2} \int_x \mathrm{Tr}\, F_{\mu\nu}^2 = \mathcal{D}_{T,\rho\gamma}\, \Pi^\perp_{\gamma\sigma}(D)\,, \tag{3.108}$$

where the trace is taken in the fundamental representation. Above, we introduced the covariant transverse and longitudinal projections,

$$\Pi^\perp_{\mu\nu}(D) = \delta_{\mu\nu} - \Pi^\parallel_{\mu\nu}(D)\,, \quad \Pi^\parallel_{\mu\nu}(D) = D_\mu \frac{1}{D^2} D_\nu\,, \tag{3.109}$$

defining a decomposition in a covariantly transverse subspace with $D_\mu \Pi^\perp(D) = 0$. It is complete, $\Pi^\perp(D) + \Pi^\parallel(D) = \mathbb{1}$, and trivially orthogonal. Finally, the operators have the projection property $(\Pi^\perp(D))^2 = \Pi^\perp(D)$ and $(\Pi^\parallel(D))^2 = \Pi^\parallel(D)$.

3.2.2.2. Ghost and gluon two-point functions

When supplemented by a wave function renormalisation $Z_A(\mathcal{D}_T)$, (3.108) provides a very good approximation of the full two-point function of the background gluon. This suggests the split in (3.106b) with the spin one Laplacian $\Delta_1 = \mathcal{D}_T$ for the transverse two-point function, and with the second term being subleading,

$$\Gamma^{(2,0)}_{AA,\mu\nu}[A,0] = Z_A(\mathcal{D}_T)\, \mathcal{D}_{T,\mu\sigma}\, \Pi^\perp_{\sigma\nu}(D) + F_{\gamma\delta}\, \Delta f_{A,\gamma\delta\mu\sigma}(D)\, \Pi^\perp_{\sigma\nu}(D)\,, \tag{3.110}$$

where $\Delta f_{A,\gamma\delta\mu\nu}$ is a combination of derivatives of $f_{A,\mu\nu\rho\sigma}$ fully contracted with powers of the field strength, see (3.106b), and $\bar{A} = A$. The transversality of (3.110) follows from the gauge invariance of the background field effective action, as does its covariance. In (3.110) we have used the notation

$$\Gamma^{(n,m)}_{\bar{A}^n \phi_{i_1}\cdots\phi_{i_m}}[\bar{A},\phi] = \frac{\Gamma[\bar{A},\phi]}{\delta \bar{A}^n \delta \phi^m}\,, \qquad \phi = (a,c,\bar{c})\,, \tag{3.111}$$

with ϕ denoting the ghost and gluon fluctuation field. We shall use the split (3.106b) leading to (3.110) and similar natural splits for the covariant versions of the momentum dependent two-point functions, thus going from the Landau gauge to the Landau-DeWitt gauge.

In particular one finds, that a similar line of arguments holds true for the kinetic operator $Z_a(p^2)p^2$ of the fluctuation field a_μ,

$$\Gamma^{(0,2)}_{aa,\mu\nu}[0,0] = Z_a(p^2)\, p^2 \Pi^\perp_{\mu\nu}(p) + \frac{1}{\xi} p^2 \Pi^\parallel_{\mu\nu}(p)\,, \tag{3.112}$$

where (3.105) was employed, and a diagonal form in the algebra, $\mathbb{1}^{ab} = \delta^{ab}$, is implied. Background gauge invariance entails that $\Gamma^{(0,2)}[A,0]$ is a covariant operator under the background gauge transformations (3.102). In consequence, the transverse part

of $\Gamma^{(0,2)}_{aa}[A,0]$ can be parametrised by the generic form of a background gauge covariant function already employed in (3.106b), i.e.,

$$\Gamma^{(0,2)}_{aa,\mu\nu}[A,0] = Z_a(\mathcal{D}_T)\,\mathcal{D}_{T,\mu\sigma}\,\Pi^{\perp}_{\sigma\nu}(D) - \frac{1}{\xi}D^2\,\Pi^{\parallel}_{\mu\nu}(D) + F_{\gamma\delta}\,\Delta f_{a,\gamma\delta\mu\sigma}(D)\,\Pi^{\perp}_{\sigma\nu}(D)\,. \quad (3.113)$$

In (3.113) we have used the spin-1 Laplacian $\Delta_1 = \mathcal{D}_T$ defined in (3.106c) in the wave function renormalisation Z_a, since the transverse fluctuating gluon is a spin-1 field. For two-flavor QCD, the validity of such covariant expansions has been confirmed explicitly for the quark-gluon vertex, whose non-classical tensor structure can be related to higher order gauge invariant terms $\bar{q}\not{D}^n q$ [166].

Finally, in the case of the ghost two-point function we parametrise

$$\Gamma^{(0,2)}_{c\bar{c}}[A,0] = -D^2 Z_c(-D^2) + F_{\mu\nu}\,\Delta f_{c,\mu\nu}(D)\,, \quad (3.114)$$

where the use of the spin zero Laplacian in (3.114) is suggested by the ghost being a spin zero field. For $A_\mu = 0$, the ghost two point function in (3.114) reduces to that in standard covariant gauges.

The infrared behaviour of $Z_a(p)$ in the Landau gauge is an extensively studied subject, both on the lattice and with functional approaches, see, e.g., [63, 107, 132, 133, 135, 136]. In particular, two types of solutions have emerged, discussed in the context of confinement in Section 3.1.5. We briefly recapitulate them here and connect to the notation used in this section:

(*i*) The *scaling* solution [88] has an infrared vanishing gluon propagator and a scaling infrared behaviour,

$$Z_{a,\mathrm{IR}} \propto (-D^2)^{-2\kappa}\,, \qquad Z_{c,\mathrm{IR}} \propto (-D^2)^{\kappa}\,, \quad (3.115)$$

with $\kappa \approx 0.6$. In (3.115) we have dropped terms proportional to the field strength. Note that in this IR solution the ghost dressing function is infrared divergent. For the present computations we shall use the fRG results from [95] within a quantitatively reliable approximation, for respective DSE results see [93].

(*ii*) An entire family of *decoupling* or *massive* solutions [142], where the gluon propagator and the ghost dressing function saturate at finite non-vanishing values at the origin, in agreement with the IR behaviour found in large-volume lattice simulations. Specifically, we have

$$Z_{a,\mathrm{IR}} \propto \frac{1 + c_a D^2 \log\left(\frac{-D^2}{\Lambda^2_{\mathrm{QCD}}}\right)}{-D^2}\,, \qquad Z_{c,\mathrm{IR}} \propto c_c\,. \quad (3.116)$$

Note that the fluctuating propagator can be mapped to the background one by means of an exact identity, characteristic of the Batalin-Vilkoviski formalism, which involves a special two-point function, see, e.g., [135, 170].

We emphasise that both types of solutions agree quantitatively for momenta $p^2 \gtrsim \Lambda^2_{\mathrm{QCD}}$, with Λ_{QCD} related to the infrared mass gap. As a result, the deviations induced to phenomenological observables by the use of either type are quantitatively minimal, see, e.g., [166, 171]. In fact, here we will cover all potential solutions listed above, and show that

their IR differences are immaterial to the central question of the presence of dynamical condensate formation.

Both types of solutions, (3.115) and (3.116), are infrared irregular, and do not admit a Taylor expansion about $-D^2 = 0$. Instead, we can expand the wave function renormalisations about the infrared asymptotics. Making use of the relation between the condensate and gluon wave function renormalisation established in (3.107), we arrive at

$$Z_{a/A}(-D^2) = Z_{a/A,\mathrm{IR}}(-D^2) + (-D^2)\, Z_{a/A,F} + \mathcal{O}(D^4)\,, \tag{3.117}$$

for both Z_a and Z_A with $Z_{a/A,\mathrm{IR}}$ defined in (3.115) and (3.116), and $Z_{a/A,F}$ is the wave function Z_F for fluctuation and background field respectively. The first term $Z_{a/A,\mathrm{IR}}$ carries the irregular infrared asymptotic behaviour, and $Z_{a/A,F}$ is the (uniquely defined) constant prefactor of the linear term in $-D^2$. The expansion (3.117) makes explicit that scaling and decoupling solutions only differ in the IR leading term $Z_{a/A,\mathrm{IR}}$, while coinciding in the expansion in powers of $-D^2$. This in particular entails that the overlap between gluon propagator and the condensate (3.87) is independent of the leading IR behaviour of the respective solution, scaling or decoupling.

We are ultimately interested in the physical mass gap m_{gap} of the fluctuation field a_μ resulting from the condensate term (3.87) in the full field $A = \bar{A} + a$. The derivation of the fluctuation field mass gap works analogously to that of (3.99) in Section 3.2.1.3, and leads to a contribution Γ_{gap} in the effective action with

$$\Gamma_{\mathrm{gap}} = \frac{1}{2} m_{\mathrm{gap}}^2 \int_x a_\mu^b a_\mu^b\,, \tag{3.118}$$

where the effective gluon mass of the fluctuation gluon a_μ is given by

$$m_{\mathrm{gap}}^2 = \frac{Z_{\mathrm{cond}}}{2} f_{\mathrm{av}}(N_c) \langle F \rangle^2\,, \tag{3.119}$$

with $Z_{\mathrm{cond}} = Z_{a,F}$ and the averaging factor $f_{\mathrm{av}}(N_c)$ introduced in (3.96) and discussed there. In particular, we have $Z_F = Z_{A,F} \neq Z_{\mathrm{cond}}$. The wave function Z_F is used in (3.99) for the mass term in a gauge invariant effective action, and in the present approach this is the background field effective action. The difference between the wave functions Z_F and Z_{cond} is the ratio of the respective wave functions of the background and fluctuation gluons.

In (3.107) we observed that the wave function renormalisation Z_{cond} of the condensate studied here generally appears in the dressing function of the respective gluon propagator, cf. (3.117). This connection will be utilised in Section 3.2.4 to determine Z_{cond} from the input gluon propagators [95] employed in the computation of the background field effective potential $\mathcal{W}_{\mathrm{eff}}(F^a)$. Supplemented with the non-trivial effective potential minimum $\langle F \rangle$, this procedure eventually lead to our heuristic estimate of the gluon mass gap in Landau gauge Yang-Mills theory.

3.2.2.3. Large N_c-scaling and self-consistency

The effective gluon masses m_A^2 in (3.99) and m_{gap}^2 in (3.119) show an explicit $1/N_c$-scaling, while no N_c-scaling is present in the large N_c limit, if the theory is formulated in the 't Hooft coupling

$$\lambda = N_c g_s^2\,. \tag{3.120}$$

This property serves as a self-consistency check of our computation and specifically our group average used to derive (3.99), (3.119) and entailed in $f_{\rm av}(N_c)$

An illustrative and relevant example are the functional relations of the two-point function $\Gamma^{(0,2)}_{aa}(p)$. Cast in a relation for the wave function $Z_a(p)$, they read

$$Z(p^2) = Z_{\rm in} + g_s^2\, N_c\, {\rm Diags}_1 + \mathcal{O}(N_c^0)\,, \tag{3.121}$$

where the right-hand side stands for the typical loop diagrams of, e.g., (integrated) fRG flows or Dyson-Schwinger equations. Here, $Z_{\rm in}$ stands for the input dressing, either the one at the initial UV cutoff scale (fRG) or the classical dressing (DSE). In most cases the $\mathcal{O}(N_c^0)$ term is dropped, for an exception as well as a respective discussion see [172]. The term ${\rm Diags}_1$ stands for the loop integral that depends on the wave functions of all the fields and the full vertex dressings. Importantly, the functional relations for all other vertex dressings and wave functions have the same form as (3.121). Accordingly, if dropping the subleading term of the order $O(N_c^0)$, all functional relations only depend on the 't Hooft coupling (3.123), and so do all correlation functions. Respective lattice studies also reveal that the large N_c-limit is achieved already for $N_c \gtrsim 3$ for most correlation functions, for a review see [173].

In summary, we deduce that in the large N_c-limit the only N_c-dependence of the effective gluon masses m_A^2 in (3.99) and $m_{\rm gap}^2$ in (3.119) is implicit in the dependence on the 't Hooft coupling (3.123). This concludes our brief discussion of the N_c-scaling of correlation functions.

The relations for the effective gluon mass, (3.99), (3.119), show an even more direct scaling consistency: $Z_{\rm F}$ is an expansion term in the two-point function of the fluctuating gluon. Moreover, in the presence of the condensate this two-point function approaches the effective gluon for vanishing momentum,

$$\lim_{p\to 0} \Pi^{\perp}_{\mu\nu}(p)\Gamma^{(0,2)}_{aa,\mu\nu}(p) = 3\, m_{\rm gap}^2\,. \tag{3.122}$$

Accordingly, both $Z_{\rm cond}$ and $m_{\rm gap}$ have the same N_c-scaling (only dependent on the 't Hooft coupling in the large N_c-limit) as well as the same RG scaling. In conclusion, the ratio $Z_{\rm cond}/m_{\rm gap}^2$ is manifestly RG invariant as well as N_c-independent in the large N_c-limit. This implies already, that the RG invariant information in the effective gluon mass is given by $f_{\rm av}(N_c)\,\langle F\rangle^2$. The value of the mass itself depends on the RG condition and should not be confused with the gluon mass gap. The latter can be defined as the inverse screening length of the gluon propagator which is indeed RG invariant.

In summary, $f_{\rm av}(N_c)\,\langle F\rangle^2$ should be N_c-independent in the large N_c-limit. This fixes the N_c-scaling of $f_{\rm av}(N_c)$, given that of $\langle F\rangle^2$. The N_c-scaling of the latter is obtained by an N_c-analysis of the effective potential, whose explicit computation is detailed in Section 3.2.3 and Appendix B.2. Here we only need that it consists out of an ultraviolet classical piece of the form (3.79) and a term that depends on N_cF^2,

$$\mathcal{W}_{\rm eff}(F^a) = \frac{1}{4g_s^2}F^2 + \Delta\mathcal{W}_{\rm eff}(N_cF^2)\,, \tag{3.123}$$

see Section 3.2.3.2. In (3.123), g_s^2 is the strong coupling at a large momentum scale $k_{\rm UV}$, and we will use $k_{\rm UV} = 20\,{\rm GeV}$ for this scale later on. We now absorb N_c into the field strength squared amplitude F^2, i.e., $\bar{F}^2 = N_cF^2$. With (3.120) this leads us to

$$\mathcal{W}_{\rm eff}(F^a) = \frac{1}{4\lambda}\bar{F}^2 + \Delta\mathcal{W}_{\rm eff}(\bar{F}^2)\,, \tag{3.124}$$

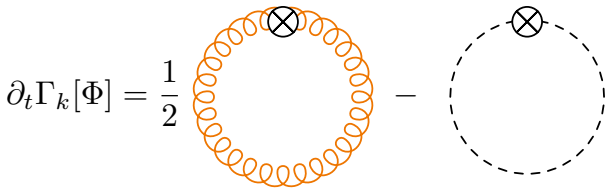

Abbildung 3.2.: Depiction of the flow equation for the effective action, (3.126). Spiralling orange lines depict the full field-dependent gluon propagator $\langle AA\rangle_c = G_{aa}[\bar{A},\phi]$, dashed back lines depicted the full field-dependent ghost propagator $\langle c\bar{c}\rangle_c = G_{c\bar{c}}[\bar{A},\phi]$, where the subscript stands for connected part. The circled cross stands for the regulator insertions $\partial_t R_a$ (gluon loop) and $\partial_t R_c$ (ghost loop).

and consequently

$$\langle \bar{F}\rangle = \bar{F}_{\min}(\lambda) \qquad \longrightarrow \qquad \langle F\rangle = \frac{1}{\sqrt{N_c}}\bar{F}_{\min}(\lambda)\,. \tag{3.125}$$

The $1/N_c$-scaling for $\langle F\rangle^2$ derived in (3.125), is confirmed numerically in Appendix B.2. There, the effective potential and its minimum is computed in a leading order N_c approximation and hence shows the asymptotic $1/N_c$ scaling even for $N_c = 2$. This N_c-scaling is rooted in the adjoint representation trace of $n^a t^a$ appearing the definition of the covariantly constant field strength in (3.77), cf. (B.3). We have confirmed its numerical presence in a comparison of $N_c = 2, 3$.

3.2.3. Background field effective potential

Now we compute the value of the field strength condensate $\langle F_{\mu\nu}\rangle$ discussed in Section 3.2.1.2. For this purpose, we update the fRG computation done in [148] to a self-consistent one with fRG precision gluon and ghost propagators from [95]. In Section 3.2.3.1 we briefly review the approach, and in Section 3.2.3.3 we report on the results for the condensate.

3.2.3.1. Flow of the background field effective potential

For the full computation we resort to the functional renormalisation group approach; see Section 2.3 for an introduction and [58, 59, 62, 63, 174, 175] for QCD-related reviews. In this approach, an infrared regulator $R_k(p)$ is added to the classical dispersion. In the infrared, that is $p/k \to 0$, the regulator endows all fields with a mass, typically proportional to the cutoff scale k. The regulator $R_k(p)$ vanishes rapidly as $p/k \to \infty$, and the ultraviolet physics is not modified; see (2.35). The change of the scale dependent effective action, Γ_k, under a variation of the cutoff scale k is described by the flow equation. In the background field approach it reads

$$\partial_t \Gamma_k[\bar{A},\phi] = \frac{1}{2}\,\mathrm{Tr}\; R_a[\bar{A}]\, G_{aa}[\bar{A},\phi] - \mathrm{Tr}\; R_c[\bar{A}]\, G_{c\bar{c}}[\bar{A},\phi]\,, \tag{3.126}$$

where $t = \log k/\Lambda$ is the (negative) RG time. G_A, G_c are the fluctuation propagators of gluon and ghost, respectively,

$$G_{\phi_1\phi_2}[\bar{A},\phi] = \left[\frac{1}{\Gamma_k^{(0,2)}[\bar{A},\phi] + R_k[\bar{A}]}\right]_{\phi_1\phi_2} . \tag{3.127}$$

The traces in (3.126) sum over momenta, Lorentz and gauge group indices, details can be found in Appendix B.1. The regulator function $R_k = (R_a, R_c)$ transforms covariantly under background gauge transformations, which preserve the background gauge invariance of the effective action. The current study utilises the propagator data from [95], which requires the use of the same regulators for our computation of the background field effective potential. For details on the regulators see Appendix B.3.

For the derivation of the (background) field strength condensate we solve the equation of motion stemming from the effective potential $\mathcal{W}_{\text{eff}}(F^a)$ of covariantly constant field strength defined in (3.76). In the fRG approach it is obtained from its scale-dependent analogue,

$$\mathcal{W}_k(F^a) = \frac{1}{\mathcal{V}}\Gamma_k[A(F^a),0]\,, \tag{3.128a}$$

with the full effective potential being defined at vanishing cutoff scale $k = 0$,

$$\mathcal{W}_{\text{eff}}(F^a) = \mathcal{W}_{k=0}(F^a)\,. \tag{3.128b}$$

The effective potential $\mathcal{W}_k$ is obtained by integrating the flow equation of the background field effective action $\partial_t\Gamma_k[A(F),0]$, derived from (3.126) from the initial ultraviolet scale k_{UV} to the running cutoff scale k. The only input in this flow are the two-point functions $\Gamma_{aa}^{(0,2)}[A(F),0]$ and $\Gamma_{c\bar{c}}^{(0,2)}[A(F),0]$, which we can infer from Landau gauge results. This is the background Landau-DeWitt gauge with $\bar{A} = 0$. For vanishing background the two-point functions only depend on momenta, $\Gamma_k^{(0,2)}(p)$. We use the results from [95], with

$$\begin{aligned}\Gamma_{aa,k}^{(0,2)}(p) &= p^2\, Z_{a,k}(p^2)\Pi^{\perp}(p) + p^2\left[\frac{1}{\xi} + Z_{a,k}^{\parallel}(p^2)\right]\Pi^{\parallel}(p)\,,\\ \Gamma_{c\bar{c}}^{(0,2)}(p) &= p^2\, Z_{c,k}(p^2)\,,\end{aligned} \tag{3.129}$$

with the transverse and longitudinal projection operators introduced in (3.105). Note that for the transverse dressing function, we omitted the $^{\perp}$-superscript in comparison to (3.63), and we will keep doing so in the further course of this work. In (3.129), $\mathbb{1}^{ab} = \delta^{ab}$ is implied in both two-point functions. The longitudinal dressing $Z_{a,k}^{\parallel}$ signals the breaking of BRST invariance due to the presence of the regulators, see Section 3.1.6, and vanishes in the limit $k \to 0$. There, the gluon two-point function in (3.129) reduces to that of (3.112). Moreover, $Z_{a,k}^{\parallel}$ is absent in the gluon propagator for the Landau gauge, $\xi \to 0$,

Now we switch on the background field and use the decomposition (3.113) for the transverse gluon two-point function. In addition, we drop the second line proportional to Δf_a comprising higher order terms. They are associated with non-classical tensor structures and can be shown to be small in the perturbative and semi-perturbative regimes. In the Landau-DeWitt gauge, only the gauge fixing survives in the longitudinal propagator, and

we can drop the cutoff contribution $Z^{\parallel}_{a,k}$. For the ghost we use (3.114), where we drop the second term proportional to Δf_c. This leads us to

$$\Gamma^{(0,2)}_{aa,k}(p) \simeq \mathcal{D}_T\, Z_{a,k}(\mathcal{D}_T)\Pi^{\perp}(-D) - \frac{1}{\xi} D_\mu D_\nu\,,$$
$$\Gamma^{(0,2)}_{c\bar{c}}(p) \simeq -\,D^2\, Z_{c,k}(-D^2)\,, \tag{3.130}$$

valid for covariantly constant field strength with $[D, F] = 0$. For these configurations, the transverse projection operator commutes with functions of the Laplacians Δ_0 and Δ_1.

3.2.3.2. RG consistent initial condition

The flow equation (3.128a) of the effective potential $\mathcal{W}_k(F^a)$ is readily obtained by inserting the approximations of (3.130) into the flow (3.126). The flow is evaluated for the generic condensate background (3.77). The details can be found in Appendix B.3. Finally, the effective potential $\mathcal{W}_{\text{eff}}(F^a)$ of Yang-Mills theory is obtained from the integrated flow. We arrive at

$$\mathcal{W}_k(F^a) = \mathcal{W}_{k_{\text{UV}}}(F^a) + \int_{k_{\text{UV}}}^{k} \frac{\mathrm{d}k'}{k'} \partial_{t'} \mathcal{W}_{k'}(F^a)\,, \tag{3.131}$$

where $\mathcal{W}_{k_{\text{UV}}}$ is well approximated by the classical potential (3.79) for a large initial cutoff scale k_{UV}. Perturbation theory is valid for these scales, and the background field effective action $\Gamma_{k_{\text{UV}}}[A]$ reduces to the classical Yang-Mills action of (3.19), augmented with a wave function renormalisation $Z_{A,k_{\text{UV}}}$. All other terms are suppressed by inverse powers of k_{UV}. This amounts to

$$\mathcal{W}_{k_{\text{UV}}}(F^a) = \frac{Z_{A,k_{\text{UV}}}}{4\, g_s^2} F^2 = \frac{F^2}{16\pi\alpha_s(k_{\text{UV}})}\,, \tag{3.132}$$

where

$$\alpha_s(k) = \frac{1}{4\pi} \frac{g_s^2}{Z_{A,k}}\,, \quad \text{with} \quad Z_{A,k_{\text{UV}}} = 1\,. \tag{3.133}$$

Here, $Z_{A,k}$ is the background wave function $Z_{A,k}(p = 0)$, and g_s^2 is the running coupling at the initial scale k_{UV}.

The onset of this asymptotic UV regime for cutoff scales $k \gtrsim k_{\text{on}}$ depends on the chosen regulator or rather its shape. Roughly speaking, the sharper the regulator drops of in momenta at about the cutoff scale, the larger is the onset scale k_{on}. For the ghost and gluon regulators underlying the computation of the propagators in [95], (B.11), we choose an initial scale $k_{\text{UV}} = 20\,\text{GeV}$. This is safely in the asymptotic UV regime of the regulators (B.11), as is also explicitly discussed in Appendix B.2. In summary, the computation is initialised at

$$\alpha_s(k_{\text{UV}}) = 0.184 \quad \text{with} \quad k_{\text{UV}} = 20\,\text{GeV}\,, \tag{3.134}$$

and the running coupling data are also taken from [95], which ensures the self-consistency of the computation.

In (3.133) we have used that the background wave function renormalisation Z_A satisfies $Z_A^{-1} = Z_{g_s}^2$, a consequence of background gauge invariance. Moreover, RG consistency, see,

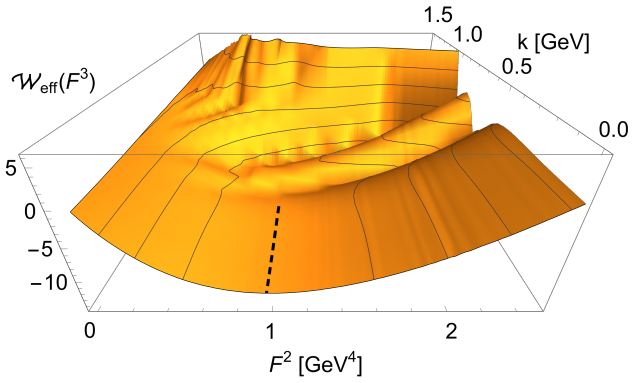

Abbildung 3.3.: Effective Potential as a function of F^2 with a field strength pointing in the t^3-direction, $(n^3, n^8) = (1, 0)$, and the cutoff scale k. The dashed line singles out the absolute minimum of $W(F)$, see (3.135). The substructure of the potential at cutoff scale $k \gtrsim 0.5\,\text{GeV}$ is related to the regulator used, see Appendix B.2. It leaves no trace in the potential for $k \to 0$.

e.g., [58, 176], enforces (3.133): the flow of the initial effective action with an infinitesimal change of the initial cutoff scale is given by the flow equation. Phrased in terms of the effective potential in (3.131), this is the simple requirement that $\mathcal{W}_k$ and in particular $\mathcal{W}_{\text{eff}} = \mathcal{W}_k$ is independent of k_{UV}. Then, differentiation of (3.131) with respect to k_{UV} readily leads to (3.132). More details are deferred to Appendix B.2.

3.2.3.3. Results

The above derivation allows the numerical computation of the scale dependent effective potential $\mathcal{W}_k(F^a)$ by performing the integration in (3.131) up to the respective RG scale k. The result is shown in Figure 3.3, which shows the k-dependent effective potential as a function of F^2, with a field strength pointing in the t^3-direction: $(n^3, n^8) = (1, 0)$. The condensate $\langle F \rangle$ is given by the solution of the equation of motion (EoM) for the effective potential $\mathcal{W}_{\text{eff}}(F^a)$, given by

$$\left.\frac{\partial \mathcal{W}_{\text{eff}}(F^a)}{\partial F}\right|_{F=\langle F\rangle} = 0\,, \tag{3.135}$$

for the generic field strengths of (3.82). The emergence of a non-trivial minimum is clearly visible in the non-perturbative regime $\lesssim 1$ GeV, and its position indicated with the black dashed line in Figure 3.3.

The gauge invariant information of the field strength $F_{\mu\nu}$ is stored in its eigenvalues, which do not change under (unitary) gauge transformations. In the present case, only the $F_{01} = F_{23}$ components and their antisymmetric counterparts are non-vanishing, and they are proportional to a combination of the Cartan generators, see (3.82). The traces in the flow equation are in the adjoint representation, and the six non-vanishing eigenvalues of $n^3 t^3 + n^8 t^8$ are given by

$$\tau_\pm^{(1)} = \pm\, n^3\,, \quad \tau_\pm^{(2)} = \pm\left(\frac{1}{2}n^3 + \frac{\sqrt{3}}{2}n^8\right), \quad \tau_\pm^{(3)} = \pm\left(\frac{1}{2}n^3 - \frac{\sqrt{3}}{2}n^8\right), \tag{3.136}$$

for more details see, e.g., [177, 178]. The global, degenerate minima in Figure 3.1 are located in the direction of the eigenvectors. The underlying Weyl symmetry maps the different minima into each other, and is seen in Figure 3.1.

From (3.135) we determine the expectation values or rather saddle point position of the condensate in both directions. We find that the expectation value in n^3-direction is a global minimum, while in the n^8-direction the EoM singles out a saddle point. Both points are indicated by the red and blue dots respectively in Figure 3.1. We determine the value of the minimum by interpolation,

$$\langle F\rangle^2_{\lambda_3} = 0.98(11)\,\mathrm{GeV}^4\,, \tag{3.137}$$

where the error is obtained by a variation of 2% in the initial coupling α_s. More details on the RG consistency of this procedure are provided in Appendix B.2. Equation (3.137) is the result of an $SU(3)$ computation without the N_c rescaling.

As discussed below (3.82), the minimum in (3.137) is composed by the condensates of both F^2 and $F\tilde{F}$. Due to the CP-violating nature of an $F\tilde{F}$ condensate, its contribution to our condensate value is tightly constrained by experimental data. Nonetheless, the value quoted in (3.137) should be interpreted as an estimate colorless condensate $\langle F^2\rangle$.

The present first-principle Yang-Mills result (3.137) corroborates the phenomenological estimates, i.e., $\langle F^2\rangle = 0.854(16)\,\mathrm{GeV}^4$ [179], as already remarked in [148]. Indeed, the normalisation procedure used here is similar to that in the phenomenological computation. In contrast, both (3.137) and the phenomenological estimates disagree with the lattice estimate $\langle F^2\rangle = 3.0(3)\,\mathrm{GeV}^4$ [180]. The latter value is extracted from $\langle G^2\rangle = 0.077(7)$ in [180], and applying $\langle F^2\rangle = 4\pi^2\langle G^2\rangle$. In this context we remark that the total normalisation may differ, even though all procedures provide RG invariant results: for example, one may multiply the respective result by the RG invariant ratio of couplings at different momenta, $\alpha_s(p_1^2)/\alpha_s(p_2^2)$, resulting in a global factor. This amounts to mapping the factor α_s from one momentum scale to another. While we lack a comprehensive interpretation, we simply point out that the lattice definition involves α_s at a low momentum scale, conversely to the present procedure, and that used in phenomenological applications.

For comparison, we also provide the saddle point value,

$$\langle F\rangle^2_{\lambda_8} = 0.85(11)\,\mathrm{GeV}^4\,, \tag{3.138}$$

which may be used for a further error estimate of the relation between octet and colorless condensates, as the octet condensate should be averaged over all color directions.

3.2.4. Gluon mass gap

The aim of this section is to use (3.119) and (3.137) for an estimate of the mass gap. Evidently, to accomplish this, the determination of the wave function renormalisation Z_{cond} is required.

Inspecting the condensate generating kinetic term, see (3.87), one finds that its analogue for the fluctuating gluon also contains contributions of the type

$$\frac{Z_{\mathrm{cond}}}{2}\int_x a^a_\mu(\partial^2)^2\Pi^\perp_{\mu\nu}(\partial)a^a_\nu + \dots\,. \tag{3.139}$$

Hence, the kinetic term for the field strength not only gives rise to the condensate, but also overlaps with the gluon propagator. More specifically, as can be read off (3.139), the p^4-term of the fluctuation gluon two-point function carries the wave function renormalisation Z_{cond} as a prefactor, as made explicit in (3.117).

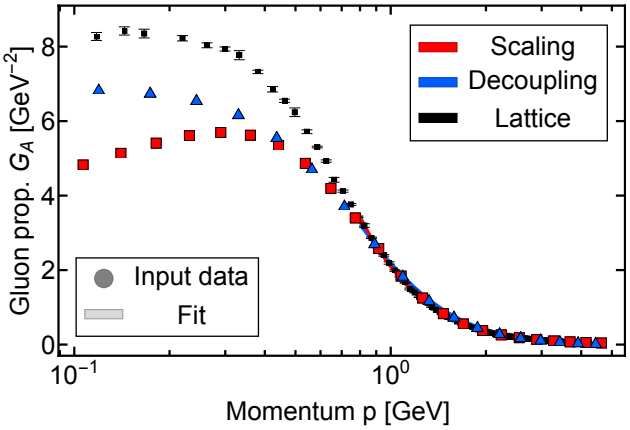

Abbildung 3.4.: Gluon propagators from the fRG [95] in the scaling (red) and decoupling (blue) scenario as well as lattice data from [128] with a continuum and infinite volume extrapolation, see [181, 182]. Coloured/black markers show the data. Solid lines show the respective fits from which the wave function renormalisation Z_{cond} (cf. (3.139)) is computed. The fit Ansätze are given in (C.1). Here, we plot fits to the propagator data over the maximal fit interval, see also Appendix C.1.1 for details.

Note that by means of (3.106a) and (3.107), the p^4-term must be solely given by (3.139), as Z_A implicitly defined in (3.106b) encodes the full gluon propagator dressing function, see (3.104). In terms of an operator product expansion, Z_{cond} can be extracted by determining the p^4-coefficient in the origin of the inverse input gluon propagator data from [95], used in the calculation of the condensate effective potential in Section 3.2.3. This is done via a fit, given by

$$Z_{\text{fit}}(p^2) = Z_{\text{as}}(p^2) + Z_{p^2} + Z_{\text{cond}}\, p^2\,, \tag{3.140}$$

where only the infrared asymptotes $Z_{\text{as}}(p^2)$ distinguish between scaling and decoupling solutions (cf. (3.115) and (3.116)). A detailed discussion of the fitting procedure is provided in Appendix C.1.1, and the respective fits in comparison to the propagator data from [95] and the lattice data of [128] are depicted in Figure 3.4.

Equation (3.140) makes it apparent that scaling and decoupling solutions differ only in the infrared, where the p^4-term is subleading. We determine Z_{cond} from the fRG scaling solution of [95] as well as the lattice decoupling solution of [128]. Combining both estimates, we arrive at the value for the wave function renormalisation

$$Z_{\text{cond}} = 0.149(19)\,\text{GeV}^{-2}\,. \tag{3.141}$$

Now we use the wave function renormalisation from (3.141), the condensate value $\langle F^2\rangle$ (3.100) as well as the saturation bound (3.100) for the averaging factor f_{av} in the relation for the effective gluon mass (3.119). This leads us to

$$m_{\text{gap}} = 0.312(27)\,\text{GeV}\,. \tag{3.142}$$

Equation (3.142) is the main result of the present study and provides an estimate for the effective gluon mass in the Landau gauge. The relatively large uncertainty in (3.142)

originates predominantly from the error for Z_{cond} in (3.141). In particular, it does not include a systematic error estimate, and is solely rooted in the small amount of data points for the gluon propagator of [95] in the deep IR.

A large source for the systematic error is the current lack of a quantitative color average as discussed in detail in Appendix A.1. Moreover, the field strength condensate (3.137) also receives contributions from the topological condensate $\langle F\tilde{F}\rangle$, see the discussion there and below (3.82). Accordingly, we simply note that inserting the literature value from phenomenological $\langle F^2\rangle$ estimates [179] reduces the value in (3.142) to $m_{\text{gap}} = 0.291(19)\,\text{GeV}$. The same value is obtained by the use of the saddle point value (3.138), which we use as an error estimate.

We can compare our result for the effective gluon mass (3.142) with that deduced from the lattice data [128] with a continuum and infinite volume extrapolation, see [181, 182]. These data are shown in Figure 3.4, and the mass gap is given by the value of the inverse lattice propagator in the origin. We find

$$m_{\text{gap}}^{(\text{lattice})} = 0.3536(11)\,\text{GeV}\,, \tag{3.143}$$

which agrees within two standard deviations with our estimate (3.142).

A further direct test of the present results is provided by the comparison with the effective gluon mass in (3.148) obtained via the Schwinger mechanism with $m_{\text{gap}} = 0.320(35)\,\text{GeV}$ after scale matching. This is an alternative approach for the dynamical emergence of a gluon mass gap in the Landau gauge, for details see Section 3.2.5. The results compare very well, which is to be expected as our propagator with the gluon mass gap agrees well with the lattice results, as does the propagator obtained with the Schwinger mechanism.

We emphasise that the estimate for the gluon mass gap depends on our choice for the color averaging factor f_{av} in (3.96): with (3.100) we have saturated the 'natural' bound $c_{\text{av}} = 1$ in (3.98), leading to (3.101). In fact, the non-trivial compatibility of the present results with that obtained from lattice propagators and via the Schwinger mechanism corroborates the aforementioned choice.

We close this section with the remark that, while the effective gluon mass or rather the gluon mass gap in the Landau or Landau-DeWitt gauge is a gauge variant quantity, its size is directly related to physical scales such as the string tension and the confinement-deconfinement temperature, see [138, 139]. Still, its value varies with the gauge as does its precise relation to the physical scales and mechanisms. Consequently, the numerical estimates of its value are rather disparate, ranging from a few hundred MeV up to 1 GeV, depending on the details of the approach and the definition employed, see, e.g., [115, 131, 142, 183–195]. Nonetheless, all these determinations convey information about the same gauge invariant physical information, namely the Yang-Mills mass gap.

3.2.5. Schwinger mechanism

For comparison compare with the estimate based on condensation of Section 3.2.4, here we present an alternative estimate for the gluon mass gap based on the Schwinger mechanism.

According to one of the main approaches put forth in a number of works [94, 196–199], the generation of an effective gluon mass proceeds through the non-Abelian implementation of the well-known Schwinger mechanism [200–203]. Within this scenario, the fundamental vertices that enter the DSE of the gluon propagator contain longitudinally coupled

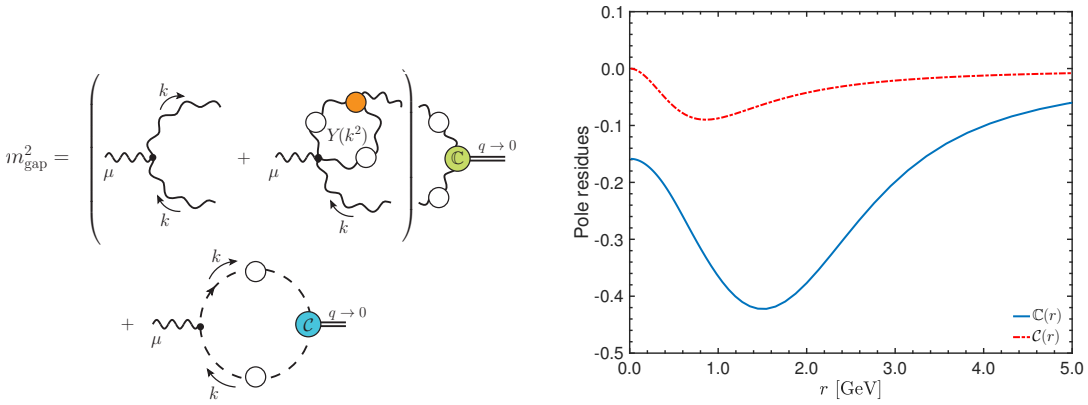

Abbildung 3.5.: Left panel: Diagrammatic representation of (3.147). As opposed the usual diagrammatic representation in this work, full propagators are marked by white blobs. The full three-gluon vertex is denoted by an orange blob. Right panel: the momentum dependence of $\mathbb{C}(q^2)$ and $\mathcal{C}(q^2)$ as obtained in [196].

massless poles. Denoting the scalar part of the transverse component of the gluon propagators as G_A (corresponding to the inverse of the transverse component of (3.63)) which eventually trigger the result $G_A^{-1}(0) := m^2_{\rm gap}$.

In particular, the three-gluon vertex, $\mathbb{I}\Gamma_{\mu\alpha\beta}(q,r,p)$, and the ghost-gluon vertex, $\mathbb{I}\Gamma_{\mu}(q,r,p)$, are composed by two distinct types of terms, namely

$$\begin{aligned}\mathbb{I}\Gamma_{\mu\alpha\beta}(q,r,p) &= \Gamma_{\mu\alpha\beta}(q,r,p) + \frac{q_\mu}{q^2} g_{\alpha\beta} C_1(q,r,p) + \cdots\,, \\ \mathbb{I}\Gamma_{\mu}(q,r,p) &= \Gamma_{\mu}(r,p,q) + \frac{q_\mu}{q^2} C(q,r,p)\,,\end{aligned} \tag{3.144}$$

where the terms $\Gamma_{\mu\alpha\beta}(q,r,p)$ and $\Gamma_{\mu}(q,r,p)$ contain all pole-free contributions, which may diverge at most logarithmically as $q \to 0$ [204]. The ellipses in the first relation of (3.144) denote terms proportional to r_α/r^2 or p_β/p^2, which are annihilated when contracted with the transverse (Landau gauge) gluon propagators inside the relevant diagrams of the DSEs, or tensorial structures that are subleading in the limit $q \to 0$.

A detailed analysis [205] based on the Slavnov-Taylor identities satisfied by the above vertices reveals that

$$C_1(0,r,-r) = C(0,r,-r) = 0\,. \tag{3.145}$$

Therefore, the Taylor expansion of $C_1(q,r,p)$ and $C(q,r,p)$ around $q=0$ yields

$$\begin{aligned}\lim_{q\to 0} C_1(q,r,p) &= 2(q\cdot r) \underbrace{\left[\frac{\partial C_1(q,r,p)}{\partial p^2}\right]_{q=0}}_{\mathbb{C}(r^2)} + \mathcal{O}(q^2)\,, \\ \lim_{q\to 0} C(q,r,p) &= 2(q\cdot r) \underbrace{\left[\frac{\partial C(q,r,p)}{\partial p^2}\right]_{q=0}}_{\mathcal{C}(r^2)} + \mathcal{O}(q^2)\,.\end{aligned} \tag{3.146}$$

Thus, inserting the vertices of (3.144) into the DSE of the gluon propagator and taking the limit $q \to 0$, one arrives at [199]

$$m_{\rm gap}^2 = \frac{3C_{\rm A}\alpha_s}{8\pi}\int_0^\infty dy\, Z_A^2(y)\,[6\pi\alpha_s C_{\rm A} Y(y) - 1]\,\mathbb{C}(y) + \frac{C_{\rm A}\alpha_s}{8\pi}\int_0^\infty dy\, Z_c^2(y)\,\mathcal{C}(y)\,, \quad (3.147)$$

depicted in Figure 3.5. In the above formula, $\alpha_s = g_s^2/4\pi$, defined at the renormalisation point μ where the ingredients of (3.147) have been renormalised, within the momentum subtraction (MOM) scheme; the renormalisation point has been chosen at $\mu = 4.3$ GeV. Moreover, $C_{\rm A}$ is the Casimir eigenvalue of the adjoint representation with $C_A = N_c$ for $SU(N)$. Finally, $Z_{A/c}$ are the gluon/ghost dressing functions $Z_{A/c}(k^2) = k^2 G_{A/c}(k^2)$, and $Y(k^2)$ is an appropriately projected contribution of the subdiagram shown in Figure 3.5.

The functional form of the pole residues $\mathbb{C}(k^2)$ and $\mathcal{C}(k^2)$ is determined from the linear homogeneous system of coupled Bethe-Salpeter equations that they satisfy. This system is derived from the corresponding DSEs governing the dynamics of $\mathbb{\Gamma}_{\mu\alpha\beta}(q,r,p)$ and $\mathbb{\Gamma}_{\mu}(q,r,p)$, in the limit $q \to 0$; for further details, see [199].

The resulting eigenvalue problem yields non-trivial solutions for $\mathbb{C}(k^2)$ and $\mathcal{C}(k^2)$, for a specific value of the coupling α_s, which depends on the details of the ingredients that enter the kernels of the Bethe-Salpeter system. It is important to emphasise that the homogeneity and linearity of the equations leaves the overall scale of the corresponding solutions undetermined. The scale setting is implemented by solving the vertex DSEs for *general kinematics*, using as input the particular α_s that was singled out by the eigenvalue condition. Then, from the general 3-D solution the particular slice that corresponds to $\mathbb{C}(k^2)$ and $\mathcal{C}(k^2)$ is identified, furnishing precisely the correctly rescaled version of the solutions obtained from the system. The final form of the scale-fixed pole residues is shown in Figure 3.5.

The next step consists in substituting into (3.147) the scale-fixed $\mathbb{C}(k^2)$ and $\mathcal{C}(k^2)$, and use refined lattice data [182] for the gluon and ghost dressing functions, $Z_A(k^2)$ and $Z_c(k^2)$. The lattice propagators have been normalised at the point $\mu = 4.3$ GeV, namely the highest momentum scale available in this simulation. For the purpose of the comparison with the results computed here we match the scales of the lattice data in [182] with that in [95], which leads us to

$$m_{\rm gap}^{\rm (Schwinger)} = 0.320(35)\,{\rm GeV}\,. \quad (3.148)$$

Equation (3.148) is in excellent agreement with the estimate $m_{\rm gap} = 0.322(34)\,{\rm GeV}$ obtained here, see (3.142). Both compare rather favourably to the central lattice value $G_A^{-1/2}(0) = 0.354\,{\rm GeV}$. The predominant source of error in the calculation using the Schwinger mechanism originates from the uncertainties in the non-perturbative structure of the pole-free vertex $\Gamma_{\mu\alpha\beta}(q,r,p)$, which affects both, the determination of the function $Y(k^2)$ in (3.147), and the kernels of the Bethe-Salpeter equations that determine the functions $\mathbb{C}(k^2)$ and $\mathcal{C}(k^2)$.

3.2.6. Conclusion

In this section, we explored the dynamical emergence of a mass gap in the Yang-Mills correlation functions via the formation of color condensate in Section 3.2.4 and compared to results from the non-Abelian Schwinger mechanism in Section 3.2.5.

In the physical case with gauge group $SU(3)$, a promising candidate for a condensate generating the gluon mass gap is the octet condensate, see (3.71). Such a condensate may be triggered by a Higgs-type mechanism in low energy QCD, similar and potentially related to dynamical chiral symmetry breaking in QCD with the pion as pseudo-Goldstone bosons. In Section 3.2.1, we have carried out a qualitative analysis within the fRG approach to QCD by computing the minimum $\langle F \rangle$ of the effective potential $W(F^a)$ in the three direction of the Cartan subgroup. This non-vanishing field strength is related to non-vanishing color condensates as discussed in Section 3.2.1.2. We have computed the effective potential $\mathcal{W}(F^a)$ for covariantly constant field strength which develops a non-trivial minimum if quantum fluctuations are successively taken into account with the fRG flow, see Figure 3.1. The condensate value (3.137) is in good agreement with phenomenological estimates, but both disagree with lattice results. As discussed in section 3.2.3.3, this latter discrepancy may be due to a difference in the normalisations employed.

The relation between the gluon condensate and the mass gap is given by (3.119). We emphasise that the mass gap (3.119) triggered by the condensate depends on the RG condition and naturally has the RG properties of a mass function: while the condensate itself is independent of the RG condition, the condensate wave function is not and carries the RG properties of the inverse gluon propagator. Consequently, the mass gap derived from (3.119) has the RG scaling of the inverse gluon propagator, as it should. Accordingly, for a comparison of the results for the mass gap obtained here with that in the literature the potentially different RG schemes and conditions have to be taken into account. Most fRG computations including the present one are done in MOM^2, for a detailed discussion see [171].

These considerations result in our estimate of the gluon mass gap, $m_{\text{gap}} = 0.312(27)\,\text{GeV}$, where our choice (3.96) for the color averaging factor f_{av} saturates the 'natural' bound, see also the discussion below (3.99). This estimate compares well to the lattice estimate $m_{\text{gap}}^{(\text{lattice})} = 0.3536(11)\,\text{GeV}$. The latter value is obtained from the continuum and infinite volume extrapolation [181] of the lattice data in [128], after matching the momentum scales and the renormalisation point.

In Section 3.2.5, we presented a result for the gluon mass gap obtained with the longitudinal Schwinger mechanism within the framework of the pinch technique [135]. This analysis leads to $m_{\text{gap}}^{(\text{Schwinger})} = 0.320(35)\,\text{GeV}$, which is in excellent agreement with the estimate from condensation.

In summary, the findings of this section suggest that the gluon condensation as well as the Schwinger mechanism work well as a mechanism for gluon mass generation. Beyond improving the systematic error of the numerical estimates, on theoretical grounds it would be desirable to establish a deeper connection between the Schwinger mechanism and the condensate formation.

4. The spectral functional approach

In this chapter, we develop the *spectral functional approach*, a novel approach for the direct computation of realtime correlation functions that is based on spectral representations. The approach comes with the advantage that we can use dimensional regularisation for the analytic computation of momentum integrals in fully numerical non-perturbative calculations. Accordingly, the respective renormalisation scheme, *spectral renormalisation*, is based on standard dimensional regularisation and respects the spacetime symmetries, internal symmetries such as chiral symmetry, and gauge symmetries of the theory at hand. Clearly, this method is applicable to a broad range of theories, including non-Abelian gauge theories, within a regularisation and renormalisation scheme which is manifestly gauge invariant.

The spectral functional approach was put forward in [1], in the framework of Dyson-Schwinger equations. Apart from the conceptual development, also a first application to a scalar ϕ^4-theory was included there. Reference [1] therefore represents the seminal work for the spectral functional approach, which we present in its entirety in Section 4.1. The extension of the spectral functional approach to the functional renormalisation group (fRG) is non-trivial, since common choices for the regulator violate causality and hence the spectral representation. This problem can be circumvented by using a causal, mass-like Callan-Symanzik (CS) regulator. However, the CS regulator comes with the loss of UV finiteness in standard flow equations. In the manifestly finite CS flow equation, this is compensated for by the counter term action, allowing for *flowing renormalisation*. Within this framework, the spectral fRG was achieved in [6], which we discuss in detail in Section 4.2. Like in the spectral DSE case, we accompany the conceptual advance with an application to the scalar ϕ^4-theory [9]. This allows for explicit comparison between the two different spectral functional approaches discussed in this thesis.

Applications of the spectral functional approach to Yang-Mills theory [2, 5] and QCD [7] are discussed in Chapter 5. For an application of the spectral fRG approach in quantum gravity, see [206]. Other advances in realtime or complex plane calculations can be found, e.g., for DSEs in [40–42, 207–211], for the fRG in [43–48, 212–231] and in Bethe-Salpeter equations (BSEs) in [49, 50, 232–235], nPI methods [236–239] or on general grounds in [240, 241].

4.1. Spectral Dyson-Schwinger equations

This section presents the results of [1].

For the introduction to the *spectral functional approach*, we resort to the scalar ϕ^4-theory. This theory is a simple strongly correlated system and serves as a good benchmark for new techniques before applying them more involved theories such as non-Abelian ones. It is also interesting in its own right and has many applications as a model theory for perturbative and non-perturbative phenomena.

The spectral functional approach centrally builds on spectral representations for correlation functions, such as the Källén-Lehmann representation of the propagator. While the spectral representations allow for analytic solution of the momentum loop integrals, they introduce additional spectral integrals. A core feature of the spectral functional approach is the *spectral renormalisation* scheme, providing consistent renormalisation of loop diagrams in functional equations in presence of spectral representations resp. integrals. We discuss two subclasses of our novel scheme, which are *spectral dimensional renormalisation* and *spectral BPHZ renormalisation*. The former renormalises the spectral integrals in a purely dimensional manner, respecting all internal symmetries of the theory at hand. In the BPHZ scheme, the spectral integrals are renormalised by a BPHZ-type subtraction using counterterms. Since spectral renormalisation yields direct access to Minkowski spacetime, it can be performed *on-shell*.

As a first application, we present results for the spectral function of the scalar field in $d = 2 + 1$ dimensions. To that end, we apply the spectral functional approach to the framework of Dyson-Schwinger equations (DSE). Using its Källén-Lehmann representation, we compute the spectral function from the gap equation of the propagator, including all two-loop diagrams. In a first step, all vertices are approximated with the classical ones. In a second step, we use a skeleton expansion of the DSE with a bubble resummation of the s-channel four-point function. The non-perturbative s-channel spectral function of the four-vertex is computed and used in the DSE.

The section is organised as follows. In Section 4.1.1, we introduce spectral renormalisation at the example of the Dyson-Schwinger approach along with the necessary technical tools. In, Section 4.1.2, we apply the spectral functional approach to the scalar propagator DSE, followed by the presentation of our results in Section 4.1.3. Finally, our conclusions are presented in Section 4.1.4.

4.1.1. Spectral renormalisation

The general realtime renormalisation scheme we develop here aims at combining a practical numerical implementation in non-perturbative applications while maintaining all underlying symmetries including gauge symmetries. This is achieved by utilising dimensional regularisation, which respects all spacetime, internal and gauge symmetries of the theory at hand. We also develop a BPHZ-type subtraction scheme which facilitates the analytical computations significantly. If such a subtraction schemes does not violate any symmetries in the theory at hand, it is the scheme of choice.

A practical implementation of dimensional regularisation requires an analytic momentum structure of the propagators and vertices in the given loop integrals. While this allows for its use in perturbation theory, non-perturbative applications, with their necessarily numerical computation of propagators and vertices, usually rely on ultraviolet

momentum cutoffs. The latter are neither consistent with spacetime symmetries nor with gauge symmetries. It is well-known that in gauge theories and supersymmetric theories such a regularisation requires symmetry-breaking counterterms. This is not a conceptual problem, but it typically triggers additional power-counting relevant terms that may lead to additional fine-tuning tasks, see, e.g. [95, 166]. Moreover, the Wick rotation to Minkowski spacetimes is hampered by the deformation of the momentum integrals, which can lead to additional poles and cuts in the integration contours.

The present renormalisation scheme achieves the requirement of analytic momentum integrals by using spectral representations of correlation functions. For the propagators this is the Källén-Lehmann spectral representation, similar spectral representations also exist for the vertices, though getting increasingly difficult. We call this renormalisation scheme *spectral renormalisation*: after inserting the spectral representations in the loop integrals, the momentum integrands take an analytic form. This form is well-suited for using dimensional regularisation or related analytic computation techniques. The loop-momentum integrations can be performed analytically, and we are left with spectral integrals. The whole non-perturbative information is contained in the spectral functions of propagators and vertices. In most non-perturbative applications the respective spectral integrals can only be computed numerically.

The scheme can be practically applied to any divergent diagram that scales in the UV with loop momentum to some natural power q^m, $m \in \mathbb{N}$ (with $m < n_{\max}$ and $n_{\max}$ given by the renormalisability constraint). This is always the case when using spectral representations for all correlation functions, but also works for classical vertices. This will be detailed in the present section within the example of the Dyson-Schwinger approach introduced in the next section, Section 4.1.1.1. For classical vertices, all momentum integrals in functional approaches, are of the standard perturbative form, but with different spectral masses for all lines. Most of these integrals are known from perturbation theory results, e.g., [242]. Note that this reparametrisation comes at the cost of spectral integrals for each propagator. Spectral representations of vertices lead to further spectral integrals as well as further classical propagators with spectral masses. In summary, in a spectral functional approach all momentum integrals are perturbative. Hence, we can implement a symmetry-preserving regularisation such as dimensional regularisation, leading to a renormalisation scheme with symmetry-consistent counterterms.

A relevant example for this important symmetry-preserving property are gauge theories. There, a momentum cutoff or standard subtraction scheme requires explicitly or implicitly a mass counterterm for the gauge field in order to keep the renormalised gauge field massless. In four dimensions this leads to a quadratic fine-tuning task instead of a logarithmic one, for a detailed discussion see [95, 166]. Spectral renormalisation with spectral regularisation removes the (explicit or implicit) necessity of a mass counterterm for the gauge field, and hence the quadratic fine-tuning task.

After briefly introducing Dyson-Schwinger equations, Section 4.1.1.1, and the Källén-Lehmann spectral representation, Section 4.1.1.2, we set up spectral renormalisation in Section 4.1.1.3 (spectral dimensional renormalisation), and Section 4.1.1.4 (spectral BPHZ renormalisation). Further examples and the discussion of the fully non-perturbative setup can be found in Section 4.1.1.5 and Section 4.1.1.6. The explicit example used for demonstrating the properties and computational details of the spectral renormalisation scheme is the gap equation for scalar ϕ^4- and ϕ^3-theories.

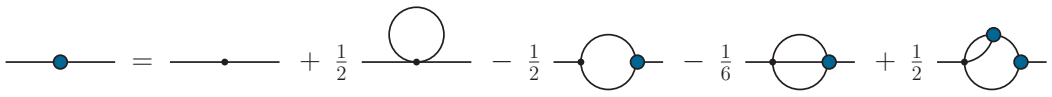

Abbildung 4.1.: DSE of the two-point function for a general background field $\phi \neq 0$. The vacuum polarisation and squint diagrams are proportional to $S^{(3)}[\phi] \propto \phi$. They vanish for $\phi = 0$, where the standard form with tadpole and sunset diagrams is obtained. The notation is given in Figure 2.1.

4.1.1.1. Dyson-Schwinger equations

For our explicit example of a ϕ^4-theory, the classical action is given by,

$$S[\varphi] = \int d^d x \left[\frac{1}{2}(\partial_\mu \varphi)^2 + \frac{m^2_{\phi,0}}{2}\varphi^2 + \frac{\lambda_{\phi,0}}{4!}\varphi^4 \right] , \tag{4.1}$$

where φ refers to the full fluctuating quantum field. The classical action (4.1) depends on two parameters or couplings, the bare four-point coupling $\lambda_{\phi,0}$ and the bare mass parameter $m_{\phi,0}$. The third parameter required for renormalisation, the wave function renormalisation Z_ϕ can be scaled out. This is conveniently done by setting it to unity at the renormalisation scale.

The underlying Z_2-symmetry of the theory, $\varphi \to -\varphi$ implies the same symmetry for the effective action under transformations of the mean field, $\phi \to -\phi$. Accordingly, the odd vertices vanish at vanishing mean field: $\Gamma^{(2n+1)}[\phi = 0] \equiv 0$. Moreover, restricting ourselves to constant background fields ϕ_c, we can formally expand the three-point function in powers of the field,

$$\Gamma^{(3)}[\phi_c](p_1, p_2, p_3) = \phi_c \left[\Gamma^{(4)}(p_1, p_2, p_3, 0) + O(\phi_c^2) \right] , \tag{4.2}$$

due to the odd vertices vanishing at the expansion point $\phi = 0$. In (4.2) we have used the Fourier transform $\tilde{\phi}_c(p) = (2\pi)^d \phi_c \delta(p)$ of the constant field. We have also introduced $\Gamma^{(n)}(p_1, p_2, p_3, 0, ..., 0)$, the n-point functions at a vanishing background and $n-3$ vanishing momenta.

Since the background field in (4.2) is constant, the propagator is diagonal in momentum space and follows from the 1PI two-point function by the simplified inverse relation (2.26). The DSE for the two-point function of the scalar theory defined by (2.1) is obtained by taking two functional derivatives w.r.t. to the field of the master DSE (2.30), see Section 2.2 for an introduction to Dyson-Schwinger equations. We depict the resulting diagrammatic form in Figure 4.1. The relation (4.2) gives rise to the polarisation and squint diagram for $\phi_c \neq 0$, which are absent for $\phi_c = 0$. In the broken phase the equation of motion (EoM) ϕ_0 for constant fields is solved for a non-vanishing expectation value of the field, i.e. $\phi_0 \neq 0$. Accordingly, if evaluating the DSEs for correlation functions on the EoM, these diagrams are present.

4.1.1.2. Källén-Lehmann spectral representation

Using the Källén-Lehmann spectral representation [51, 52], the propagator can be recast in terms of its spectral function ρ,

$$G(p_0, \vec{p}) = \int_0^\infty \frac{d\lambda}{\pi} \frac{\lambda\, \rho(\lambda, |\vec{p}|)}{p_0^2 + \lambda^2} \,. \tag{4.3}$$

For asymptotic states, the spectral function can be understood as a probability density for the transition to an excited state with energy λ. In this way, the spectral function acts as a linear response function of the two-point correlator, encoding the energy spectrum of the theory. The existence of a spectral representation imposes tight restrictions on the analytic structure of the propagator. In turn, the Euclidean propagator also constrains the spectral function; for a rather non-trivial example for the latter constraints, see [243].

From a complex analysis perspective, the spectral function naturally arises as the set of non-analyticities of the propagator. This results into the following inverse relation between spectral function and the retarded propagator,

$$\rho(\omega, |\vec{p}|) = 2 \,\mathrm{Im}\, G(-\mathrm{i}\omega_+, |\vec{p}|) \,, \tag{4.4}$$

where ω_+ denotes the retarded limit,

$$\omega_+ = \omega + \mathrm{i}0^+ \,, \tag{4.5}$$

and ω is the realtime zero momentum component. This formulation allows us to work only with the frequency argument and set the spatial momentum to zero in practice, since the full phase-space can be restored from Lorentz invariance. Hence, for the remainder of this work, $|\vec{p}|$ will be dropped.

The existence of a spectral representation restricts all non-analyticities of the propagator to lie on the real momentum axis, as manifest in (4.3) and (4.4). This crucial condition as well as the generic structure in the complex plane already mentioned above allow us to recast the spectral function into the form

$$\rho(\lambda) = \frac{\pi}{\lambda} \sum_i Z_i\, \delta(\lambda - m_i) \;+\; \tilde{\rho}(\lambda) \,. \tag{4.6}$$

The spectral function is split into a set of δ-functions and a continuous scattering part $\tilde{\rho}$, arising from branch cuts in the complex plane of the propagator. For a classical propagator the spectral function reduces to one mass-shell δ-function with $Z_1 = 1$. There are no further poles, $Z_{i>1} = 0$, and the scattering part is absent, $\tilde{\rho} \equiv 0$. Further details can be found, e.g., in [68].

In the scalar ϕ^4-theory, the spectral function of the scalar field is that of an asymptotic state, and hence is positive semi-definite and has the interpretation of a probability density. Therefore, it is convenient to normalise its integrated weight to unity within an appropriate renormalisation scheme. Within this scheme we have the sum rule,

$$\int_\lambda \lambda\, \rho(\lambda) = 1 \quad \text{with} \quad \int_\lambda \equiv \int_0^\infty \frac{d\lambda}{\pi} \,, \tag{4.7}$$

which implies $Z_i \leq 1$. The spectral weight is distributed between poles and cuts, and in the presence of scattering states the weight of the poles is less than one.

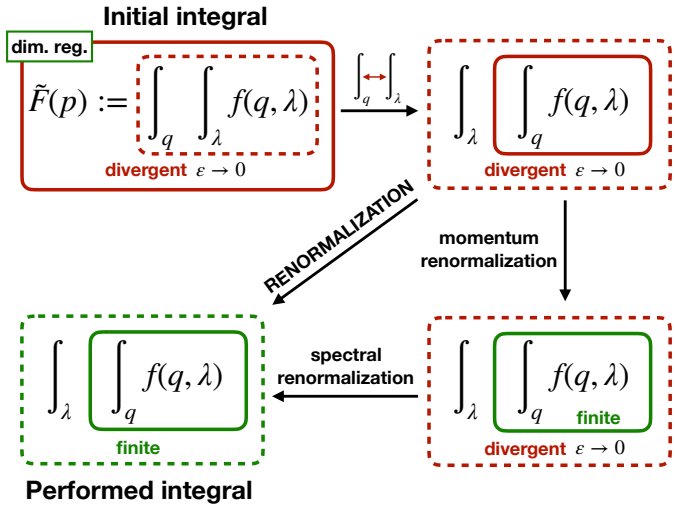

Abbildung 4.2.: Schematic illustration of the spectral renormalisation scheme. The function f is some arbitrary divergent integrand. The dependence on the external momentum p is suppressed. The upper two boxes have to be understood as finite by dimensional regularisation, but divergent in the limit $\varepsilon \to 0$ in $d-\varepsilon$ dimensions. In a first step, the momentum integrals are analytically evaluated via dimensional regularisation. Subsequently, the spectral integrals are renormalised via spectral renormalisation, either within the dimensional- (Section 4.1.1.3) or BPHZ approach (Section 4.1.1.4).

4.1.1.3. Spectral dimensional renormalisation

Next, we discuss the spectral renormalisation scheme, which is fully based on dimensional regularisation. To that end, we employ the KL representation (4.3) for all propagators in the loop diagrams of a given functional equation, such as the DSE for the scalar two-point function, see Figure 4.1. Dimensional regularisation in $d-\epsilon$ dimensions renders the loop diagrams finite, and we can swap orders of the initially outer momentum and inner spectral integrals (cf. upper part of Figure 4.2). This allows us to first perform the momentum integrals analytically. We are left with finite spectral integrals at finite $\epsilon > 0$, that in general have to be done numerically since the spectral functions may only be known numerically.

Generally, the numerical integration of the spectral integrals can be performed for finite ϵ, and in gauge theories full manifest gauge-consistency of spectral renormalisation requires that the limit $\epsilon \to 0$ is taken only after performing all integrals. However, it is convenient for the numerical performance to do the spectral integration at $\epsilon = 0$. The same holds for the access to the analytic momentum structure required for extracting Minkowski properties. In this case, for the limit $\epsilon \to 0$ we have to set up a consistent renormalisation procedure before performing the spectral integrals, which is worked out in detail in Section 4.1.1.4. In particular, it is not sufficient to only remove the $1/\epsilon$-divergences that originate in the momentum integrations, as the spectral integrations lead to further $1/\epsilon$-terms. This relates to the swapping of the integration order and performing the limit $\epsilon \to 0$ before evaluating all integrals.

This section is dedicated to the fully gauge consistent renormalisation scheme we call *spectral dimensional renormalisation*. In this scheme, the divergent parts of the spectral integrals are performed analytically before taking the limit $\epsilon \to 0$. A simple example is the tadpole contribution to the gap equation in Figure 4.1 in $d = 3$ dimensions, which comes with a momentum-independent linearly divergent term. This example is also relevant for our later computation in Section 4.1.2 and Section 4.1.3. After the momentum integration is performed, we arrive at a finite result proportional to

$$\int_0^\infty d\lambda\, \lambda \frac{\mu^{2\epsilon}\lambda^{1-2\epsilon}}{(\lambda^2+m^2)} = -\frac{\pi}{2}\frac{1}{\cos\left(\frac{\pi\epsilon}{2}\right)}\, m \left(\frac{\mu^2}{m^2}\right)^\epsilon . \tag{4.8}$$

In (4.8) we have used a trial spectral function that decays for large spectral values λ according to its momentum or spectral dimension,

$$\rho_{\text{trial}}(\lambda, m) = \frac{1}{\lambda^2+m^2}\,, \tag{4.9}$$

with a positive mass $m > 0$. The trial spectral function in (4.9) approximates the correct leading ultraviolet behaviour, if we neglect logarithmic corrections. For large spectral values, the UV-asymptotic of the spectral function can be extracted from the leading momentum dependence of the respective propagator. In the present example, the latter is assumed to decay quadratically on its branch cut on the real momentum axis.

The finiteness of the result of the momentum integration used on the left-hand side of (4.8) also points at a specific property of dimensional regularisation: in odd dimensions, $d = 2n + 1$, it already removes all momentum divergences. In even dimensions, $d = 2n$, it removes subclasses of divergent ones, a prominent being the (one-loop) tadpole in a massless theory such as a gauge theory.

If we had put $\epsilon = 0$ before the integration, (4.8) simply is (linearly) divergent. This is the price to pay for the swapping of integration orders: the divergences are not fully covered by the momentum integrals any more. The example also entails that in odd dimensions including our explicit computation in the ϕ^4-theory in $d = 3$, all divergences come via the spectral integrals.

In spectral dimensional renormalisation, spectral singularities in even dimensions show up as $1/\epsilon$-terms. In dimensional regularisation in perturbation theory, these divergences are typically removed recursively by introduction of appropriate counterterms. This procedure is applied in spectral dimensional renormalisation too, while keeping a finite ϵ as well as isolating analytically the singular part of the spectral integrals with

$$\rho(\lambda) = \rho_{\text{IR}}(\lambda) + \rho_{\text{UV,an}}(\lambda)\,. \tag{4.10}$$

In (4.10), the numerical 'infrared' part $\rho_{\text{IR}}(\lambda)$ decays sufficiently fast for large spectral values and renders the respective spectral integrals finite. In turn, the ultraviolet part $\rho_{\text{UV,an}}(\lambda)$ carries the ultraviolet asymptotics analytically. Therefore, the respective spectral integrals can be treated analytically with dimensional regularisation as done in (4.8). With (4.9) we use the IR-UV–split

$$\rho(\lambda) = \rho_{\text{IR}}(\lambda, k) + \rho_{\text{trial}}(\lambda, k)\,. \tag{4.11}$$

We also emphasise that the theory does not depend on the mass parameter k that regularises (in the infrared) the UV-part of the spectral function. In particular, we have $\partial_k \rho(\lambda) \equiv 0$, which entails the k-dependence of the infrared part of the spectral function.

The (leading) ultraviolet behaviour of the spectral function at large spectral values is governed by $\rho_{\mathrm{UV,an}} = \rho_{\mathrm{trial}}$ and the infrared part decays with the fourth power of the spectral value,

$$\lim_{\lambda\to\infty} \rho_{\mathrm{IR}}(\lambda \to \infty) \propto \frac{1}{\lambda^4} \tag{4.12}$$

Inserting the split (4.11) into (4.8) leads us to the final finite result with $\epsilon = 0$,

$$\int_0^\infty d\lambda\, \mu^{2\epsilon}\lambda^{2-\epsilon}\rho(\lambda) = \int_0^\infty d\lambda\, \lambda^2 \rho_{\mathrm{IR}}(\lambda) - \frac{\pi}{2}\, k\,, \tag{4.13}$$

with a finite (in general numerical) integral over the infrared part of the spectral function due to (4.12). The numerical convergence of this integral can be further improved systematically, if the UV-part $\rho_{\mathrm{UV}}(\lambda)$ also includes sub-leading UV-terms of the full spectral function.

The finite result of (4.13) was obtained without the introduction of any counterterms possibly breaking internal symmetries. Since the systematics of this example are general, it can be applied to all divergences of general diagrams. As the demonstrated spectral dimensional renormalisation procedure is entirely based on dimensional regularisation and the use of spectral representation, it preserves all symmetries of the theory at hand. Especially for the case of gauge theories it is manifestly gauge invariant or rather gauge consistent. For example, it reflects the peculiarity of dimensional regularisation that integrals without any external scale vanish identically. For $k = 0$ the integral over the UV-part of the spectral function vanishes, and we are left with the finite IR-part. Accordingly, no mass counterterms are needed in a massless theory such as a gauge theory.

Figure 4.2 illustrates the general renormalisation workflow, including spectral renormalisation. The schematic representation holds for the case of spectral dimensional renormalisation as well as for the subtraction-based and more universal approach of spectral BPHZ renormalisation, which is introduced in the following.

4.1.1.4. Spectral BPHZ renormalisation

In fully symmetry-consistent spectral dimensional renormalisation as described in Section 4.1.1.3, one has to perform analytic spectral integrals with dimensional regularisation on top of the momentum integrations. Already the latter are more complicated than in standard perturbation theory at the same order, since the spectral representations lead to different masses for each line. While the momentum integration has to be necessarily analytic in order to access Euclidean and Minkowski spacetime, this is not necessary for the spectral integration, whose non-perturbative infrared part has to be done numerically in most cases anyway.

The need for additional analytic computations of spectral integrals can be circumvented by performing subtractions on the spectral integrals which render the spectral integrals finite. This can be done by subtracting a Taylor expansion of the spectral integrand in momenta according to the BPHZ scheme with Dyson's formula. The procedure is called *spectral BPHZ renormalisation*. We shall see, that its workflow is still described within Figure 4.2. It is the last 'spectral' step from the bottom right to the bottom left which is changed by moving from spectral dimensional to the spectral BPHZ procedure. We emphasise that the underlying BPHZ regularisation in general does not preserve all symmetries

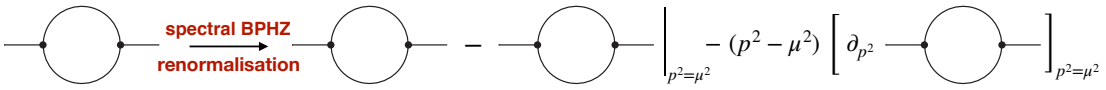

Abbildung 4.3.: Schematic spectral BPHZ renormalisation procedure at the example of the one-loop scalar propagator DSE for the ϕ^3-theory. The diagram is quadratically divergent in $d = 6$. First, the loop momentum divergences are discarded by the usual momentum renormalisation part of dimensional regularisation (i.e., implicitly assumed on the LHS). By introducing mass and wave function counterterms, the diagram is subtracted by the first two terms of its own Taylor expansion around the RG scale μ. This cancels the leading order quadratic and subleading logarithmic divergences of the spectral integrals.

of a given theory and in particular breaks gauge symmetry. This is not a conceptual problem, as the counterterms also break gauge invariance and the final result is gauge consistent, see, e.g. [244]. However, in numerical applications to gauge theories the gauge consistent spectral dimensional renormalisation is arguably worth its price, in particular for investigations of the Gribov problem and the confinement mechanism.

In the present example of a scalar ϕ^4-theory, the BPHZ scheme is consistent with both spacetime and the internal Z_2-symmetry. We will therefore utilise it for explicit computation. We introduce and explain the setup within a specific example, the sunset graph in the gap equation of the scalar ϕ^4-theory in d dimensions, see Figure 4.1. This diagram also carries sub-divergences while still being relatively simple. In Section 4.1.1.5 we additionally analyse an explicit one-loop example.

Due to the spectral representation of the sunset graph, the fully perturbative momentum integrals including the subtraction can be solved analytically in both $d = 3$ and $d = 4$:

In $d = 4$ the sunset graph is superficially quadratically divergent with logarithmic divergences in the sub-diagrams. The respective spectral power counting follows from the momentum dimension of the spectral value, $[\lambda] = 1$, where $[\mathcal{O}]$ counts the momentum dimension of $\mathcal{O}$. In particular, that of the spectral function is $[\rho(\lambda)] = -2$. This can be read off from the classical spectral function of a field with mass m with $\rho_{\mathrm{cl}}(\lambda) = 2\pi\delta(\lambda^2 - m^2)$. Trivial examples for such a power counting of spectral integrals are (4.8) and the propagator itself with $[\int d\lambda\, \lambda\rho(\lambda))/(\omega^2 + \lambda^2)] = -2$. We subtract the zeroth and first order of the Taylor expansion in external momentum about $p^2 = \mu^2$ as well as the zeroth term in Taylor expansions about the external momenta of the subdiagrams. These counterterms contribute to the mass renormalisation as well as the wave function renormalisation of the scalar field. The subtractions remove the leading and also the next-to-leading order contributions in the spectral parameters λ_i in the integrand of the spectral integral for $\lambda_i \to \infty$. Consequently, the integrand decays faster by two powers of λ_i^2 and the spectral integrals over λ_i with $i = 1, 2, 3$ are UV-finite.

In $d = 3$ there are no divergent subdiagrams and the sunset is superficially logarithmically divergent. We only subtract the zeroth order of the Taylor expansion, which contributes to the mass renormalisation.

We are left with finite spectral integrations for the sunset graph in $d = 3, 4$ at $\epsilon = 0$. The integrand depends analytically on the external momentum, the spectral values λ_i

with $i = 1, 2, 3$ of the three internal lines as well the respective spectral functions $\rho(\lambda_i)$. In general, the remaining spectral integrals have to be performed numerically.

In summary, spectral BPHZ renormalisation, as described in detail above, has the same workflow as in the last section and is depicted in Figure 4.2: First we apply dimensional regularisation to the momentum integrations and swap the order of momentum and spectral integrals. Then we perform the momentum integration analytically, right bottom corner in Figure 4.2. Finally, we apply the spectral BPHZ step: the Taylor expansion in all momenta about the renormalisation scale μ, which allows us to take the limit $\epsilon \to 0$. This leaves us with the task to perform the finite spectral integrals either analytically or numerically, depending on the application.

4.1.1.5. One-loop example: ϕ^3-theory in $d = 6$

For further illustration we now apply spectral BPHZ renormalisation within the simple perturbative example of the one-loop DSE for the two-point function of the (renormalisable) ϕ^3-theory in $d = 6$ dimensions with a coupling $g/(3!)\int_x \phi^3$. The advantage of this example is that already at one-loop it requires both a mass renormalisation and a wave function renormalisation. Hence, both can be discussed within a simple one-loop computation. In contrast, in the ϕ^4-theory the wave function renormalisation only arises at two-loop from the sunset diagram (even for $\phi_c \neq 0$).

In the ϕ^3-theory, the only diagrams in the gap equation Figure 4.1 are the polarisation diagram and the squint diagram. At one loop we only have to consider the polarisation diagram. In $d = 6$, this diagram is quadratically divergent. The respective DSE for the (inverse) propagator reads schematically,

$$\Gamma^{(2)}(p) = Z_{\phi,0}(\mu)\left(p^2 + m^2_{\phi,0}(\mu)\right) + g^2 \int_{\lambda_1,\lambda_2} \lambda_1\lambda_2\, \rho(\lambda_1)\rho(\lambda_2)\, F(p,\mu;\lambda_1,\lambda_2)\,. \tag{4.14}$$

The integrand F results from the momentum integration and depends on the renormalisation group scale μ due to dimensional regularisation. $Z_{\phi,0}$ is the wave function renormalisation and $m^2_{\phi,0}$ is the bare mass squared. Both bare parameters contain counterterms that remove the divergences in the diagrams within an expansion about $p^2 = \mu^2$: the constant quadratic divergence and the logarithmic divergence proportional to p^2. This amounts to the choices

$$\begin{aligned} Z_{\phi,0}(\mu) &= 1 - g^2 \int_{\lambda_1,\lambda_2} \lambda_1\lambda_2\, \rho(\lambda_1)\rho(\lambda_2)\, \frac{\partial F(p,\mu;\lambda_1,\lambda_2)}{\partial p^2}\bigg|_{p^2=\mu^2}\,, \\ Z_{\phi,0}(\mu) m^2_{\phi,0}(\mu) &= m^2_\phi - g^2 \int_{\lambda_1,\lambda_2} \lambda_1\lambda_2\, \rho(\lambda_1)\rho(\lambda_2) \\ &\quad \times \left[F(p,\mu;\lambda_1,\lambda_2) - \mu^2\, \frac{\partial F(p,\mu;\lambda_1,\lambda_2)}{\partial p^2}\bigg|_{p^2=\mu^2}\right], \end{aligned} \tag{4.15}$$

for wave function and mass renormalisation respectively. The counterterms proportional to g^2 in (4.15) provide the first two terms of the Taylor expansion about $p^2 = \mu^2$ of the

diagram. To see this, we insert (4.15) in the DSE (4.14),

$$\Gamma^{(2)}(p) = p^2 + m_\phi^2 + g^2 \int_{\lambda_1,\lambda_2} \lambda_1\lambda_2\, \rho(\lambda_1)\rho(\lambda_2) \times \left[F(p,\mu;\lambda_1,\lambda_2) - F(\mu,\mu;\lambda_1,\lambda_2) - \left(p^2-\mu^2\right) \frac{\partial F(p,\mu;\lambda_1,\lambda_2)}{\partial p^2}\bigg|_{p^2=\mu^2} \right] . \tag{4.16}$$

Equation (4.16) is depicted in Figure 4.3. Accordingly, (4.15) implements the standard renormalisation conditions, that the quantum corrections vanish at $p^2 = \mu^2$,

$$\begin{aligned} \Gamma^{(2)}(p^2=\mu^2) &= Z_\phi(\mu^2 + m_\phi^2) \\ \partial_{p^2}\Gamma^{(2)}(p^2=\mu^2) &= Z_\phi\,, \end{aligned} \tag{4.17}$$

for the two-point function with $Z_\phi = 1$. In the present ϕ^3-example these two renormalisation conditions are complemented by that for the coupling g, which is also logarithmically divergent in $d = 6$. As we have introduced this example only for illustration of spectral BPHZ renormalisation, we refrain from discussing this any further. Mode details on the spectral renormalisation conditions can be found in Section 4.1.2.2.

Continuing with the discussion of spectral renormalisation for the two-point function, the subtraction of F in (4.16) by its own Taylor expansion at $p^2 = \mu^2$ leads to finite spectral integrals. We emphasise that this is not achieved by simply subtracting the $1/\epsilon$-terms before performing the spectral integration: Since F scales with λ^2 for large λ with $\lambda = \lambda_1, \lambda_2$, the spectral integrals in (4.14) are quadratically divergent. After spectral BPHZ renormalisation however, the subtracted scalar integrand in (4.16) scales as $1/\lambda^2$. The subtraction scheme cancels the leading and subleading contributions in λ to F and leads to finite spectral integrals.

4.1.1.6. Non-perturbative spectral renormalisation

The discussions of the last three sections, Section 4.1.1.3 to Section 4.1.1.5, entail that spectral renormalisation leads to two different parts in the counterterms: the first part is related to the momentum divergences and has all the properties of the counterterms in dimensional regularisation. The second part comes from the spectral divergences. The counterterms in spectral dimensional renormalisation respects all symmetries including gauge symmetries and is tantamount to dimensional regularisation and renormalisation. The counterterms in spectral BPHZ renormalisation lack the full symmetries. In particular in gauge theories the BPHZ counterterms are necessarily not gauge invariant, precisely for restoring gauge consistency of the full renormalised result.

Importantly, in both spectral renormalisation schemes, the spectral counterterms follow the same recursive relations known from standard perturbation theory. This makes it a consistent renormalisation scheme to all orders of perturbation theory.

In non-perturbative applications of the present spectral approach, the non-perturbative information is solely present in the spectral functions of propagators and vertices. Moreover, within the DSE we only deal with one- and two-loop diagrams with n vertices derived from the master DSE in (2.30), see also Figure 2.2. We have one classical (bare) vertex and $n-1$ full vertices as well as full propagators. If recursively written in terms of

loops, both, the *finite* full vertices and propagators, carry subtractions of the divergences in these diagrams that render in particular subdiagrams finite. The leftover subtractions from these re-distribution renormalise the one or two explicit loops in the DSE diagrams.

In summary, non-perturbative spectral renormalisation only concerns the counterterms for the explicit loops in the DSE, while the rest of the renormalisation is carried by the finite full vertices and propagators that have to obey the renormalisation conditions. This is a consistent numerical non-perturbative renormalisation scheme.

4.1.2. ϕ^4-theory in 2+1 dimensions

The ϕ^4-theory in $2+1$ dimensions is super-renormalisable, and the initial two renormalisation conditions for the two-point function in Figure 4.1 reduce to the first one for the mass. Moreover, we do not need to renormalise the coupling. This entails that in the DSE for the scalar two-point function spectral BPHZ renormalisation as discussed in Section 4.1.1.4 simply amounts to subtracting the zeroth order term in the Taylor expansion about $p^2 = \mu^2$. After the momentum integrals are computed analytically within dimensional regularisation, we are left with the finite spectral integrals.

After completing renormalisation, the iterative solution procedure in the DSE is briefly described as follows: With a given input spectral function the renormalised DSE is evaluated in Minkowski spacetime. The input spectral function is either the initial guess or the result of the last iteration step. Then, an updated retarded two-point function is computed from the result. This allows us to extract an updated spectral function, which is fed back as input into the next iteration step. In this section we discuss the calculation sketched above in a detailed way, step by step.

4.1.2.1. Momentum integration and spectral renormalisation

The DSE can be expressed as the sum of the bare two-point function and the loop diagrams D_j,

$$\Gamma^{(2)}(p) = p^2 + m^2_{\phi,0} + \sum_{\{j\}} D_j(p) \,, \tag{4.18}$$

with $j = \text{tad,pol,sun,squint}$. In (4.18) we have used that the ϕ^4-theory in $d = 3$ is super-renormalisable and the only divergent term is the mass term. From now on, we drop the μ-dependence of the spectral integrands for notational simplicity. With the Källén-Lehmann spectral representation for the full propagator (4.3), as well as momentum-independent vertices, an arbitrary loop diagram D_j in the DSE takes the form,

$$D_j(p) = g_j \prod_i^{N_j} \left(\int_{\lambda_i} \lambda_i \rho(\lambda_i) \right) \, I_j(p; \lambda_1, ..., \lambda_{N_j}) \,. \tag{4.19}$$

The prefactors g_j are the products of the combinatorial prefactors in the DSE and the vertices of the corresponding diagram. In Table A.1 we provide the prefactors for the Minkowski version of (4.19), see (4.22).

D_j has N_j internal lines, each of them coming with one spectral integral and a corresponding spectral function. The I_j are nothing but a product of (momentum) loop integrals

over N_j classical propagators with different spectral masses λ_i,

$$I_j(p;\lambda_1,\ldots,\lambda_{N_j}) = \prod_k^{N_j^{\text{loops}}} \int \frac{d^3q_k}{(2\pi)^3} \prod_i^{N_j} \frac{1}{\lambda_i^2 + l_i^2}\,. \tag{4.20}$$

In (4.20) the momenta l_i are linear combinations of the loop-momenta q_k and the external momentum p. The number of loops is denoted by N_j^{loops} in (4.20). The analytic solutions of these integrals in $d = 3$ are known from perturbation theory, e.g. [242], and can be used here.

With the analytic expressions for I_j, we apply spectral BPHZ renormalisation, c.f. Section 4.1.1.4. Please note that only the logarithmically divergent sunset diagram D_{sun} explicitly requires renormalisation, since the bare tadpole simply can be absorbed in the definition of the bare mass squared. To cancel the logarithmic divergence of this diagram, within the BPHZ approach we subtract the zeroth order term in the Taylor expansion of D_{sun} about $p^2 = \mu^2$. The renormalised diagram reads

$$D_{\text{sun}}^{\text{ren}}(\omega) = g_{\text{sun}} \int_{\lambda_1,\lambda_2} \lambda_1\lambda_2\rho(\lambda_1)\rho(\lambda_2)\big[I_{\text{sun}}(\omega;\lambda_1,\lambda_2) - I_{\text{sun}}(\mu;\lambda_1,\lambda_2)\big]\,. \tag{4.21}$$

4.1.2.2. Evaluation at real frequencies

The $I_j(p)$ are evaluated in Minkowski spacetime for the retarded two-point function. This is done by parametrising the complex (Euclidean) frequency as $p_0 = -\mathrm{i}\omega_+$, see (4.5) and explicitly carrying out the limiting procedure. In a slight abuse of notation we denote the continued expression as $I_j(\omega)$. They are given explicitly in Appendix B.4. The DSE in Minkowski spacetime reads

$$\Gamma^{(2)}(\omega) = -\omega^2 + m_{\phi,0}^2 + \sum_{\{j\}} g_j \prod_i^{N_j} \left(\int_{\lambda_i} \lambda_i\rho(\lambda_i)\right) I_j(\omega,\mu;\lambda_1,...,\lambda_{N_j})\,. \tag{4.22}$$

The prefactors of the diagrams of the DSE (4.22) with the classical vertex approximation and the skeleton expansion can be found in Table A.1. It can be deduced from the analytic structure of the spectral integrands $I_j(\omega)$, that the support in ω of the imaginary part of the polarisation diagram starts at $\omega = \lambda_1 + \lambda_2$, as expected. Similarly, we find that the support of the sunset diagram starts at $\omega = \lambda_1 + \lambda_2 + \lambda_3$. Hence, the support of the expressions in the two-point function is given by multiples of the pole mass. This shows how the Cutkosky cutting rules can be easily extracted from the present spectral approach.

It is clear from (4.22) that the spectral renormalisation approach allows for the implementation of physical on-shell renormalisation conditions. This is in contrast to Euclidean computations, where on-shell renormalisation can only be implemented for massless modes. On-shell renormalisation has the advantage that it minimises the quantum corrections in a study of the resonance spectrum of a given theory. The renormalisation conditions (4.17) for a ϕ^4-theory in $d = 3$ dimensions reduce to

$$\Gamma^{(2)}(p^2 = -m_{\text{pole}}^2) = 0\,, \tag{4.23}$$

since both the coupling and the kinetic term do not require renormalisation. The triviality of the wave function renormalisation or rather the vanishing anomalous dimension entail,

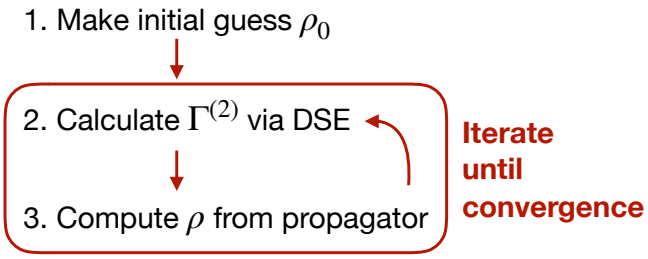

Abbildung 4.4.: Iteration procedure for computing the spectral function. With the initial guess ρ_0 for the spectral function, the two-point function $\Gamma^{(2)}$ is computed via the DSE. The resulting spectral function is fed back into the DSE for the two-point function. This procedure is iterated until the convergence for the spectral function is reached.

that the leading large momentum behaviour of the propagator is given by $1/p^2$. Accordingly, the canonical commutation relations of the scalar field are unchanged, as is the normalisation of dynamical states. The sum rule (4.7) is hence formally always satisfied in $2+1$ dimensions, and thus provides a non-trivially benchmark test of our results.

4.1.2.3. Spectral integration and iteration

The remaining multidimensional integrals over the spectral parameters λ_i in (4.22) are solved numerically. Details on the numerical part of the calculation can be found in Appendix C.2. Subsequently, the spectral function is extracted from the updated two-point function via (4.4) and fed back into the DSE. In this way, the DSE is solved iteratively by successively integrating the right-hand side of the DSE with the updated spectral function from the last step until the solution converges, comp. Figure 4.4. Note that all the dynamical information is stored in the spectral functions, and the integrands I_j do not change within the iterations. Hence, each iteration only involves the numerical solution of the respective multidimensional spectral integral of each diagram.

More details on the convergence test can be found in Appendix C.2. There, the rapid convergence is illustrated at an exemplary case, see in particular Figure C.2.

As a starting point for the iterative procedure, an initial guess for the spectral function has to be made that is close enough to the solution (in the attraction basin of the solution in terms of the iteration). In the present case with the on-shell renormalisation (4.23) the spectral function of the classical theory carries already the correct pole position by definition. In general this will improve the convergence properties of the iteration. This is yet another property that singles out on-shell renormalisation. The classical spectral function is given by,

$$\begin{aligned}\rho_0(\omega) &= \delta(\omega^2 - m_{\text{pole}}^2) \\ &= \frac{\pi}{m_{\text{pole}}}\left[\delta(\omega - m_{\text{pole}}) - \delta(\omega + m_{\text{pole}})\right] .\end{aligned} \tag{4.24}$$

The delta-function peaks are located at the physical pole mass squared, and the delta-functions at $\pm m_{\text{pole}}$, are related by anti-symmetry. With the initial guess in (4.24), the

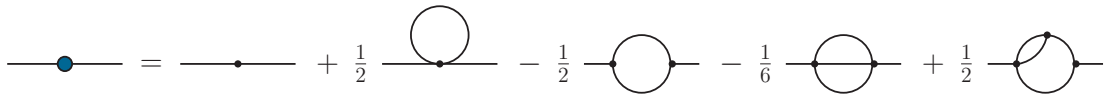

Abbildung 4.5.: DSE of the two-point function with the classical vertex approximation as used in Section 4.1.3.1. The tadpole can be absorbed into the mass renormalisation in the bare inverse propagator, for more details can be found in the main text. The two-loop terms constitute vertex corrections of the classical vertices in the one-loop diagrams. The DSE is not two-loop complete as further vertex corrections have been dropped due to the classical vertex approximation. The notation is defined in Figure 2.1.

spectral integrals in the propagator DSE (4.22) reduce to the perturbative expressions. Further iterations then lead to resummation of the respective diagram classes.

The branch cuts of the loop corrections generate a continuous tail in the spectral function when inserting the initial spectral function ρ_0 on the right-hand side of the DSE. This entails via the sum rule in (4.7), that the residue of the mass pole decreases to $Z < 1$ due to the positive weight of the tail. The mass pole residue of the updated spectral function is obtained via the relation

$$Z = -\frac{2m_{\text{pole}}}{\partial_\omega \Gamma^{(2)}(\omega)}\bigg|_{\omega=m_{\text{pole}}} . \tag{4.25}$$

The counterterm for the mass is conveniently extracted from $\text{Re}\,\Gamma^{(2)}(\omega = m_{\text{pole}}) = 0$.

The three-point function $\Gamma^{(3)}[\phi_c]$ in the gap equation is evaluated at the constant field value $\phi_c = \phi_0$, which solves the equation of motion, $\partial_\phi V_{\text{eff}}[\phi_0] = 0$, at each step of the iteration. For fields in the vicinity of ϕ_0 we can expand the effective potential in powers of $\phi^2 - \phi_0^2$ in the broken phase, leading to,

$$V_{\text{eff}}[\phi] = \sum_{n=2}^{\infty} \frac{v_n}{2n!} \left(\phi^2 - \phi_0^2\right)^n . \tag{4.26}$$

Accordingly, the two-, three- and four-point functions at vanishing momentum are given by,

$$\begin{aligned}
\Gamma^{(2)}[\phi_0] &= \frac{1}{3} v_2\, \phi_0^2 , \\
\Gamma^{(3)}[\phi_0] &= v_2\, \phi_0 \left(1 + \frac{1}{15}\frac{v_3}{v_2}\phi_0^2\right) , \\
\Gamma^{(4)}[\phi_0] &= v_2 \left(1 + \frac{1}{5}\frac{v_3}{v_2}\phi_0^2 + \frac{1}{105}\frac{v_4}{v_2}\phi_0^4\right) .
\end{aligned} \tag{4.27}$$

Dropping the higher order terms $O\big((\phi^2-\phi_0^2)^3\big)$ in (4.26), the terms in parentheses of (4.27) all reduce to unity. We introduce the curvature mass $m^2_{\text{cur}}(m_{\text{pole}}, \lambda_\phi)$ as the value of the two-point function at vanishing momentum, i.e.,

$$m^2_{\text{cur}}(m_{\text{pole}}, \lambda_\phi) \equiv \Gamma^{(2)}[\phi_0](p = 0) . \tag{4.28}$$

Note that m_{cur} is determined by the two free parameters of the theory, m_{pole} and λ_ϕ. It is no new parameter. Using (4.28) in (4.27) and dropping the higher-order contributions, the three- and four-point functions at vanishing momentum are given by,

$$\begin{aligned}\Gamma^{(3)}[\phi_0] &= \sqrt{3\, v_2}\, m_{\text{cur}}\,, \\ \Gamma^{(4)}[\phi_0] &= v_2\,. \end{aligned} \tag{4.29}$$

v_2 is nothing but the full four-vertex at vanishing momentum, $v_2 = \Gamma^{(4)}[\phi_0](p=0)$. For a general, momentum dependent four-point function in the s-channel, we find for the momentum-dependent three-point function,

$$\Gamma^{(3)}(p) = \Gamma^{(4)}(p)\sqrt{\frac{3}{v_2}} m_{\text{cur}}\,, \tag{4.30}$$

dropping the ϕ_0-dependence of the correlators from now on. Note that by choosing $\Gamma^{(3)}$ consistently with $\Gamma^{(4)}$ as done above, the three-point function becomes dynamical and is hence updated through each iteration by its dependence on the two- and four-point function.

4.1.3. Results

In this section we compute and discuss the solution to the DSE for the propagator with two different approximations for the vertices. First we solve the DSE with the classical four-point vertex and the related three-point vertex as derived in Section 4.1.2.3. Subsequently, the DSE is considered in a skeleton expansion. Both, the full three- and four-point functions $\Gamma^{(3)}, \Gamma^{(4)}$, are based on the bubble-resummed s-channel approximation to the four-point vertex derived from its Bethe-Salpeter equation. We also use the DSE for $\Gamma^{(4)}$ to compute results within a self-consistent version of this setup.

4.1.3.1. DSE with classical four-point vertex

In the present section we approximate the full vertices in the gap equation in Figure 4.1 with their classical counterparts while keeping the two-loop terms. This is depicted in Figure 4.5. The two-loop terms constitute vertex corrections to the classical four-point function in the tadpole diagram (sunset) and for the classical three-point function in the polarisation diagram (squint). In the latter case this is but half of the vertex correction, the other half has been dropped in the current approximation when approximating the full three-point function in the polarisation diagram by its classical counterpart. This approximation resums the propagator but is expected to fail in a regime where vertex corrections grow large.

For the four-point function the classical vertex approximation amounts to,

$$\Gamma^{(4)} = S^{(4)} = \lambda_\phi\,. \tag{4.31}$$

With (4.31) and (4.29), the three-point function is given by

$$\Gamma^{(3)} = S^{(3)}[\phi_0] = \sqrt{3\lambda_\phi} m_{\text{cur}}\,, \tag{4.32}$$

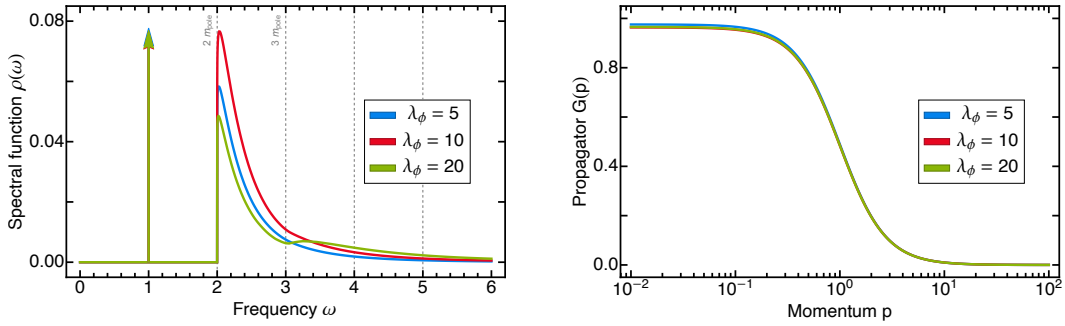

Abbildung 4.6.: Spectral function (left) and propagator (right) in the scalar theory for the coupling choices $\lambda_\phi = 5, 10, 20$ from the full DSE with classical vertices using on-shell renormalisation (4.23). All dimensionful quantities were rescaled in units of the respective mass pole result. The different height of the delta peaks encodes the magnitude of the residue relative to the other spectral functions. The grey dashed lines mark the n-particle onsets. For large enough coupling, the three-particle onset becomes visible. The propagators were computed by the Källén-Lehmann spectral representation.

see (4.29). The resulting prefactors g_j of the diagrams are listed in Table A.1. The tadpole diagram only contributes a momentum-independent term that shifts the mass, and is absorbed into the mass renormalisation.

All units will be given in the value of the pole mass. Put differently, we introduce dimensionless units

$$\lambda_\phi \to \frac{\lambda_\phi}{m_{\text{pole}}}\,, \quad \omega \to \frac{\omega}{m_{\text{pole}}}\,, \quad p \to \frac{p}{m_{\text{pole}}}\,, \tag{4.33}$$

This also entails $m_{\text{pole}} = 1$, and the massless limit is taken with $\lambda_\phi \to \infty$. The dimensionless units also emphasise the well-known fact, that the physics of the ϕ^4-theory in $d = 2+1$ is specified by one dimensionless parameter, the ratio of coupling and (pole) mass.

We solve the DSE for three different values of the classical coupling constant $\lambda_\phi = 5, 10, 20$. The renormalised mass is fixed by the on-shell RG conditions (4.23) with $m_{\text{pole}} = 1$, and the quantum corrections to the mass vanish on-shell. For the smallest classical coupling used here, $\lambda_\phi = 5$, we take the classical spectral function as initial choice. For the further couplings we use as the initial choice the full quantum spectral function of the closest coupling value available. This stabilises the iterative procedure when successively moving further to larger couplings inducing larger quantum corrections.

The resulting spectral functions, as well as the corresponding propagators, are shown in Figure 4.6 for different values of the classical four-point coupling, $\lambda_\phi = 5, 10, 20$. The mass pole as well as the onset of the two-particle threshold, $\phi \to \phi\phi$, at twice the pole mass are clearly visible. The three-particle threshold, $\phi \to \phi\phi\phi$, at $3m_{\text{pole}}$ becomes visible for large enough coupling. We emphasise that also all higher n-particle thresholds are present in the result and can be resolved numerically. Since they are suppressed by the inverse of the respective threshold energy squared, they are not visible in the plots. When further zooming in on the higher onsets which were marked by the dashed lines, the respective onsets would become visible.

The main effect of a stronger coupling (or small pole mass) can be understood intuitively very well. The residue of the mass pole becomes smaller, while the scattering cut gets

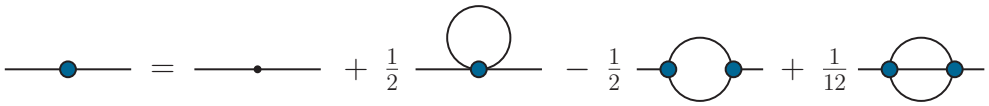

Abbildung 4.7.: Truncated DSE of the two-point function as used in Section 4.1.3.4. Notation is given in Figure 2.1. The full s-channel four-vertex in the tadpole diagram enters via its spectral representation (4.36). The full vertices in polarisation and sunset are approximated at zero frequency, see Paragraph 4.1.3.2.3. The different prefactor in front of the sunset diagram as compared to Figure 4.5 is due to the tadpole's contribution to the sunset topology, cf. Paragraph 4.1.3.2.2. Squint, kite and double-bubble topology are dropped, as motivated in Section 4.1.3.2.

larger contributions, i.e. scatterings get enhanced due to the large coupling or the small pole mass. As mentioned before, the only parameter present is $\lambda_\phi/m_{\text{pole}}$, and in the present units with $m_{\text{pole}} = 1$ this simply is λ_ϕ, see (4.33). At the largest coupling value considered here, $\lambda_\phi = 20$, also the higher scattering processes start contributing significantly: the threshold at $3m_{\text{pole}}$ is clearly visible in the spectral function for this coupling, shown in the left panel of Figure 4.6. For large couplings also the higher thresholds kick in. This scattering physics also leaves its traces in the Euclidean propagator, shown in the right panel of Figure 4.6: while first the propagator drops for small momenta with the increasing coupling (measured in the respective pole masses), it increases again for even larger ones due to the more pronounced scattering physics present in the spectral function.

The resolution of the higher particle thresholds is nearly impossible within reconstruction methods due to their exponential suppression in the Euclidean data. This emphasises once again the strength of our semi-analytic approach of calculating spectral functions directly from realtime correlators, where all these thresholds are incorporated explicitly.

4.1.3.2. Fully non-perturbative DSE

The practical applicability of the spectral renormalisation scheme has been shown in the last section within the DSE for the two-point function with classical vertices, see Figure 4.5. This approximation implements a full resummation of the propagator. The approximation also includes some corrections in the higher order diagrams in the DSE as already discussed in the last section. While these diagrams contribute to the higher-order scattering thresholds, this may not be sufficient in the limit of asymptotically large couplings $\lambda_\phi/m_{\text{pole}} \to \infty$, also tantamount to small pole masses. In this regime the vertex corrections should be taken into account consistently.

In the present section we discuss non-perturbative expansion schemes of the DSE as well as resummations of the vertices. This allows us to study the strongly correlated regime of the theory. A full quantitative study is beyond the scope of the present contribution and is deferred to future work.

A non-perturbative expansion scheme for the DSE is given by the skeleton expansion. In this expansion all vertices are full-dressed, and higher loop-order diagrams with dressed propagators and vertices have to be introduced successively. Instead of an expansion in

Abbildung 4.8.: s-channel expansion of the momentum dependent four-point function $\Gamma^{(4)}$. With a bubble resummation one arrives at (4.34). The notation is defined in Figure 2.1

classical vertices it is an expansion in fully dressed ones. This expansion is closely related to nPI-resummation schemes, in the ϕ^4-theory it is related to a 4-PI scheme.

Here we consider the two-loop order of the skeleton expansion in the broken phase. A first observation is, that the prefactor of the squint diagram vanishes: it is fully contained in the polarisation diagram with two dressed three-point functions $\Gamma^{(3)}$. At perturbative two-loop level the expansion involves a kite-diagram as well as a double-bubble diagram. Both topologies are only generated from the polarisation diagram in the DSE, more precisely from vertex corrections of the dressed three-point function. These contributions have to be subtracted in terms of explicit kite and double-bubble diagram in the skeleton expansion. For small field expectation values $\phi_0 \ll 1$, it is reasonable to neglect the kite diagram, since it scales like ϕ_0^4 due to its four three-point functions. We will also drop the double-bubble diagram which is of order ϕ_0^2. These approximations are discussed again later. The remaining diagrams are the polarisation, sunset and tadpole. The present approximation of the two-loop skeleton expansion of the gap equation is depicted in Figure 4.7.

4.1.3.2.1. Bubble-resummed s-channel four-point function It is left to specify the approximations for the three-point and four-point vertices. To begin with, we still use the relation (4.30) for the three-point function with the assumption of small field values ϕ_0^2. This leaves us with the four-point function, for which we resort to a bubble-resummed s-channel expansion, e.g., [68, 245], shown graphically in Figure 4.8. Algebraically, the momentum dependence of the s-channel in the four-point function can be expressed as

$$\Gamma^{(4)}(p) \;=\; \frac{\lambda_\phi}{1+\lambda_\phi \Pi_{\text{fish}}(p)}\,. \tag{4.34}$$

Here, Π_{fish} is the one-loop part of the s-channel self-energy (apart from λ_ϕ^2),

$$\Pi_{\text{fish}}(p) \;=\; \frac{1}{2}\int_{\lambda_1,\lambda_2} \lambda_1\lambda_2\rho(\lambda_1)\rho(\lambda_2)\; I_{\text{pol}}(p;\lambda_1,\lambda_2)\,. \tag{4.35}$$

This is exactly the polarisation diagram also appearing in the DSE with prefactor $g_{\text{pol}} = 1$, cf. Figure 4.3 and (4.14). The analytically-continued expression for $\Gamma^{(4)}(\omega)$ is obtained by simply replacing $I_{\text{pol}}(p)$ in (4.35) with $I_{\text{pol}}(\omega)$.

The resulting $\Gamma^{(4)}(\omega)$ depends on the full propagator through the spectral functions in (4.35), and the equations for $\Gamma^{(2)}$ and $\Gamma^{(4)}$ are coupled. We also note that the s-channel resummation used here is obtained in the NLO-expansion of the $1/N$-expansion of an O(N)-theory with N real scalar fields. In the present $N = 1$ case, s-channel dominance is merely an assumption. For a full quantitative study, this assumption would have to be

validated numerically. Otherwise, other scattering channels would have to be taken into account as well.

The iteration procedure does not change for such a coupled system, even though coupled systems generically show worse convergence properties. For a given input pair $\Gamma^{(2)}$ and $\Gamma^{(4)}$ we compute the next iteration from the right-hand side of the DSE for $\Gamma^{(2)}$, Figure 4.7, and the resummed representation of $\Gamma^{(4)}$, (4.34). This is repeated until convergence is reached.

4.1.3.2.2. Tadpole contribution to the sunset topology Before turning to the explicit approximation used in the skeleton scheme, we emphasise again, that the fully-dressed tadpole diagram and the fully-dressed sunset diagram are related. They both carry the s-channel of the four-point vertex. While the tadpole simply is proportional to the s-channel four-point vertex, the sunset includes the fish-diagram as a sub-diagram. Indeed, the perturbative two-loop sunset graph is a combination of the respective contributions, and the prefactor g_{sun} of the sunset diagram in the skeleton expansion is such that the perturbative prefactor, c.f. Table A.1.

The tadpole diagram is proportional to the s-channel four-point vertex, and we use the full momentum-dependent four-point vertex obtained from the bubble resummation (4.34). Inserting the diagrammatic vertex expansion explicitly into the diagram, one sees that the dressed tadpole contributes to the sunset topology on the perturbative two-loop level. However, this contribution does not account for the full prefactor of the latter. To arrive at the correct perturbative prefactor of the sunset diagram, the prefactor of the fully-dressed sunset diagram in the skeleton expansion needs to be adjusted accordingly, see Figure 4.7 and Table A.1.

4.1.3.2.3. Vertex approximation in the skeleton expansion In the sunset diagram, the two four-point vertices are averaged due to the two loop momenta that run through both vertices. This averaging holds true for both, the Euclidean branch and the Minkowski one. For this reason we approximate the full momentum-dependent four-point vertices by that at vanishing momentum, $\Gamma^{(4)}[\phi_0]$.

In our approximation with $\Gamma^{(3)}_{\text{pol}}(p) = \phi_0 \Gamma^{(4)}(p)$ with external momentum p, the vertices in the polarisation diagram are, as in the tadpole, proportional to the s-channel four-point vertex. For the sake of simplicity we also use $\Gamma^{(3)}_{\text{pol}} = \phi_0 \Gamma^{(4)}(\omega = 0)$. In any case, the spectral integrands I_{pol} and I_{sun} of polarisation and sunset diagram remain the same as in Section 4.1.3.1. However, their prefactors g_{pol} and g_{sun} are modified by the skeleton expansion, cf. Table A.1.

As outlined, our solution method requires an analytic solution of the momentum integrals for all diagrams. In the current approximation this holds true for the polarisation and sunset diagram. It is not the case for the tadpole diagram because the loop-momentum is probing the non-trivial momentum structure of the resummed four-point function (4.34). This problem can be resolved if we can use a spectral representation for the resummed four-point function, which is discussed in the following section.

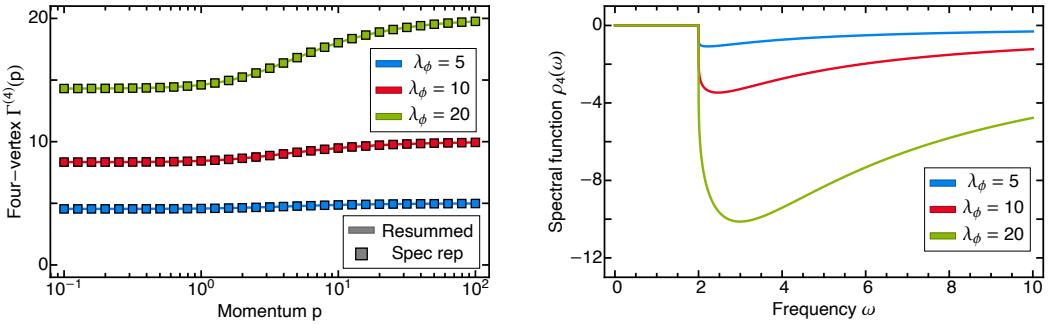

Abbildung 4.9.: Left: Comparison of the momentum dependent (Euclidean) four-vertex $\Gamma^{(4)}(p)$ in its initial form (4.34) with its spectral representation (4.36) for the coupling choices $\lambda_\phi = \{10{,}15{,}20\}$ using a classical propagator, i.e. a delta pole spectral function peaked at $m_{\text{pole}} = 1$. All dimensionful quantities were rescaled in units of the respective mass pole result. Right: Corresponding spectral functions of the four-point functions. The different height of the delta peaks encodes the magnitude of the residue relative to the other spectral functions. Also here, all dimensionful quantities were rescaled in units of the respective mass pole result.

4.1.3.3. Spectral representation for the four-point function

While the existence and practical form of spectral representations for full four-point functions pose an intricate problem, spectral representations for (approximations of) single exchange channels of the four-point function can be derived. From a practical perspective we may treat such a channel similarly to a propagator. This is well-motivated by considering that the resonant channels of a four-point function correspond to particle exchange interactions. Technically, this can be made explicit by means of a Hubbard-Stratonovich transformation. In analogy to a propagator we can make the same ansatz for a spectral representation for a single channel of the resummed vertex

$$\Gamma^{(4)}(p) \;=\; \lambda_\phi \;+ \int_\lambda \frac{\lambda\, \rho_4(\lambda)}{p^2 + \lambda^2}\,, \tag{4.36a}$$

with

$$\rho_4(\omega) \;=\; 2\,\mathrm{Im}\,\Gamma^{(4)}(-\mathrm{i}\omega_+)\,, \tag{4.36b}$$

where ω_+ again denotes the retarded limit (4.5). In (4.36) the constant classical part λ_ϕ has to be separated. It has no spectral representation and does not need one for the present purpose. Indeed, classical vertices have been already considered in Section 4.1.3.1.

Our results confirm that the analytic structure of the resummed vertex is compatible with (4.36) and works well. This can be seen in Figure 4.9, the computational details can be found in the next section, Section 4.1.3.4. The spectral function ρ_4 displayed in the right panel exhibits a continuous tail corresponding to the $\phi\phi \to \phi\phi$ scattering continuum for $\omega \geq 2m_{\text{pole}}$. The spectral representation (4.36) of the four-point function is used in the tadpole diagram in complete analogy to that of propagators.

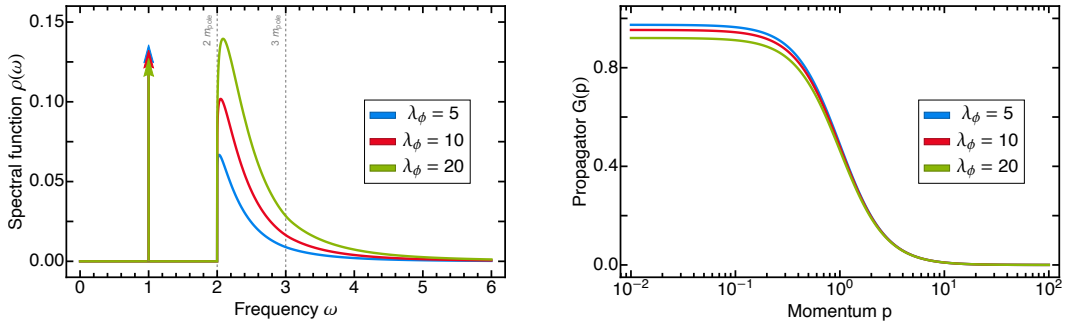

Abbildung 4.10.: Spectral function (left) and propagator (right) from the skeleton expanded DSE (comp. Figure 4.7) with a bubble-resummed s-channel expansion of the four-point function for coupling choices $\lambda_\phi = 5, 10, 20$ using on-shell renormalisation (4.23). The curves were rescaled by the respective mass poles. All vertices except for the tadpole one were approximated at $\omega = 0$. The weight of the continuous tail increases with coupling, the mass pole residue decreases. Higher n-particle onsets are not visible in the spectral function. The different height of the delta peaks encodes the magnitude of the residue relative to the other spectral functions. The propagators were computed by the Källén-Lehmann spectral representation. Increasing coupling makes the propagators deviate more from the classical propagator, which approaches 1 at momentum $p \to 0$.

Importantly, the spectral representation of the vertex effectively just leads to another classical propagator with spectral mass λ to the loop momentum integral. The momentum flowing through the four-vertex is the sum of the loop and external momentum. Thus, the momentum integral of the tadpole is identical to that of the polarisation diagram, since the internal line of the four-vertex carries $p + q$ and the initial internal line just the loop momentum q. The tadpole diagram can therefore be expressed as

$$D_{\text{tad}}(\omega) = g_{\text{tad}} \int_{\lambda_1,\lambda_2} \lambda_1\lambda_2\rho(\lambda_1)\rho_4(\lambda_2) I_{\text{pol}}(\omega;\lambda_1,\lambda_2)\,. \tag{4.37}$$

The spectral integral is logarithmically divergent, since the vertex spectral function ρ_4 drops off in the UV as λ^{-1} (as opposed to $\rho \sim \lambda^{-2}$ in the UV). Again, we employ spectral BPHZ renormalisation to subtract the zeroth order term of the Taylor expansion of I_{pol}. Finally, the renormalised diagram reads

$$D^{\text{ren}}_{\text{tad}}(\omega) = g_{\text{tad}} \int_{\lambda_1,\lambda_2} \lambda_1\lambda_2\rho(\lambda_1)\rho_4(\lambda_2)\big[I_{\text{pol}}(\omega;\lambda_1,\lambda_2) - I_{\text{pol}}(\mu;\lambda_1,\lambda_2)\big]\,. \tag{4.38}$$

4.1.3.4. Results for the coupled system of propagator and vertices

The DSE in the skeleton expansion is solved for the couplings also used in Section 4.1.3.1, $\lambda_\phi = 5, 10, 20$, measured in the pole mass $m_{\text{pole}} = 1$.

For the first iteration, initial choices $\rho_0, \rho_{4,0}$ for the spectral function of the propagator and that the four-point vertex are required. We use the classical spectral function (4.24) for ρ_0, as already done in Section 4.1.3.1. For the spectral function of the four-point function

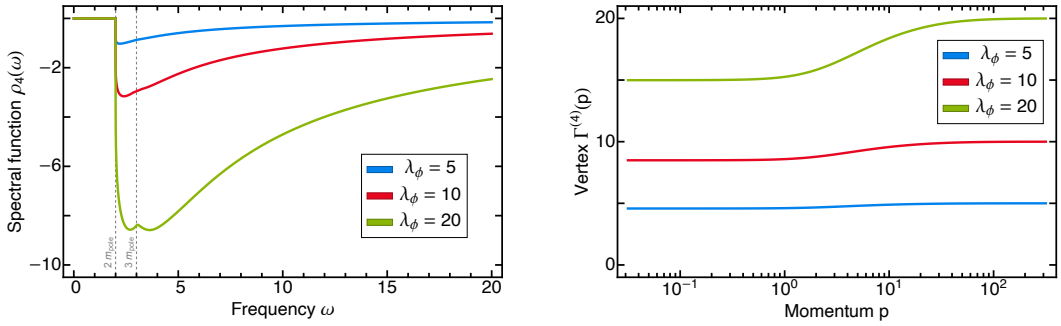

Abbildung 4.11.: Four-vertex spectral function (left) and four-vertex (right) from the skeleton expanded DSE (comp. Figure 4.7) with a bubble-resummed s-channel expansion of the four-point function for coupling choices $\lambda_\phi = 5, 10, 20$ using on-shell renormalisation (4.23). The curves were rescaled by the respective mass poles. All vertices except for the tadpole one were approximated at $\omega = 0$. The weight of the vertex spectral function increases with coupling. For the largest coupling choice, the three-particle onset is visible in the spectral function. The four-vertices were computed by their spectral-like representation (comp. (4.36)). The quantum corrections in the IR increase with coupling. All vertices approach their classical value in the UV.

$\rho_{4,0}$ compute it from the resummed representation of the four-point function, (4.34) with the initial choice of the spectral function of the propagator, ρ_0. This results in

$$\rho_{4,0}(\omega) = 2\,\mathrm{Im}\,\frac{\lambda_\phi}{1+\lambda_\phi \Pi_{\mathrm{fish},0}(\omega)}\,, \tag{4.39a}$$

with

$$\begin{aligned}\Pi_{\mathrm{fish},0} &= \frac{1}{2}\int_{\lambda_1,\lambda_2} \lambda_1\lambda_2\rho_0(\lambda_1)\rho_0(\lambda_2) I_{\mathrm{pol}}(\omega;\lambda_1,\lambda_2) \\ &= \frac{1}{2} I_{\mathrm{pol}}(\omega; m_{\mathrm{pole}}, m_{\mathrm{pole}})\,,\end{aligned} \tag{4.39b}$$

with $m_{\mathrm{pole}} = 1$. While one could also simply take the classical vertex, the convergence speed and potentially also the convergence radius (coupling range) is increased by the improved choice (4.39a). For further couplings λ_ϕ we take as initial choices ρ_0 and $\rho_{4,0}$ the full solutions ρ and ρ_4 of the closest coupling value already computed. This procedure has already been used in Section 4.1.3.1, and speeds up the convergence.

The spectral function and propagator obtained from the coupled system of resummed four-point function and DSE are displayed in Figure 4.10. As for the case of bare vertices, shown in Section 4.1.3.1, we find a distinct one-particle mass pole as well as a scattering tail. The $\phi \to \phi\phi\phi$ onset is not visible in the spectral function for any of the coupling configurations. It can be seen that for increasing coupling λ_ϕ, the tail of the spectral function becomes more enhanced, since the higher scattering states are more accessible. In turn, the mass pole residue decreases. The corresponding propagators in the right panel show similar behaviour as the for the DSE with bare vertices. The larger the coupling gets, the further the propagators deviate from the classical behaviour $G(p) \to 1$ for $p \to 0$.

In Figure 4.11 we display the spectral function of the s-channel four-point function and the Euclidean four-point function itself. The consistency of the spectral representation has been discussed already in the previous section, and is confirmed numerically, see Figure 4.9. Technically, the negativity of the spectral function displayed in Figure 4.11 can be understood from the dominant quantum correction to the classical vertex, which is negative. On the conceptual side, within the Hubbard-Stratonovich transformation ρ_4 is related to minus the spectral function of the exchange particle.

We find a continuous $2 \to 2$ scattering tail, starting at $2m_{\text{pole}}$ for all coupling choices. The spectral function is strongly enhanced with increasing coupling. Additionally, for larger coupling the spectral functions also clearly show the $1 \to 3$ scattering onsets starting at $3m_{\text{pole}}$, which was not visible in the propagator spectral functions (cf. left panel of Figure 4.10). By simple dimensional analysis it becomes clear that the higher n-particle thresholds in the propagator spectral function are suppressed by their respective energy threshold squared. This is not the case for the vertex spectral function: It decays with λ^{-1}, making the higher onsets less suppressed. In turn, the invisibility of four, five, and higher particle onsets is due to their decreasing amplitude, as every next higher onset comes with one additional loop.

Further, we note that the visible size of the $1 \to 3$ scattering onset has its sole origin in the tadpole diagram. This diagram contributes to the $1 \to 3$ scattering process due to the s-channel resummed four-point function, cf. Paragraph 4.1.3.2.2. The contribution of the sunset itself is very suppressed in comparison. This points towards a general feature of our approximation: In the large coupling (massless) limit, the tadpole becomes the dominating diagram in the spectral function (for $\omega > 3m_{\text{pole}}$). We elaborate more on the massless limit in Appendix A.2.

While presenting the spectral and correlation functions in units of the fixed mass pole $m_{\text{pole}} = 1$ allows for a comparison of the relative strength of the different contributions, the approach to the massless limit is better studied if the results are presented in units of a uniform interaction strength. This is achieved by measuring all results in units of the coupling λ_ϕ, see Appendix A.2. For the parameters $\lambda_\phi/m_{\text{pole}} = 5, 10, 20$ studied here this entails that we consider theories with the coupling $\lambda_\phi = 1$ with pole masses $m_{\text{pole}} = 1/5, 1/10, 1/20$. Evidently, within these units the spectral functions pole position moves towards zero and the onset of the scattering states gets more pronounced, see Figure 4.14.

4.1.3.5. Self-consistent skeleton expansion

Within the current approximation, we have explicitly dropped the kite and double-bubble diagrams. Implicitly we have also dropped the squint diagram, that corresponds to vertex corrections to the three-point function in the vacuum polarisation: we have used two dressed three-point vertices that are derived from the bubble resummation of the four-point function. Such an approximation of the three-point function does not contain the squint topology. An alternative approximation of the Dyson-Schwinger equation is derived as follows:

We start from the initial, full propagator DSE (Figure 4.1) and consider it in a diagrammatic expansion in orders of the constant field ϕ_0. In our approximation, these higher orders come via the three-vertices $\Gamma^{(3)}(p) = \phi_0 \Gamma^{(4)}(p) + O(\phi_0^3)$. Acting on the DSE with

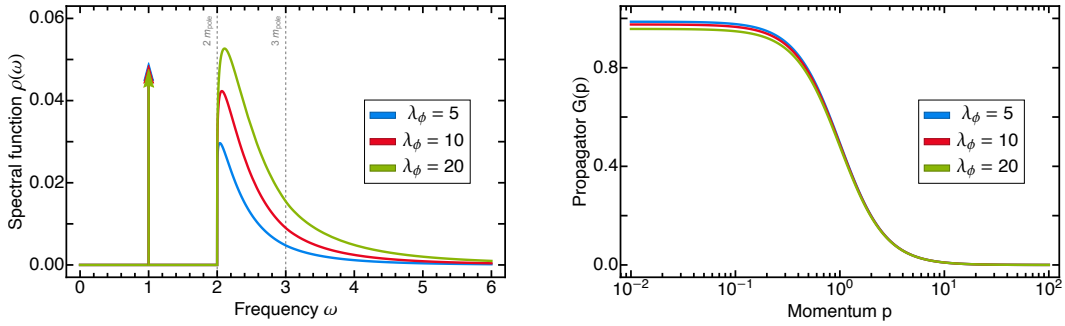

Abbildung 4.12.: Spectral function (left) and propagator (right) from the self-consistent skeleton expanded DSE (comp. Figure 4.7) with a bubble-resummed s-channel expansion of the four-point function for coupling choices $\lambda_\phi = 5, 10, 20$ using on-shell renormalisation (4.23). The polarisation diagram is here expressed through the s-channel four-vertex, cf. (4.42). The curves were rescaled by the respective mass poles. All vertices except for the tadpole one were approximated at $\omega = 0$. The weight of the continuous tail increases with coupling, the mass pole residue decreases. Higher n-particle onsets are not visible. The different height of the delta peaks encodes the magnitude of the residue relative to the other spectral functions. The propagators were computed by the Källén-Lehmann spectral representation. Increasing coupling makes the propagators deviate more from the classical propagator, which approaches 1 at momentum $p \to 0$.

two derivatives w.r.t. the constant field ϕ_0 and multiplying by $\phi_0^2/2$ afterwards, one finds the schematic relation

$$O_{\Gamma^{(2)},\mathrm{diag}}\left[\phi_0^2\right](p) = \frac{1}{2}\phi_0^2\left[\Gamma^{(4)}(p,-p,0,0) - \lambda_\phi\right] , \tag{4.40}$$

where $O_{\Gamma^{(2)},\mathrm{diag}}\left[\phi_0^2\right]$ represents all diagrams in the propagator DSE with two external constant field legs, including their initial prefactors. This includes the squint diagram and the vacuum polarisation.

On the right-hand side of (4.40), we have the full four-point function subtracted by its classical value. We also made explicit the specific momentum dependence of the four-point function. By differentiating twice w.r.t. to the momentum independent field ϕ_0, $\Gamma^{(4)}$ only depends on one external momentum p.

This entails that we can re-express all diagrams of $O_{\Gamma^{(2)},\mathrm{diag}}\left[\phi_0^2\right]$ through an s-channel four-point function. What is missing is the classical part of the vertex DSE. It is included by adding and subtracting the classical vertex contribution multiplied by an appropriate prefactor involving the constant field, $\frac{1}{2}\phi_0^2\lambda_\phi$ to the propagator DSE. This leads us to (4.40). Evidently, the additional constant part $-\frac{1}{2}\phi_0^2\lambda_\phi$ in (4.40) is absorbed in the mass renormalisation.

The expectation value ϕ_0^2 can be expressed in terms of $\Gamma^{(2)}(0) = m_{\mathrm{cur}}^2$ and $\Gamma^{(4)}[0]$. This leads us to

$$\frac{1}{2}\phi_0^2\,\Gamma^{(4)}(p) = \frac{3}{2}m_{\mathrm{cur}}^2\frac{\Gamma^{(4)}(p)}{\Gamma^{(4)}(0)} , \tag{4.41}$$

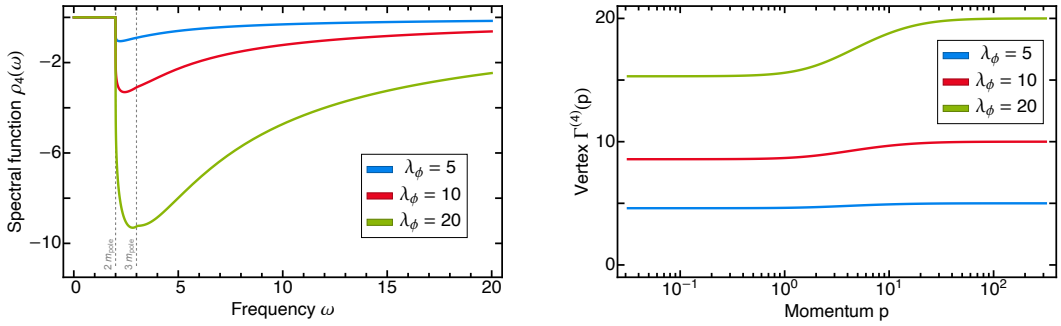

Abbildung 4.13.: Four-vertex spectral function (left) and four-vertex (right) from the self-consistent skeleton expanded DSE (comp. Figure 4.7) with a bubble-resummed s-channel expansion of the four-point function for coupling choices $\lambda_\phi = 5, 10, 20$ using on-shell renormalisation (4.23). The polarisation diagram is here expressed through the s-channel four-vertex, cf. (4.42). The curves were rescaled by the respective mass poles. All vertices except for the tadpole one were approximated at $\omega = 0$. The weight of the vertex spectral functions increases with coupling. For the largest coupling choice, the three-particle onset is visible in the spectral function. The four-vertices were computed by their spectral-like representation (comp. (4.36)). The quantum corrections in the IR increase with coupling. All vertices approach their classical value in the UV.

which has the scaling of a two-point function, and reduces to $3/2m_{\rm cur}^2$ at vanishing momentum. Making use of (4.40) and (4.41), we are led to the DSE for the propagator with Minkowski frequencies ω,

$$\begin{aligned}\Gamma^{(2)}(\omega) = &-\omega^2 + m_{\rm pole}^2 + D_{\rm tad}^{\rm ren}(\omega) + D_{\rm sun}^{\rm ren}(\omega) \\ &+ \frac{3}{2} m_{\rm cur}^2 \left[\frac{\Gamma^{(4)}(\omega) - \Gamma^{(4)}(m_{\rm pole})}{\Gamma^{(4)}(0)}\right] ,\end{aligned} \tag{4.42}$$

and $i =$ tad,sun. Note that the polarisation and squint diagram have been absorbed into the last term of (4.42) proportional to $m_{\rm cur}^2$ as a result of (4.40). Due to the on-shell renormalisation condition (4.23), all renormalised diagrams vanish at $\omega = m_{\rm pole}$, that is $D_i^{\rm ren}(m_{\rm pole}) = 0$. In summary, (4.42) is exact up to higher orders of ϕ_0^2, leaving us with a self-consistent systematic expansion scheme. The self-consistency refers to the fact that in the present order in ϕ_0^2, the polarisation diagram is given exactly in terms of the four-point vertex. Therefore, approximations to the latter are transported to the former.

4.1.3.5.1. Vertex-approximation in the self-consistent skeleton expansion As discussed above, within the self-consistent DSE in (4.42), it suffices to specify the approximation for the four-point function. Here we again resort to the bubble-resummed four-point function of (4.34), already used in the previous section. This approximation of the four-point function neglects in particular contributions in the DSE of the four-point function that originate in the squint diagram. The self-consistency of (4.42) is reflected in the fact that the contribution of the polarisation diagram is given by its bubble-resummed

$1/2\phi_0^2\Gamma^{(4)}$,

$$\frac{1}{2}\phi_0^2\,\Gamma^{(4)}(p) = \frac{1}{2}\phi_0^2\left[\lambda_\phi - \lambda_\phi \Pi_{\text{fish}}\Gamma^{(4)}(p)\right] . \tag{4.43}$$

As for the four-point function, (4.43), lacks the contributions from the squint diagram. Note also that these contributions are related to the u,t-channel. Hence, with (4.43) we consistently neglect the squint topology in the DSE if assuming dominance of the s-channel vertex corrections for the four-point vertex. We emphasise that the assumption of s-channel dominance is well-supported in the large-N limit, but less so in the present $N = 1$ case.

Diagrammatically, the DSE is still represented by Figure 4.7, with the polarisation diagram given by the last term in (4.42). The prefactors of tadpole and sunset diagram are identical to that in the standard skeleton scheme used in Section 4.1.3.4. They are listed in Table A.1. In the tadpole diagram, the four-point function again enters via its spectral representation (4.36).

4.1.3.5.2. Results Numerical results for the propagator in the self-consistent skeleton scheme are displayed in Figure 4.12. The propagator spectral function is similar in shape to that obtained in the standard skeleton approximation, see Figure 4.10. However, the magnitude of the scattering tail close to the threshold is roughly a third for all coupling choices. Comparing the two skeleton schemes one realises that the correct momentum scaling behaviour of the standard skeleton expansion came at the price of two dressed vertices. In turn, the self-consistent skeleton expansion has the correct momentum scaling as well as the correct vertex strength. Arguably, this property is particularly important in the vicinity of s-channel resonances or for asymptotically large couplings.

Higher n-particle onsets are not visible in the propagator spectral function similarly to the results in the standard skeleton expansion. We emphasise again, that they are present nevertheless, as well as easily accessible in the present spectral approach. The three-particle onset can again be seen in the vertex spectral function (bottom left panel of Figure 4.13), although it is less pronounced as in Figure 4.11. The magnitude of the vertex spectral functions matches very well in the two different schemes, however.

The corresponding Euclidean correlation functions are shown in the top and bottom right panel. Both receive slightly less quantum corrections as for the plain skeleton expansion. For the propagator this is quite clear from the much smaller spectral functions in the self-consistent approximation. The differences in the four-point vertex are less pronounced, and we refrain from discussing them. For a more detailed discussion of the general features, see Section 4.1.3.4.

4.1.3.5.3. Low-lying bound state close to phase transition Lattice simulations [246–248] show an additional low-lying excitation in the spectrum of the scalar ϕ^4-theory in $d = 2+1$ close to the phase transition with a mass of $m \approx 1.8 m_{\text{pole}}$. This state has been interpreted as a bound state of the fundamental excitation in [248]. It is also been observed within the recent functional RG study [249]. The approximation scheme underlying the Euclidean computation done in [249] is close in spirit to the s-channel approximation scheme used in the present study in Minkowski spacetime. In [249], the spectral function of the propagator, numerically reconstructed from Euclidean data, shows a bound state close to the phase transition at a mass ratio consistent with that found in the lattice

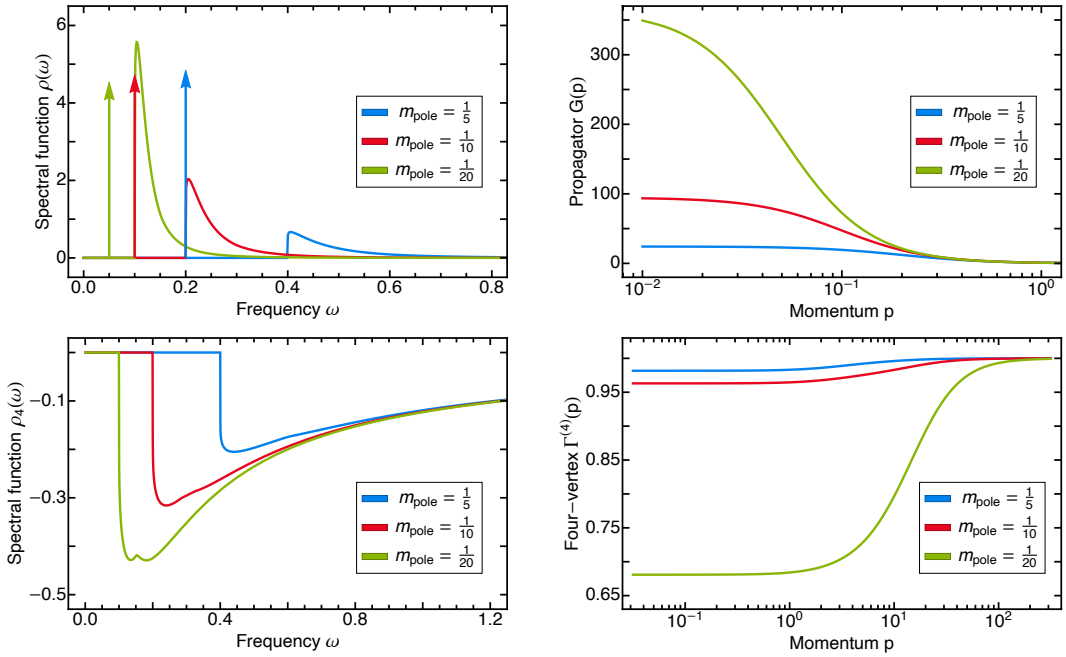

Abbildung 4.14.: Results from the skeleton expanded DSE (comp. Figure 4.7) with a bubble-resummed s-channel expansion of the four-point function for coupling choices $\lambda_\phi = 5, 10, 20$ using on-shell renormalisation (4.23). All vertices except for the tadpole one were approximated at $\omega = 0$. The curves were rescaled by their respective coupling parameters, i.e. $m_{\mathrm{pole},i} = \frac{1}{\lambda_{\phi,i}}$ and consequently $\lambda_\phi = \frac{\lambda_{\phi,i}}{\lambda_{\phi,i}} = 1$ for all curves. TOP: Spectral function (left) and propagator (right). The weight of the continuous tail decreases with larger mass pole, the mass pole residues increases. The different height of the delta peaks encodes the magnitude of the residue relative to the other spectral functions. The propagators were computed by the Källén-Lehmann spectral representation. The pole contributions are dominant, since for smaller mass pole the propagator is strongly enhanced.

studies. However, further away from the phase transition, the clear signal of the bound state is lost in [249].

The present direct computation of spectral functions is not performed close to the phase transition, that is for $m_{\mathrm{pole}} \to 0$. This regime will be studied elsewhere within the self-consistent skeleton expansion developed in the present section. Our results for $m_{\mathrm{pole}} \neq 0$ indicate that the bound state may indeed only exist close to the phase transition. However, the present s-channel approximation does not allow for a fully conclusive statement, as the latter requires a multichannel analysis. Yet, the s-channel resummation typically captures the dominant resonances and is trustworthy as next-to-leading order in a $1/N$-expansion in the large-N limit. The spectral properties of $O(N)$ models as well as the phase transition regime will be studied elsewhere.

We approach the two-particle bound state via a Bethe-Salpeter equation for the four-point function in Section 6.2.

4.1.4. Conclusion

In this section, we developed a spectral functional approach for the direct non-perturbative computation of timelike correlation functions. This approach is based on a novel renormalisation scheme called *spectral renormalisation*: This renormalisation scheme is based on the use of spectral representations and dimensional regularisation. The spectral representation allows to perform the momentum integrals within dimensional regularisation. This leaves us with the spectral integrals, whose spectral divergences can be renormalised within dimensional regularisation as well, see Section 4.1.1.3. This scheme is called *spectral dimensional renormalisation*, and respects all symmetries of the theory at hand that are maintained within dimensional regularisation. The latter set also includes gauge symmetries, and hence spectral dimensional renormalisation as developed here is a manifestly gauge invariant renormalisation scheme.

The renormalisation step can also be done with a standard subtraction procedure within a Taylor expansion in momenta as done in BPHZ renormalisation This scheme is called *spectral BPHZ renormalisation*, see Section 4.1.1.4. It maintains fewer symmetries than spectral dimensional renormalisation and in particular requires counterterms in gauge theories that break gauge symmetry (or rather BRST symmetry). The appeal of spectral BPHZ renormalisation lies in its relative numerical simplicity. In summary, spectral renormalisation allows for direct access to the real momentum axis by analytic continuation as a result of the fully analytic solution of all momentum integrals, while maintaining all symmetries of the theory at hand.

We performed explicit, non-perturbative computations within the spectral DSE approach to the scalar ϕ^4-theory in 2+1 spacetime dimensions. Our results include the spectral function of the scalar propagator and that of the s-channel four-point function, and are obtained by solving the spectral DSE recursively. We have first considered the approximation with classical vertices and full propagators in Section 4.1.3.1, but including the two-loop diagrams in the DSE. The resulting spectral functions show a distinct one-particle pole and a clear scattering tail with onset at twice the pole mass. The spectral function contains all higher scattering thresholds, which are easily accessible due to the analytic nature of the momentum integrations. For increasing couplings, the $1 \to 3$ scattering onset becomes more pronounced.

We also considered an approximation with non-perturbative vertices, based on a skeleton expansion scheme, in Section 4.1.3.4. The respective four-point function was given by an s-channel bubble resummation. The propagator spectral function again shows a distinct one-particle pole and a continuous scattering tail. The spectral function of the resummed four-vertex features a scattering tail as well and additionally shows a distinct onset for the $1 \to 3$ scattering process. For larger couplings, the fully non-perturbative nature of the approximation leads to large, though only quantitative differences compared to the classical vertex computation.

In the last part of this section, Section 4.1.3.5, we have developed a self-consistent skeleton expansion scheme. The self-consistency was obtained by relating a class of diagrams with three-point functions to the s-channel four-point function. This entails that the approximation used in the computation of the four-point function is also used within the three-point function diagrams. The results are qualitatively similar to that of the standard skeleton scheme. The magnitude of the scattering tail of the propagator spectral function turns out much smaller in the upgraded scheme, and indicates an overestimation of the polarisation diagram before. We expect that the use of such a self-consistent scheme

is important close to the phase transition of the theory or, more generally, in the presence of resonant s-channel interactions.

In conclusion, we have developed and put to work a fully non-perturbative spectral functional approach to the computation of realtime correlation functions. The approach was successfully tested within the scalar ϕ^4-theory in 2+1 dimensions.

4.2. Spectral functional renormalisation group

This section combines the derivation of the spectral fRG put forward in [6] with its application to a scalar ϕ^4-theory presented in [9]. Ref. [6] represents a jointly authored article within the fQCD collaboration [12]. In [9], all practical calculations have been carried out by Jonas Wessely during his early PhD and Master thesis, which I co-supervised.

In this section, we apply the spectral functional approach devised in [1], see Section 4.1, to the functional renormalisation group framework, amounting to the *spectral fRG*. To that end, we first set up a *finite renormalised* fRG approach, where renormalisation conditions are transported along with the flow by *flowing renormalisation*. One of its advantages is its manifest finiteness, also for regulators or regularisation schemes that do not directly implement a UV decay in the loops of the flow equation. This allows for its application to general non-perturbative truncation schemes. Our approach is manifestly finite as well as Lorentz (or Galilei/Schrödinger) invariant and gauge consistent.

In the first step, we derive a manifestly finite, renormalised functional Callan-Symanzik flow from finite fRG flows with spatial momentum regulators in the limit where these regulators turn into masslike Callan-Symanzik (CS) regulators. This allows for a derivation of the spectral fRG for the effective action by using spectral representations for correlation functions, while full Lorentz invariance is smoothly achieved in the CS limit. In particular, no regularisation of non-perturbative diagrams is implied, but all diagrams discussed are manifestly finite. The valuable benefit of gauge consistency is guaranteed as in the CS limit no momentum cutoff is involved. Finally, its realtime nature allows for an on-shell renormalisation scheme which also facilitates computations.

Furthermore, we accompany above conceptual progress with a non-perturbative application to spectral functions in the three-dimensional ϕ^4-theory. This also allows to directly compare our results with those obtained in [1] resp. Section 4.1 within the spectral DSE approach. Both functional approaches implement different resummation schemes for the theory at hand, as correlation functions obey different infinite towers of one-loop (fRG) or two-loop (DSE) exact diagrammatic relations. Moreover, within an fRG implementation, the successive momentum-shell integration of loop momenta $p^2 \approx k^2$ with the infrared cutoff scale k, already provides an average momentum dependence within simple approximations. This is particularly beneficial for vertices, since the intricacy of their spectral representations increases strongly with the number of involved field. The fRG incorporates already parts of the momentum dependence of vertices, if approximations with momentum-independent but cutoff dependent vertices are chosen.

In summary, this section lays the methodological ground for spectral fRG studies of realtime quantum field theories including QCD and quantum gravity. We discuss the application of the spectral fRG framework to Yang-Mills theory in Appendix A.3. For examples of Yukawa theories and quantum gravity, see [6]. We remark that prior to the formal derivation of the spectral fRG in [6], the spectral fRG has already been used in [206].

This section is structured as follows. In Section 4.2.1, we discuss the preservation of Lorentz invariance, causality and finiteness within given regularisation schemes and derive finite functional Callan-Symanzik flows with *flowing renormalisation* in Section 4.2.2. In Section 4.2.3, the novel setup is used to derive the Lorentz invariant spectral fRG. Its application to the scalar theory is discussed in Section 4.2.4. We present numerical results for the spectral function of the scalar field from the spectral fRG in Section 4.2.4, and

close with a short discussion in Section 4.2.6.

4.2.1. Regulators and symmetries

In order to motivate our derivation of the spectral fRG from functional Callan-Symanzik flows, where the regulator function in (2.32) is simply given by a mass term, we first illustrate the problem of causality-violating regulators in general realtime fRG setups. To that end, we start by discussing analytic properties of the functional flow equation (2.39) with respect to the choice of regulator at the example of a real scalar ϕ^4-theory, see (2.1). For an introduction to the fRG, see Section 2.3.

A specific example for a smooth shape function is

$$r_{\text{exp}}(x) = e^{-x} \,. \tag{4.44}$$

In addition to the conditions in (2.35), which guarantee the finiteness of fRG flows, we might want to impose additional, physically motivated conditions onto the regulators. For relativistic theories it is desirable that the regulators do not spoil Lorentz/Poincaré invariance. Furthermore, for studies of realtime properties, i.e., in Minkowski space, causality should also not be violated. The latter is directly related to the existence of a spectral representation for the propagator.

To maintain Lorentz invariance, the regulator should be a function of the four-momentum squared, $R_k(p^2)$. However, as discussed, e.g., in [43], such regulators might spoil causality through unphysical poles in the complex frequency plane. Typically, such regulators either do not admit a spectral representation or generate fictitious mass poles that only disappear in the vanishing cutoff limit; for a discussion of the latter, see [43, 44, 220]. As an example, consider a classical Euclidean propagator

$$G_k(p) = \frac{1}{p^2 + m_\phi^2 + R_k(p)} \,, \tag{4.45}$$

with a regulator shape function, c.f. (2.34),

$$r_{\text{rat}} = \sum_{n=n_{\text{min}}}^{n_{\text{max}}} c_n \left(\frac{k^2}{k^2 + p^2} \right)^n \,. \tag{4.46}$$

Already for such a simple propagator, the existence of a spectral representation of the regularised propagator is highly dependent on the coefficients c_n, and in general not the case, see [43, 243] for more details. For general propagators, regulators of the type (4.46) typically generate at least n_{max} poles in the propagator, whose positions in the complex plane usually spoil the spectral representation. Another choice would be a variation of the exponential regulator (4.44), see [44, 220] for more details. Regulators of this type lead to series of poles in the propagator as well as an essential singularity at infinity.

A further common choice are regulators that only depend on the spatial momenta, $R_k^{(}\vec{p}^2)$. Clearly, these regulators do not lead to additional poles in the complex frequency plane, but merely modify the dispersion of the fields. Thus, they admit a spectral representation at the cost of violating Lorentz invariance. If the system is in a medium, explicit Lorentz symmetry breaking might seem innocuous, as it is broken anyway. While this has been confirmed in specific examples [44, 250], it is a priori unclear in general. Especially

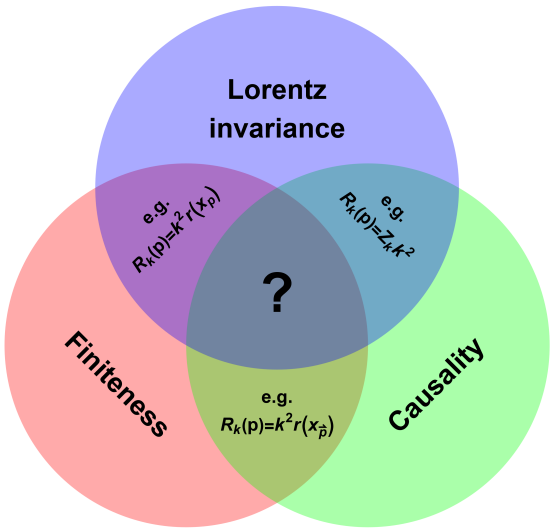

Abbildung 4.15.: Sketch of the competing requirements for regulators: finiteness of the flow, Lorentz invariance and causality of regulators. Examples for regulators with two of the properties are given. A fully systematic construction of regulators with all three properties in the flow is lacking to date.

when considering limiting cases of a phase diagram such as $T \to 0$, the question becomes much more intricate than the comparisons in the aforementioned works.

Hence, effectively we either violate (or at least complicate) causality, or we violate Lorentz invariance. All known examples of regulators rely on the regularisation conditions in (2.35). However, by relaxing at least one of these conditions, there is a natural choice for a regulator which preserves both causality and Lorentz invariance,

$$R_{k,\mathrm{CS}} = Z_\phi\, k^2\,, \qquad r_{\mathrm{CS}}(x) = 1\,, \tag{4.47}$$

which we refer to as the CS regulator. It implements IR regularisation through an explicit mass $\Delta m^2 = Z_\phi\, k^2$. In this case the flow equation (2.39) has been derived in [251]. To our knowledge, it is indeed the first occurrence of such a closed (and one loop) exact functional equation for the effective action. The insertion of the CS regulator in (2.39) leads us to the (inhomogeneous) functional CS equation. However, it violates the second condition (2.35). The CS regulator only lowers the UV degree of divergence by two, for example, quadratically divergent diagrams such as the tadpole diagram in the two-point function of the ϕ^4 theory in $d = 4$ leads to logarithmically divergent tadpole diagrams in the CS equation. In short, at each k in the flow, all loop momenta contribute. To render the flow finite, an additional UV regularisation is required in general.

The different properties of the regularisation are summarised in Figure 4.15. Restricting the discussion to vacuum for simplicity, the three different property of interest are

1. **Lorentz invariance:** The regulator is a function of p^2 and respects Lorentz symmetry.

2. **Causality:** The *regularised* propagator admits a spectral representation, c.f. (4.77). Expressed in Euclidean momenta, the right half-plane for analytically continued momenta is holomorphic.

3. **Finiteness:** All diagrams arising from (2.39) and its functional derivatives are finite.

In the overlap regions of Figure 4.15 we provide examples for regulators with the respective two properties.

No example is given in the overlap regime in the middle with all three properties: at present, no regulator keeping all three properties in Figure 4.15 simultaneously is known: indeed, the structure of the full propagator,

$$G_k(p) = \frac{1}{\Gamma_k^{(2)}(p) + R_k(p)}\,, \tag{4.48}$$

which is the inverse of the regulator and the (yet to be determined) two-point function $\Gamma_k^{(2)}$ entails that a systematic construction of such a regulator for all cutoff scales k necessarily requires the use of the complex structure of $\Gamma_k^{(2)}$ in the regulator. This leaves us with a combination of requirements: the existence of the spectral representation of the propagator (4.48) with the regulator limits (2.35) for an unknown two-point function $\Gamma_k^{(2)}$. This combination is rather obstructive, and if a systematic construction is possible at all, it evidently requires using constraints on the complex structure of the two-point function at hand.

As an illustration, let us assume we have a Lorentz invariant regulator with the properties (2.35). We observe that the regulator needs to be a decaying function as $p \to \infty$, by assumption, while $\Gamma^{(2)}(p)$ needs to be a growing function for $p \to \infty$, being the inverse of the propagator. This implies finite Lorentz invariant flow equations (properties 1 & 3). Now we show that then causality (property 2) is at stake:

A simple consideration of the Cauchy–Riemann equations suggest different signs of their imaginary parts in the top-right quadrant of $p \in \mathbb{C}$. However, the regulator needs to have a positive real part, at least for small Euclidean momenta, to provide the IR regularisation. In a partially simplified picture, this leads to lines in the complex plane where the real part of the regulator is zero. Similarly, the real part of the two-point function has lines with vanishing real part, related to the dispersion relation. The different limiting cases detailed above make it almost impossible to avoid zeros in the top right quadrant of the complex momentum plane, and consequently lead to a violation of causality in the regularised propagator. Partly, this reasoning can also be found in [47]. The argument presented here is a very pictorial, simplified version. While it is easy to construct explicit counterexamples, so far even in tailor made applications, such as spectral functions of a simple scalar theory, no regulator has been provided that escapes this problem, leave aside a generic systematic construction scheme. A full discussion of this issue is postponed to future work.

This leaves us with the situation that we may consider regulators in the three overlap regions, put differently, regulators, that lack one of the properties 1–3. In this context, we emphasise a peculiarity of the overlap regime without finiteness including the CS regulator: the structural similarity of the Wetterich equation (2.39) with regulators obeying (2.35) and the flow with the CS regulator (4.47) is misleading. While the former equation implements a Wilson-type momentum-shell integration in a fixed underlying quantum

field theory, the CS flow constitutes a flow in the space of theories. To be specific, the need for additional UV regularisation at different cutoff scales k implies that we have different theories which necessarily require a different renormalisation. Hence, the flow must be re-renormalised; only specifying the initial effective action $\Gamma_{k_{init}}$ does not lead to a finite renormalised solution of the flow equation. This renormalisation is typically done with an RG transformation, leading to finite renormalised loops as well as the β-function and anomalous dimension terms in (4.62). As we will show in the next section, this can be achieved instead by the introduction of explicit counterterms to the flow, supplemented with renormalisation conditions which are fixed at an in general k-dependent renormalisation scale μ.

4.2.2. Functional flows with flowing renormalisation

Next, we discuss the finiteness of infrared flows and the finiteness of the ultraviolet limit of the effective action. Both properties are related to the UV renormalisation that is implicitly or explicitly implemented in the flow equation. This will lead us to the concept of flowing renormalisation. Again, we will stick to a real scalar field; the generalisation to theories with arbitrary field content can be found in [6].

In Section 4.2.2.1 we discuss infrared RGs with general rescalings during the RG flows and introduce the concept of RG consistency. This setup allows us to define flows that have a finite UV limit, hence elevating the standard *bare* diverging UV effective action to a *renormalised* finite UV action. In Section 4.2.2.2 we then derive a key result of the present work, the general flow equation (4.73) with a flowing Bogoliubov-Parasiuk-Hepp-Zimmermann (BPHZ)-type UV renormalisation. This renormalised fRG flow is not based on full RG rescalings which imply a multiplicative renormalisation that typically cannot be used in non-perturbative truncation schemes. This is achieved by augmenting the infrared RG steps with explicit ultraviolet ones that are also formulated in terms of a standard functional RG. In Section 4.2.2.3 we discuss the properties of the manifestly finite CS equation (4.74) obtained from (4.73) for the CS regulator including the implementation of general renormalisation conditions, which is the basis for the spectral fRG discussed in Section 4.2.3. In Section 4.2.2.4 we summarise the results and findings of this section and emphasise some important aspects.

4.2.2.1. RG consistency and UV scaling

For standard infrared regulators with shape functions $r(x)$ that obey (2.35), the flow equation is manifestly finite as loop momenta are effectively restricted to $p^2 \lesssim k^2$. Then, choosing a specific $r(x)$ amounts to specifying a UV regularisation scheme for fRG flows. The effective action Γ_k of a general theory is then obtained by integrating (2.39) from some initial cutoff scale k_{init} to $k \leq k_{\text{init}}$,

$$\Gamma_k[\phi] = \Gamma_{k_{\text{init}}}[\phi] + \int_{k_{\text{init}}}^{k} \frac{\mathrm{d}k'}{k'} \partial_t \Gamma_{k'}[\phi] \,. \tag{4.49}$$

The renormalisation conditions are implicitly fixed through the initial effective action $\Gamma_{k_{\text{init}}}$. The theory at a given cutoff scale k should not depend on the initial cutoff scale k_{init}, which is called *RG consistency*, see [58, 176, 252],

$$k_{\text{init}} \frac{d\Gamma_k}{dk_{\text{init}}} = 0 \,. \tag{4.50}$$

Since the initial effective action implicitly fixes the renormalisation conditions, RG consistency entails renormalisation group invariance, and specifically the independence of the theory on these conditions. Inserting (4.49) into (4.50), we arrive at

$$\partial_{t_{\rm init}}\Gamma_{k_{\rm init}}[\phi] = \frac{1}{2}{\rm Tr}\, G_k[\phi]\,\partial_t R_k\Big|_{k_{\rm init}} . \tag{4.51}$$

Equation (4.51) entails that the $k_{\rm init}$-dependence of the effective action at the initial (large) cutoff scale is given by the flow equation. Hence, the running of the UV relevant parameters can be read off from the IR flow equation for asymptotically large cutoff scales, where the flow of a given coupling is proportional to

$$\lim_{k\to\infty}\partial_t\lambda_i \propto k^{d_{\lambda_i}} . \tag{4.52}$$

The right-hand side includes the full k-scaling: the combination of the scaling of the loop integrals and the vertices. Then, UV relevant and marginal couplings λ_i have scaling dimensions $d_{\lambda_i}\geq 0$, while UV irrelevant couplings have scaling dimensions $d_{\lambda_i}<0$. Consequently, for asymptotically large infrared cutoff scales, the effective action approaches the *bare* UV effective action: only the UV relevant operators survive and diverge with $k\to\infty$ according to their scaling dimension with $k^{d_{\lambda_i}}$ for $d_{\lambda_i}>0$ and logarithmically with t for $d_{\lambda_i}=0$.

As a first step towards the desired finite flow equations, also for regulators such as the CS one, we discuss how the UV scaling (4.52) can be absorbed within a general RG rescaling. Then, the UV limit of the effective action is the finite renormalised UV action and not the diverging bare action. For more details we refer the reader to [58] and in particular [61].

The underlying RG invariance of the theory at $k=0$, see [58], implies that the full effective action $\Gamma=\Gamma_{k=0}$ obeys the homogeneous renormalisation group equation

$$\mu\frac{d\Gamma[\phi]}{d\mu} = \left(\mu\partial_\mu + \beta^{(\mu)}_{\lambda_i}\partial_{\lambda_i} + \int_x \gamma^{(\mu)}_\phi\,\phi\frac{\delta}{\delta\phi}\right)\Gamma[\phi] = 0\,, \tag{4.53}$$

where $\int_x=\int d^dx$ refers to the integral over spacetime. The β-functions $\beta^{(\mu)}$ and anomalous dimensions $\gamma^{(\mu)}_\phi$ of the theory at hand are defined as

$$\gamma^{(\mu)}_\phi\phi = \mu\frac{d\phi}{d\mu}\,,\qquad \beta^{(\mu)}_\lambda = \mu\frac{d\lambda}{d\mu}\,. \tag{4.54}$$

The coupling vector $\lambda=(\lambda_1,...,\lambda_m)$ contains all relevant parameters of the theory, including the mass parameters. Note that equation (4.53) entails the invariance of the underlying quantum field theory under self-similarity transformations of the theory.

It has been shown in [58] that the RG invariance of the theory is maintained in the scale-dependent theory in the presence of the regulator term for regulators of the form of (2.34). Such regulators are called *RG-adapted* as they satisfy the RG equation

$$\left(\mu\partial_\mu + 2\gamma^{(\mu)}_\phi\right)R_k = 0\,, \tag{4.55}$$

and scale as an inverse two-point function. The respective full RG equation reads

$$\left(\mu\partial_\mu + \beta^{(\mu)}_{\lambda_i}\partial_{\lambda_i} + \int \gamma^{(\mu)}_\phi\phi\frac{\delta}{\delta\phi}\right)\Gamma_k[\phi] = 0\,. \tag{4.56}$$

From this, we obtain the general flow equation that comprises the change of a cutoff scale, here k, as well as an accompanying general RG transformation.

Using (2.39), an additional total k-derivative of (4.56) yields the flow equation with reparametrisation at each flow step [58],

$$\left(s\partial_s + \beta_{\lambda_i}^{(s)}\partial_{\lambda_i} + \int_x \gamma_\phi^{(s)}\phi\frac{\delta}{\delta\phi}\right)\Gamma_k[\phi] = \frac{1}{2}\mathrm{Tr}\, G_k[\phi]\,\left(\partial_s + 2\gamma_\phi^{(s)}\right)R_k\,, \tag{4.57}$$

where we consider $k(s)$ and $\mu(s)$ with

$$s\partial_s = \mu\partial_\mu + \partial_t\,. \tag{4.58}$$

The β-functions $\beta^{(s)}$ and anomalous dimensions $\gamma^{(s)}$ then encode the full s-scaling of a combined cutoff (k-) and RG (μ-) flow, including a reparametrisation of the theory,

$$\gamma_\phi^{(s)}\phi = s\frac{d\phi}{ds}\,,\qquad \beta_\lambda^{(s)} = s\frac{d\lambda}{ds}\,. \tag{4.59}$$

Hence, the loop term on the right-hand side of (4.57) is proportional to the full s-scaling of the cutoff term, consisting of the infrared cutoff scaling with k, the renormalisation group scaling with μ and a potential scaling of a UV cutoff scale Λ. This s-scaling reduces to (4.54) for $s\partial_s\mu = \mu$ and $s\partial_s k = 0$, and to the standard fRG anomalous dimension and β-functions for $s\partial_s k = k$ and $s\partial_s\mu = 0$. Finally, the linear combination (4.58) of k and μ scalings leads to $\gamma_\phi^{(s)} = \gamma_\phi^{(\mu)} + \gamma_\phi$ with

$$\gamma_\phi \equiv \gamma_\phi^{(k)} = -\frac{1}{2}\partial_t \log Z_\phi\,. \tag{4.60}$$

For RG-adapted regulators with (4.55) the renormalisation group scaling drops out of the right-hand side. For example, for the linear combination of the two scalings with k and μ we arrive at

$$\begin{aligned}\left(\partial_s + 2\gamma_\phi^{(s)}\right)R_k &= \left(\partial_t + 2\gamma_\phi\right)R_k + \left(\mu\partial_\mu + 2\gamma_\phi^{(\mu)}\right)R_k\\ &= \left(\partial_t + 2\gamma_\phi\right)R_k\,.\end{aligned} \tag{4.61}$$

With (4.61) the flow (4.57) reduces to

$$\left(s\partial_s + \beta_{\lambda_i}^{(s)}\partial_{\lambda_i} + \int_x \gamma_\phi^{(s)}\phi\frac{\delta}{\delta\phi}\right)\Gamma_k[\phi] = \frac{1}{2}\mathrm{Tr}\, G_k[\phi]\,\left(\partial_t + 2\gamma_\phi\right)R_k\,. \tag{4.62}$$

Due to the reparametrisation invariance, the linear field-reparametrisation $\phi \to Z_\phi^{1/2}\,\phi$ leading to the occurrence of γ_ϕ in (4.62) are optional. They might be used to simplify certain computations, e.g., in the context of critical physics, where anomalous dimensions are of central interest.

Equation (4.62) represents the fRG setup for the effective action. For regulators with the property of UV regularisation, field reparametrisations encoded in the anomalous dimensions and β-functions may facilitate the computations or implement functional optimisation schemes. In particular, we can absorb the UV scaling (4.52) of the UV-relevant couplings with d_{λ_i} into the anomalous dimensions and β-functions, leading to a finite renormalised UV effective action. This is simply a convenience for infrared flows with finite flow

equations, but is a necessity in the absence of ultraviolet finite loops, as is the case for the CS regulator, (4.47). Then, the rescalings implement the required UV renormalisation via multiplicative renormalisation. While this is a formally correct procedure, the implementation of multiplicative renormalisation within non-perturbative truncation schemes is intricate.

As the central result of this paper, we will show in the next section that the additional μ-flow can be absorbed into a well-defined flow of a non-perturbative counterterm action for the k-flow in a manifestly finite way. The flow of the counterterm action serves a two-fold purpose: First, it allows to consistently change the renormalisation conditions with the k-flow for general IR flows. We call this flowing renormalisation. Secondly, it also leads to manifestly finite flows for the CS regulator with a flowing counterterm action for general non-perturbative truncation schemes. The number of parameters in these counterterm matches that of relevant parameters in the theory.

4.2.2.2. Functional RG with flowing renormalisation

We now use the general flow equation with an infrared regulator and an ultraviolet one for deriving a flow equation which also incorporates an explicit UV renormalisation in a manifestly finite approach in terms of a generalised BPHZ scheme with the subtraction of a flowing counterterm action. In contradistinction to multiplicative schemes this leads to finite loop diagrams by subtraction. Such a construction has the benefit of a simple and robust numerical implementation.

This general setup also allows us to monitor and change the renormalisation conditions within the infrared flow. This generalises the standard fRG setup, in which the (UV) renormalisation and the respective renormalisation conditions are implicit in the choice of the finite initial action, see the discussion around (4.49).

The access to the UV behaviour of the theory is obtained by introducing a regulator $R_{k,\Lambda}(p)$, where a UV cutoff $\Lambda = \Lambda(k)$ enters as a free parameter/function. The regulator $R_{k,\Lambda}$ is chosen such that it effectively restricts loop momenta to $p^2 \lesssim \Lambda(k)^2$ in the loops of the flow equation, see the examples (4.65c) and (4.65d) below. We may also use the regulator for a full UV regularisation of the theory and not only the flow equation, see e.g., (4.65e) below.

Changing the UV scale $\Lambda = \Lambda(k)$ alongside with the infrared flow allows us to introduce a *flowing* (UV) renormalisation in the latter. For these regulators the flow (2.39) can be written as

$$\left(\partial_t\big|_\Lambda + \mathcal{D}_k\,\partial_{t_\Lambda}\right)\Gamma_{k,\Lambda} = \frac{1}{2}\mathrm{Tr}\,G_{k,\Lambda}\left(\partial_t\big|_\Lambda R_{k,\Lambda} + \mathcal{D}_k\,\partial_{t_\Lambda} R_{k,\Lambda}\right)\,, \tag{4.63}$$

where $t_\Lambda = \log(\Lambda/k_{\mathrm{ref}})$, with a reference scale k_{ref}. The factor $\mathcal{D}_k$ is a relative measure of RG steps in the $k-$ and the Λ-direction,

$$\mathcal{D}_k = \partial_t \log \Lambda(k)\,. \tag{4.64}$$

The flow (4.63) is a finite functional flow which allows us to successively integrate out momentum shells. For $\partial_{t_\Lambda} R_{k,\Lambda} = 0$ we arrive at the standard (infrared) flow in (2.39). This naive limit can only be taken for infrared momentum cutoffs that decay sufficiently fast in the ultraviolet. Most importantly, we can identify the terms $\propto \mathcal{D}_k$ in (4.63) as UV-cutoff flows that can be used for a flowing renormalisation scheme.

This derivation holds true for general infrared regulators. In the following we use as an important example regulators $R_{k,\Lambda}$, that converge towards the CS regulator with the shape function (4.47) for $\Lambda \to \infty$. In this case the flowing renormalisation can now be used to derive the finite fRG flow (4.63) for the CS regulator. For this derivation it is convenient to consider regulators $R_{k,\Lambda}$ with

$$R_{k,\Lambda}(p) = Z_\phi \, k^2 \, r(x_\Lambda) \,, \qquad x_\Lambda = \frac{\vec{p}^{\,2}}{\Lambda^2} \,, \tag{4.65a}$$

where we have considered a spatial momentum regulator in order to retain causality in a simple manner, as discussed in the previous section. Again, we emphasise that this choice is only taken for the sake of the spectral flows discussed later, it is not a necessary one. For $\Lambda \to \infty$ we require

$$\lim_{\Lambda\to\infty} R_{k,\Lambda} = Z_\phi \, k^2 \,, \tag{4.65b}$$

which leaves us with the CS flow as limit of well-defined UV-finite flows. Explicit examples for shape functions are given by

$$r_{\rm exp}(x_\Lambda) = e^{-x_\Lambda} \,. \tag{4.65c}$$

This regulator leads to an exponential damping of the UV modes in the loop via the regulator in the numerator of the flow. Another regulator of this type is given by

$$r_{\rm CS}(x_\Lambda) = \theta(1 - x_\Lambda) \,. \tag{4.65d}$$

Again the loop is rendered finite via the regulator in the numerator of the loop. We emphasise that, (4.65c) does not imply a UV regularisation of standard diagrams, e.g., in perturbation theory or a system of Dyson-Schwinger equations, but only a UV-regularisation of the loops in the flow equations.

We may augment the IR regulator with a UV regulator, leading to UV and IR finite loops with

$$r_{\rm sharp}(x_\Lambda) = \frac{1}{\theta(1 - x_\Lambda)} \,. \tag{4.65e}$$

This regulator leads to momentum loops, e.g., in perturbation theory or a system of Dyson-Schwinger equations, that do not receive any contribution from spatial loop momenta $\vec{p}^{\,2} > \Lambda^2$. Naturally, this property also holds true for the respective flow equations. All the regulators in (4.65) and the limit $\Lambda \to \infty$ satisfies the constraint (4.65b).

To understand the CS limit, we have to explicitly determine the part of the flow that comes from changing the UV cutoff Λ. For $\Lambda \to \infty$ the second part of the flow,

$$\frac{1}{2} {\rm Tr} \, G_{k,\Lambda} \, \mathcal{D}_k \, \partial_{t_\Lambda} R_{k,\Lambda} \,, \tag{4.66}$$

takes a simple form: Up to sharply peaked contributions for large momenta, see the examples in (4.65), the t_Λ-derivative of the regulator vanishes in the CS limit (4.65b) with

$$\lim_{\Lambda\to\infty} \partial_{t_\Lambda} R_{k,\Lambda} = 0 \,. \tag{4.67}$$

Note that (4.67) simply entails removing the Λ-part of the flow in the limit $\Lambda \to \infty$, so it holds true beyond the CS example. Thus, in this limit the contribution of the Λ-flow, (4.66), to the full flow, (4.63), vanishes unless this zero is compensated by a divergence in the Λ-flow.

On the more technical level we define diagrams with UV *irrelevant* power counting in the flow equation: these are the diagrams $\mathrm{Diag}_i^{(n)}\big(\partial_{t_\Lambda} R_{k,\Lambda}\big)$ in the flow of n-point functions $\Gamma_k^{(n)}$ which remains finite if the substitution $\partial_{t_\Lambda} R_k \to 1$ is done. Here, the superscript $^{(n)}$ indicates a diagram of the flow of $\Gamma_k^{(n)}$, while the subscript $_i$ labels the different diagrams in this flow. We write

$$\lim_{\Lambda\to\infty} \big|\mathrm{Diag}_i^{(n)}\big(\partial_{t_\Lambda} R_{k,\Lambda} \to \Lambda^2\big)\big| < \infty\,. \tag{4.68}$$

Diagrams with (4.68) either contain a sufficiently large number of propagators or sufficiently rapidly decaying vertices to render the integration over loop momenta finite. In the CS limit, the contribution of UV-irrelevant diagrams to the flow vanishes like Λ^{-n} with some $n > 0$.

In turn, the power counting marginal and relevant parts of the Λ-flow (4.66) will survive in this limit and indeed diverge with powers and logarithms of Λ. Importantly, these terms are also local *if* the vertices are: they only depend on powers of momenta. Note also that the Λ-flow has the same UV power counting as standard diagrams, as the regulator behaves like an inverse propagator for $\Lambda \to \infty$. This can be seen from the example regulators (4.65), whose t_Λ-derivative yields

$$\begin{aligned} \partial_{t_\Lambda} r_{\exp}(x_\Lambda) &= 2x_\Lambda e^{-x_\Lambda}\,, \\ \partial_{t_\Lambda} r_{\mathrm{CS}}(x_\Lambda) &= 2x_\Lambda \delta(1-x_\Lambda)\,. \end{aligned} \tag{4.69}$$

Hence, the Λ-flows for n-point functions diverge with the same power of Λ as standard loop diagrams, e.g., in perturbation theory.

Finally, the prefactors of the UV-relevant terms in the t flow may be different from that in the t_Λ flow, as the respective scale derivatives of the regulator have a different momentum-dependence if taken for a fixed shape function. This is remedied by using shape functions with

$$r_\Lambda = r(x_\Lambda) + \Delta r_\Lambda(x_\Lambda)\,, \tag{4.70}$$

and the correction $\Delta r_\Lambda(x_\Lambda)$ is taken such that the relative prefactors of all UV relevant terms of the t_Λ-flow equals the relative prefactors of the relevant terms in the t-flow.

In summary, this leads us to the definition of the counterterm action,

$$\partial_t S_{\mathrm{ct}}[\phi] := -\frac{1}{2}\mathrm{Tr}\, G^\phi_{k,\Lambda}\, \mathcal{D}_k\, \partial_{t_\Lambda} R_{k,\Lambda}\,, \tag{4.71}$$

which removes all terms with positive powers Λ^n as well as logarithms $\log \Lambda/k_{\mathrm{ref}}$ from (4.63) and renders the infinite UV cutoff limit finite,

$$\lim_{\Lambda\to\infty} \big|\partial_t \Gamma_{k,\Lambda}[\phi]\big| < \infty\,. \tag{4.72}$$

The counterterm action (4.71) depends on a finite set of renormalisation parameters required for the finite limit (4.72). The size of this set is equivalent to the number of UV

relevant and marginal directions. Moreover, in the limit $\Lambda \to \infty$ the counterterm action takes a local form for approximations with local vertices that reduce to the classical ones for large momenta.

Finally, we arrive at the novel flow equation with flowing renormalisation

$$\partial_t \Gamma_k[\phi] = \frac{1}{2} \mathrm{Tr}\, G[\phi]\, \partial_t R_k - \partial_t S_{\mathrm{ct}}[\phi]\,, \tag{4.73}$$

with the flow of the counterterm action (4.71) accounting for the flow of the renormalisation conditions as well as the finiteness for infrared cutoffs such as the CS regulator. This general equation constitutes a main result of our work. It can be augmented with general reparametrisations of the theory, leading to a generalisation of (4.57): we simply have to subtract $\partial_t S_{\mathrm{ct}}[\phi]$ defined in (4.71) on the right-hand side of (4.57). Note, that heuristically such a procedure is suggestive but in general a naive removal of divergent terms does not provide a consistent renormalisation. In the present section we have shown that (4.73) is correct. The derivation also offers a systematic practical way to compute the counterterms.

4.2.2.3. Finite CS flows and flowing renormalisation conditions

In the remainder of this section, we use (4.73) for setting up spectral functional flows. To that end, we consider the CS flow, for which (4.73) reduces to

$$\partial_t \Gamma_k[\phi] = \mathrm{Tr}\; G[\phi]\, k^2 - \partial_t S_{\mathrm{ct}}[\phi]\,, \tag{4.74}$$

where a CS regulator in a manifestly UV finite setting, such as given with the shape function (4.65e), is assumed and the finite limit $\Lambda \to \infty$ can be safely taken. As for the general form (4.73), the novelty of (4.74) is not its finiteness per se. Indeed, already the original functional CS equation as derived in [251] can be shown to be finite order by order in perturbation theory. However, (4.74) is manifestly finite in *general* perturbative and non-perturbative truncation schemes with a manifestly finite effective action. Moreover, the present setup allows for a direct computation of the flow of the counterterm action, only dependent on a set of renormalisation parameters which are in one-to-one correspondence to the coefficients of the UV marginal and relevant operators. Finally, the finite CS flow can be applied to perturbatively and non-perturbatively renormalisable theories. For a first application in quantum gravity, we refer to [206].

The general flow (4.73) and its finite CS limit (4.74) seemingly imply that we are left with the task of computing the non-trivial scaling factor $\mathcal{D}_k$ as well as the Λ-trajectory (4.70) at each RG step. This would exact a heavy price for the finiteness (4.72). It is therefore noteworthy that we do not have to compute $\partial_t S_{\mathrm{ct}}[\phi]$ from the flow, as it can be completely fixed by the choice of renormalisation conditions. The subtraction $\partial_t S_{\mathrm{ct}}[\phi]$ has to be simply chosen such that the flow of these conditions vanish. This choice is practically implemented by subtracting the t-flow of the correlation functions $\Gamma_k^{(n)}(p^2 = \mu^2)$, that is the renormalisation condition from the full t-flow. This renders the functional t-flow finite and guarantees the RG conditions to hold.

We illustrate this within a simple example for the finite CS flow. Again we use a real scalar field theory with the renormalised effective action $\Gamma_{k,\Lambda}$ with a given UV cutoff Λ. The renormalisation entails that the effective action $\Gamma_{k,\Lambda}$ stays finite in the limit $\Lambda \to \infty$. Moreover, it may satisfy the following on-shell renormalisation conditions at the flowing

scale $\mu = \mu(k)$,

$$\begin{aligned}
\lim_{\Lambda\to\infty} \Gamma^{(2)}_{k,\Lambda}[\phi](p)\Big|_{p_0^2=-\mu^2} &= -k^2\,, \\
\lim_{\Lambda\to\infty} \partial_{p_0^2}\Gamma^{(2)}_{k,\Lambda}[\phi](p)\Big|_{p_0^2=-\mu^2} &= 1\,, \\
\lim_{\Lambda\to\infty} \Gamma^{(4)}_{k,\Lambda}[\phi](p)\Big|_{p_0^2=-\mu^2} &= \lambda_\phi\,,
\end{aligned} \tag{4.75}$$

where p_0 is the Euclidean frequency and $p^2 = p_0^2 < 0$ is evaluated at a timelike Minkowski momentum with $\vec{p} = 0$ and the Minkowski frequency $\pm\sqrt{-p_0^2}$. Here, ϕ is a background field, which is typically given by the solution of its (quantum) equation of motion (EoM), $\phi = \phi_{\mathrm{EoM}}$.

The first condition is an on-shell mass renormalisation: the effective action in the presence of an IR regulator is defined as a modified Legendre transform excluding the regulator term. Hence, for the physical CS regulator we have to consider the full Euclidean two-point function with the CS mass term $Z_\phi k^2$, that is $\Gamma^{(2)}_k(p^2) + Z_\phi k^2$. Thus, (4.75) simply implies $\Gamma^{(2)}_k(-\mu^2) + k^2 = 0$, so the renormalisation scale determines the k-dependent pole mass, $\mu = m_k$. By setting $\mu = k$, we can enforce this pole mass to be given by the mass introduced by the CS regulator. Thus, for a given physical mass the RG flow from the initial UV scale k_{init} is terminated at $k_{\mathrm{f}in} = m_{\mathrm{phys}} = m_{k_{\mathrm{f}in}}$. Put differently, with this RG condition we flow through the space of scalar theories with the physical pole mass k^2.

The second condition in (4.75) fixes the wave function renormalisation at μ, $Z_\phi(-\mu^2) = 1$ on-shell. We remark, that this leads to a spectral function $\rho_{\phi,k}$ that is not normalised to unity if ϕ is a physical field (defining an asymptotic state), see Section 4.2.3. The last condition in (4.75) fixes the quartic interaction vertex. We have not specified the momentum configuration here, but natural choices are the symmetric point and specific momentum channels such as the s-channel. While every RG condition serves our purpose, on-shell RG conditions are in most cases a specifically convenient physical choice, only accessible for realtime formulations.

We also remark that adjusting specific renormalisation conditions in the standard fRG setting is a fine-tuning problem: One has to adjust the initial effective action at the initial cutoff scale k_{init} such, that the effective action at k_{fin} satisfies the renormalisation conditions. However, adjusting specific renormalisation conditions is not required in the fRG approach but the same finite tuning task extends to adjusting the physics parameters at the initial scale. Both tasks are solved or at least facilitated in the presence of flowing renormalisation, and (4.75) exemplifies this general pattern. With (4.75) both the adjustment of the renormalisation conditions and the adjustment of the physics parameters is done directly.

It is an additional benefit of the present formulation that the usual finite tuning of the physical parameters at $k = 0$ from a set of initial conditions at a large initial cutoff scale

k_{init} can be avoided. From (4.75) we get

$$\begin{aligned}
\lim_{\Lambda\to\infty} \partial_t \left[\Gamma^{(2)}_{k,\Lambda}[\phi](p)\Big|_{p_0^2=-\mu^2}\right] &= -2\,k^2\,,\\
\lim_{\Lambda\to\infty} \partial_t \left[\partial_{p_0^2}\Gamma^{(2)}_{k,\Lambda}[\phi](p)\Big|_{p_0^2=-\mu^2}\right] &= 0\,,\\
\lim_{\Lambda\to\infty} \partial_t \left[\Gamma^{(4)}_{k,\Lambda}[\phi](p)\Big|_{p_0^2=-\mu^2}\right] &= 0\,,
\end{aligned} \tag{4.76}$$

which completely fixes $\partial_t S_{\text{ct}}$ in (4.74).

We emphasise that the implementation of the above full flowing renormalisation is not required within the formulation. Indeed, in the ϕ^4-theory in $d = 3$ discussed in detail in Section 4.2.4, the only divergence in the flow equation is related to the mass renormalisation: The CS flow lowers the standard UV degree of divergence by two and the field-dependent part of the flow is logarithmically divergent. Thus, the flow of the counterterm action $\partial_t S_{\text{ct}}$ only needs to include one term to ensure finiteness. Additional counterterms for further fundamental couplings can still be introduced to enforce the renormalisation conditions.

We emphasise that using a 'minimal' counterterm with k-independent parameters, i.e., one that only regularises the divergent contributions, the present approach reduces to the standard infrared flow: the renormalisation group conditions at $k = 0$ are implicitly set at $k = k_{\text{init}}$ and the physics parameters and RG conditions flow into their final values, which have to be fine-tuned for given physics and RG conditions.

4.2.2.4. Wrap-up

The derivation of the general fRG flow (4.73) with flowing renormalisation and its finite CS limit (4.74) is a key result of the present section. Importantly, the counterterm action S_{ct} is all that is left from the Λ and μ-dependence of the general fRG flow in equation (4.62). Notably, the conventional finite CS equation also involves the terms proportional to the β-function on the LHS side of equation (4.62) (which follow from multiplicative renormalisation), which are missing in equation (4.74). We emphasise that the latter BPHZ-type renormalisation allows for the implementation of general non-perturbative truncation schemes which are difficult to implement in a setting with multiplicative renormalisation. Put differently, the formal finiteness of the standard CS equation is only of use in truncation schemes such as perturbation theory and does not survive in general non-perturbative truncation schemes.

Equation (4.73) and (4.74) can be augmented with β-function terms. They are present if the flow is amended with an additional standard RG transformation with $\mu(k)$. This is an option in specific cases, as it may facilitate the computations or the convergence of systematic approximation schemes. Still, it is an important result that such an additional RG transformation is not required for finiteness and equation (4.74) is exact: while the β-function terms pose no conceptual problem as they can be considered in a *closed* form by auxiliary flows, their computation constitutes in most cases a considerable additional technical challenge. For a detailed discussion of such a setup in a different context, see [253]. There, it is shown how to derive flows for the dependences of vertices or couplings on external parameters such as fundamental couplings, temperature, and chemical potential.

4.2.3. Spectral functional renormalisation group flows

One of our main motivations for using the CS regulator is that Lorentz invariance and the existence of spectral representations are manifest in the flow, see the discussion in Section 4.2.1. We exploit in particular the latter property for defining spectral, Lorentz invariant fRG flows in real time, based on the CS flow (4.74).

In Section 4.2.3.1 and Section 4.2.3.2 we give a brief overview on the spectral representation of correlation functions in quantum field theories, including sum rules for single particle spectral functions and their asymptotic behaviour that are direct consequences of the existence of a spectral representation. In Section 4.2.3.3 we show how finite flows are computed in practice, allowing for symmetry-preserving functional flows, including gauge-consistent flows. For convenience, in this section we shall mostly use a scalar theory in our discussions.

4.2.3.1. Spectral representation

The basic ingredient of spectral fRG flows are the spectral representations of the correlation functions. Foremost, this is the Källén-Lehmann (KL) representation (4.3), which for the scale-dependent propagator reads,

$$G_k(p) = \int_{-\infty}^{\infty} \frac{d\lambda}{2\pi} \frac{\lambda\, \rho_k(\lambda, \vec{p})}{\lambda^2 + p_0^2}\,, \tag{4.77}$$

with $\rho_k(-\lambda, \vec{p}) = -\rho_k(\lambda, \vec{p})$ and

$$\rho_k(\omega, \vec{p}) = 2\,\mathrm{Im}\, G_k(-\mathrm{i}\omega_+, \vec{p})\,, \tag{4.78}$$

where denotes the retarded limit (4.5). We emphasise that the spectral function is always defined with (4.78) but the relation (4.77) does not always hold. As discussed in Section 4.2.1 we have to make sure that the spectral representation of correlation functions at $k = 0$ is maintained also for $k \neq 0$ by choosing an appropriate regulator.

For the two-point function of asymptotic states, the spectral function is positive semi-definite and normalised to unity, if the states are normalised, see also the discussion in Section 4.2.4. In general this is not the case, since (4.78) and (4.77) are mere statements about the causal propagation of the associated operator.

We exemplify these statements within a more detailed discussion of the single scalar field φ in vacuum. Its two-point function $\Gamma^{(2)}(p^2)$ can be parametrised as

$$\Gamma^{(2)}(p^2) = Z_\phi(p^2)\left(p^2 + m_\phi^2\right)\,, \quad \Gamma^{(2)}(-m_\phi^2) = 0\,, \tag{4.79}$$

with the pole mass m_ϕ. The respective spectral function ρ admits a split into resonance and scattering contributions, see (4.6).

The spectral flows with a spectral CS cutoff are derived as flows in a CS limit (4.65b) of standard momentum shell cutoff flows as described in Section 4.2.2.2. Naturally, the persistence of the spectral representation (4.77) in the presence of the momentum shell regulators facilitates the derivation significantly. Hence, the CS limit may be taken with general regulators whose shape functions (2.35) are only dependent on spatial momenta squared, $x = \vec{p}^2/k^2$ or rather $x_\Lambda = \vec{p}^2/\Lambda^2$, see the two examples (4.65). It is easy to see that such regulators do not spoil the existence of a spectral representation for positive definite shape functions.

For illustration, we again consider the classical regularised propagator (4.45). Its respective scale dependent spectral function for general regulators $r(x_\Lambda)$ is given by

$$\rho_k(\lambda, \vec{p}^{\,2}) = \frac{\pi}{\lambda} \sum_{\pm} \delta\left(\lambda \pm \sqrt{\vec{p}^{\,2} + m_\phi^2 + k^2\, r(x_\Lambda)}\right) , \tag{4.80}$$

which can be shown by inserting (4.80) in (4.77),

$$G_k(p_0, \vec{p}) = \frac{1}{p_0^2 + \vec{p}^{\,2} + m_\phi^2 + k^2 r(x_\Lambda)} , \tag{4.81}$$

for general shape functions $r(x_\Lambda)$. Hence, as argued before, we may use spatial momentum regulators (2.34) with shape functions $r(x_\Lambda)$ and implement the CS limit (4.65b) in a spectral way. Note that any class of regulator can be chosen for this limit, we either drop Lorentz invariance or the spectral representation as discussed in Section 4.2.1, see Figure 4.15. The combination is only obtained in the CS limit, which in its finite form (4.74) has all three properties.

4.2.3.2. Sum rules

The KL spectral representation (4.77) links the infrared asymptote for $\lambda \to 0$ and its ultraviolet asymptote for $\lambda \to \infty$ to the IR and UV behaviour of the Euclidean propagator. This also fixes its normalisation. These properties are discussed and verified in detail in [2] resp. Appendix A.8 and [206, 243, 254]. The UV or IR asymptotic behaviour of the dimensionless Euclidean propagator can be parametrised as

$$\hat{G}(p^2 \to \mathrm{UV/IR}) = \frac{Z_\phi}{\hat{p}^2} \frac{\hat{p}^\eta}{(\log \hat{p}^2)^\gamma} , \tag{4.82}$$

with the dimensionless momentum squared $\hat{p}^2 = p^2/m_{\mathrm{gap}}^2$ and some reference scale m_{gap}. In the UV limit one has the parameters $Z_{\phi,\mathrm{UV}}$, η_{UV}, γ_{UV}, and in the IR $Z_{\phi,\mathrm{IR}}$, η_{IR}, γ_{IR}. As discussed in Section 4.2.3.1, the amplitude Z_ϕ is the inverse of the wave function of the two-point function (4.79).

This general asymptotic form of the propagator includes a power behaviour arising from the anomalous dimension η besides the canonical power -2, as well as a logarithmic dependence, see, e.g., [2] resp. Appendix A.8 and [206, 243, 254], for details. For some non-local theories, the propagator shows an exponential decay behaviour [254], which is not taken into account here. With (4.82) and the spectral representation (4.77), the UV asymptote of the spectral function reads

$$\lim_{\hat{\omega}\to\infty} \hat{\rho}(\hat{\omega}) = \frac{Z_{\phi,\mathrm{UV}}}{\hat{\omega}^2} \frac{2\hat{\omega}^{\eta_{\mathrm{UV}}}}{(\log \hat{\omega}^2)^{\gamma_{\mathrm{UV}}}} \left(\sin\left[\frac{\pi}{2}\eta_{\mathrm{UV}}\right] - \cos\left[\frac{\pi}{2}\eta_{\mathrm{UV}}\right] \frac{\pi\gamma_{\mathrm{UV}}}{\log \hat{\omega}^2} \right), \tag{4.83}$$

and the IR asymptote is given by

$$\lim_{\hat{\omega}\to 0} \hat{\rho}(\hat{\omega}) = \frac{Z_{\phi,\mathrm{IR}}}{\hat{\omega}^2} \frac{2\hat{\omega}^{\eta_{\mathrm{IR}}}}{(\log \hat{\omega}^2)^{\gamma_{\mathrm{IR}}}} \left((2 - \eta_{\mathrm{IR}}) + \frac{2\gamma_{\mathrm{IR}}}{\log \hat{\omega}^2} \right) . \tag{4.84}$$

The UV limit already entails that only for $\eta_{\mathrm{UV}} = 0$, $\gamma_{\mathrm{UV}} = 0$ we have a normalisable spectral function with

$$\int_0^\infty d\lambda\, \lambda\, \rho(\lambda) = Z_{\phi,\mathrm{UV}} , \tag{4.85a}$$

which is in one-to-one correspondence with the commutation relations $[\phi(t,\vec{x}),\partial_t\phi(t,\vec{y})] = Z_{\phi,\mathrm{UV}}\delta(\vec{x}-\vec{y})$. The standard normalisation is obtained for $Z_{\phi,\mathrm{UV}}=1$, which entails canonical commutation relations.

In turn, for $\eta_{\mathrm{UV}}<0$ or $\gamma_{\mathrm{UV}}>0$ the UV-tail of the spectral function is negative, and the respective field does not describe an asymptotic state. Moreover, the spectral function is normalised to zero,

$$\int_0^\infty d\lambda\,\lambda\,\rho(\lambda)=0\,. \tag{4.85b}$$

In QCD this is the well-known Oehme-Zimmermann super convergence property [255, 256] for the gluon in covariant gauges, for an evaluation in the Landau gauge see [243]. In asymptotically safe gravity it holds true for the background graviton, for a reconstruction see [257].

For $\eta_{\mathrm{UV}}>0$ or $\gamma_{\mathrm{UV}}<0$ the UV tail of the spectral function is positive, but the spectral function is not normalisable,

$$\lim_{\Lambda\to\infty}\int_0^\Lambda d\lambda\,\lambda\,\rho(\lambda)\to\infty\,, \tag{4.85c}$$

in the absence of IR singularities. Equation (4.85c) holds true for the spectral function of the fluctuation graviton in covariant gauges, see [257] for a reconstruction, and [206] for a direct computation with the spectral fRG. Note that also in this case the field does not generate an asymptotic state by applying it to the vacuum, $\phi|0\rangle$. However, this is not to be expected in a non-Abelian gauge theory or quantum gravity.

4.2.3.3. Spectral renormalisation & symmetries

It has been discussed in [1], see Section 4.1, how the momentum integrals of fully non-perturbative loop integrals can be computed within dimensional regularisation. It has also been shown, how a fully gauge-consistent functional renormalisation scheme can be set up by also applying *spectral dimensional renormalisation*. One also can use a Bogoliubov-Parasiuk-Hepp-Zimmermann–type (BPHZ) subtraction scheme, *spectral BPHZ renormalisation*. For details, we refer the reader to this section, here we only briefly recapitulate the important properties of spectral renormalisation.

The spectral renormalisation scheme in [1] resp. Section 4.1 has been set up for general functional approaches, and has been exemplified within the Dyson-Schwinger equation (DSE) for the scalar theory. The respective loop equations contain up to two-loop diagrams with non-perturbative propagators and vertex functions. In the present case of the spectral fRG we only have to consider the renormalisation of one-loop diagrams which facilitates the task. One of the lines carries the cutoff insertion, and the momentum routing is typically chosen such that it only depends on the loop momentum q. In terms of the frequency dependence, the line with the cutoff insertion simply leads to two classical propagators with the spectral masses λ_1^2 and λ_2^2, both carrying the loop frequency q_0. The CS or spatial regulator does not depend on the loop frequency, but only on $x=\vec{q}^{\,2}/k^2$. To facilitate numerical computations in $d>1$, it is advantageous to use a spectral representation of the full regulator line or more precisely the propagator squared,

$$G(q)\partial_t R_k(x)G(q)=\frac{\partial_t R_\phi(x)}{q^2}\int_{-\infty}^{\infty}\frac{\mathrm{d}\lambda}{2\pi}\frac{\lambda\,\rho_{G^2}(\lambda)}{\lambda^2+q^2}\,, \tag{4.86}$$

In (4.86) we have used, that Lorentz invariance allows us to reduce $\rho_i(\lambda, \vec{q})$ to $\rho_i(\lambda) = \rho_i(\lambda, 0)$ within spectral representations such as (4.77) and (4.86),

$$\int_{-\infty}^{\infty} \frac{d\lambda}{2\pi} \frac{\lambda \rho_i(\lambda, \vec{q})}{\lambda^2 + q_0^2} = \int_{-\infty}^{\infty} \frac{d\lambda}{2\pi} \frac{\lambda \rho(\lambda, 0)}{\lambda^2 + q^2} \,, \tag{4.87}$$

Note that the regulator derivative in (4.86) is simply multiplying the spectral representation of G^2. This is a consequence of the regulator not carrying the loop frequency. The spectral density ρ_{G^2} in (4.86) is defined as

$$\rho_{G^2}(\omega) = 2 \operatorname{Im}\left[\omega_+^2 G\left(\omega_+\right)^2\right] , \tag{4.88}$$

We may either use (4.86) or the product of the two spectral functions for the propagators on the right-hand side of (4.86). In both cases, general flow diagrams $\mathrm{Diag}(\mathbf{p})$ of the flow of vertex functions and inverse propagators with the external momenta $\mathbf{p} = (p_1, ..., p_n)$ have the representation

$$\mathrm{Diag}(\mathbf{p}) = \int \frac{d^d q}{(2\pi)^d} \mathrm{Vert}(\mathbf{l}, \mathbf{p}) \prod_{i=1}^{N_{\max}} \int_{-\infty}^{\infty} \frac{d\lambda_i}{2\pi} \frac{\lambda_i \rho_i(\lambda_i, \vec{l_i})}{\lambda_i^2 + (l_i)^2} \,, \tag{4.89}$$

where $\mathbf{l} = (q, q + p_1, ...,)$ is the vector of all momenta entering the propagators and vertices of the loop diagram at hand, and $N_{\max}$ is the number of spectral functions. The factor $\mathrm{Vert}(\mathbf{l}, \mathbf{p})$ stands for the momentum dependences of vertex and regulator factors and possible projections and is a rational function in the momenta $\mathbf{l}$ and $\mathbf{p}$.

For example, for constant vertex functions and using (4.86), $\mathrm{Vert}(\mathbf{l}, \mathbf{p}) \propto \frac{1}{q_0^2}$, and N_{Max} is simply the number of internal lines including the regulator line. Then, the ρ_i are the spectral functions of the fields ϕ_i propagating in the respective line and $\rho_1 = \rho_{G^2}$. In turn, if only using the spectral representation of the propagators, the vertex factor $\mathrm{Vert}(\mathbf{l}, \mathbf{p})$ has no frequency and momentum dependence, but $N_{\mathrm{Max}} \to N_{\mathrm{Max}} + 1$: it is the number of internal lines and the regulator line counts twice.

With (4.87), the momentum integral in (4.89) has the standard form of a one loop perturbative integral, and can be computed with dimensional regularisation with $d \to d - 2\epsilon$ and $\epsilon \to 0$. We are led to

$$\mathrm{Diag}(\mathbf{p}) = \prod_{i=1}^{N_{\max}} \int_{-\infty}^{\infty} \frac{d\lambda_i}{2\pi} \lambda_i \rho_i(\lambda_i, 0)\, F_{\mathrm{diag}}(\boldsymbol{\lambda}, \mathbf{p}; \epsilon) \,, \tag{4.90}$$

with

$$F_{\mathrm{diag}}(\lambda, \mathbf{p}; \epsilon) = \int \frac{d^d q}{(2\pi)^d} \mathrm{Vert}(\mathbf{l}, \mathbf{p}) \prod_{i=1}^{N_{\max}} \frac{1}{\lambda_i^2 + (l_i)^2} \,. \tag{4.91}$$

Equation (4.90) generalises the form of the spectral integrals considered in [1] resp. Section 4.1, cf. (4.19) and (4.20), by including the momentum-dependent factor Vert. Since we assume Vert to be a rational function of its momentum arguments, (4.90) can be treated the same way as the DSE diagrams. Here, we briefly recapitulate the main results obtained there and refer the reader to [1] resp. Section 4.1 for more details.

To begin with, for power-counting divergent perturbative momentum integrals, F_{diag} contains $1/\epsilon$-terms in even dimensions $d = 2n$ with $n \in \mathbb{N}$. It is tempting to apply the

minimal subtraction idea of only subtracting these divergent pieces. This would amount to simply dropping the $1/\epsilon$-terms in F_{diag}. However, as thoroughly discussed in [1] and Section 4.1, the remaining spectral integrations have the same ultraviolet degree of divergence and may not be finite. Note that these divergences are sub-divergences and are absent at one loop perturbation theory where the spectral functions are Dirac δ-functions. This leaves us with two choices:

(i) *Spectral dimensional renormalisation:* if we want to maintain all symmetry-features of dimensional regularisation, we also have to perform the UV part of the spectral integrations analytically. This can be done using splits

$$\rho(\lambda, \vec{q}) = \rho_{\text{IR}}(\lambda, \vec{q}) + \rho_{\text{UV,an}}(\lambda, \vec{q})\,, \tag{4.92}$$

where the 'IR' part decays sufficiently fast for large spectral values, and $\rho_{\text{UV,an}}$ carries the UV-tail of the spectral function and its form is chosen such that it facilitates the analytic computation of the UV-part of the spectral integrations. Finally, we are left with $1/\epsilon$ terms from both the momentum and spectral integrals, which can be subtracted by an appropriate choice of $\partial_t S_{\text{cl}}$ in (4.74).

(ii) *Spectral* BPHZ *renormalisation:* We implement the RG conditions at an RG scale μ in terms of subtractions at the level of the integrand in (4.91). This amounts to subtracting a Taylor expansion in $\mathbf{p}$ of F_{diag}. For the sake of simplicity we restrict ourselves to a case with one external momentum and a quadratic divergence, e.g., the flow of the two-point function $\Gamma^{(2)}(p)$ in a scalar theory in $d = 4$ dimensions. Then, $\mathbf{p} = p$ and the BPHZ subtraction reads schematically,

$$\begin{aligned}\text{Diag}_{\text{ren}}(\mathbf{p}) = \prod_{i=1}^{N_{\max}} \int_{-\infty}^{\infty} \frac{d\lambda_i}{2\pi} \lambda_i \rho_i(\lambda_i, 0) \Bigg[F_{\text{diag}}(\boldsymbol{\lambda}, p; \epsilon) \\ - F_{\text{diag}}(\boldsymbol{\lambda}, \mu; \epsilon) - (p^2 - \mu^2) \left.\frac{\partial F_{\text{diag}}(\boldsymbol{\lambda}, p; \epsilon)}{\partial p^2}\right|_{p^2=\mu^2} \Bigg]\,.\end{aligned} \tag{4.93}$$

In (4.93) we can take the limit $\epsilon \to 0$ before performing the spectral integrations which are manifestly finite. The showcase (4.93) straightforwardly extends to the flow of general correlation functions with the standard BPHZ procedure. Evidently, the subtraction terms constitute a specific choice of $\partial_t S_{\text{cl}}$ in (4.74).

This closes our brief recapitulation of the conceptual results in [1] resp. Section 4.1, and the discussion of their application to the spectral CS-flows: The spectral dimensional or BPHZ renormalisation is implemented by a respective choice of the flow of the counterterm action $\partial_t S_{\text{cl}}$ in (4.74). This leads us to manifestly finite spectral flows within a systematic flowing renormalisation scheme.

Evidently, the spectral BPHZ renormalisation is technically less challenging, and is the renormalisation method of choice in most cases. However, we emphasise that the $\epsilon \to 0$-limit and the integration do not commute, and hence the spectral BPHZ renormalisation and the spectral dimensional renormalisation may not agree in terms of symmetries. This may be specifically important for gauge theories. Either way this allows us to define *finite* spectral flows.

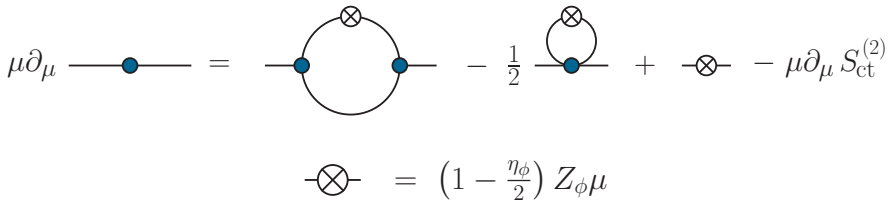

Abbildung 4.16.: Renormalised CS equation for the inverse propagator. The notation is given in Figure 2.1. As in Figure 2.3, the blob with the cross represents the regulator scale derivative $\partial_t R_k$. In the present case of the functional Callan-Symanzik flow, the regulator term is simply given by the mass term in the scale-dependent classical action, cf. (4.94), which entails the lower definition.

4.2.4. Spectral fRG in the scalar ϕ^4-theory

Next, we discuss the application of the spectral fRG framework set up in Section 4.2.3 to the scalar ϕ^4-theory in $d = 2+1$. Asymptotically free non-Abelian gauge theories are discussed in Appendix A.3, specifically concentrating on infrared and ultraviolet asymptotes of the spectral function.

In the spectral fRG approach put-forward in [6, 206], the quantum effective action of the theory at hand is obtained by starting with a theory with an asymptotically large classical pole mass $m_\phi \to \infty$, and then lowering the mass successively until the physical point is reached. For this purpose, we recast the classical action of the scalar theory (2.1) as

$$S[\varphi] = \int d^3x \left\{ \frac{1}{2}\varphi\Big(-\partial^2 + Z_\phi\,\mu\Big)\varphi + \frac{\lambda_\varphi}{4!}\varphi^4 \right\}, \tag{4.94}$$

where φ refers to the full fluctuating quantum field. $\mu > 0$ signals a classical potential with a trivial minimum. Then, the mass parameter can be identified with the classical mass squared, $m_\phi^2 = \mu$. For $\mu < 0$ in turn, the full potential exhibits non-trivial minima, and the classical mass of the theory follows from the effective potential as $m_\phi^2 = -2\mu$. The wave function Z_ϕ has been introduced for convenience, anticipating the emergence of a wave function. For asymptotically large pole masses we have $Z_\phi \to 1$, see Figure 4.17b. Then, the pole mass is given by

$$m_\phi^2 = \mu - 3\mu\,\theta(-\mu)\,, \tag{4.95}$$

capturing both, theories deep in the symmetric phase with $\mu \to +\infty$ and theories deep in the broken phase with $\mu \to -\infty$. Here, we will focus on the symmetry-broken phase $\mu < 0$ in order to facilitate comparison with the spectral DSE results of Section 4.1. The discussion of the symmetric phase results is deferred to [9].

4.2.4.1. Spectral flow of the propagator

The infinitesimal change of the quantum effective action $\Gamma[\phi]$ under a change of the mass μ is governed by the manifestly finite renormalised Callan-Symanzik equation (4.74). We

switch back to the dimensionful scale parameter to explicitly connect to the form (4.94) including the wave function renormalisation Z_ϕ. The corresponding functional CS equation for the effective action reads

$$\mu\partial_\mu\Gamma[\phi] = \frac{1}{2}\left(1-\frac{\eta_\phi}{2}\right) Z_\phi \mu\,\mathrm{Tr}\left[G[\phi]+\phi^2\right] - \frac{1}{2}\,\mu\partial_\mu S_{\mathrm{ct}}[\phi]\,, \tag{4.96a}$$

with the anomalous dimension

$$\eta_\phi = -2\frac{\mu\partial_\mu Z_\phi}{Z_\phi}\,, \tag{4.96b}$$

The factor 2 in (4.96b) takes into account that μ has mass dimension 2, and the anomalous dimension 'counts' dimensions and not 1/2 dimensions. The argument ϕ in (4.96) is the mean field. The term $\mu\partial_\mu S_{\mathrm{ct}}[\phi]$ in the second line of (4.96a) is the flow of the counterterms that renders the flow equation finite, where the factor 1/2 was added for convenience. The loop term on the right-hand side depends on the full field-dependent propagator. In momentum space, the trace in (4.96a) corresponds to a momentum integral.

Note that the effective action $\Gamma[\phi]$ in (4.96) includes the full mass term $1/2\int_x \mu\,\phi^2$ in contradistinction to the effective action used in standard fRG momentum-shell flows. There, the momentum dependent regulator part of the mass term is subtracted, and the physical theory is reached when it vanishes. In the present setup, the μ-dependent effective action is that of a physical theory with mass parameter μ, and the flow is one in (physical) theory space.

Compared to the Wetterich equation [76] with a momentum-dependent infrared regularisation, the novel ingredient in the functional Callan-Symanzik equation (4.96) is the explicit counterterm flow $\mu\partial_\mu S_{\mathrm{ct}}[\phi]$. The counterterm flow has been derived in a manifestly finite limit of standard momentum cutoff flow equations as discussed in detail in Section 4.2.2.2 resp. [6]. The derivation entails that the flow of the counterterm originates from a closed one-loop expression such as the trace in (4.96) itself, i.e., $\mu\partial_\mu S_{\mathrm{ct}}[\phi] \sim$ diagramms. Accordingly, the counterterm flow contains no tree-level contributions to the respective correlation functions. This entails that classical values of the correlation functions are solely given by the respective choice of tree-level values specified in the classical action (4.94), and in particular cannot be further changed by specification of renormalisation conditions. In consequence, the latter can only be used to renormalise the flow contributions, but not the initial conditions of the flow. This excludes, for example, that the counterterm flow rearranges the theory from the symmetric into the broken phase or vice versa by $\mu\partial_\mu S_{\mathrm{ct}} \propto \pm\mathrm{const.}\,\mu\int\phi^2$. However, the counterterm can contain similar terms proportional to $\lambda_\phi/m_{\mathrm{pole}} = \lambda_{\mathrm{eff}}$.

Here, we consider the flow of the inverse propagator within the spectral representation (4.77). This entails a particularly simple structure of the non-perturbative diagrams in the flow equations, in which the momentum loop integration can be performed analytically; see Section 4.2.3.3. The flow is diagrammatically depicted in Figure 4.16; for the algebraic form, see [9]. All quantities in the flow equation (4.96a) depend on the chosen background ϕ. For general spacetime-dependent backgrounds $\phi(x)$ this would lead us to $\Gamma^{(2)}[\phi](p,q)$. In the explicit computations we consider the background ϕ_0, which is the constant solution of the equation of motion

$$\left.\frac{\delta\Gamma[\phi]}{\delta\phi}\right|_{\phi=\phi_0} = 0\,. \tag{4.97}$$

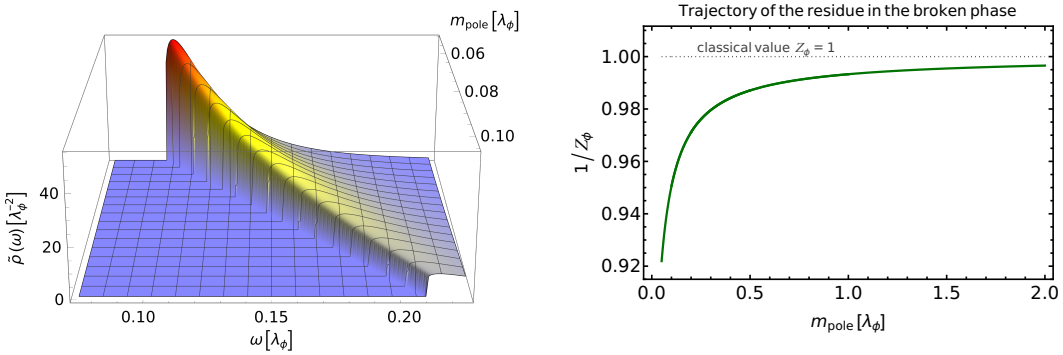

(a) Scattering tail $\tilde{\rho}_k$ for vanishing spatial momentum $\vec{p} = 0$ as a function of the spectral value ω and the pole mass m_{pole} for $1/20 \leq m_{\text{pole}}/\lambda_\phi \leq 1/10$.

(b) Amplitude $1/Z_\phi$ of the pole contribution of the spectral function (4.100) as a function of the pole mass m_{pole} for $1/20 \leq m_{\text{pole}}/\lambda_\phi \leq 1/2$. The classical value for Z_ϕ is indicated in grey.

Abbildung 4.17.: Spectral function ρ, (4.100), for different pole masses $m_{\text{pole}}/\lambda_\phi$, measured in the fixed coupling λ_ϕ.

Since we assume the physical background field ϕ_0 defined by (4.97) to be constant, the general field-dependent propagator (2.22) reduces to the physical propagator $G(p^2)$ (2.26) in the absence of source terms. From now on we drop the field argument ϕ_0. It is implicitly understood that all correlation functions are evaluated at $\phi = \phi_0$.

After this explicit discussion of functional flows with the mass scale μ, we substitute μ with $-k^2$, to keep the relations to standard fRG flows with momentum cutoffs simple, where k is commonly used. The minus sign arises from the negativity of the mass term in the broken phase, see (4.95). This facilitates the comparison and benchmarking of the realtime results obtained with the spectral fRG. For example, the three-dimensional ϕ^4-theory has been studied abundantly within the Euclidean fRG, including systematic studies of the convergence of approximation schemes, for a recent review see [63]. These results carry over straightforwardly to the present approach, and the Euclidean correlation functions obtained from the spectral functions can be directly compared. This substitution leads us to

$$k^2 = |\mu|\,, \qquad \partial_t = k\,\partial_k = 2\mu\partial_\mu\,, \tag{4.98}$$

where the (negative) RG time $t = \log(k/k_{\text{ref}})$ is measured relatively to a suitable reference scale or mass.

4.2.4.2. Spectral on-shell renormalisation

We proceed with discussing the on-shell spectral renormalisation, see Section 4.2.2.3 and Section 4.2.3.3, applied to the current setup, exploiting the direct access to Minkowski momenta. In $(2+1)$ dimensions, both diagrams in the CS flow Figure 4.16 are manifestly finite, and the flow of the counterterm action $\mu\partial_\mu S_{\text{ct}}$ only guarantees the implementation of the chosen renormalisation conditions. The (2+1)-dimensional ϕ^4-theory is superrenormalisable, and one only has the renormalisation condition for the mass. Here, we

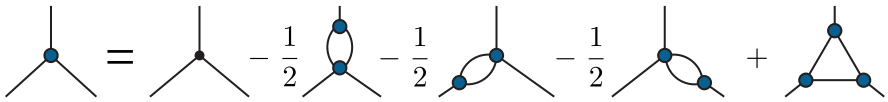

Abbildung 4.18.: Truncated DSE for the three-point function in the skeleton expansion. The notation is given in Figure 2.1.

employ flowing on-shell renormalisation, where the pole mass m_{pole} is identified with m_ϕ, $m^2_{\text{pole}} = 2k^2$. The corresponding renormalisation condition reads

$$\Gamma^{(2)}[\phi_0]\Big|_{p^2=-2k^2} = 0\,, \tag{4.99}$$

also sourcing an additional factor of 2 in front of the pole position in comparison to (4.75), where $m^2_{\text{pole}} = k^2$ was used. Furthermore, in contradistinction to (4.75), we did not subtract the trivial running of the regulator flow $1/2\int_x \mu\,\phi^2$ in (4.96a). This gives rise to the additional ϕ^2 term inside the trace in (4.96a) compared to the standard CS flow (4.73), ultimately resulting in the two-point function equating to zero in (4.99).

In our physical on-shell RG scheme, the phase transition between the symmetric and broken phase happens for $m^2_\phi = 0$. Hence, we approach the phase transition in the limit $k \to 0$, and the flow is taking place solely in the broken phase here. This also avoids flows through the phase transition as are present in momentum cutoff flows.

Due to the non-vanishing background field in the broken phase, $1 \to 2$ scattering processes are allowed. The onset of the scattering continuum of the spectral function is therefore located at twice the pole mass, and the corresponding spectral function schematically reads

$$\rho(\lambda) = \frac{2\pi}{Z_\phi}\delta(\lambda^2 - m^2_{\text{pole}}) + \theta(\lambda^2 - (2m_{\text{pole}})^2)\tilde{\rho}(\lambda)\,, \tag{4.100}$$

In Figure 4.17, we show the corresponding scale evolution of the spectral function ρ: in Figure 4.17a we depict the scattering tail $\tilde{\rho}$, and in Figure 4.17b we depict the amplitude of the pole contribution. All quantities are measured relative to the coupling λ_ϕ.

The spectral tail is rising towards smaller pole masses for a fixed classical coupling, and in turn the amplitude $1/Z_\phi$ of the pole contribution is decreasing. In combination the sum rule (4.7) holds during the evolution. The growing importance of the scattering processes can be understood from the fact that the dynamics of the theory only depends on the dimensionless ratio λ_ϕ/m_ϕ with $m_\phi \propto k$. Hence, the effective coupling grows strong for smaller pole masses and on the other hand the dynamics of the theory are vanishing for asymptotically large pole masses.

4.2.4.3. Flowing with the minimum

In general, the flow equation (4.96a) can be evaluated for arbitrary values of the external field ϕ, which requires the inclusion of the full effective potential. However, this goes beyond the scope of this work, and we simply evaluate the flow on the solution ϕ_0 of the equation of motion (4.97). This is a commonly used truncation as it gives access to the physical correlation functions.

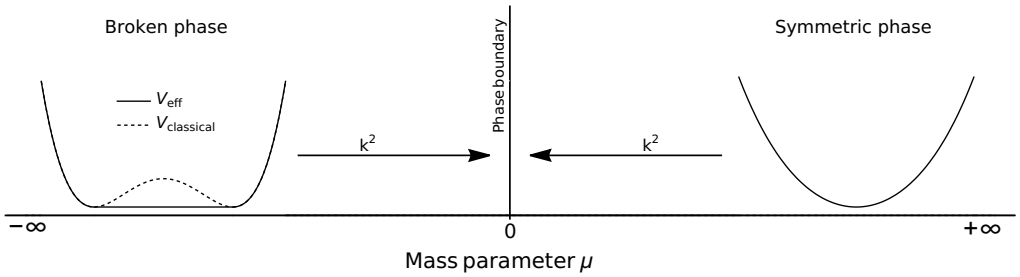

Abbildung 4.19.: Schematic phase diagram with respect to the mass-parameter μ. The phase boundary is located at $\mu = 0$. The flow is initiated in the deep UV, i.e. $|\mu| = k^2 \to \infty$ with the respective (classical) initial effective potential. Note that we are only considering the symmetry-broken phase, depicted on the left, here.

In the present fRG approach with the spectral CS regulator, the flow takes place in theory space and the effective action is physical for all values of k. In the broken phase, the minimum of the full effective potential depends on k, and the total mass flow of the two-point function is given by the flow diagrams originating from the CS equation, $\partial_t \Gamma^{(2)}[\phi_0](p)$ and a term proportional to the mass flow of ϕ_0,

$$\frac{d}{dt}\Gamma^{(2)}[\phi_0](p) = \partial_t \Gamma^{(2)}[\phi_0](p) + \left(\partial_t \phi_0 \Gamma^{(3)}[\phi_0]\right)(p)\,. \tag{4.101}$$

The novel ingredient in the present setup originates in the tree-level k-dependence of $\phi_0 \approx k\sqrt{6/\lambda_\phi}$, see (4.103). This tree-level dependence is usually absent in the flow of the minimum in standard momentum-shell flows. There $\partial_t \phi_0$ only comprises the effects of the momentum shell integration and hence is inherently one-loop and beyond. The tree-level k-dependence of ϕ_0 in the present case triggers a tree-level k-dependence of $\partial_t \phi_0 \Gamma^{(3)}(p)$ and the tree-level flow of the physical two-point function considered here reads

$$\frac{d}{dt}\,\Gamma^{(2)}\Big|_{\text{tree-level}} = -2k^2 + \partial_t \phi_0 S^{(3)}[\phi_0] = 4k^2\,, \tag{4.102}$$

where the classical three-point function is given by $S^{(3)}[\phi] = \lambda_\phi \phi$.

4.2.4.4. Approximations

To facilitate comparison with the spectral DSE results of Section 4.1, we employ the exact same approximations for the higher correlation functions. The four-point function is given by the s-channel bubble resummation (4.34), depicted in Figure 4.8, obeying a simple spectral representation (4.36).

The full momentum dependence of the three-point function in (4.101) can be incorporated via its DSE, which allows for an exact diagrammatic flow of the two-point function on the physical minimum ϕ_0. In the presence of approximations, a fully self-consistent treatment would require us to use the integrated flow of $\Gamma^{(3)}[\phi_0](p, 0)$. However, also the flow of $\Gamma^{(3)}[\phi_0]$ includes a similar additional term as in (4.102), which is proportional to the four-point function. To ensure the correct RG scaling of the flow equation, we employ

a skeleton expansion in the three-point DSE, where every vertex is dressed. Approximating $\Gamma^{(n>4)} \approx 0$ and dropping the remaining two-loop diagrams, we arrive at the simple diagrammatic structure of the three-point function depicted in Figure 4.18.

The effective potential is given by a Taylor expansion about the constant background field ϕ_0 (4.26), as in Section 4.1. With $\Gamma^{(n>4)} \approx 0$, this again allows us to relate the three- and four-point function via (4.30). Employing (4.30) on the RHS of the three-point DSE in Figure 4.18 hence allows us to close our truncation.

For the explicit form of the final flow equation including that of the counterterm action, also at real frequencies, we refer to [9].

4.2.4.5. Resume

In order to obtain intuition for the physical picture emerging within the spectral functional flow at hand, it is beneficial to consider the ultraviolet limit of the effective potential of the theory. Evidently, in the classical limit with vanishing spectral tail $\tilde{\rho}_k = 0$ and $Z_\phi = 1$, see Figure 4.17b, the curvature mass (4.28) agrees with the pole mass. This limit is approached for asymptotically large pole masses, where the effective coupling $\lambda_\phi/m_{\text{pole}}$ tends towards zero. Hence, the ultraviolet effective potential $V_{\text{UV}}(\phi)$ at $k = \Lambda \to \infty$ is augmented with a classical dispersion with $\mu = -\Lambda^2$ and the initial (classical) coupling $v_2 = \lambda_\phi$, see (3.131),

$$V_{\text{UV}}(\phi) = \frac{1}{4!}\lambda_\phi \left(\phi^2 - \phi_0^2\right)^2 , \qquad \phi_0^2 = \frac{6\Lambda^2}{\lambda_\phi} , \tag{4.103}$$

for $\phi^2 \geq \phi_0^2$. The initial curvature and pole mass are given by

$$m^2_{\text{pole}} = m^2_{\text{curv}} = 2\Lambda^2 . \tag{4.104}$$

This leads us to the following structure: the CS flow is initiated deep in the broken phase for large pole masses and a given classical coupling λ_ϕ. This entails, that also the field expectation value at the initial scale is large as it scales with Λ, see (4.103). Then, the pole mass is successively lowered and for $k = 0$ one reaches the phase transition point. In particular, the flow does not leave the symmetry-broken phase; see Figure 4.19. This is in seeming contradiction to the standard fRG picture in a scalar theory, where flows in the broken phase may end up in the symmetric phase. This apparent contradiction is resolved by the fact, that ϕ_0 in the standard fRG is defined from the subtracted EoM. There, the trivial cutoff flow, which is $\propto k^2\phi$, is subtracted from the effective potential, and one recovers physics only in the limit $k \to 0$.

4.2.5. Results

In this section, we present results for the non-perturbative spectral functions of the scalar propagator. The discussion of the numerical implementation is deferred to [9]. The results allow for an investigation of the scattering processes in both phases. The present results are in remarkable quantitative agreement with that obtained with the spectral DSE in [1], discussed in Section 4.1. This agreement of the spectral functions from these two different functional approaches hold true for a large range of effective couplings λ_ϕ/m_ϕ,

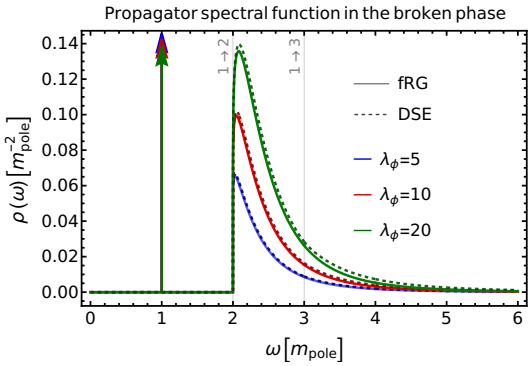

(a) Spectral function of the propagator. The $1 \to 2$ and $1 \to 3$ particle scattering onsets are indicated in grey.

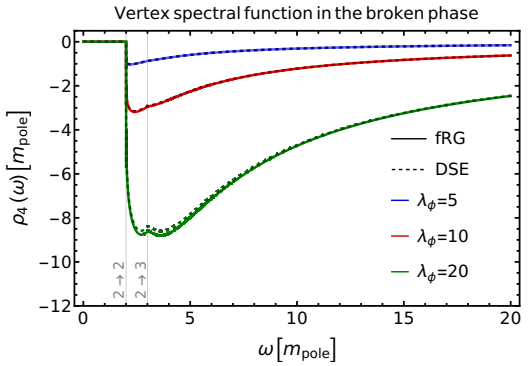

(b) Spectral function of the four-point function. The $2 \to 2$ and $2 \to 3$ particle scattering onsets are indicated in grey.

Abbildung 4.20.: Spectral functions as a function of Minkowski frequency in comparison to DSE results from [1], see Section 4.1. In contrast to Figure 4.17, all quantities are measured in units of the pole mass to facilitate the comparison with the DSE results.

see Figure 4.20a. In this coupling regime this agreement provides a non-trivial reliability check for both functional approaches, thus decreasing the respective systematic error.

In Figure 4.20a the spectral function from the current fRG approach is compared to spectral DSE results from [1] resp. Section 4.1. Every quantity is measured relative to the respective pole mass to facilitate comparison with the DSE results. This allows to compare the relative magnitude of the scattering continua for different coupling strengths. For effective couplings $\lambda_\phi/m_{\rm pole} \lesssim 20$, the spectral weight of the scattering continuum is sub-leading, as can be inferred from the combination of Figure 4.17b and the sum rule (4.7). The amplitudes of the pole contributions are listed in Section 4.2.5.

We find a remarkable agreement of both methods in the tested coupling range. For effective couplings $\lambda_\phi/m_{\rm pole} \approx 20$, the deviations start growing, specifically at the thresholds. Deviations between both methods arise due to differences in the resummation structure of the two functional equations in the current truncation. The convergence of functional techniques for a large range of couplings is non-trivial and strengthens our confidence in spectral functional approaches.

In general, the tail of the propagator spectral function is enhanced for stronger couplings, while the residue of the mass pole decreases as the scattering states become more accessible

$\lambda_\phi/m_{\rm pole}$	$1/Z_\phi$ (fRG)	$1/Z_\phi$ (DSE)
5	0.971	0.969
10	0.950	0.945
20	0.921	0.907

Tabelle 4.1.: Amplitudes $1/Z_\phi$ of the pole contribution for given effective couplings, corresponding to the scattering tails displayed in Figure 4.20a.

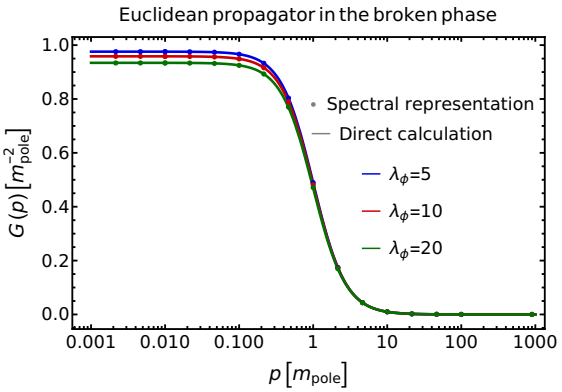

(a) Propagator as function of Euclidean frequency. This result serves as a cross-check between a direct computation via the flow and a calculation using the spectral functions.

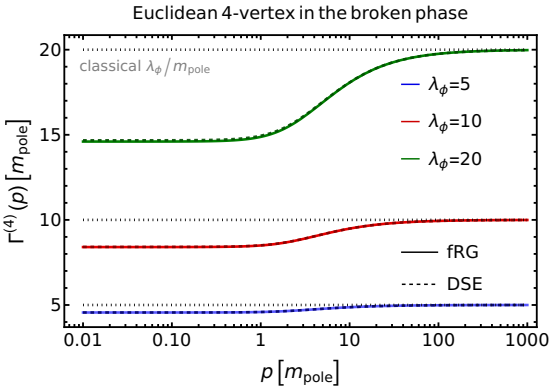

(b) Four-point vertex as function of Euclidean frequency. Results are obtained from the respective spectral functions in Figure 4.20a. The classical values of the vertices are indicated in grey.

Abbildung 4.21.: Euclidean correlators in the broken phase. All quantities are measured in units of the pole mass.

due to the rising dimensionless interaction strength. The three- and higher N-particle onsets are graphically not visible in the full spectral functions of Figure 4.20a, but present in the data. In the limit of large couplings we expect the three-particle onset to become more pronounced as the tadpole contribution becomes large.

The four-point spectral function shown in Figure 4.20b consists of only a negative scattering tail corresponding to a $2 \to 2$ scattering process. For higher couplings, the three-particle onset becomes visible. The different suppression of higher N-particle thresholds in the propagator- and four-point spectrum are explained by dimensional analysis. While for the propagator spectral function, higher N-particle onsets are suppressed by their squared energy threshold, the four-point spectral function decays only with λ^{-1}, leading to a suppression linear in their respective energy thresholds. In both cases, four-particle or higher onsets are strongly suppressed, since they come with at least one additional loop each. The corresponding Euclidean correlators are shown in Figure 4.21b, also showing remarkable agreement with the DSE.

Figure 4.21a shows the Euclidean propagators corresponding to the spectral functions of Figure 4.20a. As a cross-check, we compare the Euclidean propagator calculated from the spectral representation to the propagator directly obtained from the integrated Euclidean flow. We find the spectral representation to hold.

4.2.6. Conclusion

In this section, we have derived a novel functional flow equation with flowing renormalisation, see (4.73) in Section 4.2.2.2, and successfully put it to use in a scalar ϕ^4-theory in Section 4.2.4 for the computation of spectral functions. Flowing renormalisation entails that the renormalisation condition can be adapted with the flowing scale. This can be used for fRG flows from the finite renormalised UV effective action at large infrared cutoff scales to the full effective action at $k = 0$. Importantly, it also allows for manifestly finite fRG flows with regulators that do not implement a UV regularisation of the loop, such

as the Callan-Symanzik regulator. The respective CS flow, (4.74), is manifestly finite in general truncation schemes. The novel fRG flows (4.73) and (4.74) constitute key results of this chapter.

While finite (or homogeneous) CS equations are well-known, they are based on multiplicative renormalisation, which is not amiable to general truncation schemes, and in particular do not support most non-perturbative schemes. In turn, the present derivation is solely based on the general fRG framework with finite flow equations with respect to an infrared regulator. This embeds the Callan-Symanzik equation self-consistently in this Wilsonian framework. The current derivation also provides the full formal justification of its use in asymptotic safety [206].

We have then used the finite Lorentz invariant CS flows to set up the Lorentz invariant *spectral fRG* in Section 4.2.3, which we use to compute single particle spectral functions in Section 4.2.4. The flow equation is evaluated on the (flowing) solution to the equations of motion, corresponding to a scale-dependent background field effectively acting as an order parameter for symmetry breaking.

Together with the flowing on-shell renormalisation condition, this physical choice allowed us to formulate the flow along a physical trajectory in theory space. This trajectory connects an infinitely heavy theory in the UV, where the effective action is reduced to the classical one, with the strongly interacting massless limit $k = 0$, where the phase transition happens. In particular, our setup avoids flows through the phase transition, which are present in momentum cutoff flows. Furthermore, the implementation of a flowing renormalisation condition eliminates the need of fine-tuned initial conditions and allows for monotonous mass-flows.

The explicit results, see Section 4.2.5, are in impressive agreement with those obtained in [1] within the spectral DSE, see Section 4.1. This strengthens our confidence in spectral functional approaches to obtain reliable and fully non-perturbative realtime correlation functions.

An appealing feature of the fRG approach is that it captures average momentum dependencies of vertices. This allows to include non-trivial vertex dynamics without resorting to full spectral representations of higher correlation functions. The current spectral fRG approach is straightforwardly and easily extended to include the flow of the full effective potential, and is a pivotal step to unravel realtime correlations in QCD from first principles with spectral functional approaches.

5. Fundamental realtime correlation functions

In this chapter, we put the spectral functional approach introduced in Chapter 4 to use. We present numerical results for all fundamental QCD propagators, i.e., ghost, gluon and quark, in Minkowski space.

In Section 5.1, basing on [5], we discuss the complex structure of the coupled system of ghost and gluon propagator DSEs in Yang-Mills theory. To that end, we first analytically demonstrate how complex singularities propagate through the system by iteration in a simple truncation, posing tight consistency constraints on the analytic structure of potential solutions. The numerical solution of the system was plagued by the appearance of exactly such complex singularities. In consequence, the calculation of a gluon spectral function was not possible. A scenario fulfilling analytic consistency constraints is the one where both, the gluon and ghost propagator, obey a Källén-Lehmann representation. Under this assumption, in Section 5.2 we present results for the ghost spectral function, which are based on [2]. These are obtained using the spectral ghost DSE while resorting to spectral reconstruction results in Yang-Mills theory from [243] for the gluon spectral function.

While Yang-Mills theory offers a plethora of interesting phenomena itself, we are eventually interested in QCD correlation functions. In Section 5.3, building on [3], we move away for a bit from the direct calculation of Minkowski space correlators via functional approaches and turn towards spectral reconstruction of Euclidean high-precision correlator data from lattice QCD. We demonstrate how functional realtime results such as the ghost spectral function in Yang-Mills [2], see Section 5.2, can be used as prior information supporting the spectral reconstruction of lattice QCD data. Making use of Gaussian process regression (GPR), a non-parametric Bayesian approach, we reconstruct ghost and gluon spectral functions from 2+1 flavour lattice QCD data [100, 101]. These reconstruction results in turn, and in particular that of the gluon spectral function, feature as direct input for the direct calculation of the quark spectral function via the spectral DSE approach we present in Section 5.4, which bases on [7]. There, we also put forward a detailed discussion of sources of complex singularities in the quark propagator, focussing on STI-consistent vertex constructions and gluon propagators with and without complex poles.

5.1. Complex structure of Yang-Mills theory

This section presents results of [5].

In recent years, ghost and gluon spectral functions have been reconstructed from numerical data of Euclidean ghost and gluon propagators, see, e.g., [243, 258–261]. Also direct computations have been put forward, either perturbatively, e.g., [262, 263], with non-perturbative analytically continued DSEs [207, 264], or in a spectral approach [42]. While these direct computations unravel interesting structures, they are still inconclusive.

As a first step towards a full QCD treatment, in this section we use a coupled set of spectral DSEs to compute the ghost and gluon propagators and spectral functions in Yang-Mills theory directly in Minkowski spacetime. Apart from the numerical results, the spectral set-up allows us to unravel much of the intricate spectral structure of the Yang-Mills two-point functions. In summary, the present work serves a two-fold purpose: First, the results presented here constitute an important step towards full self-consistent functional resolution of timelike correlation functions which gives the access to the interesting scattering and resonance physics in QCD mentioned above. Second of all, both the numerical and the analytic results on the complex structure of ghost and gluon propagators provide non-trivial constraints for spectral reconstructions as well as direct computation of timelike propagators in Yang-Mills theory and QCD. Importantly, these constraints can be used to qualitatively improve the systematic error of these computations.

We close the introduction with a bird eyes view on this section: In Section 5.1.1, we briefly review the basics of Yang-Mills theory and the spectral representations of gluon and ghost are discussed. In Section 5.1.2 we set up the coupled Yang-Mills system of gluon and ghost propagator DSEs in a spectral manner. Section 5.1.3 is devoted to a discussion of the complex structure of Yang-Mills theory based on the spectral formulation introduced in Section 5.1.2. In particular, we evaluate the non-spectral scenario of a pair of complex conjugate poles in the gluon propagator. In Section 5.1.5, we present numerical solutions to the coupled DSE system of Yang-Mills. Section 5.1.6 contains a conclusion and a discussion of the consequences of our combined results.

5.1.1. Yang-Mills theory and the spectral representation

We consider functional approaches to $3+1$-dimensional Yang-Mills theory with $N_c = 3$ colors in the Landau gauge, see [58, 59, 61–63, 265] for fRG and [53–56, 132, 135, 136] for DSE reviews. The gauge-fixed classical action was introduced in Section 3.1. We iterate it here for readability,

$$S_{\mathrm{YM}} = \int \mathrm{d}^4x \left[\frac{1}{4} F^a_{\mu\nu} F^a_{\mu\nu} - \bar{c}^a \partial_\mu D^{ab}_\mu c^b + \frac{1}{2\xi} (\partial_\mu A^a_\mu)^2 \right] . \tag{5.1}$$

Landau gauge is given in the limit $\xi \to 0$.

The functional relations derived from (5.1) are one-loop exact in the fRG approach, and two-loop exact in the DSE approach, since the highest primitively divergent vertex is a four-point function. In both approaches the propagator plays a fundamental role,

$$\langle \phi_i(p) \phi_j(q) \rangle_{\mathrm{c}} = (2\pi)^4 \delta(p+q) \mathcal{T}_{\phi_i \phi_j}(p)\, G_{\phi_i}(p) \,, \tag{5.2}$$

where the subscript $_c$ stands for connected. The fields in (5.2) are $\phi = (A_\mu, c, \bar{c})$, and the tensor $\mathcal{T}_{\phi_i \phi_j}(p)$ carries the Lorenz and gauge group tensor structure. The scalar parts of

the propagators are given by $G_\phi = G_A, G_c$. In the Landau gauge, the gluon propagator is transverse,

$$[\mathcal{T}_{AA}(p)]^{ab}_{\mu\nu} = \delta^{ab}\Pi^{\perp}_{\mu\nu}(p)\,, \tag{5.3}$$

and $\Pi^{\perp}$ denotes the transverse projection operator defined in (3.64). For the computations, we parametrise the scalar part G_A of the gluon propagator as,

$$G_A(p) = \frac{1}{Z_A(p)p^2}\,, \tag{5.4}$$

where the gluon dressing function is given by $1/Z_A(p)$. Note that this convention might differ from other DSE related works and is more similar to fRG related conventions. Similarly, for the ghost we have a simple tensor structure $\mathcal{T}^{ab}_{c\bar{c}} = \delta^{ab}$, and we choose to parametrise the scalar part as

$$G_c(p) = \frac{1}{Z_c(p)p^2}\,, \tag{5.5}$$

with the ghost dressing function $1/Z_c(p)$. We will compute (5.4) and eq. (5.5) for general complex momenta, of course including timelike ones. Extensions of correlation functions to the complex plane are particularly interesting, in view of their relevance for the self-consistent treatment of bound-state problems, see, e.g., [120, 266, 267].

If the KL spectral representation is applicable, a propagator G can be recast in terms of its spectral function ρ, see (4.3).

The spectral function naturally arises as the set of non-analyticities of the propagator in the complex momentum plane. If the KL representation holds, the non-analyticities are restricted to the real momentum axis. Therefore, Equation (4.3) directly implies an inverse relation between the spectral function and the retarded propagator (4.4). Note again that as in Section 4.1 Lorentz symmetry allows us to reduce our considerations to $\vec{p} = 0$ and then use $p_0^2 \to p^2$. Hence, for the remainder of this work, $|\vec{p}|$ will be dropped.

Formally, the ghost propagator is expected to obey the KL-representation [268, 269],

$$G_c(p) = \int_0^\infty \frac{d\lambda}{\pi}\frac{\lambda\,\rho_c(\lambda)}{p^2+\lambda^2}\,, \tag{5.6}$$

if the corresponding propagator is causal. Also, recent reconstructions [260, 261] and calculations [2], see Section 5.2, show no signs of a violation of this property. The ghost spectral function must exhibit a single particle peak at vanishing spectral value, with residue $1/Z_c$. In addition, a continuous scattering tail is expected to show up in the spectral function via the logarithmic branch cut. This leads us to the general form of the ghost spectral function,

$$\rho_c(\omega) = \frac{\pi}{Z_c}\frac{\delta(\omega)}{\omega} + \tilde{\rho}_c(\omega)\,, \tag{5.7}$$

where $\tilde{\rho}_c$ denotes the continuous tail of the spectral function and $\delta(\omega)/\omega$ has to be understood as a limiting process $\delta(\omega - 0^+)/\omega$.

Inserting (5.7) in (5.6) leads us to a spectral representation for the ghost dressing function,

$$\frac{1}{Z_c(p)} = \frac{1}{Z_c^0} + p^2\int\frac{d\lambda}{\pi}\frac{\lambda\,\tilde{\rho}_c(\lambda)}{p^2+\lambda^2}\,. \tag{5.8}$$

In the case where the spectral function can be normalised by solely integrating it over the whole branch cut, the normalisation is given by the value of the inverse dressing function at infinity. A detailed derivation of this is given in [2] and Appendix A.8. Since the inverse ghost dressing tends to zero for large momenta, the ghost spectral function obeys

$$\int \frac{d\lambda}{\pi} \lambda \, \rho_c(\lambda) = 0 \,. \tag{5.9}$$

Equation (5.9) is an analogue of the Oehme-Zimmermann superconvergence property of the gluon [255, 256]. Expressed in terms of the spectral representation of the dressing (5.8), it reads

$$\int \frac{d\lambda}{\pi} \lambda \, \tilde{\rho}_c(\lambda) = -\frac{1}{Z_c^0} \,. \tag{5.10}$$

Equation (5.10) entails that the total spectral weight of the ghost vanishes. For a generic discussion, see [2] resp. Appendix A.8 and [254].

The situation for the gluon is rather similar, as it has a spectral representation under the same conditions as the ghost, i.e., the propagator must be causal. In this case we are led to

$$G_A(p) = \int_0^\infty \frac{d\lambda}{\pi} \frac{\lambda \, \rho_A(\lambda)}{p^2 + \lambda^2} \,, \tag{5.11}$$

which is covered by (4.3). The associated sum rule is

$$\int_0^\infty \frac{d\lambda}{\pi} \lambda \, \rho_A(\lambda) = 0 \,, \tag{5.12}$$

the Oehme-Zimmermann superconvergence relation. In summary, both, ghost and gluon spectral function have a vanishing total spectral weight: (5.10) and (5.12). Note that the validity of the underlying assumptions is subject of an ongoing debate; for results and discussions, see, e.g., [2, 3] resp. Section 5.2 and 5.3 and [104, 195, 207, 243, 258, 260, 263, 264, 270–276].

Independent of this debate, the IR and UV of the gluon spectral function are fixed from analytic considerations, a detailed discussion thereof can be found in [243]. We briefly summarize it here: In both, the IR and UV, the spectral function is negative. In the UV this simply follows from perturbation theory [255, 256]. For the IR, the situation is more intricate. In order to make statements, one requires that the gluon propagator is analytic in the finite, open semicircle in the upper half plane around the origin. This includes the Euclidean domain, and, e.g., (5.11) meets this criterium. With this at hand, it can be shown that the gluon spectral function is negative in the IR, owing to the contribution of the ghost loop. More details of the derivation and explicit analytic forms can be found in [243].

5.1.2. Spectral DSEs of Yang-Mills theory

In this section, we set up the spectral Yang-Mills system in order to compute the gluon and ghost spectral function ρ_A and ρ_c.

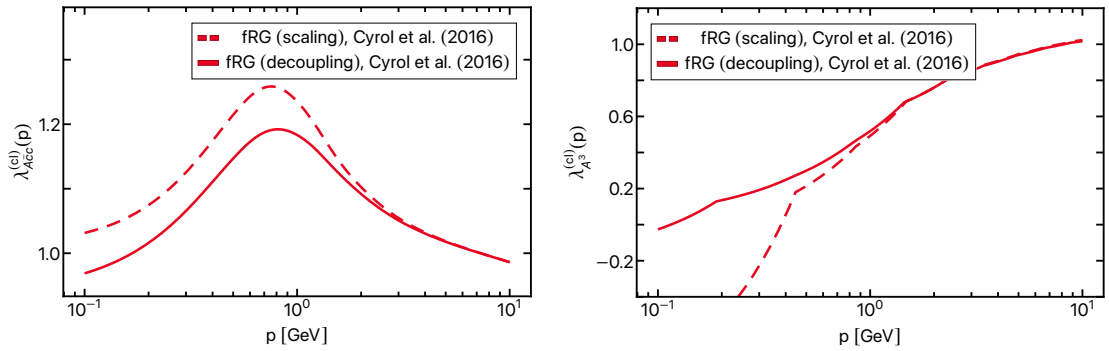

Abbildung 5.1.: Ghost-gluon vertex dressing $\lambda^{(\mathrm{cl})}_{Ac\bar{c}}(p,q)$ (left) and three-gluon vertex dressing $\lambda^{(\mathrm{cl})}_{A^3}(p,q)$ (right), see (5.13) resp. (5.16). The data is taken from [243]. The dressing functions are shown at the symmetric point $p^2 = q^2 = (p+q)^2$ for scaling and lattice-type decoupling solution, more details can be found in [243].

5.1.2.1. Vertex approximation

The full ghost-gluon vertex consists of two tensor structures, see e.g. [94, 95, 182],

$$[\Gamma_{A\bar{c}c}]^{abc}_{\mu}(p,q) = \mathrm{i} f^{abc}[q_\mu \lambda^{(\mathrm{cl})}_{A\bar{c}c}(p,q) + p_\mu \lambda^{(\mathrm{nc})}_{A\bar{c}c}(p,q)]\,, \tag{5.13}$$

and the momentum arguments p_i in our vertices $\Gamma_{\phi_1\cdots\phi_n}(p_1,...,p_{n-1})$ always indicate the incoming momentum of the field ϕ_i. In (5.13) we have the incoming gluon momentum p and anti-ghost momentum q, and we have dropped the momentum conserving δ-function.

The ghost-gluon vertex is subject to Taylor's non-renormalisation theorem, and does not require renormalisation in the Landau gauge. Within our MOM-type scheme, the dressing functions are set to unity at the renormalisation point μ_{RG}, i.e., $Z_A(\mu_{\mathrm{RG}}) = Z_c(\mu_{\mathrm{RG}}) = 1$. Accordingly, the classical ghost-gluon dressing reduces to the strong coupling g_s at the renormalisation point, which typically is chosen to be the symmetric point, $p^2 = q^2 = (p+q)^2$, or the soft gluon limit, $p \to 0, q^2 = \mu^2$. In short,

$$\lambda^{(\mathrm{cl})}_{A\bar{c}c}(p,q)\big|_{\mu_{\mathrm{RG}}} = g_s\,. \tag{5.14}$$

We emphasize that (5.14) is not an RG condition, it is a consequence of the non-renormalisation of the ghost-gluon vertex. Moreover, the non-classical dressing in (5.13) is proportional to the gluon momentum and hence drops out of the ghost DSE due to the transversality of the Landau gauge gluon propagator.

The lack of a logarithmic RG running also leads to a very mild momentum dependence of the vertex, see e.g. [93, 95, 99, 182, 277–282]. In the left panel of Figure 5.1, the ghost-gluon vertex data from [95] is depicted at the symmetric point $p^2 = q^2 = (p+q)^2$ for both, the scaling solution and a lattice-type decoupling solution. For further explanations, we refer to the detailed discussion of [94, 95].

In the present work we neglect the mild momentum dependence and identify the vertex dressing $\lambda^{(\mathrm{cl})}_{A\bar{c}c}$ with its value at the renormalisation point, (5.13), to wit,

$$\lambda^{(\mathrm{cl})}_{A\bar{c}c}(p,q) \approx g_s\,, \tag{5.15}$$

which should only introduce a small systematic error for our Euclidean results.

The three-gluon vertex can be parametrised by ten longitudinal and four transverse tensor structures. In the Landau gauge, only the transverse ones contribute, the dominant being the classical tensor structure [283]. Neglecting the subleading tensor structures, the three-gluon vertex can be written as

$$[\Gamma^{(3)}_{A^3}]^{abc}_{\mu\nu\rho}(p,q) = \mathrm{i} f^{abc} \lambda^{(\mathrm{cl})}_{A^3}(p,q)\, [\mathcal{T}^{(\mathrm{cl})}_{A^3}]_{\mu\nu\rho}(p,q)\,, \tag{5.16}$$

with the classical Lorentz structure $\mathcal{T}^{(\mathrm{cl})}_{A^3}$ defined as

$$[\mathcal{T}^{(\mathrm{cl})}_{A^3}]_{\mu\nu\rho}(p,q) = (p-q)_\nu \delta_{\mu\rho} + (2q+p)_\mu \delta_{\nu\rho} - (2p+q)_\rho \delta_{\mu\nu}\,. \tag{5.17}$$

At the symmetric momentum configuration, the dressing function $\lambda^{(\mathrm{cl})}_{A^3}$ gets negative in the deep IR region and rising for increasing momenta [93, 95, 204, 284] due to its anomalous dimension, see right panel of Figure 5.1. Since the ghost loop is known to dominate the gluon gap equation in the IR, we approximate the dressing function by its counterpart at the renormalisation point, as already done for the ghost-gluon vertex, (5.15),

$$\lambda^{(\mathrm{cl})}_{A^3}(p,q) \approx g_s\,, \tag{5.18}$$

with g_s being the strong running coupling $g_s(p)$ at the renormalisation scale $p^2 = \mu^2$. This yields a considerable technical simplification, since the realtime nature of the spectral approach requires all momentum integrals to be solved analytically, as discussed in detail in [2], see Section 5.2. However, in contradistinction to the approximation in the ghost-gluon vertex this introduces a sizeable systematic error due to the sizeable momentum dependence shown in the right panel of Figure 5.1. Accordingly, we expect our results to be of qualitative nature, and the systematic error can be evaluated by comparing the results to those obtained in quantitatively reliable approximations within functional approaches, e.g. [93, 95] and on the lattice, see e.g. [102, 125, 128].

We emphasize that our approach is by no means restricted to classical vertices: quantum corrections may be duly accounted for, as long as the momentum loops involved can be integrated analytically. Especially, upon construction of spectral representations for higher n-point-functions, see e.g., [285–297], fully dressed vertices of general form can be included. In the present work, we restrict ourselves to classical ones, as this allows us to study the emergence and interrelations of poles and generic complex structures of the propagators themselves.

5.1.2.2. Spectral DSEs

In the Landau gauge, functional relations of transverse correlation functions are closed: they do not depend on the longitudinal sector due to the transversality of the gluon propagator, see [63, 95, 107]. For the present coupled set of propagator DSEs this entails that the gluon two-point function, $\Gamma^{(2),\parallel}_{AA}$, does not enter in the system: neither the loop in the ghost DSE nor those in the gluon DSE depend on it. The ghost and gluon gap equations can be reduced to DSEs of the respective scalar parts, and we use the parametrisation,

$$[\Gamma^{(2),\perp}_{AA}]^{ab}_{\mu\nu}(p) = \Pi^{\perp}_{\mu\nu}(p) \delta^{ab} Z_A(p) p^2\,, \tag{5.19a}$$

$$[\Gamma^{(2)}_{c\bar{c}}]^{ab}(p) = \delta^{ab} Z_c(p) p^2\,. \tag{5.19b}$$

The dressings $Z_\phi(p)$ in (5.19) can be conveniently written in terms of the respective self energies, to wit,

$$Z_A(p)p^2 = Z_3 p^2 - \Sigma_{AA}(p)\,, \tag{5.20a}$$

$$Z_c(p)p^2 = \tilde{Z}_3 p^2 - \Sigma_{\bar{c}c}(p)\,, \tag{5.20b}$$

with the renormalisation constants Z_3 and $\tilde{Z}_3$ associated with the gluon and ghost fields. They contain the counter terms, that lead to finite loops as well as adjusting the renormalisation conditions in their respective DSEs.

Similarly, the classical ghost-gluon and three-gluon vertices in Figure 5.2 contain respective renormalisation constants Z_1 and $\tilde{Z}_1$, i.e.

$$S^{\mu}_{Ac\bar{c}}(p,q) = -\tilde{Z}_1 \mathrm{i} g_s f^{abc} p^\mu\,, \tag{5.21a}$$

$$S^{\mu\nu\rho}_{A^3}(p,q) = Z_1 \mathrm{i} g_s f^{abc} [\mathcal{T}^{(\mathrm{cl})}_{A^3}]^{\mu\nu\rho}(p,q)\,, \tag{5.21b}$$

As for the propagators, they contain the counterterms leading to finite loops and adjusting the renormalisation conditions in their respective DSEs. However, the ghost-gluon vertex does not require renormalisation in the Landau gauge, and we do not consider vertex DSEs. Accordingly, their consistent choice is $Z_1 = \tilde{Z}_1 = 1$, which is implemented later. For the time being, we keep the renormalisation constants as they elucidate the systematics of the spectral renormalisation applied in Section 5.1.2.3.

The gluon and ghost self-energies Σ_{AA} and $\Sigma_{\bar{c}c}$ in (5.20) contain all quantum corrections of the two-point functions, and are determined via their respective propagator DSEs. While the ghost DSE is one loop closed, the gluon DSE is two-loop closed, and we have dropped the two-loop diagrams. The corresponding system of DSEs for gluon and ghost two-point functions in (5.19) is depicted in Figure 5.2, with the notation as defined in Figure 2.1. The self-energies are then just given by the sum of all loop diagrams. We recast the gluon self-energy defined in (5.20) in terms of its two contributing one-loop diagrams as

$$\Sigma_{AA}(p) = \frac{1}{2}\Big(\mathcal{D}_{\mathrm{gluon}}(p) - \mathcal{D}_{\mathrm{ghost}}(p)\Big)\,, \tag{5.22}$$

where $\mathcal{D}_{\mathrm{gluon}}$ represents the gluon and $\mathcal{D}_{\mathrm{ghost}}$ the ghost loop. With the classical vertex approximation discussed in Section 5.1.2.1, we arrive at

$$\begin{aligned}\mathcal{D}_{\mathrm{gluon}} = g^2 C_A Z_1 \Pi^{\perp}_{\mu\nu}(p) \int_q & G_A(p+q)\Pi^{\perp}_{\gamma\delta}(p+q) G_A(q) \Pi^{\perp}_{\alpha\beta}(q) [\mathcal{T}_{A^3}]_{\mu\alpha\gamma}(p,q) \\ & \times [\mathcal{T}_{A^3}]_{\delta\beta\nu}(-q,-p)\,,\end{aligned} \tag{5.23a}$$

$$\mathcal{D}_{\mathrm{ghost}} = g^2 C_A \tilde{Z}_1 \Pi^{\perp}_{\mu\nu}(p) \int_q G_c(p) G_c(p+q) q_\nu (p+q)_\mu\,. \tag{5.23b}$$

Here, $C_A = N_c$ is the second Casimir for $\mathrm{SU}(N_c)$ in the adjoint representation.

The ghost-self energy (5.20) reads,

$$\Sigma_{\bar{c}c}(p) = g^2 C_A \tilde{Z}_1 \int_q (p^2 - \frac{(p\cdot q)^2}{q^2})\, G_A(q) G_c(p+q)\,. \tag{5.24}$$

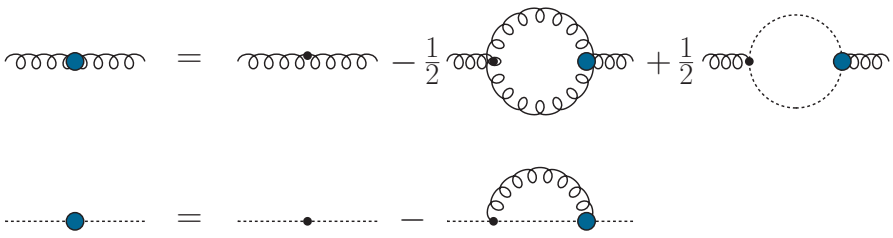

Abbildung 5.2.: Diagrammatic representation of the Dyson-Schwinger equations for of the inverse gluon (top) and ghost (bottom) propagator. Wiggly lines represent gluon and dashed lines ghost fields. Notation as defined in Figure 2.1.

Now we recast the diagrams in (5.22) and (5.24) in their spectral form, using the respective KL representation (5.11) and (5.6) for gluon and ghost propagator and contracting the Lorentz structure in (5.23) and (5.24). This leads us to

$$\mathcal{D}_{\text{gluon}} = g^2 N_c Z_1 \int_{\lambda_1,\lambda_2} \rho_A(\lambda_1)\rho_A(\lambda_2) \int_q V(p,q) \frac{1}{q^2+\lambda_1^2} \frac{1}{(p+q)^2+\lambda_2^2}\,, \tag{5.25a}$$

with

$$V(p,q) = \Pi^{\perp}_{\mu\nu}(p)\Pi^{\perp}_{\gamma\delta}(p+q)\Pi^{\perp}_{\alpha\beta}(q)[\mathcal{T}_{A^3}]_{\mu\alpha\gamma}(p,q)[\mathcal{T}_{A^3}]_{\delta\beta\nu}(-q,-p)\,, \tag{5.25b}$$

for the gluonic diagram in the gluon DSE. The function V defined in (5.25b) captures all momentum dependencies arising from contracting the Lorentz structure of vertices and projection operators in (5.23).

The ghost diagram is given by

$$\mathcal{D}_{\text{ghost}} = g^2 N_c \tilde{Z}_1 \int_{\lambda_1,\lambda_2} \rho_c(\lambda_1)\rho_c(\lambda_2) \int_q \left(q^2 - \frac{(p\cdot q)^2}{p^2}\right) \frac{1}{q^2+\lambda_1^2} \frac{1}{(p+q)^2+\lambda_2^2}\,, \tag{5.25c}$$

Finally, the spectral representation of the ghost DSE reads,

$$\Sigma_{\bar{c}c}(p) = g^2 N_c \tilde{Z}_1 \int_{\lambda_1,\lambda_2} \rho_A(\lambda_1)\rho_c(\lambda_2) \int_q \left(p^2 - \frac{(p\cdot q)^2}{q^2}\right) \frac{1}{q^2+\lambda_1^2} \frac{1}{(p+q)^2+\lambda_2^2}\,, \tag{5.25d}$$

with ρ_A and ρ_c the gluon and ghost spectral functions, respectively, and $\int_\lambda := \int_0^\infty \mathrm{d}\lambda\, \lambda/\pi$. The momentum integrals are regularised with dimensional regularisation. Importantly, this makes both, the momentum and spectral integrations, finite, and allows us to interchange the order of spectral and momentum integration, as done in (5.25).

5.1.2.3. Spectral renormalisation

The momentum integrals in (5.25) involve two classical propagators with spectral masses λ_1 and λ_2 These are readily computed in $d = 4 - 2\epsilon$ dimensions; for the computational details and the final expressions see Appendix B.5. This leaves us with two spectral integrals.

Naively one could try to resort to a momentum space subtraction scheme by simply dropping the $1/\epsilon$-term arising from the momentum integration. However, the spectral integrals suffer from the same superficial degree of divergence as their respective momentum

integral, and this naive implementation of a MOM scheme does not work. This is a generic feature in the spectral DSE, for a thorough discussion, see [1] resp. Section 4.1. There we have set up two spectral renormalisation schemes: *spectral dimensional renormalisation* and *spectral BPHZ-renormalisation*, both exploiting the advantageous properties of dimensional regularisation of the momentum loop, but treating the spectral divergences differently.

Spectral dimensional renormalisation also treats the spectral integrals in dimensional regularisation, hence manifestly respecting all internal symmetries of the theory, including gauge theory. This property entails that the gluon gap equation in Yang-Mills theory has no quadratic divergence in spectral dimension renormalisation, and only logarithmic divergences related to the gluon wave function renormalisation are present.

In turn, in spectral BPHZ renormalisation quadratic divergences are present, which is a well-known property of the BPHZ scheme in gauge theories and originates in it being a momentum cutoff scheme. For a detailed discussion see [58, 95, 96, 166] where also the direct link to Wilsonian cutoffs in the fRG approach and the ensuing modified Slavnov-Taylor identities (STIs) is discussed. In short, momentum cutoff schemes such as BPHZ-type schemes necessitate a gluon mass counterterm, which is adjusted such that the STIs are satisfied. Accordingly, the occurrence of mass counterterms in Yang-Mills theory in a BPHZ-type scheme is a property of the scheme and *restores* gauge consistency and does not (necessarily) signal its breaking.

In the present spectral BPHZ set-up, the spectral divergences are cured by introducing counterterms, including a gluon mass counterterm, through the renormalisation constants in (5.20) and taking $\epsilon \to 0$ before computing the spectral integrals. Then, gauge invariance is restored by adjusting the finite part of this counterterm such that the STIs are satisfied on the level of the renormalised correlation function. For discussions about the treatment of quadratic divergences in functional approaches to Yang-Mills theory, see e.g. [93–95, 298].

In summary, this amounts to a modification of the gluon DSE in (5.20) according to

$$Z_A(p)p^2 = Z_3 p^2 + \tilde{m}_A^2 - \Sigma_{AA}(p)\,, \tag{5.26}$$

where the mass counterterm $\tilde{m}_A^2$ is chosen such that the quadratic divergence in Σ_{AA} is cancelled. This already effectively absorbs the tadpole in the gluon DSE into the mass counterterm.

The ghost self-energy $\Sigma_{\bar{c}c}$ only carries a logarithmic divergence proportional to p^2, which can be subtracted by a proper choice of $\tilde{Z}_3$. Within spectral BPHZ renormalisation, the counterterms are chosen to be proportional to the respective self-energies Σ, evaluated at some RG scale μ_{RG}. We use standard renormalisation condition for the (inverse) dressing functions,

$$Z_A(\mu_{\mathrm{RG}}) = 1 + \frac{m_A^2}{\mu_{\mathrm{RG}}^2}\,, \qquad Z_c(\mu_{\mathrm{RG}}) = 1\,. \tag{5.27a}$$

These renormalisation conditions are implemented by the respective choice of the renormalisation constants $Z_3, \tilde{m}_A^2$ and $\tilde{Z}_3$ as

$$Z_3 = 1 + \frac{\Sigma_{AA}(\mu_{\mathrm{RG}})}{\mu_{\mathrm{RG}}^2}\,, \qquad \tilde{m}_A^2 = m_A^2 + \Sigma_{AA}(\mu_{\mathrm{RG}})\,, \qquad \tilde{Z}_3 = 1 + \frac{\Sigma_{\bar{c}c}(\mu_{\mathrm{RG}})}{\mu_{\mathrm{RG}}^2}\,, \tag{5.27b}$$

augmented with $Z_1, \tilde{Z}_1 \to 1$, reflecting the lack of vertex DSEs. For a detailed discussion of self-consistent MOM-type RG conditions for DSEs (MOM in DSEs and MOM^2 in fRG

equations and DSEs), see [171]. Eventually, this leads us to the renormalised system of DSEs for the gluon and ghost dressing functions,

$$Z_A(p)p^2 = p^2 + m_A^2 - \Big[\Sigma_{AA}(p) - \Sigma_{AA}(\mu_{\mathrm{RG}})\Big(1 + \frac{p^2 - \mu_{\mathrm{RG}}^2}{\mu_{\mathrm{RG}}^2}\Big)\Big]\,, \tag{5.28a}$$

$$Z_c(p)p^2 = p^2 - \Big[\Sigma_{\bar{c}c}(p) - \frac{p^2}{\mu_{\mathrm{RG}}^2}\Sigma_{\bar{c}c}(\mu_{\mathrm{RG}})\Big]\,. \tag{5.28b}$$

In perturbative applications the mass parameter m_A^2 is chosen such that the gluon two point function has no infrared mass, tantamount to $Z_A(p)p^2 \to 0$ for $p \to 0$. This is the requirement of perturbative BRST symmetry, implying the equivalence of the transverse mass and the longitudinal one, and the latter vanishes due to the STI. In (5.28) this amounts to

$$m_A^2 = \Sigma_{AA}(0)\,, \tag{5.29}$$

which reinstates perturbative gauge consistency with a massless gluon within the BPHZ-scheme.

In the IR, m_A^2 is linked to the dynamical emergence of the gluon mass gap in QCD, see also the discussion in Section 3.1.5 and Section 3.2. The explicit choice of m_A^2 will be discussed in Section 5.1.5.

5.1.2.4. Evaluation at real frequencies

Apart from the integration over real spectral parameters λ, the renormalised DSEs in (5.28) can be evaluated *analytically* for general complex frequencies. For the extraction of the spectral functions with (4.4) we choose $p_0 = -\mathrm{i}(\omega + \mathrm{i}0^+)$. This leads us to the Minkowski variant of (5.28),

$$Z_A(\omega)\omega^2 = \omega^2 - m_A^2 + \Big[\Sigma_{AA}(\omega) - \Sigma_{AA}(\mu_{\mathrm{RG}})\Big(1 - \frac{\omega^2 + \mu_{\mathrm{RG}}^2}{\mu_{\mathrm{RG}}^2}\Big)\Big]\,, \tag{5.30a}$$

$$Z_c(p)\omega^2 = \omega^2 + \Big[\Sigma_{\bar{c}c}(\omega) + \frac{\omega^2}{\mu_{\mathrm{RG}}^2}\Sigma_{\bar{c}c}(\mu_{\mathrm{RG}})\Big]\,, \tag{5.30b}$$

where, in a slight abuse of notation, we define $\Sigma(\omega) = \Sigma(-\mathrm{i}\omega_+)$, where ω_+ denotes the retarded limit (4.5).

The explicit spectral integral expressions for the self-energies and their renormalised counterparts can be found in Appendix B.5. The remaining finite spectral integrals have to be computed numerically, and the spectral functions $\rho_{c,A}(\omega)$ are given with (4.4) as

$$\rho_A(\omega) = -\frac{2}{\omega^2}\,\mathrm{Im}\Big[\frac{1}{Z_A(\omega)}\Big]\,, \tag{5.31}$$

for the gluon spectral function and

$$\rho_c(\omega) = \frac{\pi}{Z_c}\delta(\omega^2) - \frac{2}{\omega^2}\,\mathrm{Im}\Big[\frac{1}{Z_c(\omega)}\Big]\,, \tag{5.32}$$

for the ghost spectral function. Note that in (5.31) and (5.32), the retarded limit (4.5) has already been carried out, resulting in the delta distribution in (5.32).

The combination of (5.30), (5.31), (5.32) allows us to compute both gluon and ghost spectral functions ρ_A and ρ_c as well as the respective propagators for complex frequencies, and in particular for spacelike (Euclidean) and timelike frequencies.

5.1.2.5. Iterative procedure

The spectral DSEs for ghost and gluon propagator (5.30) are solved using an iteration procedure, discussed in detail in [1], see Section 4.1, and briefly reviewed below:

Assuming spectral representations for ghost and gluon propagator, the gluon spectral function $\rho_A^{(i)}$, obtained after the i-th iteration step with input $\rho_c^{(i)}$, is inserted together with $\rho_c^{(i)}$ into the spectral integral form of $\Sigma_{\bar{c}c}(p)$, on the right-hand side of (5.30b). Then, by means of (5.32), we arrive at the $(i+1)$-th ghost spectral function, $\rho_c^{(i+1)}$. In turn, $\rho_c^{(i+1)}$ is then inserted together with $\rho_A^{(i)}$ into the spectral integral form of $\Sigma_{AA}(p)$, on the right-hand side of (5.30a). With (5.31), we then obtain $\rho_A^{(i+1)}$. This iteration is repeated until simultaneous convergence for both spectral functions has been reached. The iteration commences with initial choices for ρ_A and ρ_c. Along with convergence properties, these choices are discussed in Appendix C.3.

Attempts to solve the system for ρ_A and ρ_c via a Newton's optimization scheme in a purely spectral manner showed worse convergence properties than the iterative approach. For this reason, the optimization approach was not pursued further.

5.1.3. Complex structure of Yang-Mills theory with complex conjugate poles

In this section, we analytically show that a gluon propagator with a simple pair of complex conjugate poles cannot be part of a consistent solution of the coupled DSE system for Yang-Mills propagators in the Landau gauge with bare vertices set up in Section 5.1.2. This is pursued in Appendix A.6.1 and Appendix A.6.2. Before we come to this discussion, we provide a brief overview of results on spectral representations and discuss the manifestation of single pairs of complex conjugate poles in Section 5.1.3.1. This is followed by a discussion of the generic impact of singularities in coupled sets of functional equations as well as the requirements for conclusive studies in Section 5.1.4.

5.1.3.1. Complex structure of Yang Mills propagators

The complex structure of the Yang-Mills propagator, and specifically the gluon propagator, is the subject of an ongoing debate. Axiomatic formulations of local QFTs forbid the existence of any further non-analytic structures beyond the real frequency axis for propagators of asymptotic states. It has been argued that this also applies to gauge theories, and in particular the case of the gluon propagator [271, 273, 299]. Scenarios such as complex conjugate poles are nevertheless used in reconstructions of the timelike structure of the gluon propagator, see e.g. [104, 195, 260, 263, 264, 270, 272, 274–276]. However, precision reconstruction of Yang-Mills propagators in a purely spectral manner and without complex conjugate poles has successfully been performed in [3], see Section 5.3 and [243, 258, 300].

In Appendix A.6.1 and Appendix A.6.2 we investigate the consequences of a single pair of complex conjugate poles in the gluon propagator on the complex structure of Yang-Mills theory *fully analytically*. While being not fully general, this scenario represents the simplest and so far only considered case of violation of the spectral representation, both in reconstructions and analytic considerations.

The spectral formulation employed in Section 5.1.2 enables us to study the general complex structure of ghost and gluon DSE, as it covers a large class of functions for the propagators and is by no means restricted to propagators satisfying the KL representation (4.3). In particular, a gluon propagator with a pair of complex conjugate poles is

realised by collapsing the (gluonic) spectral integrals at complex spectral values corresponding to complex conjugate pole positions, multiplied by the respective residues. Within the iterative approach to solving DSEs described in Section 5.1.2.5, we are able to track the propagation of these non-analyticities through the iterations of ghost and gluon DSE. This is done in an expansion about the fully analytic spectral parts of all the diagrams. In other words, we only consider the contributions arising from adding the holomorphicity violating complex conjugate pole part of the gluon propagator.

Explicitly, for both, ghost and gluon, propagators we will employ the parametrisation

$$G = G^{\mathrm{KL}} + G^{\chi} \,. \tag{5.33}$$

The non-spectral part G^{χ} encodes the respective violation of the KL representation, either directly given by the complex conjugate poles as for the gluon, or for the ghost induced by the complex conjugate poles. The spectral contribution G^{KL} is given by the KL representation (4.3) of the respective propagator. With the spectral-non-spectral split (5.33), the contributions to the single diagrams can be ordered in powers of non-spectral contributions G^{χ} entering. We only consider one-loop diagrams with two propagators in the spectral DSE setup of Section 5.1.2. Hence, the contributions coming from the additional non-analyticities that we will consider here are given by $G^{\mathrm{KL}}G^{\chi}$, $(G^{\chi})^2$. The ordinary spectral part is constituted by $(G^{\mathrm{KL}})^2$.

5.1.4. Propagation of non-analyticities

The systems of DSEs are integral equations, typically solved within an iterative procedure. In such an iteration, non-analyticities off the real frequency axis propagate through the system by the iteration. Here, we use this mechanism to study if complex poles allow for an analytically consistent solution to Yang-Mills theory. Our main results can be summarised as follows:

In Yang-Mills theory with bare vertices, a pair of complex poles in the gluon propagator

1. *violates the Källén-Lehmann representation of the ghost and*
2. *cannot be part of an analytically consistent solution of Yang-Mills theory without additional branch cuts in the complex plane.*

These results are obtained by the following analysis: We assume a gluon propagator with only a single pair of complex poles. Via the ghost self-energy diagram, these poles induce additional branch cuts off the real frequency axis in the ghost propagator. Hence, the spectral representation of the ghost propagator is violated. The additional cuts in the ghost propagator can be represented via a modified spectral representation. We use this representation to study the back-propagation of these additional cuts into the gluon propagator via the ghost loop of the gluon DSE. There, we observe that the cuts likewise induce branch cuts off the real frequency axis in the gluon propagator. This is at odds with the initial assumption of a single pair of complex conjugate poles. A consistent solution in the above scenario, involving a single pair of complex conjugate poles as well as bare vertices, is hence ruled out: an analytically consistent solution at least needs to be accompanied by the respective pair of branch cuts. The explicit calculation is carried out in Appendix A.6.

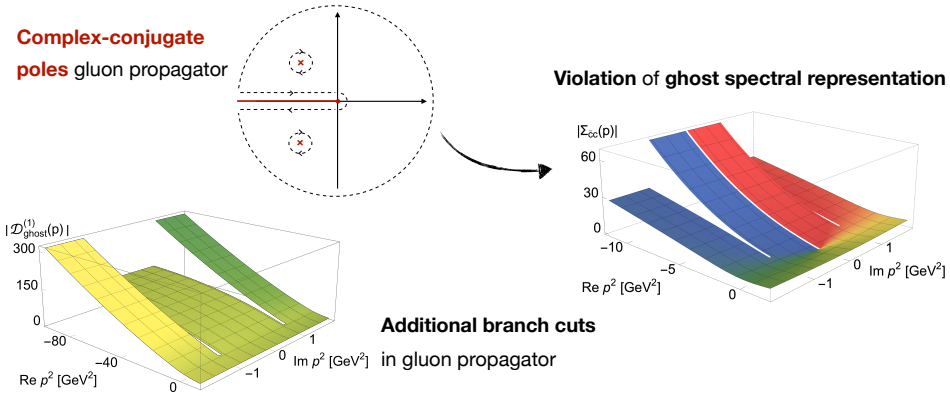

Abbildung 5.3.: Propagation of non-analyticities in the coupled Yang-Mills system with bare vertices. The displayed calculation is *fully analytic*. Complex poles in the gluon propagator cause additional branch cuts off the real axis in the ghost propagator, as shown in the plot on the right (see Figure A.2 for full size). Hence, the Källén-Lehmann representation of the ghost is violated. These additional branch cuts generate corresponding additional branch cuts also in the gluon propagator via the ghost loop, demonstrated in the bottom left figure (see Figure A.4 for full size). This violates the initial assumption of just a single pair of complex poles in the gluon propagator. In consequence, a single pair of complex poles cannot feature alone in consistent solutions in our truncation. The explicit analytic computation is presented in Appendix A.6.

We visualise the propagation of non-analyticities in the system in Figure 5.3. Note also that the performed analysis is independent of possibly different infrared scenarios such as scaling, decoupling or massive solutions.

If the non-trivial vertices do not annihilate the additional complex singular structures, this mechanism readily carries over to the full Yang-Mills system. The former annihilation either requires a respective ghost-gluon vertex that counteracts the loss of the spectral representation of the ghost, or combinations of diagrams and vertices in the gluon gap equation prohibiting the back-propagation of the additional branch cuts of the ghost.

While a full analysis goes far beyond the scope of the present work, we briefly evaluate the above-mentioned simplest possibility: a non-trivial complex structure in the classical dressing of the ghost-gluon vertex that counteract the effects of complex conjugate poles in the gluon propagator in the ghost DSE. This is seemingly reminiscent of the cancellation of complex poles in the electron propagator in QED: There one can solve the electron gap equation under the assumption, that the photon enjoys a spectral representation. Then, the solution of the electron gap equation with bare electron-photon vertices leads to complex conjugate poles for the electron. These artefacts disappear if dressed vertices are used, that satisfy the Ward-Takahashi identity. The latter vertex dressings are proportional to differences of the wave functions of the electrons, balancing the (inverse) wave function in the propagator.

This mechanism in the electron gap equation in QED does *not* apply to the ghost DSE in QCD. First, the ghost shows additional branch cuts, not complex poles as the

electron propagator in the scenario discussed above. Second, these branch cuts are due to complex poles in the gluon propagator, which was shown in [2], see Section 5.2: Using a spectral gluon propagator and bare vertices, complex poles are absent in the ghost, and the spectral representation is intact. Furthermore, no sign for a loss of the ghost spectral representation has been hinted at in all investigations so far. A cancellation of the complex singularities of the gluon in the ghost gap equation hence needs to involve the ghost-gluon vertex's scattering kernel that is usually left out in the STI construction. We consider such a delicate balance scenario as unlikely, and it has no counterpart in similar or seemingly similar systems in the literature.

Note that this assessment is merely an interpretation of our structural results. We emphasise that a conclusive analysis of the complex structure of the Yang-Mills system requires a fully non-perturbative study, as the dynamical emergence of the gluon mass gap is non-perturbative. It is difficult to envisage such a fully analytical study in the near future, and a numerical study almost by definition has to rely on approximations and hence lack a fully conclusive nature. This is already evident from the present study, as we only can exclude complex conjugate poles in the present approximation.

The above arguments emphasise the difficulty of studies in Yang-Mills theories, so one may first study variants thereof: In the past decade many studies have also exploited massive extensions of Yang-Mills, formulated in terms of the Curci-Ferrari (CF) model with mass terms for ghosts and gluons, or by simply adding a mass term for the gluon after the gauge fixing. Note that in the numerical computations in the present work we follow the latter approach. Both approaches only constitute models for Yang-Mills theory due to the presence of an additional relevant parameter, the gluon mass and the almost certain lack of unitarity. Still, they offer an analytic way for studying part of the full problem, which already has proven useful. In a massive extension of Yang-Mills theory, complex conjugate poles may occur in the gluon propagator at one-loop. This implies that their impact on the ghost propagator may be visible at two-loop in the ghost gap equation. Accordingly, the back-propagation of the ghost propagator's non-analyticities into the gluon DSE at least requires a perturbative three-loop computation. While certainly being challenging, this may be within the technical range of perturbative computations in the CF model, and is very desirable. The back-propagation of the additional cuts poses a major obstruction that only can be circumvented by intricate relations between the complex structures of propagators and that of the vertices, in particular the ghost-gluon vertex. Signs for the latter gathered in perturbation theory at least require a three-loop analysis of the ghost DSE as argued in Section 5.1.4. Such an analysis, while highly desirable, has not been undertaken yet in the literature.

To wrap up, direct or reconstructed solutions with complex conjugate poles and additional cuts should undergo a self-consistency analysis as presented in this section before being considered further. On the constructive side, the present self-consistency considerations of the complex structure can be used to devise self-consistent spectral or generalised spectral representations for correlation functions, either generic ones or restricted to a given approximation at hand.

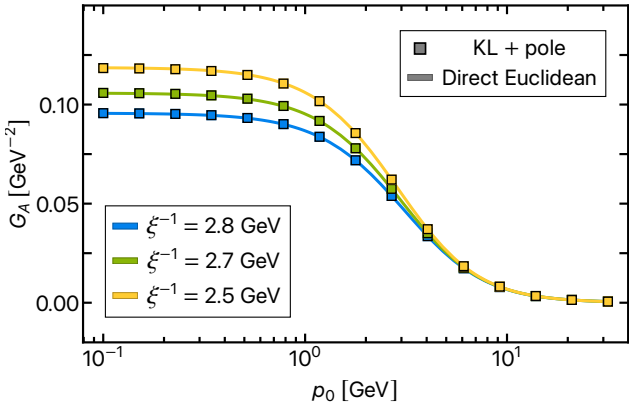

Abbildung 5.4.: Gluon propagator for different values of m_A^2. Solid lines represent the propagators computed directly via the spectral Euclidean DSE (5.28). The squared points are obtained by a sum of the spectral contribution G_A^{KL} and the fit G_A^{approx} of the spectral difference ΔG_A defined in (5.34). G_A^{KL} is computed from the realtime DSE via the spectral representation (5.11), while the fit G_A^{approx} is constituted by a pole on the real frequency axis, see (5.36). All propagators are of decoupling type, as they become constant in the IR. Their asymptotic value increases with decreasing m_A^2. The propagators have been rescaled to lie on top of each other in the perturbative region, cf. Appendix C.3.5.

5.1.5. Numerical results

In this section, we present numerical solutions of the coupled system of spectral ghost and gluon propagator DSEs of Yang-Mills theory set up in Section 5.1.2. These solutions are obtained by iteration, starting with an initial choice for ρ_A and ρ_c. Then, the coupled system of ghost and gluon gap equations is solved self-consistently for a family of input gluon mass parameters m_A^2. The value of the renormalisation scale is set to $\mu_{\mathrm{RG}} = 5$ internal units (i.u.), which is converted to physical units as described in Appendix C.3.5. This yields a slightly different renormalisation scale μ_{RG} for each input parameter m_A^2, which is always around $\mu_{\mathrm{RG}} \approx 10$ GeV. The renormalisation conditions specified in (5.27a) are employed.

5.1.5.1. Spectral violation

A simple and analytically consistent scenario for ghost and gluon propagator involves solely simple branch cuts on the real axis for both, and a massless pole for the ghost. This leaves their KL representation intact, see Section 5.1.2, and allows to solve the system iteratively in a fully spectral manner, cf. Section 5.1.2.5. Our attempts to find such a fully spectral solution were plagued by violations of the gluon spectral representation, however. In particular, we could not find an initial guess for the gluon spectral function which did not violate the KL representation in the gluon DSE (5.20). The violation of the spectral representation can be assessed by subtracting the spectral propagator from the directly computed one, i.e.

$$\Delta G_A(p) = G_A(p) - G_A^{(\mathrm{KL})}(p)\,. \tag{5.34}$$

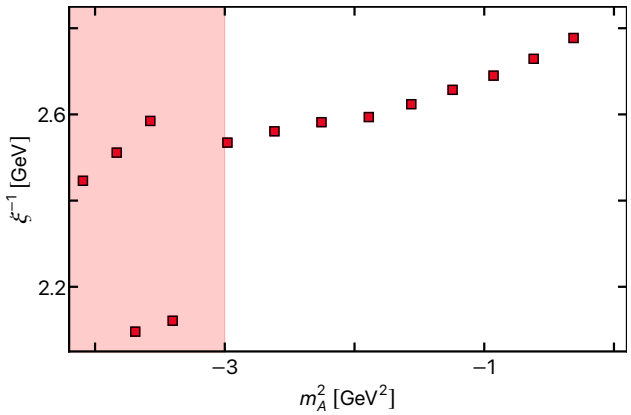

Abbildung 5.5.: Screening lengths of the gluon propagators as defined in (5.37) for the whole family of solution as a function of the input gapping parameter m_A^2. The drastic, non-monotonic change of the screening length to the left of $m_A^2 \approx 3$ GeV^2 hints at numeric instabilities in the solutions. These are most like induced by worsening of the spectral difference approximation (5.36). Therefore, all solutions in the red shaded region will neither be presented nor discussed.

Here, G_A is the propagator obtained directly from the real- and imaginary-time DSEs (5.30) and (5.28), while G_A^{KL} is calculated from the gluon spectral function (5.31) obtained from the spectral DSE (5.30).

If ΔG_A is non-zero, the spectral representation is violated, and we found $\Delta G_A \neq 0$ for all our initial guesses. In consequence, the corresponding gluon propagator must exhibit further complex structures such as (one or more pairs of) complex conjugate poles or further branch cuts in the complex plane, which violate the spectral representation. In fact, in all cases the spectral difference ΔG_A is fit quite well by a single pair of complex conjugate poles, suggesting that the violation is mainly due to a single pair of these poles. It thus seems natural to just include these additional complex poles into our approach. However, this comes along with several problems: First, in order to directly resolve these non-analytic structures and precisely determine their position, one would have to resolve the full complex momentum plane. While in the fully spectral approach, only the Euclidean and Minkowski axis have to be resolved, evaluating the DSEs in the full complex plane would drastically increase the numerical effort. Most importantly though, the analytic solutions of the momentum loop integrals presented in Appendix B.5 are a priori not valid for arbitrary complex momenta p and complex masses λ. This issue is further discussed in Appendix B.5.4.

Last but not least, from the findings of Section 5.1.3 it becomes evident that a self-consistent solution of the coupled YM system with a pair of complex conjugate poles in the gluon propagator and a spectral ghost propagator is not possible with just bare vertices. The complex conjugate pole part of the gluon propagator directly induces two additional branch cuts in the complex plane for the ghost propagator, see Figure A.2. While these can be captured via a modified spectral representation as in (A.26) and shown in Figure A.3, the additional cuts in the ghost propagator in turn induce (at least)

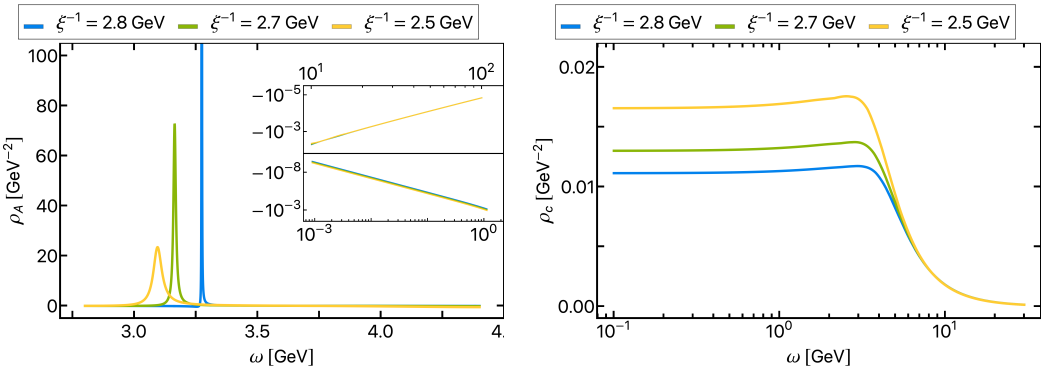

Abbildung 5.6.: Gluon (left) and ghost (right) spectral functions for different inverse screening lengths, corresponding to the values of the input gapping parameter $m_A^2 = -2.98, -1.24$ and $-0.31\,\mathrm{GeV}^2$. For decreasing inverse screening length, the peak amplitudes of the gluon spectral function decreases significantly and a second negative peak at larger frequencies becomes more pronounced. The inset shows that both IR and UV tail of all gluon spectral functions approach the axis from below. As discussed in Section 5.1.1, this property can be derived analytically by demanding a Källén-Lehmann representation for the gluon propagator. Although our gluon propagator minimally violates the spectral representation (comp. Figure 5.7), we still find the negativity of both asymptotic tails to hold. The ghost spectral function ρ_c shown in the right panel varies only in magnitude under variation of m_A^2. All ghost spectral functions coincide w.r.t. to shape. In particular, they show a constant behaviour for $\omega \to 0$, which is a manifestation of the purely logarithmic branch cut of the ghost propagator. For larger frequencies, the ghost spectral functions approach zero.

two further branch cuts in the gluon propagator via the ghost loop, see Figure A.4. In consequence, a pair of complex conjugate poles for the gluon propagator evidently leads to a cascade of additional non-analytic structures for both ghost and gluon propagator. This renders a consistent solution of the full theory including such a pair of poles highly improbable.

Note that complex conjugate poles appear generically at the one-loop level of massive extensions of Yang-Mills. This already suggests that our solutions are in the Higgs-type branch of the theory, where we do not necessarily expect a spectral representation of the gluon propagator. This is supported by the form of the gluon propagator in Figure 5.4, as well as the relation between the screening mass ξ^{-1} and the input mass parameter m_A^2 in Figure 5.5. Ultimately, we are interested in the confining branch of the theory. In order to reach this branch, the system needs to be tuned in this direction via variation of the input parameter m_A^2, for a detailed discussion see c.f. [94, 95].

If the discrepancy ΔG_A in (5.34) is non-zero, the spectral part of the gluon propagator with the spectral function ρ_A as defined in (5.31) does not account for the full gluon propagator G_A any more, as discussed above. In order to still feed back an on both axes well approximated gluon propagator, we also need to feed back the spectral difference ΔG_A. We approach this via a fit. The fit Ansatz for ΔG_A is required to avoid the above described cascade of non-analyticities induced by complex conjugate poles, while approximating the

numerically given spectral difference (5.34) as good as possible. Firstly, we note that ΔG_A is a purely real quantity, as $\mathrm{Im}\, G_A^{\mathrm{KL}} = \mathrm{Im}\, G_A$ due to

$$\begin{aligned}\mathrm{Im}\, G_A^{\mathrm{KL}}(-\mathrm{i}(\omega + \mathrm{i}0^+)) &= \mathrm{Im}\left[\int_\lambda \frac{\rho_A(\lambda)}{-(\omega+\mathrm{i}0^+)^2+\lambda^2}\right] \\ &= \frac{\rho_A(\lambda)}{2} \\ &= \mathrm{Im}\, G_A(-\mathrm{i}(\omega+\mathrm{i}0^+))\,, \end{aligned} \tag{5.35}$$

where in the last line we used the Sokhotski-Plemelj theorem. Note that ΔG_A can generally be only computed at frequencies p where the gluon DSE (5.28) is evaluated. In our case, these are either purely real or imaginary frequencies.

As discussed in Section 5.1.3, the spectral DSEs set up in Section 5.1.2 are able to account for propagators with real or complex poles or Källén-Lehmann-like integral representation, such as the modified spectral representation for the ghost (A.26). Incorporating ΔG_A into our calculation can be achieved by modelling ΔG_A by a pole on the real frequency axis,

$$\Delta G_A(p) \approx G_A^{\mathrm{approx}}(p) = \frac{Z_\chi}{p^2+\chi^2}\,, \tag{5.36}$$

with real $\chi > 0$. We emphasize that the parametrisation (5.36) of the spectral difference by a pole on the real frequency axis solely constitutes a convenient approximation of all non-holomorphicities of the gluon propagator beyond its branch cut on the real frequency axis. In particular, due to the existence of a branch cut on the real frequency axis, if such a pole existed it would directly show up as a singularity in the spectral function. This is not the case, however.

In explicit, adding G_A^{approx} to the Källén-Lehmann part $G_A^{(\mathrm{KL})}$, in (5.28) resp. (5.25) we simply substitute $\rho_A(\lambda) = \rho_A^{(\mathrm{KL})}(\lambda) + Z\,\delta(\lambda^2-\chi^2)/\pi$, where $\rho_A^{(\mathrm{KL})}$ is still given by (5.31).

5.1.5.2. Numerical solutions

Accounting for spectral violations with the procedure described in Section 5.1.5.1, the coupled DSE system of Yang-Mills theory is solved with a strong coupling constant $\alpha_s = 0.2$ for a family of input gapping parameters $m_A^2 \in [-3.69, -0.31]$. For values of m_A^2 beyond this region, we were not able to converge to a solution. The solutions corresponding to the different numerical inputs m_A^2 are labelled by the respective (inverse) screening lengths of the gluon propagators instead, which are related to the gluon mass gap. The temporal screening length ξ is defined through the Fourier transform of the propagator in momentum space $G(p)$, which is

$$\lim_{|x_0-y_0|\to\infty} \int_{-\infty}^{\infty} \frac{\mathrm{d}p_0}{2\pi}\, e^{\mathrm{i}p_0(x_0-y_0)}\, G(p) \sim e^{-|x_0-y_0|/\xi}\,. \tag{5.37}$$

According to (5.37), the screening length ξ governs how fast the propagator decays at large temporal distances. Here, it is readily evaluated by computing the Fourier transforms of

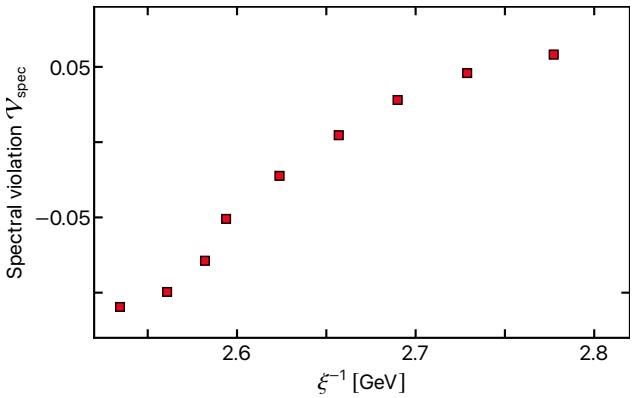

Abbildung 5.7.: Spectral violation of the gluon propagators for the whole family of solutions as a function of the inverse screening length. In the considered interval, the spectral violation exhibits a root at $2.65 < \xi^{-1} < -2.7$ GeV. Hence, the total weight of all non-analyticities flips sign.

the Euclidean propagators and determining ξ via an exponential fit of the large distance behaviour.

The gluon propagators' inverse screening length as a function of the m_A^2 is shown in Figure 5.5, and decreases monotonically with decreasing m_A^2 for all solutions considered here.

Since our self-consistent Yang-Mills system does not have inherent scales, we set the scale by rescaling all solutions to coincide with the fRG Landau gauge Yang-Mills data of [95] in the deep perturbative region; details can be found in Appendix C.3.5.

The resulting gluon spectral functions ρ_A are shown in Figure 5.6 for $m_A^2 = -2.98$, -1.24, $-0.31\,\text{GeV}^2$. For larger m_A^2, the gluon spectral function develops a strong and very sharp positive peak. At the lower end of the family of solutions w.r.t m_A^2, the gluon spectral function develops a slight negative peak at around 4 GeV, while generally the peak amplitudes decreases a lot. The inset in the left panel of Figure 5.6 shows that both IR and UV tail of all gluon spectral functions approach the axis from below. As discussed in Section 5.1.1, this property can be derived analytically by demanding a Källén-Lehmann representation for the gluon propagator. Although our gluon propagator minimally violates the spectral representation (comp. Figure 5.7), we still find the negativity of both asymptotic tails to hold.

However, all gluon propagators presented in Figure 5.4 feature a spectral violation, see Section 5.1.5.1. This means that the spectral functions displayed in the left panel of Figure 5.6 do not make up for the whole propagator. In order to quantify the size of the gluon propagator's fraction constituted by the spectral part G_A^{KL}, we define the spectral violation

$$\mathcal{V}_{\text{spec}} = \frac{1}{\|G_A\|_{\mathcal{L}_1}} \int_0^\infty \mathrm{d}p \left(G_A^{\text{KL}}(p) - G_A(p) \right) . \tag{5.38}$$

Note that only approximately $G_A \approx G_A^{\text{KL}} + G_A^{\text{approx}}$ due to (5.36), which is why we leave the difference $G_A^{\text{KL}} - G_A$ in (5.38) explicit.

The spectral violation (5.38) as a function of the screening length is visualised in Figure 5.7 for all solutions. We find that the (magnitude) of the spectral violation is increasing

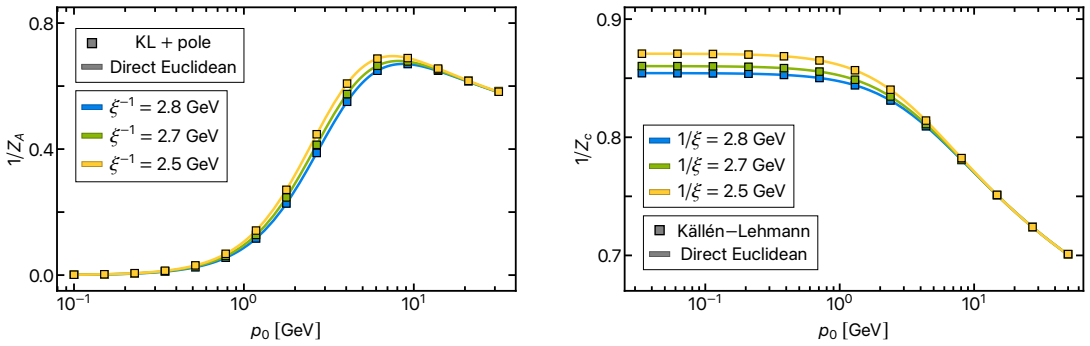

Abbildung 5.8.: Gluon (left) and ghost (right) dressing functions for different values of the input gapping parameter m_A^2. Solid lines represent the dressing functions computed directly via the spectral Euclidean DSE (5.28). In case of the gluon (left), the squared points are obtained by a sum of the dressing corresponding to the spectral contribution G_A^{KL} and the fit G_A^{approx} of the spectral difference ΔG_A defined in (5.34). G_A^{KL} is computed from the real-time DSE via the spectral representation (5.11), while the fit G_A^{approx} is constituted by a pole on the real frequency axis, see (5.36). For the ghost (right), the squared points are given solely by the spectral representation of the dressing. For decreasing m_A^2, the peak position of the gluon dressing function moves towards smaller frequencies. The ghost dressing functions shown in the right panel are of decoupling-type and become constant in the IR. barely vary and change of m_A^2. All dressing functions have been rescaled to lie on top of each other in the perturbative region, cf. Appendix C.3.5.

towards the boundary of the m_A^2-interval for which we are able to solve the system. The fact that convergence worsens for large spectral violation can be attributed to the fact the spectral difference ΔG_A is only approximately taking into account via a pole on the real frequency axis (5.36). The larger the absolute value of the spectral violation $\mathcal{V}_{\mathrm{spec}}$ gets, the larger the approximation error gets. A more in-depth discussion of the quality of the approximation, in particular on the real frequency axis, is deferred to Appendix C.3.1.

Inspecting the shape of the gluon propagators presented in Figure 5.4, we find that the value of the gluon propagator in the origin increases with decreasing m_A^2, which signals the Higgs-type branch of our solutions. In short, none of our solutions is in the confining region, for more details see [94–96, 301]. In consequence, a statement about the complex structure of Yang-Mills in the confining phase within the chosen approximation cannot be made.

The ghost spectral functions of the presented solutions are shown in the right panel of Figure 5.6. Evidently, the change of ρ_c under a variation of m_A^2 is much smaller. All ghost spectral functions coincide with respect to shape. In particular, they show a constant behaviour for $\omega \to 0$, which is a manifestation of the purely logarithmic branch cut of the ghost propagator. For larger frequencies, the ghost spectral functions approach zero. In summary, these results agree qualitatively very well with our previous studies of the ghost spectral function, which have been carried out via the stand-alone spectral ghost DSE in [2], see Section 5.2 and via reconstruction of QCD lattice data with Gaussian process regression in [3], see Section 5.3.

The corresponding gluon and ghost dressing functions are shown in Figure 5.8. For decreasing m_A^2, the peak position of the gluon dressing function moves towards smaller frequencies. In order to assess how well the approximation of the spectral difference (5.34) as a single particle pole (5.36) works, we compare the dressing computed directly via the spectral Euclidean DSE (5.28) against the one given by the sum of the spectral part and the fit of the spectral difference part, $G_A^{\mathrm{KL}} + \Delta G_A$. It can be seen that the dressings match very well, supporting the single pole approximation for the shown Euclidean solutions. In case of the propagators, see Figure 5.4, the comparison is more sensitive to the IR. Also there, single pole approximation works reasonably (on the Euclidean branch). For an in-depth discussion of the approximation on the Minkowski axis, see Appendix C.3.1. The ghost dressing functions accordingly are also all of decoupling-type as they become constant in the IR. For decreasing m_A^2, the IR value of the ghost dressing function increases. Here, the spectral representation is intact.

5.1.6. Conclusion

In this section, we investigated the complex structure of Yang-Mills theory with help of the spectral Dyson-Schwinger equation. Our approach is based on [1] resp. Section 4.1 and utilises the spectral renormalisation scheme devised there. The spectral DSE allows for analytic solution of the momentum loop integrals of all involved diagrams. In consequence, we gain direct analytic access to the complex structure of ghost and gluon propagator.

In Section 5.1.3, we studied the analytic structure of Yang-Mills theory with bare vertices and a gluon propagator with complex conjugate poles. Our findings could hint at the fact that a self-consistent solution of Yang-Mills is not possible with a gluon propagator featuring one or more pairs of complex conjugate poles. As we were able to show analytically, in the case of bare vertices a self-consistent solution with complex conjugate poles and no further branch cuts does not exist. Complex conjugate poles in the gluon propagator directly violate the spectral representation of the ghost propagator by two additional branch cuts off the real axis. This, in turn, introduces additional branch cuts off the real axis in the gluon propagator via the ghost loop. These further cuts contradict the initial assumption of single pair of complex conjugate poles. The study hence shows that by seeding complex singularities in the gluon propagator, a cascade of non-analyticities is induced, which propagate through the system by iteration. Eventually, this observation could disfavour Yang-Mills solutions with complex conjugate poles and no further branch cuts in the complex plane. We emphasize that this analytic result is independent of the different solution 'branches' of Yang-Mills such as scaling, decoupling or massive.

A central aspect of our analytic study of the complex structure of Yang-Mills theory in Section 5.1.3 is, that the existence of complex conjugate poles in the gluon propagator leads to a violation of the spectral representation for the ghost, at least for the case of bare vertices. For this not to carry over to full YM theory, an intricate cancellation of the complex poles in the gluon propagator by the full ghost-gluon vertex is required. In our opinion, this is unlikely to occur in Yang-Mills theory or QCD. In particular, a respective perturbative analysis requires at least three-loop consistency. We remark that no sign of a violation of the spectral representation has been found for the ghost propagator in various works [260, 261, 264, 302]. Therefore, our results emphasize the need for analysing consistency of analytic structure in particular in results with complex conjugate poles for the gluon propagator in QCD like regions.

In Section 5.1.5, we iteratively solve the coupled system of spectral DSEs for the YM

propagators at real and imaginary frequencies. We find decoupling-type solutions for which the Källén-Lehmann representation of the gluon propagator is partially violated, depending on the choice of input gapping parameter. The gluon spectral functions obey the known analytic constraints on the asymptotic behaviour. Solving the system for more QCD-like regions is hindered by increasing violation of the spectral representation, which is accounted for approximatively.

The analytic structure of Yang-Mills theory therefore remains unclear: In Section 5.1.3 we present an analysis implying that for a consistent solution with complex poles in full YM theory, a delicate cancellation in the analytic structure of propagators and vertices would need to happen. As we were able to show, with bare vertices, such a solution without further cuts is even ruled out. On the other hand, in our numerical study in Section 5.1.5 we were not able to solve the system with allowing for violation of the gluon's KL representation. We observed the generic appearance of complex poles for a vast range of initial conditions. Hence, a conclusive statement about the complex structure of Yang-Mills in the confining region based on the present results is not possible. However, the study reported here lays the foundation for such an analysis.

5.2. Ghost

This section presents results of [2].

As we have seen in Section 5.1, the solution of the gluon DSE without the emergence of dynamically generated complex singularities is a highly non-trivial task. Consequently, some properties of the gluon spectral functions, and in particular the potential presence and location of complex conjugate poles, are rather unstable under small variations of the vertices involved; for a detailed recent discussion, see [264].

As we have demonstrated in Section 5.1.3, the complex singularities in the gluon propagator directly violate the spectral representation of the ghost propagator in the employed truncation with classical vertices. Hence, not only the extraction of the gluon, but also of the ghost spectral function is hindered. In this section, we circumvent this problem for the ghost spectral function by considering the standalone ghost DSE, see Figure 5.9, while employing a spectral gluon propagator as input. Apart from the gluon propagator resp. spectral function, the ghost DSE requires little non-trivial input: it additionally only depends on the ghost propagator as well as the ghost-gluon vertex. The latter is protected by non-renormalisation, and hence shows a very mild momentum-dependence. Accordingly, in the present work we approximate this vertex by its classical counterpart, as done in Section 5.1.

This leaves us with a rather stable set-up: the spectral ghost DSE is solved on the basis of given input gluon spectral functions, obtained by appropriately modifying the result of [243], which was reconstructed under the assumption of a KL representation of the gluon. We also test the stability of the result under a variation of the input by tuning the whole family of scaling and decoupling solutions.

This section is organised as follows: In Section 5.1.1 we discuss spectral properties of Yang-Mills theory. In Section 5.2.1, the spectral ghost DSE is set up, and the input gluon spectral function is discussed. We present our results for the ghost propagator and spectral function in Section 5.2.2, and discuss our findings in Section 5.2.3.

5.2.1. The spectral ghost DSE in Yang-Mills theory

We again consider $3+1$-dimensional Yang-Mills theory with three colors, $N_c = 3$, in the Landau gauge, as discussed in Section 5.1.1. The gauge-fixed classical action including the ghost action is given by (5.1). We use the spectral ghost propagator DSE (5.20b) with a classical ghost-gluon vertex see (5.15) set up in Section 5.1.2.2. Renormalisation, evaluation at real frequencies as well as iterative solution are discussed in Section 5.1.2.3, Section 5.1.2.4 and Section 5.1.2.5 respectively. In contrast to Section 5.1, the gluon propagator is treated as an input here. We assume it to obey a spectral representation, see (5.11). The corresponding input gluon spectral function is discussed below. The setup is analogous to the one in Section 5.1, see Section 5.1.2, and we refer to this section or [3] for a detailed discussion.

5.2.1.1. Gluon spectral function

As discussed above, we use the spectral reconstruction result from [243] based on Yang-Mills gluon propagator fRG data from [95] for the gluon spectral function ρ_A. In both scaling and decoupling scenarios, see Section 3.1.5 for a discussion in the context of con-

Abbildung 5.9.: Diagrammatic representation of the Dyson-Schwinger equation for of the inverse ghost propagator. Notation as defined in Figure 2.1.

finement, the infrared behaviour of the gluon spectral function (assuming the validity of the KL representation) can be inferred from the respective infrared scaling of the gluon propagator in (5.4). More details can be found in [243].

For the entire family of solutions, the deep infrared limit with $p \to 0$ is parametrised by [243],

$$\hat{G}_A(p) = Z_A^{(\mathrm{IR})}\, x^{-1+2\kappa}\,, \tag{5.39a}$$

with a constant $Z_A^{(\mathrm{IR})}$. The scaling coefficient κ takes values in the range $1/2 < \kappa < 1$, and

$$x = \hat{p}^{\,2} + \gamma_G \left(\hat{m}^2_{\mathrm{gap}} + \hat{p}^{\,2} \log \hat{p}^{\,2}\right)\,, \tag{5.39b}$$

where the hatted dimensionless quantities in (5.39a) all future expressions have been rescaled with the appropriate powers of Λ_{QCD}, e.g., $\hat{p}^{\,2} = p^2/\Lambda^2_{\mathrm{QCD}}$. For $\gamma_G = 0$, the gluon propagator in (5.39a) reduces to the scaling propagator. A brief account of the scaling solution and its connection to confinement can be found in Section 3.1.5.

The lattice-type propagator is obtained for a $\gamma_G^{(\mathrm{lat})}$ that is close to the maximal one compatible with infrared QCD in the Landau gauge. The parameters $(\gamma_G, \hat{m}^2_{\mathrm{gap}})$ characterise the one-parameter family of solutions. Indeed, the actual solutions in [95] are well approximated by using the functional form of the scaling solution but with the argument of (5.39b), and an appropriate tuning of γ_G. We shall exploit this property for constructing a simple one-parameter family of gluon spectral functions, using the scaling one, $\rho^{(\mathrm{dec})}(\omega)$, as our point of departure.

For completeness, we note that, for $p \to 0$, the respective (dimensionful) ghost propagator is given by

$$G_c(p) = \frac{Z_c^{(\mathrm{IR})}}{p^2}\,\frac{1}{x^{2\kappa}}\,, \tag{5.40}$$

In the deep infrared, $\rho^{(\mathrm{scal})}(\omega)$ is determined from (5.39a) and (5.39b), setting $\gamma_G = 0$. Specifically, for $\omega \to 0_+$, we obtain

$$\hat{\rho}_A^{(\mathrm{scal})}(\omega) = -\,2\,Z_A^{(\mathrm{IR})}\,\hat{\omega}^{2(2\kappa-1)}\,, \tag{5.41}$$

which corresponds to the infrared tail of the full spectral function reconstructed [243], depicted in Figure 5.10. Similarly, in the case of the decoupling-type solutions, we arrive at

$$\hat{\rho}_A^{(\mathrm{dec})}(\omega) = -\,\frac{Z_A^{(\mathrm{IR})}}{\gamma_G}\,\frac{2\pi}{\hat{m}^4_{\mathrm{gap}}}\hat{\omega}^2\,. \tag{5.42}$$

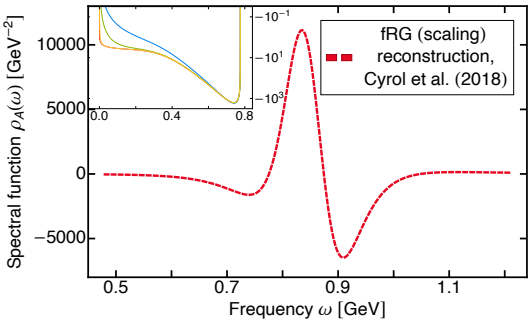

(a) Gluon spectral functions (scaling and decoupling), see (5.43), based on the reconstruction of the scaling spectral function in [243] (red-dashed line). The spectral functions differ only in the infrared, shown in the inset.

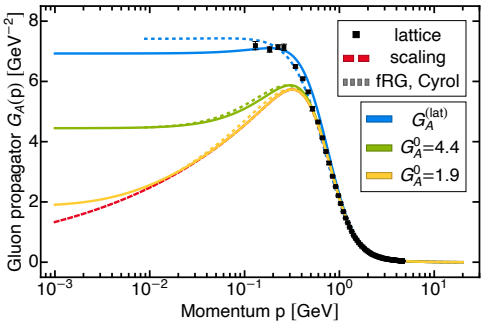

(b) Euclidean gluon propagators obtained from the KL representation (5.11) with the gluon spectral functions in Figure 5.10a. The small IR-difference for $\omega \lesssim 0.7\,\text{GeV}$ shown in the inset in Figure 5.10a translate into the IR-differences for $p \lesssim 1\,\text{GeV}$. The lattice data is taken from [98].

Abbildung 5.10.: Reconstructed gluon spectral function (left) based on [243] and (5.43) and the respective gluon propagators (right). The spectral functions and propagators differ in the infrared and are labelled by $G_A^{(\text{lat})}$ (blue) for our lattice-type input, and $G_A(0)\,[\text{GeV}^{-2}]$=4.4 (green), 1.9 (yellow).

While (5.41) and (5.42) describe the different behaviour of the scaling and decoupling spectral functions in the deep infrared, for larger spectral values the two sets of spectral functions coincide. This regime is approximately bounded from below by the first zero, ω_0, of the scaling spectral function, shown in Figure 5.10, with $\omega_0 \approx 0.78$. A simple interpolation to the decoupling solution, based on the scaling spectral function in [243], is therefore given by

$$\rho_A^{(\text{dec})}(\omega,\chi) = Z_\chi \left(\frac{\omega^2}{\omega^2+\chi^2}\right)^{2-2\kappa} \rho_A^{(\text{scal})}(\omega)\theta(\omega_0-\omega+\rho_A^{(\text{scal})}(\omega)\theta(\omega-\omega_0)\,, \tag{5.43a}$$

with

$$Z_\chi := \frac{\int_0^{\omega_0} d\lambda\,\lambda\,\rho_A^{(\text{scal})}(\lambda)}{\int_0^{\omega_0} d\lambda\,\lambda\,\rho_A^{(\text{scal})}(\lambda)\left(\frac{\omega^2}{\omega^2+\chi^2}\right)^{2-2\kappa}}\,, \tag{5.43b}$$

dictated by the Oehme-Zimmermann superconvergence relation for the gluon spectral function,

$$\int_0^\infty d\lambda\,\lambda\,\rho_A(\lambda) = 0\,. \tag{5.44}$$

With (5.43b) the total spectral weight of $\rho_A^{(\text{dec})}(\omega,\chi)$ is the same as that of $\rho_A^{(\text{scal})}(\omega)$. Hence, given that the latter satisfies (5.44), so does the former. The scaling spectral function reconstructed in [243], satisfies (5.44) analytically for $\epsilon \to 0^+$ in (4.4). In the present work we take a small $\epsilon \approx 10^{-7}$ leading to

$$\frac{\int d\lambda\,\lambda\,\rho_A(\lambda)}{\int d\lambda\,\lambda\,|\rho_A(\lambda)|} \approx 10^{-4}\,, \tag{5.45}$$

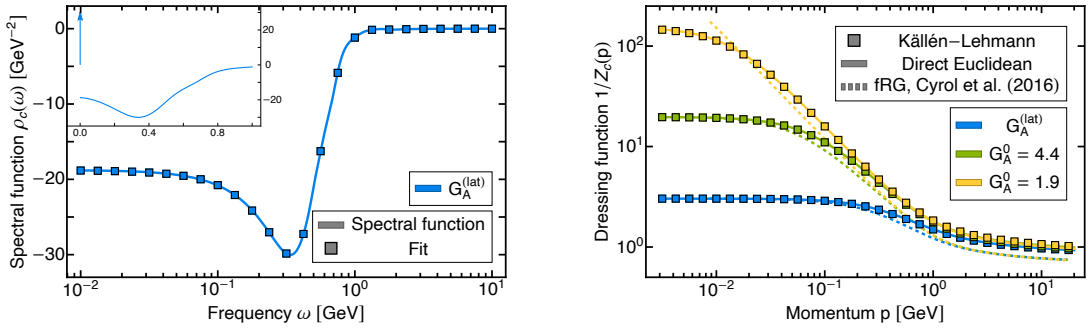

(a) Ghost spectral function: direct computation by iteration with the spectral DSE (5.25d) and the gluon spectral function from Figure 5.10 for $G_A^{(\mathrm{lat})}$. The inlay also indicates the δ-function contribution in the origin, indicated by an arrow. Its amplitude is given by the value of corresponding Euclidean dressing function $1/Z_c(p)$ at $p = 0$. The squares show our best fit, comp. Section 5.2.2.2.

(b) Euclidean ghost dressings: $1/Z_c(p)$ from KL representation via the ρ_c's in Figure 5.11a (squares), $1/Z_c(p)$ from the direct solution with the Euclidean DSE (straight lines), $1/Z_c(p)$ from the Euclidean fRG computations in [95]: we have taken the solutions with matching values of G_A^0 (dashed lines).

Abbildung 5.11.: Ghost spectral functions (left) and respective Euclidean dressings (right), obtained with the decoupling gluon spectral functions in Figure 5.10, with the same color coding by $G_A^{(\mathrm{lat})}$ (blue), $G_A(0)$ [GeV^{-2}]=4.4 (green), 1.9 (yellow).

for all spectral functions. For $\chi = 0$, we get back the scaling solution with $\gamma_G = 0$. The lattice gluon is achieved via (5.43a) for $\chi^{(\mathrm{lat})} = \frac{3}{4}\,\mathrm{GeV}^2$ with $Z_\chi^{(\mathrm{lat})} = 1.86$.

We emphasise that fully quantitative gluon spectral functions $\rho_A^{(\mathrm{dec})}$ may be achieved by means of reconstructions. While possible, this is beyond the scope of the present work. Note also that the simple analytic spectral functions $\rho_A(\omega, \chi)$ give semi-quantitative results for the gluon propagators, while at the same time allowing for analytic access to the relative changes.

5.2.2. Results

With the preparation of the previous sections we now compute the ghost spectral function. The ghost DSE is solved for the three different input decoupling gluon spectral functions in Figure 5.10 and propagators, labelled by $G_A^{(\mathrm{lat})}$ resp. the infrared value of the related gluon propagators $G_A(0) = 4.4, 1.9\,[\mathrm{GeV}^{-2}]$. For $G_A^{(\mathrm{lat})}$, we tune the mass parameter χ in (5.43a) such that we best agree with the lattice results from [98]. We pair each of our input G_A's with a gluon propagator from the family of self-consistent YM solutions of [95], indicated by dashed lines in the right panel of Figure 5.10. For $G_A^{(\mathrm{lat})}$ (blue curve), we chose the solution which also matches the lattice results from [98] best. The green and yellow curves are matched with the respective solution with the same $G_A(0)$.

The renormalisation condition $\tilde{Z}_c$ is now chosen such that the value of the ghost dressing function $1/Z_c(p)$ matches that of [95] at the RG scale $\mu_{\mathrm{RG}} = 20$ MeV for the respective

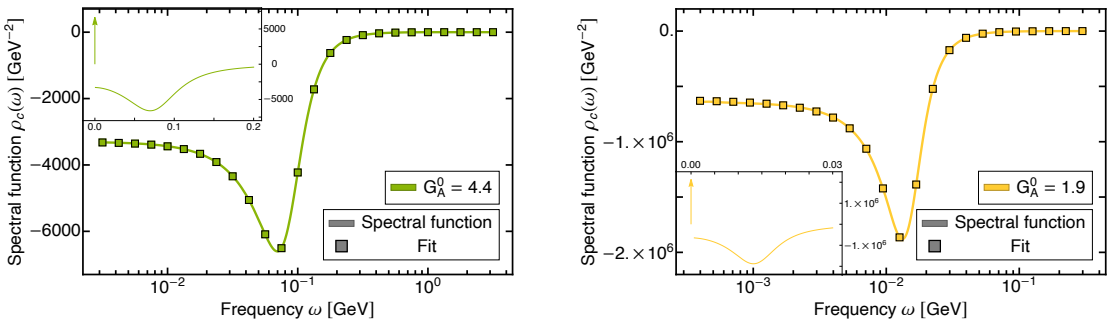

Abbildung 5.12.: Ghost spectral functions: direct computation by iteration with the spectral DSE (5.25d) and the gluon spectral functions from Figure 5.10 with the same color coding, i.e. $G_A(0)$ [GeV^{-2}] = 4.4 (green), 1.9 (yellow). The inlays also show the δ-function pole in the origin, indicated by an arrow. The residue is given by the value of corresponding Euclidean dressing function $1/Z_c(p)$ at $p = 0$. The squares show our best fits, comp. Section 5.2.2.2.

gluon propagator. This IR renormalisation procedure is necessary in order to compensate for the lack of self-consistency when considering the ghost DSE with fixed gluon input. The strong coupling constant is fixed to $\alpha_s = 0.26$.

In Figure 5.11a and Figure 5.12 we show the respective ghost spectral functions. All spectral functions show a positive particle peak at vanishing momentum, constituted by a delta distribution. The magnitude of the corresponding residue, i.e. the particle peaks amplitude, rises with decreasing $G_A(0)$, and the residue's positivity reflects the chosen positive classical dispersion of the ghost. The spectral function also has a negative scattering spectrum starting at vanishing frequency. For decreasing $G_A(0)$, one gradually approaches the scaling solution, and the spectral weight increases drastically. This also mirrors the increasing amplitude of the particle peak, which is enforced by the Oehme-Zimmermann-type superconvergence relation (5.10) for the ghost, for more details see Appendix A.8 and [254]. This also leads to the known UV-asymptotics for the ghost spectral function,

$$\hat{\rho}^{(\mathrm{UV})}(\hat{\lambda}) = \frac{Z_c^{(\mathrm{UV})}}{1 + \hat{\lambda}^2 (\log \hat{\lambda}^2)^{\gamma_c}} , \tag{5.46}$$

with the ghost anomalous dimension γ_c, and the UV wave function renormalisation $Z_c^{(\mathrm{UV})}$. The gluon spectral function for $G_A^{(\mathrm{lat})}$ represents the lattice-type case, see Figure 5.10b. The respective lattice data for the ghost propagator is depicted in Figure 5.11b, and confirms the semi-quantitative nature of the classical vertex approximation in the ghost DSE. For smaller $G_A(0) \to 0$, the gluon propagator approaches the scaling solution. This entails, that also the ghost propagators approaches the scaling solution with $1/Z_c(p) \propto (p^2)^{-\kappa}$.

The Euclidean dressing functions corresponding to the computed spectral functions for the different gluon propagator inputs are shown in Figure 5.11b. We show both the dressing functions obtained from the spectral Euclidean and realtime DSE and find that the spectral representation for the ghost propagator (and dressing function) holds. We also compare to the Yang-Mills results from [95], which we also used in the renormalisation condition

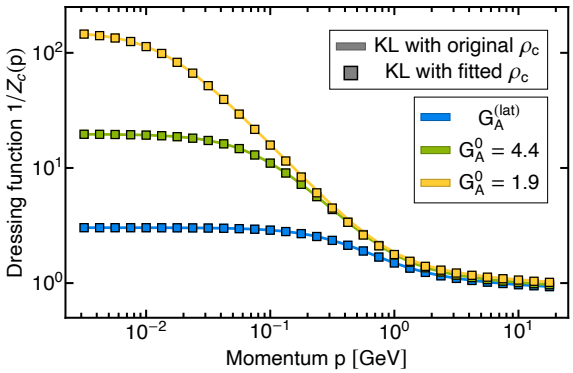

Abbildung 5.13.: Comparison of the ghost dressing function obtained via the KL representation (5.8) from the spectral function (solid line) and its fit (squares) for the different input gluon propagators.

as described above, and see that we reach very good qualitative agreement. In particular, our most scaling-like solution shows the typical scaling behaviour down to about 30 MeV. The deviations from [95] in the UV originate in the classical approximation for the full ghost-gluon vertex used here.

5.2.2.1. Comparison with previous works

In this section we compare our results on the ghost spectral function with that in the literature, for results with different approaches see [260–262, 302]. The spectral function also allows us to map out the ghost propagator in the complex momentum plain, which is discussed in Section 5.2.2.3 including a comparison with respective results in the literature from a DSE analysis, see [264].

In [261], the ghost spectral function has been reconstructed from lattice QCD data. The results are in good agreement with our direct computation: both show a massless particle pole and a negative scattering tail. The reconstruction in [261] lacks reliability for spectral values smaller than roughly 100 MeV, as the smallest Euclidean data point used for the reconstruction is at about $p = 150$ MeV. In this regime, the present results from a direct spectral computation can be used as an input for future reconstructions by restricting the respective infrared completion. The same qualitative features are also found in the ghost spectral function obtained via a massive propagator expansion in [262], i.e. a massless particle pole as well as negative spectral tail.

In [260], Pade-type reconstructions of the ghost dressing spectral function from DSE and lattice data in Yang-Mills theory has been performed. These results are in contradistinction to the present result and [261, 262], as the scattering tails in [260] show significant negative contributions. This corresponds to positive contributions in the propagator spectral function due to a relative sign in the definition. In addition, the UV tail of the reconstruction of DSE data is not shown in [260], and the spectral function appears to approach a constant value. A UV-positive (negative) as well as a non-vanishing tail in the propagator (dressing) spectral function violates the analytically given asymptotic fixed by Equation (4.4), for a detailed derivation see Appendix A.8.

The study of the analytic structure of the ghost propagator put forward in [302] also suggests the existence of a massless pole as well as a branch cut along the real frequency axis. As already mentioned above, Yang-Mills propagators in the whole complex momentum plane have been investigated with DSEs in [264]. The findings show good qualitative agreement with the propagators obtained from the ghost spectral function computed in the present work, but do not support a KL spectral representation of the ghost. This is discussed further in Section 5.2.2.3.

5.2.2.2. Spectral fits

The results for the ghost spectral function with the UV asymptotics $\rho^{(\mathrm{UV})}(\lambda)$ in (5.46), the IR asymptotics ρ_0 allow for a simple fit in terms of the both asymptotics and Breit-Wigner functions for intermediate spectral values. The split into these three regimes allows for a simple parametrisation $\rho_c^{(\mathrm{fit})}$ of the ghost spectral function,

$$\rho_c^{(\mathrm{fit})}(\lambda) = \kappa\left[\hat{\rho}_0\,\sigma_{\mathrm{IR}}(\lambda) + \sigma_1(\lambda)\hat{f}^{(\mathrm{BW})}_{\mathrm{peak}}(\lambda)\sigma_2(\lambda) + \sum_j^N \hat{f}^{(\mathrm{BW})}_j(\lambda) + \sigma_{\mathrm{UV}}(\lambda)\hat{\rho}^{(\mathrm{UV})}(\lambda)\right]. \tag{5.47a}$$

In (5.47a) we use the sigmoid function for projecting on the three regimes,

$$\sigma_x(y) = \frac{1}{1+e^{-\nu_x(y-\Lambda_x)}}\,, \tag{5.47b}$$

where κ only carries the appropriate dimension. The intermediate regime is expanded in Breit-Wigner kernels,

$$\hat{f}^{(\mathrm{BW})}_x(\hat{y}) = \frac{c_x}{(\hat{y}-\hat{M}_x)^2+\hat{\Gamma}_x}\,. \tag{5.47c}$$

For our best fit, we use $N = 3$. The respective fit parameters are listed in Appendix C.4, Table C.2, and the fits are depicted together with the spectral functions in Figure C.7.

The accuracy of the fits is best evaluated within a comparison between the ghost dressing functions $1/Z_c(p)$ obtained from the computed spectral functions and their fits. This comparison if depicted in Figure 5.13 for all three different input gluon propagators.

5.2.2.3. Results in the complex plane

We close this section with a short discussion of the potential application of the present results within bound state and resonance computations in QCD. To begin with, the behaviour of QCD correlation functions for complex-valued momenta is instrumental for the reliable computation of bound-state properties within the frameworks of the Bethe-Salpeter equations (BSEs). In this quest, the gluon and ghost propagators are of paramount importance, as may be exemplified by considering the BSEs that control the formation of glueballs in a pure Yang-Mills theory [118, 119, 121–123, 303] (for lattice studies, see [114] and references therein). In fact, the present results are specifically useful for the scalar glueball: in contradistinction to its pseudo-scalar counterpart, it involves *both* the gluon and ghost propagators, as shown in Figure 5.15.

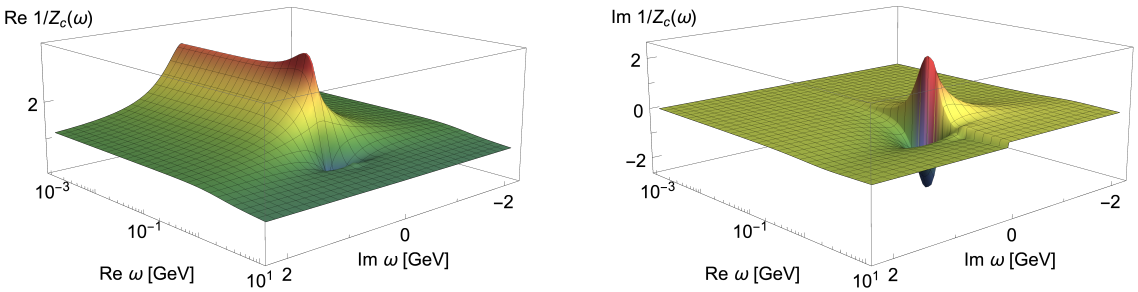

Abbildung 5.14.: Real (left) and imaginary (right) part of the ghost dressing function $1/Z_c(\omega)$ for the lattice-like gluon input (comp. Figure 5.11) as a function of complex frequencies. Purely real ω correspond to Minkowski frequencies, purely imaginary ω to Euclidean frequencies. The color coding serves to guide the eye. The branch cut along the real frequency axis is clearly visible.

As is well-known, the need to extend the aforementioned propagators to the complex plane stems from the fact that the momentum P of the bound-state in question must satisfy $P^2 = -M^2$, where M is the corresponding mass. This condition is typically implemented by introducing the rest-frame parametrisation $P = M(0, 0, 0, \mathrm{i})$ (see, e.g., [304]). Invariably, this complexifies the arguments of $G_A(q_\pm)$ and $G_c(q_\pm)$ in the BSE of Figure 5.15, since $q_\pm^2 = |q|^2 - M^2/4 \pm \mathrm{i}\,|q|\,M$.

These considerations motivate the computation of the dressing function $1/Z_c(p)$ in the entire complex plane. To that end, we employ the KL representation of (A.47), utilising the $\rho_c(\lambda)$ found above, and setting $\mathrm{i}p = \mathrm{Re}\,\omega + \mathrm{i}\,\mathrm{Im}\,\omega$. The results of this computation are shown in Figure 5.14.

We now compare our results for the ghost propagator in the complex plane with the spectral DSE with those from [264]. There, ghost and gluon propagators in the complex plane have been computed with complex DSEs. The gluon propagators in [264] exhibit complex conjugate singularities, and their nature and position varies greatly under small changes in the ansatz for the vertex. We emphasise, that these singularities simply indicate the limited radius of convergence of the method both for the gluon and for the ghost, for a detailed discussion see [264]. For large (angular) distances to the Euclidean axis analyticity is lost, and the method used does not produce reliable results. If reconstructed with the Schlessinger point method, the singularities observed in [264] take the form of complex conjugate poles. This has also been seen in [260], where similar reconstruction methods have been used. For further studies of the complex structure of QCD-like theories in the presence of complex conjugate poles see also the recent work [263, 275].

Despite the lack of reliability for sufficiently large Minkowski frequencies, we have compared ghost dressing from [264] with the present result in this region. The imaginary part of the ghost dressing function computed there is strictly positive for timelike momenta, in qualitative agreement with our result, in particular in view of the different approximations. We have also confirmed the absence of a spectral representation of the ghost by computing the spectral function from the Minkowski dressing of [264] via Equation (4.4). Then, the Euclidean dressing is computed via the KL representation of Equation (5.8) and compared to the direct calculation. This comparison showed a significant violation of the

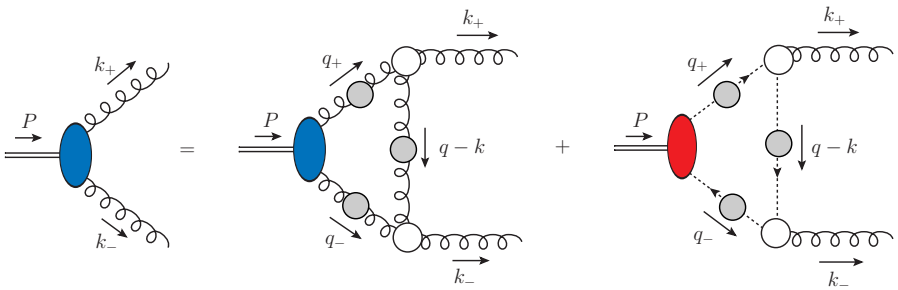

Abbildung 5.15.: One of the two BSEs comprising the system that controls the scalar glueball formation. The blue (red) ellipses denote the glueball-gluon (ghost) BS amplitudes, and $k_\pm = k \pm P/2$, $q_\pm = q \pm P/2$, where q denotes the loop momentum. Note that we are employing a different notation than that in Figure 2.1 here. Grey blobs represent full propagators and white blobs full vertices here.

spectral representation especially for larger Euclidean frequencies. This is to be expected, since by nature of the kernel of the spectral representation Equation (4.3), large Euclidean frequencies are sensitive to large spectral values, i.e. large Minkowski frequencies. These lie beyond the radius of convergence of the method used in [264], as discussed.

In summary, this analysis strongly suggests that complex conjugate poles as well as other non-analyticities in the gluon propagator beyond the real frequency axis invalidate the KL representation for both the gluon *and* the ghost. A more detailed discussion is deferred to future work. In particular, this casts serious doubts on mixed reconstructions with a KL representation for the ghost and cc poles for the gluons. In turn, the gluon spectral function in [243] was reconstructed with the assumption of a KL representation, as outlined in Section 5.2.1.1. As shown in the present work, this also leads to a KL representation of the ghost. Whether this property holds true in a self-consistent solution of the coupled system, remains to be seen and is deferred to future work.

5.2.3. Conclusion

In this section, we solved the Dyson-Schwinger equation for the ghost propagator in the complex plane on the basis of a given input gluon spectral functions, spanning the whole family of decoupling solutions, including the scaling limit. Our spectral DSE approach is based on the spectral DSE put forward in [1], see Section 4.1, and uses the spectral renormalisation devised there. The procedure allows for analytic solution of the momentum loop integrals by utilising the KL representation and dimensional regularisation. This facilitates the access to the full complex momentum plane, constituting the central aspect of our scheme. The present truncation uses classical vertices in the ghost gap equation, but we emphasise that the spectral DSE approach also allows for non-trivial vertex approximations, see [1] resp. Section 4.1.

The input data for the gluon spectral function is constructed via a decoupling-type modification of the scaling spectral function from [243]. The latter spectral function has been obtained via a reconstruction of the scaling solution fRG data of [95].

The spectral function for the ghost shows a massless pole as well as a continuous scattering tail. The classical massless mode dominates up to momenta close to the position of

the maximum of the input gluon propagator. For larger momenta, the perturbative logarithmic behaviour starts to dominate, ultimately causing the dressing function to vanish in the ultraviolet. The present results and the current realtime approach with a realtime renormalisation scheme yields systematic spectral access to dynamical, timelike properties of QCD. The respective results are pivotal for following studies of the resonance properties and the dynamics of QCD within the present approach.

5.3. Spectral reconstruction of ghost and gluon

This section presents the results of [3]. All practical calculations have been performed by then fellow PhD student Julian Urban.

In the previous sections, we presented results for Minkowski space correlation functions obtained via the spectral functional approach. In contradistinction to this direct realtime scheme, Minkowski correlation functions can also be obtained via spectral reconstruction of Euclidean correlation functions, which are well accessible within lattice simulations and functional approaches. As the spectral functional approach, spectral reconstruction exploits the Källén-Lehmann representation by computing the spectral function via an inverse integral transform. Here, we approach this problem with Gaussian process regression (GPR). The applicability of GPR to inverse problems of this type has been discussed in [305]. Specifically, it was shown how GPs can be used to obtain probabilistic models of functions for which only weighted averages are available.

Utilising numerical reconstruction techniques to compute spectral functions has a long history in non-perturbative QCD. The underlying problem is inherently ill-conditioned, prompting the development and application of a plethora of approaches over the last couple of decades, such as the maximum entropy method [258, 306, 307], Bayesian inference techniques [308, 309], Tikhonov regularisation [261, 310, 311], neural networks [312–316], kernel ridge regression [317, 318], and basis expansions [243, 319–322].

We apply GPR to the reconstruction of ghost and gluon spectral functions based on recent results from 2+1 flavor lattice QCD with domain wall fermions at a pion mass of 139 MeV [100, 101]. Furthermore, we improve the systematic error control by incorporating additional data in the infrared (IR) and ultraviolet (UV) regimes from functional renormalization group (fRG) and Dyson-Schwinger (DSE) computations in Yang-Mills theory and QCD [2] resp. Section 5.2, [38, 39, 95, 166, 171, 243], mostly obtained within the fQCD collaboration [12].

This section is structured as follows. In Section 5.3.1, we briefly recapitulate the spectral representation for ghost and gluon propagator. In Section 5.3.2, we give a short introduction to spectral reconstruction with GPR. We discuss the input data for our reconstruction in Section 5.3.3, present our results in Section 5.3.4 and conclude in Section 5.3.5.

5.3.1. Spectral representation

In this section, we express the KL representation (4.3) of the propagator in momentum as

$$G(p) = \int_{-\infty}^{\infty} \frac{d\lambda}{2\pi} \frac{\lambda\,\rho(\lambda)}{\lambda^2 + p^2} \equiv \int_0^{\infty} \mathrm{d}\lambda\, K(p,\lambda)\,\rho(\lambda)\,, \tag{5.48}$$

implicitly defining the KL kernel $K(p,\lambda)$. The spectral function is defined via the imaginary part of the retarded propagator, see (4.4).

For the propagators of physical particles, the spectral function is the probability density for (multi-)particle excitations to be created from the vacuum in the presence of the corresponding quantum field. Consequently, in this case, the spectral function is positive semi-definite and normalisable. For propagators of 'unphysical' fields, such as gauge fields, positive semi-definiteness is no longer required and the spectral representation reduces to

a statement about the analytic structure of the corresponding correlation function; see, e.g., [2, 5] resp. Section 5.1 and 5.2 and [243, 254, 269, 273].

In this section, we reconstruct ghost and gluon spectral functions of 2+1 flavor QCD under the assumption that both, ghost and gluon propagator G_c and G_A, admit a KL representation (5.48), with the respective spectral functions ρ_c and ρ_A. Their total spectral weight vanishes,

$$\int_0^\infty \mathrm{d}\omega\, \omega \rho_{A/c}(\omega) = 0\,, \tag{5.49}$$

for both, the ghost and gluon spectral functions, see also (5.9) and (5.44). For the gluon, this is the well-known Oehme-Zimmermann superconvergence (OZS) condition [256, 323]; for recent discussions with general fields, see [2] resp. Appendix A.8 and [243, 254]. These works also include a treatment of the analytic low-frequency behaviour of continuous parts of the spectral functions, initiated in [243].

A general spectral function ρ can be composed of a continuous part $\tilde{\rho}$ and a sum of particle and resonance peaks (proportional to the δ-function and its derivatives), see (4.6). Here, we assume that the gluon spectral function only consists of a continuous part $\rho_A = \tilde{\rho}_A$ satisfying (5.49). This is the generic structure suggested by all functional equations describing the gluon propagator due to the ghost being massless. While derivatives of δ-functions are formally also allowed, we exclude these structures from our ansatz due to the absence of a generic mechanism generating the required roots of the inverse gluon propagator on the real momentum axis. In turn, due to the $1/p^2$ behaviour of the Euclidean lattice ghost propagator in the IR, the associated spectral function exhibits a particle peak at vanishing frequency in addition to its continuous part, see (5.7) and (5.8).

Euclidean correlators obtained from lattice simulations are generally only available in terms of discrete sets of observations G_i at N_G Euclidean momenta p_i with finite precision. Relating the results to the associated Minkowski propagators via Equation (4.4) is problematic; see, e.g., [319, 320]. In such a numerical setup the analytic continuation via $p \to -\mathrm{i}(\omega + \mathrm{i}0^+)$ is ill-conditioned, since further assumptions about the complex structure need to be made. Instead, the usual strategy is the numerical inversion of the integral transformation. A variety of approaches has been explored to tackle this issue, such as the maximum entropy method [258, 306, 307], Bayesian inference techniques [308, 309], suitable expansions in functional spaces [243, 319–322], Padé-type approximants [260, 302], Tikhonov regularisation [261, 310, 311], neural networks [312–315], and kernel ridge regression [317, 318]. Alternative approaches based on the existence of complex conjugate poles have also been considered, see, e.g., [260, 263, 272, 274, 275, 324–327], but are orthogonal to the method presented here.

5.3.2. Reconstruction with GPR

Starting from early developments in the context of geostatistics in the 1950s [328], today GPR is widely employed in a variety of settings for the probabilistic modelling of functions from a finite number of observations; see [329, 330] for reviews and [331] for a modern textbook account. Recently, the method has been applied to the reconstruction of parton distribution functions from lattice QCD [332]. In this section, we summarize the main ingredients for spectral reconstruction with GPR based on the developments reported in [305]. A short introduction to GPR for function prediction as well as further details and references are provided in Appendix A.9.

We assume our knowledge of the spectral function $\rho(\omega)$ to be described by a GP, written as

$$\rho(\omega) \sim \mathcal{GP}(\mu(\omega), C(\omega, \omega')) \,, \tag{5.50}$$

where $\mu(\omega), C(\omega, \omega')$ denote the mean and covariance functions. Importantly, in this approach we do not restrict the space of possible solutions by choosing a specific functional basis, which often leads to spurious artefacts in the reconstruction in order to compensate for unrepresentable features. Instead, the GP defines a distribution over families of functions with rather generic properties, specified via the kernel parametrization described below.

The KL integral in (5.48) is a linear transformation that preserves Gaussian statistics. Hence, given (5.50) one may obtain statistical predictions G_i at N_G specified momenta p_i as

$$G_i \sim \mathcal{N}\left(\int \mathrm{d}\omega \; K(p_i, \omega)\mu(\omega), \int \mathrm{d}\omega \, \mathrm{d}\omega' K(p_i, \omega) C(\omega, \omega') K(p_j, \omega')\right) \equiv \mathcal{N}\big(\tilde{\mu}_i, \tilde{C}_{ij}\big) \,. \tag{5.51}$$

Here, $\mathcal{N}$ denotes a multivariate normal distribution, to be distinguished from distributions over function space denoted by $\mathcal{GP}$. Statistical uncertainties associated with individual prediction points $\tilde{\mu}_i$ may be computed from the diagonal of the covariance matrix as $\tilde{\sigma}_i = \sqrt{\tilde{C}_{ii}}$.

Conversely, the framework also enables inference in the opposite direction. The inherent analytic tractability associated with Gaussian statistics allows formulating the conditional distribution for $\rho(\omega)$ given observations G_i in closed form. The full expression may then be derived as

$$\begin{aligned} \rho(\omega) \,\big|\, G_i \sim \mathcal{GP}\Big(\mu(\omega) \; &+ \sum_{i,j=1}^{N_G} \int \mathrm{d}\eta \, K(p_i, \eta) C(\eta, \omega) \left(\tilde{C} + \sigma_n^2 \cdot \mathbf{1}\right)^{-1}_{ij} (G_j - \tilde{\mu}_j) \;, \\ C(\omega, \omega') &- \sum_{i,j=1}^{N_G} \int \mathrm{d}\eta \mathrm{d}\eta' \, K(p_i, \eta) C(\eta, \omega) \left(\tilde{C} + \sigma_n^2 \cdot \mathbf{1}\right)^{-1}_{ij} K(p_j, \eta') C(\eta', \omega')\Big) \;. \end{aligned} \tag{5.52}$$

The GP in (5.52) encodes our knowledge of the spectral function after making observations of the propagator and accounting for observational noise with variance σ_n^2. The corresponding expressions for the dressing function instead of the propagator can be immediately obtained by inserting an additional factor of p_i^2 at every occurrence of the KL kernel $K(p_i, \omega)$ in (5.51) and (5.52).

The flexibility of the approach makes it possible to also incorporate further available prior information in various forms into the predictive distribution in the same manner, yielding similar though somewhat more complicated expressions. This may include, e.g., direct observations of ρ and its derivatives, assumptions about the asymptotic behaviour (see Section 6.1), or global normalization constraints.

In order for GPs to be useful for modelling, the covariance $C(\omega, \omega')$ may be defined via a so-called kernel function. It is commonly parametrized using few hyperparameters, which may be subjected to optimization based on the associated likelihood. The mean function $\mu(\omega)$ is often set to zero, since its contribution can be fully absorbed by the kernel. Typically, the latter is the sole focus of the optimization procedure. However, a custom mean function may still be useful in certain situations in order to incorporate

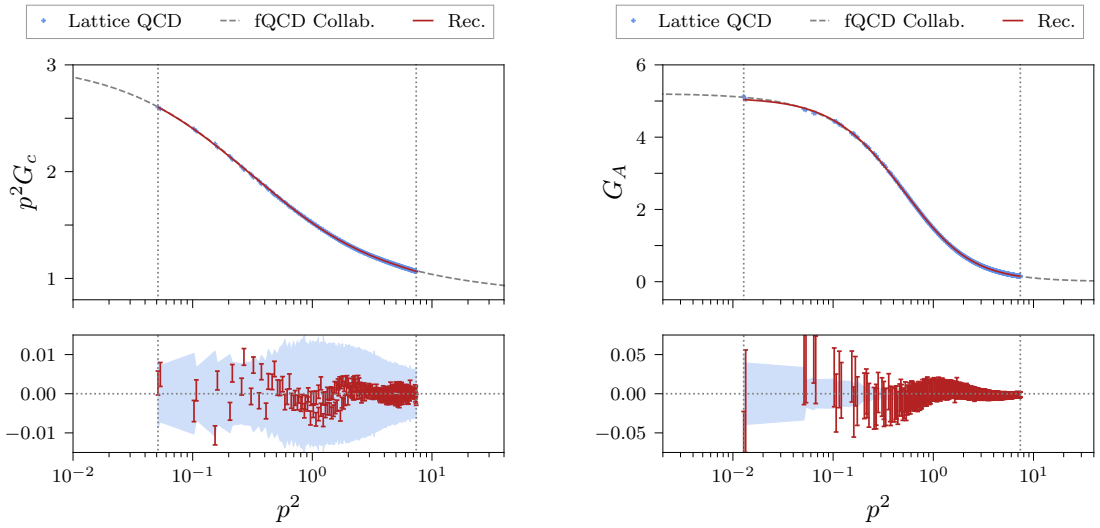

Abbildung 5.16.: Plots showing the ghost dressing function (left) and gluon propagator (right) from 2+1 flavor lattice QCD simulations, extended by functional computations in Yang-Mills theory and QCD and compared against the correlators obtained from the reconstructed spectral functions shown in Figure 5.17. The results agree within the given statistical uncertainties as shown in the bottom panels, where the posterior GPs for the correlators are evaluated at the fixed momenta provided by the lattice data, which is then subtracted leaving the error bars intact. The total mean squared errors amount to ∼5e–6 for the ghost and ∼4e–5 for the gluon.

prior beliefs about the functional form of the expected solution. This can improve the calculation by providing a better starting point for the optimization routine.

A frequently used kernel parametrization is the radial basis function (RBF) kernel, also called squared exponential. It is defined as

$$C(\omega, \omega') = \sigma_C^2 \exp\left(-\frac{(\omega - \omega')^2}{2l^2} \right), \tag{5.53}$$

where the parameter σ_C controls the overall magnitude and l is a generic length scale. The RBF kernel has been established as the standard choice for many applications due to a number of attractive features, such as universality [333] and every function in its prior being infinitely differentiable. It is also used for our first results on spectral reconstruction with GPR presented here.

Nevertheless, designing custom kernels for specific problems has been shown to greatly increase the usefulness of the approach in various settings and is also promising here. In particular, it may be interesting to construct kernel functions that can be integrated analytically against the KL kernel, such that the frequency integrals in (5.51) and (5.52) may be carried out analytically instead of numerically. To this end, one could potentially employ functions of Breit-Wigner type as done for the spectral function itself in [243]. In contradistinction, we may use them to instead define a suitable GP kernel, thereby still

avoiding the restriction to a specific functional basis as previously mentioned. We comment on this and other possible improvements to our reconstruction approach in the conclusion.

Furthermore, we emphasize that the present approach in principle does not require us to choose a specific set of nodes ω_i. In fact, instead of computing a discrete set of point predictions or coefficients of a predefined functional basis, the prediction for ρ is obtained as a function of ω, albeit only implicitly via the kernel formulation. In particular, the GP also allows computing all the derivatives of the prediction analytically at any point—including the associated statistical uncertainties—by differentiating the expressions in (5.52) with respect to ω (as well as ω' for the covariance). A finite set of nodes ω_i is chosen only at inference time in order to evaluate the GP, however, the choice is completely arbitrary within the given domain. This property is one of the most attractive features of GPR for spectral reconstruction and probabilistic function prediction in general.

5.3.3. Input data

In the past two decades, increasing interest in the momentum behaviour of the fundamental two-point Green's functions in QCD as well as further correlation functions of higher order has triggered respective lattice calculations in particular of Yang-Mills and QCD propagators; see, e.g., [97, 128, 182, 334–345]. The lattice data for the ghost dressing function and gluon propagator employed here are shown in Figure 5.16. They are obtained from recent simulations of 2+1 flavor QCD at the physical point [100, 101]; see Appendix A.10.1 for further details and references. Additional input data and benchmarks are provided by one-parameter families of solutions from functional computations in Yang-Mills theory and QCD [2], see Section 5.2, and [95, 171, 243], which are matched to the continuum-extrapolated lattice data as shown in Figures A.5 and A.6; see Appendix A.10.2 for details.

5.3.4. Reconstruction results

The GPR for the reconstruction of the ghost spectral function is performed using the aforementioned standard RBF kernel. We extend the lattice input data for the dressing function into the deep IR. Simultaneously, we fix the low-frequency asymptotics of the spectral function using a direct realtime result in Yang-Mills theory obtained via the spectral ghost DSE, see Section 5.2 and also Appendix A.10.2. This is achieved by treating the spectral DSE result as an additional observation. Our procedure uniquely determines the non-zero value of ρ_c for $\omega \to 0^+$, but also increases the reliability of the solution in the most interesting central region with respect to the kernel hyperparameters. Using just the lattice data without the extension by the spectral DSE result leads to a much higher variance in the solution space, with widely different asymptotic behaviours of solution candidates in the IR. The kernel hyperparameters are chosen by optimizing the associated likelihood of observations with an additional Gaussian hyperprior, which we achieve through a fine-grained grid scan; see Appendix C.5 for details. The reconstructed spectral function in the left panel ofFigure 5.17 accurately reproduces the dressing function data within the uncertainties displayed in the left panel of Figure 5.16, with a total mean squared error of ∼5e–6.

The features of our prediction are strikingly similar to the aforementioned Yang-Mills result shown in the left panel of Figure A.6 in Appendix A.10, even though only the

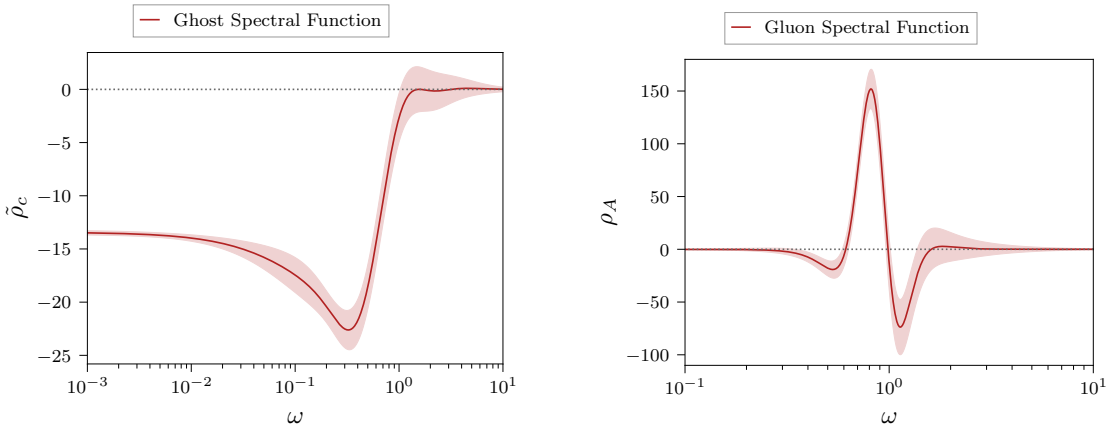

Abbildung 5.17.: Plots showing the continuous part of the ghost (left) and the gluon spectral function (right) reconstructed from the lattice QCD correlators shown in Figure 5.16 using GPR. Shaded areas represent the 1σ-bands of plausible solutions around the mean prediction based on the available observations and precision. The ghost spectral function ρ_c features an additional massless particle pole in the origin; cf. (5.7).

IR limit is incorporated into the reconstruction. This is expected heuristically, since the ghost only interacts with the quarks indirectly via the gluon vertices, and the effects of introducing dynamical quarks must hence be of higher order. The similarity is particularly notable considering that the methods are conceptually very different.

For the reconstruction of the gluon spectral function, the lattice input data are extended into the UV using an earlier fRG computation [243], which is quantitatively reliable in this regime. We discuss this in more detail in the next paragraph and in Appendix A.10.2. As for the ghost, this extension leads to greatly enhanced stability of the reconstruction with respect to the kernel hyperparameters. In particular, it ensures convergence to zero for $\omega \to \infty$, whereas with just the lattice data we often observe convergence to a non-zero constant and in some cases even pathological divergences. We use a modified frequency scale in the RBF kernel in order to suppress spurious oscillations in the IR and UV tails. The hyperparameters are again obtained via optimization of the likelihood with Gaussian hyperpriors while approximately enforcing the OZS condition; see Appendix C.5 for details. The reconstruction shown in the right panel of Figure 5.17 accurately reproduces the lattice data within the given uncertainties, as shown in the left panel of Figure 5.16, with a total mean squared error of ∼4e–5. While also being fully consistent, deviations from the lattice propagator are somewhat stronger than for the ghost dressing function and seem to become more pronounced in the IR. This is likely caused by the comparably large uncertainties of the lattice data at small momenta.

The peak structure of the spectral function appears similar to an earlier reconstruction of the Yang-Mills propagator in the fRG framework [243], shown in the right panel of Figure A.6 in Appendix A.10. We emphasize that the UV extension is done with the Yang-Mills data of [95] instead of the full 2+1 flavor results from [171]. This is detailed in Appendix A.10.2 and facilitates the comparison with the Yang-Mills reconstruction [243]. In particular, the positions of the leading positive peaks approximately coincide, with

$\omega \approx 0.818$ for the present result and $\omega \approx 0.835$ for the fRG reconstruction. This reflects the approximate coincidence of the peaks of the Euclidean gluon dressing functions shown in the left panel of Figure A.5 in Appendix A.10. We also note that a small peak to the right of the second local minimum is present in both reconstructions. This feature may be a generic reconstruction artefact since it is not necessitated by theoretical considerations, but is observed in both results from conceptually very distinct methods. However, the comparably large uncertainties in this region also include plausible solutions without additional zero-crossings.

We observe significant differences between the two reconstructions mainly in the overall peak height and width. Generally, we expect the QCD result for the gluon to differ more strongly from the pure gauge theory than the ghost due to the direct coupling to quarks. However, differences may also be attributed in part to the limited availability and precision of data and the resulting difficulty in resolving highly peaked structures. We find that generating narrower peaks with greater amplitudes by allowing the kernel's magnitude parameter σ_C to increase and the length scale l to decrease leads to stronger oscillations in the solution. This is a common feature of conceptually similar reconstruction approaches, such as linear regression with a Tikhonov regulariser (also called ridge regression), which has been applied, e.g., in [261]. Introducing such a regularisation scheme, which is equivalent to assuming a Gaussian prior, leads to a favouring of solutions that are closer to zero. This additional bias can introduce the unwanted oscillations. Within the GPR approach, the kernel hyperparameters provide more detailed control over the regularisation and can be tuned to deliberately suppress such unphysical features. However, this may result in reconstructions that are naturally flatter, which must be taken into account when interpreting and utilizing the result. This demonstrates one of the key advantages of GPR, namely the possibility to dynamically adjust the resolution depending on the available amount and quality of the input data, while still matching the observations as accurately as possible.

Although the obtained spectral functions reproduce the lattice data to high accuracy, the asymptotic behaviours of the mean predictions in the deep IR and UV differ from the analytic results derived in [243]. In particular, different scaling exponents are observed, and the gluon spectral function shows the opposite sign in the UV. Nevertheless, the analytically expected behaviour is still plausibly contained within the computed errors, which are comparably large in these regimes. This indicates that not enough prior information is available to the GP from just the data in order to accurately resolve the tails of the spectral functions, which may come as no surprise. While this issue does not affect the reconstruction in the region of interest, it may be problematic for precision computations that use these results as inputs. In order to directly enforce the correct asymptotics, potential approaches are the incorporation of the analytically known behaviours into the prior means of the GPs or finding more suitable choices for the kernel functions. Furthermore, exploiting the available analytic results to provide additional prior information about the derivative structure may be particularly helpful in stabilizing the tail behaviour. To achieve this, one may again write down the joint distribution of the predicted spectral function at any frequency and its associated derivatives to arbitrary order in closed form and derive the conditional posterior distribution similar to (5.52).

5.3.5. Conclusion

In this section, we applied Gaussian process regression to the reconstruction of ghost and gluon spectral functions in 2+1 flavor QCD at the physical point. These spectral functions are the pivotal building blocks of diagrammatic representations for bound state equations such as Bethe-Salpeter and Faddeev equations, see, e.g., [120, 266, 267], as well as transport coefficients, see, e.g., [258, 346].

Importantly, the gluon spectral function has a pronounced quasi-particle peak, the position of which is related to the mass gap in QCD. This extends previous vacuum and finite-temperature results in Yang-Mills theory [243, 258] to physical QCD. Our findings provide non-trivial QCD support to the phenomenological use of quasi-particle gluon spectral functions for transport computations; see [347] for a recent review. Moreover, the present results can be directly employed as first-principle QCD inputs in order to systematically improve the respective phenomenological approaches towards a first-principle treatment of QCD transport processes.

These promising phenomenological applications of the present results also highlight the necessity of further improving the reconstruction approach itself, for which a number of potential directions can be envisaged. This includes the aforementioned possibility of designing custom kernels for the problem at hand, potentially with analytic integrability against the KL kernel. Constructing suitable, expressive kernels may also be automated and improved through the use of hyperkernels [348] or techniques such as deep kernel learning [349]. To account for some variability in the kernel hyperparameters, one may replace the maximum likelihood approach by an integral over parameter space using a suitable hyperprior which encodes any prior assumptions. Alternatively, optimal hyperparameters may also be selected based on a data-driven machine learning approach, using datasets consisting of pairs of correlators and associated spectral functions.

Furthermore, the flexibility of the GPR framework allows the incorporation of various supplementary constraints derived from theoretical arguments, such as information about derivatives, known asymptotic behaviours, or normalization conditions. This is expected to further improve the accuracy and reliability of the reconstruction, in particular for the IR and UV tails of the spectral functions that are otherwise difficult to resolve. This will be the subject of future work, accompanied by direct functional computations of further spectral properties along the lines of [1, 2, 5], see Section 4.1, 5.1 and 5.2.

The immediate next steps in our endeavour towards unveiling realtime properties of QCD are the application and extension of the present numerical method to quark propagators as well as correlation functions computed at finite temperature. This will enable quantitative studies of hitherto theoretically inaccessible non-equilibrium dynamics of QCD in the transport phase of heavy-ion collisions within a first-principle approach.

5.4. Quark

This section presents results of [7].

In this section we apply the spectral functional approach to the quark gap equation and present a direct calculation of the spectral function of light quark flavors in 2+1 flavor vacuum QCD using the isospin-symmetric approximation. For the gluon propagator, we use the Gaussian Process Regression (GPR) reconstruction results for the gluon spectral function of 2+1 flavor lattice QCD data [100, 101] presented in [3], see Section 5.3. In addition to the numerical results, we present a general discussion of the impact of the quark-gluon vertex and the gluon propagator on the analytic structure of the quark propagator. Based on this discussion, we formulate conditions under which complex conjugate poles are present or absent in the quark propagator, and discuss their sources. Reconstructions of the quark spectral function from Euclidean lattice and DSE data in QCD have been previously put forward in [350] respectively [351–353]. Investigations of the quark propagator on the real axis and in the complex plane with various vertex models, also in the context of solving BSEs in the timelike domain, have been put forward in, e.g., [266, 354–370].

Realtime results for the quark propagator have a wide range of possible direct applications: in the case of heavy quarks, the propagator can be directly used to calculate the heavy quark diffusion coefficient, which is a necessary ab-initio input in hydrodynamical simulations of the quark gluon plasma. In the calculation of the QCD resonance spectrum from functional methods the quark propagator is needed for general complex momenta. Using the Källén-Lehmann representation, the quark propagator is readily evaluated in the full complex momentum plane solely using information on the realtime axis.

This section is organised as follows. A general discussion of the analytic structure of the quark propagator can be found in Section 5.4.1. In Section 5.4.2, we introduce the spectral quark propagator DSE. Results for the quark spectral function and a discussion of the complex structure of the propagator are presented in Section 5.4.3. We conclude in Section 5.4.4.

5.4.1. Analytic properties of the quark propagator

The quark propagator can be parametrised as

$$G_q(p) = \frac{1}{Z_q(p)} \frac{-i\not{p} + M_q(p)}{p^2 + M_q(p)^2}\,, \tag{5.54}$$

with dressing $1/Z_q$ and mass function M_q. The singularity structure of G_q is encoded in its universal part

$$g(p) = \frac{1}{p^2 + M_q(p)^2}\,. \tag{5.55}$$

The singularities of the quark propagator appear as roots of the denominator of (5.55). The dressing function $1/Z_q$ can be assumed to be singularity-free in the complex plane.

By its gapped nature, the universal part (5.55) of the quark propagator has to have one or more poles close to the gapping scale $M_q(0)$. These poles can be located either on the first or second Riemann sheet or on their boundary, which is the real axis. On the boundary and on the first sheet, the poles directly show up in the quark propagator as

real respectively complex conjugate poles. On the second Riemann sheet, the poles do not directly show up in propagator, but only leave an imprint on the real axis. In the latter case as well as when the pole is on the real axis, the quark propagator obeys a Källén-Lehmann representation. In the vacuum, it can then be described by a single scalar function ρ_q via

$$G_q(p) = \int_{-\infty}^{\infty} \frac{\mathrm{d}\lambda}{2\pi} \frac{\rho_q(\lambda)}{\mathrm{i}\not{p} + \lambda} \,. \tag{5.56}$$

We drop the spatial momentum argument in the subsequent calculation, as it can be restored from the $\vec{p} = 0$ case via a Lorentz boost due to Lorentz invariance.

The quark spectral function ρ_q can be decomposed into a frequency-even and -odd component,

$$\rho_q(\omega) = \rho_q^{(d)}(\omega) + \rho_q^{(s)}(\omega) \,, \tag{5.57}$$

with

$$\rho_q^{(d)}(-\omega) = \rho_q^{(d)}(\omega) \,, \qquad \rho_q^{(s)}(-\omega) = -\rho_q^{(s)}(\omega) \,. \tag{5.58}$$

$\rho_q^{(d)}$ and $\rho_q^{(s)}$ account for the Dirac respectively scalar part of the propagator,

$$G_q(p) = -\mathrm{i}\not{p} \int_\lambda \frac{\rho_q^{(d)}(\lambda)}{p^2 + \lambda^2} + \int_\lambda \frac{\lambda\, \rho_q^{(s)}(\lambda)}{p^2 + \lambda^2} \,, \tag{5.59}$$

with $\int_\lambda = \int_0^\infty \mathrm{d}\lambda/\pi$, again. The components of the spectral function can be obtained separately from the propagator via

$$\rho_q^{(d)}(\omega) = \frac{1}{2} \operatorname{tr}\left[\gamma_0 \operatorname{Im} G_q(-\mathrm{i}\omega_+)\right] , \qquad \rho_q^{(s)}(\omega) = \frac{1}{2} \operatorname{tr}\left[\operatorname{Im} G_q(-\mathrm{i}\omega_+)\right] , \tag{5.60}$$

with ω_+ as defined in (4.5). An isolated pole on the real axis shows up as a single Dirac delta contribution in the spectral function. These contributions are associated with stable asymptotic vacuum states, located at the pole mass of the corresponding particle. Note that in gauge theories, these asymptotic states do not necessarily correspond to physically measurable particles [371]. Continuous contributions to the spectral function usually encode the scattering spectrum of the theory. In vacuum, they come with a sharp onset at the energy of the lowest lying scattering state. The quark propagators analytic structure has been intensively studied in the literature [355–357, 367, 370].

The spectral representation (5.56) also entails the sum rules

$$\int_\lambda \rho_q^{(d)}(\lambda) = \frac{1}{Z_q(p \to \infty)} \,, \qquad \int_\lambda \lambda\, \rho_q^{(s)}(\lambda) = 0 \,. \tag{5.61}$$

Equation (5.61) can be derived in analogy to Appendix A in [2], see Appendix A.8.

5.4.1.1. Singularity structure

In the case of poles on the first sheet, the spectral representation (5.60) is violated. Below, we summarise the discussion of the analytic structure of the quark propagator presented in Appendix A.11. This discussion eventually motivates the use of the spectral representation of the propagator independent of its precise analytic structure.

Abbildung 5.18.: Quark propagator Dyson-Schwinger equation. Notation as defined in Figure 2.1. Solid lines represent quark and wiggly lines represent gluon fields.

Under a small set of well-justified assumptions, which Riemann sheet the poles of the quark propagator appear on is directly linked to the imaginary part of its mass function on the real axis. We assume the mass function to be smooth and well-behaved, which is monotonously decaying for large complex momenta. Note that this usually holds true due to the logarithmic nature of the branch cut of the propagator. In summary, we find:

The quark propagator shows a pair of complex conjugate poles on the first Riemann sheet, if

$$\operatorname{Im} M_q(\omega_0) > 0\,, \qquad \text{for} \qquad \omega_0^2 - \operatorname{Re} M_q(\omega_0)^2 = 0\,. \tag{5.62}$$

We emphasise that the above condition for complex poles in the quark propagator is an empirical observation based on a generic mechanism which applies under fairly general conditions in fermionic DSEs. Turning observations such as (5.62) into rigorous statements is a notoriously hard task in functional methods since analytic structures of correlation functions are highly truncation-dependent. We discuss this matter for the quark gap equation in Paragraph 5.4.3.2.2. Details as well as a heuristic derivation of (5.62) are presented in Appendix A.11.

In (5.62), ω_0 is the root of the real part of the universal part g's (5.55) denominator. It therefore gives the position of the (quasi-) pole of the quark propagator on the real axis. If (5.62) is fulfilled, the denominator of g has a root in the upper (and lower) right half of the complex plane. If $\operatorname{Im} M_q(\omega_0) = 0$, the quark propagator has a real pole. For $\operatorname{Im} M_q(\omega_0) < 0$, the denominator of (5.55) most likely will not have a root, and the complex poles move to the second Riemann sheet.

In one-loop perturbation theory, (5.62) holds true, and the quark propagator shows complex poles. There, as well as in other practical calculations, the imaginary part of the mass function is usually very small in a neighbourhood of ω_0, $\operatorname{Im} M_q(\omega_0) \ll 1$. This entails that independent of which sheet the complex poles lie on, the (quasi-)pole in the universal part (5.55) can be well approximated by a real pole at ω_0. On the level of the spectral function, this approximation translates into

$$\rho(\omega) = R\,\delta(\omega - \omega_0) + \tilde{\rho}(\omega)\,, \tag{5.63}$$

for both vector and scalar component, where R is a residue. We call (5.63) the *resonance-scattering split*.

Equation (5.63) represents a central approximation of this work. It is used in obtaining all numerical results presented in Section 5.4.3. For a detailed discussion of this approximation we refer to Appendix A.11. There, we also provide the relations between the respective residues and scattering tails of scalar and vector component of the quark spectral function in the resonance-scattering split (5.63) and the full Minkowski space quark propagator.

5.4.2. Spectral quark DSE

In this section, we briefly introduce the spectral quark propagator DSE. This equation is used in obtaining all numerical and analytical results in this work.

The quark propagator DSE can be parametrised as

$$\Gamma^{(2)}_{\bar{q}q}(p) = \mathrm{i}Z_2\,\not{p} + Z_{m_q} m_q - \Sigma_{\bar{q}q}(p)\,, \tag{5.64}$$

with the quark self-energy $\Sigma_{\bar{q}q}(p)$ and the wave function renormalisation Z_2 and mass renormalisation Z_{m_q} of the quark. In (5.64) we have used the notation (2.13) for 1PI correlation functions, derived from the 1PI effective action.

The quark-gluon vertex is proportional to $(t^a)^{AB}$ with the gluon color index a and quark and anti-quark indices A, B. We can write schematically

$$[\Gamma^{(3)}_{\bar{q}qA}]^a(q,p) = t^a \Gamma_\mu(q,p)\,, \tag{5.65}$$

where we suppressed the color indices of the quark. The quark self-energy $\Sigma_{\bar{q}q}$ in (5.64) has the general form

$$\Sigma_{\bar{q}q}(p) = -\mathrm{i}g_s \mathrm{C_f} \delta^{ab} Z_1^f \gamma_\mu \int_q G_A^{\mu\nu}(q+p) G_q(q) \Gamma_\nu(q,-p)\,, \tag{5.66}$$

with the strong coupling constant g_s and Z_1^f the quark-gluon vertex renormalisation constant. The combination of (5.64) and (5.66) is depicted in Figure 5.18 with the diagrammatic rules of Figure 2.1.

In (5.66), the color contractions have already been carried out, yielding the Casimir operator in the fundamental representation, $C_f = 4/3$ for $SU(3)$. G_A and G_q are the gluon respectively quark propagator. The following computation is carried out in the Landau gauge.

We employ the KL representation for the quark and gluon propagators inside the quark self-energy. Then, we apply the scheme of spectral renormalisation [1], see Section 4.1. Within this scheme, the momentum integrals in the quark DSE can be solved analytically via standard dimensional regularisation. As a consequence, the quark gap equation can be evaluated *analytically* in the full complex momentum plane, and in particular on the timelike axis. The remaining spectral integrals also require regularisation, which is provided by the spectral renormalisation scheme. The finite spectral integrals are straightforwardly evaluated numerically, and the quark spectral function can be obtained by simply using (5.60).

Due to its genuine realtime nature, spectral renormalisation permits specifying renormalisation conditions in the Euclidean or Minkowski domain. In particular for massive theories, this allows for on-shell renormalisation. Since the position of the mass (quasi-)pole of the quark is unknown, we refrain from doing so however, and fix the propagator at a large perturbative scale μ instead,

$$Z_q(p^2 = \mu^2) = 1\,, \quad M_q(p^2 = \mu^2) = m_q\,, \tag{5.67}$$

where m_q is the current quark mass. For the explicit calculation we refer to Appendix B.6.

5.4.2.1. Gluon propagator

In Landau gauge, the gluon propagator is fully transverse,

$$G_A^{\mu\nu}(p) = \Pi_\perp^{\mu\nu}(p) G_A(p)\,, \tag{5.68}$$

where $\Pi_\perp^{\mu\nu}$ is the transverse projection operator defined in (5.3). We employ a spectral representation for the scalar part $G_A(p)$ of the gluon propagator (5.11), implying that all non-analyticities of the gluon propagator are confined to the real momentum axis. In particular, this entails that the gluon propagator does not have complex poles. In fact, the complex structure of the gluon propagator is subject of an ongoing debate. Equation (5.11) is therefore to an assumption. We discuss implications as well as deviations of it by, e.g., complex conjugate poles in Paragraph 5.4.3.2.2.

The gluon spectral function ρ_A represents a non-trivial input for our calculation. We use reconstruction results of 2+1 flavor lattice QCD data [100, 101] obtained via Gaussian process regression in [3] for ρ_A, shown in the right panel of Figure 5.17. The lattice data corresponds to a decoupling-type solution, i.e., the gluon propagator approaches a finite, non-zero value in the origin, as shown in the right panel of Figure 5.16.

5.4.2.2. Quark-gluon vertex

The existence of analytic solutions for the momentum loop integrals is at the heart of spectral functional approaches. This imposes restrictions on the representations of the correlation functions entering. For example, full vertices or particular momentum channels thereof can be included via their spectral representations, as done, e.g., in [1] resp. Chapter 4.

Due to the transversality of the gluon propagator in the Landau gauge, only the transverse part $\mathbf{\Gamma}_\mu(p,q)$ of the quark-gluon vertex $\Gamma_\mu(p,q)$ enters the gap equation. We define

$$\mathbf{\Gamma}_\mu(p,q) = \Pi_{\mu\nu}^\perp(p+q)\Gamma_\nu(q,p)\,, \tag{5.69}$$

with the transverse projection operator (5.68). While the full quark-gluon vertex can be expanded in a basis with twelve tensor components, the transverse vertex $\mathbf{\Gamma}_\nu$ is expanded in eight transverse tensor structures,

$$\mathbf{\Gamma}_\mu(p,q) = g_s \sum_{i=1}^{8} \lambda_i(p,q)\mathcal{T}_i(p,q)\,. \tag{5.70}$$

Here, q, p are the (incoming) anti-quark and quark momenta respectively and the incoming gluon momentum is $-(p+q)$, see, e.g., [171].

While the tensor basis $\{\mathcal{T}_i\}$ is not unique, it can be ordered such that it only hosts three dominant components [166, 171, 372–374]. Naturally, one of them is the chirally symmetric classical tensor structure, and we choose $\mathcal{T}_1 = \gamma_\mu$, or rather its transverse projection,

$$\mathcal{T}_1(q,p) = -\mathrm{i}\,\gamma_\mu\,\Pi_{\mu\nu}^\perp(p+q)\,. \tag{5.71}$$

The choice for the dominant components is completed by a further chirally symmetric tensor structure and one, that breaks chiral symmetry. The dressing λ_1 of the classical tensor structure can be related to the wave function renormalisation of the quark as well as a scattering kernel via the Slavnov-Taylor identities (STIs), see, e.g., the reviews [54, 56]

for more details and Section 3.1.6 for a general introduction. The representation of the STIs and their impact here relies on [166, 171], and we refer to these works for further discussions.

Roughly speaking, the STIs for the quark-gluon vertex express the four longitudinal dressings in terms of the quark propagator and additional scattering kernels, that carry the quantum modifications of BRST transformations. While the general relations are rather complicated, they are significantly reduced under the assumption that the quantum BRST transformations are approximated well by the classical ones. Indeed, in general the scattering kernels show a rather mild momentum dependence which supports this approximation. An exception is triggered by the Schwinger mechanism for confinement that necessarily leads to longitudinal poles in the ghost-gluon scattering kernels. Without the scattering kernels, the STI for the quark-gluon vertex takes the simple Abelian form

$$(p_\mu + q_\mu)\Gamma_\mu(q,p) = g_s \left[\Gamma^{(2)}_{\bar{q}q}(q) - \Gamma^{(2)}_{\bar{q}q}(p)\right] , \tag{5.72}$$

identical to the form of the Ward identity in QED.

The approximation of the quantum BRST transformations as classical ones discussed above are at the heart of the Ball-Chiu construction [375, 376] and variants thereof, e.g., [377–379], for a discussion see [54]. All these vertices are constructed around a unique combination of the quark dressings Z_q and M_q. The difference between the variants of this construction is an undetermined additional transverse part dropping out of the STIs. Effectively, STI vertices rely on the smallness of this additional piece. The construction is Abelian and also works in $U(1)$ theories such as QED.

Consistent approximations of the quark-gluon vertex, leading to the right amount of chiral symmetry breaking, are intricate: To begin with, as discussed before, quantitatively reliable results are only obtained self-consistently from the coupled set of propagator and quark-gluon vertex DSEs, if we consider at least three out of the eight transverse tensor structures.

In gauge theories we face the situation that the correct complex structure of propagators and vertices may only be obtained in a fully gauge consistent approximation, for a discussion see, e.g., [5] resp. Section 5.1. This suggests an investigation of the quark gap equation with STI quark-gluon vertices. However, while the dressing of the classical tensor structure is constrained by the STIs, the dressings of the other two relevant tensor structures are not. Hence, one may drop them in a first attempt on the complex structure of the quark. In this case, the physical amount of chiral symmetry breaking can only be obtained by an infrared enhancement of the dressing λ_1. This may introduce an additional complex structure into the gap equation, whose impact is hard to control. A similar analysis has been done very thoroughly in the pure Yang-Mills system, see [264]: the ensuing location and strength of complex singularities of ghost and gluon varied greatly, depending on the vertex dressings. This suggests that a conclusive study involves a self-consistent computation using all the three dominant tensor structures and an STI-consistent dressing for the classical tensor structure. We discuss the complex structure of the quark propagator in the scenario with STI vertices in Paragraph 5.4.3.2.2. A quantitative computational analysis of this scenario goes beyond the scope of the present study and will be presented elsewhere.

Here, we close the remaining gap in approximations studied in the literature: We numerically solve the gap equation with the input of a full realtime gluon propagator augmented

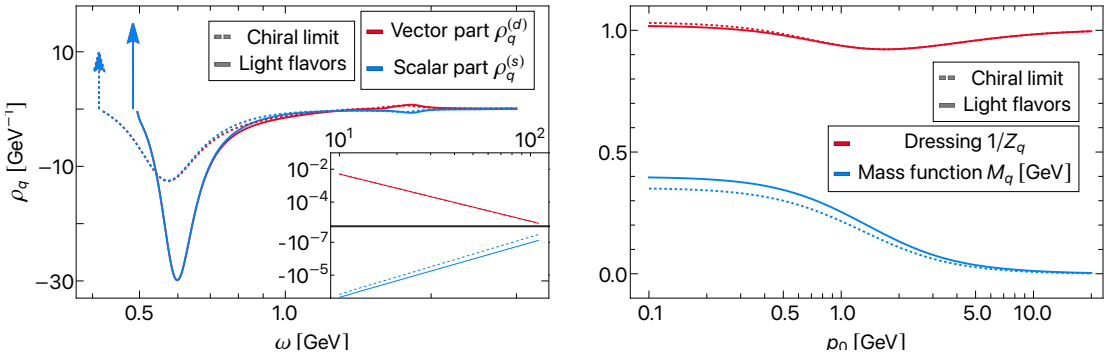

Abbildung 5.19.: DSE results for the quark propagator in the chiral limit (dashed) and for light quark flavors (solid). Left: Spectral function in the resonance-scattering split (5.63). Arrows indicate delta poles. Their height encodes the relative size of the residues. The numerical values of the pole positions and residues are given in Table 5.1. Note that the appearance of the delta poles is due to the resonance-scattering split. The scattering tail is predominantly negative, as necessitated by the sum rules (5.61). While the large negative peak in the scattering tail can be understood as part of the pole structure, the bump at about 1.8 GeV is connected to quark-gluon scattering. Right: Euclidean dressing and mass function. In the chiral limit, a constituent quark mass of $M_\chi(0) = 353$ MeV is obtained. For light quark flavors in the isospin symmetric approximation, we find $M_l(0) = 398$ MeV. The dressing function approaches a value above one in the IR. This feature is investigated in Appendix A.12 and attributed the use of a classical quark-gluon vertex in Landau gauge.

with classical vertices,

$$\mathbf{\Gamma}_\nu \approx -\mathrm{i} g_s \gamma_\nu \,. \tag{5.73}$$

In this approximation, the gap equation takes the simple form

$$\Sigma_{\bar{q}q}(p) = -g_s^2 \mathrm{C_f} \delta^{ab} Z_1^f \int_\lambda \int_q G_A^{\mu\nu}(q+p) \gamma_\mu \frac{1}{\mathrm{i}\not{q} + \lambda} \rho_q(\lambda) \gamma_\nu \,. \tag{5.74}$$

To account for a sufficient amount of chiral symmetry breaking, we amplify the value of the coupling constant such that the correct constituent quark masses are produced. Note that such a qualitative procedure necessarily leads to quark propagators with an enhanced ultraviolet tail. We emphasise that in this work, we do not aim at quantitatively improving its description in the Euclidean domain. Instead, the purpose of this study is a non-perturbative, direct investigation of the complex structure of the quark propagator using a full 2+1 flavor QCD gluon propagator.

5.4.3. Results

The spectral quark DSE introduced in Section 5.4.2 is solved in 2+1 flavor QCD for light quark flavors using the isospin-symmetric approximation. For the gluon propagator, we use the input discussed in Section 5.4.2.1. Our quark-gluon vertex truncation, the classical vertex approximation, is discussed in detail in Section 5.4.2.2. The strong coupling constant is set to $\alpha_s = 1.11$ such that in the chiral limit, a dynamical constituent quark mass of $M_\chi(0) \approx 350$ MeV is generated. Formally, the current quark mass for light flavors is fixed through the pion mass m_π and decay constant f_π by the Gell-Mann-Oakes-Renner (GMOR) relation. Here, we treat m_q as a phenomenological parameter instead. For $m_q = 1.2$ MeV, we obtain a constituent quark mass for light quark flavors of $M_l(0) \approx 400$ MeV.

The renormalisation conditions (5.67) are employed at $\mu = 30$ GeV. All solutions are obtained using the resonance-scattering split (5.63).

5.4.3.1. Numerical results

Our results for the quark spectral function for light quark flavors and in the chiral limit are shown in the left panel of Figure 5.19. Since the resonance-scattering split was employed, all spectral functions feature a genuine delta pole, with positive residue. The pole position is identical for both components, since it follows from the universal part of the quark propagator (5.55).

The peak moves towards larger frequencies going from the chiral limit towards the light flavors, as expected from the increase of the constituent quark mass. The residues of both components increase accordingly, since the mass function respectively the peak position appear in the residues, cf. (A.79). The residues of both components are nearly identical, as anticipated from (A.80). The numerical values of the peak positions and residues can be found in Table 5.1. We note that while the constituent quark mass increases about 50 MeV from the chiral limit to light flavors, the pole position moves up about 70 MeV. Since also the scattering tail grows in amplitude, a larger increase in the pole mass than in the constituent mass is necessary. The scattering tail is negative and therefore yields a negative contribution to the value of the mass function in the origin.

The scattering tails of both, vector and scalar components are predominantly negative. Since the residues are positive, this is necessitated by the quark spectral functions normalisation condition (5.61). Remarkably, for both components we find the sum rules to be fulfilled with an accuracy of about 1 ‰. We interpret the negative bump directly to the right of the delta pole as part of the actual pole structure, part of which is approximated by a delta pole in the resonance-scattering split. We discuss this in more detail in Section 5.4.1.1.

The second particular structure in the scattering tail is a small bump at about 1.8 GeV, which has opposite sign for vector and scalar components. We relate this structure to quark-gluon scattering: for the light flavors, its position is approximately at twice the quark mass pole position ω_0 plus the peak position of the gluon spectral function ω_A, i.e., $\omega_{\text{bump}} \approx 2\omega_0 + \omega_A$. Hence, the structure can be understood as a washed-out onset for quark-gluon scattering. This interpretation is supported by the fact that, when using a more strongly peaked gluon spectral function, e.g., the Yang-Mills reconstructions results of [243], the structure becomes much sharper and more pronounced. In the chiral limit, the bump position is less pronounced and difficult to locate, appears at a similar scale, however.

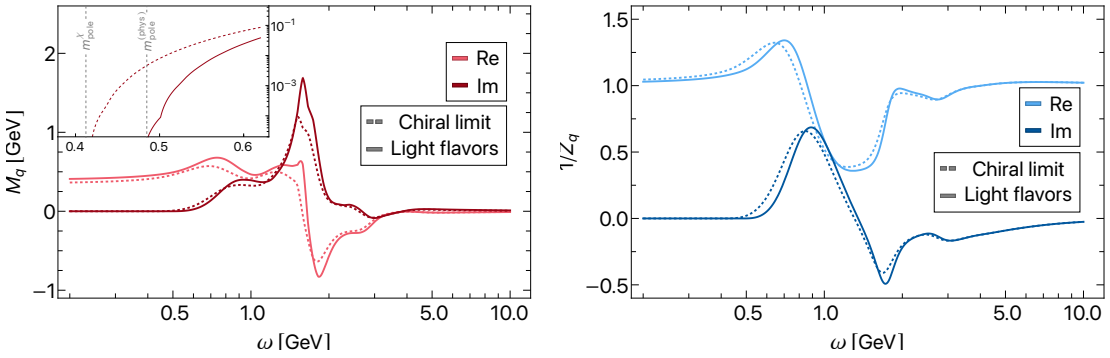

Abbildung 5.20.: Results for the quark propagator in Minkowski space in the chiral limit (dashed) and for light quark flavors (solid). Left: Mass function. The imaginary part shows a sharp onset at the respective pole mass m_{pole}, as shown in the inset. At about 1.8 GeV, the imaginary part shows a peak, while the real part has a zero crossing. These structures are attributed to quark-gluon scattering, compare the corresponding bump in the spectral function in the left panel of Figure 5.19. Right: Dressing function. The imaginary part shows a (negative) peak at about the quark-gluon scattering scale as well.

The inset in the left panel of Figure 5.19 shows the ultraviolet tails of both spectral function components. The opposite sign follows from the different anomalous dimensions of the quark wave and mass functions.

In the right panel of Figure 5.19 we display the Euclidean quark mass and dressing function. In the chiral limit, we obtain $M_\chi(0) = 353$ MeV, whereas for the light flavors, we have $M_l(0) = 398$ MeV. The dressing function $1/Z_q(p)$ rises above one in the deep IR, in contrast to results using more sophisticated vertex truncations [166, 171, 373, 380, 381]. We therefore attribute this feature to our vertex truncation, which can be considered too crude to yield quantitative statements about the Euclidean domain. In Appendix A.12 we demonstrate that at one-loop level, the IR behaviour of the dressing function is strongly gauge parameter dependent.

5.4.3.2. Analytic structure

Next, we present a general discussion of the analytic structure of the quark propagator in light of the numerical findings presented in the previous section. We start by discussing the effects of our truncation with classical vertices and the resonance-scattering split on the analytic structure of the result in Paragraph 5.4.3.2.1. In Paragraph 5.4.3.2.2, in particular the impact of STI vertex constructions and non-spectral gluon propagators are discussed.

	Chiral limit	Light flavors
m_{pole} [GeV]	0.412	0.485
$R^{(s)}$	0.768	1.15
$R^{(d)}$	0.766	1.15

Tabelle 5.1.: Results for the numerical parameters in the resonance-scattering split (5.63) describing the pole contribution of the quark spectral functions in Figure 5.19. We numerically verify that $R^{(s)} \approx R^{(d)}$, according to (A.80).

5.4.3.2.1. Present truncation Our truncation of the spectral quark DSE, discussed in detail in Section 5.4.2, along with resonance-scattering split (5.63) allows us to discuss the analytic structure of the quark propagator within the following scenario:

(i) The gluon propagator obeys a Källén-Lehmann representation and does not exhibit poles,

(ii) the quark propagator has a pole on the real axis at $\omega_0 = m_{\text{pole}}$,

(iii) only the classical tensor structure of the quark-gluon vertex contributes and its dressing is constant.

Note that certainly, (iii) does not hold true for the full quark-gluon vertex. The latter can be expected to show an imaginary part as well as a branch cut for specific combinations of real frequencies. As vertex models with (iii) are still used in practical calculations, we include this situation in the present discussion.

Under the above conditions, the universal part of the propagator (5.55) features a branch cut with support in $[m_{\text{pole}}, \infty)$. Since the branch cut of the gluon propagator starts in the origin, the branch point $m_{\text{pole}} \in \mathbb{R}$ of the quark propagator arises at the same point as its pole. This can be easily seen from the scalar part of the quark self-energy diagram, see (B.44). In consequence, the universal part shows a *branch point singularity*. Note that this alone does not necessarily violate the KL representation.

In addition to the branch point singularity, the propagator can show complex poles. As argued in Section 5.4.1, the presence or absence of complex poles depends on the sign of the mass functions imaginary part in the neighbourhood of the branch point m_{pole}. If the imaginary part is negative, the poles are on the second Riemann sheet and the quark propagator obeys the KL representation. If it is positive, the pole are on the first sheet and the KL representation is violated, see (5.62). In the left panel of Figure 5.20 we display the mass function on the real axis. We find that the imaginary part of the mass function approaches zero from above at m_{pole}. Although strictly speaking, (5.62) does not apply here since $\text{Im}\, M_q(m_{\text{pole}}) = 0$, our quark propagator still shows *complex poles*. This can be validated by calculating the corresponding spectral function with (5.60) without the resonance-scattering split (5.63): it shows a negative instead of a positive peak around m_{pole}, entailing that the propagators branch point singularity is negative. In consequence, the corresponding Euclidean propagator obtained through the spectral representation (5.56) does not reproduce the Euclidean results in the right panel of Figure 5.19.

We emphasise that the real pole of the spectral function is a built-in feature of the resonance-scattering split (5.63) and does not correspond to the quark propagators analytic structure described above. Rather, our results suggest that the quark propagator can

be very well approximated by the spectral functions in this approximation, displayed in Figure 5.19. In contradistinction, the condition for the appearance of complex poles formulated in (5.62) is general. An evaluation confirming the applicability of the resonance-scattering split at the level of the Euclidean propagator is presented in Appendix A.11.1.

5.4.3.2.2. STI vertices & non-spectral gluon propagators The full analytic structure of the quark propagator is a long-standing question. A clear answer is hindered by the need to truncate the infinite tower of diagrammatic equations for QCD correlation functions in functional approaches. For example, in [264] a strong dependence of the analytic structure of the gluon propagator on vertex models has been observed via a direct calculation in Yang-Mills theory for complex frequencies. For the quark propagator such a strong dependence has been observed in [266, 357, 359, 382], where complex conjugate poles in the quark propagator where found depending on the vertex model. In the following, we discuss the impact of the two input correlation functions in the quark gap equation on the analytic structure of the quark propagator: the quark-gluon vertex and gluon propagator. The discussion will put focus on sources of complex non-analyticities, which are consistent approximation of the full quark-gluon vertex and the complex structure of the gluon. To that end, we will use the examples of an STI vertex construction and a non-spectral gluon propagator.

Quark-gluon vertex As discussed in Section 5.4.2.2, the quark-gluon vertex is constrained by an STI which implements gauge consistency of the solution. A spectral vertex model fulfilling the particularly simple Abelian approximation (5.75) of the STI has been introduced in [383] and reads,

$$G_q(q)\Gamma_\mu(q,p)G_q(p) \approx \mathrm{i}g_s \int_\lambda \frac{1}{\mathrm{i}\not{q}+\lambda}\gamma_\mu \frac{1}{\mathrm{i}\not{p}+\lambda}\rho_q(\lambda)\,. \tag{5.75}$$

Equation (5.75) directly builds on the quark spectral representation (5.56) with the spectral function of the quark propagator ρ_q. Contracting (5.75) with $(p+q)_\mu$ leads to (5.72), multiplied from the left and right by quark propagators.

The STI vertex (5.75) can be directly used in the gap equation (5.66) when multiplying the latter with the quark propagator $G_q(p)$. Then, (5.66) reduces to

$$1 = \left(\mathrm{i}Z_2\not{p} + Z_{m_q}m_q\right)G_q(p) + g_s^2\mathrm{C_f}Z_1^f \int_\lambda\int_q G_A^{\mu\nu}(q+p)\gamma_\mu\frac{1}{\mathrm{i}\not{q}+\lambda}\gamma_\nu\frac{1}{\mathrm{i}\not{p}+\lambda}\rho_q(\lambda)\,. \tag{5.76}$$

By taking the imaginary part of (5.76), we project onto the spectral function of the quark propagator in the first term on the right hands side. Hence, the Abelian STI vertex defined in (5.75) reduces the gap equation from an initially non-linear to a linear equation for the quark spectral function. This greatly simplifies the task of numerically solving the equation.

In QED, (5.76) can be solved analytically if augmented with a classical spectral function ρ_A of a photon, i.e., a simple delta pole, as done in [40]. The resulting spectral function of the electron has the pole contribution at the electron mass as well as a scattering tail. Hence, no violation of the KL representation of the electron propagator has been found there. In turn, the electron propagator derived from the gap equation with classical vertices (5.74) has complex conjugate poles, in analogy to our results, see the discussion

in Paragraph 5.4.3.2.1. This shows impressively that gauge consistency of correlation functions plays a pivotal role for the existence of spectral representations. This observation can also heuristically be linked to the form of the gap equation with STI vertices: the STI turns the initially non-linear equation for the quark spectral function (5.64) with a complex solution into a linear one with a real solution (5.76).

Gluon propagator A pivotal ingredient in above discussion is the simple *spectral* structure of the photon/gluon propagator. In contrast to the photon spectral function, the spectral representation of the gluon is far more complicated. An extended representation features a spectral (KL) part and additional complex singularities.

The spectral part necessarily show negative parts at asymptotically large and small spectral values [243] in contradistinction to the positive photon spectral function. Moreover, complex poles have been observed in direct realtime calculations of the gluon propagator in different truncations of Yang-Mills theory [5], see Section 5.1, [264]. It has been argued in [5] resp. Section 5.1 that these poles render a consistent solution difficult and, as stated above, might ultimately be linked to inconsistencies in the respective truncation. Finally, precision reconstructions of Yang-Mills and QCD gluon propagators have been performed in a purely spectral manner without complex poles [3], see Section 5.3, [243, 258, 300], and with complex poles [104, 260, 270, 327].

A gauge boson propagator with complex conjugate poles can lead to further complex conjugate cuts in the quark propagator, violating the KL representation. This has been shown in [5] resp. Section 5.1 in the ghost-gluon system. The mechanism is very general: The complex singularities of the gluon propagator are dragged along by the loop momentum integration to form branch cuts in the ghost self-energy. Note that in the same fashion, the ordinary branch cut on the real axis in polarisation diagrams emerges from integrating two massive propagators. Therefore, the mechanism also applies in the quark gap equation with bare vertices, and complex conjugate cuts are produced when using a gluon with complex poles. The analytic structure w.r.t to loop momentum of the integrands in the gap equation with classical vertices (5.64) and with STI vertex (5.76) is identical, however. This leads us to the following result about the analytic structure of the quark propagator:

For a gluon with complex conjugate poles, the quark gap equation with either classical vertices (5.73) or STI vertices (5.75) leads to a violation of the spectral representation of the quark by complex conjugate cuts.

This observation may have far-reaching consequences for the direct realtime computation of scattering elements via DSE, Bethe-Salpeter, Faddeev and four-body equations, which will be discussed elsewhere.

5.4.4. Conclusion

In this section, we computed the quark spectral function of vacuum QCD for light quark flavors assuming isospin symmetry. The full quark propagator was obtained by solving its spectral Dyson-Schwinger equation using 2+1 flavor lattice QCD gluon propagator data [100, 101] and a classical quark-gluon vertex. We employed a spectral representation for the gluon propagator and used reconstruction results from Gaussian process regression [3], see Section 5.3, for the gluon spectral function.

In this approximation, the quark propagator shows a pair of complex conjugate poles located very close to the real axis. Nevertheless, the quark propagator can be very well

approximated to obey a Källén-Lehmann representation by using an analytic split into resonance and scattering contribution for the quark spectral function, cf. Section 5.4.1.1. Within this approximation, the quark spectral function shows a delta pole and a continuous scattering contribution. While the delta pole features a positive residue, the scattering tail is predominantly negative. The latter fact is necessitated by the sum rule of the quark spectral function.

In QED, it has been found that complex poles in the electron gap equation disappear when using STI-consistent vertex constructions. Similar observations have been made indirectly in QCD, implying that the quark obeys a spectral representation in this case. Even in the case of STI-consistent vertices this property is lost again when using a gluon propagator with complex conjugate poles also, as we argue in Paragraph 5.4.3.2.2.

Our investigation represents a further major step towards understanding the timelike structure of fundamental correlation functions of QCD. To further deepen this understanding, the impact of different quark-gluon vertex models on the complex structure of the quark propagator should be studied. Using an STI-consistent vertex construction together with a full gluon propagator in the spectral quark DSE can be regarded as a natural next step in this direction. Our approach enables to directly resolve the full complex momentum plane for different vertex models and gluon propagators.

Our results have a wide range of possible direct applications. In hydrodynamical simulations of the quark gluon plasma, QCD transport coefficients represent necessary input which can only be calculated from ab initio methods such as functional methods. The transport coefficients are linked to fundamental correlation functions via Kubo relations. Of particular interest is the heavy quark diffusion coefficient. Due to their massive nature, heavy quarks act as probes of the thermodynamic evolution of the quark gluon plasma. Our calculation for light quarks extends straightforwardly to that of the heavy quark propagators in realtime. Indeed, the systematic error of the present approximation is significantly reduced in the latter case, as both the quark propagator and the respective vertex carry less (chiral) dynamics. The calculation of the QCD hadron spectrum represents another promising application. Resonances can be determined from functional methods by solving resonance equations such as the Bethe-Salpeter equation in the timelike domain. As an input, the fundamental QCD correlation functions in the complex momentum plane are required. Here, our results for the quark propagator can directly be used.

6. Observables

In this chapter, we demonstrate how the spectral functional approach introduced in [1], see Chapter 4, can facilitate the calculation of various observables which directly base on fundamental realtime correlation function input. The computations cover a broad range of observables, encompassing transport coefficients, bound states, anomalous magnetic moments and scattering amplitudes, and directly make use of results for timelike correlators presented in Chapter 5.

In Section 6.1, basing on [8], we compute the non-perturbative strong coupling constant in the timelike domain, which finds direct application in the computation of, e.g., physical scattering amplitudes or the resonance spectrum of QCD. The computation is facilitated by the reconstruction results of [3], see Section 5.3: Establishing a spectral representation for the strong coupling constant, we use the reconstructed QCD gluon and ghost spectral functions to directly compute the spectral function of the coupling. This result is compared to a direct GPR reconstruction of the spectral function of the coupling constant from lattice data, demonstrating the reliability of GPR as a tool for spectral reconstruction.

In Section 6.2, we present preliminary results for a two-particle bound state in the scalar ϕ^4-theory in 2+1 dimensions facilitated by the realtime propagator results from the spectral DSE discussed in Section 4.1 resp. [1]. With this study, we lay the conceptual basis for the computation of hadronic resonances in QCD by combination of the spectral functional approach with resonance equations such as Bethe-Salpeter equations.

In Section 6.3, we compute the hadronic vacuum polarisation (HVP) in the full complex plane, including the calculation of the quark-photon vertex from a Bethe-Salpeter equation. The HVP represents the leading QCD contribution the anomalous magnetic moment of the muon, g–2. Our investigation focusses on the connection of the analytic structure of the HVP to that of its fundamental input correlation functions such as the quark propagator. This could yield insight into existence of complex singularities in the fundamental correlators, as the analytic structure of the HVP is tightly constrained.

In Section 6.4, we present results for the shear viscosity of Yang-Mills theory, based on an exact diagrammatic expression for the corresponding shear correlator of the energy momentum tensor. The shear viscosity is the dominant transport coefficient in the hydrodynamic evolution of the quark-gluon plasma, representing a crucial input for the simulation of ultrarelativistic heavy-ion collisions. Our setup only requires realtime gluon propagator data as an input, and we model the corresponding gluon spectral function by a Breit-Wigner peak.

6.1. Non-perturbative timelike strong coupling constant

This section presents results of [8]. The practical calculations were performed in collaboration with PhD student Jonas Turnwald from TU Darmstadt.

Physical scattering processes or the hadronic resonance spectrum represent prominent examples requiring first-principle input in the form of fundamental correlation functions in Minkowski spacetime. The strong coupling constant of QCD is a central ingredient in any of those, as it describes the interaction strength between the fundamental fields. One of its most salient features is asymptotic freedom, i.e., the decay towards small distances, which is well captured by perturbation theory. In contrast, the large distance or low energy behaviour, where the coupling grows large, can only be described via non-perturbative approaches such as lattice field theory or functional methods.

While the spectral functional approach introduced in [1], see Chapter 4, enables a direct realtime formulation of functional methods, on the lattice field theory side, direct realtime calculations are plagued by a severe sign problem. However, Minkowski correlation functions may also be obtained indirectly via spectral reconstruction of Euclidean data. This requires inverting the Källén-Lehmann (KL) spectral representation. The applicability of Gaussian process regression (GPR) to inverse problems of this type was discussed in [305]. The method has since been employed for the spectral reconstruction of ghost and gluon propagator data in [3], see Section 5.3, and the computation of glueball masses in [384].

In this section, we establish a spectral representation for the strong coupling constant and compute its spectral function, both directly and via spectral reconstruction. The calculation is facilitated by the reconstruction results for the ghost and gluon spectral functions of [3], see Section 5.3, based on propagator data from 2+1 flavor lattice QCD calculations with domain wall fermions at a physical pion mass [100, 101]. In doing so, we improve on the previous reconstruction approach by incorporating known asymptotic behaviour into the GP kernel. Based on this data, we also apply GPR directly to the reconstruction of the Taylor coupling. This non-trivial benchmark of our reconstruction method yields remarkable agreement between the direct and indirect results, thereby making a strong case for the reliability of spectral reconstruction via probabilistic inversion with GPR. On the other hand, our results feature a broad range of applications in the calculation of physical observables. Knowledge of the coupling constant in the full complex plane is required, e.g., in the treatment of hadronic bound states via Bethe-Salpeter equations. Furthermore, in the calculation of physical scattering amplitudes, the strong coupling in Minkowski space is a necessary ingredient.

This section is organised as follows. In Section 6.1.1, we connect the timelike strong coupling to scattering processes and derive its spectral representation. The extension of our spectral reconstruction approach granting improved control over the asymptotics is described in Section 6.1.2. Our results are presented in Section 6.1.3, and we conclude in Section 6.1.4.

6.1.1. Scattering processes & the timelike QCD coupling

Scattering processes and decays in QCD are described in terms of S-matrix elements. At low energies, the operators of the physical in and out states are complicated objects in terms of the fundamental QCD degrees of freedom. For instance, a description of the Compton scattering of protons requires the definition of the proton or, more generally, the

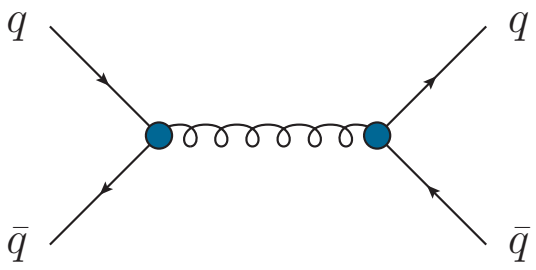

Abbildung 6.1.: $q\bar{q}$-scattering process with a one-gluon exchange. At sufficiently large timelike exchange momenta, this process plays an important role in its respective S-matrix elements. Consequently, all internal quantities are dressed. Blue blobs represent full vertices, and the wiggly internal line is a full gluon propagator.

nucleon operator in terms of its partonic constituents. Since, on the fundamental level, the partons are related to quarks and gluons, the building blocks of the respective S-matrix elements are quark-gluon and quark-photon scattering processes.

In most partonic models the fundamental scattering processes are approximated by effective models for the exchange process, such as one-gluon exchange potentials that carry the qualitative property of the gluon mass gap in QCD in terms of an effective mass. Ideally, however, they should be constructed from tree-level processes in QCD with full propagators and vertices, both of which carry on-shell, timelike, and spacelike momenta. The final S-matrix is gauge invariant, while the tree-level components making up the individual S-matrix element contributions are not. Moreover, the S-matrix admits a spectral representation, which is not necessarily present for the gauge-fixed correlation functions.

6.1.1.1. Cross-section of quark–anti-quark scattering events and the S-matrix element

In the present work, we undertake a first step towards such a determination of non-perturbative S-matrix building blocks in QCD. To that end, we compute the timelike strong coupling in 2+1 flavor QCD that governs the quark–anti-quark scattering process depicted in Figure 6.1. This diagram is at the core of many of the scattering processes used to determine the strong running coupling,

$$\alpha_s(p) = \frac{g_s^2(p)}{4\pi} \,. \tag{6.1}$$

It is also one of the fundamental building blocks of scattering processes in the Pomeron model [385–388]—such as the aforementioned Compton scattering of the proton—where it is typically estimated by one-gluon exchange models. For a review, see [389]; for a recent application related to the present work, see [390].

Assuming the incoming and outgoing quarks $q(p)$ and anti-quarks $\bar{q}(\bar{p})$ to be on-shell, $q\bar{q}$-scattering is similar to e^+e^- scattering. We expect this analogy to hold for sufficiently large timelike exchange momenta $p^2 \gtrsim 1\,\mathrm{GeV}^2$, whereas for $p^2 \lesssim 1\,\mathrm{GeV}^2$ we enter the hadronic, strongly correlated regime. There, the non-trivial embedding of the scattering

quarks and anti-quarks in hadrons becomes increasingly relevant, and quark–anti-quark scattering should be also considered off-shell alongside with further, more complicated processes; for a formulation in functional approaches, see [387].

Here, we concentrate on the one-gluon exchange diagram as one of the building blocks of the full S-matrix element. The associated tree-level process shown in Figure 6.1 consists of two full quark-gluon vertices, $\Gamma^{(3)}_{q\bar{q}A}(p_1,p_2,p)$ with the on-shell momenta p_1,p_2 for the incoming as well as $\Gamma^{(3)}_{q\bar{q}A}(p_3,p_4,-p)$ with on-shell $-p_3,-p_4$ for the outgoing quark and anti-quark, respectively. The relative minus sign is due to the notational convention in functional computations treating all momenta as incoming. The momentum p is that of the exchange gluon with the full gluon propagator $G_A(p)$. In combination, this process can be expressed as

$$\begin{aligned}\langle q(p_3)\bar{q}(p_4)|\,S\,|q(p_1)\bar{q}(p_2)\rangle \simeq \prod_{i=1}^{4} Z_q^{-1/2}(p_i)\Bigg\{ &\Big[\bar{u}_q(p_3)\Gamma^{(3)}_{q\bar{q}A}(p_3,p_4,p)v_q(p_4)\Big]^a_\mu \\ &\times G_A(p)\,\delta^{ab}\left(g^{\mu\nu}-\frac{p^\mu p^\nu}{p^2}\right)\Big[\bar{v}_q(p_2)\Gamma^{(3)}_{q\bar{q}A}(p_1,p_2,-p)u_q(p_1)\Big]^b_\nu\Bigg\}\,,\end{aligned} \tag{6.2}$$

where the (on-shell) quark wave functions Z_q originate in the LSZ reduction formula. Note that the quark and gluon wave functions are defined such that the quark and gluon propagators $G_q(p), G_A(p)$ are proportional to $1/Z_q(p), 1/Z_A(p)$, respectively. The scalar parts of the Euclidean propagators read

$$G_A(p)=\frac{1}{Z_A(p)}\frac{1}{p^2}\,,\quad G_q(p)=\frac{1}{Z_q(p)}\frac{1}{p^2+M_q^2(p)}\,, \tag{6.3}$$

where the full propagators are proportional to the identity in color space in the adjoint (gluon) and fundamental (quark) representations. The gluon propagator in the Landau gauge also carries the projection operator on the transverse subspace (see (6.2)), and the quark propagator is multiplied by $\mathrm{i}\not{p}+M_q(p)$. With (6.3), the standard LSZ factors carrying the pole residues are simply $Z_q^{-1/2}$, as already used in (6.2).

The S-matrix element (6.2) is renormalisation group (RG) invariant, as required. To see this explicitly, we reparametrise the vertices in terms of wave functions of the legs and an RG invariant core,

$$\Gamma^{(3)}_{q\bar{q}A}(p_i,p_j,p)=Z_q^{\frac{1}{2}}(p_i)Z_q^{\frac{1}{2}}(p_j)Z_A^{\frac{1}{2}}(p)\,\bar{\Gamma}^{(3)}_{q\bar{q}A}(p_i,p_j,p)\,, \tag{6.4}$$

where $\bar{\Gamma}^{(3)}_{q\bar{q}A}$ has the transformation properties of a running coupling, and naturally occurs in the S-matrix element. Inserting (6.4) into the S-matrix element (6.2) leads us to

$$\begin{aligned}\langle q(p_3)\bar{q}(p_4)|\,S\,|q(p_1)\bar{q}(p_2)\rangle \simeq &\Big[\bar{u}_q(p_3)\bar{\Gamma}^{(3)}_{q\bar{q}A}(p_3,p_4,p)v_q(p_4)\Big]^a_\mu \\ &\times\frac{1}{p^2}\,\delta^{ab}\left(g^{\mu\nu}-\frac{p^\mu p^\nu}{p^2}\right)\Big[\bar{v}_q(p_2)\bar{\Gamma}^{(3)}_{q\bar{q}A}(p_1,p_2,-p)u_q(p_1)\Big]^b_\nu\,.\end{aligned} \tag{6.5}$$

We restrict ourselves to the limit of large transfer momentum $p^2\equiv s$ of the scattering event with $p_1p_3=p_2p_4=s(1-\cos\theta)/4$ and scattering angle $\cos\theta=\boldsymbol{p}_1\boldsymbol{p}_3/(|\boldsymbol{p}_1||\boldsymbol{p}_3|)$. For small

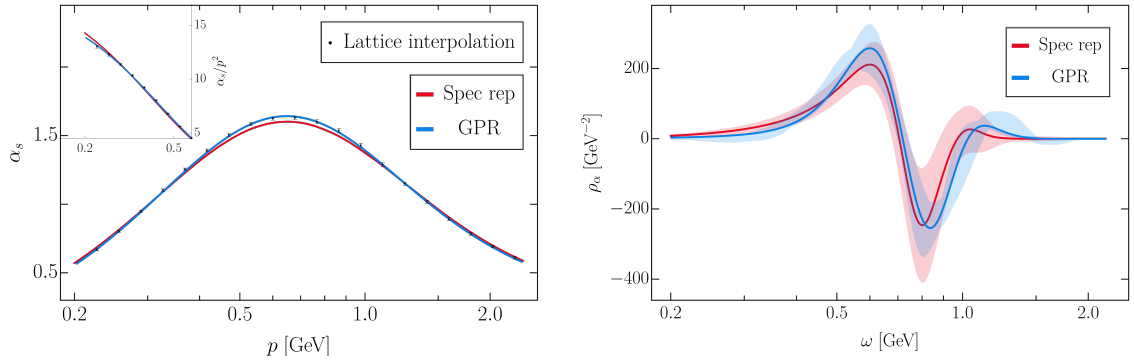

Abbildung 6.2.: Spacelike Taylor coupling α_s in QCD (left) and its spectral function $\rho_\alpha(\omega)$ (right). We compare the spectral function computed directly via (6.13) (red) to that obtained via reconstruction with GPR (blue). The direct calculation uses the reconstruction results for gluon and ghost spectral functions from [3] resp. Section 5.3. For the reconstruction, we use the gluon and ghost propagator data in 2+1 flavor lattice QCD from [100, 101]. Both the input spectral functions and the corresponding lattice data are displayed in Figure 6.3. The coupling spectral functions obtained via these two complementary approaches share all qualitative features, such as peak positions and heights as well as asymptotic behaviour. The peak structure can be connected to the respective peak structure of the gluon spectral function; see the right panel of Figure 6.3. The error band of the reconstruction result accounts for the change in the spectral function when varying the GP kernel parameters, whereas that of the direct calculation originates from propagating the uncertainty of the input. The Euclidean lattice data for the Taylor coupling α_s are displayed as grey squares in the left panel. We compare it to the data from its spectral representation (6.11) (red) as well as the reconstruction result (blue), showing that the representation holds and that the reconstruction accurately describes the lattice data.

s, we approach the reliability limit of our approximations. We return to the respective discussion after deriving our results.

Additionally, in a last approximation step we concentrate on the classical tensor structure $\gamma_\mu T^a$ in the full quark-gluon vertex,

$$\left[\bar{\Gamma}^{(3)}_{q\bar{q}A}(p_i, p_j, p)\right]^a_\mu \approx \mathrm{i}\,\gamma_\mu T^a \sqrt{4\pi\alpha_s(s)}\,. \tag{6.6}$$

Here, T^a is the $SU(3)$ generator in the fundamental representation and $\alpha_s(s)$, defined in (6.1), is the strong coupling of the quark-gluon scattering process in the s-channel. On the equation of motion, the $\not{p}_i$ terms vanish, and we obtain

$$|\bar{u}_q(p_3)\gamma_\mu T^a v_q(p_4)\,\bar{v}_q(p_2)\gamma_\mu T^a u_q(p_1)|^2 \to \frac{s^2}{9}\left(1+\cos^2\theta\right)\,, \tag{6.7}$$

in the high energy limit. In (6.7), we have performed an average/sum over spins and color

in the initial/final state. With (6.5) and (6.7), we arrive at

$$|\langle q(p_3)\bar{q}(p_4)|\, S\, |q(p_1)\bar{q}(p_2)\rangle|^2 \to \frac{1}{9}\left[4\pi\alpha_s(s)\right]^2\left(1+\cos^2\theta\right)\,, \tag{6.8}$$

with $\alpha_s(p)$ defined in (6.1). Equation (6.8) highlights the importance of the strong coupling constant $\alpha_s(s)$ for physical scattering processes. For the remainder of this work, we adopt the linear momentum argument $p=\sqrt{s}$ for the coupling.

In the present work, we shall compute the strong coupling $\alpha_s(p)$ and, hence, the above S-matrix element from its spectral representation for general complex frequencies, including the timelike momenta relevant for (6.8). We utilise that the strong coupling can be computed from the quark-gluon vertex, the three- and four-gluon vertices, as well as the ghost-gluon vertex. The computation involves the wave functions $Z_q(p), Z_A(p)$ of quarks and gluons as defined in (6.3) and the ghost wave function $Z_c(p)$ from (5.5). The avatars of the strong couplings are then defined as the (symmetric point) dressings of the classical tensor structures, see (6.4) and (6.6).

A final definition of the strong coupling in the Landau gauge is given by the propagator or Taylor coupling, that utilises Taylor's non-renormalisation theorem for the ghost-gluon vertex. This leads to the Taylor coupling, solely defined by the ghost and gluon dressing functions,

$$\alpha_s(p) = \frac{g_s^2}{4\pi}\frac{1}{Z_A(p)Z_c^2(p)}\,. \tag{6.9}$$

All strong coupling avatars have the same universal two-loop running but differ for infrared momenta; see [166]. For an evaluation of the infrared differences between the Taylor coupling and the quark-gluon coupling, see [171]. The latter regime is not accessible within the present approximation. Hence, we use the Taylor coupling (6.9) for the evaluation of (6.8). Its corresponding spectral function ρ_α is depicted in Figure 6.2. It allows us to compute the coupling $\alpha_s(p)$ for complex frequencies including timelike momenta; see Figure 6.4. Timelike result for the strong coupling in the perturbative domain can be found, e.g., in [391, 392].

6.1.1.2. Spectral representation

For the computation of (6.9), and hence of (6.8), we require the ghost and gluon propagators for timelike momenta. We assume that the propagators admit a KL representation, see (4.3).

The ghost propagator is known to exhibit a massless particle pole in the origin, entailing a delta pole at vanishing frequency in its spectral function ρ_c [2], see Section 5.2. The gluon spectral function ρ_A is continuous along the whole real frequency axis and is not expected to show distributional contributions. Taking into account the explicit forms of the spectral functions, the ghost and gluon dressing functions can be expressed as

$$\begin{aligned}\frac{1}{Z_A(p)} &= p^2\int_0^\infty \frac{\mathrm{d}\lambda}{\pi}\frac{\lambda\,\rho_A(\lambda)}{\lambda^2+p^2}\,,\\ \frac{1}{Z_c(p)} &= \frac{1}{Z_c^0}+p^2\int_0^\infty \frac{\mathrm{d}\lambda}{\pi}\frac{\lambda\,\tilde{\rho}_c(\lambda)}{\lambda^2+p^2}\,,\end{aligned} \tag{6.10}$$

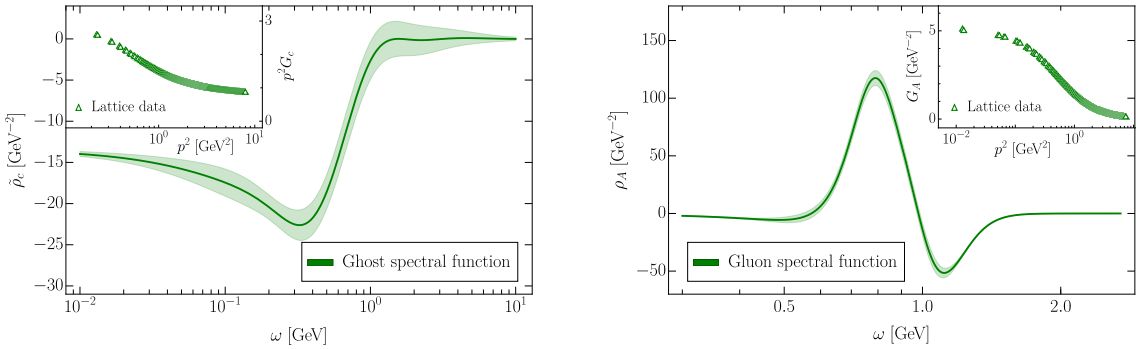

Abbildung 6.3.: The continuous parts of the ghost (left) and gluon (right) spectral functions obtained in [2] resp. Section 5.3 (see also Section 6.1.1.3), used here as input for the calculation of the coupling spectral function shown in the left panel of Figure 6.2 via its spectral representation (6.11). Shaded areas represent 1σ-bands of the statistical error of the mean prediction based on the available observations and precision. Note that we improved on the reconstruction of the gluon spectral function of [2], see Section 5.3, by including information of the asymptotic IR and UV behaviour; for details, see Appendix C.7.2. The UV and IR asymptotic regimes are assumed to be maximally large. This leads to a small reconstruction error without accounting for systematics, which is different from the error in Figure 5.17; see Appendix C.7.3 for a detailed discussion.

where $1/Z_c^0$ is the residue of the massless delta pole of ρ_c, and $\tilde{\rho}_c$ denotes the continuous part.

Given the existence of a spectral representation, the associated correlation function must obey certain symmetries and fulfil requirements about its infrared (IR) and ultraviolet (UV) asymptotics. It can be shown that the existence of spectral representations for the ghost and gluon propagators implies the existence of such a representation also for the Taylor coupling as defined in (6.9); see Appendix A.4 for details. Specifically, it is given by

$$\alpha_s(p) = p^2 \int_0^\infty \mathrm{d}\lambda \, \frac{\lambda \rho_\alpha(\lambda)}{p^2 + \lambda^2} \,. \tag{6.11}$$

With (6.11), the strong coupling spectral function is obtained from its retarded correlator via

$$\rho_\alpha(\omega) = -\frac{2}{\omega^2} \mathrm{Im}\, \alpha_s\big(-\mathrm{i}(\omega + \mathrm{i}0^+)\big) \,. \tag{6.12}$$

Now we use the definition of the Taylor coupling (6.9) and insert the spectral representations of ghost and gluon dressing functions (6.10). Then, the spectral function (6.12) of the coupling can be written as

$$\rho_\alpha(\omega) = -2\,\mathrm{Im}\left[\left(\int_0^\infty \frac{\mathrm{d}\lambda}{\pi} \frac{\lambda\, \rho_A(\lambda)}{\lambda^2 - \omega^2 + \mathrm{i}0^+}\right)\left(\frac{1}{Z_c^0} - \omega^2 \int_0^\infty \frac{\mathrm{d}\lambda}{\pi} \frac{\lambda\, \tilde{\rho}_c(\lambda)}{\lambda^2 - \omega^2 + \mathrm{i}0^+}\right)^2\right] . \tag{6.13}$$

Since the Taylor coupling decays logarithmically in the UV, its spectral function obeys a superconvergence condition [2], see Appendix A.8, [254], given by

$$\int_0^\infty \mathrm{d}\lambda\, \lambda \rho_\alpha(\lambda) = 0\,. \tag{6.14}$$

A treatment of the analytic low-frequency behaviour of continuous parts of the spectral functions has been initiated in [243]. In particular, it was shown that for correlation functions obeying a KL representation, a simple relation between the IR asymptotics of the correlator and its spectral function can be derived by differentiating with respect to the frequency. For the Taylor coupling we explicitly find

$$\lim_{\omega\to 0^+} \partial_\omega \rho_\alpha(\omega) = -2 \lim_{p\to 0^+} \partial_p \frac{\alpha_s(p)}{p^2}\,. \tag{6.15}$$

Hence, if the coupling approaches zero in the origin faster than p^2, we expect the spectral function to approach zero from below, and vice versa.

6.1.1.3. Lattice data

During the past two decades, lattice QCD results for Landau gauge two-point functions have advanced to an impressive quantitative level of precision; see, e.g., [97, 128, 182, 334–341, 343–345, 393, 394]. A recent review of lattice and functional results can be found in [395]. The lattice ghost dressing function and gluon propagator data used here have been obtained from recent calculations with 2+1 dynamical fermion flavors at the physical point [100, 101]. In particular, the ensembles of gauge configurations were generated by the RBC/UKQCD collaboration in [396–400], leveraging the Iwasaki gauge action [401] and the domain wall fermion action [402, 403] with a pion mass of 139 MeV. This choice of action (with a particular implementation of the Möbius kernel [404]) exhibits favourable chiral properties with a much smaller size in the fifth dimension than required by conventional domain wall fermions. These ensembles were utilised in [100, 101] for the calculation of the ghost and gluon propagators as well as the running of the strong coupling in the Taylor (miniMOM) scheme [405–407], and an associated effective charge [408].

The continuum limit of the lattice data is only obtained within a proper treatment of discretisation. For the Landau gauge propagators this is done via an analysis of the physical scaling violation described in [181], leading to continuum extrapolated propagators with the correct momentum running. The resulting gluon propagator and ghost dressing data are displayed in the insets of Figure 6.3. This data alongside with data from functional Yang-Mills theory and QCD [38, 95, 166, 171] have also been reconstructed in [3], see Section 5.3.

Since the lattice data for the propagators is available only on different momentum grids, the coupling, as defined in (6.9), is computed from a GP interpolation of the respective dressings. These interpolations are performed by direct GPR and therefore assume no general features of the underlying dressings apart from continuity. From this, we sample $N = 600$ logarithmically spaced values for the coupling (including errors) in the interval 0.23 GeV to 2.69 GeV, to be used in the reconstruction. For technical convenience, the coupling is extended perturbatively in the UV in order to control the amplitude of the UV asymptotics, see Appendix A.13. A subset of these points is shown in Figure 6.2. Here, we replace the error with the difference between the values computed as described above,

and the coupling obtained from the product of the ghost and gluon spectral functions, described around (6.13) and in Section 6.1.3.

6.1.2. GPR reconstruction with controlled asymptotics

GPR is a popular framework for the probabilistic modelling of functions from a finite number of data points; see [329, 330] for recent reviews and [331] for a textbook account. Example applications in high energy physics include the computation of parton distribution functions [332] and modelling backgrounds in detectors [409]. The method can also be used to predict solutions to linear inverse problems [305], i.e., when the only available data are indirect observations of the desired function after a linear forward process. This makes the approach suitable for spectral reconstruction. Importantly, it does not in general require choosing a particular functional basis. This avoids many of the numerical artefacts like additional peak structures that are commonly encountered when employing reconstruction algorithms with predetermined families of solutions, due to the presence of unrepresentable features. We summarise the main concepts in Appendix C.7.1; see also [3] resp. Section 5.3 and [384] for a comprehensive introduction as well as further details and references.

As an extension to this approach, in this paper we introduce a novel technical improvement that allows us to explicitly control the asymptotic behaviour of the predictions by specifying concrete functional forms in the appropriate limits only, without restricting the expressivity of the GP model in the region of interest. When considering different design choices for GPs, one often opts for so-called *universal* kernels. One prominent example also used in the present study is the radial basis function (RBF) kernel (5.53). The basis of kernel eigenfunctions of such universal kernels is infinite-dimensional. This allows for great flexibility in the reconstruction—universal kernels can describe any continuous function [410]. However, the GPR framework allows us to also incorporate further available prior information into the predictive distribution. In the context of spectral functions, the asymptotics in the IR and UV are often analytically tractable with perturbative or functional calculations, as well as formal relations to Euclidean data like (6.15). Hence, it is beneficial to introduce a bias by reducing the space of kernel eigenfunctions to the known behaviour of the target function. This can be achieved by applying Mercer's theorem [411] and constructing a kernel from the known asymptotic function $\phi(\omega)$ as

$$C(\omega, \omega') = \phi(\omega) \cdot \phi(\omega') \,. \tag{6.16}$$

Since the asymptotic behaviour is only specified in the appropriate limits, the full kernel is constructed as a combination of universal and restricted kernels using smooth step functions. With this approach, it becomes possible to smoothly transition between regions with an unknown functional basis—where a generic kernel like RBF is used—and regions with a specified basis; see Appendix C.7.2 for further details.

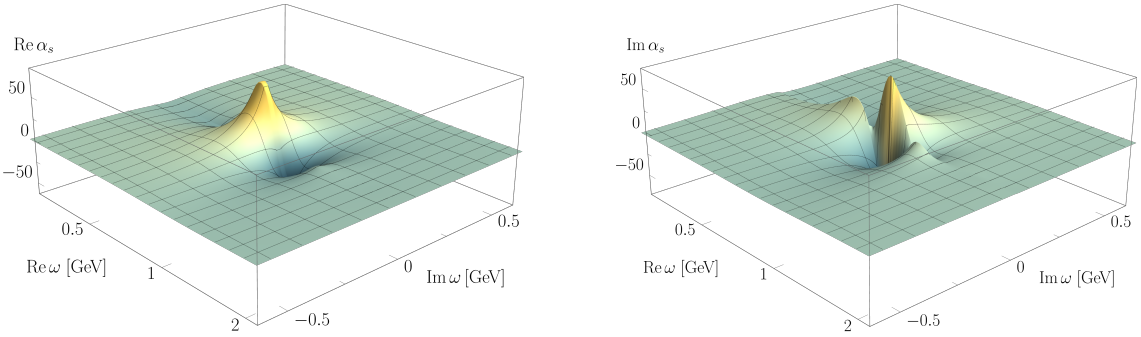

Abbildung 6.4.: Taylor coupling $\alpha_s(\omega)$ of 2+1 flavor QCD defined in (6.9) in the complex frequency right half plane (positive real frequencies), real (left) and imaginary part (right). The imaginary part explicitly shows the branch cut along the real frequency axis. The corresponding spectral function (red graph in the right panel of Figure 6.2) corresponds to the imaginary part of α_s at the upper half plane boundary of the branch cut, divided by ω^2. Both, the real and imaginary part, exhibit distinctive peaks which can be connected to the peak structure of the gluon spectral function; see right panel of Figure 6.3. The coupling decays logarithmically for increasing $|\omega|$.

6.1.3. Results

Our main result, the spectral function of the Taylor coupling (6.12) in QCD, is displayed in the right panel of Figure 6.2. It shows two variants: $\rho_\alpha^{\mathrm{GP}}$ from the reconstruction of the lattice QCD data via GPR, and $\rho_\alpha^{\mathrm{spec}}$ from the direct calculation based on the spectral representations of ghost and gluon propagators (6.13). The associated input spectral functions are shown in Figure 6.3. In this context, we have improved the reconstruction of the gluon propagator reported in [3] resp. Section 5.3 by explicitly incorporating the known IR and UV asymptotics with the method described in Section 6.1.2. The error band of $\rho_\alpha^{\mathrm{spec}}$ is obtained by propagating the errors of these input data. Importantly, the coupling spectral functions obtained via these two different approaches agree well within errors and share all qualitative features, such as peaks and asymptotic behaviour. In both results, we can identify two prominent peaks of similar size in positive and negative direction at roughly $\sim 0.6\,\mathrm{GeV}$ and $\sim 0.8\,\mathrm{GeV}$, along with a smaller positive peak at $\sim 1.1\,\mathrm{GeV}$. The spectral function $\rho_\alpha^{\mathrm{spec}}$ (6.13) allows for a direct interpretation of this behaviour: it is connected to the peak structure of the gluon spectral function, which carries information about the gluon mass gap; see the right panel of Figure 6.3. This information is extracted reliably from the lattice data with the GPR reconstruction.

In the reconstruction of the coupling, the correct asymptotic behaviour is enforced by smooth step functions at transition points μ_{IR} and μ_{UV}, while fully retaining the flexibility in the enclosed region where the GP kernel remains unrestricted and universal, see Appendix C.7.2 for details. As mentioned above, this procedure has also been applied to the ghost and gluon spectral functions used here. It enhances significantly the stability and reliability of the prediction by connecting it to analytic results at low and high frequencies, ensuring agreement with functional and perturbative results in the relevant limits without reducing the expressivity of the GP model in the domain of interest. While the prediction shows some variation with the choice of the transition midpoints, the peak positions and

heights remain remarkably stable; see Figure C.9. Hence, we choose the size of the regions dominated by the asymptotics to be as large as possible without increasing the χ^2 error of the reconstruction significantly; see Appendix C.7.3 and Figure C.10 for details. Furthermore, changing the parameters controlling the transition to the asymptotic behaviour accounts for the majority of the variation in the spectral function, while changing the parameters of the RBF kernel produces errors at least one order of magnitude smaller; see Appendix C.7.3 for details. The numerical values of all kernel hyperparameters are listed in Table C.3. Accordingly, the size of the dynamical region carrying information about the QCD mass gap is minimised, supporting the gluonic quasi-particle picture employed in various applications such as bound state studies and transport computations. Specifically, this suggests dismissing smaller negative peaks close to the dominant quasi-particle peak—they merely reflect the asymptotic behaviour and the superconvergence condition (6.14). As such, they are sensitive to changes in the gauge fixing parameter and infrared closure. This suggests that they carry physically relevant information only on a subleading level.

In the left panel of Figure 6.2, we compare the reconstructed Euclidean Taylor couplings to the result computed from the lattice data for the ghost and gluon propagators, as described in Section 6.1.1.3. Using the dressing function data obtained in this way, the resulting coupling is shown to decay towards small and large momenta. In correspondence to the scale of the peaks of the spectral function—reflecting the mass gap of the theory—also the peak of the coupling itself appears at $\sim 0.6\,\mathrm{GeV}$.

The blue curve in the left panel of Figure 6.2 represents the GPR reconstruction of the Taylor coupling lattice data, corresponding to $\rho_\alpha^{\mathrm{GP}}$. The red curve represents the coupling obtained via its spectral representation (6.11) using the directly computed spectral function $\rho_\alpha^{\mathrm{spec}}$. The calculation involves finite precision, both in the input data and in the integration. Hence, we expect a small, but not negligible, relative error. The decent agreement between this result and the lattice/GPR reconstruction result provides a highly non-trivial benchmark check. The error is well within our expectations, since the result obtained from the directly computed spectral function depends on the reconstructions of the gluon and ghost propagators. If the ghost and gluon spectral functions were describing their respective propagator data to infinite precision, we would also expect perfect agreement from analytic considerations; see Appendix A.4. Hence, the small difference can be attributed to systematic uncertainties present in the calculation. Please note that they do not contribute to the error bands, corresponding to the purely statistical error, shown in Figure 6.2.

In the inset of the left panel of Figure 6.2, we also show the Taylor coupling divided by p^2 for small Euclidean momenta p. The derivative of this quantity is connected to the asymptotic behaviour of the spectral function in the IR by (6.15). We observe that in the region where lattice data are available, the slope of α_s/p^2 is negative. In accordance with the analytic requirement (6.15), the slope of the spectral function is observed to be positive in this regime.

Finally, in Figure 6.4 we display the real and imaginary parts of the coupling in the full complex momentum plane. The data are obtained by evaluating the coupling spectral representation (6.11) with the directly calculated spectral function $\rho_\alpha^{\mathrm{spec}}$ in the complex plane. The branch cut in the imaginary part, responsible for the spectral representation, is clearly visible. As expected, no further non-analyticities in the complex plane are encountered and the coupling shows the expected decay behaviour towards large frequencies.

6.1.4. Conclusion

In this section, we have presented results for the spectral function of the strong coupling constant in QCD obtained through a direct calculation as well as a reconstruction via GPR. Assuming spectral representations for the ghost and gluon, we have derived the spectral representation of the Taylor coupling, which is fully determined by the ghost and gluon dressing functions. With this relation, we have calculated the associated spectral function as well as the coupling constant itself in the full complex plane. The required ghost and gluon spectral functions have been obtained from the reconstruction method put forward here, that takes into account explicitly the known asymptotic infrared and ultraviolet behaviour. They are depicted in Figure 6.3.

This result is complemented by a direct reconstruction of the Taylor coupling from its Euclidean data obtained from the spectral representation of the Euclidean ghost and gluon dressing functions. A comparison of the results, depicted in Figure 6.2, shows the excellent agreement between both approaches. The independent verification provides strong support for the accuracy of the result and also underlines the power of probabilistic inversion with GPR as a spectral reconstruction approach.

By expanding the GP kernel in suitable eigenfunctions based on Mercer's theorem, we extend the algorithm previously applied in [3], see Section 5.3 and [384], to now explicitly enforce the known asymptotic behaviour of the spectral function in the IR and UV. This substantially improves the reliability of the approach by properly encoding the analytically tractable regimes into the prediction while preserving the expressivity and universality of the GP model in the region of interest. The proposed modification is completely generic and may also be useful in other contexts where some analytic properties of a function to be modelled are known a priori, in particular if data scarcity is an issue.

Our results find direct application in the calculation of non-perturbative, physical scattering processes, where the strong coupling constant needs to be known at timelike momenta. While neglecting angular dependencies, the Taylor coupling considered here carries the correct RG running and hence scale-dependence of the strong coupling constant. Furthermore, it encodes genuine non-perturbative information through the input ghost and gluon dressing functions obtained from 2+1 flavor lattice QCD. This study hence paves the way for incorporating non-perturbative information from lattice field theory to functional methods in the calculation of physical, timelike scattering processes.

6.2. Two-particle bound state of the scalar ϕ^4-theory

This section presents preliminary results of [10]. All practical calculations have been carried out by Andrés Gómez in the context of his Master thesis, which I co-supervised.

Describing and understanding how the hadronic bound state spectrum emerges from the fundamental QCD degrees of freedom is a key theoretical challenge. Quark models represent a phenomenological approach to the description of in particular baryonic bound states. In this approach, gluonic interactions are integrated out and massive constituent quarks represent the fundamental degrees of freedom; for reviews, see [412, 413]. In lattice field theory, hadronic bound states are usually studied through their respective Euclidean quark n-point correlation functions. Fermionic determinants render computations at realistic bare quark masses computationally expensive up to infeasible, however, which is why one often resorts to quenched approximations where the quarks are treated as static; for recent reviews on hadronic bound states from lattice QCD, see [33, 34]. In functional approaches, bound states can be approached within the framework of Bethe-Salpeter equations (BSE) [414, 415]. Directly accessing the hadronic resonances through their respective poles in the timelike domain once again requires knowledge of the fundamental QCD correlation functions, which enter the BSE, at real and complex frequencies. Therefore, resonance computations represent another important application for the spectral functional approach. Other approaches of accessing the timelike region in BSEs involve, e.g., contour deformation or Cauchy's theorem, see, [94, 233, 266, 355, 357, 358, 360, 361, 363, 365, 366, 368–370].

In this section, we extend the toolbox of direct, timelike resonance computations by combining the BSE framework with the spectral functional approach. To that end, we employ the BSE of the four-point function in a scalar ϕ^4-theory in 2+1 dimensions to compute a low-lying two-particle bound state. In our setup, the BSE uses timelike propagator input from the spectral DSE of the scalar theory discussed in detail in [1] resp. Section 4.1. At the second order phase transition between the symmetric and broken regime of the theory, the bound state under investigation has been located at ~ 1.83 times the single-particle particle pole mass [247, 248]. Here, we approach the phase transition by considering the infinite coupling/vanishing mass gap limit of the theory.

This section is structured as follows. In Section 6.2.1, we briefly introduce our spectral BSE-DSE setup, and discuss explicit truncations thereof in Section 6.2.2. We present our results in Section 6.2.3 and conclude in Section 6.2.4.

6.2.1. Setup

We study a scalar ϕ^4-theory in $d = 2{+}1$. An introduction to the ϕ^4-theory is provided in [1], see Section 4.1, to which we refer for details. Here, we simply recap the most important aspects, and focus on the BSE-DSE system that we use to calculate the two-particle bound state in the scalar theory.

The classical action of our theory is given by

$$S[\varphi] = \int \mathrm{d}^3x \left[\frac{1}{2}(\partial_\mu\varphi)^2 + \frac{\lambda_\phi}{4!}(\varphi^2 - \phi_0^2)^2\right], \tag{6.17}$$

where φ refers to the full, fluctuating quantum field, and the action exhibits a $\mathbb{Z}_2$-symmetry. The field expectation value ϕ_0 in (6.17) is determined by the solution to the quantum equation of motion of the theory (4.97). At $\phi_0 = 0$, all odd n-point functions vanish, i.e.,

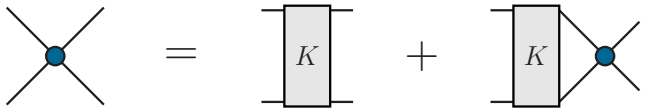

Abbildung 6.5.: The inhomogeneous BSE for the four-point function, see (6.18a). Notation as defined in Figure 2.1. The BSE kernel K is discussed in Section 6.2.2.3.

.

$\Gamma^{(2n+1)} \equiv 0$. A non-vanishing background $\phi_0 \neq 0$, however, gives rise to non-vanishing $\Gamma^{(2n+1)}$, and most importantly the three-vertex $\Gamma^{(3)}$.

6.2.1.1. Spectral Dyson-Schwinger equation for the propagator

In our setup, the propagator is determined from the spectral DSE, precisely as in Section 4.1, see also Figure 4.1, to which we refer for details. The propagator is hence parametrised by the Källén-Lehmann representation (4.3) in this section. We discuss particular truncations to the spectral DSE used in this section in Section 6.2.2.

6.2.1.2. Bethe-Salpeter equation for the four-point function

The four-point vertex obeys the inhomogeneous BSE [416, 417]

$$\Gamma^{(4)}(Q,p) = K(Q,p) + \int_q K(Q,q)G(q_+)G(q_-)\Gamma(Q,q)\,, \tag{6.18a}$$

with

$$q_\pm = q \pm \frac{Q}{2}\,, \tag{6.18b}$$

diagrammatically depicted in Figure 6.5. Due to the s-channel kinematics of the equation, a particularly symmetric momentum configuration for the four-point function is realised, i.e., $\Gamma^{(4)}(Q,p) := \Gamma^{(4)}(p_+,p_-,p_+,p_-)$, where Q is the total and p the relative incoming momentum, and $p_\pm$ is defined in analogy to (6.18b). In (6.18a), λ_ϕ is the tree-level four-vertex, and $K(P,k)$ is the two-particle interaction kernel, using the same notation for the momentum arguments as for the four-point function.

In proximity of a (bound state) pole, the four-point function can be parametrised via its Bethe-Salpeter amplitude Ψ,

$$\Gamma^{(4)}(Q,p) = \frac{\Psi(Q,p)\bar{\Psi}(Q,p)}{Q^2 - M^2}\,, \tag{6.19}$$

corresponding to the residue of the bound state pole. Accordingly, the Bethe-Salpeter amplitude Ψ can also be understood as measuring the overlap between the bound state and the four-point function.

Using the parametrisation (6.19), we are lead to the homogeneous BSE in terms of Ψ by evaluating the inhomogeneous BSE (6.18a) on the bound state pole $Q^2 = M^2$,

$$\Psi(Q,p) = \int_q K(Q,q)G(q_+)G(q_-)\Psi(Q,q), \tag{6.20}$$

A diagrammatic representation of the homogeneous BSE is given in Figure 6.6.

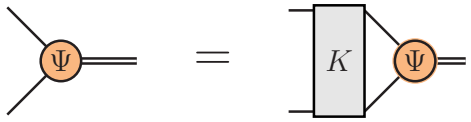

Abbildung 6.6.: The homogeneous Bethe-Salpeter equation for the Bethe-Salpeter wave function Ψ, defined via (6.19). Notation as defined in Figure 2.1. The BS wave function is denoted by an orange blob, while the bound state is marked by a double line. The BSE kernel K is discussed in Section 6.2.2.3.

Solution strategy In practical calculations, the BSE is solved on discrete grids for its momentum arguments. This allows to recast the BSE as a matrix equation

$$\Psi_a = \sum_b \mathcal{M}_{ab}\Psi_b \,, \tag{6.21}$$

where the indices a and b capture both momentum arguments, and

We resort to the usual procedure of solving the BSE by writing at as an eigenvalue equation,

$$\Lambda(M, \lambda_\phi)\Psi_a = \mathcal{M}_{ab}\Psi_b \,, \tag{6.22}$$

from which for a given coupling λ_ϕ, the solution is determined by numerically finding the bound state mass M such that $\Lambda(M, \lambda_\phi) = 1$. For details on the numerical procedure, we refer to [10].

6.2.2. Scaling truncations

Next, we turn towards the description of the truncations of our BSE-DSE system, see Section 6.2.1.2, used to study the two-particle bound state in the vicinity of the phase transition. In order to study the system close to the phase transition, the truncations which we employ should be suitable to study the infinite coupling limit of the theory. More precisely, since the system is known to exhibit scaling behaviour close to the phase transition, it is beneficial to employ truncations in which this scaling behaviour is easy to observe.

The constant background field ϕ_0 corresponds to the solution of the equation of motion (4.97). It is of particular relevance since it does not only act as an order parameter, expressing the amount of symmetry breaking, but also appears in practical calculations, e.g., in the spectral DSE for the propagator, see [1] resp. Section 4.1. ϕ_0 can be accessed by a Taylor expansion of the effective potential of the theory about ϕ_0 (4.26). The moments of the effective potential simply correspond to the 1PI correlation functions at vanishing momentum, cf. (4.27). We again neglect all correlations which vanish classically,

$$\Gamma^{(n>4)} \approx 0 \,, \tag{6.23}$$

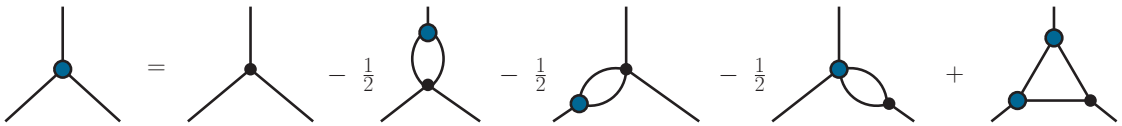

Abbildung 6.7.: Dyson-Schwinger equation for the three-point function $\Gamma^{(3)}$, truncated at one-loop. Notation as defined in Figure 2.1.

which allows us to link the field expectation value to the remaining vertices $\Gamma^{(3)}$ and $\Gamma^{(4)}$ via

$$\phi_0 = \frac{3\Gamma^{(3)}(0) - \sqrt{9\Gamma^{(3)}(0)^2 - 15\Gamma^{(4)}(0)m_{\text{cur}}^2}}{\Gamma^{(4)}(0)} \,. \tag{6.24}$$

The curvature mass m_{cur} is defined via (4.28). The sign in the solution of the corresponding quadratic equation for ϕ_0 is fixed by requiring to obtain the tree-level value $\phi_0 = \sqrt{3/\lambda_\phi}m$ in the limit $\lambda_\phi/m \to 0$.

6.2.2.1. Vertex approximations

Since we are dropping higher correlation functions (6.23), specifying approximations for the three- and four-point function closes our system of correlation functions. These vertices feature in the field expectation value in (6.24) as well as in the respective DSE/BSE for the propagator/four-point function. The approximations we are specifying below will be used in all of them. Since our focus lies on the infinite coupling limit, for simplicity we approximate both vertices at all incoming momenta vanishing,

$$\Gamma^{(3)}(p_1, p_2) \approx \Gamma^{(3)}(0) \,, \qquad \Gamma^{(4)}(p_1, p_2, p_3) \approx \Gamma^{(4)}(0) \,. \tag{6.25}$$

A particularly suitable model for the full four-vertex for studying the large coupling limit is the s-channel resummation already used in Section 4.1, given by

$$\Gamma^{(4)}(p) = \frac{\lambda_\phi}{1 + \lambda_\phi \Pi_{\text{fish}}(p)} \,, \tag{6.26}$$

with $\Pi_{\text{fish}}(p)$ defined as in (4.35). This form of the four-vertex (6.26) originates as a solution to the inhomogeneous BSE depicted in Figure 6.5 in an s-channel approximation for the loop-momentum-independent choice $K = \lambda_\phi$ for the kernel. Due to its resummation structure, (6.26) exhibits a well-behaved large coupling behaviour, making it suitable for the study at hand, see also the discussion below. The expansion in bubble diagrams corresponding to (6.26) is shown in Figure 4.8. We remark that for different choices of the kernel K, also the resummation (6.26) exhibits the two-particle bound state under investigation here, see [247, 248].

For determination of the bound state location, we do not want to restrict ourselves to the type of simplified BSE kernels leading to (6.26). In the homogeneous BSE (6.20), we employ a more general K, which we discuss in Section 6.2.2.3. Nevertheless, (6.26) represents a viable model for the s-channel dynamics in particular in the limit of large coupling. Furthermore, it has the welcome property of admitting a spectral representation, see (4.36).

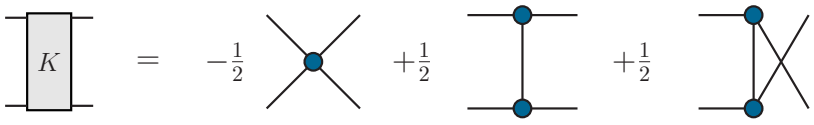

Abbildung 6.8.: BSE kernel K as obtained via its 2PI-exact relation (6.30) to the DSE self-energy from the one-loop diagrams skeleton-expanded DSE, see Figure 4.7. Note that the skeleton expansion violates the 2PI hierarchy underlying (6.30). Notation as defined in Figure 2.1.

As a simple model for the three-point function, we employ its corresponding DSE truncated at one-loop, see Figure 6.7. Evaluated at vanishing momentum, it reads

$$\begin{aligned}\Gamma^{(3)}(0) = S^{(3)}[\phi_0] - 2\lambda_\phi \Gamma^{(3)}(0)\Pi_{\text{fish}}(0) - S^{(3)}[\phi_0]\Gamma^{(4)}(0)\Pi_{\text{fish}}(0) \\ + \Gamma^{(3)}(0)^2 S^{(3)}[\phi_0]\Pi_{\text{tr}}(0)\,,\end{aligned} \tag{6.27}$$

where Π_{tr} is the triangle diagram and $S^{(3)}[\phi_0] = \lambda_\phi \phi_0$. Evaluated at vanishing momentum, the triangle diagram reads

$$\Pi_{\text{tr}}(0) = \frac{1}{4\pi}\int_{\lambda_1,\lambda_2,\lambda_3} \frac{\lambda_1\lambda_2\lambda_3\rho(\lambda_1)\rho(\lambda_2)\rho(\lambda_3)}{(\lambda_1+\lambda_2)(\lambda_2+\lambda_3)(\lambda_3+\lambda_1)}\,. \tag{6.28}$$

$S^{(3)}$ again depends on the full vertex $\Gamma^{(3)}(0)$ through ϕ_0, see (6.24). Equation (6.27) can be solved for $\Gamma^{(3)}(0)$ analytically, which completes our vertex truncation. The resulting expression for $\Gamma^{(3)}(0)$ is rather lengthy and not very illuminating, and will be presented in [10].

Large coupling scaling Our expansion is constructed to be suitable for studying the infinite coupling limit, since we wish to study the system close to the phase transition. It can be explicitly checked that for $\lambda_\phi \to \infty$, the three- and four-point function behave as

$$\Gamma^{(3)}(0) = \sqrt{\frac{2}{3}\frac{\Pi_{\text{fish}}(0)}{2\Pi_{\text{fish}}(0) - \frac{5}{2}\Gamma^{(2)}(0)\Pi_{\text{tr}}(0)}\frac{1}{\Pi_{\text{tr}}(0)}}\,, \qquad \Gamma^{(4)}(0) = \frac{1}{\Pi_{\text{fish}}(0)}\,. \tag{6.29}$$

Since both expressions are directly proportional to Feynman diagrams, scaling behaviour in the propagator will induce a corresponding scaling behaviour in the vertices, including a non-trivial anomalous dimension, as desired.

6.2.2.2. DSE in the skeleton expansion

We now discuss the explicit truncations for propagator DSE, cf. Figure 4.1. While in the infinite coupling limit, the full solution of the standard 1PI DSE of course shows the desired scaling behaviour, due to the classical vertices involved, the single diagrammatic contributions do not do so by themselves, but only in combination. Accessing the scaling behaviour in this form hence requires a delicate balance between the diagrams, which is most certainly destroyed by applying arbitrary truncations. Well suited for studying

scaling properties in DSEs is the skeleton expansion, in which all vertices are dressed. This ensures proper scaling behaviour of all diagrams, facilitated by our choice of vertex approximations, discussed in Section 6.2.2.1. Since the field expectation value ϕ_0 acts as an order parameter here, we expect it to become small towards the phase transition. This justifies dropping diagrams in the skeleton expansion with high powers of ϕ_0. For feasibility, we only consider diagrams up to order ϕ_0^2. The resulting diagrammatic representation of the propagator DSE in the skeleton expansion is depicted in Figure 4.7

6.2.2.3. BSE kernel

In usual BSE-DSE systems, the inherent 2PI hierarchy connects the BSE kernel K to the DSE self-energy Σ via

$$K(q_1 + q_2, q_1 - q_2) = 2\frac{\delta\Sigma(q_1)}{\delta G(q_2)}\,, \tag{6.30}$$

here with total/relative momentum $q_1 \pm q_2$; see, e.g., [417]. The derivative in (6.30) corresponds to cutting open one internal line of the self-energy diagrams. Resorting to the skeleton expansion, see Section 6.2.2.2, violates the usual 2PI hierarchy of the diagrams, and the previous exact connection (6.30) between Σ and K is lost. We will nevertheless use this relation as a guiding principle for the construction of the kernel here.

Restricting ourselves to the one-loop diagrams of the self-energy for the kernel construction via (6.30) suggests the following form for K,

$$K(Q,p) = K_{\text{contact}} + K_{\text{exchange}}(Q,p)\,, \tag{6.31a}$$

with

$$K_{\text{contact}} = -\frac{1}{2}\Gamma^{(4)}(0)\,, \qquad K_{\text{exchange}}(Q,p) = \frac{1}{2}\Gamma^{(3)}(0)^2\Big[G(Q) + G(p)\Big]\,, \tag{6.31b}$$

where we already substituted the vanishing-momentum approximation (6.25) for the vertices discussed in Section 6.2.2.1. The tadpole resp. polarisation diagram in Figure 4.7 gives rise to the contact term resp. t- and u-channel diagrams in Figure 6.8.

Since (6.30) is no longer exact, neither is (6.31b), despite being truncated. We exploit this fact in order to arrive at an error estimate for our truncation by replacing the full four-vertex in the contact term of the kernel, K_{contact}, by a classical vertex, i.e.,

$$K_{\text{contact}} = -\frac{\lambda_\phi}{2}\,. \tag{6.32}$$

Since the contact term constitutes the dominant contribution, we expect (6.32) to yield a conservative error estimate.

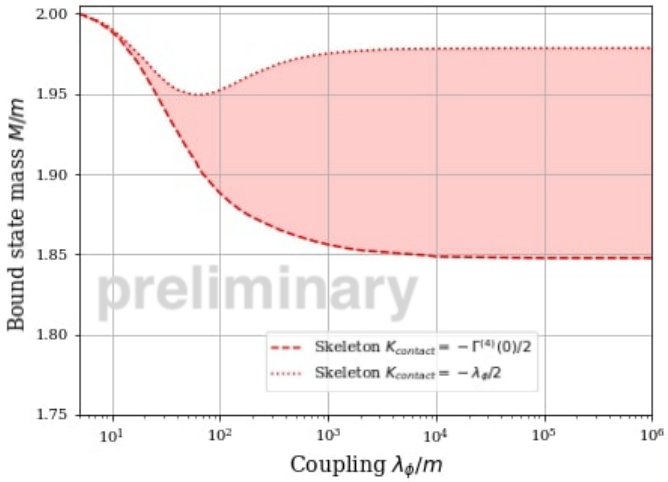

Abbildung 6.9.: Evolution of the two-particle bound state position M in units of the single particle pole mass m. We vary the contact term of the kernel in order to arrive at an uncertainty band for the bound state mass, see Section 6.2.2.3. The DSE for the propagator entering the BSE is solved in the skeleton expansion, see Section 6.2.2.2. The presented results are preliminary.

6.2.3. Results

We display our preliminary results for the evolution of the bound state mass as a function of the coupling in Figure 6.9. We observe a saturation of the bound state location in the infinite coupling limit, yielding the result

$$\frac{M}{m} \approx 1.85 - 1.98\,. \tag{6.33}$$

The error bands are obtained as discussed in Section 6.2.2.3. While the uncertainty is relatively large, the value for the bound state mass at the phase transition quoted in the literature, $M/m \approx 1.83$ [247, 248], is not included.

In Figure 6.10, we show the value of the background field ϕ_0 as obtained from the solution of the propagator DSE via (6.24). Towards infinite coupling, ϕ_0 saturates at a non-zero value. We conclude that within our present truncation, we are not able to reach the phase transition signalled by $\phi_0 \to 0$. This might explain the deviation of our result for the bound state mass from the literature. We further note that the field expectation does not reach its minimum towards infinite coupling, but at about $\lambda_\phi/m \approx 100$. The origin of this effect remains to be understood. Comparing with other DSE truncations should clarify if the effect is a truncation artefact.

On the other hand, we observe that the position of the bound state obtained using the BSE kernel constructed from the 2PI exact relation (6.30) is in fact relatively close to the literature value. In contrast, the value obtained using the classical contact kernel (6.32) differs significantly. Furthermore, it shows a non-monotonicity at about $\lambda_\phi/m \approx 70$ in form of a clear dip, before increasing again and approach its asymptotic value. While variation of truncations is a well-established technique for uncertainty estimation in functional approaches, this could also suggest that our particular choice of kernel variation is not well-chosen.

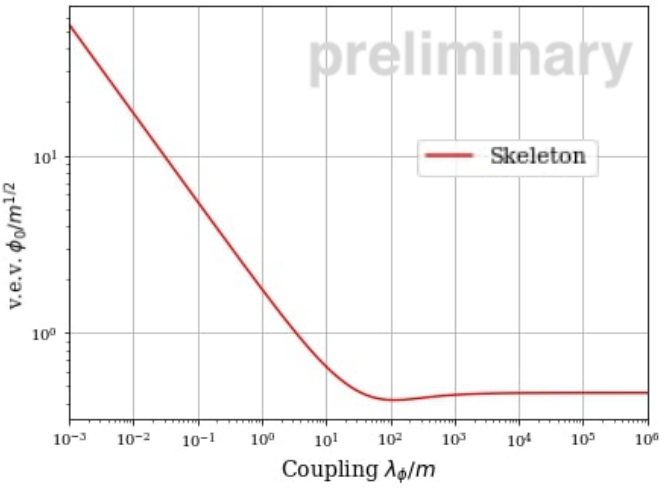

Abbildung 6.10.: Evolution of the field expectation value ϕ_0 in units of the single particle pole mass m. ϕ_0 acts as an order parameter, signalling the symmetry-broken regime for $\phi_0 \neq 0$, and is obtained via (6.24). The corresponding DSE for the propagator is solved in the skeleton expansion, see Section 6.2.2.2. We observe that ϕ_0 saturates in the infinite coupling limit. Hence, we do not seem to fully reach the phase boundary between to the symmetric regime. The presented results are preliminary.

More details on in particular from the DSE solution, including the three- and four-point function, can be found in [10].

6.2.4. Conclusion

In this section, we computed the mass of the low-lying two-particle bound state of the scalar ϕ^4-theory in $d = 2+1$. To that end, we used the homogeneous Bethe-Salpeter equation of the four-point function based on spectral function results from the spectral DSE presented in Section 4.1. To that end, we solve the corresponding DSE-BSE system over six orders of magnitude in the coupling parameter λ_ϕ, numerically approaching the infinite coupling limit where the system is expected to exhibit a phase transition. The bound state mass at the phase transition is known from lattice simulations to be $M/m \approx 1.83$. This does not agree with our estimate $M/m \approx 1.85 - 1.98$. Possible reasons for this deviation include a too large distance from the phase boundary, see Figure 6.10, and an unsuitable uncertainty estimate, see the discussion in Section 6.2.3.

As a natural next step, vertex truncations in which larger classes of diagrams are resummed than in the current s-channel resummation (4.34) could be employed. This could potentially lead to smaller background fields in the infinite coupling limit and hence closer to the phase transition. Furthermore, more sophisticated kernel variations for error estimation should be employed.

Despite the observed deviation from the literature value for the bound state mass, the present study demonstrates how the spectral functional approach can facilitate the determination of bound states from resonance equations. The current setup therefore constitutes the foundation for future investigation of glueballs and hadronic bound states in Yang-Mills theory and QCD with spectral functional realtime correlator input.

6.3. Hadronic vacuum polarisation & g–2

This project originated from a research stay at the Laboratory of Instrumentation and Experimental Particle Physics (LIP) in Lisbon with Gernot Eichmann. By the time of completion of this thesis, the investigation presented below was not yet completed. Since the project constitutes an important potential application of the spectral functional approach connected to observables, we nevertheless chose to document the work in progress.

The anomalous magnetic moment of the muon a_μ, better known as g–2, is one of the most precisely measured numbers in the Universe. Its theoretical prediction represents an important success story of the Standard Model of particle physics, combining quantum corrections from QED, QCD and the weak sector. Here, we will focus on the leading QCD contribution to g–2, whose calculation in particular involves the hadronic vacuum polarisation (HVP).

The HVP is commonly assumed to underlie tight restrictions on its analytic structure, entailing dispersive relations which allow for using high precision Euclidean lattice data for the corresponding g–2 contribution; for recent reviews, see [418, 419]. The great agreement between the theoretical prediction and experimental observations for g–2 and the HVP can be understood as a validation of these dispersive relations and, in consequence, the assumptions on the analytic structure of the HVP. A violation of these restrictions in a functional calculation that can be directly connected to complex non-analyticities of the input correlation functions, such as those in Section 5.1, would represent a strong case against such complex singularities in the fundamental correlation functions of QCD.

On the other hand, finding that independent of the analytic structure of the input, the HVP always keeps its analyticity, would allow investigating how complex non-analyticities present in the input disappear on the level of the HVP. These considerations lead to the idea of the project discussed in this section. Calculating the HVP requires the full quark propagator as well as the full quark-photon vertex as an input. While the quark propagator can be computed quite easily via a Dyson-Schwinger equation, see, e.g., Section 5.4, the quark-photon vertex is obtained via solving an inhomogeneous Bethe-Salpeter equation (BSE). The quark-photon vertex also requires the quark propagator as an input. Investigation of the analytic structure of the HVP in dependence of the analytic structure of its input could hence yield arguments for or against the existence of complex singularities in particular in the quark propagator.

After briefly introducing the defining relations for a_μ and its connection to the HVP in Section 6.3.1, we detail the calculation of the HVP in Section 6.3.2. In Section 6.3.3, we dive in into the calculation of the quark-photon vertex from its inhomogeneous BSE, including the computation of the quark propagator via its DSE.

6.3.1. Anomalous magnetic moment

The anomalous magnetic moment of the muon can be calculated from the muon-photon vertex Γ^μ_{muon}, which has the general tensorial decomposition

$$\Gamma^\mu_{\text{muon}}(Q,q) = \mathrm{i}\Lambda(p_+)\left[F_1(Q^2)\gamma^\mu + F_2(Q^2)\frac{\mathrm{i}}{4m_\mu}[\gamma^\mu,\not{Q}]\right]\Lambda(p_-)\,, \tag{6.34}$$

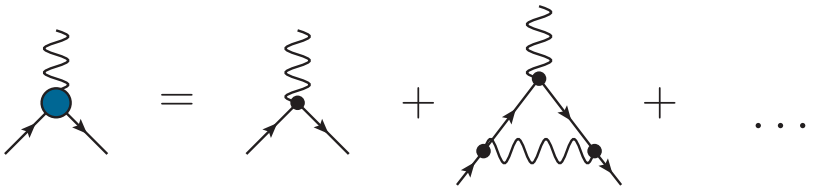

Abbildung 6.11.: Leading corrections in powers of the fine structure constant to the muon-photon vertex (6.34). Notation as defined in Figure 2.1. The leading correction is obtained by taking the muon propagators in the loop diagram to be classical.

with the positive energy projector

$$\Lambda(p) = \frac{1}{2}\left(\mathbb{1} + \frac{\not{p}}{\mathrm{i}m_\mu}\right) . \tag{6.35}$$

In (6.34), Q is the incoming photon momentum, while the in- and outgoing (anti-)muon momenta $p_\pm$ are defined in analogy to (6.18b).

Since the in- and outgoing muons are physical particles, they are on-shell, and we find

$$p_\pm^2 = -m_\mu^2 \qquad \Rightarrow \qquad p^2 = -m_\mu^2 - \frac{Q^2}{4} , \tag{6.36}$$

where m_μ is the muon mass. The on-shell condition for the muon momenta significantly simplifies the kinematics of the muon-photon vertex, eventually resulting in the simple two-dimensional tensor basis for the muon-photon vertex (6.34).

The dressing functions F_1 and F_2 appearing in (6.34) are called Dirac resp. Pauli form factor. The magnetic moment a_μ is obtained from the Pauli form Factor F_2 at vanishing momentum, which can be expanded in powers of the fine structure constant $\alpha \approx 1/137$,

$$a_\mu = F_2(0) = \frac{\alpha}{2\pi} + \mathcal{O}(\alpha^2) . \tag{6.37}$$

The corresponding diagrammatic expansion of the muon-photon vertex is depicted in Figure 6.11. The leading QCD contribution to a_μ is given by the first loop diagram, assuming the muon propagators to be classical, which is of leading order α^2. The hadronic vacuum polarisation Π enters a_μ via the dressed photon propagator, cf. Figure 6.12. Naive evaluation of the respective one-loop diagram in Figure 6.11 requires knowledge of the HVP at complex photon momenta $Q^2 \in \mathbb{C}$. Under the assumption that all non-analyticities of the HVP are restricted to the real frequency axis, one can derive the following simplified expression for its g–2 contribution,

$$a_\mu^{\mathrm{HVP}} = -\frac{\alpha}{4\pi m_\mu^4} \int_0^\infty \mathrm{d}Q^2 \frac{\left(Q^2 + 2m_\mu^2 - \sqrt{Q^2}\sqrt{Q^2+4m_\mu^2}\right)^2}{\sqrt{Q^2}\sqrt{Q^2+4m_\mu^2}} \Pi(Q^2) , \tag{6.38}$$

only requiring Π to be given at Euclidean photon momenta $Q^2 > 0$. This is the case, e.g., in lattice simulations or most functional approaches. Equation (6.38) therefore represents

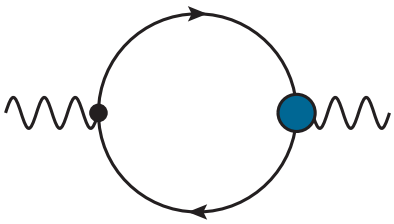

Abbildung 6.12.: Diagrammatic representation of the hadronic vacuum polarisation (6.39). The HVP enters g–2 as the leading QCD contribution to the full photon propagator in the leading order loop diagram of the muon-photon vertex depicted in Figure 6.11. Notation as defined in Figure 2.1.

a cornerstone of the theoretical efforts of calculating the muon's anomalous magnetic moment. Equation (6.38) has yield theoretical predictions that have been verified to great accuracy by experiments. By calculating the HVP in the full complex plane, our study allows for testing if the underlying analyticity assumption holds in functional approaches independent of truncation schemes. If so, this further could yield insight into possible mechanisms how complex singularities in the input correlation functions, existing in particular in the truncation discussed below, are cancelled and do not show up in the HVP.

6.3.2. HVP

The hadronic vacuum polarisation encodes the QCD contribution to the photon self-energy, see Figure 6.12. It is defined by

$$\Pi^{\mu\nu}(Q) = e^2 \int_q \mathrm{Tr}\left[Z_2 \mathrm{i}\gamma^\mu G_q(q_+)\Gamma^\mu(Q,q)G_q(q_-)\right], \tag{6.39}$$

where $e^2 = 4\pi\alpha$ is the electric charge, Z_2 the quark wave function renormalisation and G_q the full quark propagator, see (5.54). The momenta $q_\pm$ are defined as in (6.18b). Γ^μ here represents the dressed quark-photon vertex, which can be parametrised as

$$\Gamma^\mu(Q,q) = \sum_{j=1}^{4} g_j\left(p^2,\omega,Q^2\right) iG_j^\mu(Q,p) + \sum_{j=1}^{8} f_j\left(p^2,\omega,Q^2\right) iT_j^\mu(Q,p), \tag{6.40}$$

where the g_j and f_j represent the transverse resp. longitudinal dressing functions of the quark-photon vertex. The corresponding tensor basis elements G_j^μ, F_j^μ are defined in Appendix B.7. The Lorentz traces are carried out explicitly in Appendix B.8 [420].

We can decompose the unrenormalised HVP into a transverse and diagonal part as

$$\Pi^{\mu\nu}(Q) = \Pi(Q^2)Q^2\Pi_\perp^{\mu\nu}(Q) + \widetilde{\Pi}(Q^2)\delta^{\mu\nu}, \tag{6.41}$$

with the transverse projection operator $\Pi_\perp$ as defined in (3.64). In (6.41), we made explicit that the dressing functions Π and $\tilde{\Pi}$ are functions of Q^2 and hence Lorentz invariant.

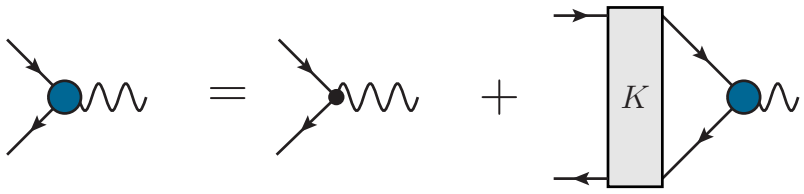

Abbildung 6.13.: Inhomogeneous Bethe-Salpeter equation for the quark-photon vertex (6.48). Here, we use the rainbow ladder truncation (6.45) for the kernel K. Notation as defined in Figure 2.1.

Projecting (6.39) onto the diagonal part of the tensor decomposition (6.41) yields that the diagonal part vanishes,

$$\widetilde{\Pi}(Q^2) \equiv 0\,, \tag{6.42}$$

by means of the WTI for the quark-photon vertex,

$$Q^\mu \Gamma^\mu(Q,p) = \Gamma^{(2)}_{\bar{q}q}(p_+) - \Gamma^{(2)}_{\bar{q}q}(p_-)\,. \tag{6.43}$$

Unlike for the Abelian STI of the quark-gluon vertex (5.72), we absorbed the gauge coupling into the vertex in (6.43).

We are left with the renormalisation of the transverse part of the HVP. In QED, the perturbative domain is the low energy region. The renormalised transverse HVP component entering the g–2 predictions is hence

$$\Pi_R(Q) = \Pi(Q) - \Pi(0)\,. \tag{6.44}$$

6.3.3. Quark-photon vertex

The quark-photon vertex (QPV) can be determined from its BSE, for a recent review, see [266]. Here, we employ the rainbow ladder truncation, approximating the BSE kernel K by a one-gluon exchange. To that end, we define the quark-gluon interaction kernel

$$g(p) = Z_2^2 \frac{16\pi}{3} \frac{\alpha(p^2)}{p^2}\,. \tag{6.45}$$

For the gauge coupling, we employ the Maris-Tandy model [421, 422],

$$\alpha(p) = \pi\eta^7 x^2 e^{-\eta^2 x} + \frac{2\pi\gamma_m \left(1 - e^{-p^2/\Lambda_t^2}\right)}{\ln\left[e^2 - 1 + \left(1 + p^2/\Lambda_{\mathrm{QCD}}^2\right)^2\right]} \qquad \text{with} \qquad x = \frac{p^2}{\Lambda^2}\,. \tag{6.46}$$

The first summand models the infrared behaviour of the interaction, effectively controlling the dynamical generation of the quark masses. The second term is responsible for the correct perturbative behaviour. Typical values for the interaction parameters in (6.46) are $\eta = 1.8, \gamma_m = 12/25, \Lambda_t = 1\,\mathrm{GeV}, \Lambda_{\mathrm{QCD}} = 0.234\,\mathrm{GeV}$ and $\Lambda = 0.72\,\mathrm{GeV}$.

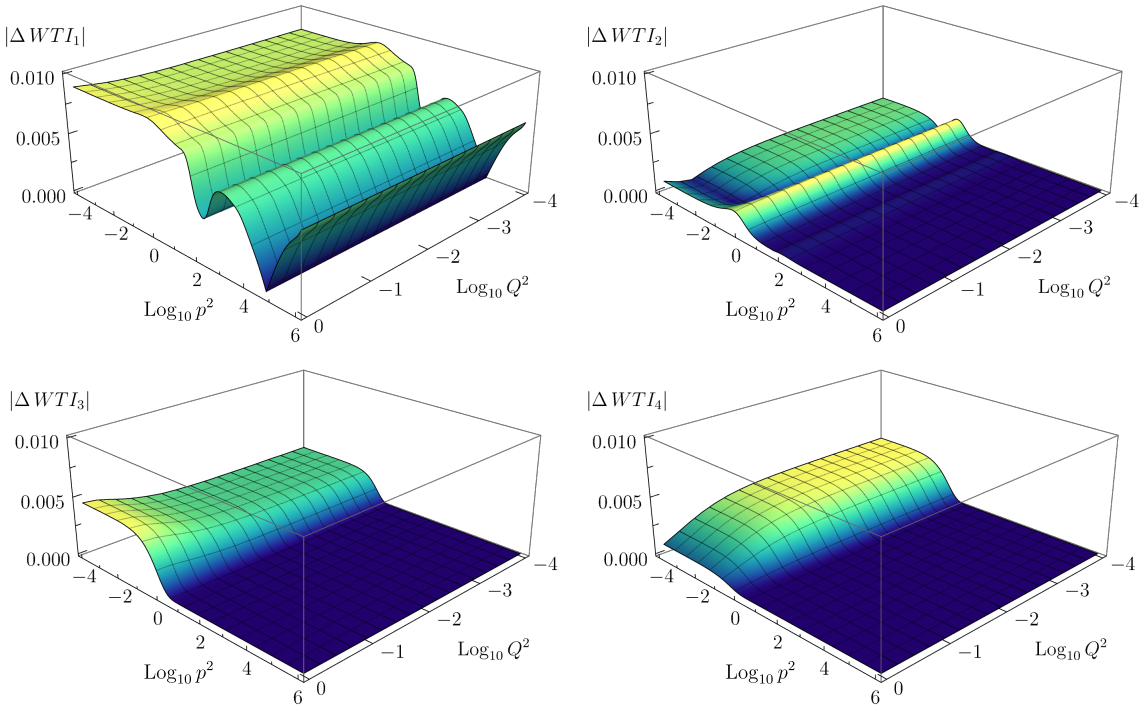

Abbildung 6.14.: Ward-Takahashi identities of the quark-photon vertex for Euclidean total momentum Q^2 and relative momentum k^2. Plotted are difference in absolute value of the left and right-hand side of (6.43), numbered accordingly. The dressing functions of the QPV (except for g_4) are of order 1. Hence, the WTIs are well fulfilled. We observed that the fulfilment of the WTIs improves with finer grids; details on the numerical implementation are given in Appendix C.8.

In practical calculations, it has been found that the introduction of a Pauli-Villars cutoff in the interaction kernel is advantageous for the fulfilment of the WTI (6.43), see, e.g., [266]. This amounts to multiplying the interaction kernel (6.45) by a factor

$$\frac{1}{1+p^2/\Lambda_{\mathrm{PV}}^2}\,. \tag{6.47}$$

For the cutoff scale, we use $\Lambda_{\mathrm{PV}} = 200$ GeV.

The resulting BSE with rainbow ladder interaction kernel (6.45) reads

$$\Gamma^\mu(Q,p) = Z_2 \mathrm{i}\gamma^\mu - \int_q g(p-q)\Pi_\perp^{\alpha\beta}(p-q)\gamma^\alpha G_q(q_+)\Gamma^\mu(Q,q)G_q(q_-)\gamma^\beta\,. \tag{6.48}$$

The transverse projection operator $\Pi_\perp$ (3.64) arises from the Landau gauge gluon propagator. The quark propagator G_q represents an input for the equation, which is directly connected to the quark-photon vertex via the WTI (6.43), however. We will determine the quark propagator from its Dyson-Schwinger equation in Section 6.3.3.1, and postpone the details of the calculation to that section. Instead, we focus on the explicit consequences of the WTI (6.43). To that end, we make use of the decomposition (6.40), splitting the

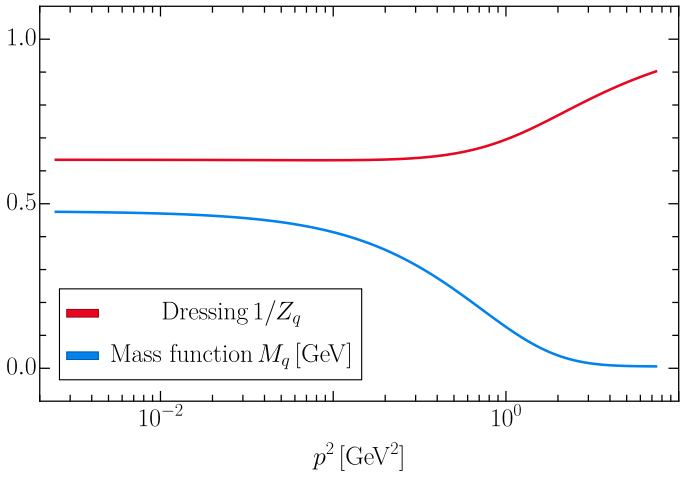

Abbildung 6.15.: Solution for the quark DSE in the rainbow ladder truncation (6.50) with Maris-Tandy interaction (6.46). Left, we show the Euclidean dressing functions. The mass function shows dynamical chiral symmetry breaking with a constituent quark mass between 450 and 500 MeV. On the right, we show the leading complex poles of the quark propagator which are known to appear in the Maris-Tandy model [354]. These poles are linked to the complex poles appearing in the hadronic vacuum polarisation, cf. Figure 6.17.

QPV into longitudinal and transverse tensor structures. Contraction with the photon momentum in the WTI then projects onto the longitudinal tensor structures, and entails the explicit relations

$$g_1 = \frac{1}{2}\big(Z_q(q_+) + Z_q(q_-)\big)\,, \qquad g_2 = 2\,\frac{Z_q(q_+) - Z_q(q_-)}{q_+^2 - q_-^2}\,,$$
$$g_3 = 2\,\frac{M_q(q_-)Z_q(q_-) - M_q(q_+)Z_q(q_+)}{q_+^2 - q_-^2}\,, \qquad g_4 = 0\,. \tag{6.49}$$

Due to the large amount of tensor structure of the quark-gluon vertex, numerically solving the BSE (6.48) is a costly task. The dynamics is carried by the twelve dressing functions, for which the BSE forms a system of twelve coupled equations. Getting the equation into a form which can be handled well numerically requires a considerable amount of algebraic work, which is detailed in Appendix B.7 [420]. In the following, we will just discuss the results. Numerical details on the solution of the BSE are discussed in Appendix C.8.

6.3.3.1. Quark propagator DSE

The quark propagator for calculation of the quark-photon vertex is obtained from its Dyson-Schwinger equation. Since the quark propagator DSE was already introduced in Section 5.4, we will be brief here.

The quark DSE has the general form (5.64), for a diagrammatic representation see Figure 5.18. While in Section 5.4, we were free to specify a truncation for the DSE and

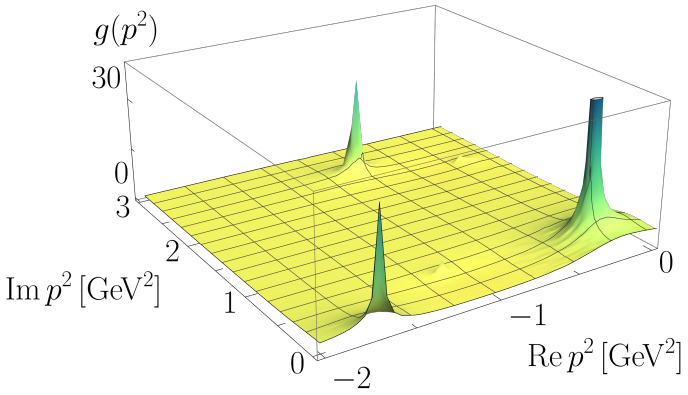

Abbildung 6.16.: Solution for the quark DSE in the rainbow ladder truncation (6.50) with Maris-Tandy interaction (6.46). We show the leading complex poles of the quark propagator, here in the universal part of the quark propagator (5.55), which are known to appear in the Maris-Tandy model [354]. These poles are linked to the complex poles appearing in the hadronic vacuum polarisation, cf. Figure 6.17.

employed a full gluon propagator, here, the situation is different. The 2-PI BSE and 1-PI DSE kernels are related via functional derivative with respect to an internal propagator line (6.30), see also, e.g., [417, 423]. For a consistent treatment of coupled BSE-DSE systems like ours, these relations need to be taken into account. Violation of these constraints typically manifests itself at the level of symmetry identities like the WTI (6.43). For mechanisms which are sensitive to the amount of symmetry breaking in the system, such as dynamical chiral symmetry breaking, a consistent treatment of the kernels is hence crucial.

Since we want to use the quark propagator in the quark-photon vertex BSE, our DSE truncation is fixed by the truncation specified for the BSE kernel, or vice versa. This is the rainbow ladder truncation, and the resulting quark self-energy diagram reads

$$\Sigma_{\bar{q}q}(p) = \int_q g(p-q)\Pi_\perp^{\alpha\beta}(p-q)\gamma^\alpha G_q(q)\gamma^\beta\,. \tag{6.50}$$

The rainbow ladder interaction kernel g is given by (6.45), in which the gauge coupling again is specified by the Maris-Tandy model (6.46). Renormalisation is performed as detailed in Appendix B.6.2. We employ a renormalisation scale of $\mu = 19\,\mathrm{GeV}$ with a current quark mass of $m_q = 4$ MeV.

The resulting solution is displayed in Figure 6.15. The mass function exhibits dynamical chiral symmetry breaking, yielding a constituent quark mass between 450 and 500 MeV. In the Euclidean domain, the quark dressing functions of the Maris-Tandy model are similar to those obtained with a bare quark-gluon vertex and a full gluon propagator, see right panel of Figure 5.19. The situation is different in the complex plane, however. In the Maris-Tandy model, the interaction kernel leads to numerous poles in the $\mathrm{Re}\ p^2 < 0$ half-plane, see Figure 6.16 and also [266, 354, 362]. In Section 5.4, however, only a single pair of complex poles is present in direct vicinity of the real axis. This demonstrates the strong influence of truncations and particular vertex models on the complex structure of correlation functions and in particular propagators. Numerical details on the solution of the DSE are discussed in Appendix C.8.

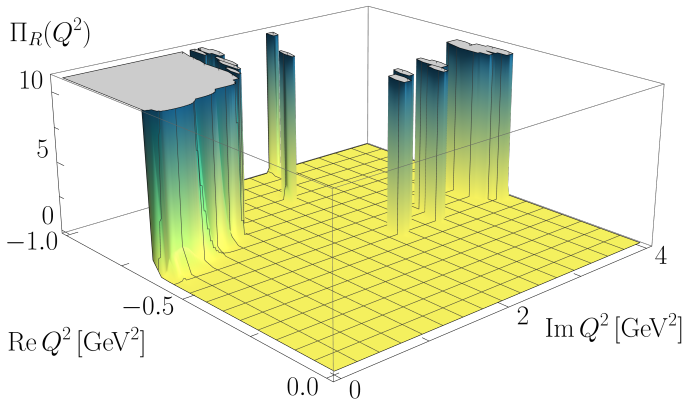

Abbildung 6.17.: Renormalised hadronic vacuum polarisation in the upper half of the timelike region in the complex plane. The sharp structure on the negative real Q^2 is the ρ-meson pole, located at $\sqrt{Q^2} \approx 740$ MeV. Beyond the ρ-meson pole, the power method employed for solving the quark-photon vertex BSE (6.48) no longer converges, resulting in the grey shaded region. Hence, only the leading singularity can be resolved, as seen in the figure. The isolated sharp peaks at non-vanishing Im Q^2 arise from the complex singularities of the quark propagator in the Maris-Tandy model (6.46) in the integration domain, see Figure 6.16 and also [266, 354, 362]. These complex spikes are expected to vanish when properly treating the quark propagator's poles, e.g., via contour deformation or Cauchy's theorem.

6.3.4. Results

In Figure 6.17, we display the renormalised hadronic vacuum polarisation in the upper half of the timelike region in the complex plane. The ρ-meson resonance can be identified as the leading singularity on the negative real Q^2 axis. The iteration fails to converge beyond the first pole, which is a known feature of iterative solution schemes. We can hence identify the location of the ρ-meson pole as the onset of the grey shaded area on the real axis, yielding a pole position of about $\sqrt{Q^2} \approx 740$ MeV.

The sharp peaks at non-vanishing Im Q^2 however can be assigned to the improper treatment of the complex poles of the quark propagator in the Maris-Tandy model, see Figure 6.16 and also [266, 354, 362]. In the current implementation, integration over internal momenta in the BSE (6.48) is performed parallelly to the real q^2 axis, regardless of possible poles of the quark propagator in the integration domain. When such a pole is encountered, the integral converges to a wrong result, leading to corresponding spikes in the QPV. The unphysical peaks of the QPV then propagate into the HVP. While for the ρ-meson pole visible in Figure 6.17, this is indeed a desired physical effect since this pole in the QPV is not due to the poles of the quark propagators, for the complex spikes shown this is not the case. In a proper treatment of the quark propagator's complex singularities, these are explicitly taken into account by, e.g., contour deformation or Cauchy's theorem. Implementation of these methods will be deferred to future work. That being said, it is still not clear how the complex singularities of the quark propagator will influence the

complex structure of the QPV and, in consequence, the HVP. A reasonable scenario is that these complex poles draw branch cuts in the complex domain, analogous to the case of complex poles in the gluon propagator discussed in Section 5.1. In this case, the explicit expression (6.39) for the HVP suggests that these additional complex cuts will directly show up in the HVP as well. The reason for this is that the external momentum of the diagram appears without addition of loop momentum in the second argument of the QPV on the RHS, i.e., is not integrated over. Hence, the complex structure of the QPV w.r.t. the total momentum Q^2, which carries the resonances such as that of the ρ-meson, directly carries over to the HVP.

6.3.5. Conclusion

In this section, we presented a calculation of the hadronic vacuum polarisation, the leading QCD contribution to $g-2$, in the complex plane. The investigation focusses in particular on how the analytic structure of the HVP is influenced by the analytic structure of the fundamental input correlation functions such as the quark propagator and the quark-photon vertex. In particular, this could yield insight into how, if so, complex non-analyticities in the quark propagator and the quark-photon vertex cancel on the level of the HVP. The assumption that the HVP is an analytic function in the upper half plane is explicitly exploited in computing the respective contribution to g–2 using Euclidean lattice data. Note that by the time of completion of this thesis, the investigation presented here was not yet completed. Since the project constitutes an important example for potential applications of the spectral functional approach connected to observables, we nevertheless chose to document the calculation and progress that has been made so far.

The intermediate results presented in this chapter are summarised in Figure 6.17, displaying the HVP in a quadrant of the complex momentum plane. While the leading ρ-meson pole can be clearly identified, the (non-)existence of complex poles could not be verified, since the complex peaks appearing in the plot are due to an insufficient numerical treatment of the complex poles of the quark propagator, cf. Figure 6.16. In order to arrive at a conclusive statement about the implications of complex poles in the quark propagator for the complex structure of the HVP, a few steps are necessary.

First, it is necessary to upgrade our numerical routine to correctly account for the complex poles in the integration domain. Then, if in the discussed scenario it can be shown that additional complex non-analyticities appear in the HVP, it remains to be studied how these are affected by the choice of scattering kernel in the QPV BSE. Furthermore, comparison of different truncations for the quark DSE, also without complex quark poles, as discussed for the case of STI-consistent vertices in [7] resp. Paragraph 5.4.3.2.2, would add to understanding the nature of additional non-analyticities in the HVP. Assuming that no complex singularities show up in the HVP, an investigation of the mechanism protecting the HVP from the non-analyticities of its input would be in order. Evaluation of the WTI (6.43) in the complex plane, in particular in the vicinity of the complex singularities of the QPV and quark propagator, could potentially yield insights about the connection of such a mechanism to the internal symmetries.

Due to the necessity of resolving the quark propagator in the complex plane makes, the spectral functional approach, already applied to the quark propagator DSE in [7], see Section 5.4, could be applied for studying DSE truncations beyond rainbow ladder Maris-Tandy.

6.4. Shear viscosity of Yang-Mills theory

This chapter presents results of [11]. All practical calculations have been carried out by Jakob Dolgner in the context of his Master thesis, which I co-supervised.

Relativistic heavy ion collisions (HIC) represent a central experimental technique for testing the phase structure as well as dynamical properties of QCD. In modern phenomenological approaches to HIC, the dynamical evolution of the quark-gluon plasma is described by viscous relativistic hydrodynamics, see, e.g., [424–428]. Within the hydrodynamical description, transport coefficients parametrise the response of the fluid to linear perturbations in particular kinematic channels around local thermal equilibrium. These fluid properties ultimately follow from the underlying microscopic equilibrium theory, and its correlation functions. Hence, transport coefficients establish a link between the macroscopic properties and the microscopic description of QCD, which is formalised within the Kubo relations [429]. The most important transport coefficients for the hydrodynamical description of the quark-gluon plasma are the shear and bulk viscosity. In this section, we are going to focus on the shear channel.

Experimental measurements suggest a relatively small value for the shear viscosity over entropy ratio [430–434], with a current estimate of $1/(4\pi) < \eta/s < 2/(4\pi)$ [435]. This estimate is close to the KSS bound predicting $\eta/s = 1/(4\pi)$, which be inferred from AdS/CFT correspondence [436]. Recent lattice studies tend to predict somewhat larger values, see [437–440].

In this section, calculate the shear viscosity of $SU(3)$ Yang-Mills theory from Kubo relations solely based on fundamental realtime correlator input, i.e., the gluon propagator resp. its spectral function. In doing so, we follow a similar approach to that of [346], extending the previous calculation by including a temperature dependent normalisation factor into the calculation of the shear spectral function. This normalisation is determined by comparing to lattice data for the Euclidean shear channel two-point function, accessible in our calculation via a spectral representation. For a pedagogical introduction into the calculation of the shear viscosity in QCD from fundamental correlators, see [441].

6.4.1. Diagrammatic representation of the Kubo relation

Kubo relations link transport coefficients to fundamental, microscopic correlation functions. Since transport coefficients describe collective, macroscopic properties of the system, they are inherently linked to long-range behaviour. Emerging from a hydrodynamical framework, it is natural that the correlation functions featuring in the Kubo relations are that of the energy-momentum tensor (EMT) of the theory, which is related to the quantum effective action via

$$T_{\mu\nu}(x) = \frac{2}{\sqrt{-g(x)}} \frac{\delta\Gamma[\Phi, g]}{\delta g^{\mu\nu}(x)} \,. \tag{6.51}$$

Here, g represents the metric tensor, and Φ captures all fields of the effective action Γ. We will evaluate (6.51) in flat Minkowski spacetime, i.e., set $g = \eta$ after differentiation.

In Fourier space, long range behaviour is encoded in the low frequency and momentum limit. For the case of the shear viscosity, the corresponding Kubo relation reads

$$\eta = \lim_{\omega \to 0} \frac{1}{20} \frac{\rho_{\pi\pi}(\omega, \vec{p} = 0)}{\omega} \,, \tag{6.52}$$

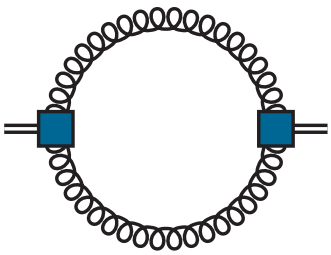

Abbildung 6.18.: One-loop contribution to the shear correlator in (6.53). Notation as defined in Figure 2.1, with curly lines representing gluon fields. Blue boxes with n gluon legs represent EMT n-vertices, defined as in (6.58).

where $\rho_{\pi\pi}$ is the spectral function of the corresponding EMT two-point function, defined as

$$\rho_{\pi\pi}(\omega,\vec{p}) = \int \mathrm{d}^4x e^{\mathrm{i}px}\langle[\pi_{ij}(x)\pi_{ij}(0)]\rangle\,. \tag{6.53}$$

π_{ij} is defined as the spatial traceless part of the EMT, being related to the full EMT by

$$\pi_{ij}(x) = T_{ij}(x) - \frac{\delta_{ij}}{3}T_{kk}(x)\,. \tag{6.54}$$

The corresponding spectral representation relating the shear channel spectral function (6.53) to the Euclidean two-point function reads

$$C(\tau) = \int \frac{\mathrm{d}\lambda}{2\pi}\rho_{\pi\pi}(\lambda,\vec{0})\frac{\cosh(\lambda(\beta/2-\tau))}{\sinh(\lambda\beta/2)}\,, \tag{6.55}$$

where $C(\tau) = \int_{\vec{x}}\langle\pi_{ij}(x)\pi_{ij}(0)\rangle$ for spacelike x. Equation (6.55) will be useful to relate the computed shear spectral function to Euclidean lattice data later.

The expectation value in (6.53) can be evaluated explicitly by means of the composite operator identity (2.20),

$$\langle\pi_{ij}[A]\pi_{ij}[A]\rangle = \pi_{ij}\big[G_{A\phi_i}\cdot\frac{\delta}{\delta\phi_i}+\mathbf{A}\big]\pi_{ij}\big[G_{A\phi_i}\cdot\frac{\delta}{\delta\phi_i}+\mathbf{A}\big]\,, \tag{6.56}$$

with $\mathbf{A} = \langle A\rangle$, resulting in a seven-loop exact diagrammatic expression for the shear correlator, cf. [346]. Here, we focus on its dominant one-loop term, depicted in Figure 6.18. Its corresponding contribution to the shear viscosity (6.53) reads

$$\rho_{\pi\pi}(\omega,\vec{p}) = \mathrm{Im}\int\frac{\mathrm{d}^4q}{(2\pi)^4}\pi^{(2)}_{ij}(q,p+q)G_A(p+q)\pi^{(2)}_{ij}(p+q,q)G_A(q)\,, \tag{6.57}$$

where the imaginary part results from commutator in (6.53), and we use $G_A = G_{AA}$ to match previous notation. $\pi^{(n)}$ is an EMT n-vertex, represented by grey squares with n gluon legs in Figure 6.18, for which we employ the notation (2.13) for functional derivatives,

$$\pi^{(n)}_{ij}(p_1,\ldots,p_n) = \frac{\delta^n\pi_{ij}}{\delta A(p_1)\ldots\delta A(p_n)}\,. \tag{6.58}$$

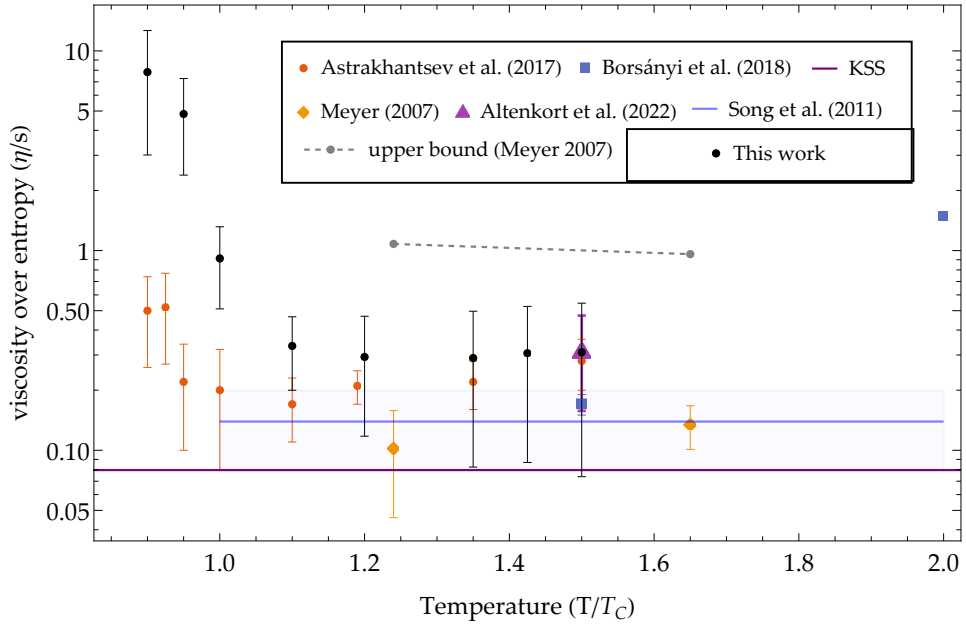

Abbildung 6.19.: Shear viscosity over entropy ratio from the shear Kubo relation (6.52). We employ a diagrammatic representation for the shear correlator, truncated at one-loop, see Figure 6.18. The input gluon spectral function is modelled by a Breit-Wigner peak, whose parameters are adjusted by fitting to the Euclidean lattice shear correlator data of [438]. We compare to the lattice results of [437–440]. The entropy density data is taken from [447]. A lower bound on η/s, the KSS bound, can be inferred from AdS/CFT correspondence [436]. The solid blue line is obtained from viscous hydrodynamical simulations by fitting to measured particle yields [448].

Here, we approximate the two-point EMT vertices in (6.57) by their classical counterparts, i.e., derive the EMT vertices starting from the classical action in (6.51). For the gluon propagators in (6.57), we employ a spectral representation, cf. (5.11). The frequency integral can be solved, e.g., at imaginary frequencies via the Matsubara formalism and then continued to real frequencies or directly in a realtime formalism such as the Keldysh formalism [442–444]; for pedagogical introductions to both formalisms see, e.g., [445, 446]. We employ the Keldysh formalism here, following the approach of [346]. We refrain from giving the resulting algebraic expressions here for this reason, and provide them in [11].

6.4.2. Gluon spectral function and temperature dependent normalisation

By truncating the diagrammatic representation for the shear correlator (6.53) at one-loop, we are neglecting higher loops which contribute to the temperature dependence of the shear viscosity. This can be partially remedied by introducing a temperature dependent normalisation factor in (6.53),

$$\rho_{\pi\pi}(\omega) \to c(T)\rho_{\pi\pi}(\omega)\,. \tag{6.59}$$

The temperature dependent normalisation $c(T)$ can be fixed by comparing the corresponding Euclidean shear correlator, evaluated with (6.55), to lattice data such as that of [438]. This procedure allows to efficiently incorporate the temperature dependence of higher loop corrections into the calculation, while only dealing with a simple one-loop computation. Furthermore, it allows to fix the generally arbitrary global normalisation of correlation functions from functional approaches, which is usually done by comparing to normalised results from other methods.

It turned out that with the above procedure, vacuum gluon spectral functions such as the ones discussed in [3], see Section 5.3, and [243], do not yield values for the shear viscosity compatible with previous calculations. We will defer the in-depth discussion of possible reasons for this to a future publication. Instead, in this section we focus on an analytic model for the gluon spectral function allowing to control features such as peak scale or width in a temperature dependent manner, given by a combination of Breit-Wigner (BW) peaks,

$$\rho_A^{\mathrm{BW}}(\omega,\vec{p};m,\gamma) = \frac{1}{2\omega_{\mathbf{p}}}\left(\frac{2\gamma_{\vec{p}}}{\left(\omega-\omega_{\vec{p}}\right)^2+\gamma_{\vec{p}}^2} - \frac{2\gamma_{\vec{p}}}{\left(\omega+\omega_{\vec{p}}\right)^2+\gamma_{\vec{p}}^2}\right), \tag{6.60a}$$

with

$$\omega_{\vec{p}} = \sqrt{m^2+\vec{p}^2}\,, \qquad \gamma_{\vec{p}} = \frac{\gamma}{\omega_{\vec{p}}}\,. \tag{6.60b}$$

Here, we treat the parameters m and γ, related to the peak position and width, as additional fit parameters when fitting the temperature dependent normalisation $c(T)$ in (6.59) to the Euclidean lattice data of [438]. This allows to infer the temperature evolution of the characteristic features of the gluon spectral function, as the χ^2-fits are performed separately for each temperature of the data of [438]. The shape of the vacuum YM spectral function [243] acts as an orientation for sensible shapes of the BW spectral function, effectively shrinking the volume of the two-dimensional BW parameter space (m,γ). After fixing the parameters of our gluon spectral functions by this procedure, we eventually evaluate the shear viscosity as a function of temperature via (6.52).

6.4.3. Results

In hydrodynamic equations, transport coefficients usually appear in ratio with the entropy density s. It is common practice to present results for transport coefficients as such a ratio. We use the entropy density results of [447] for this here.

In Figure 6.19, we display our result for the viscosity over entropy ratio as a function of temperature in the range $T/T_c \in [0.9-1.5]$, where T_c is the critical temperature. The temperature range is fixed by the available lattice data for Euclidean shear correlator which we use to fix the T-dependent normalisation factor of our shear correlator, see Section 6.4.2.

For temperatures above T_c, our result is well compatible with data from various lattice calculations, predicting a viscosity over entropy ratio of $\eta/s \approx 0.3$. For temperatures below T_c, the lattice data is surpassed by approximately an order of magnitude, however. We remark that this type of overshooting of the lattice data close to the phase transition is a feature already seen in previous studies [346]. Accordingly, for decreasing temperature,

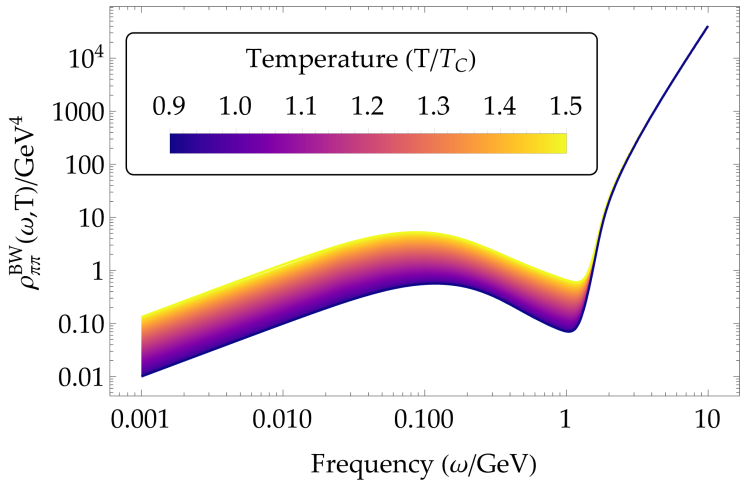

Abbildung 6.20.: Shear spectral function (6.53) interpolated between different temperatures using Breit-Wigner fits for the gluon spectral function. While all curves show the same ω^4 large frequency behaviour, the IR slope determining the shear viscosity (6.52) is clearly temperature dependent. The corresponding viscosities are displayed in Figure 6.19.

our procedure seems to describe the low frequency asymptotics of the shear spectral function worse than for higher ones. This could be related to the fact that in particular in the infrared, our model gluon spectral function does not match the analytically known behaviour [243]. For decreasing thermal gap, we become more sensitive to this regime, which could explain the observed deviation. Including higher loop diagrams acting as vertex corrections could yield insight into this matter.

The shear spectral functions from which the viscosities are obtained via the Kubo relation (6.52) are shown in Figure 6.20. Note that we interpolated between the shear spectral functions for the eight different temperatures for which we present viscosity results in Figure 6.19. Describing a physical correlation function, the shear spectral function is positive, accordingly. The slope of the spectral function in the IR, determining the shear viscosity, is monotonically decreasing with temperature. At about 1 GeV, the spectral function shows a dip, which is related to the dominant mass scale of the gluon spectral function. In the perturbative large frequency domain, the spectral functions fall on top of each other and show the expected ω^4-behaviour, see also [449] for perturbative hard thermal loop (HTL) results in that regime, for instance.

In Figure 6.21, we display the Euclidean shear correlators corresponding to the spectral functions shown in Figure 6.20. As detailed in Section 6.4.2, we performed a χ^2-fit with respect to the parameters of the Breit-Wigner gluon spectral function (6.60) entering the spectral function of the displayed correlators to the respective lattice data of [438]. The fits agree very well within errors with the lattice data, which is also confirmed by the reduced χ^2-values given in the plot legend. On the basis of the Euclidean correlator, a Breit-Wigner peak appears to model the gluon spectral function well enough to describe the data. Inspecting the best fits for the Breit-Wigner parameters width and mass scale reveals a very mild temperature dependence, and their values are in particular close to the mass scale and width of the reconstructed gluon spectral function in [243]. It therefore

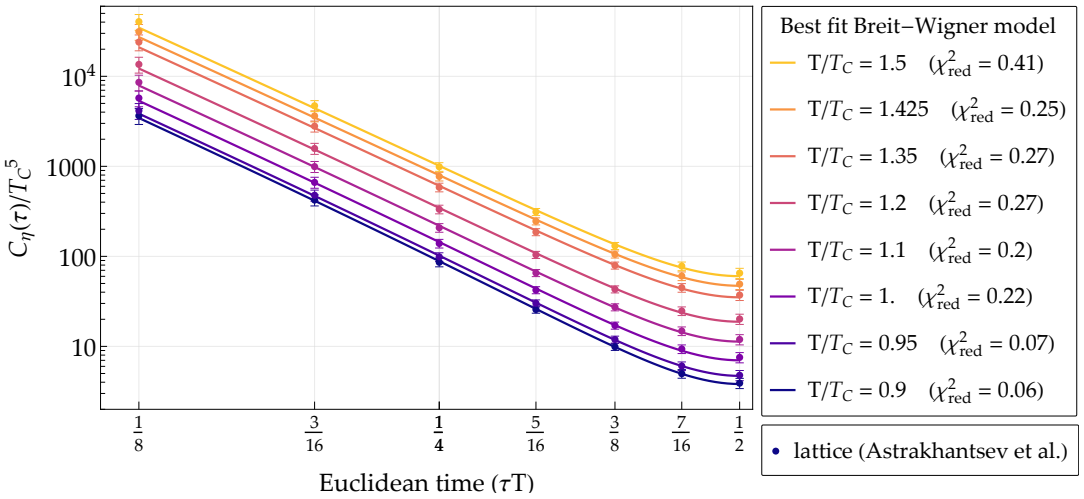

Abbildung 6.21.: Euclidean shear correlators for different temperatures corresponding to the spectral functions shown in Figure 6.20, with the spectral representation (6.55), compared to lattice results [438]. The width and mass scale of the Breit-Wigner gluon spectral function (6.60) entering the calculation of the shear spectral function is fixed by fitting the above displayed corresponding Euclidean shear correlators to the respective lattice data. The fits describe the lattice data very well within errors.

remains to be fully understood why results for the viscosity in agreement with the lattice could only be obtained in case of the Breit-Wigner model for the gluon spectral function, and not for the reconstruction results discussed in Section 5.3 resp. [3] or that of [243]. Our investigation showed that the EMT spectral function was particularly sensitive gauge dependent features of the gluon spectral functions such as deep IR and UV behaviour. The full shear correlator is physical and hence gauge invariant, a property which is hence violated by our one-loop truncation of its seven-loop exact diagrammatic expansion. Future investigations could go into the direction of systematically constructing gauge invariant truncations for the full expansion, guided by invariance under changes of the gluon spectral function's gauge variant features.

6.4.4. Conclusion

In this section, we calculated the shear viscosity of Yang-Mills theory from Kubo relations based on fundamental realtime correlation function input. To that end, we modelled the gluon spectral function by a Breit-Wigner peak. Our results for the shear viscosity over entropy ratio, displayed in Figure 6.19, are well compatible with existing results from the literature. Our approach has the advantage of full access to the shear correlator spectral function, shown in Figure 6.20, and in consequence also to the corresponding Euclidean shear correlator, displayed in Figure 6.21. Since the shear correlator is also the subject of lattice simulations, this yields an additional benchmark for results, representing an important extension of the approach of [346]. Here, we exploited this feature to fix the model parameters of the gluon spectral function by a fit of the Euclidean shear correlator to the corresponding lattice data in a temperature dependent manner. This enabled us

to include temperature dependent EMT-vertex loop corrections while retaining the low analytic complexity of our one-loop calculation.

A natural next step in our investigation is to replace the model input for the gluon spectral function by real data. This data can be obtained via direct calculation, e.g., via the spectral functional approach, which was applied to Yang-Mills theory in [5], see Section 5.1. The calculation was plagued by spurious complex poles in the gluon propagator, also observed in other realtime DSE approaches [264], preventing the computation of a gluon spectral function. On the other hand, spectral reconstructions have efficiently reconstructed gluon spectral functions from Euclidean lattice data for the propagator in for Yang-Mills theory [243] and QCD [3], see Section 5.3. Our investigation appeared to be sensitive to gauge variant features of these reconstruction results, however. In consequence, future investigations should involve the construction of gauge invariant truncations the diagrammatic expansion of the shear correlator.

7. Summary & Conclusion

In this thesis, we presented advances in the calculation of realtime observables in the non-perturbative domain of QCD. These observables are of utmost importance for understanding dynamical properties of the theory, which includes, for instance, transport phenomena or resonances. From the experimental side, the QCD phase diagram is only indirectly accessible, e.g., through heavy-ion collisions under lab conditions or in nature via neutron stars. These extreme and inherent non-equilibrium conditions render dynamical properties crucial for understanding the phase structure of QCD. The theoretical description of realtime properties is notoriously difficult, since lattice field theory and conventional functional approaches are usually formulated in Euclidean spacetime. To tackle this issue, we put forward the *spectral functional approach*, which allows for the efficient calculation of fundamental correlation functions directly in Minkowski spacetime within functional, diagrammatic approaches. We demonstrate the power of the spectral functional approach by computing spectral functions of all fundamental QCD degrees of freedom and show how they can be used to calculate different physical observables.

The first major part of this thesis is the development of the spectral functional approach in Chapter 4. This development constitutes the technical and methodical core of the majority of numerical results presented in this thesis. The spectral functional approach utilises integral representations for correlation functions, so-called spectral representations, to analytically solve momentum loop integrals in general diagrammatic expressions by dimensional regularisation. This grants access to the entire complex momentum plane and in particular the Minkowski domain of the respective diagram. We applied this technique to Dyson-Schwinger equations and the functional renormalisation group in Section 4.1 and 4.2. For both, we presented results for spectral functions in a scalar ϕ^4-theory, serving as a proof of concept for computations in more intricate theories such as QCD. The application of the spectral functional approach to two different functional methods enabled direct comparison between both of them. We observed very good agreement, which establishes the reliability of our direct functional realtime approach.

In Chapter 5, we used the spectral functional approach for the calculation of fundamental QCD correlation functions in Minkowski spacetime, which represents a pivotal step on our avenue to realtime observables in QCD. Since observable correlation functions underlie tight restrictions on their analytic structure rooted in locality, causality and unitarity requirements, it is crucial to understand the analytic structure of the underlying fundamental correlators. For this reason, in Section 5.1, we investigated the analytic structure of the arguably most central correlation functions of Yang-Mills theory, i.e., the gluon and ghost propagator. We demonstrated how complex non-analyticities in these propagators can lead to inconsistencies in the solutions of the corresponding coupled set of DSEs. Based on this, we argued that a mechanism for the cancellation of these complex poles requires a delicate balance between these singularities and roots in vertex functions, which, if not imposed by a symmetry, is unlikely to exist. In a scenario without such complex singularities, we found that the spectral representation of the ghost propagator is intact, and

computed the corresponding spectral function non-perturbatively from its corresponding DSE in Section 5.2. We proceeded similarly for the case of the quark propagator, whose spectral function we calculated in Section 5.4. An important input for the calculation of the quark spectral function is given by the gluon propagator or spectral function, for which we used spectral reconstruction results based on 2+1 flavor lattice QCD data using Gaussian process regression, presented in Section 5.3. The reconstruction also encompasses results for the ghost spectral function, which shows remarkable agreement with the direct calculation from the spectral DSE in Section 5.2.

In Chapter 6, we turned towards the computation of observables from fundamental timelike correlation functions. To demonstrate the wide range of potential use cases for the spectral functional approach, we considered four observables of different types: the strong coupling constant, a two-particle bound state in the scalar ϕ^4-theory, the anomalous magnetic moment of the muon and the shear viscosity of Yang-Mills theory. We started with the discussion of the strong coupling constant of QCD in the timelike domain in Section 6.1, directly building on the spectral reconstruction results of Section 5.3. We established a spectral representation for the strong coupling and calculated its spectral function via two different methods; directly based on the spectral functions of its input correlation functions and via Gaussian process regression from lattice data, showing very good agreement. Furthermore, we discussed scattering amplitudes that can be calculated directly based on our results. In Section 6.2, we demonstrated how the spectral functional approach can facilitate the computation of bound states, which can be described via resonance equations in functional approaches. To that end, we calculate the position of a low-lying two-particle bound state in a scalar ϕ^4-theory. This investigation lays the groundwork for future investigation of hadronic resonances in QCD aided by the spectral functional approach. Moreover, we investigated the complex structure of the hadronic vacuum polarisation (HVP), the leading QCD contribution to the magnetic moment of the muon, g–2, in Section 6.3. The motivation for our investigation are the discussed causality and unitarity requirements, which are exploited in quantitative g–2 calculations to determine the timelike HVP from Euclidean lattice data via dispersion formulae. A central element of our investigation is the computation of the full quark-photon vertex in the complex momentum plane. Here, we only reported on interim results for the purpose of documentation, since the study has not been finished at the time of completion of this thesis. Finally, in Section 6.4 we turned towards the QCD transport coefficients, and used Kubo relations to calculate the shear viscosity as a function of temperature in Yang-Mills theory. The computation features the gluon propagator at real frequencies as an input, therefore representing a prototypical use case for direct realtime results from functional approaches. We observed good agreement within errors with the corresponding lattice data for the relevant temperatures.

To conclude, in this thesis we put forward the spectral functional approach, a novel technique for the calculation of fundamental realtime correlation functions in functional approaches, and demonstrated its potential for the calculation of observables in QCD—ranging from scattering amplitudes over hadronic resonances to transport coefficients. In the past, access to these observables has often been hindered by the Euclidean nature of non-perturbative results from lattice simulations or functional approaches. Hence, this work can be understood as a foundation for future precision calculations of observables in QCD with functional techniques. An obvious next step in this endeavour is the extension of the spectral functional approach to finite temperature, which appears to be even necessary for the calculation of particular transport coefficients. On the avenue to

quantitative precision, embedding higher vertices in the spectral functional approach will be a crucial obstacle to overcome. This will most certainly necessitate the construction of generic spectral representation for higher n-point functions.

Despite the outlined short and long term challenges, the path towards the overarching goal of precision calculations of QCD observables from functional methods is clearly visible today. Advancing on this path will require concerted conceptual and numerical efforts, whose merit will not be limited to QCD, however. The generality of the discussed concepts promises applicability to strongly correlated quantum systems on the most different energy scales—from ultracold atoms to quantum gravity.

Appendices

A. Additional material

A.1. Expansions around condensates and color averages

In this section we discuss the implementation of expansions around non-trivial condensates in connection to Section 3.2, and comment on the subtleties of the color averaging procedure associated with the central mass formula in (3.101). To illustrate the properties and subtleties, we employ two simple examples: spontaneous symmetry breaking in a scalar $O(N)$ theory, and (color) centre symmetry breaking in finite temperature Yang-Mills theory.

Let us first consider a scalar field theory with an $O(N)$ field ϕ (including the discrete Z_2 symmetry when $N = 1$) in the symmetric phase. In the symmetric phase, both, the effective action $\Gamma[\phi]$, and expectation values of observables, are typically expanded around $\phi = \phi_0$, where

$$\phi_0^2 = \lim_{\mathcal{V}\to\infty} \frac{1}{\mathcal{V}} \int_{\mathcal{V}} \langle \phi(x)\phi(0)\rangle \,, \tag{A.1}$$

is defined by the order parameter of the theory. The order parameter (A.1) can also be obtained from

$$\phi_0 = \lim_{J\to 0} \langle \phi \rangle \,, \tag{A.2}$$

where J indicates an external current (or magnetisation) coupled to the field, $\lim_{J\to 0} \int_x J\phi$, which is finally removed. Alternatively, within a finite volume one may use boundary conditions that break the symmetry, and then take the infinite volume limit.

Either way, the effective action Γ is invariant under the full symmetry group of the underlying theory by definition, whereas the vacuum state (the solution of the equations of motion) breaks the symmetry.

Thus, quite importantly, the apparent symmetry breaking in Γ, seemingly induced by the expansion point, is absent for the full effective action. In turn, a given approximation scheme may break this symmetry (for example a finite order of a Taylor expansion about $\phi = \phi_0$). This symmetry can be restored subsequently by averaging the approximated effective action $\Gamma_{\rm app}[\phi]$ over the symmetry group, $\Gamma[\phi] = \langle \Gamma_{\rm app}[\phi]\rangle_{\rm av}$. Note in this context, that in our example case of an $O(N)$ theory the averaged expectation value of the field vanishes, $\langle\phi\rangle_{\rm av} = 0$, as it must. Moreover, the operator in (A.1) has the full symmetry and hence does not change under the averaging procedure, while $\langle\phi\rangle$ does.

In the case of the effective gluon mass, the underlying symmetry is a gauge symmetry. For this reason we also consider a second, closer, example, the expectation value of the Polyakov loop $\langle L\rangle$ in finite temperature Yang-Mills theory,

$$L = \frac{1}{N_c} \,\mathrm{Tr}\, \mathcal{P} \exp\{ig_s \oint A_0(x)\} \,, \tag{A.3}$$

where the integral $\oint$ in (A.3) is over $x_0 \in [0, 1/T]$, and the trace is taken in the fundamental representation. Here, T denotes the temperature and $\mathcal{P}$ is the path ordering operator. The underlying symmetry is the centre symmetry Z_{N_c} of the gauge group with $L \to z\,L$ and $z \in Z_{N_c}$. We have the order parameter

$$L_0^2 = \lim_{\mathcal{V}\to\infty} \frac{1}{\mathcal{V}} \int_{\mathcal{V}} \langle L(0) L^\dagger(x) \rangle \,, \tag{A.4}$$

which is non-vanishing in the confining disordered low temperature phase. Typically, in both, functional approaches and on the lattice, (A.4) is obtained by an infinitesimal explicit centre symmetry breaking in the Cartan direction t^3, similar to introducing an infinitesimal explicit breaking of $O(N)$ symmetry described above. In the t^3 direction the Polyakov loop takes real values, and we get

$$L_0 = \langle L(x) \rangle \,, \tag{A.5}$$

with a real positive L_0, which is a non-trivial solution of the equation of motion (of A_0) at finite temperature. The expectation value of the order parameter serves as a physical expansion point for observables as well as the effective action in functional approaches, both in first principle QCD computation and low energy effective theories of QCD. In quantitative approximations the results for observables agree very well with lattice simulations, for the Polyakov loop itself see [178]: The observables are either color-blind in the first place and hence do not require a color average and are insensitive to it, or, as in the case of the Polyakov loop, a color direction was singled out for the computation in the first place.

However, the comparison of gauge-fixed correlation functions or parts of it is more intricate, as then the averaging is required and may also affect the gauge fixing, for more details and further literature see in particular [166, 450] and the recent review [63]. This intricacy also applies in the present situation and makes a direct comparison of the effective gluon mass difficult.

The lack of a quantitative averaging procedure has forced us to introduce the averaging factor $f_{\rm av}(N_c)$ in our results, see (3.96) and the definition of the effective gluon mass, (3.99) and (3.119). In the present work we have only determined its N_c-dependence with the consistency of the large N_c scaling. As mentioned in the main text, the value of $f_{\rm av}(N_c)$ is the largest source of systematic error for the effective gluon mass.

A.2. Massless limit in the scalar theory

The scalar ϕ^4-theory in 2+1 dimensions depends on one dimensionless parameter, $\lambda_\phi/m_{\text{pole}}$. In the present work we have shown all results in terms of the respective pole mass. Hence, the above parameter simply relates to different couplings λ_ϕ, measured in units of the pole mass $m_{\text{pole}} = 1$. If interested in the massless limit of the theory, it is more convenient to keep the coupling fixed $\lambda_\phi = 1$, and to depict all results for different pole masses. For example, in the work we have used $\lambda_\phi = 5, 10, 20$ with $m_{\text{pole}} = 1$, which can be read as $\lambda_\phi = 1$ and $m_{\text{pole}} = 1/5, 1/10, 1/20$. This leads us to the spectral functions for propagator and four-vertex as well as the respective Euclidean correlators itself of the scalar field, depicted or rather redrawn in Figure 4.14. Rescaling the results in this way it gets clear the massless limit is readily investigated through the limit $\lambda_\phi \to \infty$. For a consistent treatment of the DSE, the vertices need to be well-defined and have the appropriate scaling properties in this limit. This is given for the resummed s-channel four-point function that was introduced in Section 4.1.3.2 and used in calculation of Section 4.1.3.4 and Section 4.1.3.5.

Note that in the skeleton expansion as approximated in Section 4.1, the only other appearing vertex, which is the three-point function, is obtained directly from $\Gamma^{(4)}$ and hence has the same property. The resummation is hence suitable for studying the massless case in our skeleton expansion. In all diagrams except for the tadpole, all vertices are approximated at frequency zero. In consequence, they do not carry loop momentum and merely enter as multiplicative factor, which makes them well under control in the large coupling limit. For the tadpole however, this is not the case. Here, the four-point function enters via its spectral representation (4.36). The additive classical contribution drops out by renormalisation, as it contributes momentum-independently. What is left is the vertex spectral function contributing to the tadpole loop integral, cf. (4.38). With increasing coupling, this spectral function gets larger, see Figure 4.10 or Figure 4.12. Since the multidimensional spectral

	Classical vertices	Skeleton
g_{pol}	$-\frac{3}{2}\Gamma^{(2)}(\omega=0)\lambda_\phi$	$-\frac{3}{2}\Gamma^{(2)}(\omega=0)\Gamma^{(4)}(\omega=0)$
g_{sunset}	$-\frac{1}{6}\lambda_\phi^2$	$\frac{1}{12}\Gamma^{(4)}(\omega=0)^2$
g_{squint}	$\frac{3}{2}\lambda_\phi^2\Gamma^{(2)}(\omega=0)$	0
g_{tad}	0	$\frac{1}{2}$

Tabelle A.1.: Prefactors of the propagator DSE diagrams in the different approximation schemes. The prefactors are obtained by the standard DSE prefactors and the loop-momentum and spectral parameter independent parts of the vertices. The tadpole factor in the approximation with classical vertices is set to zero, as the tadpole is absorbed completely in the mass renormalisation. The sunset prefactor in the skeleton expansion compensates the two-loop contributions of the tadpole with full four-vertex. In the self-consistent approximation of Section 4.1.3.5, the skeleton prefactors apply with exception to the polarisation diagram, which is given by (4.43).

integrals need to be evaluated numerically, a UV cutoff for the integrals needs to be chosen that minimises the error caused by doing so. This results in increasingly long-range integrals for the large coupling limit. The appropriate treatment of these integrals hence results in a technical obstacle, which will be the subject of a follow-up project. Apart from the technical aspect, this suggests that the tadpole diagram is the dominant contribution to the DSE and thus to the spectral function for $\omega > 3m_{\text{pole}}$ in the s-channel approximation. As a result, one is left solely with polarisation and tadpole diagram, further simplifying the setup.

A.3. Spectral flows in gauge theories

The scope of the spectral Callan-Symanzik flow equations introduced in Section 4.2 also extends to the particularly interesting case of gauge theories, which we elaborate on in this section. Especially the non-perturbative infrared regime of QCD has been studied intensively within the fRG approach [63, 95, 137, 138, 166, 172, 451–454]. In this section we discuss the application of the spectral renormalisation group to gauge theories at the example of Yang-Mills theory, for respective works with the spectral DSE see [2, 5] resp. Section 5.2 and Section 5.1. The classical gauge-fixed Yang-Mills action including the ghost term is given by (3.41) in Landau gauge, i.e., evaluated at $\xi = 1$, reads

$$S_{\mathrm{YM}} = \int_x \left[\frac{1}{4} F^a_{\mu\nu} F^a_{\mu\nu} - \bar{c}^a \partial_\mu D^{ab}_\mu c^b + \frac{1}{2\xi} (\partial_\mu A^a_\mu)^2 \right] . \tag{A.6}$$

Generally, setting up spectral flow equations for gauge theories works analogously as for scalar theories, discussed in Section 4.2.4. The flow equations are derived in the usual manner, and spectral representations are used for the propagators of all fields, i.e., ghost and gluon propagator.

A.3.1. Ghost propagator

Formally, the ghost propagator is expected to obey the KL-representation [268, 269], if the corresponding propagator is causal. A recent direct calculation of the ghost spectral function with the spectral Dyson-Schwinger equation in [2], which we present in Section 5.2, has confirmed this expectation. This computation has utilised a spectral representation for the gluon, which is discussed in Appendix A.3.2. Moreover, recent reconstructions [260, 261] show no signs of a violation of this property. It is found that the ghost spectral function exhibits a single particle peak at vanishing frequency with residue $1/Z_c$, whose value may depend on the non-perturbative infrared closure of the Landau gauge. Specifically, the scaling solution is obtained for the limit $Z_c \to 0$, see [2, 243] resp. Section 5.2. In this case, the particle pole in the origin is no longer present. Instead, in the origin there is the branch point of the non-integer power scaling law branch cut of the scaling solution. Note that in this case, the ordinary KL representation can no longer be applied, since the corresponding spectral function would show an IR divergence. For the current discussion, we will stick to the case of a massless particle pole in the IR.

Independent of the IR behaviour addition, a continuous scattering tail shows up in the spectral function via the logarithmic branch cut. This leads us to the general form of the ghost spectral function,

$$\rho_c(\omega) = \frac{\pi}{Z_c} \frac{\delta(\omega)}{\omega} + \tilde{\rho}_c(\omega) , \tag{A.7}$$

where $\tilde{\rho}_c$ denotes the continuous tail of the spectral function. In [2], see Section 5.2 and in particular Appendix A.8, it has been shown that the ghost spectral function obeys an analogue of the Oehme-Zimmermann superconvergence property of the gluon [255, 256]. Expressed in terms of the spectral representation of the dressing, it reads

$$\int \frac{d\lambda}{\pi} \lambda \, \tilde{\rho}_c(\lambda) = -\frac{1}{Z_c} . \tag{A.8}$$

Equation (A.8) entails that the total spectral weight of the ghost vanishes. A generic discussion can also be found in [2, 254] resp. Section 5.2.

Since the ghost spectral function (A.7) shows a (massless) particle pole, as for scalar theories, on-shell renormalisation conditions like (4.75) can be applied. This fixes the pole position of the scale-dependent ghost spectral function to $p^2 = -k^2$. In analogy to (A.7), the flowing ghost spectral function reads

$$\rho_{c,k}(\omega) = \frac{\pi}{Z_{c,k}} \frac{\delta(\omega - k) + \delta(\omega + k)}{\omega} + \tilde{\rho}_{c,k}(\omega) \,, \tag{A.9}$$

where $\tilde{\rho}_{c,k}(\omega)$ has support for $|\omega| > 2k$. In the limit of vanishing cutoff, pole position and scattering onset move into the origin, and (A.7) is recovered.

A.3.2. Gluon propagator

The above discussion of the ghost spectral function and its existence was done under the assumption of a spectral representation of the gluon. In contrast to the ghost spectral function, there is an ongoing debate in the community whether this assumption is justified. In local QFTs, only the existence of a spectral representation for asymptotic, physical states is guaranteed. It has been argued that in Landau gauge this also applies to the gluon propagator [271, 273, 299]. While high precision spectral reconstructions are not in contradiction to this assumption and do work for the gluon propagator [3, 243, 258, 300] resp. Section 5.3, extensions with complex conjugate poles are also commonly entertained in reconstructions, see, e.g., [104, 195, 260, 263, 264, 270, 272, 274–276]. A recent computation has shown, that the situation is indeed exceedingly intricate: its resolution may only be possible by also resolving the problem of a consistent non-perturbative gauge fixing [5], see Section 5.1. The self-consistent implementation of the latter for propagators *and* vertices is subject to a non-perturbative infrared realisation of the respective Slavnov-Taylor identities. For a detailed discussion of the complex structure of Yang-Mills theory see [5] resp. Section 5.1. There, we show that a solution of the Yang-Mills system with a spectral ghost and a non-spectral gluon would require non-trivial relations between the complex structures of vertices and propagators. In turn, while less conclusive, in [5] resp. Section 5.1, it is found that numerical indications that a self-consistent solution system with spectral representations for both ghost and gluon propagators, if existent, may also require self-consistent or rather STI-consistent solutions for non-trivial vertices.

In the present chapter we add nothing new to the resolution of this intricate problem, but simply consider the flow of the gluon spectral function under the assumption of its existence. Likewise, we assume a spectral representation for the ghost, with a pole at $\omega^2 = k^2$, c.f. (A.9). The branch point of the ghost loop contribution to the gluon propagator's branch cut lies at $\omega^2 = (2k)^2$. Due to the massless nature of the ghost, the position of the branch point in the gluon propagator thus necessarily is in the origin for vanishing cutoff scale, $k = 0$. However, due to the lack of a gluon particle peak, a direct identification of a flowing mass scale k as in the scalar theory Section 4.2.4, is not possible for the gluon. Consequently, there is no unique way to stop the flow at some $k_{\mathrm{IR}} = m_{\mathrm{phys}}$, where the physical limit of the theory is recovered. Furthermore, the lack of unique gluon mass scale entails that we cannot use on-shell renormalisation here. Eventually, we wish to recover the IR behaviour of the gluon propagator known from other non-perturbative studies, e.g., via functional approaches [93–95]. In consequence, we can define the IR scale only implicitly, and k_{IR} depends directly on the initial conditions employed. This poses the

question of how to consistently couple the gluonic flow to that of the ghost. A consistent, coupled flow is required to simultaneously reach the explicitly resp. implicitly defined IR scales $k_{\mathrm{IR}}^{(\mathrm{ghost})} = 0$ and $k_{\mathrm{IR}}^{(\mathrm{gluon})}$. This can be implemented by flowing both equations with a common scale k down to 0, where the IR limit of the ghost propagator is reached. We then proceed to further lower k solely in the gluon propagator flow equation down to the point where we reach $k_{\mathrm{IR}}^{(\mathrm{gluon})}$ defined by, e.g., scaling as IR behaviour, c.f. [94, 95]. Note that this procedure needs to be supplemented with an appropriate choice of initial conditions guaranteeing $k_{\mathrm{IR}}^{(\mathrm{gluon})} \leq 0$. This clarifies that the described procedure of flowing with two seemingly different scales simply amounts to an implicit choice of initial conditions and does not lead to an inconsistency between the different flow equations. In such a procedure, adjusting the initial conditions is similar to common fRG calculations. We therefore expect a similar fine-tuning problem for the Yang-Mills system as for example encountered in [95].

The proper choice of initial conditions comes in case of the gluon propagator with another technical complication. It is well-known that in massive Yang-Mills theory, the gluon propagator exhibits complex conjugate poles. It has been demonstrated in [5], see Section 5.1, that these can also violate the spectral representation of the ghost propagator, in turn inducing a cascade of non-analyticities in both propagators. Since the Callan-Symanzik cutoff effectively constitutes a mass term, the construction of an initial condition respecting the spectral representation poses a crucial challenge. On the other hand, using modified spectral representations that explicitly take into account complex singularities as done in Section 5.1, one is able to track the evolution of the complex poles through the flow. This allows to make a statement about their existence in the full correlation function at k_{IR}. It has been studied e.g., in [47] how regulator-induced poles vanish in the $k \to 0$ limit in a quantum mechanical system.

A.4. Spectral representation of general operators

Any product of correlation functions obeying a spectral representation allows for such a representation itself. This follows from a set of sufficient conditions for the existence of a spectral representation for an arbitrary correlation function $\mathcal{C}$:

(i) *Holomorphicity:* $\mathcal{C}$ is holomorphic in the upper half plane $\mathbb{H} = \{z \,|\, \mathrm{Im}\, z > 0\}$;

(ii) *Mirror symmetry:* $\mathcal{C}(z) = \bar{\mathcal{C}}(\bar{z})$ and $\mathrm{Im}\,\mathcal{C}(z) = 0$ for $\mathrm{Im}\, z = 0$, $\mathrm{Re}\, z > 0$;

(iii) *Asymptotic decay:* $|z\,\mathcal{C}(z)| \to 0$ for $|z| \to \infty$;

(iv) *Spectral convergence:*

$$\begin{aligned} &\text{(IR)} \quad |z\,\mathrm{Im}\,\mathcal{C}(z)| < \infty \quad \text{for} \quad z \to 0\,, \\ &\text{(UV)} \quad |\log z\,\mathrm{Im}\,\mathcal{C}(z)| \to 0 \quad \text{for} \quad z \to -\infty\,. \end{aligned}$$

Heuristically, (i) and (ii) guarantee that the spectral kernel has the form $1/(z+\lambda^2)$ and the spectral function is defined via (4.4). The integration domain is restricted to $\lambda^2 > 0$ by (iii). Condition (iv) guarantees the convergence of the spectral integral. We remark that (iv) only applies to non-distributional contributions.

It is immediately clear that for any two correlation functions $\mathcal{C}_1$, $\mathcal{C}_2$ satisfying (i)-(iii), their product $\mathcal{C} = \mathcal{C}_1\mathcal{C}_2$ does as well. Similarly, this also applies to (iv) (UV), stating that the spectral function $\rho \sim \mathrm{Im}\,\mathcal{C}$ decays fast enough for the spectral integral to converge in the UV, due to (iii). The infrared convergence condition (iv) (IR) does not need to be fulfilled; consider, e.g., $\mathcal{C}_1 = \mathcal{C}_2 = (1/z)^\alpha$ with $1/2 < \alpha < 1$. Nevertheless, this can be always remedied by multiplying with an appropriate power of z. Note that this does not violate the other conditions.

The spectral representation for the strong coupling constant is then constructed as follows: by the assumption of ghost and gluon propagator obeying the KL representation, their dressing functions obey (i) and (ii). Since by its definition (6.9) the coupling is dimensionless, (iii) does not hold. However, division by p^2 makes (iii) and (iv) hold true. Hence, a KL representation for $\alpha_s(p)/p^2$ is constructed. Multiplying this representation by p^2, we obtain the spectral representation for α_s (6.11).

A.5. Integral representation for propagators with multiple branch cuts

In this section, we construct a general in integral representation for propagators for multiple branch cuts in the complex plane. To that end, we start by deriving the ordinary Källén-Lehmann from Cauchy's theorem and the set of sufficient analytic properties given in Appendix A.4.

Ordinary Källén-Lehmann representation The analytic structure of a propagator G obeying the KL representation (4.3) is tightly constrained by the nature of the former integral representation, see Appendix A.4. With properties (i–iv), the spectral representation can be derived explicitly via Cauchy's integral formula. It states for a holomorphic function G defined an open set $U \subset \mathbb{C}$, $G : U \to \mathbb{C}$, that the value of G at any point z_0 enclosed by an arbitrary, closed rectifiable curve γ in U is given by

$$G(z_0) = \frac{1}{2\pi \mathrm{i}} \oint_\gamma \mathrm{d}z \frac{G(z)}{z - z_0} \,. \tag{A.10}$$

We want to find γ such that we can use (A.10) for all $z_0 \in \mathbb{C}$, for which the easiest choice would be the circle around the origin $\mathcal{C}_R$ and taking $R \to \infty$. Since $\operatorname{Im} G(z) \neq 0$ for $z < 0$, G is discontinuous along the negative real axis according to (ii). Hence, we explicitly need to exclude this region from the integration contour. This can be done by going from negative infinity towards the origin along just above the negative real axis, turning at the origin and then returning to negative infinity along below the real axis. We can then recast (A.10) as

$$G(z_0) = \frac{1}{2\pi \mathrm{i}} \lim_{R\to\infty} \left(\int_{\mathcal{C}_R} \mathrm{d}z \frac{G(z)}{z - z_0} - \int_0^R \mathrm{d}z \frac{G(-z + \mathrm{i}\varepsilon)}{z + z_0 - \mathrm{i}\varepsilon} + \int_0^R \mathrm{d}z \frac{G(-z - \mathrm{i}\varepsilon)}{z + z_0 + \mathrm{i}\varepsilon} \right), \tag{A.11}$$

where in the second term, the integration boundaries were interchanged, and we substituted $z \to -z$ in the last two terms. Due to (iii), the first term vanishes according to Jordan's Lemma. Exploiting the mirror symmetry (ii), we can combine the latter two terms, since their real parts cancel. We find that

$$G(z_0) = \int_0^\infty \frac{\mathrm{d}z}{2\pi} \frac{2 \operatorname{Im} G(-z - \mathrm{i}\varepsilon)}{z + z_0} \,, \tag{A.12}$$

which is the well-known Källén-Lehmann representation. Note that formally, G receives another contribution in the limit $\varepsilon \to 0$ due to the opposite signs of ε in the denominators in the last two terms of (A.11), which is

$$- \int_0^\infty \frac{\mathrm{d}z}{\pi} \operatorname{Re} G(-z - \mathrm{i}\varepsilon) \frac{\varepsilon}{(z + z_0)^2 + \varepsilon^2} \,. \tag{A.13}$$

Generally, $\lim_{\varepsilon\to 0} \varepsilon/((z + z_0)^2 + \varepsilon^2)$ is a representation of the delta distribution $\delta(z + z_0)$. Here, however, for $\varepsilon \to 0$ this term vanishes since $z = -z_0$ is not contained in the integration domain. By definition of Cauchy's formula, $z \in \gamma$, while z_0 is enclosed by γ.

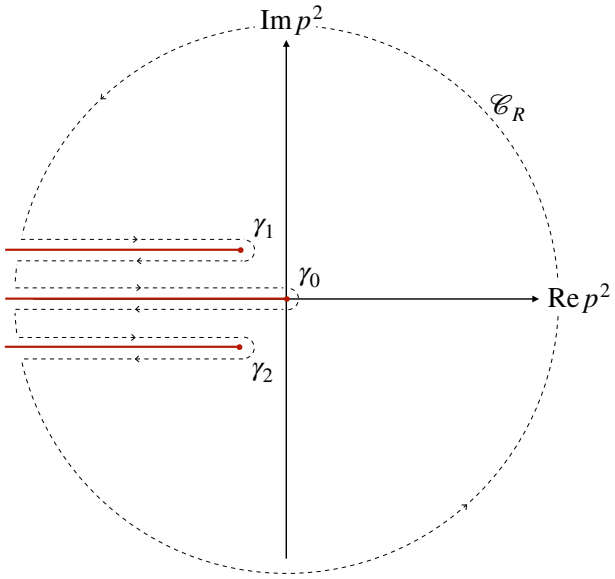

Abbildung A.1.: Integration contour γ in Cauchy's theorem (A.10) for construction of an integral representation of the ghost propagator from Appendix A.6.1, which uses an input gluon propagator with complex conjugate poles. Branch cuts are marked with red lines. The ghost propagator shows the ordinary branch cut along the negative real axis and two additional branch cuts, starting at χ and $\bar{\chi}$ and stretching in parallel to the real axis towards negative infinity, compare also Figure A.2. All branch cuts are explicitly excluded from the integration contour by the γ_i's.

Propagators with multiple branch cuts In the case of a gluon propagator with complex conjugate poles as considered in Appendix A.6.1, the ghost propagator shows two additional branch cuts, see Figure A.2. These additional cuts start at $p^2 = -\chi^2$ and $-\bar{\chi}^2$ respectively and stretch parallel to the real axis towards negative infinity. This general integral representation for propagators with multiple branch cuts $\mathcal{B}_i$ can now be constructed in analogy to (A.10)–(A.12). By the existence of additional branch cuts we need to relax property (i), still assuming holomorphicity everywhere except for the cuts, however. As for the derivation of the KL representation above, this is done by choosing the integration contour to wind around the cuts by simply excluding these additional branch cuts from the integration contour γ. We go from the cuts asymptotic limit to the branch point χ_i infinitesimally above/below the cut, turning at the branch point at returning the same path just infinitesimally below/above the cut. For the case of the ghost propagator of Appendix A.6.1 which has three branch cuts, the integration contour is displayed in Figure A.1.

The full integration contour can then conveniently be written as

$$\gamma = \lim_{R\to\infty} \mathcal{C}_R \bigoplus_i \gamma_i \,, \tag{A.14}$$

where γ_0 is the contour winding around the usual branch cut of the KL representation along the negative real axis. As before, due to property (iii), the integration along $\mathcal{C}_R$

vanishes. From (A.10), by above choice of γ we arrive at

$$G(z_0) = \frac{1}{2\pi \mathrm{i}} \sum_i \int_{\gamma_i} \mathrm{d}z \frac{G(z)}{z - z_0} \,. \tag{A.15}$$

We now split γ_i into the parts above/below the cut, which we call $\mathcal{B}_i^{+/-} = \mathcal{B}_i \pm \mathrm{i}\varepsilon$, such that $\gamma_i = \mathcal{B}_i^+ \bigoplus \mathcal{B}_i^-$. Since we integrate along the path in the mathematically positive direction, if the asymptotic value at infinity of the cut $\mathcal{B}_i$, B_i^∞, lies in the left half plane, γ_i starts above the cut with $\mathcal{B}_i^+$. The direction of integration is then such that we integrate along $\mathcal{B}_i^+$ from $B_i^\infty + \mathrm{i}\varepsilon$ to $\chi_i + \mathrm{i}\varepsilon$, and then go back along $\mathcal{B}_i^-$ from $\chi_i - \mathrm{i}\varepsilon$ to $B_i^\infty - \mathrm{i}\varepsilon$. If the asymptotic value lies in the right half plane, this works vice versa, going along $\mathcal{B}_i^-$ from $B_i^\infty - \mathrm{i}\varepsilon$ to $\chi_i - \mathrm{i}\varepsilon$ first and then back. Plugging in the split of γ_i explicitly and assuming the appropriate directionality along $\mathcal{B}_i^{+/-}$, we arrive at

$$\begin{aligned} G(z_0) &= \frac{1}{2\pi \mathrm{i}} \sum_i \int_{\mathcal{B}_i^+ \bigoplus \mathcal{B}_i^+} \mathrm{d}z \frac{G(z)}{z - z_0} \\ &= \frac{1}{2\pi \mathrm{i}} \sum_i \int_{\mathcal{B}_i} \mathrm{d}z \frac{G(z + \mathrm{i}\varepsilon) - G(z - \mathrm{i}\varepsilon)}{z - z_0} \,, \end{aligned} \tag{A.16}$$

where in the second line we used that we integrate along $\mathcal{B}_i^{+/-}$ in opposite directions.

With the general integral representation (A.16) for propagators with multiple branch cuts at hand, we can now directly arrive at the modified spectral representation for the ghost propagator (A.26). With the complex structure as shown in Figure A.2, the corresponding integration contour γ is sketched in Figure A.1. As demonstrated in (A.11) and (A.12), the branch cut $\mathcal{B}_0$ just yields the usual KL part G_c^{KL}. $\mathcal{B}_1$ and $\mathcal{B}_2$ then constitute the modification of the ordinary spectral representation, explicitly given by

$$\begin{aligned} G_c^\chi(z_0) &= \frac{1}{2\pi \mathrm{i}} \int_{\mathcal{B}_1 \bigoplus \mathcal{B}_2} \mathrm{d}z \frac{G_c(z + \mathrm{i}\varepsilon) - G_c(z - \mathrm{i}\varepsilon)}{z - z_0} \\ &= \frac{-1}{2\pi \mathrm{i}} \left(\int_{-\chi^2}^{-\infty - \chi^2} \mathrm{d}z \frac{G_c(z + \mathrm{i}\varepsilon) - G_c(z - \mathrm{i}\varepsilon)}{z - z_0} + \int_{-\bar{\chi}^2}^{-\infty - \bar{\chi}^2} \mathrm{d}z \frac{G_c(z + \mathrm{i}\varepsilon) - G_c(z - \mathrm{i}\varepsilon)}{z - z_0} \right) \\ &= \frac{1}{2\pi \mathrm{i}} \int_0^\infty \mathrm{d}z \left(\frac{G_c(-z - \chi^2 - \mathrm{i}\varepsilon) - G_c(-z - \chi^2 + \mathrm{i}\varepsilon)}{z + \chi^2 + z_0} \right. \\ &\qquad \left. + \frac{G_c(-z - \bar{\chi}^2 - \mathrm{i}\varepsilon) - G_c(-z - \bar{\chi}^2 + \mathrm{i}\varepsilon)}{z + \bar{\chi}^2 + z_0} \right) . \end{aligned} \tag{A.17}$$

Note that in (A.17), we already dropped the contributions corresponding to (A.13) here when combining the dominators with different signs of ε. We can now use that G_c is only discontinuous in its imaginary part across the branch cuts $\mathcal{B}_1$ and $\mathcal{B}_2$, such that, as for the KL branch cut, the real parts in the propagator difference in the denominators of (A.17)

cancel. We find that

$$G_c^{\chi}(z_0) = \frac{1}{2\pi}\int_0^{\infty} \mathrm{d}z \left\{ \frac{2\,\mathrm{Im}\Big[G_c(-z-\chi^2+\mathrm{i}\varepsilon) - G_c(-z-\chi^2-\mathrm{i}\varepsilon)\Big]}{z+\chi^2+z_0} \right.$$
$$\left. + \frac{2\,\mathrm{Im}\Big[G_c(-z-\bar{\chi}^2+\mathrm{i}\varepsilon) - G_c(-z-\bar{\chi}^2-\mathrm{i}\varepsilon)\Big]}{z+\bar{\chi}^2+z_0} \right\}. \tag{A.18}$$

Exploiting the mirror symmetry (ii), we finally arrive at

$$G_c^{\chi}(z_0) = \frac{1}{2\pi}\int_0^{\infty} \mathrm{d}z \left(\frac{1}{z+\chi^2+z_0} + \frac{1}{z+\bar{\chi}^2+z_0} \right)$$
$$\times\, 2\,\mathrm{Im}\Big[G_c(-z-\chi^2+\mathrm{i}\varepsilon) - G_c(-z-\chi^2-\mathrm{i}\varepsilon)\Big]. \tag{A.19}$$

With $G_c = G_c^{\mathrm{KL}} + G_c^{\chi}$, we end up with the modified spectral representation for the ghost propagator, which is

$$G_c(z_0) = \int_0^{\infty} \frac{\mathrm{d}z}{2\pi} \left\{ \frac{\rho_c^{\mathrm{KL}}(z)}{p^2+z^2} + \rho_c^{\chi}(z) \left(\frac{1}{z+\chi^2+z_0} + \frac{1}{z+\bar{\chi}^2+z_0} \right) \right\} \tag{A.20a}$$

with

$$\rho_c^{\chi}(z) = 2\,\mathrm{Im}\Big[G_c(-z-\chi^2+\mathrm{i}\varepsilon) - G_c(-z-\chi^2-\mathrm{i}\varepsilon)\Big] \tag{A.20b}$$

and ρ_c^{KL} the usual KL spectral function (4.4).

A.6. Propagation of non-analyticities through the coupled YM system

In this section, we provide details on the analytic calculation showing the propagation of non-analyticities through the coupled YM system present in Section 5.1.

A.6.1. Ghost DSE

As a starting point of the following investigation, we study the effect of a single pair of complex conjugate poles in the gluon propagator on the ghost propagator. This is done via the spectral ghost DSE, set up in Section 5.4.2. Owing to the spectral-non-spectral split (5.33), for the complex conjugate pole contribution to the gluon propagator we then explicitly have

$$G_A^\chi(p) = \frac{R_\chi}{p^2+\chi^2} + \frac{\bar{R}_\chi}{p^2+\bar{\chi}^2}\,, \tag{A.21}$$

where one of the poles is located at $p^2 = -\chi^2$ and has residue R_χ. The relevant correction to the fully spectral part of the ghost loop $\sim G_A^{\mathrm{KL}} G_c^{\mathrm{KL}}$ is then $\sim G_A^\chi G_c^{\mathrm{KL}}$. We assume the ghost propagator to be given solely by its classical contribution, i.e.

$$G_c^{\mathrm{KL}} \approx G_c^{\mathrm{cl}} \qquad \text{with} \qquad G_c^{\mathrm{cl}}(p) = \frac{1}{p^2}\,. \tag{A.22}$$

For the ghost spectral function, this corresponds to just having the massless pole with residue $1/Z_c = 1$ in the origin, cf. (5.7). Note that the results of the following discussion are not altered by also including scattering tails for ghost and gluon spectral functions due to superposition with the contributions of (A.22). For the same reason, the following investigation is independent of particular infrared scenarios of Yang-Mills such as scaling/decoupling or massive solutions.

With choice (A.22) and the complex conjugate pole gluon propagator (A.21), we arrive at the ghost self-energy

$$\begin{aligned}
\Sigma_{\bar{c}c}^{(1)}(p) &= g^2 N_c \int_q \left(p^2 - \frac{(p\cdot q)^2}{q^2}\right) G_c^{\mathrm{cl}}(p+q) G_A^\chi(q) \\
&= g^2 N_c \int_q \left(p^2 - \frac{(p\cdot q)^2}{q^2}\right) \frac{1}{(p+q)^2} \\
&\quad \times \left(\frac{R_\chi}{p^2+\chi^2} + \frac{\bar{R}_\chi}{p^2+\bar{\chi}^2}\right)\,,
\end{aligned} \tag{A.23}$$

which is readily integrated analytically via dimensional regularisation in analogy to Appendix B.5 with the appropriate choice of the gluon and ghost spectral functions. The respective gluon and ghost spectral functions of the propagators (A.21) and (A.22) read,

$$\begin{aligned}
\rho_A(\omega) &= \rho_A^\chi(\omega)\,, \\
\rho_c(\omega) &= \rho_c^{\mathrm{cl}}(\omega)\,,
\end{aligned} \tag{A.24a}$$

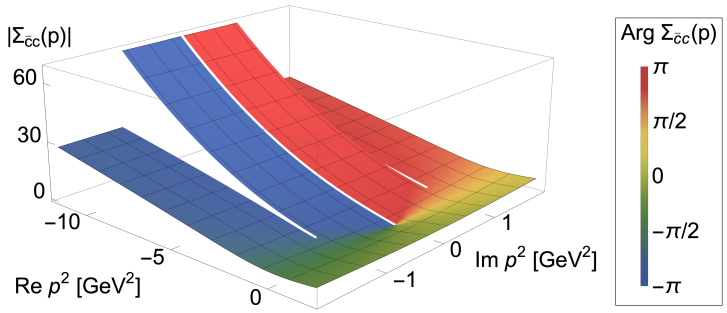

Abbildung A.2.: Ghost self energy $\Sigma_{\bar{c}c}$ in the complex plane as defined in (A.23), yielding two additional branch cuts in the ghost propagator. In $\Sigma_{\bar{c}c}$, a gluon propagator with a pair of complex conjugate poles (A.21) is used. This choice directly results in two additional branch cuts, running parallelly to the negative real axis. Hence, we observe a violation of the ghost propagators Källén-Lehmann representation induced by a pair of complex conjugate poles in the gluon propagator.

with

$$\rho_A^{\chi}(\omega) = \pi\left[Z_\chi \delta(\omega^2 - \chi^2) + \bar{Z}_\chi \delta(\omega^2 - \bar{\chi}^2)\right],$$
$$\rho_c^{\mathrm{cl}} = \pi\delta(\omega^2)\,. \tag{A.24b}$$

The δ-distributions for complex arguments $\chi^2, \bar{\chi}^2 \in \mathbb{C}$ in the gluon spectral functions should then be understood as

$$\int_0^\infty \mathrm{d}\omega\, \delta(\omega - \chi)\Phi(\omega) = \Phi(\chi)\,, \tag{A.25}$$

for a test function $\Phi(\omega)$. Evidently, the complex frequencies $\chi, \bar{\chi}$ are not inside the spectral integration domain $\omega \in [0, \infty)$. In order to make sense in a distributional sense, a proper integration contour for the spectral integration has to be chosen, since the complex conjugate pole positions are not element of the usual spectral integration domain, for details see Appendix A.5.

The analytic result for the ghost self-energy (A.23) is depicted in the full complex p^2-plane in Figure A.2. In addition to the usual branch cut along the negative p^2-axis, two additional branch cuts are present, and are clearly visible in Figure A.2. Starting at their respective branch points at χ and $\bar{\chi}$, the additional cuts extend parallelly to the negative real axis towards infinity. In consequence, the KL representation is violated, since it requires all non-analyticities to be confined to the negative real p^2-axis.

In the absence of a KL spectral representation one can devise an alternative integral representation for the ghost propagator. This representation will maintain the analytical solvability of loop momentum integrals featuring ghost propagators despite violation of its spectral representation. In consequence, also in a scenario like shown in Figure A.2 functional equations can still be evaluated on the real frequency axis. Given the complete complex structure of $\Sigma_{\bar{c}c}$, this can be done in analogy to the construction of the KL

representation (4.3) by help of Cauchy's integral theorem. We end up with a *modified spectral representation* for the ghost propagator by excluding also the two additional branch cuts from the circular integration contour with radius $R \to \infty$ around the origin. In the spectral-non-spectral split (5.33), this leads us to a non-spectral contribution of the ghost propagator given by

$$G_c^\chi(p) = \int_\lambda \rho_c^\chi(\lambda)\Big(\frac{1}{p^2+\lambda^2+\chi^2} + \frac{1}{p^2+\lambda^2+\bar{\chi}^2}\Big)\,. \tag{A.26a}$$

We also introduced the additional spectral function ρ_c^χ defined via

$$\rho_c^\chi(\omega) = \mathrm{Im}\Big[G(-\mathrm{i}\sqrt{\omega^2+\chi^2+\mathrm{i}0^+}) - G(-\mathrm{i}\sqrt{\omega^2+\chi^2-\mathrm{i}0^+})\Big]\,. \tag{A.26b}$$

Note that in the Källén-Lehmann case, the imaginary parts of the two propagators in (A.26b) are related by mirror (anti)symmetry. Here, this symmetry is spoiled by the fact the branch cuts are shifted into the complex plane through the appearance of the complex mass parameter χ. The spectral functions encoding the weight of the branch cuts in the upper and lower half are related by this exact mirror symmetry, however. This symmetry has been exploited in obtaining (A.26), since there only one spectral function appears. The full derivation of the modified spectral representation (A.26) as well as its generalisation to an arbitrary number of branch cuts is presented in Appendix A.5.

In Figure A.3, we compare the directly computed Euclidean ghost propagator corresponding to the ghost self-energy defined in (A.23) with its KL as well as its modified spectral representation. The violation of the KL representation by the complex conjugate poles of the gluon propagator is validated. In addition, the validity of the modified spectral representation (A.26) is confirmed. In particular, this confirms the analytic structure of the ghost self-energy presented in Figure A.2, since the modified spectral representation is a direct consequence.

A.6.2. Gluon DSE

We proceed with the analysis of the complex structure of Yang-Mills theory by investigating the back-propagation of a pair of complex conjugate poles in the gluon propagator into the spectral gluon DSE: in the ghost loop we insert the modified spectral representation (A.26) for the ghost, and investigate the contribution of the additional cuts. For a complete picture, the complex conjugate gluon propagator poles also have to be fed back via the gluon loops. The latter part will be deferred to future work, however, since the feedback of the additional cuts in the ghost propagator suffices to arrive at a conclusive picture. Nevertheless, we will provide the relevant expressions in this section. Note also that the tadpole is absorbed in the renormalisation.

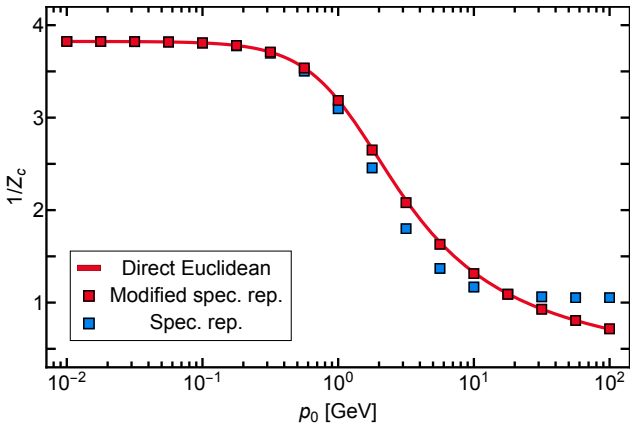

Abbildung A.3.: Violation of the ghost propagators Källén-Lehmann representation by using a gluon propagator featuring a pair of complex conjugate poles and validation of the ghost propagators modified spectral representation (A.26). The solid line represents the ghost dressing function computed directly via the spectral Euclidean DSE (5.28), using a complex conjugate pole gluon propagator. The squared points are obtained from the corresponding realtime DSE via the ordinary spectral representation (4.3) (blue) and the modified spectral representation (A.26), also taking into account the two additional branch cuts (comp. Figure A.2) induced by the gluon propagators complex conjugate poles. While the dressing function obtained from the modified spectral representation matches the directly computed Euclidean ghost dressing perfectly, the Källén-Lehmann one is clearly off. Note that this not only proves the violation of the ordinary spectral representation, but in particular validates the result for the ghost self-energy (A.23) presented in Figure A.2.

Ghost loop We use the spectral DSEs set-up Section 5.4.2, similarly to Appendix A.6.1 and concentrate on the leading order correction $G^{\mathrm{KL}}G^{\chi}$. The computation and the analytic results are deferred to Appendix B.5. In the spectral gluon DSE, we now consider the modified spectral representation for the ghost, where the non-spectral part G_c^{χ} is constituted by (A.26). For the spectral part of the ghost propagator, we again only consider the classical contribution, see (A.22). This leads us to

$$\begin{aligned}\mathcal{D}^{(1)}_{\mathrm{ghost}} &= g^2 N_c \int_q \left(q^2 - \frac{(p\cdot q)^2}{p^2}\right) G_c^{\chi}(p+q) G_c^{\mathrm{KL}}(q) \\ &= g^2 N_c \int_\lambda \rho_c^{\chi}(\lambda) \int_q \left(q^2 - \frac{(p\cdot q)^2}{p^2}\right) \frac{1}{(p+q)^2} \left(\frac{1}{q^2+\lambda^2+\chi^2} + \frac{1}{q^2+\lambda^2+\bar{\chi}^2}\right).\end{aligned} \tag{A.27}$$

Again, the loop momentum integral in (A.27) can be evaluated analytically via dimensional regularisation, see Appendix B.5.2. The result is obtained by adding to copies of the expression for the ghost loop quoted in Appendix B.5.2 where one spectral parameter is taken to zero and the other one is substituted such that the ordinary KL kernel is transformed into that of the modified spectral representation (A.26) featuring in (A.27). In explicit, this is $\lambda_1 \to 0$ and $\lambda_2 \to \sqrt{\lambda_2^2+\chi^2}$ resp. $\sqrt{\lambda_2^2+\bar{\chi}^2}$. The validity range of this

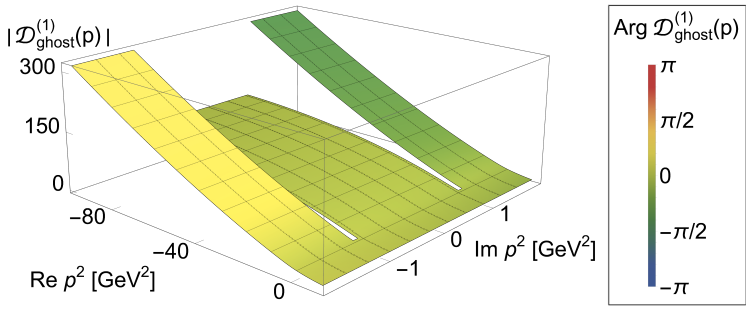

Abbildung A.4.: Contribution to the ghost loop $\mathcal{D}_{\text{ghost}}$ in the complex plane as defined in (A.27), causing additional branch cuts in the gluon propagator. In $\mathcal{D}^{(1)}_{\text{ghost}}$, one of the ghost propagators is given by the violation of the spectral representation G^{χ}_{c} of the ghost propagator, as defined in (A.26). The modification of the ordinary spectral representation is constituted by two additional branch cuts in the ghost propagator (comp.Figure A.2), which are themselves induced by a pair of complex conjugate poles in the gluon propagator through the ghost DSE (5.28). In consequence, a consistent solution of Yang-Mills theory with one or more pairs of complex conjugate poles in the gluon propagator (on top of the usual branch cut) is ruled out, since we were able to show that a pair of complex conjugate poles always produces an additional, corresponding pair of branch cuts.

substitution is discussed in Appendix B.5.4, since by above the substitutions the spectral parameters are effectively complex.

We now aim for a closed symbolic form for (A.27), which necessitates analytic access to the spectral integral. For the present purpose of studying the complex structure, it suffices to choose a well-behaved trial spectral function $\rho^{\chi}_{c} = \rho^{(\text{trial})}$ with appropriate decay behaviour. Here, a convenient choice is $\rho^{(\text{trial})}(\lambda) = 1/(1+\lambda^2)$. The superficially divergent spectral integral is rendered finite via application of spectral BPHZ regularisation, see Section 5.1.2.3. We emphasise that both the procedure of spectral regularisation and the choice of $\rho^{(\text{trial})}$, do not affect the complex structure of the diagram.

In the right panel of Figure A.4 we show the leading order correction (A.27) in the complex momentum plane. We find two additional branch cuts, stretching in parallel to the real axis from $p^2 = -\chi^2$ and $-\bar{\chi}^2$ towards negative real infinity. Thus, a pair of complex conjugate poles in the gluon propagator also leads to additional branch cuts in the gluon propagator. This can be seen via the modified spectral representation for the ghost propagator (A.26), itself induced by the complex conjugate poles of the gluon propagator via the ghost DSE, see Appendix A.6.1.

At order $(G^{\chi}_{c})^2$, the contribution to the ghost loop arising from the complex conjugate

pole gluon propagator reads

$$\begin{aligned}\mathcal{D}^{(2)}_{\text{ghost}} &= g^2 N_c \int_q \left(q^2 - \frac{(p\cdot q)^2}{p^2}\right) G_c^\chi(q) G_c^\chi(p+q) \\ &= g^2 N_c \int_{\lambda_1,\lambda_2} \rho_c^\chi(\lambda_1)\rho_c^\chi(\lambda_2) \int_q \left(q^2 - \frac{(p\cdot q)^2}{p^2}\right) \left(\frac{1}{q^2+\lambda^2+\chi^2} + \frac{1}{q^2+\lambda^2+\bar{\chi}^2}\right) \\ &\quad \times \left(\frac{1}{(p+q)^2+\lambda^2+\chi^2} + \frac{1}{(p+q)^2+\lambda^2+\bar{\chi}^2}\right). \end{aligned} \tag{A.28}$$

Equation (A.28) involves two spectral integrals, obstructing a fully analytic evaluation of this contribution. Inspecting the analytic structure of the integrand in comparison to the $G_c^\chi G_c^{\text{KL}}$-contribution of (A.27), we see that the previously massless classical ghost propagator is replaced by the modified spectral kernel $1/(p^2+\lambda^2+\chi^2)$ and $1/(p^2+\lambda^2+\bar{\chi}^2)$. The complex structure of these integrals is dominated by the imaginary parts of the logarithmic terms, that occur after evaluating the momentum integrals via dimensional regularisation. Hence, we anticipate, that the complex structure of this contribution is similar to that of the leading order correction shown in Figure A.4.

The direct investigation of this term is not performed here, as the leading order contribution already shows two additional branch cuts. The latter are already inconsistent with the assumption of a single pair of complex conjugate poles in the gluon propagator, which was the starting point of this investigation. Nonetheless, in the following we will also quote the expressions for the complex conjugate poles induced corrections to the gluon loop for the sake of completeness.

Gluon loop The first order contribution in G_A^χ to the gluon loop is given by

$$\begin{aligned}\mathcal{D}^{(1)}_{\text{gluon}} &= g^2 N_c \int_q V(p,q) G_A^\chi(q) G_A^{\text{KL}}(p+q) \\ &= g^2 N_c \int_\lambda \rho_A^{\text{KL}}(\lambda) \int_q V(p,q) \frac{1}{(p+q)^2+\lambda^2} \left(\frac{R_\chi}{q^2+\chi^2} + \frac{\bar{R}_\chi}{q^2+\bar{\chi}^2}\right), \end{aligned} \tag{A.29}$$

with $V(p,q)$ as defined in (5.25). The $\mathcal{O}({G_A^\chi}^2)$ contribution is given by

$$\begin{aligned}\mathcal{D}^{(2)}_{\text{gluon}} &= g^2 N_c \int_q V(p,q) G_A^\chi(q) G_A^\chi(p+q) \\ &= g^2 N_c \int_q V(p,q) \left(\frac{R_\chi}{q^2+\chi^2} + \frac{\bar{R}_\chi}{q^2+\bar{\chi}^2}\right)\left(\frac{R_\chi}{(p+q)^2+\chi^2} + \frac{\bar{R}_\chi}{(p+q)^2+\bar{\chi}^2}\right). \end{aligned} \tag{A.30}$$

The computation of $\mathcal{D}^{(1)}_{\text{gluon}}$ and $\mathcal{D}^{(2)}_{\text{gluon}}$ in the full complex momentum plane requires the evaluation of the respective momentum integrals for two arbitrary complex masses $\chi, \bar{\chi}$ and momenta p^2. The analytic evaluation of this integral is significantly more challenging than with just one complex mass parameter, as for the ghost loop (A.27). In particular, the employed technique of Feynman parametrisation is not applicable in this scenario, as we discuss in Appendix B.5.4.

However, we have already shown in Appendix A.6.1, that a complex conjugate pole gluon propagator leads to additional branch cuts in the gluon propagator via the ghost loop.

Thus, the input assumption of a spectral function plus a pair of complex conjugate poles for the gluon propagator is violated independently of the complex structure of the gluon loop $\mathcal{D}_{\text{gluon}}$. While an investigation of the effect of the complex conjugate pole contribution of the gluon propagator on the complex structure of the gluon loop might nevertheless yield additional valuable insight into the analytic structure of Yang-Mills theory, we defer this to future work. Still, we remark that in our opinion a cancellation between the shifted branch cuts of $\mathcal{D}_{\text{ghost}}$ and those possibly existing in $\mathcal{D}_{\text{gluon}}$ cannot be expected. This would require the vertices to compensate for the different weights of the cuts, since the ghost diagram cuts are induced by the ghost and the (possible) gluon diagram cuts by the gluon propagator.

A.7. Ghost loop with massive non-integer power propagators

The scaling solution of Yang-Mills theory is characterised by the IR behaviour of the ghost and gluon propagator dressing functions as

$$\lim_{p\to 0} Z_A(p) \sim (p^2)^{-2\kappa}\,, \qquad \lim_{p\to 0} Z_c(p) = (p^2)^{\kappa}\,, \tag{A.31}$$

while for a decoupling behaviour, we have

$$\lim_{p\to 0} Z_A(p) \sim \frac{1}{p^2}\,, \qquad \lim_{p\to 0} Z_c(p) = Z_c\,, \tag{A.32}$$

A particularly useful analytic form of the ghost propagator which allows to smoothly interpolate between scaling and decoupling behaviour in the IR is given by

$$G_c(p,m) = \frac{1}{p^2(p+m)^{\kappa}}\,, \tag{A.33}$$

with the non-integer scaling exponent $0 < \kappa < 1$. The scaling solution is realised for $m \to 0$. Non-perturbative studies of Yang-Mills theories suggest $\kappa \approx 0.57$ [95]. In an approximation with bare vertices, the value of κ can be determined analytically from the DSE to be $\kappa = \frac{93+\sqrt{1201}}{98} \approx 0.59535$ [92].

In cases like the scaling or decoupling scenario where the infrared behaviour of a propagator is known, it can be beneficial to analytically split off the IR part as $G = G^{\mathrm{IR}} + \Delta G$. Here, we study the ghost loop $\mathcal{D}_{\mathrm{ghost}}$ in the gluon DSE where the ghost propagator is entirely given by the IR parametrisation of (A.33), reading

$$\mathcal{D}_{\mathrm{ghost}} = g^2 N_c \tilde{Z}_1 \int_q \left(q^2 - \frac{(p\cdot q)^2}{p^2}\right) \frac{1}{q^2}\,\frac{1}{(p+q)^2}\,\frac{1}{(q^2+m^2)^{\kappa}}\,\frac{1}{((p+q)^2+m^2)^{\kappa}}\,. \tag{A.34}$$

Analytic solutions of integrals of this kind have, to our knowledge, not been quoted in the literature so far. The non-integer exponent κ increases the difficulty of the integral enormously. Since only the non-integer part of the propagator power carries the mass m, from the mathematical perspective (A.34) represents a Feynman diagram with four propagators in a particular momentum-configuration with two massive propagators of the same mass. The large number of propagators renders the approach of introducing Feynman parameters as in Appendix B.5 non-feasible. A more powerful technique to solve integrals of this kind has been proposed by Davydychev and Boos [455], representing massive denominators by Mellin-Barnes integrals as

$$\frac{1}{(k^2+m^2)^{\alpha}} = \frac{1}{(k^2)^{\alpha}}\,\frac{1}{\Gamma(\alpha)}\,\frac{1}{2\pi\mathrm{i}}\int_{-\mathrm{i}\infty}^{\mathrm{i}\infty} \mathrm{d}s \left(\frac{m^2}{k^2}\right)^{s} \Gamma(-s)\Gamma(\alpha+s)\,, \tag{A.35}$$

which follows from the Barnes integral representation of the hypergeometric function ${}_1F_0\big(a\big|z\big)$. A pedagogical introduction to the technique can be found e.g. in [456]. The generalised hypergeometric function of one variable is defined by

$${}_AF_B\left(\begin{matrix} a_1,\ldots,a_A \\ b_1,\ldots,b_B \end{matrix}\,\middle|\, z\right) = \sum_{j=0}^{\infty} \frac{(a_1)_j\ldots(a_A)_j}{(b_1)_j\ldots(b_B)_j}\,\frac{z^j}{j!}\,, \tag{A.36}$$

where $(a)_j = \Gamma(a+j)/\Gamma(a)$ is the Pochhammer symbol.

Using (A.35) for the non-integer power propagators in (A.34) and dropping the prefactor $g^2 N_c \tilde{Z}_1$, we get

$$\mathcal{D}_{\text{ghost}} = \frac{-1}{4\pi^2}\frac{1}{\Gamma(\kappa)^2}\int_{-\mathrm{i}\infty}^{\mathrm{i}\infty}\mathrm{d}s\int_{-\mathrm{i}\infty}^{\mathrm{i}\infty}\mathrm{d}t\,(m^2)^{s+t}\Gamma(-s)\Gamma(-t)\Gamma(\kappa+s)\Gamma(\kappa+t)I^{\text{MB}}_{\text{ghost}}(p,m)\,, \tag{A.37a}$$

with

$$I^{\text{MB}}_{\text{ghost}} = \int_q \Big(q^2 - \frac{(p\cdot q)^2}{p^2}\Big)\frac{1}{(q^2)^{\kappa+s+1}}\frac{1}{((p+q)^2)^{\kappa+t+1}}\,. \tag{A.37b}$$

Defining $k = p+q$, we can rewrite the momentum integral as

$$I^{\text{MB}}_{\text{ghost}} = \frac{1}{2}\int_q \mathcal{P}(p,q,k)\frac{1}{(q^2)^{\kappa+s+1}}\frac{1}{(k^2)^{\kappa+t+1}} \tag{A.38a}$$

where

$$\mathcal{P}(p,q,k) = q^2 + k^2 - \frac{1}{2}p^2 - \frac{1}{2p^2}\big(k^4 - 2k^2q^2 + q^4\big)\,. \tag{A.38b}$$

Equation (A.38) is now evaluated with help of the well-known integration formula

$$\int\frac{\mathrm{d}^d q}{(2\pi)^d}\Big(\frac{1}{q^2}\Big)^{d/2-\alpha}\Big(\frac{1}{p^2}\Big)^{\alpha-\beta}\Big(\frac{1}{k^2}\Big)^{\beta} = \frac{1}{(4\pi)^{d/2}}\frac{\Gamma(\alpha)\Gamma(\frac{d}{2}-\beta)\Gamma(\beta-\alpha)}{\Gamma(\beta)\Gamma(\frac{d}{2}-\alpha)\Gamma(\frac{d}{2}+\alpha-\beta)}\,. \tag{A.39}$$

Convergence of (A.39) is only ensured for $\mathrm{Re}(\alpha) > 0$, $\mathrm{Re}(\beta-\alpha) > 0$ and $\mathrm{Re}(\beta) < d/2$. Although the convergence requirements do not hold for all summands of $\mathcal{P}$ defined in (A.38) separately, it holds for its initial form $\mathcal{P} = q^2 - (p\cdot q)^2/p^2$. Application of (A.39) is hence justified, and setting $d=4$ we find

$$I^{\text{MB}}_{\text{ghost}}(p,m) = \frac{3}{2(4\pi)^2}(p^2)^{1-2\kappa-s-t}\frac{\Gamma(s+t+2\kappa+2)\Gamma(2-s-\kappa)\Gamma(2-t-\kappa)}{\Gamma(s+\kappa+1)\Gamma(t+\kappa+1)\Gamma(4-s-t-2\kappa)}\,. \tag{A.40}$$

Using $\Gamma(z+1) = z\Gamma(z)$ and the result of the momentum integration (A.40), (A.37) becomes

$$\begin{aligned}\mathcal{D}_{\text{ghost}} = \frac{-3}{128\pi^4}\frac{1}{\Gamma(\kappa)^2}\int_{-\mathrm{i}\infty}^{\mathrm{i}\infty}\mathrm{d}s\int_{-\mathrm{i}\infty}^{\mathrm{i}\infty}\mathrm{d}t\Big(\frac{m^2}{p^2}\Big)^{s+t}(p^2)^{1-2\kappa} \\ \times\frac{\Gamma(-s)\Gamma(-t)\Gamma(s+t+2\kappa+2)\Gamma(2-s-\kappa)\Gamma(2-t-\kappa)}{(s+\kappa)(t+\kappa)\Gamma(4-s-t-2\kappa)}\,.\end{aligned} \tag{A.41}$$

The two remaining integrals in (A.41) along the imaginary axis can be evaluated via the residue theorem, closing the integration contour at real positive/negative infinity for $p^2 > m^2/p^2 < m^2$. This step can be automated using the Mathematica packages *MB* [457] and *MBsums* [458]. The result is quoted as

$$\mathcal{D}_{\text{ghost}} = \frac{-3}{128\pi^4}\frac{1}{\Gamma(\kappa)^2}\begin{cases}(m^2)^{1-2\kappa}\mathcal{M}^{\text{IR}}(p,m) & p<4m \\ (p^2)^{1-2\kappa}\mathcal{M}^{\text{UV}}(p,m) & \text{else}\end{cases}\,. \tag{A.42}$$

The functions $\mathcal{M}$ are given by the sums of the residues of (A.41), and explicitly read

$$\mathcal{M}^{\mathrm{IR}} = \mathcal{M}_1^{\mathrm{IR}} + \mathcal{M}_2^{\mathrm{IR}} + \mathcal{M}_3^{\mathrm{IR}} \tag{A.43}$$

with

$$\mathcal{M}_1^{\mathrm{IR}} = \frac{-1}{24}\Big(\frac{p^2}{m^2}\Big)^2 \Gamma(\kappa)\Gamma(\kappa+1)\,{}_3F_2\Big(\begin{matrix}1,1,1+\kappa\\2,5\end{matrix}\Big|-\frac{p^2}{m^2}\Big)\,,$$

$$\begin{aligned}\mathcal{M}_2^{\mathrm{IR}} = &-\sum_{n_1,n_2=0}^{\infty} \frac{(-1)^{n_1+n_2}\Gamma(n_1+n_2+\kappa+1)\big(\frac{m^2}{p^2}\big)^{-n_1}}{n_1!(n_1+2)!n_2!(n_2+2)!(n_1+n_2+1)!\Gamma(n_2+\kappa+1)\Gamma(-n_1-n_2+2-\kappa)}\\
&\times\Big[(n_2+1)!\Gamma(-n_2-2-\kappa)\Gamma(n_2+\kappa+1)(n_1+n_2)!(n_1+n_2+2)!\Gamma(-n_1-n_2+2-\kappa)\\
&\quad-(n_2+2)!\Gamma(2-\kappa-n_2)\Gamma(n_2+\kappa)(n_1+n_2+1)!\Gamma(-n_1-n_2+1-\kappa)\\
&\qquad\times\Gamma(n_1+n_2+2\kappa-1)\Big]\,,\end{aligned}$$

$$\mathcal{M}_3^{\mathrm{IR}} = \Gamma(\kappa)^2\left(\frac{1}{2(\kappa-1)}+\frac{1}{6}\frac{p^2}{m^2}\Big[\frac{1}{6}\Big(\psi(\kappa)-\log\frac{m^2}{p^2}+\gamma_E\Big)-\frac{11}{6}\Big]\right), \tag{A.44}$$

where ψ is the digamma function and

$$\mathcal{M}_1^{\mathrm{UV}} = \sum_{n_1,n_2=0}^{\infty} \frac{(-1)^{n_1+n_2}\big(\frac{m^2}{p^2}\big)^{n_1+n_2}\Gamma(-\kappa-n_1+2)\Gamma(-\kappa-n_2+2)\Gamma(2\kappa+n_1+n_2-1)}{(\kappa+n_1)(\kappa+n_2)\Gamma(n_1+1)\Gamma(n_2+1)\Gamma(-2\kappa-n_1-n_2+4)}\,,$$

$$\begin{aligned}\mathcal{M}_2^{\mathrm{UV}} = &\sum_{n_1,n_2=0}^{\infty} \frac{(-1)^{n_1+n_2}(n_1+1)!\big(\frac{m^2}{p^2}\big)^{-\kappa+n_1+n_2+2}\Gamma(\kappa-n_1-2)\Gamma(-\kappa-n_2+2)}{n_1!(n_1+2)!n_2!\Gamma(-\kappa-n_1-n_2+2)\Gamma(\kappa+n_2+1)}\\
&\qquad\times\Gamma(\kappa+n_2)\Gamma(\kappa+n_1+n_2+1)\,,\end{aligned}$$

$$\begin{aligned}\mathcal{M}_3^{\mathrm{UV}} = &\sum_{n_1,n_2=0}^{\infty} \frac{(-1)^{n_1+n_2}(n_2+1)!\big(\frac{m^2}{p^2}\big)^{-\kappa+n_1+n_2+2}\Gamma(-\kappa-n_1+2)\Gamma(\kappa+n_1)}{n_1!n_2!(n_2+2)!\Gamma(\kappa+n_1+1)\Gamma(-\kappa-n_1-n_2+2)}\\
&\qquad\times\Gamma(\kappa-n_2-2)\Gamma(\kappa+n_1+n_2+1)\,.\end{aligned} \tag{A.45}$$

The double sums appearing in (A.44) and (A.45) can be represented as Kampé de Fériet functions, which generalise the hypergeometric function of two variables to

$$\begin{aligned}F_{C:D;D'}^{A:B;B'}\Big(\begin{matrix}a_1,\dots,a_A:b_1,\dots,b_B;b'_1,\dots,b'_{B'}\\c_1,\dots,c_C:d_1,\dots,d_D;d'_1,\dots,d'_{d'}\end{matrix}\Big|z_1,z_2\Big) = \qquad\qquad (A.46)\\
\sum_{j_1,j_2=0}^{\infty}\frac{(a_1)_{j_1+j_2}\dots(a_A)_{j_1+j_2}(b_1)_{j_1}\dots(b_B)_{j_1}(b'_1)_{j_2}\dots(b'_{B'})_{j_2}}{(c_1)_{j_1+j_2}\dots(c_C)_{j_1+j_2}(d_1)_{j_1}\dots(d_D)_{j_1}(d'_1)_{j_2}\dots(d'_{D'})_{j_2}}\frac{z_1^{j_1}z_2^{j_2}}{j_1!j_2!}\,,\end{aligned}$$

by identifying the respective Pochhammer symbols. Since in numerical implementations special functions such as the Kampé de Fériet function defined in (A.46) are often evaluated via their series representation, we do not reformulate the double sums in (A.44) and (A.45) here. The presented analytic result can be validated by evaluating (A.34) numerically. Note that in particular, with the above expressions at hand, also here we can directly evaluate the diagram at real frequencies ω.

A.8. Spectral sum rules from perturbative dressing functions

In a general manner, given a KL representation, the normalisation relation for the corresponding spectral function can be inferred from the perturbative behaviour of the propagator. Multiplying (4.3) by p^2, one has

$$\frac{1}{Z(p)} = p^2 \int \frac{d\lambda^2}{\pi} \frac{\rho(\lambda)}{p^2+\lambda^2} = \int \frac{d\lambda^2}{\pi} \frac{\rho(\lambda)}{1+\lambda^2/p^2} \,. \tag{A.47}$$

In the UV, the behaviour of the dressing function $Z(p)$ can be inferred from perturbation theory, $\lim_{p\to\infty} 1/Z(p) = Z_\infty^{-1}$. For large p^2, we can also expand the integrand, yielding

$$\begin{aligned} Z_\infty^{-1} &= \lim_{p\to\infty} \sum_{n=0}^{\infty} (-1)^n \int \frac{d\lambda^2}{\pi} \rho(\lambda) \left(\frac{\lambda^2}{p^2}\right)^n \\ &= \int \frac{d\lambda^2}{\pi} \rho(\lambda) + \lim_{p\to\infty} \Delta(p) \,, \end{aligned} \tag{A.48}$$

defining

$$\Delta(p) = \sum_{n=1}^{\infty} (-1)^n (p^2)^{-n} \int \frac{d\lambda^2}{\pi} \rho(\lambda)\, \lambda^{2n} \,. \tag{A.49}$$

We want to show $\lim_{p\to\infty} \Delta(p) = 0$ in order to obtain a normalisation condition for ρ via (A.48) using the known perturbative asymptotics of the corresponding dressing function. In doing that, we first note that for the spectral integral in the left term of the lower line in (A.48) to converge, the spectral function must obey

$$\lim_{\omega\to\infty} \rho(\omega)\, \omega^2 \log \omega^2 \to 0 \,. \tag{A.50}$$

If this requirement does not hold, ρ cannot be normalised in the above form.

Based on the assumption of the existence of above representation (A.47), ρ can be taken to be integrable on $[0,\infty)$. We choose a scale Λ such that for frequencies $\lambda > \Lambda$, ρ is given solely by the leading UV behaviour of its corresponding propagator via (4.4), see also [243]. Denoting the known UV asymptotics as ρ_{UV}, we then distinguish

$$\rho(\omega) = \begin{cases} \rho_\Lambda(\omega) & \text{if } \omega \leq \Lambda \,, \\ \rho_{\mathrm{UV}}(\omega) & \text{else} \,, \end{cases} \tag{A.51}$$

where ρ_{UV} now obeys (A.50). Note that by the nature of the spectral function being a tempered distribution, it can have distributional contributions such as (higher order) poles. These are allowed in our consideration as long as integrability is not violated. The parametrisation (A.51) is chosen such that these contributions are contained in ρ_Λ. We now split the spectral integration interval of (A.49) along the split of the spectral function and conclude for finite Λ that

$$\int_0^\Lambda \frac{d\lambda^2}{\pi} \rho_\Lambda(\lambda)\, \lambda^{2n} < \infty \quad \forall\, n \geq 1 \,, \tag{A.52}$$

such that for large momenta, the contribution (A.52) to the spectral representation of the dressing function vanishes,

$$\lim_{p\to\infty} (p^2)^{-n} \int_0^\Lambda \frac{d\lambda^2}{\pi} \rho_\Lambda(\lambda)\, \lambda^{2n} \to 0\,. \tag{A.53}$$

Hence, in the limit of large p we are only left with spectral integral over ρ_{UV} contributing to $\Delta(p)$ in (A.49). Taking into account the known asymptotics of ρ_{UV} from (A.50) however, we find that

$$\lim_{p\to\infty} (p^2)^{-n} \int_\Lambda^\infty \frac{d\lambda^2}{\pi} \rho_{\mathrm{UV}}(\lambda)\, \lambda^{2n} < C \lim_{p\to\infty} (p^2)^{-n} \int_\Lambda^\infty \frac{d\lambda^2}{\pi} \frac{\lambda^{2n-2}}{\log \lambda^2}\,, \tag{A.54}$$

where the lower line can already be anticipated to vanish for arbitrary constants C. However, this can also be shown rigorously by noting that upon substitution, the last line of (A.54) can be expressed as the exponential integral function E_1,

$$\int_\Lambda^\infty \frac{d\lambda^2}{\pi} \frac{\lambda^{2n-2}}{\log \lambda^2} = -\frac{1}{\pi} \mathrm{E}_1(-n \log \lambda^2)\Big|_\Lambda^\infty\,. \tag{A.55}$$

The contribution from the lower integral boundary is finite and thus vanishes in (A.54). For the upper limit we utilise the asymptotic expansion of the exponential integral and plug this back into (A.54), yielding, while dropping the constant prefactor,

$$\begin{aligned} \lim_{p\to\infty} (p^2)^{-n}\, \mathrm{E}_1(-n \log p^2) &= \lim_{p\to\infty} (p^2)^{-n} \frac{e^{n\log p^2}}{-n \log p^2} \sum_{m=0}^\infty \frac{m!}{(n \log p^2)^m} \\ &= \lim_{p\to\infty} \sum_{m=0}^\infty \frac{-m!}{(n \log p^2)^{m+1}} \;\to\; 0\,. \end{aligned} \tag{A.56}$$

In conclusion, recalling (A.49), we arrive at

$$\lim_{p\to\infty} \Delta(p) = 0\,, \tag{A.57}$$

which, with (A.48), eventually yields the desired normalisation for the spectral function,

$$\int \frac{d\lambda^2}{\pi} \rho(\lambda) = Z_\infty^{-1}\,. \tag{A.58}$$

We thus see that, in the fairly general case where ρ can be normalised via the integral in (A.58), the normalisation is given by the value of the dressing function at infinity.

A.9. Introduction to GPR

This section serves as a brief introduction to GPR for function prediction using a finite number of direct or indirect observations, based primarily on [305]. We adopt the notation used in the main text for consistency, however, the general formalism presented here is also applicable outside the specific context of spectral reconstruction for quantum field theory. For a modern, comprehensive textbook treatment of the topic, we refer the interested reader to [331]. For a brief, pedagogical introduction to GPR with simple code examples, we recommend [459]. In the context of inverse theory, [460] provides a recent review.

We first discuss GPR for the case where direct observations are available for the function to be modelled. We assume our knowledge of the function $\rho(\omega)$ to be encoded in a GP with mean and covariance functions $\mu(\omega), C(\omega, \omega')$, denoted by

$$\rho(\omega) \sim \mathcal{GP}\left(\mu(\omega), C(\omega, \omega')\right) \ , \tag{A.59}$$

where the covariance is assumed to be symmetric, i.e. $C(\omega, \omega') = C(\omega', \omega)$. As per the definition of a GP, any finite set of function evaluations at N sample points ω_i follows a multivariate normal distribution,

$$\begin{pmatrix} \rho(\omega_1) \\ \vdots \\ \rho(\omega_N) \end{pmatrix} \sim \mathcal{N}\left(\begin{pmatrix} \mu(\omega_1) \\ \vdots \\ \mu(\omega_N) \end{pmatrix}, \begin{pmatrix} C(\omega_1, \omega_1) & \dots & C(\omega_1, \omega_N) \\ \vdots & \ddots & \vdots \\ C(\omega_N, \omega_1) & \dots & C(\omega_N, \omega_N) \end{pmatrix}\right) . \tag{A.60}$$

Similarly, we can write down the joint distribution of a set of observations $\hat{\rho}_i$ at points $\hat{\omega}_i$ and the value of the function at an arbitrary point ω as

$$\begin{pmatrix} \rho(\omega) \\ \hat{\boldsymbol{\rho}} \end{pmatrix} \sim \mathcal{N}\left(\begin{pmatrix} \mu(\omega) \\ \hat{\boldsymbol{\mu}} \end{pmatrix}, \begin{pmatrix} C(\omega, \omega) & \hat{\mathbf{C}}^T(\omega) \\ \hat{\mathbf{C}}(\omega) & \hat{\mathbf{C}} + \sigma_n^2 \cdot \mathbf{1} \end{pmatrix}\right) \ , \tag{A.61}$$

where boldface type denotes vector and matrix quantities. Here, we have defined $\hat{\boldsymbol{\mu}} \equiv \mu(\hat{\omega}_i)$, $\hat{\mathbf{C}}_i(\omega) \equiv C(\hat{\omega}_i, \omega)$, and $\hat{\mathbf{C}}_{ij} \equiv C(\hat{\omega}_i, \hat{\omega}_j)$. σ_n^2 defines the point-wise variance of additional measurement noise which may be present in the observations $\hat{\boldsymbol{\rho}}$. Due to the analytic tractability of multivariate Gaussian distributions, the conditional distribution of function values $\rho(\omega)$ given observations $\hat{\boldsymbol{\rho}}$ may then be derived as

$$\begin{aligned} \rho(\omega)|\hat{\boldsymbol{\rho}} \sim \mathcal{N}\Bigg(&\mu(\omega) + \hat{\mathbf{C}}^T(\omega)\left(\hat{\mathbf{C}} + \sigma_n^2 \cdot \mathbf{1}\right)^{-1}\left(\hat{\boldsymbol{\rho}} - \hat{\boldsymbol{\mu}}\right) , \\ &C(\omega, \omega) - \hat{\mathbf{C}}^T(\omega)\left(\hat{\mathbf{C}} + \sigma_n^2 \cdot \mathbf{1}\right)^{-1}\hat{\mathbf{C}}(\omega)\Bigg) \ . \end{aligned} \tag{A.62}$$

The covariance is parametrized by a suitable kernel function, whereby one may encode any prior beliefs about the types of solutions one expects by choosing an appropriate form for the problem at hand. For an introduction to constructing GP kernels of various types as well as strategies to apply and combine them, we recommend the kernel cookbook [461].

A kernel's hyperparameters, denoted here by $\hat{\boldsymbol{\alpha}}$, may be subjected to optimization by maximizing the associated likelihood,

$$p(\hat{\boldsymbol{\rho}}|\boldsymbol{\alpha}) = \left((2\pi)^N \det\left(\hat{\mathbf{C}}_\alpha + \sigma_n^2 \cdot \mathbf{1}\right)\right)^{-\frac{1}{2}} \exp\left(-\frac{1}{2}(\hat{\boldsymbol{\rho}} - \hat{\boldsymbol{\mu}})^T\left(\hat{\mathbf{C}}_{\boldsymbol{\alpha}} + \sigma_n^2 \cdot \mathbf{1}\right)^{-1}(\hat{\boldsymbol{\rho}} - \hat{\boldsymbol{\mu}})\right) \ , \tag{A.63}$$

where we have written $\hat{\mathbf{C}}_{\hat{\boldsymbol{\alpha}}}$ to emphasise the dependence on the hyperparameters. Instead of directly maximizing $p(\hat{\boldsymbol{\rho}}|\boldsymbol{\alpha})$ as a function of $\hat{\boldsymbol{\alpha}}$, one conventionally minimises the negative log likelihood (NLL),

$$-\log p(\hat{\mathbf{f}}|\boldsymbol{\alpha}) = \frac{1}{2}(\hat{\boldsymbol{\rho}} - \hat{\boldsymbol{\mu}})^T \left(\hat{\mathbf{C}}_{\boldsymbol{\alpha}} + \sigma_n^2 \cdot \mathbf{1}\right)^{-1} (\hat{\boldsymbol{\rho}} - \hat{\boldsymbol{\mu}}) + \frac{1}{2}\log\det\left(\hat{\mathbf{C}}_{\alpha} + \sigma_n^2 \cdot \mathbf{1}\right) + \frac{N}{2}\log 2\pi \ . \tag{A.64}$$

Since simply finding and employing the maximum likelihood configuration of hyperparameters may ignore relevant additional structures in the distribution, one can also integrate out $\hat{\boldsymbol{\alpha}}$ using suitable hyperpriors to account for some variability.

Based on the formulation of GPR for direct observations $\hat{\boldsymbol{\rho}}$ at points $\hat{\boldsymbol{\omega}}$, one can derive the expressions for inference from indirect observations $\hat{\mathbf{G}}$ at points $\hat{\mathbf{p}}$ as discussed in the main text by applying the forward process of the associated linear inverse problem, in our case the KL integral defined in (4.3). This involves all terms related to the observations that depend on the discrete set of points $\hat{\boldsymbol{\omega}}$, which are promoted back to the continuous domain and subsequently integrated out to yield the nodes $\hat{\mathbf{p}}$ instead.

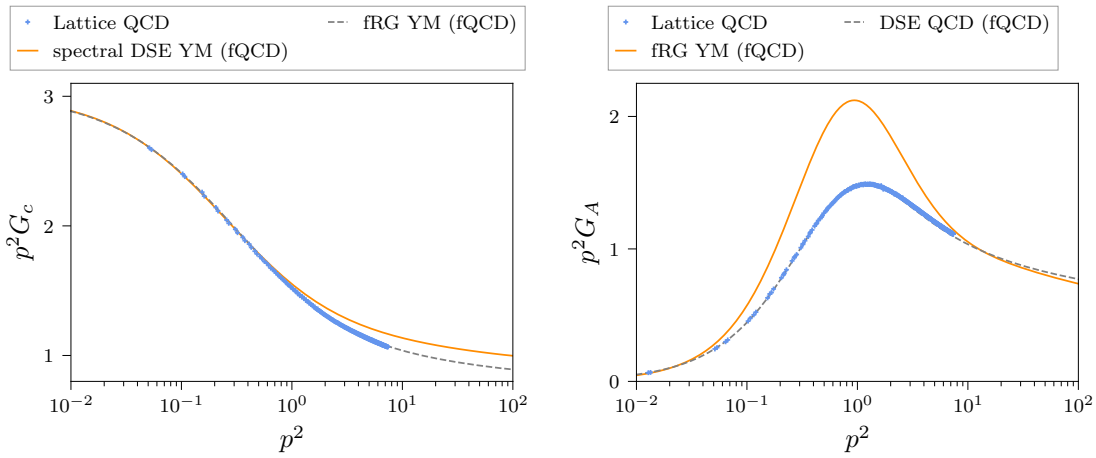

Abbildung A.5.: Plots showing ghost (left) and gluon (right) dressing functions in 2+1 flavor QCD and Yang-Mills (YM) theory, obtained from the lattice simulations and functional computations discussed in Appendix A.10.

A.10. Input Data for the spectral reconstruction of ghost and gluon

Combining the data from lattice simulations and functional computations as described in Section 5.3 requires matching the scales through renormalisation. Here, we always rescale the functional methods results to match the lattice data in the appropriate regime.

A.10.1. Lattice simulations

The lattice data employed in Section 5.3 for the reconstruction were obtained from lattice configurations generated by the RBC/UKQCD collaboration, and firstly introduced in [396–400], with 2+1 dynamical quark flavors using the Iwasaki [401] and domain wall fermion [402, 403] actions, respectively for the gauge and quark sectors, at the physical point (a pion mass amounting to 139 MeV) by the particular implementation of the Möbius kernel [404]. These developments were then exploited in [100, 101] in order to calculate the gluon and ghost propagators as well as the strong coupling in a particular scheme [405–407], and an effective charge stemming from it [408]. A description of this calculation is given, for instance, in [341].

In computing propagators that properly feature the physical running with momenta, data should be thoroughly cured of lattice regularisation artefacts. In particular, as explained in [100], our results are obtained after a careful scrutiny of discretization artefacts, thereby accounting for the continuum-limit extrapolation, following [181]. As a noteworthy remark, a recent work [182] has revealed the key role played by the procedure of [181] for an adequate removal of discretization artefacts in achieving a consistent description of Yang-Mills two- and three-point correlators, involving both lattice and DSE results.

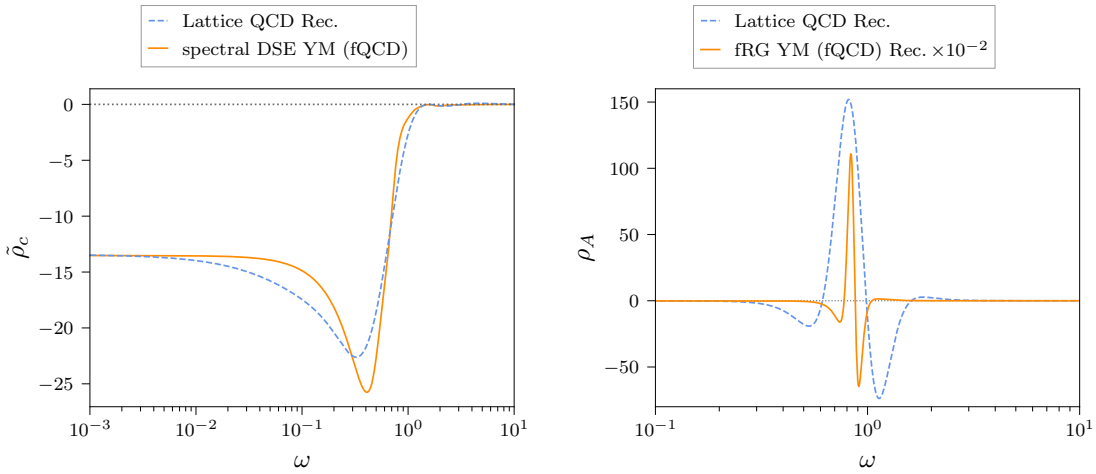

Abbildung A.6.: Plots comparing the continuous part of the ghost (left) and the gluon spectral function (right) from different approaches in 2+1 flavor QCD and Yang-Mills (YM) theory, as discussed in the results section and Appendix A.10. The ghost spectral function ρ_c features an additional massless particle pole in the origin; cf. (5.7).

The resulting ghost dressing function and gluon propagator data are displayed in Figure 5.16, respectively. They are compared against their counterparts obtained from evaluating (4.3) for the reconstructed spectral functions shown in Figure 5.17, as well as the results from functional methods described in the following section. The dressing functions of all input datasets are compared in Figure A.5 to further illustrate their similarities and differences.

A.10.2. Functional methods

We briefly summarize results from functional computations in Yang-Mills theory and QCD that are employed in Section 5.3 to provide additional prior information for the reconstruction. For reviews on the application of functional methods in this context, see e.g. [37, 63, 135, 136].

We use the realtime Yang-Mills results from [2] to extend the lattice QCD data of the ghost dressing function into the deep infrared, as shown in the left panel of Figure A.5. The approach also provides direct access to the associated spectral function, which we employ to fix the low-frequency asymptotic behaviour of the reconstruction. It is obtained via the spectral ghost DSE, building upon the technique of spectral renormalisation [1], see Section 4.1. Making use of (4.3) for the ghost and gluon propagator, the momentum integrals appearing in the loop diagrams of the ghost propagator DSE can be solved analytically. This preserves the full analytic momentum dependence and allows evaluating the equation on the real momentum axis. The spectral function can then be directly extracted from the realtime propagator DSE via (4.4); see the left panel of Figure A.6 for a comparison to the reconstruction result of the present work. As input gluon spectral function, the reconstruction result of [243] based on the scaling solution obtained via the fRG in [95] is used. Assuming a spectral representation for the gluon propagator, in both scaling and decoupling scenario the infrared behaviour of the gluon spectral function

follows directly from the propagator [243]. We utilise this to modify the given scaling spectral function such that we obtain a decoupling-type gluon propagator matching the value of the given lattice propagator well within the given uncertainties. Due to its mild momentum dependence, the ghost-gluon vertex is assumed to be classical.

The lattice QCD data for the gluon propagator are extended towards the UV using earlier results from functional computations in Yang-Mills theory [95]. Differences to the 2+1 flavor QCD result for the gluon propagator reported in [171], being based on [166], are comparably small in the relevant momentum range. A stronger deviation can be observed in the dressing functions, as shown in the right panel ofFigure A.5. Despite these differences, the reconstruction still produces remarkably reliable results, cf. the right panel of Figure 5.17. Nevertheless, we aim to replace the Yang-Mills UV extension by the 2+1 flavor QCD data from [171] in order to further optimize the accuracy of the result and mitigate any potential issues. For related results and further correlation functions see [38, 39, 374, 462]. More specifically, the fRG results in [95] are derived within an advanced approximation where the momentum dependence of all vertices is approximated at the symmetric point, for respective DSE results see [93]. For our purposes, this data set provides the optimal trade-off for momentum range versus accuracy. Due to the high numerical precision, the results are particularly well-suited as an input for spectral reconstruction. The Yang-Mills data have already been employed for this purpose in [243], and we use this earlier reconstruction for comparison; see the right panel of Figure A.6. In summary, the extension of the 2+1 flavor lattice data with the high precision Yang-Mills data up to momenta $p^2 = 10^2\,\mathrm{GeV}^2$ allows a more direct comparison (in terms of scales) with the Yang-Mills reconstruction in [243], while only modifying the large frequency tail of the gluon spectral function for frequencies $\omega \gtrsim 5\,\mathrm{GeV}$, see Figure A.6.

A.11. Resonance-scattering split of the quark spectral function

The singularity structure of the quark propagator in Section 5.4 is entirely determined by its universal part g. For real frequencies, it reads

$$g(\omega_+) = \frac{1}{M_q(\omega_+)^2 - \omega_+^2}\,. \tag{A.65}$$

In (A.65) and in the following, we make use of the notation $M_q(\omega_+) = M_q(p = -\mathrm{i}\omega_+)$, with the retarded limit $\omega_+ = \omega + \mathrm{i}0^+$. If G_q obeys the KL representation, so does g, with a spectral function

$$\rho_g(\omega) = 2\,\mathrm{Im}\,g(\omega_+)\,. \tag{A.66}$$

Since in (A.65) the retarded limit ω_+ is considered, the subsequent discussion applies to the complex upper half plane. The pole(s) of the quark propagator appear as the roots of the denominator of (A.65). We distinguish three cases: real, complex and no roots. For a real root,

$$\omega_0 - M_q(\omega_0) = 0\,, \tag{A.67}$$

with $\omega_0 \in \mathbb{R}$, one simply obtains an ordinary massive particle pole. Already at one-loop order in perturbation theory however, the mass function M_q obtains a non-vanishing imaginary part on the positive real axis, such that a real root is no longer possible. We consider this imaginary part to be a small, constant imaginary perturbation in a neighbourhood of the previously real pole ω_0 of the mass function in (A.67), i.e.,

$$M_\varepsilon(\omega_c) = M_q(\omega_c) \pm \mathrm{i}\varepsilon \quad \text{for} \quad |\omega_c - \omega_0| \ll 1\,, \tag{A.68}$$

with $\varepsilon \ll 1$ and $\omega_c \in \mathbb{C}$ now. In (A.68), M_q is to be understood as the real part of M_ε, i.e., $M_q(\omega) \in \mathbb{R}$. Then, M_q has no branch cut, we can omit the retarded limit reminding us which side of the branch cut we are on and simply write $M_q(\omega)$ on the real axis. Due to the propagators mirror symmetry, also the mass function obeys

$$M_\varepsilon(\bar{\omega}_c) = \bar{M}_\varepsilon(\omega_c)\,. \tag{A.69}$$

With (A.68), the quark propagators complex poles are given by the solution to

$$\omega_c - M_\varepsilon(\omega_c) = 0\,. \tag{A.70}$$

Since we are working in the upper half plane, we have $\mathrm{Im}\,\omega_c > 0$. Then, as M_ε obeys (A.69), (A.70) only has a solution for $\mathrm{Im}\,M_\varepsilon > 0$, i.e. the plus case in (A.68). In this case, the complex poles appear on the first Riemann sheet, and show up in the propagators. For the $\mathrm{Im}\,M < 0$ case, the complex poles are located on the second Riemann sheet, and hence do not appear in calculations.

For the quark spectral representation, above consideration have the following consequences: For $\mathrm{Im}\,M_\varepsilon < 0$, the spectral representation is intact. The corresponding universal quark spectral function shows a distinct, sharp positive peak structure around ω_0 plus a scattering continuum. We will focus on the peak structure in the following.

Since the imaginary part of the mass function (A.68) is small, due to the Sokhotski-Plemelj theorem,

$$\lim_{\varepsilon\to 0} \operatorname{Im} \frac{1}{(M_q(\omega) \pm \mathrm{i}\varepsilon)^2 - \omega^2} = \pm \frac{\pi}{2\omega_0}\, \delta(\omega - \omega_0)\,, \tag{A.71}$$

the peak is well approximated by a delta distribution. Note that also in (A.71), we only considered the positive frequency contribution. We thus have

$$\rho_g(\omega) \approx \frac{\pi}{\omega_0} \delta(\omega - \omega_0)\,. \tag{A.72}$$

On the contrary, for $\operatorname{Im} M_\varepsilon > 0$ the KL representation is violated by the complex poles. In this case, the universal part of the quark propagator (A.65) can be described by a modified spectral representation which explicitly takes the complex poles into account. On the real axis, it reads

$$g(\omega_+) = \frac{1}{(\omega_0 + \mathrm{i}\varepsilon)^2 - \omega_+^2} + \frac{1}{(\omega_0 - \mathrm{i}\varepsilon)^2 - \omega_+^2} + \int_\lambda \frac{\lambda\, \rho_g(\lambda)}{\lambda^2 - \omega_+^2}\,, \tag{A.73}$$

with ρ_g as defined in (A.66). As for the $\operatorname{Im} M_\varepsilon > 0$ case, with (A.71) we find that the spectral functions ρ_g shows a sharp peak around ω_0 with negative residue

$$\rho_g(\omega) \approx -\frac{\pi}{\omega_0} \delta(\omega - \omega_0)\,. \tag{A.74}$$

In this case, the universal part (A.73) then evaluates to

$$g(\omega_+) \approx \frac{1}{(\omega_0 + \mathrm{i}\varepsilon)^2 - \omega_+^2} + \frac{1}{(\omega_0 - \mathrm{i}\varepsilon)^2 - \omega_+^2} - \frac{1}{\omega_0^2 - \omega_+^2}\,. \tag{A.75}$$

Taking the imaginary part in (A.75), we recover (A.74).

Note that the real pole part in (A.73) enters with a minus sign. Since $\varepsilon \ll 1$ in (A.75), for any complex frequency not in the direct vicinity of ω_0, the real pole effectively cancels on of the complex poles. In other words, the complex pole universal part (A.75) is practically indistinguishable from a single massive propagator, i.e.,

$$g(\omega_c) \approx \frac{1}{\omega_0^2 - \omega_c^2} \quad \text{for} \quad |\omega_c - \omega_0| \gtrsim \varepsilon\,, \tag{A.76}$$

which applies in particular on the Euclidean axis. From the perspective of a generic lower limit on the numerical resolution in the complex plane, the approximation (A.76) is therefore well justified. It says that the sum of the two complex poles with positive residue and the negative real quasi-pole is well approximated by a single real positive pole. In terms of the spectral function, this has the consequence that the spectral representation of the universal part and hence of the quark propagator itself is restored. The spectral function is then simply given by the $\operatorname{Im} M_\varepsilon < 0$ case (A.72).

Above considerations suggest that in the case of a small imaginary part in the mass function, independent of its sign and the resulting particular analytic structure, the quark propagator can be well approximated to obey a KL representation. In this case, the universal spectral function is well represented by an analytical split into a genuine pole contribution plus a continuous scattering tale, which is

$$\rho_g(\omega) = \frac{\pi}{\omega_0} \delta(\omega - \omega_0) + \tilde{\rho}_g(\omega)\,, \tag{A.77}$$

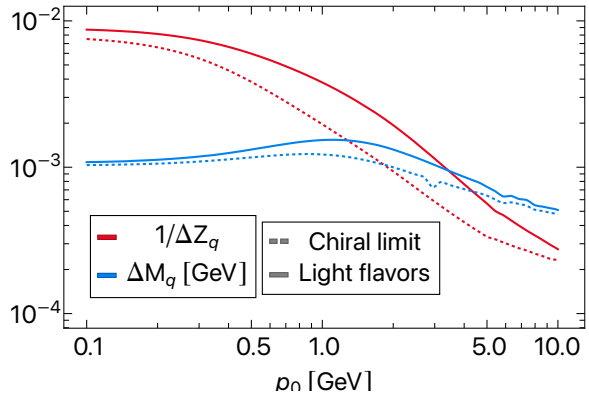

Abbildung A.7.: Evaluation of the quality of the resonance-scattering split (5.63) introduced in Section 5.4.1. We consider the Euclidean mass and dressing function and compare their difference in absolute value from the spectral representation to that directly obtained from the spectral Euclidean DSE. The deviation in the mass function does not supersede 10 MeV, while that for the dressing function is about 10^{-3}. Comparing to the absolute values of mass and dressing function Figure 5.19, we conclude that the resonance-scattering split represents the quark propagator quantitatively very well.

with scattering tail $\tilde{\rho}_g$. In terms of the Dirac and mass components of the spectral function, this pole-tail split reads

$$\rho^{(d/s)}(\omega) = R^{(d/s)}\delta(\omega - \omega_0) + \tilde{\rho}^{(d/s)}(\omega)\,. \tag{A.78}$$

The scattering contribution $\tilde{\rho}^{(d/s)}$ was neglected in above consideration but does not influence the discussion, as the quasi-pole structure is extremely sharp and distinct. The pole structure dominates the entire IR behaviour of the propagator in the sense of a gapping, while the scattering tail gets relevant towards in the UV and in particular carries the perturbative information. We emphasise that the applicability of this split depends on the imaginary part of the mass function and always has to be tested empirically.

In the pole-tail split (A.78), the residues $R^{(d/s)}$ are given by

$$R^{(d)} = \pi\omega_0 \operatorname{Re}\frac{1}{Z_q(\omega_0)}\,, \quad R^{(s)} = \pi \operatorname{Re}\frac{M_\varepsilon(\omega_0)}{Z_q(\omega_0)}\,. \tag{A.79}$$

Note that since $M_q(\omega_0) = \omega_0 \pm \mathrm{i}\varepsilon$, we have

$$R^{(d)} \approx R^{(s)}\,. \tag{A.80}$$

The scattering tails in (A.77) are still given by (5.60), augmented with a suitable lower for the spectral tail such that the pole contribution is not included. This cut-off is related to the width of the pole and hence to the distance of the complex poles to the real axis. The numerical value for the cut-off used in our implementation is specified in Appendix C.6.4.

A.11.1. Quality of the approximation

The validity of the resonance-scattering split is tested by comparing the Euclidean mass and dressing function obtained through the spectral representation (5.56) with the spectral functions shown in Figure 5.19 against their counterparts obtained directly from the spectral Euclidean DSE. In Figure A.7, we show their absolute difference. If the spectral representation is intact, the difference should be zero within the accuracy of our numerical integration. Our numerical integration routine aims at relative accuracy of about 10^{-3}. We conclude that the approximation works well on a quantitative level. The error from neglecting the imaginary part of the poles is visible in particular in the mass function, but seems to be of negligible size.

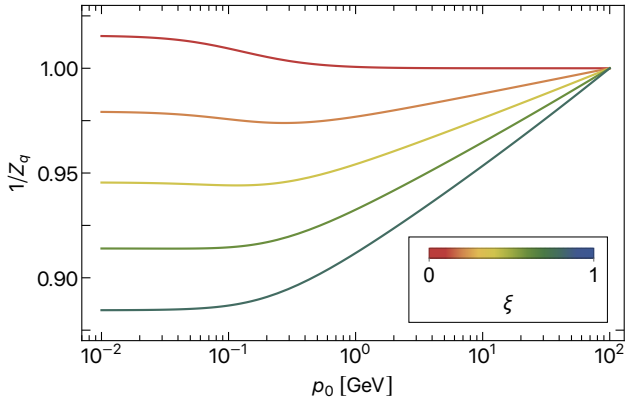

Abbildung A.8.: Gauge parameter dependence of the quark dressing function $1/Z$ at one-loop order in perturbation theory using a small gluon mass $m_A = 10$ MeV. A strong dependence of the IR asymptotic behaviour on the gauge parameter is observed. In Feynman gauge ($\xi = 1$), the dressing function is smaller than one in the deep IR. Similar to our non-perturbative Landau gauge results, in Landau gauge ($\xi = 0$) the dressing function rises above one.

A.12. Gauge parameter dependence of the quark dressing function

The infrared asymptotics of our result for the quark dressing function $1/Z_q$ presented in Section 5.4, see Figure 5.19, differs qualitatively from that in other works in Landau gauge. Our result approaches a value above one, while in, e.g., [166, 171, 373, 380, 381] it is found that the dressing function saturates below one in the deep IR. In contrast to former references though, we only consider a classical quark-gluon-vertex in order to facilitate the realtime calculation. It is known that at one-loop order in perturbation theory, the dressing function does not receive quantum corrections. In Figure A.8 we demonstrate the gauge parameter dependence of the IR behaviour of the quark dressing function in one-loop perturbation theory using a small gluon mass of $m_A = 10$ MeV. Although we are not using a massive gluon in obtaining our DSE results Figure 5.19, our gluon propagator has a characteristic mass scale given by the peak position of its spectral function, cf. the right panel of Figure 5.17. In conclusion, we attribute the IR behaviour of our quark dressing function to the combination of the classical quark-gluon-vertex with a gapped gluon propagator. Including other tensor structures as well as a momentum-dependent dressing functions in the quark-gluon-vertex, we expect the IR value of the dressing function to drop below one, as seen in [171].

A.13. Asymptotic behaviour of the strong coupling

Here, we provide details on the asymptotic IR and UV behaviour of the strong coupling spectral function, computed in Section 6.1.

For the gluon and the ghost propagators, the leading order IR and UV asymptotics are known analytically; see [243] and references therein. In the infrared, the decoupling solution of the ghost is characterised by a constant propagator dressing $Z_c \equiv Z_c(p=0)$. On the other hand, the gluon propagator is dominated by the ghost loop polarisation diagram in the IR, since the gluon propagator itself has a mass gap and decouples in the infrared. This results in a $p^2 \log p^2$ contribution in the IR regime; for a detailed discussion thereof, see [243].

Using the definition of the strong coupling (6.9), we see that it has the same, but negative, IR behaviour as the inverse gluon dressing, up to a constant contribution from the ghost dressing. From (6.15), we can then infer the asymptotic behaviour of the spectral function as

$$\rho_{\alpha,\mathrm{IR}}(\omega) \sim \omega^2 \,, \tag{A.81}$$

analogously to [243]. The UV asymptotic behaviour of the strong coupling is well known from perturbative calculations and reads

$$\alpha_{s,\mathrm{UV}}(p) \sim \frac{1}{\log(p^2)} \,. \tag{A.82}$$

The asymptotic behaviour of the spectral function follows directly from (6.12), and we obtain

$$\rho_{\alpha,\mathrm{UV}}(\omega) \sim -\frac{1}{\omega^2(\pi^2 + \log(\omega^2)^2)} \,. \tag{A.83}$$

B. Analytical supplements

B.1. Spectral properties of Laplacians

In this section we comment on the background-covariant Laplacians employed in Section 3.2, which were used for the momentum dependence of the Landau-gauge propagators in (3.126) and (B.10). Their explicit form follows from the gauge-invariant background field effective action [463] and is given by

$$\mathcal{D}_{T\,\mu\nu} = -D^2\delta_{\mu\nu} + 2ig\,F_{\mu\nu}\,, \quad \mathcal{D}_{L\,\mu\nu} = -D_\mu D_\nu\,, \tag{B.1}$$

and $\mathcal{D}_{\rm gh} = -D^2$. The transverse Laplacian also contains the spin-1 coupling to the background field.

The traces over the Laplace-type operators in (B.10) can be evaluated upon introduction of Laplace transforms using standard heat-kernel techniques. The subtleties arising from the presence of a self-dual background are discussed in-depth in e.g. [167, 464, 465]. Here, we just quote the relevant spectra in self-dual backgrounds from [148],

$$\begin{aligned} \mathrm{Spec}\Big\{-D^2\Big\} &= F_l(n+m+1), \quad n,m = 0,1,2,\ldots \\ \mathrm{Spec}\Big\{\mathcal{D}_{\rm T}\Big\} &= \begin{cases} F_l(n+m+2) & , \quad \text{multiplicity} \quad 2 \\ F_l(n+m) & , \quad \text{multiplicity} \quad 2 \end{cases} \end{aligned} \tag{B.2}$$

where $F_l = |\nu_l|F/\sqrt{2}$. Here, dividing by $\sqrt{2}$ accounts for the multiplicity in a self-dual formulation of $F_{\mu\nu}$, and ν_l are the eigenvalues to the adjoint color matrix $n^a t^a$. The covariant spin-1 Laplacian $\mathcal{D}_{\rm T}$ has a double zero mode for $n = m = 0$ which is due to the symmetry between color-electric and color-magnetic field. The spectral problem of the longitudinal Laplacian $\mathcal{D}_{\rm L}$ can be mapped onto that of $-D^2$, such that (B.2) is sufficient for the calculation in the main part of the paper, see e.g. [167, 464, 465]. The trace Tr' is defined as that without the zero mode, and for a general function $\mathcal{F}$ we get,

$$\begin{aligned} \mathrm{Tr}'\,\mathcal{F}(\mathcal{D}_{\rm T}) &= 2\sum_{l=1}^{N_c^2-1}\left(\frac{F_l}{4\pi}\right)^2\Bigg\{\sum_{n,m=0}^{\infty}\mathcal{F}\big(F_l(n+m+2)\big) + \sum_{n=0}^{\infty}\sum_{m=1}^{\infty}\mathcal{F}\big(F_l(n+m)\big) \\ &\qquad + \sum_{n=1}^{\infty}\mathcal{F}\big(nF_l\big)\Bigg\} \\ &= 4\sum_{l=1}^{N_c^2-1}\left(\frac{F_l}{4\pi}\right)^2\sum_{n,m=0}^{\infty}\mathcal{F}\big(F_l(n+m+1)\big) = 4\,\mathrm{Tr}_{xc}\,\mathcal{F}(-D^2), \end{aligned} \tag{B.3}$$

where the trace Tr sums over momentum or spacetime, internal indices and Lorentz indices of the respective field mode. Equation (B.3) displays an isospectrality relation between

$-D^2$ and the non-zero eigenvalues of $\mathcal{D}_{\mathrm{T}}$. As a consequence, all gluon and ghost modes except for the two zero modes couple in the same fashion to the selfdual background. This allows us to compute (B.10).

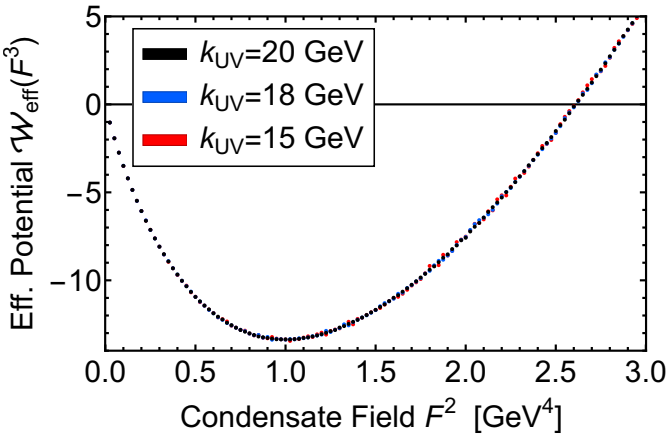

Abbildung B.1.: RG consistency of the effective potential $\mathcal{W}_{\rm eff}(F^a)$, shown for integrating the effective potential (B.4) starting from different initial cutoff scales $k_{\rm UV} = 20, 18, 15$ GeV to $k = 0$. The result is independent of the initial scale (RG consistency).

B.2. UV Asymptotics of the effective potential and regulator independence

The present work utilises the ghost and gluon propagators from [95]; which has been obtained within a quantitative approximation to the full Yang-Mills system. There, and in respective works in QCD, [166, 172, 373] it has been checked that the choice of the regulator is of subleading importance for the propagators at vanishing cutoff scale, which is one of the self-consistency checks that goes into an estimate of the systematic error.

As mentioned at the end of Appendix B.3, the relatively sharp regulator here delays the onset of UV asymptotics and hence the onset cutoff scale $k \gtrsim k_{\rm on}$ of the regime in which the effective potential reduces to the classical form (3.132). For the sake of convenience we recall it,

$$\mathcal{W}_k(F^a) \overset{k\gtrsim k_{\rm on}}{\longrightarrow} \frac{F^2}{16\pi\alpha_s(k)}\,, \qquad \alpha_s(k) = \frac{1}{4\pi}\frac{g_s^2}{Z_{A,k}}\,, \tag{B.4}$$

with $Z_{A,k} = Z_{A,k}(p=0)$. In this regime the flow is simply a linear function in F^2 with the slope $\partial_t 1/(16\pi\alpha_s)$. Hence, for large cutoff scales we have,

$$\partial_t \mathcal{W}_k(F^a) \to -\frac{\partial_t\alpha_s(k)}{\alpha_s(k)}\frac{1}{16\pi\alpha_s(k)}F^2\,. \tag{B.5}$$

The coupling α_s in (B.4) is the background coupling which has the same (two-loop) universal β-function as the fluctuation coupling $\alpha_{s,\rm fluc} = g_s^2/(4\pi Z_a\, Z_c^2)$ computed in [95]. However, the equivalence of the perturbative β-functions still allows for a global rescaling $\alpha_s = \bar\gamma\,\alpha_{s,\rm fluc}$ whose value is checked by comparing the two flows for $k \to k_{\rm UV}$,

$$\bar\gamma = \lim_{F^2\to 0}\frac{16\pi\alpha_{s,\rm fluc}^2}{\partial_t\alpha_{s,\rm fluc}}\frac{\partial_t\mathcal{W}_k}{F^2} \approx 1\,. \tag{B.6}$$

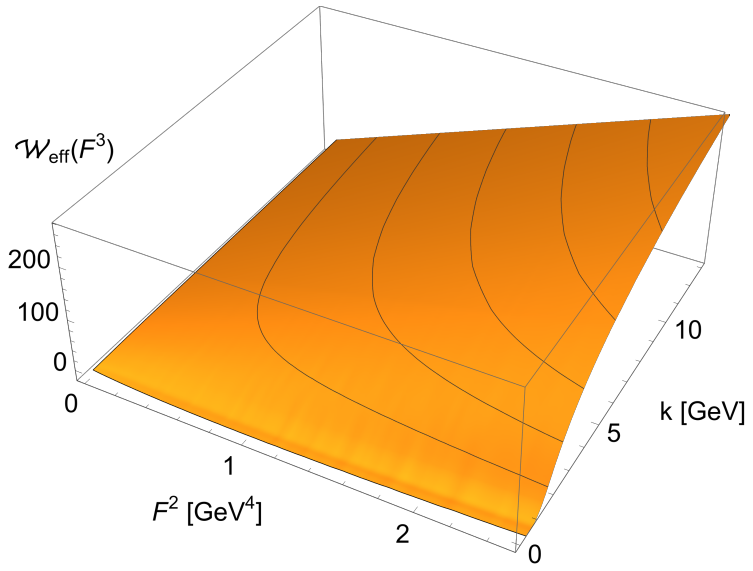

Abbildung B.2.: Effective Potential $\mathcal{W}_k(F^a)$, defined in (3.131), for $F^a = F\delta^{a3}$ as a function of F^2 obtained from integrating the flow with the regulator (B.8). In comparison to Figure B.3b the regulator is much smoother, which translates to the smoothness in $k_{\text{on}} \gtrsim k \gtrsim 1\,\text{GeV}$.

This fixes our initial condition, and in Figure B.3 we show both, the respective integrated flow, Figure B.3a, and the full cutoff dependent effective potential that also involves the initial condition, Figure B.3b. The integrated flow from the UV scale $k_{\text{UV}} = 20\,\text{GeV}$ to a general cutoff scale k is given by

$$\mathcal{W}_k(F^a) - \mathcal{W}_{k_{\text{UV}}}(F^a) = -\int_k^{k_{\text{UV}}} \frac{\mathrm{d}k}{k} \partial_t \mathcal{W}_k(F^a)\,. \tag{B.7}$$

One clearly sees the linear dependence on F^2 for $k \to k_{\text{UV}}$. At lower scales $k \to k_{\text{on}}$ with $k_{\text{on}} \approx 14\,\text{GeV}$ the transition regime sets in, in which the integrated flow resolves the shape function. Finally, for physical cutoff scales $k \lesssim 1\,\text{GeV}$, the form of the shape function gets irrelevant, and the integrated flow is getting smooth again. This shows very impressively that the information about the shape function is integrated out and disappears in the physical limit $k \to 0$.

We have also checked that the effective potential $\mathcal{W}_{\text{eff}}(F^a)$ is RG consistent [58, 176]. This is the simple requirement that $\mathcal{W}_{\text{eff}}(F^a)$ does not vary if the flow is initiated at another cutoff scale k_{UV}. Accordingly, it is a consistency check on the initial effective potential $\mathcal{W}_{k_{\text{UV}}}$. Figure B.1 depicts the physical effective potential $\mathcal{W}_{\text{eff}}(F^a)$, obtained from computations with $k_{\text{UV}} = 15, 18, 20\,\text{GeV}$. The initial effective potentials are given by (B.4), where the scale dependency of the coupling α_s is obtained from the 1-loop beta function of the background coupling. These computations confirm the quantitative validity of the one-loop estimate for $\mathcal{W}_{k_{\text{UV}}}$ for these large initial cutoff scales. In turn, for lower cutoff scales, the one-loop form is gradually lost which can be easily seen by the substructure (in F^2) of the flow.

Finally, we also report on results for the effective potential obtained by integrating the flow with a smoother regulator

$$R_k(p) = k^2\, e^{-p^2/k^2}\,. \tag{B.8}$$

Such a regulator decreases the numerical effort considerably. Note that this is not a self-consistent computation as it also requires cutoff dependent propagators computed with the same regulator (B.8). However, we use this as a stability test of our results, and hence a further systematic error control. The respective result for the cutoff dependent effective potential is shown in Figure B.2, and one clearly sees that the use of a smoother regulator removes the substructures in the flow. The minimum value of F^2 at $k = 0$ is given by

$$\langle F^2\rangle_{\lambda_3} = 0.93(14)\,\mathrm{GeV}^4\,, \tag{B.9}$$

to be compared with (3.137). These values compare well, which informs our estimate of the systematic error.

B.3. Flow of the effective potential

Here we provide some details of the computation of the integrated flow (3.131) of the effective potential, (3.128a) from the flow equation (3.126) and the propagators (3.129). Inserting the latter into (3.126) yields,

$$\begin{aligned}\partial_t \mathcal{W}_k(F^a) =& \frac{3}{2}\,\mathrm{Tr}\,\frac{\partial_t R_a^{\perp}(\mathcal{D}_T)}{\mathcal{D}_T Z_{a,k}(\mathcal{D}_T)+R_a^{\perp}(\mathcal{D}_T)}+\frac{1}{2}\,\mathrm{Tr}\,\frac{\partial_t R_a^{\parallel}(-D^2)}{-D^2+R_a^{\parallel}(-D^2)}\\ &+\frac{1}{2}\,\mathrm{Tr}\,P_0\frac{\partial_t R_a^{\perp}(-D^2)}{-D^2\,Z_{a,k}(-D^2)+R_a^{\perp}(-D^2)}-\mathrm{Tr}\,\frac{\partial_t R_c(-D^2)}{-D^2 Z_{c,k}(-D^2)+R_{k,c}(-D^2)}\\ &-\frac{3}{2}\,\mathrm{Tr}\,\frac{\partial_t R_a^{\perp}(p^2)}{p^2\,Z_a(p^2)+R_a^{\perp}(p^2)}-\frac{1}{2}\,\mathrm{Tr}\,\frac{\partial_t R_a^{\parallel}(p^2)}{p^2\,Z_a(p^2)+R_a^{\parallel}(p^2)}\\ &-\mathrm{Tr}\,\frac{\partial_t R_c(p^2)}{p^2\,Z_{c,k}(p^2)+R_{k,c}(p^2)}\,,\end{aligned}\tag{B.10}$$

where the contributions in the first line are the glue contributions, and P_0 denotes the projection on the zero-mode. The traces in (B.10) sum over momenta or spacetime, as well as internal and Lorentz indices of the respective field modes. We have three covariant transverse modes and one covariant longitudinal mode, the trivial gauge mode. The term in the second line is the ghost contribution, and the field-independent subtraction in the third line normalises the potential to $\mathcal{W}_k(F^a=0)=0$. We choose the regulator in consistency with the input data. The regulators in [95] are defined as,

$$\begin{aligned}R_{a,k}(p) =& p^2\,r(x)\left(\tilde{Z}_{a,k}\Pi^{\perp}(p)+\Pi^{\parallel}(p)\right),\\ R_{a,k}(p) =& p^2\,r(x)\tilde{Z}_{c,a}\,.\end{aligned}\tag{B.11}$$

with the projection operators $\Pi^{\perp,\parallel}$ defined in (3.105). In (B.11), x is the dimensionless momentum variable, $x=p^2/k^2$, and the shape function $r(x)$ used in [95] is given by,

$$r(x)=\left(\frac{1}{x}-1\right)\frac{1}{1+e^{\frac{x-1}{a}}}\,,\qquad a=2\times 10^{-2}\,.\tag{B.12}$$

The shape function (B.12) is a smoothened version of the Litim shape function, [466]. The cutoff dependent prefactors $\tilde{Z}_{a/c}$ are given by

$$\tilde{Z}_{a,k}=Z_{a,k}([k^n+\tilde{k}^n]^{1/n})\,,\qquad \tilde{Z}_{c,k}=Z_{c,k}(k)\,,\tag{B.13}$$

with $k=1\,\mathrm{GeV}$. The choice (B.13) ensures that the regulators have the same (average) momentum scaling as the two-point functions, regulators proportional to the respective wave function renormalisations of the fields are RG-adapted, see [58]. Moreover, the scale $k=1\,\mathrm{GeV}$ is introduced for computations convenience; it leads to a gluon regulator, that does not diverge at $p=0$ for $k\to 0$. While even a singular regulator choice at $p=0$ does not contribute to the momentum integral, it complicates the numerics.

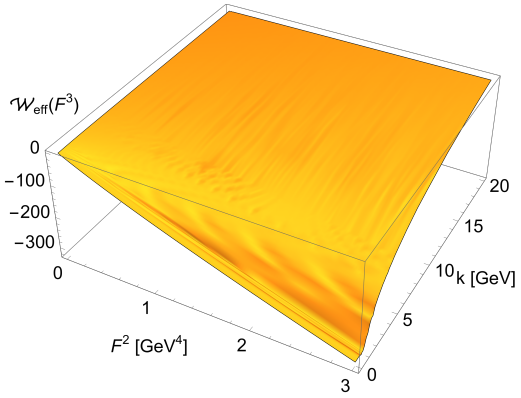

(a) Integrated UV Flow of the effective potential, $\mathcal{W}_k(F^a) - \mathcal{W}_{k_{\text{UV}}}(F^a)$, defined in (B.7), for $F^a = F\delta^{a3}$ as a function of F^2. Here, $k_{\text{UV}} = 20\,\text{GeV}$. The substructure for $k_{\text{on}} \gtrsim k \gtrsim 1\,\text{GeV}$ resolves the shape of the regulator (B.12).

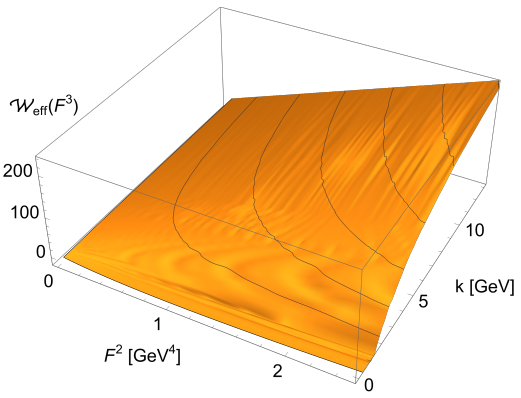

(b) Effective Potential $\mathcal{W}_k(F^a)$, defined in (3.131), for $F^a = F\delta^{a3}$ as a function of F^2 in the regime $0 \leq k \leq k_{\text{UV}} = 20\,\text{GeV}$. The substructure for $k_{\text{on}} \gtrsim k \gtrsim 1\,\text{GeV}$ resolves the shape of the regulator (B.12). For $k = 0$ see also Figure 3.1.

Abbildung B.3.: Cutoff dependence of the effective potential.

In [166] the regulator was used as it optimises fully momentum dependent approximations, see [58]. However, the resolution of (B.10) requires the computation of $\text{Tr}\,\mathcal{F}(-D^2)$ and $\text{Tr}\,\mathcal{F}(-D_T)$ in terms of the discrete Eigenvalues or spectrum of the Laplacians $-D^2$ and D_T. The spectral properties of the Laplacians are discussed in Appendix B.1, see also [148].

The optimisation of the approximation in terms of its momentum dependence as used in [166] comes at the price that soft but sharp regulators delay the onset of the asymptotic ultraviolet scaling in the presence of a discrete momentum spectrum, see [467]. Here, asymptotic UV scaling entails, that the effective action reduces to the classical one with a running prefactor, see (3.132). Indeed, for non-analytic regulators such as the Litim regulator or the sharp regulator the asymptotic UV scaling. In Appendix B.2 we investigate the asymptotic UV scaling in the present set up as well as the regulator (in)dependence of our results.

B.4. Scalar theory self-energy calculation

Analytic expressions for the spectral integrands of the spectral scalar propagator DSE in Section 4.1, (4.22) before and after analytic continuation:

Polarization:

$$\begin{aligned} I_{\mathrm{pol}}(p;\lambda_1,\lambda_2) &= \frac{1}{4\pi p}\arctan\left(\frac{p}{\lambda_1+\lambda_2}\right), \\ I_{\mathrm{pol}}(\omega;\lambda_1,\lambda_2) &= \frac{1}{4\pi\omega}\left[\operatorname{artanh}\left(\frac{\omega}{\lambda_1+\lambda_2}\right)+\mathrm{i}\arg\left(1-\frac{\omega}{\lambda_1+\lambda_2}\right)\right] \end{aligned} \tag{B.14}$$

Sunset:

$$\begin{aligned} I_{\mathrm{sun}}(p;\lambda_1,\lambda_2,\lambda_3) &= \frac{1}{(4\pi)^2}\left(\frac{1}{2}\log\left(\frac{1}{(\lambda_1+\lambda_2+\lambda_3)^2+p^2}\right)\right. \\ &\quad \left.-\frac{\lambda_1+\lambda_2+\lambda_3}{p}\arctan\left(\frac{p}{\lambda_1+\lambda_2+\lambda_3}\right)\right), \\ I_{\mathrm{sun}}(\omega;\lambda_1,\lambda_2,\lambda_3) &= \frac{1}{(4\pi)^2}\left(\frac{1}{2}\log\left(\frac{1}{(\lambda_1+\lambda_2+\lambda_3)^2-\omega^2}\right)\right. \\ &\quad \left.-\frac{\lambda_1+\lambda_2+\lambda_3}{\omega}\left[\operatorname{artanh}\left(\frac{\omega}{\lambda_1+\lambda_2+\lambda_3}\right)+\mathrm{i}\arg\left(1-\frac{\omega}{\lambda_1+\lambda_2+\lambda_3}\right)\right]\right) \end{aligned} \tag{B.15}$$

Squint:

$$
\begin{aligned}
I_{\text{squint}}(p;\lambda_1,\lambda_2,\lambda_3,\lambda_4) \;=\; & \frac{1}{(8\pi)^2\omega\lambda_4}\Bigg(2\log\left(\frac{\lambda_2+\lambda_3+\lambda_4}{\lambda_2+\lambda_3-\lambda_4}\right)\operatorname{artanh}\left(\frac{\omega}{\lambda_1+\lambda_4}\right) \\
& + \mathrm{i}\Bigg[\mathrm{Li}_2\left(\frac{\mathrm{i}p-\lambda_1-\lambda_4}{\lambda_2+\lambda_3-\lambda_4}\right) - \mathrm{Li}_2\left(\frac{\mathrm{i}p-\lambda_1+\lambda_4}{\lambda_2+\lambda_3+\lambda_4}\right) \\
& + \mathrm{Li}_2\left(\frac{-\mathrm{i}p-\lambda_1+\lambda_4}{\lambda_2+\lambda_3+\lambda_4}\right) - \mathrm{Li}_2\left(\frac{-\mathrm{i}p-\lambda_1-\lambda_4}{\lambda_2+\lambda_3-\lambda_4}\right)\Bigg]\Bigg), \\
I_{\text{squint}}(\omega;\lambda_1,\lambda_2,\lambda_3,\lambda_4) \;=\; & \frac{1}{(8\pi)^2\omega\lambda_4}\Bigg(\mathrm{Re}\Bigg[2\log\left(\frac{\lambda_2+\lambda_3+\lambda_4}{\lambda_2+\lambda_3-\lambda_4}\right)\operatorname{artanh}\left(\frac{\omega}{\lambda_1+\lambda_4}\right) \\
& - \mathrm{Li}_2\left(\frac{\omega-\lambda_1-\lambda_4}{\lambda_2+\lambda_3-\lambda_4}\right) + \mathrm{Li}_2\left(\frac{-\omega-\lambda_1-\lambda_4}{\lambda_2+\lambda_3-\lambda_4}\right) \\
& + \mathrm{Li}_2\left(\frac{\omega-\lambda_1+\lambda_4}{\lambda_2+\lambda_3+\lambda_4}\right) - \mathrm{Li}_2\left(\frac{-\omega-\lambda_1+\lambda_4}{\lambda_2+\lambda_3+\lambda_4}\right)\Bigg] \\
& - \mathrm{i}\,\theta\Big(\omega-|\lambda_1+\lambda_4|\Big)\,\mathrm{Im}\Bigg[2\log\left(\frac{\lambda_2+\lambda_3+\lambda_4}{\lambda_2+\lambda_3-\lambda_4}\right)\operatorname{artanh}\left(\frac{\omega}{\lambda_1+\lambda_4}\right) \\
& - \mathrm{Li}_2\left(\frac{\omega-\lambda_1-\lambda_4}{\lambda_2+\lambda_3-\lambda_4}\right) + \mathrm{Li}_2\left(\frac{-\omega-\lambda_1-\lambda_4}{\lambda_2+\lambda_3-\lambda_4}\right) \\
& + \mathrm{Li}_2\left(\frac{\omega-\lambda_1+\lambda_4}{\lambda_2+\lambda_3+\lambda_4}\right) - \mathrm{Li}_2\left(\frac{-\omega-\lambda_1+\lambda_4}{\lambda_2+\lambda_3+\lambda_\phi}\right)\Bigg]\Bigg).
\end{aligned}
\tag{B.16}
$$

B.5. Yang-Mills self-energy calculation

In this section, we detail the analytic solution of the loop momentum integrals of the Yang-Mills self-energy diagrams in Section 5.1, (5.25) in the spectral DSEs (5.20) at the example of the ghost self energy diagram $\Sigma_{\bar{c}c}$. Starting at (5.24), we express the ghost-gluon diagram as

$$\Sigma_{\bar{c}c}(p) = g^2 \delta^{ab} C_A \int_{\lambda_1,\lambda_2} \rho_A(\lambda_2)\rho_c(\lambda_2)\, I(p,\lambda_1,\lambda_2)\,, \tag{B.17}$$

with the now dimensionally regularised momentum integral

$$I(p,\lambda_1,\lambda_2) = \int_q \left(p^2 - \frac{(p\cdot q)^2)}{q^2}\right) \frac{1}{q^2+\lambda_1^2}\frac{1}{(p+q)^2+\lambda_2^2}\,. \tag{B.18}$$

The measure is now $\int_q = \int d^dq/(2\pi)^d$.

B.5.1. Momentum integration

Next, we employ partial fraction decomposition

$$\frac{1}{q^2}\frac{1}{q^2+\lambda^2} = \frac{1}{\lambda^2}\left(\frac{1}{q^2} - \frac{1}{q^2+\lambda^2}\right), \tag{B.19}$$

and introduce Feynman parameters, i.e. utilise

$$\frac{1}{AB} = \int_0^1 dx \frac{1}{xA+(1-x)B}\,. \tag{B.20}$$

Upon a shift in the integration variable $q \to q - xp$ and after some manipulation, we arrive at

$$I(p,\lambda_1,\lambda_2) = \int_{q,x} \sum_{i=0}^{2} (q^2)^i \left[\frac{A_i}{(q^2+\tilde{\Delta}_1)^2} + \frac{B_i}{(q^2+\tilde{\Delta}_2)^2}\right], \tag{B.21}$$

with

$$\begin{aligned}\tilde{\Delta}_1 &= (1-x)\lambda_1^2 + x\lambda_2^2 + x(1-x)p^2\,,\\ \tilde{\Delta}_2 &= \tilde{\Delta}_1 - x\lambda_2^2\,.\end{aligned} \tag{B.22}$$

We will not make all intermediate results explicit, such as giving the full expressions for A_i and B_i, which are functions of external momentum p, the spectral parameter λ_1 as well as the Feynman parameter x. Ultimately, the complete final result will be stated explicitly.

The momentum integrals are now readily solved via the standard integration formulation,

$$\int \frac{d^dq}{(2\pi)^d}\frac{q^{2m}}{(q^2+\Delta)^n} = \frac{1}{(4\pi)^{d/2}}\frac{\Gamma(m+\frac{d}{2})\Gamma(n-\frac{d}{2}-m)}{\Gamma(\frac{d}{2})\Gamma(n)}\Delta^{m+d/2-n}\,, \tag{B.23}$$

with m a non-negative and n a positive integer.

B.5.2. Feynman parameter integration

Reordering the expression in powers of the Feynman parameter x and taking the limit $d \to 4 - 2\varepsilon$, we arrive at

$$I(p,\lambda_1,\lambda_2) = \left(\frac{1}{\varepsilon} + \log\frac{4\pi\mu^2}{e^{\gamma_E}}\right)\sum_{i=0}^{3}\frac{\alpha_i^{(\mathrm{f})} - \alpha_i^{(\mathrm{g})}}{i+1} - \int_x \sum_{i=0}^{3} x^i \left(\alpha_i^{(\mathrm{f})}\log\tilde{\Delta}_1 - \alpha_i^{(\mathrm{g})}\log\tilde{\Delta}_2\right) + \mathcal{O}(\varepsilon)\,, \tag{B.24}$$

with γ_E the Euler-Mascheroni constant. The coefficients α_i and β_i do not depend on x, and will be given down below. We can solve the Feynman parameter integrals analytically and simplify the first sum to obtain the final result,

$$I(p,\lambda_1,\lambda_2) = \left(\frac{1}{\varepsilon} + \log\frac{4\pi\mu^2}{e^{\gamma_E}}\right)\frac{3}{4}p^2 - \sum_{i=0}^{3}\left[\alpha_i^{(\mathrm{f})} f_i - \alpha_i^{(\mathrm{g})} g_i\right]. \tag{B.25}$$

The coefficients $\alpha_i^{(\mathrm{f,g})}$ are defined as follows:

$$\begin{aligned}
\alpha_0^{(\mathrm{f})} &= \frac{p^2}{2}\,, & \alpha_0^{(\mathrm{g})} &= 0\,,\\
\alpha_1^{(\mathrm{f})} &= -\frac{p^2(p^2 - 5\lambda_1^2 + \lambda_2^2)}{2\lambda_1^2}\,, & \alpha_1^{(\mathrm{g})} &= -\frac{p^2(p^2 + \lambda_2^2)}{2\lambda_1^2}\,,\\
\alpha_2^{(\mathrm{f})} &= \frac{3p^2(3p^2 - 2\lambda_1^2 + 2\lambda_2^2)}{2\lambda_1^2}\,, & \alpha_2^{(\mathrm{g})} &= \frac{3p^2(3p^2 + 2\lambda_2^2)}{2\lambda_1^2}\,,\\
\alpha_3^{(\mathrm{f})} &= -\frac{4p^4}{\lambda_1^2}\,, & \alpha_3^{(\mathrm{g})} &= -\frac{4p^4}{\lambda_1^2}\,,
\end{aligned} \tag{B.26}$$

The functions f_i and g_i carry the branch cuts ultimately giving rise to the spectral function and are defined by integrals over the Feynman parameter x via

$$f_i = \int_0^1 dx\, x^i \log\tilde{\Delta}_1\,, \qquad g_i = \int_0^1 dx\, x^i \log\tilde{\Delta}_2\,, \tag{B.27}$$

yielding

$$
\begin{aligned}
f_0 &= \frac{\zeta}{2p^2} D_{\text{cut}} + 2\log\lambda_2 + \frac{p^2-\lambda_1^2+\lambda_2^2}{p^2}\log\Big(\frac{\lambda_1}{\lambda_2}\Big) - 2\,,\\
f_1 &= \frac{1}{4p^4\zeta} D_{\text{cut}}\Big[\big((\lambda_1-\lambda_2)^2+p^2\big)\big((\lambda_1+\lambda_2)^2+p^2\big)\big(p^2-\lambda_1^2+\lambda_2^2\big)\Big]\\
&\quad + \log\lambda_2 - \frac{p^2-\lambda_1^2+\lambda_2^2}{2p^2} + \frac{(\lambda_1^2-\lambda_2^2)^2+2\lambda_2^2p^2+p^4}{2p^4}\log\Big(\frac{\lambda_1}{\lambda_2}\Big) - \frac{1}{2}\,,\\
f_2 &= \frac{1}{6p^6\zeta} D_{\text{cut}}\Big[(\lambda_1^2-\lambda_2^2)^4 + p^6(\lambda_1^2+4\lambda_2^2) - 2\lambda_2^2p^4(\lambda_1^2-3\lambda_2^2)\\
&\quad + p^2(\lambda_1^2-\lambda_2^2)^2(\lambda_1^2+4\lambda_2^2) + p^8\Big] + \frac{1}{3}\log\lambda_2^2 - \frac{\lambda_2^2-\lambda_1^2+p^2}{6p^2}\\
&\quad - \frac{(\lambda_1^2-\lambda_2^2)^2+2\lambda_2^2p^2+p^4}{3p^4}\\
&\quad + \frac{3\lambda_2^2p^2(\lambda_2^2-\lambda_1^2+p^2)-(\lambda_1^2-\lambda_2^2)^3+p^6}{3p^6}\log\Big(\frac{\lambda_1}{\lambda_2}\Big) - \frac{2}{9}\,,\\
f_3 &= \frac{1}{8p^8\zeta} D_{\text{cut}}\Big[\big((\lambda_1-\lambda_2)^2+p^2\big)\big(\lambda_2^2-\lambda_1^2+p^2\big)\big(\lambda_1^4+\lambda_2^4+p^4+2\lambda_2^2(p^2-\lambda_1^2)\big)\\
&\qquad\qquad \times\big((\lambda_1+\lambda_2)^2+p^2\big)\Big]\\
&\quad - \frac{1}{8}\log(-\lambda_2^2) + \frac{1}{4}\log(\lambda_2^2) + \frac{\lambda_1^2-13\lambda_2^2}{12p^2} - \frac{\lambda_1^4-8\lambda_1^2\lambda_2^2+7\lambda_2^4}{8p^4} + \frac{(\lambda_1^2-\lambda_2^2)^3}{4p^6} - \frac{7}{12}\\
&\quad + \frac{\log(-\lambda_1^2)}{8p^8}\Big[\big(\lambda_1^2-\lambda_2^2\big)^4 + p^4\big(6\lambda_2^4-4\lambda_1^2\lambda_2^2\big) + 4\lambda_2^2p^2\big(\lambda_1^2-\lambda_2^2\big)^2 + 4\lambda_2^2p^6 + p^8\Big]\\
&\quad - \frac{\log(-\lambda_2^2)}{8p^8}\Big[\lambda_1^8+\lambda_2^8+4\lambda_2^6(p^2-\lambda_1^2) + 2\lambda_2^4\big(3\lambda_1^4-4\lambda_1^2p^2+3p^4\big)\\
&\qquad\qquad + 4\lambda_2^2(p^2-\lambda_1^2)\big(\lambda_1^4+p^4\big)\Big]\,,
\end{aligned}
\tag{B.28}
$$

where we defined

$$
\begin{aligned}
D_{\text{cut}} &= \log\big(\zeta+\lambda_1^2-\lambda_2^2+p^2\big) - \log\big(\zeta+\lambda_1^2-\lambda_2^2-p^2\big) + \log\big(\zeta-\lambda_1^2+\lambda_2^2+p^2\big)\\
&\quad - \log\big(\zeta-\lambda_1^2+\lambda_2^2-p^2\big)\,,
\end{aligned}
\tag{B.29a}
$$

with

$$
\zeta = \sqrt{\lambda_2^4 + \big(\lambda_1^2+p^2\big)^2 + 2\lambda_2^2\big(p^2-\lambda_1^2\big)}\,,
\tag{B.29b}
$$

and

$$
\begin{aligned}
g_0 &= \log\lambda_2^2 - \frac{\left(\lambda_2^2+p^2\right)\log -\lambda_2^2}{p^2} + \left(\frac{\lambda_2^2}{p^2}+1\right)\log\left(-\lambda_2^2-p^2\right) - 2\,,\\
g_1 &= \frac{1}{2p^4}\Big[-p^2\left(\lambda_2^2+2p^2\right) + p^4\log\lambda_2^2 - \log -\lambda_2^2\left(\lambda_2^2+p^2\right)^2 + \left(\lambda_2^2+p^2\right)^2\log\left(-\lambda_2^2-p^2\right)\Big]\,,\\
g_2 &= -\frac{1}{18p^6}\Big[15\lambda_2^2p^4 + 6\lambda_2^4p^2 - 6p^6\log\lambda_2^2 + 6\log -\lambda_2^2]\left(\lambda_2^2+p^2\right)^3\\
&\qquad - 6\left(\lambda_2^2+p^2\right)^3\log\left(-\lambda_2^2-p^2\right) + 13p^6\Big]\,,\\
g_3 &= \frac{1}{24p^8}\Big[-p^2\left(6\lambda_2^6+26\lambda_2^2p^4+21\lambda_2^4p^2+14p^6\right) + 6p^8\log\lambda_2^2 - 6\log -\lambda_2^2\left(\lambda_2^2+p^2\right)^4\\
&\qquad + 6\left(\lambda_2^2+p^2\right)^4\log\left(-\lambda_2^2-p^2\right)\Big]\,.
\end{aligned}
\tag{B.30}
$$

The gluon and ghost loops $\mathcal{D}_{\text{gluon}}$ and $\mathcal{D}_{\text{ghost}}$ featuring in the gluon self-energy Σ_{AA} defined in (5.22) are computed analogously. As for the ghost self-energy, we first define

$$
\mathcal{D}_{\text{gluon}}(p) = g^2\delta^{ab}C_A\int_{\lambda_1,\lambda_2}\rho_A(\lambda_2)\rho_A(\lambda_2)\,I_{\text{glu}}(p,\lambda_1,\lambda_2)\,,
\tag{B.31a}
$$

$$
\mathcal{D}_{\text{ghost}}(p) = g^2\delta^{ab}C_A\int_{\lambda_1,\lambda_2}\rho_c(\lambda_2)\rho_c(\lambda_2)\,I_{\text{ghost}}(p,\lambda_1,\lambda_2)\,.
\tag{B.31b}
$$

We just quote the results for the momentum integrals I_{glu} and I_{ghost} as

$$
\begin{aligned}
I_{\text{glu}}(p,\lambda_1,\lambda_2) &= \left(\frac{1}{\varepsilon}+\log\frac{4\pi\mu^2}{e^{\gamma_E}}\right)\left[\frac{25}{12}p^2+\frac{3}{2}\left(\lambda_1^2+\lambda_2^2\right)\right]\\
&\qquad - \sum_{i=0}^{4}\left(\beta_i^{(\text{f})}\,f_i + \beta_i^{(\text{h})}h_i - \beta_i^{(\text{g})}\,g_i - \beta_i^{(\text{j})}j_i\right)\,,
\end{aligned}
\tag{B.32a}
$$

$$
I_{\text{ghost}}(p,\lambda_1,\lambda_2) = \left(\frac{1}{\varepsilon}+\log\frac{4\pi\mu^2}{e^{\gamma_E}}\right)\left[\frac{1}{12}p^2+\frac{1}{4}\left(\lambda_1^2+\lambda_2^2\right)\right] - \mathcal{F}_{\text{ghost}}\,.
\tag{B.32b}
$$

The coefficients $\beta_i^{(\cdot)}$ are defined as

$$\begin{aligned}
\beta_0^{(f)} =& \frac{27\big(\lambda_1^4 - 3\lambda_1^2\lambda_2^2\big) + 6p^4 + 6p^2\big(6\lambda_1^2 + 5\lambda_2^2\big)}{8\lambda_2^2}\,,\\
\beta_1^{(f)} =& -\frac{3}{4\lambda_1^2\lambda_2^2}\Big[9\big(\lambda_1^3 - \lambda_1\lambda_2^2\big)^2 + p^6 + p^4\big(6\lambda_2^2 - 7\lambda_1^2\big)\\
&+ p^2\big(5\lambda_2^4 - 3\lambda_1^4 - 20\lambda_1^2\lambda_2^2\big)\Big]\,,\\
\beta_2^{(f)} =& \frac{3}{8\lambda_1^2\lambda_2^2}\Big[2p^6 + 9\big(\lambda_1^2 - \lambda_2^2\big)^2\big(\lambda_1^2 + \lambda_2^2\big)\\
&+ p^4\big(79\lambda_2^2 - 11\lambda_1^2\big) + p^2\big(62\lambda_2^4 - 58\lambda_1^4 - 40\lambda_1^2\lambda_2^2\big)\Big]\,,\\
\beta_3^{(f)} =& -\frac{15p^2\Big[-2\lambda_1^4 + 2\lambda_2^4 + p^2\big(2\lambda_1^2 + 5\lambda_2^2\big)\Big]}{2\lambda_1^2\lambda_2^2}\,,\\
\beta_4^{(f)} =& \frac{105p^4\big(\lambda_1^2 + \lambda_2^2\big)}{8\lambda_1^2\lambda_2^2}\,,
\end{aligned} \tag{B.33a}$$

$$\begin{aligned}
\beta_0^{(g)} =& 0\,,\\
\beta_1^{(g)} =& -\frac{3p^2\big(p^2 + \lambda_2^2\big)\big(p^2 + 5\lambda_2^2\big)}{4\lambda_1^2\lambda_2^2}\,,\\
\beta_2^{(g)} =& \frac{3\big(2p^6 + 79p^4\lambda_2^2 + 62p^2\lambda_2^4 + 9\lambda_2^6\big)}{8\lambda_1^2\lambda_2^2}\,,\\
\beta_3^{(g)} =& -\frac{15\big(5p^4 + 2p^2\lambda_2^2\big)}{2\lambda_1^2}\,,\\
\beta_4^{(g)} =& \frac{105p^4}{8\lambda_1^2}\,,
\end{aligned} \tag{B.33b}$$

$$\begin{aligned}
\beta_0^{(h)} =& \beta_3^{(h)} = \beta_4^{(h)} = 0\,,\\
\beta_1^{(h)} =& -\beta_2^{(h)} = -\frac{3p^6}{4\lambda_1^2\lambda_2^2}\,,
\end{aligned} \tag{B.33c}$$

$$\begin{aligned}
\beta_0^{(j)} =& \frac{3\big(2p^4 + 12p^2\lambda_1^2 + 9\lambda_1^4\big)}{8\lambda_2^2}\,,\\
\beta_1^{(j)} =& -\frac{3\big(p^6 - 7p^4\lambda_1^2 - 3p^2\lambda_1^4 + 9\lambda_1^6\big)}{4\lambda_1^2\lambda_2^2)}\,,\\
\beta_2^{(j)} =& \frac{3\big(2p^6 - 11p^4\lambda_1^2 - 58p^2\lambda_1^4 + 9\lambda_1^6\big)}{8\lambda_1^2\lambda_2^2}\,,\\
\beta_3^{(j)} =& \frac{15p^2\big(-p^2 + \lambda_1^2\big)}{\lambda_2^2}\,,\\
\beta_4^{(j)} =& \frac{105p^4}{8\lambda_2^2}\,.
\end{aligned} \tag{B.33d}$$

The functions f_i and g_i appearing in (B.32a) have already been defined in (B.28) and (B.30). The functions h_i and j_i are given by

$$\begin{aligned} h_0 &= 2h_1 = -2 + \log p^2 \,, \\ h_2 &= \frac{1}{18}\big(-13 + 6\log p^2\big) \,, \\ h_3 &= \frac{1}{12}\big(-7 + 3\log p^2\big) \,, \\ h_4 &= -\frac{149}{300} + \frac{1}{5}\log p^2 \,, \end{aligned} \tag{B.34}$$

as well as

$$\begin{aligned} j_0 &= \frac{\lambda_1^2\big[\log\big(\lambda_1^2+p^2\big) - \log\lambda_1^2\big]}{p^2} - 2 + \log\big(\lambda_1^2+p^2\big) \,, \\ j_1 &= \frac{\lambda_1^4\log\lambda_1^2 - 2p^4 + \lambda_1^2p^2 + \big(p^4-\lambda_1^4\big)\log\big(\lambda_1^2+p^2\big)}{2p^4} \,, \\ j_2 &= \frac{1}{18p^6}\Big[-13p^6 + 3p^4\lambda_1^2 - 6p^2\lambda_1^4 - 6\lambda_1^6\log\lambda_1^2 \\ &\quad + 6\big(p^6+\lambda_1^6\big)\log\big(p^2+\lambda_1^2\big)\Big] \,, \\ j_3 &= \frac{1}{24p^8}\Big[-14p^8 + 2p^6\lambda_1^2 - 3p^4\lambda_1^4 + 6p^2\lambda_1^6 \\ &\quad + 6\lambda_1^8\log\lambda_1^2 + 6\big(p^8-\lambda_1^8\big)\log\big(p^2+\lambda_1^2\big)\Big] \,, \\ j_4 &= \frac{1}{300p^{10}}\Big[-149p^{10} + 15p^8\lambda_1^2 - 20p^6\lambda_1^4 + 30p^4\lambda_1^6 \\ &\quad - 60p^2\lambda_1^8 - 60\lambda_1^{10}\log\lambda_1^2 + 60\big(p^{10}+\lambda_1^{10}\big)\log\big(p^2+\lambda_1^2\big)\Big] \,. \end{aligned} \tag{B.35}$$

The function $\mathcal{F}_{\text{ghost}}$ in (B.31a) is defined as

$$\begin{aligned} \mathcal{F}_{\text{ghost}} = \frac{1}{36}\Bigg(&-24\big(\lambda_1^2+\lambda_2^2\big) - \frac{6\big(\lambda_1^2-\lambda_2^2\big)^2}{p^2} + 6\Big[3\big(\lambda_1^2+\lambda_2^2\big)+p^2\Big]\log\lambda_2^2 - 10p^2 \\ &+ \frac{3}{p^4}\Bigg\{\Big[\lambda_1^4 + \lambda_1^2\big(4p^2-2\lambda_2^2\big) + \big(\lambda_2^2+p^2\big)^2\Big]\big(p^2-\lambda_1^2+\lambda_2^2\big) \\ &\quad\times\Big(\log\big(-\lambda_1^2\big) - \log\big(-\lambda_2^2\big)\Big) \\ &- 2\mathrm{i}\zeta^3\left[\arctan\left(\frac{p^2+\lambda_1^2-\lambda_2^2}{\mathrm{i}\zeta}\right) + \arctan\left(\frac{p^2-\lambda_1^2+\lambda_2^2}{\mathrm{i}\zeta}\right)\right]\Bigg\}\Bigg) \,. \end{aligned} \tag{B.36}$$

B.5.3. Real frequencies

For realtime expressions of the DSE diagrams, we need (B.25) and (B.32a) at real frequencies ω, i.e. $I(\omega,\lambda_1,\lambda_2) := I(-\mathrm{i}(\omega+\mathrm{i}0^+))$. From the definitions of the respective

functions and coefficients, the corresponding realtime expressions are obtained by replacing $p \to -\mathrm{i}(\omega + \mathrm{i}\varepsilon)$ and explicitly taking the limit $\varepsilon \searrow 0$. The calculations here were performed in WOLFRAM MATHEMATICA 12.1 with the convention $\operatorname{Im} \log x = \pi$ for $x < 0$ for the logarithmic branch cut. In this case, for the ghost self-energy (B.25) as well as I_{ghost} in (B.32a) taking the above limit corresponds to the mere substitution $p \to \mathrm{i}\omega$. For I_{glu} in (B.32a) this is not the case due to symbolic manipulations that have been performed in order to simplify the expressions. Here, appropriate imaginary parts need to be added in order to get the correct limit when explicitly taking the limit $\varepsilon \searrow 0$. Note that the manual addition of appropriate imaginary parts might also be necessary for other branch cut conventions.

B.5.4. Complex frequencies and spectral masses

The non-trivial analytic solutions of the Feynman parameter integrals in this work (Appendix B.5.2), such as (B.24), always require numerical cross-check. Especially for arbitrary complex spectral values and frequencies $\lambda_{1/2}^2, p^2 \in \mathbb{C}$, this is crucial. This becomes clear when considering the in Appendix B.5 presented solutions for the loop momentum integrals of the diagrams in this work. For $\lambda_{1/2}^2, p^2 \in \mathbb{C}$, (B.25) and (B.32a) generally do not need to hold. We will discuss this at the example of the calculation presented in Appendix B.5. While, after introduction of Feynman parameters (B.20), the solution of momentum integration (B.23) is still valid for $\lambda_{1/2}^2, p^2 \in \mathbb{C}$, this is generally not true for the analytic solution of the Feynman parameter integral in (B.24). For the diagrams involved in this work, the (non-trivial) Feynman parameter integrals takes the general form

$$J_{\text{FP}}^i(p) = \int_0^1 \mathrm{d}x\, x^i \log\left((1-x)\lambda_1^2 + x\lambda_2^2 + x(1-x)p^2\right). \tag{B.37}$$

For certain combinations $\lambda_{1/2}^2, p^2$, the integration contour in (B.37), which is the straight line connecting 0 and 1, is now crossing the logarithmic branch of the integrand. To study the case of a pair of complex conjugate poles, the case $\lambda_2 = \bar{\lambda}_1$ is of particular interest. There, for $p^2 \leq 2\operatorname{Re}\lambda_1^2$, the integration contour always crosses the branch cut. In this case, the Feynman parameter integral in (B.37) becomes ill-defined. The reason for that lies in the introduction of Feynman parameters in the first place. The Feynman trick (B.20) is only valid if the straight line connecting A and B does not cross the origin, i.e. the RHS of (B.20) has no (non-integrable) pole in the integration contour. For the above described case of $\lambda_2 = \bar{\lambda}_1$ and $p^2 < 2\operatorname{Re}\lambda_1^2$, this is exactly what happens, however. After a shift in the loop momentum, the order of the momentum and Feynman parameter integration are interchanged. For $\lambda_2 = \bar{\lambda}_1$ and $p^2 < 2\operatorname{Re}\lambda_1^2$, there always exists a value of the loop momentum q for which the Feynman parameter integration contour crosses a non-integrable pole. Since the q integration is performed first, this pole manifests itself as a branch cut in the Feynman parameter integration. The Feynman parameter integral becomes ill-defined, since the Feynman trick (B.20) is not well-defined in the first place in this case and can not be used to solve the momentum integral in this case.

For certain combinations of $\lambda_{1/2}^2, p^2 \in \mathbb{C}$ the branch cuts resulting from poles in the Feynman parameter integration domain can be avoided by contour deformation for the Feynman parameter integral. The Feynman parameter x is then integrated between 0 and 1 along an arbitrary curve in the complex plane which avoids the branch cut(s). In that case, a numeric solution of the Feynman parameter in can be well treated numerically

along with possible spectral integrals. In Section 5.1.3, we apply the described contour deformation to verify the analytic solutions for the Feynman parameter integrals. The development of a systematic procedure for finding contours avoiding these branch cuts is deferred to the future.

A possible other approach to tackle the momentum integral for arbitrary complex spectral parameters and frequencies lies in the Mellin-Barnes representation of propagators (A.35), which also holds for complex masses. In Appendix A.7, we utilise this representation to calculate the ghost loop of the gluon DSE in a particular parametrisation of the ghost propagator (A.33) involving a massive non-integer propagator power part.

B.6. Quark self-energy calculation

In this section, we detail the calculation of the quark self-energy in the spectral quark DSE in Section 5.4.

(5.59) makes explicit how the components of the spectral function are related to those of the propagator, i.e.,

$$\begin{aligned}\int_\lambda \frac{\rho_q^{(d)}(\lambda)}{p^2+\lambda^2} &= \frac{1}{Z_q(p)}\frac{1}{p^2+M_q(p)^2}\,,\\ \int_\lambda \frac{\lambda\rho_q^{(s)}(\lambda)}{p^2+\lambda^2} &= \frac{M_q(p)}{Z_q(p)}\frac{1}{p^2+M_q(p)^2}\,.\end{aligned} \tag{B.38}$$

We will use (5.59) in the following calculation of the spectral quark self-energy diagram. Using a bare quark-gluon vertex, the diagram reads

$$\Sigma_{\bar{q}q}(p) = -g^2\mathrm{C_f}\delta^{ab}\gamma_\mu\int_q \Pi_\perp^{\mu\nu}(q)G_A(q)G_q(p+q)\gamma_\nu\,. \tag{B.39}$$

Employing a split into the Dirac and mass components for the self-energy,

$$\Sigma_{\bar{q}q} = \Sigma_{\bar{q}q}^{(s)} + \mathrm{i}\not{p}\Sigma_{\bar{q}q}^{(d)}\,, \tag{B.40}$$

one obtains

$$\Gamma_{\bar{q}q}^{(2)}(p) = \mathrm{i}\not{p}\left(1-\Sigma_{\bar{q}q}^{(d)}\right) + m - \Sigma_{\bar{q}q}^{(s)}(p)\,, \tag{B.41}$$

By the fact that $\left(\Gamma_{\bar{q}q}^{(2)}\right)^{-1} = G_q$, we can now identify

$$\begin{aligned}Z_q(p) &= 1-\Sigma_{\bar{q}q}^{(d)}(p)\,,\\ M_q(p) &= \frac{1}{Z_q(p)}\left(m-\Sigma_{\bar{q}q}^{(s)}(p)\right)\,.\end{aligned} \tag{B.42}$$

B.6.1. Analytic calculation of the momentum integral

Using spectral representations for quark, (5.59), and gluon, (5.11), in the self-energy (B.39), one obtains

$$\begin{aligned}\Sigma_{\bar{q}q}(p) = &-g^2\mathrm{C_f}\delta^{ab}\gamma_\mu\int_{\lambda_A,\lambda_q}\lambda_A\rho_A(\lambda_A)\lambda_q\rho_q^{(s)}(\lambda_q)\int_q\Pi_\perp^{\mu\nu}(q)\gamma_\nu\frac{1}{q^2+\lambda_A^2}\frac{1}{(p+q)^2+\lambda_q^2}\\ &+\mathrm{i}g^2\mathrm{C_f}\delta^{ab}\gamma_\mu\int_{\lambda_A,\lambda_q}\lambda_A\rho_A(\lambda_A)\rho_q^{(d)}(\lambda_q)\int_q\Pi_\perp^{\mu\nu}(q)\left(\not{p}+\not{q}\right)\gamma_\nu\frac{1}{q^2+\lambda_A^2}\frac{1}{(p+q)^2+\lambda_q^2}\,.\end{aligned} \tag{B.43}$$

Using the split into Dirac and mass part of the self-energy (B.40), we identify

$$\begin{aligned}\Sigma_{\bar{q}q}^{(s)}(p) &= -g^2\mathrm{C_f}\delta^{ab}\int_{\lambda_A,\lambda_q}\mathrm{d}\mu_\lambda^{(s)}I^{(s)}(p,\lambda_A,\lambda_q)\,,\\ \not{p}\Sigma_{\bar{q}q}^{(d)}(p) &= g^2\mathrm{C_f}\delta^{ab}\int_{\lambda_A,\lambda_q}\mathrm{d}\mu_\lambda^{(d)}I^{(d)}(p,\lambda_A,\lambda_q)\,,\end{aligned} \tag{B.44a}$$

where we defined the spectral measures

$$\begin{aligned} \mathrm{d}\mu_\lambda^{(d)} &:= \lambda_A \rho_A(\lambda_A)\rho^{(d)}(\lambda_q)\,, \\ \mathrm{d}\mu_\lambda^{(s)} &:= \lambda_A \rho_A(\lambda_A)\lambda_q\rho_q^{(s)}(\lambda_q)\,, \end{aligned} \tag{B.44b}$$

and introduced the momentum integral functions

$$\begin{aligned} I^{(s)}(p,\lambda_A,\lambda_q) &= \gamma_\mu \int_q \Pi_\perp^{\mu\nu}(q)\gamma_\nu \frac{1}{q^2+\lambda_A^2}\frac{1}{(p+q)^2+\lambda_q^2}\,, \\ I^{(d)}(p,\lambda_A,\lambda_q) &= \gamma_\mu \int_q \Pi_\perp^{\mu\nu}(q)\left(\not{p}+\not{q}\right)\gamma_\nu \frac{1}{q^2+\lambda_A^2}\frac{1}{(p+q)^2+\lambda_q^2}\,. \end{aligned} \tag{B.44c}$$

Performing the Lorentz contractions and commutation of the Dirac structure yields

$$\begin{aligned} I^{(s)}(p,\lambda_A,\lambda_q) &= (d-1)\int_q \frac{1}{q^2+\lambda_A^2}\frac{1}{(p+q)^2+\lambda_q^2}\,, \\ I^{(d)}(p,\lambda_A,\lambda_q) &= \int_q \tau^{(d)}\frac{1}{q^2+\lambda_A^2}\frac{1}{(p+q)^2+\lambda_q^2}\,, \end{aligned} \tag{B.45a}$$

with

$$\tau^{(d)} = \not{p}\,(3-d) + \not{q}\left(1-d-2\,\frac{p\cdot q}{q^2}\right)\,. \tag{B.45b}$$

In order to get rid of the $1/q^2$-term in $\tau^{(d)}$, we apply partial fraction decomposition. This yields

$$I^{(d)}(p,\lambda_A,\lambda_q) = \int_q \left(\tau_1^{(d)}\frac{1}{q^2+\lambda_A^2} + \tau_2^{(d)}\frac{1}{q^2}\right)\frac{1}{(p+q)^2+\lambda_q^2}\,, \tag{B.46a}$$

where

$$\tau_1^{(d)} = \not{p}\,(3-d) + \not{q}\left(1-d-2\,\frac{p\cdot q}{\lambda_A^2}\right)\,, \qquad \tau_2^{(d)} = -2\not{q}\frac{p\cdot q}{\lambda_A^2}\,. \tag{B.46b}$$

In a next step, we perform the Feynman trick on each product of two propagator kernels,

$$\begin{aligned} \frac{1}{q^2+\eta_1^2}\frac{1}{(p+q)^2+\eta_2^2} &= \int_x \frac{1}{\left(q^2+\Delta(\eta_1,\eta_2,p)\right)^2}\,, \\ \Delta(\eta_1,\eta_2,p) &= x\eta_1 + (1-x)\,\eta_2 + x(1-x)p^2\,, \end{aligned} \tag{B.47}$$

where $\int_x := \int_0^1 \mathrm{d}x$. Performing the Feynman trick (B.47) necessitates shifting the loop momentum as $q \to q - xp$. This also shifts the tensor structure functions τ. Also dropping off powers of loop momentum q, which vanish under the integral, and symmetrizing $\not{q}(p\cdot q) = \not{p}q^2/d$, yields

$$\begin{aligned} \tau_1^{(d)} &\to \not{p}\tilde{\tau}_1^{(d)} \qquad \text{with} \qquad \tilde{\tau}_1 = \left[3-d+\frac{2}{d}\frac{p^2}{\lambda_A^2} + x\left(d-1+2x\frac{p^2}{\lambda_A^2}\right)\right]\,, \\ \tau_2^{(d)} &\to \not{p}\tilde{\tau}_2^{(d)} \qquad \text{with} \qquad \tilde{\tau}_2^{(d)} = \left[-\frac{2}{d}\frac{q^2}{\lambda_A^2} - 2x\frac{p^2}{\lambda_A^2}\right]\,, \end{aligned} \tag{B.48}$$

such that eventually

$$I^{(s)}(p,\lambda_A,\lambda_q) = (d-1)\int_q\int_x \frac{1}{\left(q^2+\Delta(\lambda_A,\lambda_q,p)\right)^2}\,,$$
$$I^{(d)}(p,\lambda_A,\lambda_q) = \not{p}\int_q\int_x \tilde{\tau}_1^{(d)}\frac{1}{\left(q^2+\Delta(\lambda_A,\lambda_q,p)\right)^2} + \tilde{\tau}_2^{(d)}\frac{1}{\left(q^2+\Delta(0,\lambda_q,p)\right)^2}\,. \tag{B.49}$$

The momentum integrals can now be evaluated using standard integration formulae. Re-ordering the resulting expression in powers of the Feynman parameter x and taking the limit $d \to 4-2\varepsilon$, we arrive at

$$I^{(s)}(p,\lambda_A,\lambda_q) = \frac{3}{(4\pi^2)}\left(\frac{1}{\varepsilon}+\log\frac{4\pi\mu^2}{e^{\gamma_E}} - \int_x \log\Delta(\lambda_A,\lambda_q,p)\right)+\mathcal{O}(\varepsilon)\,,$$
$$I^{(d)}(p,\lambda_A,\lambda_q) = \frac{\not{p}}{(4\pi)^2}\left\{\left(\frac{1}{\varepsilon}+\log\frac{4\pi\mu^2}{e^{\gamma_E}}\right)\sum_{i=0}^{3}\frac{\alpha_i+\beta_i}{i+1}\right.$$
$$\left. - \int_x \sum_{i=0}^{3} x^i\,\left(\alpha_i\log\Delta(\lambda_A,\lambda_q,p)+\beta_i\log\Delta(0,\lambda_q,p)\right)\right\}+\mathcal{O}(\varepsilon)\,, \tag{B.50}$$

with γ_E the Euler-Mascheroni constant. The coefficients α_i and β_i appearing in the Dirac part $I^{(d)}$ of (B.49) do not depend on x, and will be given down below. Since we work in Landau gauge, the one-loop anomalous momentum is expected to vanish, i.e.,

$$\sum_{i=0}^{3}\frac{\alpha_i+\beta_i}{i+1} = 0\,, \tag{B.51}$$

serving as a consistency check for our calculation. Indeed, we find them to satisfy the condition (B.51).

The Feynman parameter integrals can be solved analytically. Using (B.51) and dropping the $1/\varepsilon$ term as well as the $\mathcal{O}(\varepsilon)$ contribution, we obtain the final result,

$$I^{(s)}(p,\lambda_A,\lambda_q) = \frac{3}{(4\pi^2)}\left(\log\frac{4\pi\mu^2}{e^{\gamma_E}} - f_0\right)\,,\qquad I^{(d)}(p,\lambda_A,\lambda_q) = -\frac{\not{p}}{(4\pi)^2}\left(\alpha_i f_i+\beta_i g_i\right)\,, \tag{B.52}$$

with $i=0,...,3$. Using $C_\mathrm{f}(SU(3)) = 4/3$ and $g^2 = 4\pi\alpha_s$, we ultimately arrive at

$$\Sigma^{(s)}_{\bar{q}q}(p) = -\frac{\alpha_s}{4\pi}\frac{4}{3}\delta^{ab}3\int \mathrm{d}\mu^{(s)}_\lambda\left(\log\frac{4\pi\mu^2}{e^{\gamma_E}} - f_0\right)\,,$$
$$\Sigma^{(d)}_{\bar{q}q}(p) = -\frac{\alpha_s}{4\pi}\frac{4}{3}\delta^{ab}\int \mathrm{d}\mu^{(d)}_\lambda\left(\alpha_i f_i+\beta_i g_i\right)\,. \tag{B.53}$$

The analytic result agrees quantitatively with that of [468]. Performing above calculation for arbitrary values of the gauge fixing parameter ξ, we reproduce the well-known one-loop perturbation theory results for wave function renormalisation $Z_\psi = 1-\alpha_s C_\mathrm{f}\xi$.

The coefficients α_i, β_i implicitly defined in (B.50) read

$$\begin{aligned} \alpha_0 &= -2\,, & \alpha_1 &= -\frac{p_0^2 - 4\lambda_A^2 + \lambda_q^2}{\lambda_A^2}\,, & \alpha_2 &= \frac{3p_0^2}{\lambda_A^2}\,, \\ \beta_0 &= 0\,, & \beta_1 &= \frac{p_0^2 + \lambda_q^2}{\lambda_A^2}\,, & \beta_2 &= -\frac{3p_0^2}{\lambda_A^2}\,. \end{aligned} \tag{B.54}$$

The functions f_i and g_i are defined as in Appendix A of [5] with $\lambda_1 = \lambda_A$, $\lambda_2 = \lambda_q$.

B.6.2. Spectral renormalisation

The quark self-energy diagram is linearly divergent. While the momentum integrals are finite due to dimensional regularisation, the spectral integrals are not. This is due to the fact that the dimensional limit $\varepsilon \to 0$ is taken before performing the spectral integrals. This is necessary however in order to solve the spectral integrals in a fully numerical fashion. In consequence, the spectral integrals require regularisation. To that end, we apply spectral BPHZ renormalisation. This scheme renormalises the spectral integral by subtracting a Taylor expansion of the spectral integrand such that the integral converges. For details on the procedure, we refer to [1]. Below, we only provide the renormalised expressions corresponding to the renormalisation conditions (5.67).

Since the superficial degree of divergence of the quark self-energy is one, it is sufficient to subtract the 0th order Taylor expansion. The renormalised DSE reads

$$\Gamma^{(2)}_{\bar{q}q}(p) = \mathrm{i}\not{p} + m - \left(\Sigma_{\bar{q}q}(p) - \Sigma_{\bar{q}q}(\mu)\right). \tag{B.55}$$

B.6.3. Evaluation at real frequencies

In order to obtain the realtime expression for the quark self-energy diagram, in all coefficients α_i, β_i as well as in the functions f_i and g_i the substitution $p_0 \to -\mathrm{i}(\omega + \mathrm{i}0^+)$ is performed. The limit 0^+ is taken analytically. It is crucial to stay on the correct side of the branch cut. A cross-check if this is the case is can be done by comparing the analytic limit to the numeric expression using a small, finite (positive) value for 0^+.

B.7. Solving the quark-photon vertex BSE

The algebraic expressions presented in this section were provided by [420].

In this section, we will detail how the quark-photon vertex BSE in Section 6.3.3 is solved.

B.7.1. Basis transformations

The tensor basis of the quark-photon vertex is twelve-dimensional. A particularly useful basis is given by a split into transverse and longitudinal tensor structures T_j^μ resp. G_j^μ, which we employ in (6.40) and repeat here,

$$\Gamma^\mu(Q,p) = \sum_{j=1}^{4} g_j(p^2,\omega,Q^2) i G_j^\mu(Q,p) + \sum_{j=1}^{8} f_j(p^2,\omega,Q^2) i T_j^\mu(Q,p)\,, \tag{B.56}$$

with the respective dressing functions g_j, f_j. The basis elements explicitly read

$$\begin{aligned}
G_1^\mu &= \gamma^\mu, & T_1^\mu &= t_{QQ}^{\mu\nu}\gamma^\nu, & T_5^\mu &= t_{QQ}^{\mu\nu}\mathrm{i}q^\nu,\\
G_2^\mu &= q^\mu \not{q}, & T_2^\mu &= \omega\, t_{QQ}^{\mu\nu}\frac{\mathrm{i}}{2}\left[\gamma^\nu,\not{q}\right], & T_6^\mu &= t_{QQ}^{\mu\nu} q^\nu \not{q}\\
G_3^\mu &= \mathrm{i}q^\mu, & T_3^\mu &= \frac{\mathrm{i}}{2}\left[\gamma^\mu, Q\right], & T_7^\mu &= \omega\, t_{Qq}^{\mu\nu}\gamma^\nu\\
G_4^\mu &= \omega\frac{\mathrm{i}}{2}\left[\gamma^\mu,\not{q}\right], & T_4^\mu &= \frac{1}{6}\left[\gamma^\mu,\not{Q},q\right], & T_8^\mu &= t_{Qq}^{\mu\nu}\frac{\mathrm{i}}{2}\left[\gamma^\nu,\not{q}\right],
\end{aligned} \tag{B.57}$$

where

$$\omega = q\cdot Q = z|q||Q|, \qquad t_{ab}^{\mu\nu} = a\cdot b\,\delta^{\mu\nu} - b^\mu a^\nu\,. \tag{B.58}$$

The commutators are defined as

$$[A,B] = AB - BA\,, \qquad [A,B,C] = [A,B]\,C + [B,C]\,A + [C,A]\,B\,. \tag{B.59}$$

Writing the quark-photon vertex as

$$\Gamma^\mu(Q,p) = \sum_{j=1}^{12} F_j(p^2,\omega,Q^2) i t_j^\mu(Q,p)\,, \tag{B.60}$$

with $F_j \in \{g_j, f_j\}$ and $t_j^\mu \in \{G_j^\mu, T_j^\mu\}$, we notice that the basis (B.57) is not orthonormal,

$$\frac{1}{4}\,\mathrm{Tr}\left[\bar{t}_i^\mu(Q,p) t_j^\mu(Q,p)\right] \neq \delta_{ij}\,. \tag{B.61}$$

This makes it unsuitable for practical numerical calculations. An orthonormal basis can be constructed efficiently by going to the coordinate frame defined by,

$$Q^\mu = \sqrt{Q^2}\begin{bmatrix}0\\0\\0\\1\end{bmatrix}, \quad k^\mu = \sqrt{p^2}\begin{bmatrix}0\\0\\\sqrt{1-z^2}\\z\end{bmatrix}, \quad k'^\mu = \sqrt{q^2}\begin{bmatrix}0\\\sqrt{1-z'^2}\sqrt{1-y^2}\\\sqrt{1-z'^2}y\\z'\end{bmatrix}. \tag{B.62}$$

There, we can define the vectors

$$d^\mu = \hat{Q}^\mu = \frac{Q^\mu}{\sqrt{Q^2}}, \quad r^\mu = \widehat{k_\perp}^\mu = \frac{k_\perp^\mu}{\sqrt{k_\perp^2}}, \quad k_\perp^\mu = k^\mu - \frac{k\cdot Q}{Q^2}Q^\mu\,, \tag{B.63}$$

implying

$$d^\mu = \begin{bmatrix} 0 \\ 0 \\ 0 \\ 1 \end{bmatrix}, \quad r^\mu = \begin{bmatrix} 0 \\ 0 \\ 1 \\ 0 \end{bmatrix}, \quad r'^\mu = \begin{bmatrix} 0 \\ \sqrt{1-y^2} \\ y \\ 0 \end{bmatrix}, \tag{B.64}$$

which are orthonormal, as can be easily verified.

Next, we define transversely projected γ-matrices by

$$\gamma_\perp^\mu = \gamma^\mu - d^\mu \not{d} - r^\mu \not{r}, \quad \left(\gamma_\perp^\mu\right)' = \gamma^\mu - d^\mu \not{d} - r'^\mu \not{r}'\,, \tag{B.65}$$

eventually allowing us to express the quark-photon vertex in the desired orthonormal tensor basis as

$$\Gamma^\mu(Q,p) = \sum_{j=1}^{12} a_j(p^2, z, Q^2) i\tau_j^\mu(Q,p)\,, \tag{B.66}$$

with

$$\begin{aligned}
\tau_1^\mu &= \frac{1}{\sqrt{2}}\gamma_\perp^\mu\,, & \tau_5^\mu &= r^\mu \mathbb{1}\,, & \tau_9^\mu &= d^\mu \mathbb{1}\,,\\
\tau_2^\mu &= \frac{1}{\sqrt{2}}\gamma_\perp^\mu \not{d}\,, & \tau_6^\mu &= r^\mu \not{d}\,, & \tau_{10}^\mu &= d^\mu \not{d}\,,\\
\tau_3^\mu &= \frac{1}{\sqrt{2}}\gamma_\perp^\mu \not{r}\,, & \tau_7^\mu &= r^\mu \not{r}\,, & \tau_{11}^\mu &= d^\mu \not{r}\,,\\
\tau_4^\mu &= \frac{1}{\sqrt{2}}\gamma_\perp^\mu \not{r}\not{d}\,, & \tau_8^\mu &= r^\mu \gamma\not{d}\,, & \tau_{12}^\mu &= d^\mu \gamma\not{d}\,.
\end{aligned} \tag{B.67}$$

The basis (B.67) indeed obeys

$$\frac{1}{4}\operatorname{Tr}\bar{\tau}_i^\mu \tau_j^\mu = \delta_{ij}\,. \tag{B.68}$$

Perform the change of basis from (B.57) to (B.67), the new dressing functions a_j can be related to the old ones via

$$g_1 = a_{10} - \frac{z}{s}a_{11}, \quad g_2 = \frac{1}{p^2 zs}a_{11}, \quad g_3 = -\frac{\mathrm{i}}{pz}a_9, \quad g_4 = \frac{\mathrm{i}}{p^2 Qzs}a_{12}\,, \tag{B.69}$$

and

$$\begin{aligned}
f_1 &= \frac{1}{Q^2 s^2}\left(\frac{a_1}{\sqrt{2}} + zs\,(a_6 + a_{11}) - z^2 a_7 - s^2 a_{10}\right), & f_5 &= -\frac{\mathrm{i}}{pQ^2 s}\left(a_5 - \frac{s}{z}a_9\right),\\
f_2 &= -\frac{\mathrm{i}}{p^2 Q^3 s^2}\left(\frac{a_2}{\sqrt{2}} - a_8 + \frac{s}{z}\left(\frac{a_3}{\sqrt{2}} + a_{12}\right)\right), & f_6 &= -\frac{1}{p^2 Q^2 s^2}\left(\frac{a_1}{\sqrt{2}} - a_7 + \frac{s}{z}a_{11}\right)\\
f_3 &= \frac{\mathrm{i}}{\sqrt{2}Q}\left(-a_2 + \frac{z}{s}a_3\right), & f_7 &= -\frac{1}{p^2 Q^2 s^2}\left(\frac{a_1}{\sqrt{2}} - a_7 + \frac{s}{z}a_6\right)\\
f_4 &= \frac{1}{\sqrt{2}pQs}a_4, & f_8 &= \frac{\mathrm{i}}{p^2 Qs^2}\left(\frac{a_2}{\sqrt{2}} - a_8\right).
\end{aligned} \tag{B.70}$$

The combination of the two quark propagators and the QPV on the RHS of the BSE (6.48) has exact same momentum and tensor structure as the QPV itself. Hence, it must have the same tensor decomposition, and we can write

$$G_q(p_+)\Gamma^\mu(Q,p)G_q(p_-) = \sum_{j=1}^{12} b_j(p^2,z,Q^2)\mathrm{i}\tau_j(Q,p)\,. \tag{B.71}$$

Substituting this into the RHS of the BSE (6.48) while working with the same tensor decomposition for the QVP (B.66), we can exploit the orthonormality relations (B.68) to arrive at a purely scalar form of the equation,

$$\begin{aligned} a_i\left(p^2,z,Q^2\right) &= Z_2 a_i^0 + \sum_{j=1}^{12}\int_q g(p-q)K_{ij}\left(p^2,q^2,z,z',y,Q^2\right)b_j\left(q^2,z',Q^2\right), \\ b_i\left(p^2,z,Q^2\right) &= \sum_{j=1}^{12} G_{ij}\left(p^2,z,Q^2\right)a_j\left(p^2,z,Q^2\right)\,, \end{aligned} \tag{B.72}$$

where the kernels K_{ij}, G_{ij} are given by

$$\begin{aligned} K_{ij}\left(p^2,q^2,z,z',y,Q^2\right) &= T_l^{\alpha\beta}\frac{1}{4}\,\mathrm{Tr}\left\{\bar\tau_i^\mu(Q,p)\gamma^\alpha\tau_j^\mu\left(Q,q\right)\gamma^\beta\right\} \\ G_{ij}\left(p^2,z,Q^2\right) &= \frac{1}{4}\,\mathrm{Tr}\left\{\bar\tau_i^\mu(Q,p)S\left(p_+\right)\tau_j^\mu(Q,p)S\left(p_-\right)\right\}\,, \end{aligned} \tag{B.73}$$

and $a_i^0 = \frac{1}{4}\,\mathrm{Tr}\,\bar\tau_i^\mu\gamma^\mu$.

B.7.2. Lorentz traces

The Lorentz traces in (B.73) can be worked out explicitly. The inhomogeneous term in the BSE reads

$$a_i^0 = \frac{1}{4}\,\mathrm{Tr}\left\{\bar\tau_i^\mu\gamma^\mu\right\} = \begin{cases}\sqrt{2} & i=1\\ 1 & i=7,10\\ 0 & \text{else.}\end{cases}\,. \tag{B.74}$$

For the sake of a more compact notation, using $l = p-q$, we define

$$\begin{aligned} u &= p\sqrt{1-z^2}\,, & u' &= q\sqrt{1-z'^2}, & V &= \frac{pz-qz'}{l^2}\,, \\ w &= \frac{u^2}{l^2}\,, & w' &= \frac{u'^2}{l^2}\,, & X &= \frac{uu'}{l^2}\,. \end{aligned} \tag{B.75}$$

The kernel entries of (B.73) are then completely determined by

$$\begin{aligned}
K_{11} &= -\frac{1+y^2}{2} - y\left(1-y^2\right)X, & K_{16} &= \sqrt{2}\left(1-y^2\right)u'V,\\
K_{22} &= -\frac{1+y^2}{2}\left(1-2l^2V^2\right) + y\left(1-y^2\right)X, & K_{61} &= -\sqrt{2}\left(1-y^2\right)uV,\\
K_{33} &= y\left(1-2l^2V^2\right) - \left(1-y^2\right)X, & K_{17} &= -\frac{1-y^2}{\sqrt{2}}\left(1+2w'-2yX\right),\\
K_{44} &= y + \left(1-y^2\right)X, & K_{71} &= -\frac{1-y^2}{\sqrt{2}}(1+2w-2yX),\\
K_{55} &= 3y, & K_{23} &= \left(2yu - \left(1+y^2\right)u'\right)V,\\
K_{66} &= -y\left(1+2l^2V^2\right), & K_{32} &= -\left(2yu' - \left(1+y^2\right)u\right)V,\\
K_{77} &= -y^2\left(3-2l^2V^2\right) + 2y\left(1-y^2\right)X, & K_{67} &= 2y\left(u'-yu\right)V,\\
K_{88} &= y^2 - 2y\left(1-y^2\right)X, & K_{76} &= -2y\left(u-yu'\right)V\,,
\end{aligned} \tag{B.76}$$

and

$$\begin{aligned}
K_{28} &= K_{71} + \sqrt{2}\left(1-y^2\right),\\
K_{82} &= K_{17} + \sqrt{2}\left(1-y^2\right),\\
K_{38} &= -K_{61},\\
K_{83} &= -K_{16},
\end{aligned}
\qquad
\begin{bmatrix} K_{99}\\ K_{10,10}\\ K_{10,11}\\ K_{11,10}\\ K_{11,11}\\ K_{12,12}\end{bmatrix} = \frac{1}{y}\begin{bmatrix} K_{55}\\ K_{66}\\ K_{67}\\ K_{76}\\ K_{77}\\ K_{88}\end{bmatrix}, \tag{B.77}$$

and all other elements zero.

The propagator kernel can be decomposed as

$$G_{ij}\left(p^2,z,Q^2\right) = \sigma_v\left(p_+^2\right)\sigma_v\left(p_-^2\right)\widetilde{G}_{ij}\left(p^2,z,Q^2\right)\,. \tag{B.78}$$

Defining

$$\Sigma_M = \frac{M\left(p_+^2\right)+M\left(p_-^2\right)}{2}, \quad \Delta_M = \frac{M\left(p_+^2\right)-M\left(p_-^2\right)}{p_+^2-p_-^2}, \quad \bar{M}^2 = M\left(p_+^2\right)M\left(p_-^2\right)\,, \tag{B.79}$$

we can write the kernel entries $\widetilde{G}_{ij}$ as

$$\begin{aligned}
\widetilde{G}_{11} &= \bar{M}^2 + p^2 - \frac{Q^2}{4}, & \widetilde{G}_{12} &= \mathrm{i}Q\left(\Sigma_M - 2p^2z^2\Delta_M\right),\\
\widetilde{G}_{22} &= \bar{M}^2 - \left(1-2z^2\right)p^2 - \frac{Q^2}{4}, & \widetilde{G}_{13} &= -2\mathrm{i}p^2Qz\sqrt{1-z^2}\Delta_M,\\
\widetilde{G}_{33} &= \bar{M}^2 + \left(1-2z^2\right)p^2 + \frac{Q^2}{4}, & \widetilde{G}_{23} &= 2p^2z\sqrt{1-z^2},\\
\widetilde{G}_{44} &= \bar{M}^2 - p^2 + \frac{Q^2}{4}, & \widetilde{G}_{24} &= 2\mathrm{i}p\sqrt{1-z^2}\Sigma_M,\\
\widetilde{G}_{14} &= -pQ\sqrt{1-z^2} & \widetilde{G}_{34} &= \mathrm{i}pz\left(Q^2\Delta_M - 2\Sigma_M\right),
\end{aligned} \tag{B.80}$$

The other elements follow from the fact that G is symmetric,

$$\begin{bmatrix} G_{55} \\ G_{56} \\ G_{66} \\ G_{77} \\ G_{78} \\ G_{88} \end{bmatrix} = \begin{bmatrix} G_{99} \\ G_{9,10} \\ G_{10,10} \\ G_{11,11} \\ G_{11,12} \\ G_{12,12} \end{bmatrix} = \begin{bmatrix} G_{44} \\ G_{34} \\ G_{33} \\ G_{22} \\ G_{12} \\ G_{11} \end{bmatrix}, \quad \begin{bmatrix} G_{57} \\ G_{58} \\ G_{67} \\ G_{68} \end{bmatrix} = \begin{bmatrix} G_{9,11} \\ G_{9,12} \\ G_{10,11} \\ G_{10,12} \end{bmatrix} = - \begin{bmatrix} G_{24} \\ G_{14} \\ G_{23} \\ G_{13} \end{bmatrix}, \tag{B.81}$$

and all other elements vanish.

B.8. Calculating the hadronic vacuum polarisation

The algebraic expressions in this section were provided by [420].

In this section, we details the calculation of the hadronic vacuum polarisation carried out in Section 6.3.2.

Substituting (6.40) into (6.39) yields

$$\Pi_0^{\mu\nu}(Q) = 4e^2 Z_2 \int_q \frac{g_q(q_+)q_q(q_-)}{Z_q(q_+)Z_q(q_-)} \left[\sum_{j=1}^{4} g_j G_j^{\mu\nu} + \sum_{j=1}^{8} f_j T_j^{\mu\nu}\right], \tag{B.82}$$

where

$$\begin{aligned} G_j^{\mu\nu} &= \frac{1}{4}\,\mathrm{Tr}\left[\mathrm{i}\gamma^\mu\left(-\mathrm{i}q_+ + M(q_+^2)\right)\mathrm{i}G_j^\nu\left(-iq_- + M(q_-^2)\right)\right], \\ T_j^{\mu\nu} &= \frac{1}{4}\,\mathrm{Tr}\left[i\gamma^\mu\left(-\mathrm{i}q_+ + M(q_+^2)\right)\mathrm{i}T_j^\nu\left(-iq_- + M(q_-^2)\right)\right]. \end{aligned} \tag{B.83}$$

Here and in the following, we parametrise the four-dimensional momentum integral as

$$\int_q = \int \frac{\mathrm{d}^4 q}{(2\pi)^4} = \frac{1}{(2\pi)^4}\int_0^\infty \mathrm{d}q^2 q^2 \int_{-1}^1 \mathrm{d}z\sqrt{1-z^2}\int_{-1}^1 \mathrm{d}y \int_0^{2\pi}\mathrm{d}\phi\,. \tag{B.84}$$

The transverse and diagonal parts of the HVP (6.41) can be projected onto via

$$\Pi_0(Q) = \frac{\delta^{\mu\nu} - 4\Pi_\parallel^{\mu\nu}(Q)}{3Q^2}\Pi_0^{\mu\nu}(Q)\,, \qquad \widetilde{\Pi}_0(Q^2) = \Pi_\parallel^{\mu\nu}(Q)\Pi_0^{\mu\nu}(Q)\,, \tag{B.85}$$

with the longitudinal projection operator $\Pi_\parallel^{\mu\nu}$ as defined in (3.64). Explicitly carrying out the projections in (B.85) yields that the diagonal part vanishes by means of the WTI, see (6.42). The transverse part takes the form

$$\Pi_0(Q^2) = 4e^2 Z_2 \int_k \frac{g_q(q_+)q_q(q_-)}{Z_q(q_+)Z_q(q_-)} \left[\sum_{j=1}^{4} g_j c_j + \sum_{j=1}^{8} f_j d_j\right], \tag{B.86}$$

where the functions c_j, d_j are defined by

$$c_j = \frac{\delta^{\mu\nu} - 4\Pi_\parallel^{\mu\nu}(Q)}{3Q^2}G_j^{\mu\nu}\,, \qquad d_j = \frac{\delta^{\mu\nu} - 4\Pi_\parallel^{\mu\nu}(Q)}{3Q^2}T_j^{\mu\nu}\,. \tag{B.87}$$

Explicitly, they read

$$\begin{aligned} c_1 &= \frac{1}{2} + \mathbf{V}, & d_3 &= \mathbf{Z}\,, \\ c_2 &= \frac{1}{4}\left(\mathbf{w} + 2\mathbf{V}\mathbf{X}_-\right), & d_4 &= \mathbf{w}\,, \\ c_3 &= -q^2 z^2 \Delta_M - \mathbf{V}\Sigma_M\,, & d_5 &= -\mathbf{w}\Sigma_M\,, \\ c_4 &= q^2 z^2\left(\Sigma_M + Q^2\mathbf{V}\Delta_M\right), & d_6 &= \mathbf{w}\left(q^2 - \frac{1}{2}\mathbf{X}_+\right), \\ d_1 &= \mathbf{w} - \mathbf{X}_+, & d_7 &= -q^2 z^2 \mathbf{X}_+\,, \\ d_2 &= q^2 Q^2 z^2\left(\mathbf{Z} - 2\mathbf{w}\Delta_M\right), & d_8 &= q^2\mathbf{Z} - \mathbf{w}\Sigma_M\,. \end{aligned} \tag{B.88}$$

In (B.88), we made use of the definitions

$$\begin{aligned}
\mathbf{X}_{\pm} &= q^2 - \frac{Q^2}{4} \pm \left(\Sigma_M^2 - q^2 Q^2 z^2 \Delta_M^2\right), \\
\mathbf{Z} &= \Sigma_M - 2q^2 z^2 \Delta_M, \\
\mathbf{w} &= \frac{2q^2}{3}\left(1 - z^2\right), \\
\mathbf{V} &= \frac{2q^2}{3Q^2}\left(1 - 4z^2\right). \qquad \text{(B.89)}
\end{aligned}$$

C. Numerical procedures

In this appendix, we present details on the numerical procedures used in the investigations presented in this thesis. To allow for a clear assignment, the structure of this appendix follows that of the main body of this thesis. Accordingly, the following sections carry the names of the respective sections in the thesis.

C.1. Mass generation for the gluon

In this section, we elaborate on the numerical procedures of Section 3.2.

C.1.1. Fitting procedure

Formally, the coefficient Z_{cond} in (3.117) is defined via an operator product expansion of the gluon propagator, and stems from the local operator (3.87). The present computation of the effective potential $\mathcal{W}_{\text{eff}}$ is detailed in Appendix B.2, Appendix B.1, Appendix B.3 and uses the scaling propagator from [95]. The latter is obtained within a quantitative approximation of the coupled set of functional equations for Yang-Mills correlation functions, for respective DSE results see [93]. In [95], also decoupling solutions have been computed including a lattice-type solution, for respective lattice propagators see [98, 182].

The extraction of the p^4-coefficient stemming from (3.87) requires the distinction of the infrared dynamics in the propagator, which in the present approach relates to the emergence of the color condensates, from the coefficients of the local operators. This mixing for small momenta makes it impossible to extract the p^4-coefficient in an expansion about $p = 0$ without further information on the momentum dependence of the condensate. We shall evaluate the propagator for sufficiently large momentum scales, for which the

	Z_{cond} [GeV^{-2}]
scaling (fRG)	0.168(31)
decoupling (lattice)	0.129(19)
decoupling (fRG)	0.1147(22)
Estimate	0.149(19)

Tabelle C.1.: Extrapolation results for the wave function renormalisation Z_{cond} at $p = 0$ based on the fit results for $Z_{\text{cond}}(p_{\text{min}})$ as a function of the lower fit interval bound p_{min}, see Figure C.1. The final estimate is obtained as the average of the scaling fRG and decoupling lattice data. In order to conservatively estimate possible systematic uncertainties (see text), we use the separate scaling fRG and lattice results as error bars.

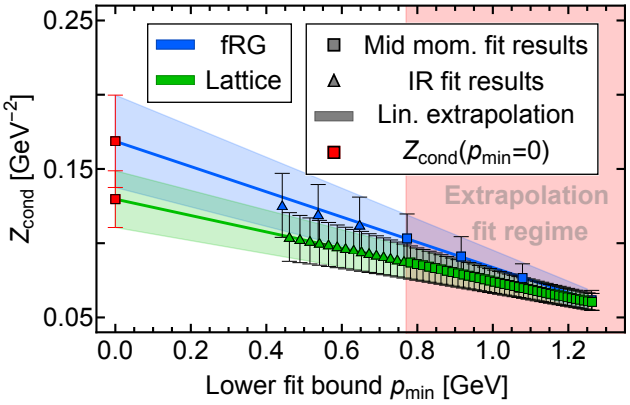

Abbildung C.1.: Linear extrapolation of $Z_{\rm cond}$ to the lower fit interval bound $p_{\rm min} = 0$, yielding $Z_{\rm cond} = 0.149(19)$. The explicit fit results for $Z_{\rm cond}$ are obtained via a fit of (C.1) to the scaling fRG data of [95] (blue squares), and to the lattice data of [128, 182] (green squares). $Z_{\rm cond}$, being defined as the operator product expansion coefficient should be extracted at $p = 0$: we extract this information from an extrapolation of the fit results towards $p = 0$ (red squares), and use as a minimal $p_{\rm min} \approx 0.8\,\text{GeV}$, below which the details of the implementation of the IR dynamics begin to matter. The triangular data points mark fit results for $p_{\rm min}$ below the fit regime for the interpolation. The final estimate for $Z_{\rm cond}$ ((C.5) and (3.141)) is obtained as the mean of the lattice and scaling fRG results for $Z_{\rm cond}$, whose numerical values can be found in Table C.1.

condensate vanishes, $\langle F\rangle \to 0$. The cutoff scale resembles the momentum scale p, indeed it is introduced in the two-point function itself as a momentum cutoff. Hence, we deduce from the flow of the minimum of $\mathcal{W}_{\rm eff}$ depicted in Figure 3.3, that the condensate vanishes for $p \gtrsim 1/2$ GeV. Accordingly, we determine $Z_{\rm cond}$ from fits

$$Z_a^{\rm fit}(p^2) = \frac{Z_m}{p^2} + Z_{p^2} + Z_{\rm cond}\, p^2 \tag{C.1}$$

to the gluon wave function $Z_a(p^2)$ in the momentum regime

$$p \in [p_{\rm min}\,,\, p_{\rm max}]\,, \tag{C.2}$$

with

$$p_{\rm min} \in [0.77, 1.27]\,\text{GeV}\,, \quad p_{\rm max} \in [1.95, 2.23]\,\text{GeV}\,, \tag{C.3}$$

where the range of values for $p_{\rm min}$ is adapted to the data points of the sparse fRG data.

The upper bound $p_{\rm max}$ is chosen such, that the interval sustains a Taylor expansion while containing a sufficient amount of data points for fitting, also adapted to the fRG data points. Its maximum value is further constrained by the UV boundary of the lattice data from [182], which are used for comparison as well as the error estimate, together with the lattice data from [128].

The constants Z_m, Z_{p^2} and $Z_{\rm cond}$ in (C.1) are fit parameters. Here Z_m takes care of the infrared gapping dynamics, and Z_{p^2} related to a standard (infrared) wave function

renormalisation. Both parts carry the details of the IR behaviour of the propagator and may vary largely for different solutions. In turn, the coefficient Z_{cond} should not.

We perform the fits for different values of the lower fitting interval bound p_{min}. For every fit, p_{max} is varied between the points in the p_{max} interval, comp. (C.3). In addition, we transform the lattice and fRG data sets into the respective (inverse) dressing function and inverse propagator, and fit those with the respective fit functions corresponding to (C.1). This provides us with a $Z_{\mathrm{cond}}(p_{\mathrm{min}})$ given as the average over the single fit results for the different values of p_{max} and representations of the data set, with uncertainty given by the standard deviation.

Eventually, we extract the wave function renormalisation Z_{cond} at $p = 0$ via a limiting procedure as

$$Z_{\mathrm{cond}} = \lim_{p_{\mathrm{min}} \to 0} Z_{\mathrm{cond}}(p_{\mathrm{min}}) \,. \tag{C.4}$$

The limit is obtained within an extrapolation of the $Z_{\mathrm{cond}}(p_{\mathrm{min}})$ discussed below. We extract Z_{cond} from both, the scaling fRG data of [95] and the lattice solution [182], see Figure C.1 and Table C.1 for the numerical values. We also provide Z_{cond} from a lattice-type fRG decoupling solution for comparison in Table C.1. When lowering the lower fit interval bound p_{min}, the results for Z_{cond} differ more and more. This can be attributed to the different infrared behaviour of the two data sets. Accordingly, we exclude as many incompatible data points as possible from the extrapolation fit regime while keeping enough data for a meaningful prediction of $Z_{\mathrm{cond}}(p = 0)$.

As the data from [95] are relatively sparse and hence the respective $Z_{\mathrm{cond}}(p_{\mathrm{min}})$ and the extrapolation show large error bars, we support this extrapolation with one obtained from dense fRG data provided in [96, 469]. While the approximation used in the latter computations is not as sophisticated as that used in [95], it allows for a relatively quick production of dense data. The scaling solution of [96] yields $Z_{\mathrm{cond}} = 0.166(33)$, which agrees extremely well with the scaling solution estimate of [95], comp. Table C.1.

Our final estimate for Z_{cond} is obtained by averaging the scaling fRG and lattice result, yielding

$$Z_{\mathrm{cond}} = 0.149(19) \,. \tag{C.5}$$

The error bars are given by the separate extrapolation results for scaling fRG and lattice data in order to incorporate systematic uncertainties such as the influence of the different infrared behaviours.

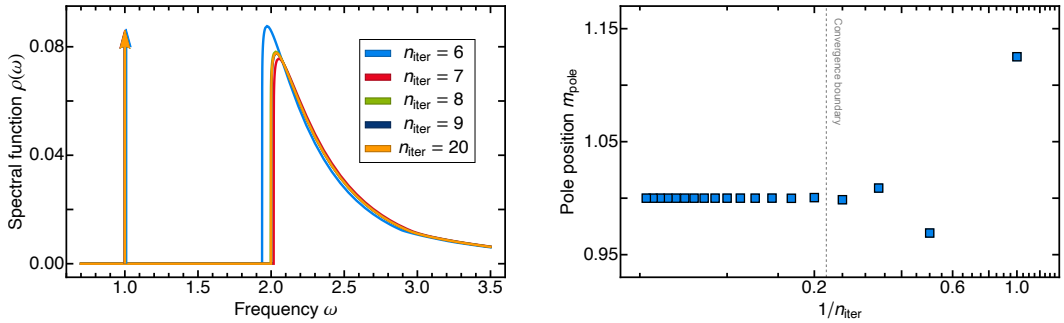

Abbildung C.2.: Example of a convergent iteration of the scalar DSE with classical vertices. The curves were *not* rescaled by the respective mass poles to demonstrate convergence of the iteration also for the pole mass. Instead, renormalisation was done at $\mu = 0$. Units thus given by the input parameters. The spectral functions are alternating, approaching the final orange curve (left). 20 iterations have been performed. The curves from iterations 10 to 19 were left out as they were graphically indistinguishable from the final curve. An iterative behaviour as displayed is taken to be convergent, i.e. signalling a solution to the DSE where left and right-hand side of the equation coincide. The corresponding pole positions also converge very quickly (right). Left of the convergence boundary, assuming a (relative) precision of 10^{-4}, all points are identical.

C.2. Spectral Dyson-Schwinger equations

This section elaborates on the numerical procedures in Section 4.1.

In order to compute the spectral integrals in (4.22), the integrands I_j are discretised on suitable, evenly spaced momentum grids of usually around 100 points. The grids are chosen differently for each diagram such that peaked or discontinuous structures like the onset jumps in the imaginary parts are ideally resolved. The spectral integrations are performed numerically in MATHEMATICA with standard global adaptive integration strategies using a relative precision goal of 10^{-3}. All diagrams are interpolated separately in real and imaginary part in order to treat the sharp onset of the imaginary parts properly. All interpolations are performed using B-splines up to order 2 as all interpolants are real due to the split of real and imaginary part. The spectral function is then computed from the interpolated diagrams.

For a given set of parameters, convergence was usually reached within less than 10 iterations. Figure C.2 demonstrates convergent behaviour. We estimate the relative precision of our routine to be $\geq 10^{-4}$. Based on that, all mass poles shown in the right panel of Figure C.2 left of the convergence boundary are indistinguishable. Normalising the scattering onsets of all spectral functions in the left panel to be identical, the continuous tail also converges pointwise beyond the convergence boundary, based on above precision estimate.

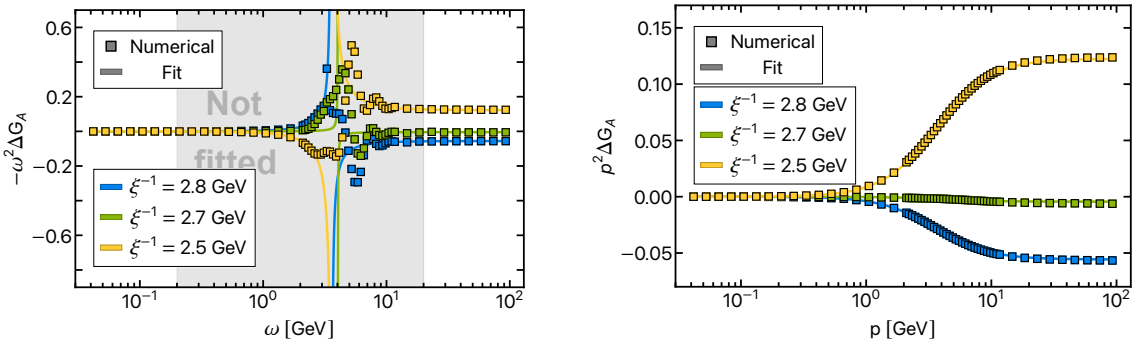

Abbildung C.3.: Spectral difference ΔG_A on the real (left) and imaginary (right) frequency axis. Squares indicate the numerical values of ΔG_A, while solid lines mark the corresponding fit G_A^{approx} by a pole on the real frequency axis, cf. (5.36). The best fit for the spectral difference is constructed on the level of the dressing function, as displayed above. The fit describes the Euclidean well. On the Minkowski axis, only the asymptotic tails are fitted, and the fit works well in this regime. In the mid-momentum regime of the real axis however, numerous wiggles suggests that multiple pairs of complex conjugate poles are present. The region is explicitly excluded from the fit.

C.3. Complex structure of Yang-Mills theory

This section details the numerical procedures in Section 5.1.

C.3.1. Spectral difference

This appendix discusses the fitting procedure that is used to take the spectral difference (5.34), i.e., the difference between the spectral and full gluon propagator, into account. The spectral difference is evaluated on both real and imaginary frequency axis. The obtained result is fit with a simple pole on the real frequency axis, comp. (5.36), using Mathematica's NonlinearModelFit routine. We select Newton's method for the optimisation and explicitly specify gradient and hessian of the fit function. The trust region method is employed for step control. Further, we assign weights w_i to the (real and imaginary) frequency grid points. It turned out to be beneficial for the convergence to choose $w_i = |p_0^2|$, where p_0 stands for both real or imaginary frequencies. This results simply in fitting the spectral difference of the gluon dressing function instead of the propagator. In consequence, the fitting routine puts a lot more weight on the UV instead of the IR, which is the case when fitting the propagator. The fact that this increases stability can be well understood considering that the effect of the deep IR behaviour of the gluon propagators in the DSE diagrams (comp. Figure 5.2) is relatively subleading compared to the UV behaviour.

In order to assess the quality of the employed fit, it is hence sensible to consider the spectral difference for the gluon dressing function, as shown in Figure C.3. The left panel shows the spectral difference as compared to the fit on the realtime axis. The grey shaded area is explicitly excluded from the fit, such that only the asymptotic tails are taken into account. As emphasised in Section 5.1.5.1, it can be clearly seen that the employed fit

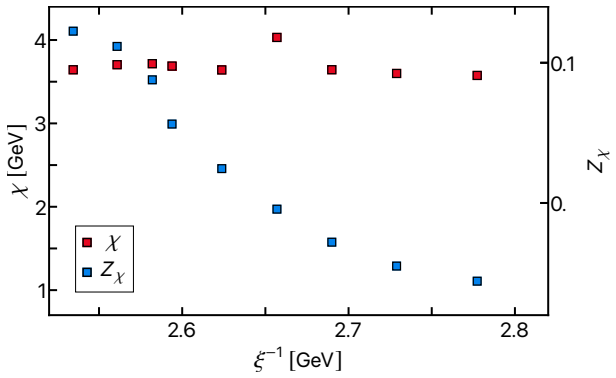

Abbildung C.4.: Evolution of the pole positions (red) and residues (blue) of the spectral difference fit G_A^χ defined in (5.36) under change of m_A^2. The residues mirror the spectral violations $\mathcal{V}_{\text{spec}}$ defined in (5.38) and shown in Figure 5.7. If the spectral violation is negative, i.e. the Källén-Lehmann part G_A^χ is smaller than the full gluon propagator G_A, the spectral difference and, correspondingly the residue, are positive, and vice versa. Decreasing stability of the iteration and worsening fit precisions towards smaller m_A^2, which can be also seen when comparing the spectral difference ΔG_A and its fit G_A^χ, shown in Figure C.3, also manifest themselves in non-monotonous behaviour of χ.

function is not able to capture the full structure of the spectral difference. The asymptotic tails are well fit, however. Taking a closer look at the excluded region in fact suggest the existence of multiple pairs of complex conjugate poles. A single complex conjugate pole term accounts for each one local maximum and minimum in the spectral difference. A rough estimate for the number of (leading order) pairs of poles can thus be obtained by just counting positive/negative peaks.

The Euclidean spectral difference for the gluon dressing is displayed in the left panel of Figure C.3. As for the asymptotic regions on the real frequency axis, the fit works well here. However, comparing the fit quality between the different values of m_A^2, the worst fit is obtained for smallest m_A^2.

C.3.2. Spectral integration

This section elaborates on the numerical treatment of the spectral integrals, which are of the form

$$\int_{\{\lambda_i\}} \prod_i \lambda_i \rho_i(\lambda_i) I_{\text{ren}}\big(p, \{\lambda_i\}\big) \,, \tag{C.6}$$

where I_{ren} is the renormalised spectral integrand (comp. (5.28) or (5.30)), are evaluated numerically on a logarithmic momentum grid of 100-200 grid points with boundary $(p_{\min}, p_{\max}) = (10^{-4}, 10^2)$, identically for the Euclidean and Minkowski axis. We use a global adaptive integration strategy with default multidimensional symmetric cubature integration rule. After spectral integration, the diagram is interpolated with splines in the Euclidean and Hermite polynomials in the Minkowski domain, both of order 3. The

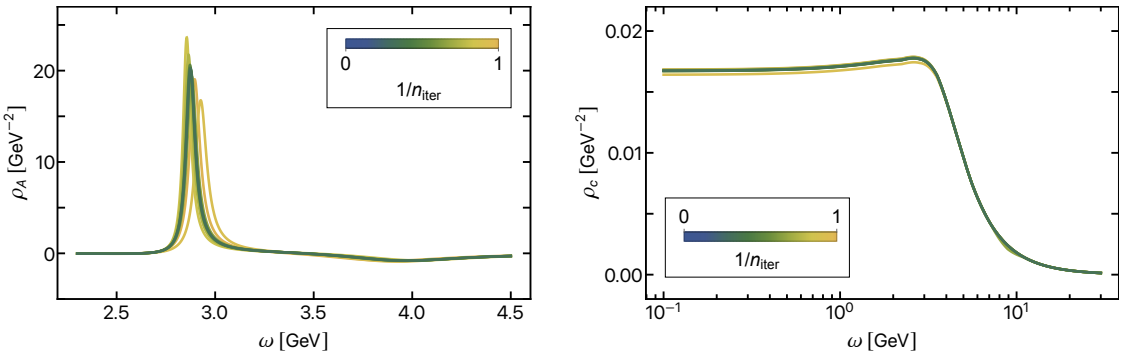

Abbildung C.5.: Convergence of a gluon (left) and ghost (right) spectral function through iteration of the DSE for $m_A^2 = -1.1$. As an initial guess, the solution for $m_A^2 = -1$ is used. The colour coding indicates the iteration number n_{iter}. After about 10 iterations, the curves become visually indistinguishable, i.e. the iteration converges.

spectral function is then computed from the interpolants. Note that, a priori, due to (4.4), the domain of the ghost spectral function is given by the momentum grid. The integration domain of the spectral integral of the ghost spectral parameter has to be bounded by $(p_{\min}, p_{\max})$, in order to not rely on the extrapolation of the spectral function beyond the grid points. Due to numerical oscillations at the very low end of the grid, we choose $(\lambda_c^{\min}, \lambda_c^{\max}) = (10^{-3.5}, 10^2)$. Convergence of the integration result with respect to increase of the integration domain has been explicitly checked.

C.3.3. Spectral integrands

The numerical performance of the spectral integrations presented in Appendix B.5 is sped-up by up to two orders of magnitude by using interpolating functions of the numerical data. The interpolants are constructed by first discretising the integrand inside the three-dimensional $(p, \lambda_1, \lambda_2)$ cuboid defined by $p \in 10^{\{-4,2\}}$, $\lambda_{1,2} \in 10^{\{-4,4\}}$. As for the momentum grid for the spectral integration, we use the same cuboid for the real- and imaginary-time domain. We use 60 grid points in the momentum and 160 grid points in the spectral parameter integration, both with logarithmic grid spacing. For the realtime expressions, we divide into real and imaginary part of the integrands. Both real and imaginary parts of the discretised Minkowski as well as the Euclidean expressions are then interpolated by three-dimensional splines inside the cuboid. The resulting interpolating functions are then used in the spectral integration.

C.3.4. Convergence of iterative solution

The iterative procedure applied to solve the coupled system of DSEs in this work is described in Section 5.1.2.5. For each value of m_A^2, the iterations is initiated with spectral functions from the previous (larger) value of m_A^2. It converges rapidly, see Figure C.5. The very first initial guess for the gluon spectral function has been obtained heuristically by trial-and-error from previous iteration results and has not been stored. For the ghost spectral function, a massless pole in the origin with residue 1 was used.

C.3.5. Scale setting and normalisation

In order to provide data which can be compared to the lattice, we need to fix the momentum scale and global normalisation of both fields. This is done by introducing two rescaling factors via

$$Z_{c/A}^{(\mathrm{lat})}(p_{\mathrm{GeV}}) = \mathcal{N}_{c/A}\, Z_{c/A}(c \cdot p_{\mathrm{internal}})\,, \tag{C.7}$$

The normalisation of ghost and gluon field $\mathcal{N}_{c/A}$ as well as (common) momentum rescaling factor c are then determined by fitting the Euclidean ghost and gluon dressing functions in (C.7) to the Yang-Mills fRG data of [95], which is itself properly rescaled to match the lattice data of [98]. For the gluon, during the fit an additional constant term Δm_A^2 needs to be allowed on the level of $\Gamma^{(2)}_{AA}$ in order to compensate for possible differences in the constant part of $\Gamma^{(2)}_{AA}$. Note that this term is only introduced to correctly determine $\mathcal{N}_A$ and c, and is removed again after rescaling.

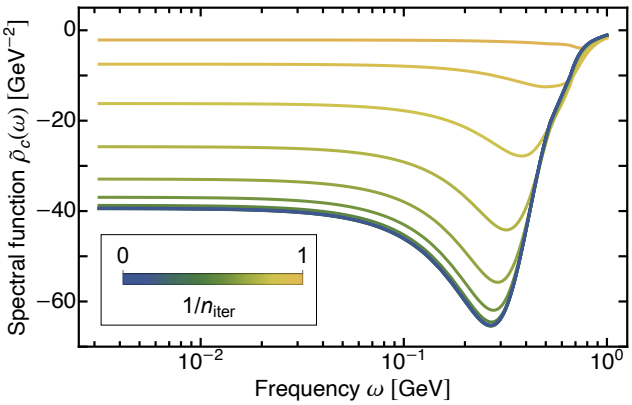

Abbildung C.6.: Convergence of an exemplary spectral function through iteration of the DSE. The colour coding indicates the iteration number n_{iter}. After about 10 iterations, the curves become visually indistinguishable, i.e., the iteration converges.

C.4. Ghost

This section elaborates on the numerical treatment of the spectral integrals as well as the spectral integrands in Section 5.2.

C.4.1. Spectral integration and convergence

The spectral integrals of the form

$$\int_{\{\lambda_i\}} \prod_i \lambda_i \rho_i(\lambda_i) I_{\text{ren}}\big(p, \{\lambda_i\}\big) \,, \tag{C.8}$$

where I_{ren} is the renormalised spectral integrand (comp. (5.28) or (5.30)), are evaluated numerically on a logarithmic momentum grid of about 200 grid points with boundary $(p_{\min}, p_{\max}) = (10^{-4}, 10^2)$, identically for the Euclidean and Minkowski axis. We use a global adaptive integration strategy with default multidimensional symmetric cubature integration rule. After spectral integration, the diagram is interpolated with splines in the Euclidean and Hermite polynomials in the Minkowski domain, both of order 3. The spectral function is then computed from the interpolants. Note that, a priori, due to (4.4), the domain of the ghost spectral function is given by the momentum grid. The integration domain of the spectral integral of the ghost spectral parameter has to be bounded by $(p_{\min}, p_{\max})$, in order to not rely on the extrapolation of the spectral function beyond the grid points. Due to numerical oscillations at the very low end of the grid, we choose $(\lambda_c^{\min}, \lambda_c^{\max}) = (10^{-3.5}, 10^2)$. Convergence of the integration result with respect to increase of the integration domain has been explicitly checked.

For the gluon spectral integral, the situation is different, as the spectral function is given in an algebraic form from [243]. We use the integration boundary $(\lambda_A^{\min}, \lambda_A^{\max}) = (10^{-4}, 10^2)$.

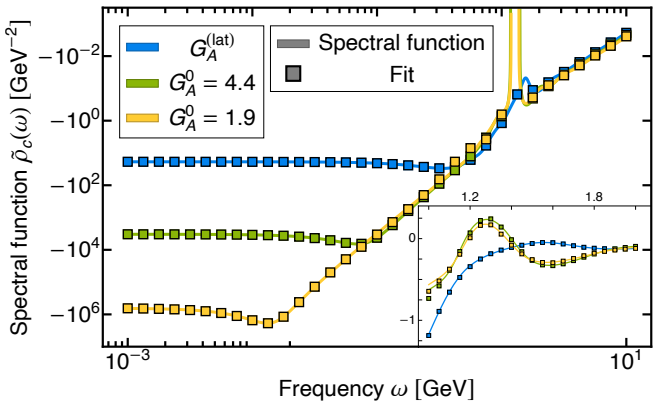

Abbildung C.7.: Ghost spectral functions (solid lines) compared to their fits via ansatz (5.47). The best fit parameters are listed in Table C.2. The change of sign around 1.2 GeV is an imprint of the oscillations of the input reconstructed gluon spectral function from [243] and is discussed in Appendix C.4.4.

C.4.2. Spectral integrands

The numerical performance of the spectral integrations presented in Appendix B.5 is sped-up by up to two orders of magnitude by using interpolating functions of the numerical data. The interpolants are constructed by first discretising the integrand inside the three-dimensional $(p, \lambda_c, \lambda_A)$ cuboid defined by $p \in 10^{\{-4,2\}}$, $\lambda_{c/A} \in 10^{\{-4,4\}}$. As for the momentum grid for the spectral integration, we use the same cuboid for the real- and imaginary-time domain. We use 60 grid points in the momentum and 160 grid points in the spectral parameter integration, both with logarithmic grid spacing. For the realtime expressions, we divide into real and imaginary part of the integrands. Both real and imaginary parts of the discretised Minkowski as well as the Euclidean expressions are then interpolated by three-dimensional splines inside the cuboid. The resulting interpolating functions are then used in the spectral integration.

C.4.3. Convergence of iterative solution

The DSE is solved iteratively, as described in Section 5.1.2.5. It is initiated with a classical spectral function, $\rho_c^{(0)}(\omega) = \pi\,\delta(\omega^2)$. It converges rapidly, see Figure C.6.

C.4.4. Spectral fits

As discussed in Section 6.1.3, we provide a ready-to-use analytic fit formula for the ghost spectral function, see (5.47). For our best fit we use $N = 3$, the fit parameters for the ghost spectral functions for all input gluon propagators are listed in Table C.2. We show the spectral functions and their respective fits on a log-log scale in Figure C.7. For $G_A(0)\,[\mathrm{GeV}^{-2}] = 4.4$ and 1.9, the spectral functions feature a change of sign between 1.2 and 1.3 GeV. These wiggles are imprints of the oscillations in the input reconstructed

$\mathbf{G_A(0)}$	δ_{peak}	δ_1	δ_2	δ_3
(lat)	1.89930	10.7596	2.14185	2.15831
4.4	1.61917	3.91085	1.34667	1.88137
1.9	1.13871	20.5415	1.07826	19.8684
γ_c	$\hat{\Gamma}_{\text{peak}}$	$\hat{\Gamma}_1$	$\hat{\Gamma}_2$	$\hat{\Gamma}_3$
0.891763	0.221917	1.21044	0.408565	0.410932
0.916629	0.0435632	0.978503	0.245856	0.285878
0.794928	0.00641307	0.837894	0.151710	0.890227
Z_{UV}	$\hat{M}_{\text{peak}}$	$\hat{M}_1$	$\hat{M}_2$	$\hat{M}_3$
0.746555	0.374992	0.589509	1.59738	1.59758
0.933136	0.0146429	1.12309	1.26385	1.55235
0.859889	0.0134048	0.654315	1.26661	1.55657
$\hat{\rho}_0$	c_{peak}	c_1	c_2	c_3
18.4661	0.656878	231.204	-1.1422	1.13776
3235.78	1.90835	1.02717	-0.0321321	0.00133668
417864	37.4574	0.00294505	-0.0113776	0.00148406
ν_{UV}	ν_{IR}	ν_1	ν_2	
13.5935	-9.99927	16.953	-28.7442	
9.49617	-49.8529	80.9258	-13.3501	
19.5468	-195.657	7800.45	- 6.45	
$\hat{\Lambda}_{\text{UV}}$	$\hat{\Lambda}_{\text{IR}}$	$\hat{\Lambda}_1$	$\hat{\Lambda}_2$	
1.92012	0.374992	0.0998299	0.759367	
2.18064	0.0775041	0.0721607	0.762104	
0.967466	0.0816488	-0.0648268	0	

Tabelle C.2.: Best fit parameters for the ansatz (5.47) of the spectral functions for the different solutions. As indicated in the top right cell, in each cell the first line contains the fit parameter of the ghost spectral function corresponding to the lattice-like input gluon propagator $G_A^{(\text{lat})}$, the second to $G_A(0) = 4.4\,\text{GeV}^{-2}$ and the last line to the scaling-like $G_A(0) = 1.9\,\text{GeV}^{-2}$.

gluon spectral function of [243], and can be understood as numerical artefacts from the reconstruction process. However, in order to match the original Euclidean dressing function $1/Z_c(p)$ in the UV (comp. Figure 5.13), it is necessary to keep the respective oscillatory behaviour in the fit.

C.5. Spectral reconstruction of ghost and gluon

In this section, we comment on certain points of the numerical implementation of Section 5.3 in more detail. We first address numerical aspects of the optimisation and a discussion of the required computational effort. Subsequently, we provide further information about data usage, kernel design choices and theoretical constraints for the particular reconstructions reported in Section 5.3.

C.5.1. Hyperparameter optimisation and computational cost

To find optimal values for the kernel's hyperparameters, we perform a fine-grained grid scan of the NLL with additional hyperpriors where necessary. Alternatively, the NLL may also be minimized with a gradient-based ansatz using a standard optimizer such as L-BFGS. However, mapping out the posterior distribution in more detail tends to be highly instructive for the problem at hand. It is also less prone to numerical problems such as unstable directions and violation of positive definiteness of the covariance, as these can be identified early on, and should hence be preferred when feasible. This is also where the bulk of the computational effort goes, as it involves calculating for each individual grid point the comparably expensive inverse and determinant of the covariance matrix, which naively scales like $\mathcal{O}(N^3)$. For very large datasets where their direct evaluation becomes infeasible, one may resort to cheaper linear solvers for the inverse and stochastic approximations of the determinant, but this is unlikely to become necessary in this particular context. Cost may also be mitigated by scanning the parameter space hierarchically, starting at low resolution and zooming into the interesting regions.

The whole procedure is trivially parallelisable, as each grid point can be treated independently. At the scale of the present work, each instance was handled by a standard CPU node with low performance requirements. Some first tests were also conducted on a single machine, where mapping out the parameter space for each reconstruction with medium resolution took a few hours at most. In comparison to finding the optimal hyperparameters, the subsequent inference step is negligibly cheap. Of course, the total computational effort for the reconstruction is dwarfed by the requirements of the large-scale lattice simulations described in Appendix A.10.1, which are orders of magnitude more expensive.

C.5.2. Reconstruction Details

C.5.2.0.1. Ghost In the case of the ghost spectral function, we treat the low-frequency asymptotics extracted from the direct DSE computation in Yang-Mills theory as an additional observation for the GP. This is only possible for the ghost, as a similarly direct determination of the Yang-Mills gluon spectral function is currently not available. The procedure is implemented by including the value of ρ at $\omega = 0$ in the construction of the joint distribution of observations and predictions. In particular, one needs to compute additional expressions for the covariances of the point $\rho(0)$ and the correlator data. This requires some programming headache, but carries no further conceptual difficulty.

As stated in the main text, we use the standard RBF kernel and identify optimal hyperparameters via a high-resolution grid scan. We note an unstable direction in the magnitude parameter σ_C, which is cured by subjecting it to a zero-mean Gaussian hyperprior. As an

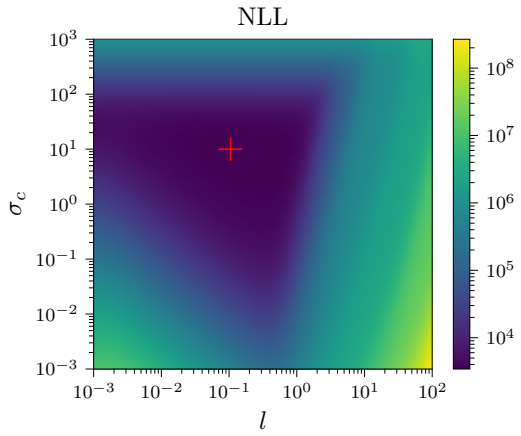

Abbildung C.8.: Heatmap of the NLL as a function of the RBF kernel hyperparameters σ_C, l for the reconstruction of the ghost spectral function, with an additional zero-mean Gaussian hyperprior for σ_C. A unique minimum can be identified, which provides the optimal values used for the results shown in the left panels of Figure 5.16 and 5.17.

illustrative example, the heatmap for the NLL including this additional regularization term for σ_C is shown in Figure C.8.

C.5.2.0.2. Gluon In the case of the gluon spectral function, no realtime result in Yang-Mills theory is available to fix the asymptotics. However, as an additional theoretical constraint we require the solution to respect the aforementioned OZS condition defined in (5.49). While one might expect this to further complicate the reconstruction, it actually helps in narrowing down the space of plausible solutions. The condition can simply be enforced approximately by treating it as an additional indirect observation and checking it a posteriori. The associated transformation is here just the convolution with ω instead of the KL integral. We confirm that the OZS condition is fulfilled with a relative accuracy of $\sim$1%, computed by evaluating the ratio of the left-hand side of (5.49) and the same expression using the modulus of the integrand, i.e. $\int_0^\infty \mathrm{d}\omega\, |\omega\rho_A(\omega)|$.

As mentioned in the main text, we find it helpful to modify the standard RBF kernel by non-linearly rescaling the frequency as $\omega \to \tilde{\omega} = \omega^4(1+\omega^4)^{-1}$ before computing the squared distance. This leads to a strongly improved asymptotic stability of the reconstructed spectral function, in particular at large frequencies, compared to just using ω itself. The procedure may be interpreted either as a non-stationary modification of the kernel or as a preprocessing step for the data to the same effect.

C.6. Quark

This section elaborates on the numerical procedure of Section 5.4.

C.6.1. Iterative procedure

The spectral DSE is solved using a power iteration. The RHS of the DSE (5.64) is evaluated for a given quark spectral function $\rho_q^{(i)}$, where the superscript $^{(i)}$ now relates to the iteration number and not the component of the quark spectral function. We then calculate the spectral function of the next iteration $\rho_q^{(i+1)}$ via (5.60). This procedure is iterated until convergence of the pole position as well as the spectral tail by eyesight is reached. The iteration is initialised with quark spectral function corresponding to the classical propagator. In terms of vector and scalar component, they read

$$\rho^{(d/s)}(\omega) = \frac{\pi}{2}\delta(\omega - m)\,. \tag{C.9}$$

Note that we omitted the $\omega < 0$ contributions in (C.9). They can be obtained via the symmetry relations (5.58).

C.6.2. Analytic structure during iterative solution

In this work, we solve the DSE iteratively via a power method, as described in Appendix C.6.1. There arises a subtlety when solving the DSE this way while employing the resonance-scattering split (A.78). Although the solution must exhibit a branch point singularity, this property usually does not hold while solving the equation. Staring from an initial guess for the spectral function with pole position ω_0, the pole positions ω_i of subsequent iterations moves to the right, i.e., $\omega_i > \omega_0$. Thus, ω_i will always lie within the support of the mass functions imaginary part, such that instead of a branch point singularity, a very sharp peak appears. Once converged however, the pole position is no longer moving and directly lies on the branch point, and the branch point singularity appears. Technically, this property could be enforced by renormalisation during the iterations, i.e., we could use on-shell renormalisation to fix the pole position to always lie on the branch point. Since, while keeping the coupling constant fixed, this would modify the scales of our system which are already fixed by the gluon propagator input, we refrain from doing so.

C.6.3. Determination of residues

Formally, the residues of the delta pole contributions in the resonance-scattering split (5.63) are related to the quark propagator by (A.79). It turned out to be numerically more stable to determine them by a fit to the Euclidean propagator data instead. For that, a momentum scale p_{fit} needs to be chosen. For the residue of the scalar part, we chose $p_{\text{fit}} = \mu = 30$ GeV. This ensured that also the propagator obtained from the spectral representation respects the renormalisation condition for the mass function. This is in fact important for numerical stability. The mass function becomes very small in the UV. A lack of numerical precision can violate positivity of the Euclidean mass function (obtained through the spectral representation) in the UV. These negative parts introduce unstable directions in the iteration which must be avoided in order to avoid a solution.

For the vector part, we specified $p_{\text{fit}} = 1$ GeV.

C.6.4. Spectral integration domain

In the resonance-scattering split (5.63), an onset for scattering tail needs to be chosen such that the spectral representation is well satisfied. This needs to be done such that the pole contribution has decayed sufficiently without neglecting relevant scattering contributions. The onset scale is chosen such that the resonance-scattering split is reproduces the Euclidean propagator as good as possible, see Appendix A.11.1. We use $\omega_{\text{onset}} = m_{\text{pole}} + 0.1$ GeV, where m_{pole} is the pole position of the respective resonance contribution.

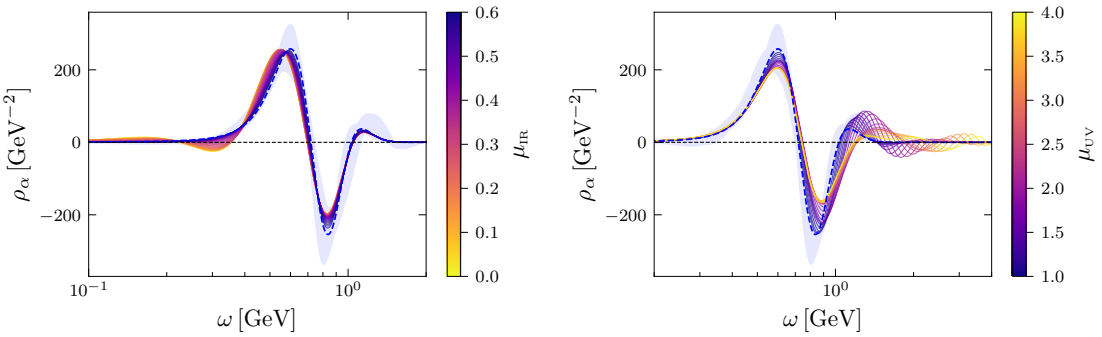

Abbildung C.9.: Behaviour of the spectral function when varying the midpoints $\mu_{\mathrm{IR/UV}}$ of the transition kernels to the asymptotic IR (left) and UV regimes (right). The respective values of the parameters are colour-coded. The resulting scan of the spectral functions is compared to the final result with maximally enhanced asymptotics, displayed with a dashed blue line. The error band obtained by varying the parameters of the asymptotics—as indicated in Figure C.10—is given by the shaded blue area.

C.7. Non-perturbative timelike strong coupling constant

In this section, we comment on certain points of the numerical implementation of Section 6.1 in more detail. We start with a brief recap of the GPR basics, followed by a discussion of the incorporation of asymptotic information and details on the hyperparameter optimisation.

C.7.1. GPR basics

Here, we briefly summarise the main aspects of the GPR reconstruction procedure. For a more detailed overview, we refer to earlier works [3, 384] as well as Appendix A.9.

We assume our knowledge of the spectral function $\rho(\omega)$ before making observations of the correlator to be described by a GP prior, written as

$$\rho(\omega) \sim \mathcal{GP}(\mu(\omega), C(\omega,\omega))\,, \tag{C.10}$$

where μ, C denote the mean and covariance. The conditional posterior distribution for $\rho(\omega)$ given observations of the propagator G_i at N_G discrete Euclidean frequencies $p_i \equiv [\boldsymbol{p}]_i$ can be derived in closed form,

$$\begin{aligned}\rho(\omega)|G(\boldsymbol{p}) \sim \mathcal{GP}\Big(&\boldsymbol{w}^T(\omega)(\boldsymbol{W}+\sigma_n^2\mathbb{1})^{-1}G(\boldsymbol{p}),\\ &k(\omega,\omega)-\boldsymbol{w}^T(\omega)(\boldsymbol{W}+\sigma_n^2\mathbb{1})^{-1}\boldsymbol{w}(\omega)\Big)\,,\end{aligned} \tag{C.11}$$

where

$$\begin{aligned}[\boldsymbol{w}]_i(\omega) &= \int \mathrm{d}\omega'\, K(p_i,\omega')C(\omega',\omega)\,,\\ [\boldsymbol{W}]_{ij} &= \int \mathrm{d}\omega'\mathrm{d}\omega''\, K(p_i,\omega')K(p_j,\omega'')C(\omega',\omega'')\,.\end{aligned} \tag{C.12}$$

This is essentially equivalent to a standard result in probability theory for the closed-form expression of a conditional multivariate normal distribution, but defined with a continuum of random variables due to being a Gaussian *process*, as well as additional applications of the integral transformation one seeks to invert. The equivalence becomes more concrete in practice when the GP is evaluated for a finite set of predictions; however, the choice of inference points ω is arbitrary within the given domain. In the above expressions, $\mu(\omega)$ has been set to zero since a GP can be fully specified by its second-order statistics and the prior mean can be absorbed into C. The GP in (C.12) encodes our knowledge of the spectral function after making observations of the correlator and accounting for observational noise with variance σ_n^2.

The covariance $C(\omega, \omega')$ is commonly defined via a so-called kernel function with few hyperparameters, which may be subject to optimisation based on the associated likelihood. A widely used parametrisation is the radial basis function (RBF) kernel, defined in (5.53).

C.7.2. Incorporating asymptotic information

With the knowledge of the IR and UV asymptotics, cf. Appendix A.13, an appropriate bias can be introduced. It is chosen such that the kernel is restricted to the specified functional basis as described in Section 6.1.2, while retaining the flexibility of the RBF kernel C_{RBF}, see (5.53), in the central region.

In order to achieve a smooth transition between the biased and unbiased kernels, we employ smooth step functions of the form

$$\theta^{\pm}(\omega; \mu, \ell) = \frac{1}{1 + \exp(\pm 2(\omega - \mu)/\ell)} \,. \tag{C.13}$$

The full kernel can then be written simply as a sum of the individual contributions,

$$k(\omega, \omega') = k_{\mathrm{RBF}}(\omega, \omega') + k_{\mathrm{IR}}(\omega, \omega') + k_{\mathrm{UV}}(\omega, \omega') \,, \tag{C.14}$$

where

$$\begin{aligned}
k_{\mathrm{RBF}}(\omega, \omega') &= \theta^{+}_{\mathrm{IR}}(\omega)\, \theta^{+}_{\mathrm{IR}}(\omega')\, \theta^{-}_{\mathrm{UV}}(\omega)\, \theta^{-}_{\mathrm{UV}}(\omega')\, C_{\mathrm{RBF}}(\omega, \omega') \\
k_{\mathrm{IR}}(\omega, \omega') &= \theta^{-}_{\mathrm{IR}}(\omega)\, \theta^{-}_{\mathrm{IR}}(\omega')\, \rho_{\mathrm{IR}}(\omega)\, \rho_{\mathrm{IR}}(\omega') \\
k_{\mathrm{UV}}(\omega, \omega') &= \theta^{+}_{\mathrm{UV}}(\omega)\, \theta^{+}_{\mathrm{UV}}(\omega')\, \rho_{\mathrm{UV}}(\omega)\, \rho_{\mathrm{UV}}(\omega') \,.
\end{aligned}$$

The midpoints of the transition functions $\theta_{\mathrm{IR/UV}}$ are specified by $\mu_{\mathrm{IR/UV}}$ and their steepness is controlled by $\ell_{\mathrm{IR/UV}}$.

C.7.3. GP kernel hyperparameters

Since the hyperparameters of the GP kernel control the behaviour of the resulting spectral function, their choice is a pivotal step in the reconstruction. They are commonly determined via numerical optimisation by minimising (conventionally) the negative log-likelihood (NLL),

$$\begin{aligned}
-\log p(\hat{\boldsymbol{\rho}}|\boldsymbol{\sigma}) = \frac{1}{2} \hat{\boldsymbol{\rho}}^T \left(\boldsymbol{W}_{\boldsymbol{\sigma}} + \sigma_n^2 1 \right)^{-1} \hat{\boldsymbol{\rho}} + \\
\frac{1}{2} \log\det(\boldsymbol{W}_{\boldsymbol{\sigma}} + \sigma_n^2 1) + \frac{N}{2} \log 2\pi \,,
\end{aligned} \tag{C.15}$$

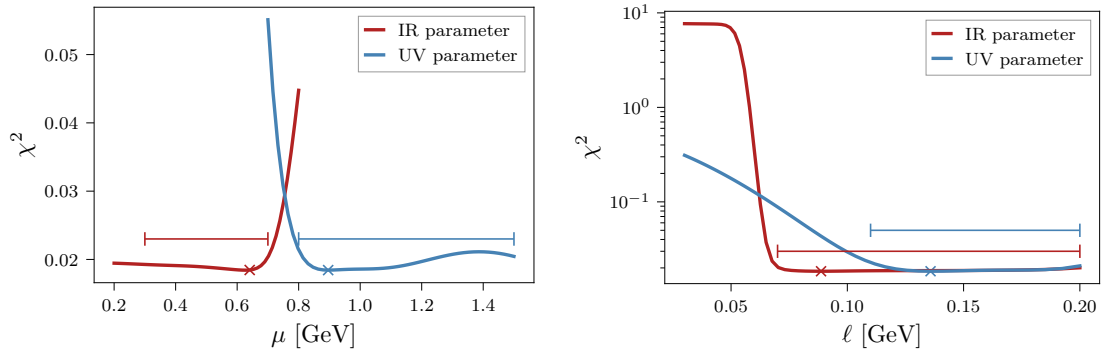

Abbildung C.10.: Scans of the bias parameters defined in (C.14). We compare the quality of the dressing reconstruction—quantified by χ^2—when varying the midpoint positions of the bias transition $\mu_{\mathrm{IR/UV}}$ (left) as well as its steepness $\ell_{\mathrm{IR/UV}}$ (right). The values of the bias parameters chosen for the reconstruction are marked by crosses. This choice maximises the size of the regions dominated by the coupling infrared and ultraviolet asymptotics while producing small χ^2 reconstructions of the data. Additionally, the parameters are then scanned in the flat directions, indicated by the horizontal bars, in order to obtain the error estimation for the reconstruction results shown in Figure 6.2.

where the dependence on the kernel hyperparameters $\boldsymbol{\sigma}$ is emphasised by an index.

The number of hyperparameters increases significantly when including the bias term that enforces the correct asymptotics (C.14). Hence, the two parameters of the bare RBF kernel are chosen first by minimising (C.15). The asymptotics are then introduced in the far IR/UV and shifted towards the centre, all while monitoring the quality of the interpolation of the dressing by computing χ^2 at each step. We compare χ^2 instead of the NLL for different bias parameters, since the second term in (C.15) constitutes a complexity penalty term. When considering an explicit functional basis, such a term is inherently in opposition to the constraint for the analytically known asymptotics and is therefore excluded. We observe that the bias kernel parameters have an open direction towards vanishing bias, e.g., for small μ_{IR} and large μ_{UV}. Spectral functions with $\mu_{\mathrm{UV}} > 1.5\,\mathrm{GeV}$ show a growing number of smaller oscillations in the UV which are a remnant of the global length scale introduced in the RBF kernel; see the right panel ofFigure C.9. Accordingly, models in this parameter region can be ruled out as sensible descriptions of the underlying physics of the coupling. For $\mu_{\mathrm{IR}} < 0.25\,\mathrm{GeV}$, the resulting spectral functions do not change significantly; see the left panel of Figure C.9. The change of χ^2 when varying the asymptotic kernel parameters is shown in Figure C.10, with the final settings used for the reconstruction indicated by crosses. These parameters are explicitly chosen to maximise the regions dominated by the asymptotics, without significantly increasing the error of the coupling reconstruction. All final parameters of the GP model used to compute the results reported in this work are listed in Table C.3.

The error estimation for the spectral function via the covariance of the posterior distribution does not include the systematic error that arises from the choice of the model, in particular regarding different values of the hyperparameters. However, we observe that

Parameter	σ_{RBF}	l_{RBF}	μ_{UV}	ℓ_{UV}	μ_{IR}	ℓ_{IR}
Value	67.399	0.074	0.890	0.137	0.637	0.090

Tabelle C.3.: Hyperparameters for the combined RBF and fixed-asymptotics kernel, as defined in (C.14) and (5.53).

enforcing the maximally large asymptotic regimes leads to the predicted posterior covariance being comparatively small as the model is now highly restricted; see the right panel of Figure 6.3. Hence, the error is estimated by varying the bias parameters in a region where χ^2 is small, but the effect of different parameter choices is non-negligible, while unphysical oscillations remain largely suppressed. This region is marked in Figure C.10 by horizontal bars. When considering μ_{UV} larger than indicated in this region, a substantial amount of oscillations is introduced in the spectral function as mentioned above. For μ_{IR} smaller than indicated in the left panel of Figure C.10, the spectral function vanishes in the IR. However, it can then differ from the expected ω^2 behaviour. The largest variations in the resulting spectral functions under these changes of the hyperparameters are then used as error estimates for the reconstruction results shown in Figure 6.2. Since the deviations of the predictions at the edges of the parameter space tend to be maximised in particular regions for certain parameter combinations, e.g., when μ_{UV} and ℓ_{UV} are both small, the error band shows a few distinct kinks.

C.8. Hadronic vacuum polarisation & g–2

In this section we give numerical details on the implementation of Section 6.3.

C.8.1. Quark-photon vertex & HVP

We solve the quark-photon vertex BSE (6.48) via a power method, i.e., substituting the result of the RHS back into RHS until convergence is reached. While this technique is numerically efficient, it becomes unstable close to resonances due to its iterative nature. Alternatively, matrix inversion could be employed, which is much more costly, however.

The internal momentum integrals are computed via Gauss Legendre quadrature in each integration variable. For that, we parametrise the integrals as

$$\int_q = \int \frac{d^4q}{(2\pi)^4} = \frac{1}{(2\pi)^4}\frac{1}{2}\int_{\Lambda^2_{\mathrm{IR}}} \Lambda^2_{\mathrm{UV}} dq q^2 \int_{-1}^{1} dz\sqrt{1-z2}\int_{-1}^{1} dy \int_0^{2\pi} d\phi\,, \tag{C.16}$$

where the infrared and ultraviolet momentum cutoffs the system are chosen as $\Lambda_I R = 10^-3$ GeV, $\Lambda_{UV} = 10^{-3}$ GeV. The ϕ integral can simply be performed right away since no integrand depends on it.

For the y and z integrals, we use 16 grid points each. For the q^2 integral we employ a logarithmic grid with 128 grid points in order to resolve the peaked structure of the integrand and in particular the Maris-Tandy coupling (6.46) properly.

The momentum integral of the HVP (6.39) is treated as the internal ones of the quark-photon vertex, as described above.

C.8.2. Quark DSE

The quark DSE for the quark-photon vertex Section 6.3.3.1 is solved via Gauss Legendre quadrature as well with the parametrisation (C.16) with 512 grid point for the logarithmic k^2-grid and 32 grid point for the z-grid. Here, both ϕ and y can be integrated out beforehand. The DSE is solved via a power method as, as is the BSE. We employ the same values for the momentum cutoffs for the DSE as for the BSE described in Appendix C.8.1.

For timelike and complex external momenta Q, the quark propagator is needed at complex external momenta, cf. (6.48). The range of these momenta can be deduced from the combination of external momentum Q of the QPV BSE and the parametrisation of the internal momentum integrals, as discussed in Appendix C.8.1.

Danksagung

Mein großer Dank gilt meinem Doktorvater Jan M. Pawlowski für seine hervorragende Betreuung und freundschaftliche Zusammenarbeit. Die unzähligen Diskussionen, in denen er mir Physik vermittelt hat, waren ein prägendes Element meiner Promotion, von dem ich sowohl wissenschaftlich als auch persönlich stark profitiert habe.

Manfred Salmhofer danke ich für seine Bereitschaft, das Zweitgutachten für diese Doktorarbeit zu verfassen.

Großen Dank möchte ich auch gegenüber Nicolas Wink ausdrücken, der mich als Freund und Mentor stets begleitet hat. Ich habe es als Privileg wahrgenommen, in zahlreichenz Kollaborationen und Diskussionen von seinen Ideen zu profitieren. Auch für das Korrekturlesen dieser Arbeit möchte ich mich bei ihm bedanken.

Besonderer Dank gilt auch allen meinen Co-Autoren für die produktive Zusammenarbeit, aus der große Teile dieser Arbeit hervorgegangen sind.

Bei Gernot Eichman möchte ich mich für seine Gastfreundschaft während meines Besuchs in Lissabon bedanken und dafür, dass er das daraus resultierende Kapitel dieser Doktorarbeit korrekturgelesen hat.

Zu großem Dank bin ich auch meinen Kollegen am Institut für Theoretische Physik verpflichtet. Die anregende und zugleich familiäre Atmosphäre am Institut habe ich stets als besonders empfunden. Besonders hervorgehoben seien meine Bürokollegen Coralie Schneider, Friederike Ihssen und Jonas Wessely, die hierzu besonders beigetragen haben. Letzteren beiden gilt auch Dank für das Korrekturlesen dieser Arbeit.

Speziellen Dank möchte ich auch gegenüber meinem Physiklehrer Herrn Wolf ausdrücken, welcher in mir die Begeisterung für die Physik geweckt hat.

Auch meinen Studienkollegen, welche mich während meiner Zeit in Heidelberg begleitet haben, möchte ich danken. Meine Erinnerungen an die Studienzeit werden für immer untrennbar mit ihrer Kameradschaft verbunden sein.

Meiner Freundin Greta möchte ich für ihre emotionale Unterstützung insbesondere in der finalen Phase meiner Promotion danken.

Meine Eltern waren für mich eine währende Stütze und haben es mir stets ermöglich, meinen Interessen nachzugehen. Ihnen bin ich zu tiefem Dank verpflichtet.

Literaturverzeichnis

[1] J. Horak, J. M. Pawlowski, and N. Wink, "Spectral functions in the ϕ^4-theory from the spectral DSE," Phys. Rev. D 102, 125016 (2020), arXiv:2006.09778 [hep-th].

[2] J. Horak, J. Papavassiliou, J. M. Pawlowski, and N. Wink, "Ghost spectral function from the spectral Dyson-Schwinger equation," (2021), arXiv:2103.16175 [hep-th].

[3] J. Horak, J. M. Pawlowski, J. Rodríguez-Quintero, J. Turnwald, J. M. Urban, N. Wink, and S. Zafeiropoulos, "Reconstructing QCD Spectral Functions with Gaussian Processes," (2021), arXiv:2107.13464 [hep-ph].

[4] J. Horak, F. Ihssen, J. Papavassiliou, J. M. Pawlowski, A. Weber, and C. Wetterich, "Gluon condensates and effective gluon mass," SciPost Phys. 13, 042 (2022), arXiv:2201.09747 [hep-ph].

[5] J. Horak, J. M. Pawlowski, and N. Wink, "On the complex structure of Yang-Mills theory," (2022), arXiv:2202.09333 [hep-th].

[6] J. Braun *et al.*, "Renormalised spectral flows," (2022), arXiv:2206.10232 [hep-th].

[7] J. Horak, J. M. Pawlowski, and N. Wink, "On the quark spectral function in QCD," (2022), arXiv:2210.07597 [hep-ph].

[8] J. Horak, J. M. Pawlowski, J. Turnwald, J. M. Urban, N. Wink, and S. Zafeiropoulos, "Non-perturbative strong coupling at timelike momenta," (2023), arXiv:2301.07785 [hep-ph].

[9] J. Horak, F. Ihssen, J. M. Pawlowski, J. Wessely, and N. Wink, "Scalar spectral flows in (2+1) dimensions," (2022).

[10] "Scalar bound states from the spectral BSE," (2023).

[11] xxx, "Shear viscosity and spectral function in Yang-Mills theory," (2021), arXiv:2104.13413 [hep-th].

[12] J. Braun, Y.-r. Chen, W.-j. Fu, F. Ihssen, J. Horak, C. Huang, J. M. Pawlowski, F. Rennecke, F. Sattler, B. Schallmo, C. Schneider, Y.-y. Tan, S. Töpfel, R. Wen, N. Wink, and S. Yin, (2021).

[13] A. Jaffe and E. Witten, "Quantum yang-mills theory," The millennium prize problems 1 (2006).

[14] Relativistic Heavy Ion Collider (RHIC), https://www.bnl.gov/rhic/.

[15] Large Hadron Collider (LHC), https://home.cern/.

[16] Facility for Antiproton and Ion Research (FAIR), http://www.fair-center.eu/.

[17] Nuclotron-based Ion Collider Facility (NICA), http://nica.jinr.ru/.

[18] M. Stephanov, "QCD phase diagram: An Overview," PoS LAT2006, 024 (2006), arXiv:hep-lat/0701002 [hep-lat].

[19] J. O. Andersen, W. R. Naylor, and A. Tranberg, "Phase diagram of QCD in a magnetic field: A review," Rev. Mod. Phys. 88, 025001 (2016), arXiv:1411.7176 [hep-ph].

[20] A. Andronic, P. Braun-Munzinger, K. Redlich, and J. Stachel, "Decoding the phase structure of QCD via particle production at high energy," Nature 561, 321 (2018), arXiv:1710.09425 [nucl-th].

[21] X. Luo and N. Xu, "Search for the QCD Critical Point with Fluctuations of Conserved Quantities in Relativistic Heavy-Ion Collisions at RHIC : An Overview," Nucl. Sci. Tech. 28, 112 (2017), arXiv:1701.02105 [nucl-ex].

[22] L. Adamczyk *et al.* (STAR), "Bulk Properties of the Medium Produced in Relativistic Heavy-Ion Collisions from the Beam Energy Scan Program," Phys. Rev. C 96, 044904 (2017), arXiv:1701.07065 [nucl-ex].

[23] R. A. Briceno, J. J. Dudek, and R. D. Young, "Scattering processes and resonances from lattice QCD," Rev. Mod. Phys. 90, 025001 (2018), arXiv:1706.06223 [hep-lat].

[24] M. Mai and M. Doring, "Finite-Volume Spectrum of $\pi^+\pi^+$ and $\pi^+\pi^+\pi^+$ Systems," Phys. Rev. Lett. 122, 062503 (2019), arXiv:1807.04746 [hep-lat].

[25] B. Hörz and A. Hanlon, "Two- and three-pion finite-volume spectra at maximal isospin from lattice QCD," Phys. Rev. Lett. 123, 142002 (2019), arXiv:1905.04277 [hep-lat].

[26] M. T. Hansen, R. A. Briceño, R. G. Edwards, C. E. Thomas, and D. J. Wilson (Hadron Spectrum), "Energy-Dependent $\pi^+\pi^+\pi^+$ Scattering Amplitude from QCD," Phys. Rev. Lett. 126, 012001 (2021), arXiv:2009.04931 [hep-lat].

[27] M. Fischer, B. Kostrzewa, L. Liu, F. Romero-López, M. Ueding, and C. Urbach, "Scattering of two and three physical pions at maximal isospin from lattice QCD," Eur. Phys. J. C 81, 436 (2021), arXiv:2008.03035 [hep-lat].

[28] Y. Aoki, G. Endrodi, Z. Fodor, S. Katz, and K. Szabo, "The Order of the quantum chromodynamics transition predicted by the standard model of particle physics," Nature 443, 675 (2006), arXiv:hep-lat/0611014 [hep-lat].

[29] S. Borsanyi, Z. Fodor, C. Hoelbling, S. D. Katz, S. Krieg, C. Ratti, and K. K. Szabo (Wuppertal-Budapest), "Is there still any T_c mystery in lattice QCD? Results with physical masses in the continuum limit III," JHEP 09, 073 (2010), arXiv:1005.3508 [hep-lat].

[30] S. Borsanyi *et al.*, "Calculation of the axion mass based on high-temperature lattice quantum chromodynamics," Nature 539, 69 (2016), arXiv:1606.07494 [hep-lat].

[31] A. Bazavov *et al.*, "The QCD Equation of State to $\mathcal{O}(\mu_B^6)$ from Lattice QCD," Phys. Rev. D 95, 054504 (2017), arXiv:1701.04325 [hep-lat].

[32] C. Gattringer and C. B. Lang, *Quantum chromodynamics on the lattice* (Lect. Notes Phys., 2010) p. 211.

[33] Z. Fodor and C. Hoelbling, "Light Hadron Masses from Lattice QCD," Rev.Mod.Phys. 84, 449 (2012), arXiv:1203.4789 [hep-lat].

[34] S. Aoki *et al.*, "Review of lattice results concerning low-energy particle physics," Eur. Phys. J. C77, 112 (2017), arXiv:1607.00299 [hep-lat].

[35] M. Troyer and U.-J. Wiese, "Computational complexity and fundamental limitations to fermionic quantum Monte Carlo simulations," Phys. Rev. Lett. 94, 170201 (2005), arXiv:cond-mat/0408370 [cond-mat].

[36] P. de Forcrand, "Simulating QCD at finite density," *Proceedings, 27th International Symposium on Lattice field theory (Lattice 2009): Beijing, P.R. China, July 26-31, 2009*, PoS LAT2009, 010 (2009), arXiv:1005.0539 [hep-lat].

[37] C. S. Fischer, "QCD at finite temperature and chemical potential from Dyson–Schwinger equations," Prog. Part. Nucl. Phys. 105, 1 (2019), arXiv:1810.12938 [hep-ph].

[38] W.-j. Fu, J. M. Pawlowski, and F. Rennecke, "QCD phase structure at finite temperature and density," Phys. Rev. D 101, 054032 (2020), arXiv:1909.02991 [hep-ph].

[39] F. Gao and J. M. Pawlowski, "QCD phase structure from functional methods," Phys. Rev. D 102, 034027 (2020), arXiv:2002.07500 [hep-ph].

[40] S. Jia and M. R. Pennington, "Exact Solutions to the Fermion Propagator Schwinger-Dyson Equation in Minkowski space with on-shell Renormalization for Quenched QED," Phys. Rev. D96, 036021 (2017), arXiv:1705.04523 [nucl-th].

[41] V. Sauli, "The quark spectral functions and the Hadron Vacuum Polarization from application of DSEs in Minkowski space," Few Body Syst. 61, 23 (2020), arXiv:1809.07644 [hep-ph].

[42] V. Sauli, "Confinement within the use of Minkowski space integral representation," (2020), arXiv:2011.00536 [hep-lat].

[43] S. Floerchinger, "Analytic Continuation of Functional Renormalization Group Equations," JHEP 05, 021 (2012), arXiv:1112.4374 [hep-th].

[44] J. M. Pawlowski, N. Strodthoff, and N. Wink, "Finite temperature spectral functions in the O(N)-model," Phys. Rev. D98, 074008 (2018), arXiv:1711.07444 [hep-th].

[45] S. Huelsmann, S. Schlichting, and P. Scior, "Spectral functions from the real-time functional renormalization group," Phys. Rev. D 102, 096004 (2020), arXiv:2009.04194 [hep-ph].

[46] C. Jung, J.-H. Otto, R.-A. Tripolt, and L. von Smekal, "Self-consistent O(4) model spectral functions from analytically continued functional renormalization group flows," Phys. Rev. D 104, 094011 (2021), arXiv:2107.10748 [hep-ph].

[47] J. V. Roth, D. Schweitzer, L. J. Sieke, and L. von Smekal, "Real-time methods for spectral functions," Phys. Rev. D 105, 116017 (2022), arXiv:2112.12568 [hep-ph].

[48] Y.-y. Tan, Y.-r. Chen, and W.-j. Fu, "Real-time dynamics of the $O(4)$ scalar theory within the fRG approach," SciPost Phys. 12, 026 (2022), arXiv:2107.06482 [hep-ph].

[49] C. Gutierrez, V. Gigante, T. Frederico, G. Salmè, M. Viviani, and L. Tomio, "Bethe–Salpeter bound-state structure in Minkowski space," Phys. Lett. B 759, 131 (2016), arXiv:1605.08837 [hep-ph].

[50] V. A. Karmanov, J. Carbonell, and T. Frederico, "Equation for the Nakanishi weight function using the inverse Stieltjes transform," Few Body Syst. 59, 27 (2018), arXiv:1802.05515 [hep-ph].

[51] G. Kallen, "On the definition of the Renormalization Constants in Quantum Electrodynamics," Helv. Phys. Acta 25, 417 (1952).

[52] H. Lehmann, "On the Properties of propagation functions and renormalization contants of quantized fields," Nuovo Cim. 11, 342 (1954).

[53] C. D. Roberts and A. G. Williams, "Dyson-Schwinger equations and their application to hadronic physics," Prog.Part.Nucl.Phys. 33, 477 (1994), arXiv:hep-ph/9403224 [hep-ph].

[54] R. Alkofer and L. von Smekal, "The Infrared behavior of QCD Green's functions: Confinement dynamical symmetry breaking, and hadrons as relativistic bound states," Phys. Rept. 353, 281 (2001), arXiv:hep-ph/0007355.

[55] P. Maris and C. D. Roberts, "Dyson-Schwinger equations: A Tool for hadron physics," Int.J.Mod.Phys. E12, 297 (2003), arXiv:nucl-th/0301049 [nucl-th].

[56] C. S. Fischer, "Infrared properties of QCD from Dyson-Schwinger equations," J.Phys.G G32, R253 (2006), arXiv:hep-ph/0605173 [hep-ph].

[57] J. Polonyi, "Lectures on the functional renormalization group method," Central Eur.J.Phys. 1, 1 (2003), arXiv:hep-th/0110026 [hep-th].

[58] J. M. Pawlowski, "Aspects of the functional renormalisation group," Annals Phys. 322, 2831 (2007), arXiv:hep-th/0512261 [hep-th].

[59] H. Gies, "Introduction to the functional RG and applications to gauge theories," Lect. Notes Phys. 852, 287 (2012), arXiv:hep-ph/0611146.

[60] B. Delamotte, "An Introduction to the nonperturbative renormalization group," Lect. Notes Phys. 852, 49 (2012), arXiv:cond-mat/0702365 [cond-mat.stat-mech].

[61] O. J. Rosten, "Fundamentals of the Exact Renormalization Group," Phys. Rept. 511, 177 (2012), arXiv:1003.1366 [hep-th].

[62] J. Braun, "Fermion Interactions and Universal Behavior in Strongly Interacting Theories," J. Phys. G 39, 033001 (2012), arXiv:1108.4449 [hep-ph].

[63] N. Dupuis, L. Canet, A. Eichhorn, W. Metzner, J. M. Pawlowski, M. Tissier, and N. Wschebor, "The nonperturbative functional renormalization group and its applications," Phys. Rept. 910, 1 (2021), arXiv:2006.04853 [cond-mat.stat-mech].

[64] W.-j. Fu, "QCD at finite temperature and density within the fRG approach: an overview," Commun. Theor. Phys. 74, 097304 (2022), arXiv:2205.00468 [hep-ph].

[65] S. Weinberg, *The Quantum theory of fields. Vol. 1: Foundations* (Cambridge University Press, Cambridge, 1995) cambridge, UK: Univ. Pr. (1995) 609 p.

[66] S. Weinberg, *The quantum theory of fields. Vol. 2: Modern applications* (Cambridge University Press, Cambridge, 1996) cambridge, UK: Univ. Pr. (1996) 489 p.

[67] R. Haag, *Local quantum physics: Fields, particles, algebras* (Springer, Berlin, 1992) p. 356, berlin, Germany: Springer (1992) 356 p. (Texts and monographs in physics).

[68] M. E. Peskin and D. V. Schroeder, *An Introduction to quantum field theory* (Addison-Wesley, Reading, 1995) p. 842.

[69] J. Zinn-Justin, *Quantum field theory and critical phenomena* (Int. Ser. Monogr. Phys., 2002) p. 1054.

[70] J. S. Schwinger, "On the Green's functions of quantized fields. 1." Proc. Nat. Acad. Sci. 37, 452 (1951).

[71] J. S. Schwinger, "On the Green's functions of quantized fields. 2." Proc. Nat. Acad. Sci. 37, 455 (1951).

[72] F. J. Dyson, "The S matrix in quantum electrodynamics," Phys. Rev. 75, 1736 (1949).

[73] L. P. Kadanoff, "Scaling laws for Ising models near T(c)," Physics Physique Fizika 2, 263 (1966).

[74] K. G. Wilson, "Renormalization group and critical phenomena. 1. Renormalization group and the Kadanoff scaling picture," Phys.Rev. B4, 3174 (1971).

[75] K. G. Wilson, "Renormalization group and critical phenomena. 2. Phase space cell analysis of critical behavior," Phys.Rev. B4, 3184 (1971).

[76] C. Wetterich, "Exact evolution equation for the effective potential," Phys.Lett. B301, 90 (1993).

[77] J. Polchinski, "Renormalization and Effective Lagrangians," Nucl. Phys. B 231, 269 (1984).

[78] M. Bonini, M. D'Attanasio, and G. Marchesini, "Perturbative renormalization and infrared finiteness in the Wilson renormalization group: The Massless scalar case," Nucl. Phys. B 409, 441 (1993), arXiv:hep-th/9301114.

[79] U. Ellwanger, "FLow equations for N point functions and bound states," Z. Phys. C 62, 503 (1994), arXiv:hep-ph/9308260.

[80] T. R. Morris, "The Exact renormalization group and approximate solutions," Int. J. Mod. Phys. A9, 2411 (1994), arXiv:hep-ph/9308265.

[81] J. M. Pawlowski, J. A. Bonnet, S. Rechenberger, and N. Wink, "The functional renormalization group & applications to gauge theories and gravity," available on request.

[82] C.-N. Yang and R. L. Mills, "Conservation of Isotopic Spin and Isotopic Gauge Invariance," Phys.Rev. 96, 191 (1954), yang-Mills.

[83] C. Itzykson and J. B. Zuber, *Quantum Field Theory*, International Series In Pure and Applied Physics (McGraw-Hill, New York, 1980).

[84] V. N. Gribov, "Quantization of Nonabelian Gauge Theories," Nucl. Phys. B 139, 1 (1978).

[85] A. Fuster, M. Henneaux, and A. Maas, "BRST quantization: A short review," Int. J. Geom. Meth. Mod. Phys. 2, 939 (2005), arXiv:hep-th/0506098.

[86] J. Greensite, "The confinement problem in lattice gauge theory," Prog. Part. Nucl. Phys. 51, 1 (2003), arXiv:hep-lat/0301023.

[87] D. Diakonov, "Topology and confinement," Nucl. Phys. B Proc. Suppl. 195, 5 (2009), arXiv:0906.2456 [hep-ph].

[88] T. Kugo and I. Ojima, "Local Covariant Operator Formalism of Nonabelian Gauge Theories and Quark Confinement Problem," Prog. Theor. Phys. Suppl. 66, 1 (1979).

[89] L. von Smekal, R. Alkofer, and A. Hauck, "The Infrared behavior of gluon and ghost propagators in Landau gauge QCD," Phys. Rev. Lett. 79, 3591 (1997), arXiv:hep-ph/9705242 [hep-ph].

[90] L. von Smekal, A. Hauck, and R. Alkofer, "A Solution to Coupled Dyson–Schwinger Equations for Gluons and Ghosts in Landau Gauge," Annals Phys. 267, 1 (1998), [Erratum: Annals Phys. 269, 182 (1998)], arXiv:hep-ph/9707327.

[91] D. Zwanziger, "Non-perturbative Landau gauge and infrared critical exponents in QCD," Phys. Rev. D65, 094039 (2002), arXiv:hep-th/0109224.

[92] C. Lerche and L. von Smekal, "On the infrared exponent for gluon and ghost propagation in Landau gauge QCD," Phys. Rev. D65, 125006 (2002), arXiv:hep-ph/0202194.

[93] M. Q. Huber, "Correlation functions of Landau gauge Yang-Mills theory," Phys. Rev. D 101, 114009 (2020), arXiv:2003.13703 [hep-ph].

[94] G. Eichmann, J. M. Pawlowski, and J. a. M. Silva, "Mass generation in Landau-gauge Yang-Mills theory," Phys. Rev. D 104, 114016 (2021), arXiv:2107.05352 [hep-ph].

[95] A. K. Cyrol, L. Fister, M. Mitter, J. M. Pawlowski, and N. Strodthoff, "Landau gauge Yang-Mills correlation functions," Phys. Rev. D 94, 054005 (2016), arXiv:1605.01856 [hep-ph].

[96] J. M. Pawlowski, C. S. Schneider, and N. Wink, "On Gauge Consistency In Gauge-Fixed Yang-Mills Theory," (2022), arXiv:2202.11123 [hep-th].

[97] A. Sternbeck, E. M. Ilgenfritz, M. Muller-Preussker, and A. Schiller, "Towards the infrared limit in SU(3) Landau gauge lattice gluodynamics," Phys. Rev. D 72, 014507 (2005), arXiv:hep-lat/0506007.

[98] A. Sternbeck, E. M. Ilgenfritz, M. Muller-Preussker, A. Schiller, and I. L. Bogolubsky, "Lattice study of the infrared behavior of QCD Green's functions in Landau gauge," PoS LAT2006, 076 (2006), arXiv:hep-lat/0610053.

[99] A. Sternbeck, *The infrared behavior of lattice QCD Green's functions*, Ph.D. thesis, Humboldt-University Berlin (2006), arXiv:hep-lat/0609016.

[100] S. Zafeiropoulos, P. Boucaud, F. De Soto, J. Rodríguez-Quintero, and J. Segovia, "Strong Running Coupling from the Gauge Sector of Domain Wall Lattice QCD with Physical Quark Masses," Phys. Rev. Lett. 122, 162002 (2019), arXiv:1902.08148 [hep-ph].

[101] Z.-F. Cui, J.-L. Zhang, D. Binosi, F. de Soto, C. Mezrag, J. Papavassiliou, C. D. Roberts, J. Rodríguez-Quintero, J. Segovia, and S. Zafeiropoulos, "Effective charge from lattice QCD," Chin. Phys. C 44, 083102 (2020), arXiv:1912.08232 [hep-ph].

[102] A. Maas, "Constraining the gauge-fixed Lagrangian in minimal Landau gauge," SciPost Phys. 8, 071 (2020), arXiv:1907.10435 [hep-lat].

[103] D. Dudal, J. Gracey, S. Sorella, N. Vandersickel, and H. Verschelde, "The Landau gauge gluon and ghost propagator in the refined Gribov-Zwanziger framework in 3 dimensions," Phys.Rev. D78, 125012 (2008), arXiv:0808.0893 [hep-th].

[104] D. Dudal, J. A. Gracey, S. P. Sorella, N. Vandersickel, and H. Verschelde, "A Refinement of the Gribov-Zwanziger approach in the Landau gauge: Infrared propagators in harmony with the lattice results," Phys.Rev. D78, 065047 (2008), arXiv:0806.4348 [hep-th].

[105] D. Zwanziger, "Local and Renormalizable Action From the Gribov Horizon," Nucl. Phys. B 323, 513 (1989).

[106] D. Zwanziger, "Fundamental modular region, Boltzmann factor and area law in lattice gauge theory," Nucl. Phys. B412, 657 (1994).

[107] C. S. Fischer, A. Maas, and J. M. Pawlowski, "On the infrared behavior of Landau gauge Yang-Mills theory," Annals Phys. 324, 2408 (2009), arXiv:0810.1987 [hep-ph].

[108] H. Fritzsch and M. Gell-Mann, "Current algebra: Quarks and what else?" eConf C720906V2, 135 (1972), arXiv:hep-ph/0208010.

[109] H. Fritzsch and P. Minkowski, "Psi Resonances, Gluons and the Zweig Rule," Nuovo Cim. A 30, 393 (1975).

[110] C. Michael and M. Teper, "The Glueball Spectrum in SU(3)," Nucl. Phys. B 314, 347 (1989).

[111] G. S. Bali, K. Schilling, A. Hulsebos, A. C. Irving, C. Michael, and P. W. Stephenson (UKQCD), "A Comprehensive lattice study of SU(3) glueballs," Phys. Lett. B 309, 378 (1993), arXiv:hep-lat/9304012.

[112] C. J. Morningstar and M. J. Peardon, "The Glueball spectrum from an anisotropic lattice study," Phys. Rev. D 60, 034509 (1999), arXiv:hep-lat/9901004.

[113] E. Gregory, A. Irving, B. Lucini, C. McNeile, A. Rago, C. Richards, and E. Rinaldi, "Towards the glueball spectrum from unquenched lattice QCD," JHEP 10, 170 (2012), arXiv:1208.1858 [hep-lat].

[114] A. Athenodorou and M. Teper, "The glueball spectrum of SU(3) gauge theory in 3 + 1 dimensions," JHEP 11, 172 (2020), arXiv:2007.06422 [hep-lat].

[115] A. Szczepaniak, E. S. Swanson, C.-R. Ji, and S. R. Cotanch, "Glueball spectroscopy in a relativistic many body approach to hadron structure," Phys. Rev. Lett. 76, 2011 (1996), arXiv:hep-ph/9511422.

[116] A. P. Szczepaniak and E. S. Swanson, "The Low lying glueball spectrum," Phys. Lett. B 577, 61 (2003), arXiv:hep-ph/0308268.

[117] V. Mathieu, N. Kochelev, and V. Vento, "The Physics of Glueballs," Int. J. Mod. Phys. E 18, 1 (2009), arXiv:0810.4453 [hep-ph].

[118] D. Dudal, M. S. Guimaraes, and S. P. Sorella, "Glueball masses from an infrared moment problem and nonperturbative Landau gauge," Phys. Rev. Lett. 106, 062003 (2011), arXiv:1010.3638 [hep-th].

[119] J. Meyers and E. S. Swanson, "Spin Zero Glueballs in the Bethe-Salpeter Formalism," Phys. Rev. D 87, 036009 (2013), arXiv:1211.4648 [hep-ph].

[120] I. C. Cloet and C. D. Roberts, "Explanation and Prediction of Observables using Continuum Strong QCD," Prog. Part. Nucl. Phys. 77, 1 (2014), arXiv:1310.2651 [nucl-th].

[121] H. Sanchis-Alepuz, C. S. Fischer, C. Kellermann, and L. von Smekal, "Glueballs from the Bethe-Salpeter equation," Phys. Rev. D 92, 034001 (2015), arXiv:1503.06051 [hep-ph].

[122] E. V. Souza, M. Narciso Ferreira, A. C. Aguilar, J. a. Papavassiliou, C. D. Roberts, and S.-S. Xu, "Pseudoscalar glueball mass: a window on three-gluon interactions," Eur. Phys. J. A 56, 25 (2020), arXiv:1909.05875 [nucl-th].

[123] M. Q. Huber, C. S. Fischer, and H. Sanchis-Alepuz, "Spectrum of scalar and pseudoscalar glueballs from functional methods," Eur. Phys. J. C 80, 1077 (2020), arXiv:2004.00415 [hep-ph].

[124] A. Cucchieri and T. Mendes, "What's up with IR gluon and ghost propagators in Landau gauge? A puzzling answer from huge lattices," PoS LATTICE2007, 297 (2007), arXiv:0710.0412 [hep-lat].

[125] A. Cucchieri and T. Mendes, "Constraints on the IR behavior of the gluon propagator in Yang-Mills theories," Phys. Rev. Lett. 100, 241601 (2008), arXiv:0712.3517 [hep-lat].

[126] A. Cucchieri and T. Mendes, "Landau-gauge propagators in Yang-Mills theories at beta = 0: Massive solution versus conformal scaling," Phys. Rev. D 81, 016005 (2010), arXiv:0904.4033 [hep-lat].

[127] I. L. Bogolubsky, E. M. Ilgenfritz, M. Muller-Preussker, and A. Sternbeck, "The Landau gauge gluon and ghost propagators in 4D SU(3) gluodynamics in large lattice volumes," PoS LATTICE2007, 290 (2007), arXiv:0710.1968 [hep-lat].

[128] I. L. Bogolubsky, E. M. Ilgenfritz, M. Muller-Preussker, and A. Sternbeck, "Lattice gluodynamics computation of Landau gauge Green's functions in the deep infrared," Phys. Lett. B 676, 69 (2009), arXiv:0901.0736 [hep-lat].

[129] O. Oliveira and P. J. Silva, "The Lattice infrared Landau gauge gluon propagator: The Infinite volume limit," PoS LAT2009, 226 (2009), arXiv:0910.2897 [hep-lat].

[130] J. M. Pawlowski, D. Spielmann, and I.-O. Stamatescu, "Lattice Landau gauge with stochastic quantisation," Nucl. Phys. B 830, 291 (2010), arXiv:0911.4921 [hep-lat].

[131] O. Oliveira and P. Bicudo, "Running Gluon Mass from Landau Gauge Lattice QCD Propagator," J. Phys. G 38, 045003 (2011), arXiv:1002.4151 [hep-lat].

[132] A. Maas, "Describing gauge bosons at zero and finite temperature," Phys. Rept. 524, 203 (2013), arXiv:1106.3942 [hep-ph].

[133] A. C. Aguilar, D. Binosi, and J. Papavassiliou, "Gluon and ghost propagators in the Landau gauge: Deriving lattice results from Schwinger-Dyson equations," Phys. Rev. D 78, 025010 (2008), arXiv:0802.1870 [hep-ph].

[134] P. Boucaud, J.-P. Leroy, A. L. Yaouanc, J. Micheli, O. Pene, and J. Rodriguez-Quintero, "IR finiteness of the ghost dressing function from numerical resolution of the ghost SD equation," JHEP 06, 012 (2008), arXiv:0801.2721 [hep-ph].

[135] D. Binosi and J. Papavassiliou, "Pinch Technique: Theory and Applications," Phys. Rept. 479, 1 (2009), arXiv:0909.2536 [hep-ph].

[136] M. Q. Huber, "Nonperturbative properties of Yang–Mills theories," Phys. Rept. 879, 1 (2020), arXiv:1808.05227 [hep-ph].

[137] J. M. Pawlowski, D. F. Litim, S. Nedelko, and L. von Smekal, "Infrared behavior and fixed points in Landau gauge QCD," Phys.Rev.Lett. 93, 152002 (2004), arXiv:hep-th/0312324 [hep-th].

[138] J. Braun, H. Gies, and J. M. Pawlowski, "Quark Confinement from Color Confinement," Phys.Lett. B684, 262 (2010), arXiv:0708.2413 [hep-th].

[139] L. Fister and J. M. Pawlowski, "Confinement from Correlation Functions," Phys. Rev. D 88, 045010 (2013), arXiv:1301.4163 [hep-ph].

[140] E. Farhi and R. Jackiw, eds., *Dyanamical gauge symmetry breaking. A collection of reprints* (1982).

[141] I. J. R. Aitchison and A. J. G. Hey, *Gauge Theories in Particle Physics: A Practical Introduction, Volume 2: Non-Abelian Gauge Theories : QCD and The Electroweak Theory, Fourth Edition* (Taylor & Francis, 2013).

[142] J. M. Cornwall, "Dynamical Mass Generation in Continuum QCD," Phys. Rev. D 26, 1453 (1982).

[143] M. J. Lavelle and M. Schaden, "Propagators and Condensates in QCD," Phys. Lett. B 208, 297 (1988).

[144] M. Lavelle, "Gauge invariant effective gluon mass from the operator product expansion," Phys. Rev. D 44, 26 (1991).

[145] C. Wetterich, "Phase transition between three and two flavor QCD?" (2001), arXiv:hep-ph/0102248.

[146] C. Wetterich, "Spontaneously broken color," Phys. Rev. D 64, 036003 (2001), arXiv:hep-ph/0008150.

[147] C. Wetterich, "Higgs picture of the QCD-vacuum," AIP Conf. Proc. 739, 123 (2004), arXiv:hep-ph/0410057.

[148] A. Eichhorn, H. Gies, and J. M. Pawlowski, "Gluon condensation and scaling exponents for the propagators in Yang-Mills theory," Phys. Rev. D 83, 045014 (2011), [Erratum: Phys.Rev.D 83, 069903 (2011)], arXiv:1010.2153 [hep-ph].

[149] C. Wetterich, "Gluon meson duality," Phys. Lett. B 462, 164 (1999), arXiv:hep-th/9906062.

[150] C. Wetterich, "Gluon meson duality in the mean field approximation," Eur. Phys. J. C 18, 577 (2001), arXiv:hep-ph/9908514.

[151] H. Gies, J. Jaeckel, J. M. Pawlowski, and C. Wetterich, "Do instantons like a colorful background?" Eur.Phys.J. C49, 997 (2007), arXiv:hep-ph/0608171 [hep-ph].

[152] C. T. Hill, "Are There Significant Gravitational Corrections to the Unification Scale?" Phys. Lett. B 135, 47 (1984).

[153] Q. Shafi and C. Wetterich, "Modification of GUT Predictions in the Presence of Spontaneous Compactification," Phys. Rev. Lett. 52, 875 (1984).

[154] U. Ellwanger and C. Wetterich, "Evolution equations for the quark - meson transition," Nucl. Phys. B 423, 137 (1994), arXiv:hep-ph/9402221.

[155] H. Gies and C. Wetterich, "Renormalization flow of bound states," Phys.Rev. D65, 065001 (2002), arXiv:hep-th/0107221 [hep-th].

[156] F. Lamprecht, "Confinement in Polyakov gauge and flow equation of dynamical degrees of freedom," (2007), diploma thesis Heidelberg.

[157] S. Floerchinger and C. Wetterich, "Exact flow equation for composite operators," Phys.Lett. B680, 371 (2009), arXiv:0905.0915 [hep-th].

[158] F. Isaule, M. C. Birse, and N. R. Walet, "Application of the functional renormalization group to Bose gases: from linear to hydrodynamic fluctuations," Phys. Rev. B 98, 144502 (2018), arXiv:1806.10373 [cond-mat.quant-gas].

[159] A. Baldazzi, R. B. A. Zinati, and K. Falls, "Essential renormalisation group," (2021), arXiv:2105.11482 [hep-th].

[160] R. Daviet and N. Dupuis, "Flowing bosonization in the nonperturbative functional renormalization-group approach," (2021), arXiv:2111.11458 [cond-mat.quant-gas].

[161] F. J. Wegner, "Some invariance properties of the renormalization group," Journal of Physics C: Solid State Physics 7, 2098 (1974).

[162] H. Gies and C. Wetterich, "Universality of spontaneous chiral symmetry breaking in gauge theories," Phys.Rev. D69, 025001 (2004), arXiv:hep-th/0209183 [hep-th].

[163] J. Braun, "The QCD Phase Boundary from Quark-Gluon Dynamics," Eur. Phys. J. C64, 459 (2009), arXiv:0810.1727 [hep-ph].

[164] J. Braun, L. Fister, J. M. Pawlowski, and F. Rennecke, "From Quarks and Gluons to Hadrons: Chiral Symmetry Breaking in Dynamical QCD," Phys. Rev. D94, 034016 (2016), arXiv:1412.1045 [hep-ph].

[165] F. Rennecke, "Vacuum structure of vector mesons in QCD," Phys. Rev. D92, 076012 (2015), arXiv:1504.03585 [hep-ph].

[166] A. K. Cyrol, M. Mitter, J. M. Pawlowski, and N. Strodthoff, "Nonperturbative quark, gluon, and meson correlators of unquenched QCD," Phys. Rev. D 97, 054006 (2018), arXiv:1706.06326 [hep-ph].

[167] M. Reuter and C. Wetterich, "Indications for gluon condensation for nonperturbative flow equations," (1994), arXiv:hep-th/9411227.

[168] M. Reuter and C. Wetterich, "Gluon condensation in nonperturbative flow equations," Phys. Rev. D 56, 7893 (1997), arXiv:hep-th/9708051.

[169] L. F. Abbott, "The Background Field Method Beyond One Loop," Nucl. Phys. B 185, 189 (1981).

[170] D. Binosi and J. Papavassiliou, "Pinch technique and the Batalin-Vilkovisky formalism," Phys. Rev. D 66, 025024 (2002), arXiv:hep-ph/0204128.

[171] F. Gao, J. Papavassiliou, and J. M. Pawlowski, "Fully coupled functional equations for the quark sector of QCD," Phys. Rev. D 103, 094013 (2021), arXiv:2102.13053 [hep-ph].

[172] L. Corell, A. K. Cyrol, M. Mitter, J. M. Pawlowski, and N. Strodthoff, "Correlation functions of three-dimensional Yang-Mills theory from the FRG," SciPost Phys. 5, 066 (2018), arXiv:1803.10092 [hep-ph].

[173] B. Lucini and M. Panero, "Introductory lectures to large-N QCD phenomenology and lattice results," Prog. Part. Nucl. Phys. 75, 1 (2014), arXiv:1309.3638 [hep-th].

[174] D. F. Litim and J. M. Pawlowski, "On gauge invariant Wilsonian flows," in *Workshop on the Exact Renormalization Group* (1998) pp. 168–185, arXiv:hep-th/9901063.

[175] J. Berges, N. Tetradis, and C. Wetterich, "Nonperturbative renormalization flow in quantum field theory and statistical physics," Phys. Rept. 363, 223 (2002), arXiv:hep-ph/0005122.

[176] J. Braun, M. Leonhardt, and J. M. Pawlowski, "Renormalization group consistency and low-energy effective theories," SciPost Phys. 6, 056 (2019), arXiv:1806.04432 [hep-ph].

[177] P. van Baal, "QCD in a finite volume," (2000), arXiv:hep-ph/0008206.

[178] T. K. Herbst, J. Luecker, and J. M. Pawlowski, "Confinement order parameters and fluctuations," (2015), arXiv:1510.03830 [hep-ph].

[179] S. Narison, "Power corrections to alpha(s)(M(tau)),—V(us)— and anti-m(s)," Phys. Lett. B 673, 30 (2009), arXiv:0901.3823 [hep-ph].

[180] G. S. Bali and A. Pineda, "Phenomenology of renormalons and the OPE from lattice regularization: the gluon condensate and the heavy quark pole mass," AIP Conf. Proc. 1701, 030010 (2016), arXiv:1502.00086 [hep-ph].

[181] P. Boucaud, F. De Soto, K. Raya, J. Rodríguez-Quintero, and S. Zafeiropoulos, "Discretization effects on renormalized gauge-field Green's functions, scale setting, and the gluon mass," Phys. Rev. D 98, 114515 (2018), arXiv:1809.05776 [hep-ph].

[182] A. C. Aguilar, C. O. Ambrósio, F. De Soto, M. N. Ferreira, B. M. Oliveira, J. Papavassiliou, and J. Rodríguez-Quintero, "Ghost dynamics in the soft gluon limit," (2021), arXiv:2107.00768 [hep-ph].

[183] G. Parisi and R. Petronzio, "On Low-Energy Tests of QCD," Phys. Lett. B 94, 51 (1980).

[184] C. W. Bernard, "Monte Carlo Evaluation of the Effective Gluon Mass," Phys. Lett. B 108, 431 (1982).

[185] C. W. Bernard, "Adjoint Wilson Lines and the Effective Gluon Mass," Nucl. Phys. B 219, 341 (1983).

[186] J. F. Donoghue, "The Gluon 'Mass' in the Bag Model," Phys. Rev. D 29, 2559 (1984).

[187] J. E. Mandula and M. Ogilvie, "The Gluon Is Massive: A Lattice Calculation of the Gluon Propagator in the Landau Gauge," Phys. Lett. B 185, 127 (1987).

[188] C.-R. Ji and F. Amiri, "Perturbative QCD Analysis of the Pion Form-factor Using a Frozen Coupling Constant," Phys. Rev. D 42, 3764 (1990).

[189] F. Halzen, G. I. Krein, and A. A. Natale, "Relating the QCD pomeron to an effective gluon mass," Phys. Rev. D 47, 295 (1993).

[190] F. J. Yndurain, "Limits on the mass of the gluon," Phys. Lett. B 345, 524 (1995).

[191] J. H. Field, "A Phenomenological analysis of gluon mass effects in inclusive radiative decays of the J / psi and Upsilon," Phys. Rev. D 66, 013013 (2002), arXiv:hep-ph/0101158.

[192] O. Philipsen, "On the nonperturbative gluon mass and heavy quark physics," Nucl. Phys. B 628, 167 (2002), arXiv:hep-lat/0112047.

[193] E. G. S. Luna, A. F. Martini, M. J. Menon, A. Mihara, and A. A. Natale, "Influence of a dynamical gluon mass in the pp and p anti-p forward scattering," Phys. Rev. D 72, 034019 (2005), arXiv:hep-ph/0507057.

[194] A. Deur, S. J. Brodsky, and G. F. de Teramond, "The QCD Running Coupling," Nucl. Phys. 90, 1 (2016), arXiv:1604.08082 [hep-ph].

[195] S. W. Li, P. Lowdon, O. Oliveira, and P. J. Silva, "The generalised infrared structure of the gluon propagator," Phys. Lett. B 803, 135329 (2020), arXiv:1907.10073 [hep-th].

[196] A. C. Aguilar, M. N. Ferreira, and J. Papavassiliou, "Exploring smoking-gun signals of the Schwinger mechanism in QCD," (2021), arXiv:2111.09431 [hep-ph].

[197] A. C. Aguilar, D. Ibanez, V. Mathieu, and J. Papavassiliou, "Massless bound-state excitations and the Schwinger mechanism in QCD," Phys. Rev. D 85, 014018 (2012), arXiv:1110.2633 [hep-ph].

[198] D. Binosi, D. Ibanez, and J. Papavassiliou, "The all-order equation of the effective gluon mass," Phys. Rev. D 86, 085033 (2012), arXiv:1208.1451 [hep-ph].

[199] A. C. Aguilar, D. Binosi, C. T. Figueiredo, and J. Papavassiliou, "Evidence of ghost suppression in gluon mass scale dynamics," Eur. Phys. J. C 78, 181 (2018), arXiv:1712.06926 [hep-ph].

[200] J. S. Schwinger, "Gauge Invariance and Mass," Phys. Rev. 125, 397 (1962).

[201] J. S. Schwinger, "Gauge Invariance and Mass. 2." Phys. Rev. 128, 2425 (1962).

[202] R. Jackiw and K. Johnson, "Dynamical Model of Spontaneously Broken Gauge Symmetries," Phys. Rev. D 8, 2386 (1973).

[203] E. Eichten and F. Feinberg, "Dynamical Symmetry Breaking of Nonabelian Gauge Symmetries," Phys. Rev. D 10, 3254 (1974).

[204] A. C. Aguilar, D. Binosi, D. Ibañez, and J. Papavassiliou, "Effects of divergent ghost loops on the Green's functions of QCD," Phys. Rev. D 89, 085008 (2014), arXiv:1312.1212 [hep-ph].

[205] A. C. Aguilar, D. Binosi, C. T. Figueiredo, and J. Papavassiliou, "Unified description of seagull cancellations and infrared finiteness of gluon propagators," Phys. Rev. D 94, 045002 (2016), arXiv:1604.08456 [hep-ph].

[206] J. Fehre, D. F. Litim, J. M. Pawlowski, and M. Reichert, "Lorentzian quantum gravity and the graviton spectral function," (2021), arXiv:2111.13232 [hep-th].

[207] S. Strauss, C. S. Fischer, and C. Kellermann, "Analytic structure of the Landau gauge gluon propagator," Phys. Rev. Lett. 109, 252001 (2012), arXiv:1208.6239 [hep-ph].

[208] A. Windisch, M. Q. Huber, and R. Alkofer, "On the analytic structure of scalar glueball operators at the Born level," Phys.Rev. D87, 065005 (2013), arXiv:1212.2175 [hep-ph].

[209] S. M. Dorkin, L. P. Kaptari, T. Hilger, and B. Kampfer, "Analytical properties of the quark propagator from a truncated Dyson-Schwinger equation in complex Euclidean space," Phys. Rev. C89, 034005 (2014), arXiv:1312.2721 [hep-ph].

[210] S. M. Dorkin, L. P. Kaptari, and B. Kampfer, "Accounting for the analytical properties of the quark propagator from the Dyson-Schwinger equation," Phys. Rev. C91, 055201 (2015), arXiv:1412.3345 [hep-ph].

[211] S. Dorkin, M. Viebach, L. Kaptari, and B. Kampfer, "Extending the truncated Dyson-Schwinger equation to finite temperatures," J. Mod. Phys. 7, 2071 (2016), arXiv:1512.06596 [nucl-th].

[212] G. Aarts and J. Berges, "Nonequilibrium time evolution of the spectral function in quantum field theory," Phys. Rev. D 64, 105010 (2001), arXiv:hep-ph/0103049.

[213] G. Aarts, "Spectral function at high temperature in the classical approximation," Phys. Lett. B 518, 315 (2001), arXiv:hep-ph/0108125.

[214] Yu. B. Ivanov, F. Riek, H. van Hees, and J. Knoll, "Renormalization of a gapless Hartree-Fock approximation to a theory with spontaneously broken O(N) symmetry," Phys. Rev. D72, 036008 (2005), arXiv:hep-ph/0506157 [hep-ph].

[215] D. Röder, J. Ruppert, and D. H. Rischke, "Self-consistent calculations of spectral densities in the o (n) model: improving the hartree–fock approximation by including nonzero decay widths," Nuclear Physics A 775, 127 (2006).

[216] T. Gasenzer and J. M. Pawlowski, "Functional renormalisation group approach to far-from-equilibrium quantum field dynamics," (2007), arXiv:0710.4627 [cond-mat.other].

[217] T. Gasenzer, S. Kessler, and J. M. Pawlowski, "Far-from-equilibrium quantum many-body dynamics," Eur.Phys.J. C70, 423 (2010), arXiv:1003.4163 [cond-mat.quant-gas].

[218] K. Kamikado, N. Strodthoff, L. von Smekal, and J. Wambach, "Real-Time Correlation Functions in the O(N) Model from the Functional Renormalization Group," Eur.Phys.J. C74, 2806 (2014), arXiv:1302.6199 [hep-ph].

[219] R.-A. Tripolt, N. Strodthoff, L. von Smekal, and J. Wambach, "Spectral Functions for the Quark-Meson Model Phase Diagram from the Functional Renormalization Group," Phys. Rev. D89, 034010 (2014), arXiv:1311.0630 [hep-ph].

[220] J. M. Pawlowski and N. Strodthoff, "Real time correlation functions and the functional renormalization group," Phys. Rev. D92, 094009 (2015), arXiv:1508.01160 [hep-ph].

[221] T. Yokota, T. Kunihiro, and K. Morita, "Functional renormalization group analysis of the soft mode at the QCD critical point," PTEP 2016, 073D01 (2016), arXiv:1603.02147 [hep-ph].

[222] K. Kamikado, T. Kanazawa, and S. Uchino, "Mobile impurity in a Fermi sea from the functional renormalization group analytically continued to real time," Phys. Rev. A95, 013612 (2017), arXiv:1606.03721 [cond-mat.quant-gas].

[223] C. Jung, F. Rennecke, R.-A. Tripolt, L. von Smekal, and J. Wambach, "In-Medium Spectral Functions of Vector- and Axial-Vector Mesons from the Functional Renormalization Group," Phys. Rev. D95, 036020 (2017), arXiv:1610.08754 [hep-ph].

[224] T. Yokota, T. Kunihiro, and K. Morita, "Tachyonic instability of the scalar mode prior to the QCD critical point based on the functional renormalization-group method in the two-flavor case," Phys. Rev. D96, 074028 (2017), arXiv:1707.05520 [hep-ph].

[225] Z. Wang and P. Zhuang, "Meson spectral functions at finite temperature and isospin density with the functional renormalization group," Phys. Rev. D96, 014006 (2017), arXiv:1703.01035 [hep-ph].

[226] M. Bluhm, Y. Jiang, M. Nahrgang, J. M. Pawlowski, F. Rennecke, and N. Wink, "Time-evolution of fluctuations as signal of the phase transition dynamics in a QCD-assisted transport approach," *Proceedings, 27th International Conference on Ultrarelativistic Nucleus-Nucleus Collisions (Quark Matter 2018): Venice, Italy, May 14-19, 2018*, Nucl. Phys. A982, 871 (2019), arXiv:1808.01377 [hep-ph].

[227] R.-A. Tripolt, C. Jung, N. Tanji, L. von Smekal, and J. Wambach, "In-medium spectral functions and dilepton rates with the Functional Renormalization Group," *Proceedings, 27th International Conference on Ultrarelativistic Nucleus-Nucleus*

Collisions (Quark Matter 2018): Venice, Italy, May 14-19, 2018, Nucl. Phys. A982, 775 (2019), arXiv:1807.04952 [hep-ph].

[228] R.-A. Tripolt, J. Weyrich, L. von Smekal, and J. Wambach, "Fermionic spectral functions with the Functional Renormalization Group," Phys. Rev. D98, 094002 (2018), arXiv:1807.11708 [hep-ph].

[229] Z. Wang and L. He, "Fermion spectral function in hot strongly interacting matter from the functional renormalization group," Phys. Rev. D98, 094031 (2018), arXiv:1808.08535 [hep-ph].

[230] L. Corell, A. K. Cyrol, M. Heller, and J. M. Pawlowski, "Flowing with the temporal renormalization group," Phys. Rev. D 104, 025005 (2021), arXiv:1910.09369 [hep-th].

[231] M. Heller and J. M. Pawlowski, "Causal Temporal Renormalisation Group Flow of the Energy-Momentum Tensor," (2021), arXiv:2112.12652 [hep-th].

[232] K. Kusaka and A. G. Williams, "Solving the Bethe-Salpeter equation for scalar theories in Minkowski space," Phys. Rev. D 51, 7026 (1995), arXiv:hep-ph/9501262.

[233] G. Eichmann, P. Duarte, M. T. Peña, and A. Stadler, "Scattering amplitudes and contour deformations," Phys. Rev. D100, 094001 (2019), arXiv:1907.05402 [hep-ph].

[234] N. Santowsky and C. S. Fischer, "Light scalars: Four-quark versus two-quark states in the complex energy plane from Bethe-Salpeter equations," Phys. Rev. D 105, 034025 (2022), arXiv:2109.00755 [hep-ph].

[235] V. Sauli, "Timelike behavior of the pion electromagnetic form factor in the functional formalism," Phys. Rev. D 106, 034030 (2022), arXiv:2204.08424 [hep-ph].

[236] L. Shen and J. Berges, "Spectral, statistical and vertex functions in scalar quantum field theory far from equilibrium," Phys. Rev. D 101, 056009 (2020), arXiv:1912.07565 [hep-ph].

[237] G. Markó, U. Reinosa, and Z. Szép, "O(N) model within the Φ-derivable expansion to order λ^2: On the existence and UV/IR sensitivity of the solutions to self-consistent equations," Phys. Rev. D92, 125035 (2015), arXiv:1510.04932 [hep-ph].

[238] L. Shen, J. Berges, J. Pawlowski, and A. Rothkopf, "Thermalization and dynamical spectral properties in the quark-meson model," (2020), arXiv:2003.03270 [hep-ph].

[239] J. Berges, S. Schlichting, and D. Sexty, "Dynamic critical phenomena from spectral functions on the lattice," Nucl. Phys. B 832, 228 (2010), arXiv:0912.3135 [hep-lat].

[240] A. Windisch, R. Alkofer, G. Haase, and M. Liebmann, "Examining the Analytic Structure of Green's Functions: Massive Parallel Complex Integration using GPUs," Comput. Phys. Commun. 184, 109 (2013), arXiv:1205.0752 [hep-ph].

[241] A. Windisch, T. Gallien, and C. Schwarzlmüller, "Deep reinforcement learning for complex evaluation of one-loop diagrams in quantum field theory," Phys. Rev. E 101, 033305 (2020), arXiv:1912.12322 [hep-ph].

[242] A. K. Rajantie, "Feynman diagrams to three loops in three-dimensional field theory," Nucl. Phys. B480, 729 (1996), [Erratum: Nucl. Phys.B513,761(1998)], arXiv:hep-ph/9606216 [hep-ph].

[243] A. K. Cyrol, J. M. Pawlowski, A. Rothkopf, and N. Wink, "Reconstructing the gluon," SciPost Phys. 5, 065 (2018), arXiv:1804.00945 [hep-ph].

[244] E. Kraus, "Renormalization of the Electroweak Standard Model to All Orders," Annals Phys. 262, 155 (1998), arXiv:hep-th/9709154.

[245] K. Fukushima and J. M. Pawlowski, "Magnetic catalysis in hot and dense quark matter and quantum fluctuations," Phys. Rev. D 86, 076013 (2012), arXiv:1203.4330 [hep-ph].

[246] V. Agostini, G. Carlino, M. Caselle, and M. Hasenbusch, "The Spectrum of the (2+1)-dimensional gauge Ising model," Nucl. Phys. B484, 331 (1997), arXiv:hep-lat/9607029 [hep-lat].

[247] M. Caselle, M. Hasenbusch, and P. Provero, "Nonperturbative states in the 3-D phi**4 theory," Nucl. Phys. B556, 575 (1999), arXiv:hep-lat/9903011 [hep-lat].

[248] M. Caselle, M. Hasenbusch, P. Provero, and K. Zarembo, "Bound states and glueballs in three-dimensional Ising systems," Nucl. Phys. B623, 474 (2002), arXiv:hep-th/0103130 [hep-th].

[249] F. Rose, F. Benitez, F. Léonard, and B. Delamotte, "Bound states of the Φ^4 model via the nonperturbative renormalization group," Phys. Rev. D93, 125018 (2016), arXiv:1604.05285 [cond-mat.stat-mech].

[250] R.-A. Tripolt, L. von Smekal, and J. Wambach, "Flow equations for spectral functions at finite external momenta," Phys.Rev. D90, 074031 (2014), arXiv:1408.3512 [hep-ph].

[251] K. Symanzik, "Small distance behavior in field theory and power counting," Commun. Math. Phys. 18, 227 (1970).

[252] J. M. Pawlowski, M. M. Scherer, R. Schmidt, and S. J. Wetzel, "Physics and the choice of regulators in functional renormalisation group flows," (2015), arXiv:1512.03598 [hep-th].

[253] W.-j. Fu and J. M. Pawlowski, "On the relevance of matter and glue dynamics for baryon number fluctuations," Phys. Rev. D92, 116006 (2015), arXiv:1508.06504 [hep-ph].

[254] A. Bonanno, T. Denz, J. M. Pawlowski, and M. Reichert, "Reconstructing the graviton," (2021), arXiv:2102.02217 [hep-th].

[255] R. Oehme and W. Zimmermann, "QUARK AND GLUON PROPAGATORS IN QUANTUM CHROMODYNAMICS," Phys. Rev. D21, 471 (1980).

[256] R. Oehme, "On superconvergence relations in quantum chromodynamics," Phys. Lett. B252, 641 (1990).

[257] T. Denz, J. M. Pawlowski, and M. Reichert, "Towards apparent convergence in asymptotically safe quantum gravity," (2016), arXiv:1612.07315 [hep-th].

[258] M. Haas, L. Fister, and J. M. Pawlowski, "Gluon spectral functions and transport coefficients in Yang–Mills theory," Phys. Rev. D 90, 091501 (2014), arXiv:1308.4960 [hep-ph].

[259] D. Dudal, O. Oliveira, and P. J. Silva, "Källén-Lehmann spectroscopy for (un)physical degrees of freedom," Phys. Rev. D 89, 014010 (2014), arXiv:1310.4069 [hep-lat].

[260] D. Binosi and R.-A. Tripolt, "Spectral functions of confined particles," Phys. Lett. B 801, 135171 (2020), arXiv:1904.08172 [hep-ph].

[261] D. Dudal, O. Oliveira, M. Roelfs, and P. Silva, "Spectral representation of lattice gluon and ghost propagators at zero temperature," Nucl. Phys. B 952, 114912 (2020), arXiv:1901.05348 [hep-lat].

[262] F. Siringo, "Analytic structure of QCD propagators in Minkowski space," Phys. Rev. D 94, 114036 (2016), arXiv:1605.07357 [hep-ph].

[263] Y. Hayashi and K.-I. Kondo, "Complex poles and spectral functions of Landau gauge QCD and QCD-like theories," Phys. Rev. D 101, 074044 (2020), arXiv:2001.05987 [hep-th].

[264] C. S. Fischer and M. Q. Huber, "Landau gauge Yang-Mills propagators in the complex momentum plane," Phys. Rev. D 102, 094005 (2020), arXiv:2007.11505 [hep-ph].

[265] J. M. Pawlowski, "Equation of state and phase diagram of strongly interacting matter," Nucl.Phys. A931, 113 (2014).

[266] G. Eichmann, H. Sanchis-Alepuz, R. Williams, R. Alkofer, and C. S. Fischer, "Baryons as relativistic three-quark bound states," Prog. Part. Nucl. Phys. 91, 1 (2016), arXiv:1606.09602 [hep-ph].

[267] H. Sanchis-Alepuz and R. Williams, "Recent developments in bound-state calculations using the Dyson–Schwinger and Bethe–Salpeter equations," Comput. Phys. Commun. 232, 1 (2018), arXiv:1710.04903 [hep-ph].

[268] N. N. Bogolyubov, A. A. Logunov, A. I. Oksak, and I. T. Todorov, *General principles of quantum field theory* (1990).

[269] P. Lowdon, "Non-perturbative constraints on the quark and ghost propagators," Nucl. Phys. B 935, 242 (2018), arXiv:1711.07569 [hep-th].

[270] S. P. Sorella, "Gluon confinement, i-particles and BRST soft breaking," J.Phys.A A44, 135403 (2011), arXiv:1006.4500 [hep-th].

[271] P. Lowdon, "Nonperturbative structure of the photon and gluon propagators," Phys. Rev. D 96, 065013 (2017), arXiv:1702.02954 [hep-th].

[272] Y. Hayashi and K.-I. Kondo, "Complex poles and spectral function of Yang-Mills theory," Phys. Rev. D 99, 074001 (2019), arXiv:1812.03116 [hep-th].

[273] P. Lowdon, "On the analytic structure of QCD propagators," PoS Confinement2018, 050 (2018), arXiv:1811.03037 [hep-th].

[274] Y. Hayashi and K.-I. Kondo, "Reconstructing confined particles with complex singularities," Phys. Rev. D 103, L111504 (2021), arXiv:2103.14322 [hep-th].

[275] K.-I. Kondo, Y. Hayashi, R. Matsudo, Y. Suda, and M. Watanabe, "Complex poles, spectral function and reflection positivity violation of Yang-Mills theory," PoS LC2019, 053 (2019), arXiv:1912.06261 [hep-th].

[276] K.-I. Kondo, M. Watanabe, Y. Hayashi, R. Matsudo, and Y. Suda, "Reflection positivity and complex analysis of the Yang-Mills theory from a viewpoint of gluon confinement," Eur. Phys. J. C 80, 84 (2020), arXiv:1902.08894 [hep-th].

[277] W. Schleifenbaum, A. Maas, J. Wambach, and R. Alkofer, "Infrared behaviour of the ghost gluon vertex in Landau gauge Yang-Mills theory," Phys. Rev. D72, 014017 (2005), arXiv:hep-ph/0411052.

[278] E. M. Ilgenfritz, M. Müller-Preussker, A. Sternbeck, A. Schiller, and I. L. Bogolubsky, "Landau gauge gluon and ghost propagators from lattice QCD," Braz. J. Phys. 37, 193 (2007), arXiv:hep-lat/0609043.

[279] P. Boucaud, D. Dudal, J. P. Leroy, O. Pene, and J. Rodriguez-Quintero, "On the leading OPE corrections to the ghost-gluon vertex and the Taylor theorem," JHEP 12, 018 (2011), arXiv:1109.3803 [hep-ph].

[280] D. Dudal, O. Oliveira, and J. Rodriguez-Quintero, "Nontrivial ghost-gluon vertex and the match of RGZ, DSE and lattice Yang-Mills propagators," Phys.Rev. D86, 105005 (2012), arXiv:1207.5118 [hep-ph].

[281] A. C. Aguilar, D. Ibáñez, and J. Papavassiliou, "Ghost propagator and ghost-gluon vertex from Schwinger-Dyson equations," Phys. Rev. D87, 114020 (2013), arXiv:1303.3609 [hep-ph].

[282] N. Barrios, M. Peláez, U. Reinosa, and N. Wschebor, "The ghost-antighost-gluon vertex from the Curci-Ferrari model: Two-loop corrections," Phys. Rev. D 102, 114016 (2020), arXiv:2009.00875 [hep-th].

[283] G. Eichmann, R. Williams, R. Alkofer, and M. Vujinovic, "The three-gluon vertex in Landau gauge," Phys.Rev. D89, 105014 (2014), arXiv:1402.1365 [hep-ph].

[284] M. Pelaez, M. Tissier, and N. Wschebor, "Three-point correlation functions in Yang-Mills theory," Phys.Rev. D88, 125003 (2013), arXiv:1310.2594 [hep-th].

[285] T. S. Evans, "N point finite temperature expectation values at real times," Nucl. Phys. B 374, 340 (1992).

[286] P. Aurenche and T. Becherrawy, "A Comparison of the real time and the imaginary time formalisms of finite temperature field theory for 2, 3, and 4 point Green's functions," Nucl.Phys. B379, 259 (1992).

[287] R. Baier and A. Niegawa, "Analytic continuation of thermal N point functions from imaginary to real energies," Phys. Rev. D 49, 4107 (1994), arXiv:hep-ph/9307362.

[288] F. Guerin, "Retarded-advanced n-point green functions in thermal field theories," Nuclear Physics B 432, 281–311 (1994).

[289] N. Wink, *Towards the spectral properties and phase structure of QCD.*, Ph.D. thesis, U. Heidelberg, ITP (2020).

[290] M. Carrington and U. Heinz, "Three-point functions at finite temperature," The European Physical Journal C 1, 619–625 (1998).

[291] J. Bros and D. Buchholz, "Axiomatic analyticity properties and representations of particles in thermal quantum field theory," Ann. Inst. H. Poincare Phys. Theor. 64, 495 (1996), arXiv:hep-th/9606046 [hep-th].

[292] H. Defu and U. Heinz, "Three-point spectral functions in ϕ_6^3 theory at finite temperature," The European Physical Journal C 4, 129–137 (1998).

[293] H. Weldon, "Finite-temperature retarded and advanced fields," Nuclear Physics B 534, 467–490 (1998).

[294] D. Hou, E. Wang, and U. Heinz, "n-point functions at finite temperature," Journal of Physics G: Nuclear and Particle Physics 24, 1861–1868 (1998).

[295] D.-f. Hou, M. E. Carrington, R. Kobes, and U. W. Heinz, "Four point spectral functions and Ward identities in hot QED," Phys. Rev. D 61, 085013 (2000), [Erratum: Phys.Rev.D 67, 049902 (2003)], arXiv:hep-ph/9911494.

[296] H. A. Weldon, "Thermal four-point functions with analytic extensions," Phys. Rev. D 72, 096005 (2005).

[297] D. Bodeker and M. Sangel, "Lepton asymmetry rate from quantum field theory: NLO in the hierarchical limit," JCAP 1706, 052 (2017), arXiv:1702.02155 [hep-ph].

[298] M. Peláez, U. Reinosa, J. Serreau, M. Tissier, and N. Wschebor, "A window on infrared QCD with small expansion parameters," Rept. Prog. Phys. 84, 124202 (2021), arXiv:2106.04526 [hep-th].

[299] P. Lowdon, "Dyson–Schwinger equation constraints on the gluon propagator in BRST quantised QCD," Phys. Lett. B 786, 399 (2018), arXiv:1801.09337 [hep-th].

[300] E.-M. Ilgenfritz, J. M. Pawlowski, A. Rothkopf, and A. Trunin, "Finite temperature gluon spectral functions from $N_f = 2 + 1 + 1$ lattice QCD," Eur. Phys. J. C 78, 127 (2018), arXiv:1701.08610 [hep-lat].

[301] U. Reinosa, J. Serreau, M. Tissier, and N. Wschebor, "How nonperturbative is the infrared regime of Landau gauge Yang-Mills correlators?" Phys. Rev. D 96, 014005 (2017), arXiv:1703.04041 [hep-th].

[302] A. F. Falcão, O. Oliveira, and P. J. Silva, "Analytic structure of the lattice Landau gauge gluon and ghost propagators," Phys. Rev. D 102, 114518 (2020), arXiv:2008.02614 [hep-lat].

[303] C. A. Meyer and E. S. Swanson, "Hybrid Mesons," Prog. Part. Nucl. Phys. 82, 21 (2015), arXiv:1502.07276 [hep-ph].

[304] H. Sanchis-Alepuz and R. Williams, "Hadronic Observables from Dyson-Schwinger and Bethe-Salpeter equations," J. Phys. Conf. Ser. 631, 012064 (2015), arXiv:1503.05896 [hep-ph].

[305] A. P. Valentine and M. Sambridge, "Gaussian process models—I. A framework for probabilistic continuous inverse theory," Geophysical Journal International 220, 1632 (2019).

[306] M. Jarrell and J. E. Gubernatis, "Bayesian inference and the analytic continuation of imaginary-time quantum Monte Carlo data," Phys. Rept. 269, 133 (1996).

[307] M. Asakawa, T. Hatsuda, and Y. Nakahara, "Maximum entropy analysis of the spectral functions in lattice QCD," Prog. Part. Nucl. Phys. 46, 459 (2001), arXiv:hep-lat/0011040 [hep-lat].

[308] Y. Burnier and A. Rothkopf, "Bayesian Approach to Spectral Function Reconstruction for Euclidean Quantum Field Theories," Phys. Rev. Lett. 111, 182003 (2013), arXiv:1307.6106 [hep-lat].

[309] A. Rothkopf, "Bayesian inference of nonpositive spectral functions in quantum field theory," Phys. Rev. D95, 056016 (2017), arXiv:1611.00482 [hep-ph].

[310] M. Ulybyshev, C. Winterowd, and S. Zafeiropoulos, "Collective charge excitations and the metal-insulator transition in the square lattice Hubbard-Coulomb model," Phys. Rev. B 96, 205115 (2017), arXiv:1707.04212 [cond-mat.str-el].

[311] D. Dudal, O. Oliveira, and M. Roelfs, "Källén-Lehmann Spectral Representation of the Scalar SU(2) Glueball," (2021), arXiv:2103.11846 [hep-lat].

[312] R. Fournier, L. Wang, O. V. Yazyev, and Q. Wu, "Artificial neural network approach to the analytic continuation problem," Physical Review Letters 124, 056401 (2020), arXiv:1810.00913 [physics.comp-ph].

[313] H. Yoon, J.-H. Sim, and M. J. Han, "Analytic continuation via domain knowledge free machine learning," Physical Review B 98, 245101 (2018), arXiv:1806.03841 [cond-mat.str-el].

[314] L. Kades, J. M. Pawlowski, A. Rothkopf, M. Scherzer, J. M. Urban, S. J. Wetzel, N. Wink, and F. P. G. Ziegler, "Spectral Reconstruction with Deep Neural Networks," Phys. Rev. D 102, 096001 (2020), arXiv:1905.04305 [physics.comp-ph].

[315] M. Zhou, F. Gao, J. Chao, Y.-X. Liu, and H. Song, "Application of radial basis functions neutral networks in spectral functions," (2021), arXiv:2106.08168 [hep-ph].

[316] T. Lechien and D. Dudal, "Neural network approach to reconstructing spectral functions and complex poles of confined particles," SciPost Phys. 13, 097 (2022), arXiv:2203.03293 [hep-lat].

[317] L.-F. Arsenault, R. Neuberg, L. A. Hannah, and A. J. Millis, "Projected regression methods for inverting fredholm integrals: Formalism and application to analytical continuation," (2016), arXiv:1612.04895 [cond-mat.str-el].

[318] S. Offler, G. Aarts, C. Allton, J. Glesaaen, B. Jäger, S. Kim, M. P. Lombardo, S. M. Ryan, and J.-I. Skullerud, "News from bottomonium spectral functions in thermal QCD," PoS LATTICE2019, 076 (2019), arXiv:1912.12900 [hep-lat].

[319] G. Cuniberti, E. De Micheli, and G. A. Viano, "Reconstructing the thermal Green functions at real times from those at imaginary times," Commun. Math. Phys. 216, 59 (2001), arXiv:cond-mat/0109175 [cond-mat.str-el].

[320] Y. Burnier, M. Laine, and L. Mether, "A Test on analytic continuation of thermal imaginary-time data," Eur. Phys. J. C71, 1619 (2011), arXiv:1101.5534 [hep-lat].

[321] J. Fei, C.-N. Yeh, and E. Gull, "Nevanlinna analytical continuation," Physical Review Letters 126, 056402 (2021), arXiv:2010.04572 [cond-mat.str-el].

[322] J. Fei, C.-N. Yeh, D. Zgid, and E. Gull, "Analytical continuation of matrix-valued functions: Carathéodory formalism," (2021), arXiv:2107.00788 [cond-mat.str-el].

[323] R. Oehme and W. Zimmermann, "Gauge Field Propagator and the Number of Fermion Fields," Phys. Rev. D21, 1661 (1980).

[324] M. A. L. Capri, M. S. Guimaraes, I. Justo, L. F. Palhares, and S. P. Sorella, "On general ultraviolet properties of a class of confining propagators," Eur. Phys. J. C 76, 141 (2016), arXiv:1510.07886 [hep-th].

[325] F. Siringo, "Dispersion relations for unphysical particles," *Proceedings, 12th Conference on Quark Confinement and the Hadron Spectrum (Confinement XII): Thessaloniki, Greece*, EPJ Web Conf. 137, 13017 (2017), arXiv:1606.03769 [hep-ph].

[326] D. Dudal, D. M. van Egmond, M. S. Guimarães, O. Holanda, B. W. Mintz, L. F. Palhares, G. Peruzzo, and S. P. Sorella, "Some remarks on the spectral functions of the Abelian Higgs Model," Phys. Rev. D 100, 065009 (2019), arXiv:1905.10422 [hep-th].

[327] Y. Hayashi and K.-I. Kondo, "Reconstructing propagators of confined particles in the presence of complex singularities," Phys. Rev. D 104, 074024 (2021), arXiv:2105.07487 [hep-th].

[328] D. G. Krige, "A statistical approach to some basic mine valuation problems on the witwatersrand," Journal of the Southern African Institute of Mining and Metallurgy 52, 119 (1951).

[329] M. Kanagawa, P. Hennig, D. Sejdinovic, and B. K. Sriperumbudur, "Gaussian processes and kernel methods: A review on connections and equivalences," (2018), arXiv:1807.02582 [stat.ML].

[330] H. Liu, Y.-S. Ong, X. Shen, and J. Cai, "When gaussian process meets big data: A review of scalable gps," (2019), arXiv:1807.01065 [stat.ML].

[331] C. E. Rasmussen and C. K. I. Williams, *Gaussian Processes for Machine Learning (Adaptive Computation and Machine Learning)* (The MIT Press, 2005).

[332] C. Alexandrou, G. Iannelli, K. Jansen, and F. Manigrasso (Extended Twisted Mass), "Parton distribution functions from lattice QCD using Bayes-Gauss-Fourier transforms," Phys. Rev. D 102, 094508 (2020), arXiv:2007.13800 [hep-lat].

[333] C. A. Micchelli, Y. Xu, and H. Zhang, "Universal kernels," J. Mach. Learn. Res. 7, 2651–2667 (2006).

[334] F. D. R. Bonnet, P. O. Bowman, D. B. Leinweber, and A. G. Williams, "Infrared behavior of the gluon propagator on a large volume lattice," Phys. Rev. D 62, 051501 (2000), arXiv:hep-lat/0002020.

[335] P. Boucaud, J. P. Leroy, A. Le Yaouanc, A. Y. Lokhov, J. Micheli, O. Pene, J. Rodriguez-Quintero, and C. Roiesnel, "Asymptotic behavior of the ghost propagator in SU3 lattice gauge theory," Phys. Rev. D 72, 114503 (2005), arXiv:hep-lat/0506031.

[336] P. J. Silva and O. Oliveira, "Infrared Gluon Propagator from lattice QCD: Results from large asymmetric lattices," Phys. Rev. D 74, 034513 (2006), arXiv:hep-lat/0511043.

[337] A. Cucchieri, A. Maas, and T. Mendes, "Exploratory study of three-point Green's functions in Landau-gauge Yang-Mills theory," Phys. Rev. D 74, 014503 (2006), arXiv:hep-lat/0605011.

[338] A. Cucchieri, A. Maas, and T. Mendes, "Three-point vertices in Landau-gauge Yang-Mills theory," Phys. Rev. D 77, 094510 (2008), arXiv:0803.1798 [hep-lat].

[339] O. Oliveira and P. J. Silva, "Does The Lattice Zero Momentum Gluon Propagator for Pure Gauge SU(3) Yang-Mills Theory Vanish in the Infinite Volume Limit?" Phys. Rev. D 79, 031501 (2009), arXiv:0809.0258 [hep-lat].

[340] T. Iritani, H. Suganuma, and H. Iida, "Gluon-propagator functional form in the Landau gauge in SU(3) lattice QCD: Yukawa-type gluon propagator and anomalous gluon spectral function," Phys. Rev. D 80, 114505 (2009), arXiv:0908.1311 [hep-lat].

[341] A. Ayala, A. Bashir, D. Binosi, M. Cristoforetti, and J. Rodriguez-Quintero, "Quark flavour effects on gluon and ghost propagators," Phys. Rev. D 86, 074512 (2012), arXiv:1208.0795 [hep-ph].

[342] A. Athenodorou, P. Boucaud, F. De Soto, J. Rodríguez-Quintero, and S. Zafeiropoulos, "On the zero-crossing of the three-gluon Green's function from lattice simulations," EPJ Web Conf. 175, 12012 (2018), arXiv:1802.00698 [hep-lat].

[343] A. G. Duarte, O. Oliveira, and P. J. Silva, "Further Evidence For Zero Crossing On The Three Gluon Vertex," Phys. Rev. D 94, 074502 (2016), arXiv:1607.03831 [hep-lat].

[344] A. C. Aguilar, F. De Soto, M. N. Ferreira, J. Papavassiliou, J. Rodríguez-Quintero, and S. Zafeiropoulos, "Gluon propagator and three-gluon vertex with dynamical quarks," Eur. Phys. J. C 80, 154 (2020), arXiv:1912.12086 [hep-ph].

[345] A. C. Aguilar, F. De Soto, M. N. Ferreira, J. Papavassiliou, and J. Rodríguez-Quintero, "Infrared facets of the three-gluon vertex," Phys. Lett. B 818, 136352 (2021), arXiv:2102.04959 [hep-ph].

[346] N. Christiansen, M. Haas, J. M. Pawlowski, and N. Strodthoff, "Transport Coefficients in Yang–Mills Theory and QCD," Phys. Rev. Lett. 115, 112002 (2015), arXiv:1411.7986 [hep-ph].

[347] M. Bluhm *et al.*, "Dynamics of critical fluctuations: Theory – phenomenology – heavy-ion collisions," Nucl. Phys. A 1003, 122016 (2020), arXiv:2001.08831 [nucl-th].

[348] C. S. Ong, A. J. Smola, and R. C. Williamson, "Learning the kernel with hyperkernels," Journal of Machine Learning Research 6, 1043 (2005).

[349] A. G. Wilson, Z. Hu, R. Salakhutdinov, and E. P. Xing, "Deep kernel learning," (2015), arXiv:1511.02222 [cs.LG].

[350] F. Karsch and M. Kitazawa, "Quark propagator at finite temperature and finite momentum in quenched lattice QCD," Phys. Rev. D80, 056001 (2009), arXiv:0906.3941 [hep-lat].

[351] J. A. Mueller, C. S. Fischer, and D. Nickel, "Quark spectral properties above Tc from Dyson-Schwinger equations," Eur. Phys. J. C 70, 1037 (2010), arXiv:1009.3762 [hep-ph].

[352] S.-x. Qin and D. H. Rischke, "Quark Spectral Function and Deconfinement at Nonzero Temperature," Phys. Rev. D 88, 056007 (2013), arXiv:1304.6547 [nucl-th].

[353] C. S. Fischer, J. M. Pawlowski, A. Rothkopf, and C. A. Welzbacher, "Bayesian analysis of quark spectral properties from the Dyson-Schwinger equation," Phys. Rev. D98, 014009 (2018), arXiv:1705.03207 [hep-ph].

[354] P. Maris and H. A. Holties, "Determination of the singularities of the Dyson-Schwinger equation for the quark propagator," Int. J. Mod. Phys. A 7, 5369 (1992).

[355] S. J. Stainsby and R. T. Cahill, "IS SPACE-TIME EUCLIDEAN 'INSIDE' HADRONS?" Phys. Lett. A 146, 467 (1990).

[356] M. S. Bhagwat, M. A. Pichowsky, C. D. Roberts, and P. C. Tandy, "Analysis of a quenched lattice QCD dressed quark propagator," Phys. Rev. C 68, 015203 (2003), arXiv:nucl-th/0304003.

[357] R. Alkofer, W. Detmold, C. S. Fischer, and P. Maris, "Analytic properties of the Landau gauge gluon and quark propagators," Phys. Rev. D70, 014014 (2004), arXiv:hep-ph/0309077.

[358] C. S. Fischer, P. Watson, and W. Cassing, "Probing unquenching effects in the gluon polarisation in light mesons," Phys. Rev. D72, 094025 (2005), arXiv:hep-ph/0509213.

[359] C. S. Fischer, D. Nickel, and R. Williams, "On Gribov's supercriticality picture of quark confinement," Eur. Phys. J. C60, 1434 (2008), arXiv:0807.3486 [hep-ph].

[360] A. Krassnigg, "Excited mesons in a Bethe-Salpeter approach," PoS CONFINEMENT8, 075 (2008), arXiv:0812.3073 [nucl-th].

[361] G. Eichmann, *Hadron properties from QCD bound-state equations*, Ph.D. thesis, Karl-Franzens-University Graz (2009), arXiv:0909.0703 [hep-ph].

[362] A. Windisch, "Analytic properties of the quark propagator from an effective infrared interaction model," Phys. Rev. C 95, 045204 (2017), arXiv:1612.06002 [hep-ph].

[363] E. Weil, G. Eichmann, C. S. Fischer, and R. Williams, "Electromagnetic decays of the neutral pion," Phys. Rev. D 96, 014021 (2017), arXiv:1704.06046 [hep-ph].

[364] E. P. Biernat, F. Gross, M. T. Peña, A. Stadler, and S. Leitão, "Quark mass function from a one-gluon-exchange-type interaction in Minkowski space," Phys. Rev. D 98, 114033 (2018), arXiv:1811.01003 [hep-ph].

[365] R. Williams, "Vector mesons as dynamical resonances in the Bethe–Salpeter framework," Phys. Lett. B 798, 134943 (2019), arXiv:1804.11161 [hep-ph].

[366] A. S. Miramontes and H. Sanchis-Alepuz, "On the effect of resonances in the quark-photon vertex," Eur. Phys. J. A 55, 170 (2019), arXiv:1906.06227 [hep-ph].

[367] E. L. Solis, C. S. R. Costa, V. V. Luiz, and G. Krein, "Quark propagator in Minkowski space," Few Body Syst. 60, 49 (2019), arXiv:1905.08710 [hep-ph].

[368] N. Santowsky, G. Eichmann, C. S. Fischer, P. C. Wallbott, and R. Williams, "σ-meson: Four-quark versus two-quark components and decay width in a Bethe-Salpeter approach," Phys. Rev. D 102, 056014 (2020), arXiv:2007.06495 [hep-ph].

[369] A. S. Miramontes, H. Sanchis Alepuz, and R. Alkofer, "Elucidating the effect of intermediate resonances in the quark interaction kernel on the timelike electromagnetic pion form factor," Phys. Rev. D 103, 116006 (2021), arXiv:2102.12541 [hep-ph].

[370] A. F. Falcão and O. Oliveira, "The analytic structure of the Landau gauge quark propagator from Padé analysis," (2022), arXiv:2209.14815 [hep-lat].

[371] R. Oehme, "Analytic structure of amplitudes in gauge theories with confinement," Int. J. Mod. Phys. A 10, 1995 (1995), arXiv:hep-th/9412040.

[372] R. Williams, "The quark-gluon vertex in Landau gauge bound-state studies," Eur. Phys. J. A51, 57 (2015), arXiv:1404.2545 [hep-ph].

[373] M. Mitter, J. M. Pawlowski, and N. Strodthoff, "Chiral symmetry breaking in continuum QCD," Phys.Rev. D91, 054035 (2015), arXiv:1411.7978 [hep-ph].

[374] R. Williams, C. S. Fischer, and W. Heupel, "Light mesons in QCD and unquenching effects from the 3PI effective action," Phys. Rev. D 93, 034026 (2016), arXiv:1512.00455 [hep-ph].

[375] J. S. Ball and T.-W. Chiu, "Analytic Properties of the Vertex Function in Gauge Theories. 1." Phys.Rev. D22, 2542 (1980).

[376] J. S. Ball and T.-W. Chiu, "ANALYTIC PROPERTIES OF THE VERTEX FUNCTION IN GAUGE THEORIES. 2," Phys. Rev. D22, 2550 (1980), three-gluon vertex.

[377] D. C. Curtis and M. R. Pennington, "Truncating the Schwinger-Dyson equations: How multiplicative renormalizability and the Ward identity restrict the three point vertex in QED," Phys. Rev. D 42, 4165 (1990).

[378] A. Aguilar, D. Binosi, D. Ibáñez, and J. Papavassiliou, "New method for determining the quark-gluon vertex," Phys.Rev. D90, 065027 (2014), arXiv:1405.3506 [hep-ph].

[379] A. C. Aguilar, J. C. Cardona, M. N. Ferreira, and J. Papavassiliou, "Quark gap equation with non-abelian Ball-Chiu vertex," Phys. Rev. D 98, 014002 (2018), arXiv:1804.04229 [hep-ph].

[380] C. S. Fischer and R. Alkofer, "Non-perturbative Propagators, Running Coupling and Dynamical Quark Mass of Landau gauge QCD," Phys. Rev. D67, 094020 (2003), arXiv:hep-ph/0301094.

[381] R. Alkofer, C. S. Fischer, F. J. Llanes-Estrada, and K. Schwenzer, "The quark-gluon vertex in Landau gauge QCD: Its role in dynamical chiral symmetry breaking and quark confinement," Annals Phys. 324, 106 (2009), arXiv:0804.3042 [hep-ph].

[382] F. E. Serna, R. C. da Silveira, J. J. Cobos-Martínez, B. El-Bennich, and E. Rojas, "Distribution amplitudes of heavy mesons and quarkonia on the light front," Eur. Phys. J. C 80, 955 (2020), arXiv:2008.09619 [hep-ph].

[383] R. Delbourgo and P. C. West, "A Gauge Covariant Approximation to Quantum Electrodynamics," J. Phys. A 10, 1049 (1977).

[384] J. M. Pawlowski, C. S. Schneider, J. Turnwald, J. M. Urban, and N. Wink, "Yang-Mills glueball masses from spectral reconstruction," (2022), arXiv:2212.01113 [hep-ph].

[385] P. V. Landshoff and O. Nachtmann, "Vacuum Structure and Diffraction Scattering," Z. Phys. C 35, 405 (1987).

[386] A. Donnachie and P. V. Landshoff, "Gluon Condensate and Pomeron Structure," Nucl. Phys. B 311, 509 (1989).

[387] C. Ewerz and O. Nachtmann, "Towards a nonperturbative foundation of the dipole picture. I. Functional methods," Annals Phys. 322, 1635 (2007), arXiv:hep-ph/0404254.

[388] C. Ewerz and O. Nachtmann, "Towards a nonperturbative foundation of the dipole picture. II. High energy limit," Annals Phys. 322, 1670 (2007), arXiv:hep-ph/0604087.

[389] S. Donnachie, H. G. Dosch, O. Nachtmann, and P. Landshoff, *Pomeron physics and QCD*, Vol. 19 (Cambridge University Press, 2004).

[390] G. B. Bopsin, E. G. S. Luna, A. A. Natale, and M. Peláez, "Nonperturbative gluon exchange in pp elastic scattering at TeV energies," (2022), arXiv:2212.04007 [hep-ph].

[391] K. A. Milton and O. P. Solovtsova, "Analytic perturbation theory: A New approach to the analytic continuation of the strong coupling constant alpha-s into the timelike region," Phys. Rev. D 57, 5402 (1998), arXiv:hep-ph/9710316.

[392] A. I. Alekseev, "Strong coupling constant to four loops in the analytic approach to QCD," Few Body Syst. 32, 193 (2003), arXiv:hep-ph/0211339.

[393] A. Athenodorou, D. Binosi, P. Boucaud, F. De Soto, J. Papavassiliou, J. Rodriguez-Quintero, and S. Zafeiropoulos, "On the zero crossing of the three-gluon vertex," Phys. Lett. B 761, 444 (2016), arXiv:1607.01278 [hep-ph].

[394] P. Boucaud, F. De Soto, J. Rodríguez-Quintero, and S. Zafeiropoulos, "Refining the detection of the zero crossing for the three-gluon vertex in symmetric and asymmetric momentum subtraction schemes," Phys. Rev. D 95, 114503 (2017), arXiv:1701.07390 [hep-lat].

[395] M. N. Ferreira and J. Papavassiliou, "Gauge Sector Dynamics in QCD," (2023), arXiv:2301.02314 [hep-ph].

[396] C. Allton *et al.* (RBC, UKQCD), "2+1 flavor domain wall QCD on a (2 fm)*83 lattice: Light meson spectroscopy with L(s) = 16," Phys. Rev. D76, 014504 (2007), arXiv:hep-lat/0701013 [hep-lat].

[397] C. Allton *et al.* (RBC-UKQCD), "Physical Results from 2+1 Flavor Domain Wall QCD and SU(2) Chiral Perturbation Theory," Phys. Rev. D78, 114509 (2008), arXiv:0804.0473 [hep-lat].

[398] R. Arthur *et al.* (RBC, UKQCD), "Domain Wall QCD with Near-Physical Pions," Phys. Rev. D87, 094514 (2013), arXiv:1208.4412 [hep-lat].

[399] T. Blum *et al.* (RBC, UKQCD), "Domain wall QCD with physical quark masses," Phys. Rev. D93, 074505 (2016), arXiv:1411.7017 [hep-lat].

[400] P. A. Boyle, L. Del Debbio, A. JÃ¼ttner, A. Khamseh, F. Sanfilippo, and J. T. Tsang, "The decay constants $\mathbf{f_D}$ and $\mathbf{f_{D_s}}$ in the continuum limit of $\mathbf{N_f = 2 + 1}$ domain wall lattice QCD," JHEP 12, 008 (2017), arXiv:1701.02644 [hep-lat].

[401] Y. Iwasaki, "Renormalization Group Analysis of Lattice Theories and Improved Lattice Action: Two-Dimensional Nonlinear O(N) Sigma Model," Nucl. Phys. B258, 141 (1985).

[402] D. B. Kaplan, "A Method for simulating chiral fermions on the lattice," Phys. Lett. B288, 342 (1992), arXiv:hep-lat/9206013 [hep-lat].

[403] Y. Shamir, "Chiral fermions from lattice boundaries," Nucl. Phys. B406, 90 (1993), arXiv:hep-lat/9303005 [hep-lat].

[404] R. C. Brower, H. Neff, and K. Orginos, "Mobius fermions: Improved domain wall chiral fermions," *Lattice field theory. Proceedings, 22nd International Symposium, Lattice 2004, Batavia, USA, June 21-26, 2004*, Nucl. Phys. Proc. Suppl. 140, 686 (2005), arXiv:hep-lat/0409118 [hep-lat].

[405] A. Sternbeck, K. Maltman, L. von Smekal, A. G. Williams, E. M. Ilgenfritz, and M. Muller-Preussker, "Running alpha(s) from Landau-gauge gluon and ghost correlations," *Proceedings, 25th International Symposium on Lattice field theory (Lattice 2007): Regensburg, Germany, July 30-August 4, 2007*, PoS LATTICE2007, 256 (2007), arXiv:0710.2965 [hep-lat].

[406] P. Boucaud, F. De Soto, J. Leroy, A. Le Yaouanc, J. Micheli, O. Pène, and J. Rodríguez-Quintero, "Ghost-gluon running coupling, power corrections and the determination of Lambda(MS-bar)," Phys.Rev. D79, 014508 (2009), arXiv:0811.2059 [hep-ph].

[407] A. Sternbeck *et al.*, "QCD Lambda parameter from Landau-gauge gluon and ghost correlations," PoS LAT2009, 210 (2009), arXiv:1003.1585.

[408] D. Binosi, C. Mezrag, J. Papavassiliou, C. D. Roberts, and J. Rodriguez-Quintero, "Process-independent strong running coupling," Phys. Rev. D 96, 054026 (2017), arXiv:1612.04835 [nucl-th].

[409] M. Frate, K. Cranmer, S. Kalia, A. Vandenberg-Rodes, and D. Whiteson, "Modeling Smooth Backgrounds and Generic Localized Signals with Gaussian Processes," (2017), arXiv:1709.05681 [physics.data-an].

[410] I. Steinwart, "Support vector machines are universally consistent," Journal of Complexity 18, 768 (2002).

[411] J. Mercer, "Xvi. functions of positive and negative type, and their connection the theory of integral equations," Philosophical transactions of the royal society of London. Series A, containing papers of a mathematical or physical character 209, 415 (1909).

[412] S. Capstick and W. Roberts, "Quark models of baryon masses and decays," Prog. Part. Nucl. Phys. 45, S241 (2000), arXiv:nucl-th/0008028.

[413] E. Klempt and J.-M. Richard, "Baryon spectroscopy," Rev. Mod. Phys. 82, 1095 (2010), arXiv:0901.2055 [hep-ph].

[414] E. Salpeter and H. Bethe, "A Relativistic equation for bound state problems," Phys.Rev. 84, 1232 (1951).

[415] E. E. Salpeter, "Wave Functions in Momentum Space," Phys. Rev. 84, 1226 (1951).

[416] M. Carrington, W.-J. Fu, P. Mikula, and D. Pickering, "Four-point vertices from the 2PI and 4PI effective actions," Phys.Rev. D89, 025013 (2014), arXiv:1310.4352 [hep-ph].

[417] J.-P. Blaizot, J. M. Pawlowski, and U. Reinosa, "Functional renormalization group and 2PI effective action formalism," Annals Phys. 431, 168549 (2021), arXiv:2102.13628 [hep-th].

[418] T. Aoyama *et al.*, "The anomalous magnetic moment of the muon in the Standard Model," Phys. Rept. 887, 1 (2020), arXiv:2006.04822 [hep-ph].

[419] G. Colangelo *et al.*, "Prospects for precise predictions of a_μ in the Standard Model," (2022), arXiv:2203.15810 [hep-ph].

[420] G. Eichmann, "private communication," (2022).

[421] P. Maris and P. C. Tandy, "The Quark photon vertex and the pion charge radius," Phys. Rev. C 61, 045202 (2000), arXiv:nucl-th/9910033.

[422] P. Maris and P. C. Tandy, "Bethe-Salpeter study of vector meson masses and decay constants," Phys. Rev. C60, 055214 (1999), arXiv:nucl-th/9905056.

[423] J. Berges, "Introduction to nonequilibrium quantum field theory," AIP Conf. Proc. 739, 3 (2005), arXiv:hep-ph/0409233.

[424] M. Luzum and P. Romatschke, "Conformal Relativistic Viscous Hydrodynamics: Applications to RHIC results at s(NN)**(1/2) = 200-GeV," Phys. Rev. C 78, 034915 (2008), [Erratum: Phys.Rev.C 79, 039903 (2009)], arXiv:0804.4015 [nucl-th].

[425] D. A. Teaney, "Viscous Hydrodynamics and the Quark Gluon Plasma," in *Quark-gluon plasma 4*, edited by R. C. Hwa and X.-N. Wang (2010) pp. 207–266, arXiv:0905.2433 [nucl-th].

[426] C. Gale, S. Jeon, and B. Schenke, "Hydrodynamic Modeling of Heavy-Ion Collisions," Int. J. Mod. Phys. A28, 1340011 (2013), arXiv:1301.5893 [nucl-th].

[427] R. Derradi de Souza, T. Koide, and T. Kodama, "Hydrodynamic Approaches in Relativistic Heavy Ion Reactions," Prog. Part. Nucl. Phys. 86, 35 (2016), arXiv:1506.03863 [nucl-th].

[428] A. Dubla, S. Masciocchi, J. M. Pawlowski, B. Schenke, C. Shen, and J. Stachel, "Towards QCD-assisted hydrodynamics for heavy-ion collision phenomenology," Nucl. Phys. A 979, 251 (2018), arXiv:1805.02985 [nucl-th].

[429] R. Kubo, "Statistical mechanical theory of irreversible processes. 1. General theory and simple applications in magnetic and conduction problems," J. Phys. Soc. Jap. 12, 570 (1957).

[430] K. H. Ackermann *et al.* (STAR), "Elliptic flow in Au + Au collisions at (S(NN))**(1/2) = 130 GeV," Phys. Rev. Lett. 86, 402 (2001), arXiv:nucl-ex/0009011.

[431] S. S. Adler *et al.* (PHENIX), "Elliptic flow of identified hadrons in Au+Au collisions at s(NN)**(1/2) = 200-GeV," Phys. Rev. Lett. 91, 182301 (2003), arXiv:nucl-ex/0305013.

[432] K. Aamodt *et al.* (ALICE), "Higher harmonic anisotropic flow measurements of charged particles in Pb-Pb collisions at $\sqrt{s_{NN}}$=2.76 TeV," Phys. Rev. Lett. 107, 032301 (2011), arXiv:1105.3865 [nucl-ex].

[433] G. Aad *et al.* (ATLAS), "Measurement of event-plane correlations in $\sqrt{s_{NN}} = 2.76$ TeV lead-lead collisions with the ATLAS detector," Phys. Rev. C 90, 024905 (2014), arXiv:1403.0489 [hep-ex].

[434] J. Adam *et al.* (ALICE), "Correlated event-by-event fluctuations of flow harmonics in Pb-Pb collisions at $\sqrt{s_{\rm NN}} = 2.76$ TeV," Phys. Rev. Lett. 117, 182301 (2016), arXiv:1604.07663 [nucl-ex].

[435] D. Everett *et al.* (JETSCAPE), "Multisystem Bayesian constraints on the transport coefficients of QCD matter," Phys. Rev. C 103, 054904 (2021), arXiv:2011.01430 [hep-ph].

[436] P. Kovtun, D. T. Son, and A. O. Starinets, "Viscosity in strongly interacting quantum field theories from black hole physics," Phys. Rev. Lett. 94, 111601 (2005), arXiv:hep-th/0405231 [hep-th].

[437] H. B. Meyer, "A Calculation of the shear viscosity in SU(3) gluodynamics," Phys.Rev. D76, 101701 (2007), arXiv:0704.1801 [hep-lat].

[438] Astrakhantsev, N.Yu., Braguta, V.V., and Kotov, A.Yu., "Temperature dependence of shear viscosity of su(3)-gluodynamics within lattice simulation," EPJ Web Conf. 164, 07046 (2017).

[439] S. Borsányi, Z. Fodor, M. Giordano, S. D. Katz, A. Pasztor, C. Ratti, A. Schäfer, K. K. Szabo, and B. C. Tóth, "High statistics lattice study of stress tensor correlators in pure $SU(3)$ gauge theory," Phys. Rev. D 98, 014512 (2018), arXiv:1802.07718 [hep-lat].

[440] L. Altenkort, A. M. Eller, A. Francis, O. Kaczmarek, L. Mazur, G. D. Moore, and H.-T. Shu, "Viscosity of pure-glue QCD from the lattice," (2022), arXiv:2211.08230 [hep-lat].

[441] G. D. Moore, "Shear viscosity in QCD and why it's hard to calculate," in *Criticality in QCD and the Hadron Resonance Gas* (2020) arXiv:2010.15704 [hep-ph].

[442] J. S. Schwinger, "Brownian motion of a quantum oscillator," J. Math. Phys. 2, 407 (1961).

[443] L. V. Keldysh, "Diagram technique for nonequilibrium processes," Zh. Eksp. Teor. Fiz. 47, 1515 (1964).

[444] G. Baym and N. D. Mermin, "Determination of thermodynamic green's functions," Journal of Mathematical Physics 2, 232 (1961).

[445] M. Le Bellac, *Thermal field theory* (Cambridge University Press, 2000).

[446] M. Laine and A. Vuorinen, *Basics of Thermal Field Theory*, Vol. 925 (Springer, 2016) arXiv:1701.01554 [hep-ph].

[447] S. Borsanyi, G. Endrodi, Z. Fodor, S. Katz, and K. Szabo, "Precision SU(3) lattice thermodynamics for a large temperature range," JHEP 1207, 056 (2012), arXiv:1204.6184 [hep-lat].

[448] H. Song, S. A. Bass, U. Heinz, T. Hirano, and C. Shen, "200 A GeV Au+Au collisions serve a nearly perfect quark-gluon liquid," Phys. Rev. Lett. 106, 192301 (2011), [Erratum: Phys.Rev.Lett. 109, 139904 (2012)], arXiv:1011.2783 [nucl-th].

[449] G. D. Moore, "Transport coefficients in large N(f) gauge theory: Testing hard thermal loops," JHEP 05, 039 (2001), arXiv:hep-ph/0104121.

[450] D. M. van Egmond, U. Reinosa, J. Serreau, and M. Tissier, "A novel background field approach to the confinement-deconfinement transition," (2021), arXiv:2104.08974 [hep-ph].

[451] U. Ellwanger, "Flow equations and BRS invariance for Yang-Mills theories," Phys. Lett. B335, 364 (1994), arXiv:hep-th/9402077.

[452] U. Ellwanger, M. Hirsch, and A. Weber, "Flow equations for the relevant part of the pure Yang-Mills action," Z.Phys. C69, 687 (1996), arXiv:hep-th/9506019 [hep-th].

[453] C. S. Fischer and H. Gies, "Renormalization flow of Yang-Mills propagators," JHEP 10, 048 (2004), arXiv:hep-ph/0408089.

[454] A. K. Cyrol, M. Mitter, J. M. Pawlowski, and N. Strodthoff, "Non-perturbative finite-temperature Yang-Mills theory," (2017), arXiv:1708.03482 [hep-ph].

[455] E. E. Boos and A. I. Davydychev, "A Method of evaluating massive Feynman integrals," Theor. Math. Phys. 89, 1052 (1991).

[456] V. A. Smirnov, "Evaluating multiloop Feynman integrals by differential equations," PoS LL2014, 018 (2014).

[457] M. Czakon, "Automatized analytic continuation of Mellin-Barnes integrals," Comput. Phys. Commun. 175, 559 (2006), arXiv:hep-ph/0511200.

[458] M. Ochman and T. Riemann, "MBsums - a Mathematica package for the representation of Mellin-Barnes integrals by multiple sums," Acta Phys. Polon. B 46, 2117 (2015), arXiv:1511.01323 [hep-ph].

[459] M. Krasser, "Gaussian processes," .

[460] W. Menke and R. Creel, "Gaussian process regression reviewed in the context of inverse theory," Surveys in Geophysics 42, 473 (2021).

[461] D. Duvenaud, "The kernel cookbook," .

[462] A. C. Aguilar, D. Binosi, and J. Papavassiliou, "Unquenching the gluon propagator with Schwinger-Dyson equations," Phys. Rev. D 86, 014032 (2012), arXiv:1204.3868 [hep-ph].

[463] M. Reuter and C. Wetterich, "Effective average action for gauge theories and exact evolution equations," Nucl. Phys. B 417, 181 (1994).

[464] H. Gies, "Running coupling in Yang-Mills theory: A flow equation study," Phys. Rev. D 66, 025006 (2002), arXiv:hep-th/0202207.

[465] G. V. Dunne and C. Schubert, "Two loop selfdual Euler-Heisenberg Lagrangians. 1. Real part and helicity amplitudes," JHEP 08, 053 (2002), arXiv:hep-th/0205004.

[466] D. F. Litim, "Optimization of the exact renormalization group," Phys. Lett. B 486, 92 (2000), arXiv:hep-th/0005245.

[467] L. Fister and J. M. Pawlowski, "Functional renormalization group in a finite volume," Phys. Rev. D 92, 076009 (2015), arXiv:1504.05166 [hep-ph].

[468] M. Peláez, M. Tissier, and N. Wschebor, "Two-point correlation functions of QCD in the Landau gauge," Phys. Rev. D90, 065031 (2014), arXiv:1407.2005 [hep-th].

[469] J. M. Pawlowski, C. S. Schneider, and N. Wink, "QMeS-Derivation: Mathematica package for the symbolic derivation of functional equations," (2021), arXiv:2102.01410 [hep-ph].